TECHNISCHE UNIVERSITÄT DARMSTADT

Theoretical Screening of 2D Materials as High-Efficiency Catalysts for Energy Conversion and Storage Applications

Theoretisches Screening von 2D-Materialien als hocheffiziente Katalysatoren für Energieumwandlungs- und Speicheranwendungen

Vom 11 Fachbereich Material und Geowissenschaften, Materialwissenschaft, Fachgebiet Theorie Magnetischer Materialien der Technischen Universität Darmstadt

Zur Erlangung des Grades eines Doktors der Naturwissenschaften (Dr.rer.nat.)

Genehmigte Dissertation von Yi Xiao, M. Sc. aus Sichuan, China

Tag der Einreichung: den 04. Oktober 2021

Tag der Prüfung: den 02. Juni 2022

1. Gutachten: Prof. Dr. Hongbin Zhang, Technische Universität Darmstadt

2. Gutachten: Prof. Dr. Karsten Albe, Technische Universität Darmstadt

Darmstadt 2022

Theoretical Screening of 2D Materials as High-Efficiency Catalysts for Energy Conversion and Storage Applications

Accepted doctoral thesis by Yi Xiao

1. Review: Prof. Dr. Hongbin Zhang
2. Review: Prof. Dr. Karsten Albe

Date of submission: 04. 10. 2021
Date of thesis defense: 02. 06. 2022

Darmstadt 2022

Theoretisches Screening von 2D-Materialien als hocheffiziente Katalysatoren für Energieumwandlungs- und Speicheranwendungen
Genehmigte Dissertation von Yi Xiao.

Jahr der Veröffentlichung der Dissertation auf TUprints: 2022
Bitte zitieren Sie dieses Dokument als:
URN: urn:nbn:de:tuda-tuprints-225645
URI: https://tuprints.ulb.tu-darmstadt.de/id/eprint/22564

Erklärung zur Dissertation

Hiermit versichere ich, die vorliegende Dissertation ohne Hilfe Dritter nur mit den angegebenen Quellen und Hilfsmitteln angefertigt zu haben. Alle Stellen, die aus Quellen entnommen wurden, sind als solche kenntlich gemacht. Diese Arbeit hat in gleicher oder ähnlicher Form noch keiner Prüfungsbehörde vorgelegen.

Darmstadt, den den Oktober, 04, 2021.

Yi Xiao

MSc (Yi. Xiao)

“Although were Side in Far Corners of the World,

Having a Good Friend is Akin to Having a Good Neighbor.”

Bo Wang

ABSTRACT

This Ph.D. thesis focuses on the exploration and design of new electrocatalysts; the theoretical screening and establishment of new high-efficiency catalysts for electrochemical reactions on 2D materials is based on extensive research, which provides a new route for designing heterogeneous catalysis and paves the way for the development of better electrochemical energy storage and conversion. Theoretical screening focuses on designing more selective, stable, and catalytically active electrocatalysts at a lower cost and finally replace commonplace catalysts. Achieving this requires sufficient theoretical knowledge of how a catalyst functions and works, including the active sites, reaction mechanisms, and expected products. The ultimate goal is to have a sufficient understanding of the significant influencing factors that determine the performance of a catalyst, which can be evaluated using the binding energy of the intermediates or D band center as descriptors. However, it is challenging to provide detailed information on reaction mechanisms using only experimental techniques. Extensive theoretical screening based on density functional theory (DFT) approaches has been employed to obtain basic guidelines for catalyst design. In this thesis, the electrocatalytic mechanisms of some representative electrochemical reactions are taken as examples to comprehensively analyze the present situation in terms of electrocatalyst technology that is to be used for application in energy storage and conversion devices, such as the oxygen reduction reaction (ORR) in fuel cells, carbon dioxide reduction (CO_2RR) in capturing CO_2, nitrogen reduction (NRR) in nitrogen fixation, and the nitric oxide (NO) reduction of ammonia (NORR) on two-dimensional (2D) materials. Theoretical screening is utilized to summarize the detailed design of the electrocatalyst. The understanding of 2D materials as catalysts for electrochemical catalysis can be broadened from various perspectives. The theoretical screening method guides the further development and discovery of highly efficient and inexpensive electrochemical catalysts, which can help confirm the preferable mechanism path to develop the control step of a reaction system. Achieving efficient catalytic activity for electrochemical reactions in promising future catalysts requires people to focus on highly flexible active sites, sufficient activity, selectivity, and a large species. Here, several great and novel 2D materials are considered as catalysts for electrochemical reduction, including the graphene family, 2D metal-organic framework M_3(2,3,6,7,10,11-hexaiminotriphenylene)$_2$ [$M_3(HITP)_2$], 2D transition metal carbides and carbonitrides (MXenes), and the novel 2D material MBenes that are based on boron analogs of MXenes. Our results suggest that these 2D materials can achieve high activity and selectivity in electrochemical reactions under extensive theoretical screening. The family of a single transition metal atom nitrogen co-coordination (MN_4)-embedded graphene catalyst is known for its excellent activity, selectivity, and high atomic efficiency in the oxygen reduction reaction (ORR), and systematic theoretical research has proved that ORR works along a complete four-electron transfer pathway in acidic conditions, indicating that direct hydrogenation pathways are preferred over the O_2 dissociative mechanism in ORR. Furthermore, 2D metal-organic frameworks $M_3(HITP)_2$ and 2D transition metal carbides (MXenes) have been proven to possess high activity and low overpotentials when used for carbon dioxide electrochemical reduction reactions (CO_2RR). We performed density functional theory (DFT) calculations combined with the theoretical screening method and found that both 2D MOF and MXene materials are promising electrocatalysts for reducing CO_2 to produce C1 hydrocarbons. Finally, 2D Metal Boride (MBenes) catalysts have the significant catalytic potential for the electroreduction of CO_2 to CH_4; MBenes are also great prospects for application in efficient electrocatalysts with high activity and high selectivity for the nitrogen reduction reaction (NRR) and nitric oxide reduction (NORR). 2D MBene catalysts have a low limiting potential, and their high selectivity is particularly desirable. Still, challenges surrounding the inadequate understanding of the catalytic mechanism need to be met if these materials are used commercially. To reduce nitric oxide to ammonia by electrochemical conversion as an efficient approach to solving air pollution, MBene materials are an attractive electroreduction

catalyst with which ammonia can be synthesized from nitric oxide (NO) in a process driven by renewable energy, such as wind and solar power. One promising strategy is the use of the Haber–Bosch process to synthesize ammonia under ambient conditions. Ammonia synthesis depends on the fixation of industrial nitrogen. It is important that the synthesis of chemicals and fertilizers while removing NO to solve air pollution is attractive and challenging in electrocatalysis. Current research generally focuses on these issues separately. However, the direct electrochemical reduction of N_2 to NH_3 is seldom mentioned. We propose a new electrocatalyst, metal boride (MBene), as a promising candidate catalyst for achieving the direct electroreduction of N_2 to NH_3. Therefore, our study evaluates a novel 2D material for use as a high-efficiency metal boride (MBene) electrocatalyst that can fix chemical nitrogen and remove NO, purifying exhaust gas. MBenes are also an effective alternative to the Haber–Bosch process currently used to synthesize ammonia.

Zusammenfassung

Diese Dissertation konzentriert sich auf die Erforschung und Gestaltung neuer Elektrokatalysatoren; das theoretische Screening und die Etablierung neuer hocheffizienter Katalysatoren für elektrochemische Reaktionen auf 2D-Materialien basiert auf umfangreicher Forschungen, die einen neuen Weg für die Gestaltung der heterogenen Katalyse eröffnen und den Weg für die Entwicklung besserer elektrochemischer Energiespeicherung und -umwandlung ebnen. Das theoretische Screening konzentriert sich auf die Entwicklung selektiverer, stabilerer und katalytisch aktiverer Elektrokatalysatoren zu geringeren Kosten, um herkömmliche Katalysatoren zu ersetzen. Um dieses Ziel zu erreichen, ist ein ausreichendes theoretisches Wissen darüber erforderlich, wie ein Katalysator funktioniert und arbeitet, einschließlich der aktiven Stellen, Reaktionsmechanismen und der erwarteten Produkte. Das ultimative Ziel ist ein ausreichendes Verständnis der signifikanten Einflussfaktoren, die die Leistung eines Katalysators bestimmen, die anhand der Bindungsenergie der Zwischenprodukte oder des D-Band-Zentrums als Deskriptoren bewertet werden können. Es ist jedoch äußerst schwierig, allein mit experimentellen Techniken detaillierte Informationen über Reaktionsmechanismen zu erhalten. Ein umfangreiches theoretisches Screening, das auf Ansätzen der Dichtefunktionaltheorie (DFT) basiert, wurde eingesetzt, um grundlegende Richtlinien für das Katalysatordesign zu erhalten. In dieser Arbeit werden die elektrokatalytischen Mechanismen einiger repräsentativer elektrochemischer Reaktionen als Beispiele herangezogen, um die gegenwärtige Situation in Bezug auf die Elektrokatalysatortechnologie umfassend zu analysieren, die für die Anwendung in Energiespeicher- und -umwandlungsgeräten verwendet werden soll, wie z. B. die Sauerstoffreduktionsreaktion (ORR) in Brennstoffzellen, die Kohlendioxidreduktion (CO2RR) bei der Abscheidung von CO2, die Stickstoffreduktion (NRR) bei der Stickstofffixierung und die Stickoxid (NO)-Reduktion von Ammoniak (NORR) auf zweidimensionalen (2D) Materialien. Theoretisches Screening wird genutzt, um das detaillierte Design des Elektrokatalysators zusammenzufassen. Das Verständnis von 2D-Materialien als Katalysatoren für die elektrochemische Katalyse kann aus verschiedenen Perspektiven erweitert werden, und die theoretische Screening-Methode bietet eine Anleitung für die weitere Entwicklung und Entdeckung hocheffizienter und kostengünstiger elektrochemischer Katalysatoren, die dabei helfen kann, den bevorzugten Mechanismuspfad zu bestätigen und den Kontrollschritt eines Reaktionssystems zu entwickeln. Um eine effiziente katalytische Aktivität für elektrochemische Reaktionen in vielversprechenden zukünftigen Katalysatoren zu erreichen, werden hochflexible aktive Stellen, ausreichende Aktivität, Selektivität und eine breite spezifische Oberfläche benötigt. Hier werden mehrere herausragende und neuartige 2D-Materialien als Katalysatoren für die elektrochemische Reduktion betrachtet, darunter die Graphen-Familie, das metallorganische 2D-Gerüst M_3(2,3,6,7,10,11-Hexaiminotriphenylen)$_2$ [$M_3(HITP)_2$], 2D-Übergangsmetallcarbide und -carbonitride (MXene) und das neuartige 2D-Material MBenes, das auf Bor-Analoga von MXenen basiert. Unsere Ergebnisse deuten darauf hin, dass diese 2D-Materialien nach umfangreichen theoretischen Untersuchungen eine hohe Aktivität und Selektivität in elektrochemischen Reaktionen erreichen können. Die Familie der Graphen-Katalysatoren mit einem einzigen Übergangsmetall-Atom und Stickstoff-Koordination (MN_4) ist für ihre ausgezeichnete Aktivität, Selektivität und hohe atomare Effizienz in der Sauerstoff-Reduktionsreaktion (ORR) bekannt. Systematische theoretische Untersuchungen haben bewiesen, dass die ORR unter sauren Bedingungen entlang eines vollständigen Vier-Elektronen-Transfer-Weges funktioniert, was darauf hindeutet, dass direkte Hydrierungswege gegenüber dem dissoziativen O_2-Mechanismus in der ORR bevorzugt werden. Darüber hinaus wurde nachgewiesen, dass 2D metallorganische Gerüste $M_3(HITP)_2$ und 2D Übergangsmetallcarbide (MXene) eine hohe Aktivität und niedrige Überspannungen besitzen, wenn sie für die elektrochemische Kohlendioxid-Reduktionsreaktion (CO_2RR) verwendet werden. Wir haben Dichtefunktionaltheorie (DFT)-Berechnungen in Kombination mit der theoretischen Screening-Methode durchgeführt und festgestellt, dass sowohl 2D-MOF- als

auch MXene-Materialien vielversprechende Elektrokatalysatoren für die Reduktion von CO_2 zur Herstellung von C1-Kohlenwasserstoffen sind. Schließlich haben 2D-Metallborid (MBene)-Katalysatoren ein signifikantes katalytisches Potenzial für die Elektroreduktion von CO_2 zu CH_4; MBene sind auch vielversprechend für die Anwendung in effizienten Elektrokatalysatoren mit hoher Aktivität und hoher Selektivität für die Stickstoffreduktionsreaktion (NRR) und die Stickoxidreduktion (NORR). 2D-MBen-Katalysatoren haben ein niedriges Begrenzungspotenzial und ihre hohe Selektivität ist besonders wünschenswert, aber die Herausforderungen, die mit dem unzureichenden Verständnis des katalytischen Mechanismus verbunden sind, müssen bewältigt werden, wenn diese Materialien auf kommerzieller Basis eingesetzt werden sollen. MBen-Materialien sind ein attraktiver Elektroreduktionskatalysator, mit dem Ammoniak aus Stickstoffoxid (NO) in einem Prozess synthetisiert werden kann, der mit erneuerbaren Ressourcen wie Wind- und Sonnenenergie betrieben wird, um Stickstoffoxid zu Ammoniak zu reduzieren - ein effektiver Ansatz zur Lösung der Nitratverschmutzung. Eine vielversprechende Strategie ist die Nutzung des Haber-Bosch-Prozesses zur Synthese von Ammoniak unter Umgebungsbedingungen. Die Ammoniaksynthese hängt von der Fixierung des industriellen Stickstoffs ab und ist wichtig für die Synthese von Chemikalien und Düngemitteln, während die Entfernung von NO zur Lösung des Problems der Luftverschmutzung attraktiv und eine Herausforderung auf dem Gebiet der Elektrokatalyse ist. Die derzeitige Forschung konzentriert sich in der Regel auf diese Themen getrennt. Die direkte elektrochemische Reduktion von N_2 zu NH_3 wird jedoch nur selten erwähnt, und wir schlagen eine neue Art von Elektrokatalysator, Metallborid (MBene), als vielversprechenden Katalysatorkandidaten für die Erreichung der direkten Elektroreduktion von N_2 zu NH_3 vor. Ziel dieser Forschungsarbeit ist es daher, ein neuartiges 2D-Material für den Einsatz als hocheffizienten Metallborid (MBene)-Elektrokatalysator zu evaluieren, der in der Lage ist, chemischen Stickstoff zu fixieren und NO zu entfernen und somit das Abgas zu reinigen. MBene sind auch eine praktikable Alternative zum Haber-Bosch-Verfahren, das üblicherweise zur Herstellung von Ammoniak verwendet wird.

List of Figures

List of Tables

Content

Introduction

1.1 Motivation (Energy Issues)

The total energy sources of the Earth are constant. While the world in its current state will not change, [1] methods to meet the requirements of human society and economic development for energy and related services and returning to clean, sustainable energy can help solve these energy issues and slow climate change [2] for the sustainable development of the energy demands of future generations. The focus areas for renewable energy sources may include energy security, energy production, energy and economics, and climate change. [3] In these cases, some challenges impede sustainable energy sources, such as climate change and market variations. Sustainable and clean energy sources include solar energy, bioenergy, hydropower, wind, geothermal, and ocean energy. They would become ideal sustainable energy sources. These renewable energy sources can help reduce carbon dioxide gases and could play a significant role in replacing fossil fuels that are important to human social and economic development. Renewable energy must be unlimited and include environmentally friendly goods and services. For example, sustainable energy should ideally be clean green fuel, carbon neutral, energy rich, and energy secure. Renewable energy technologies are defined as the storage and conversion of clean sources. They would optimally utilize these resources and decrease or limit environmental pollution, producing minimum secondary waste and accommodating future economic and social development requirements. Renewable energy technologies offer a rare opportunity to reduce greenhouse gas emissions and mitigate climate change to stop global warming by replacing fossil fuel energy sources. (Figure 1-1a)

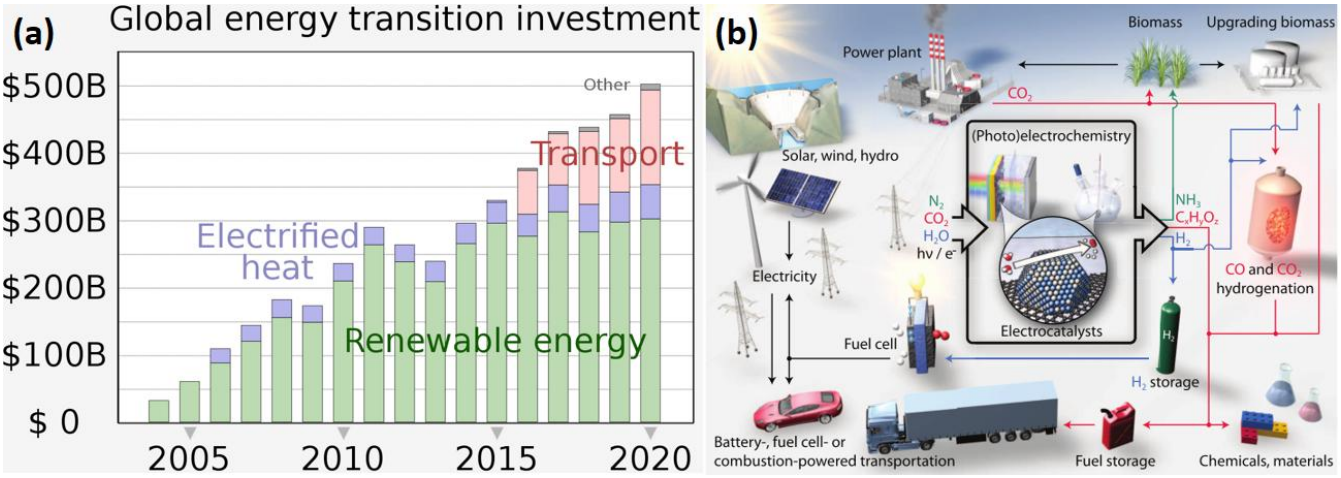

Figure 1-1. (a) Renewable energy commercialization. (Reprinted with authorization from RSC, adopted from [4] (b) Schematic of a sustainable energy landscape based on electrocatalysis. (Reprinted with permission from the American Association for the Advancement of Science, adopted from [5])

Currently, due to population growth and the industrialization of developing countries, the continuous growth in the global energy demand has led to an increase in the consumption of fossil fuels, which may be the most significant problem that humanity is facing in the 21st century. [5] How can we provide adequate clean and safe energy for billions of people in the future? [6] Various renewable energy sources have been considered to solve this problem, including wind, [7] biomass conversion, [8] and geothermal sources, [9] with solar [10] and hydrogen energy [11] considered feasible in terms of producing sustainable energy on a large scale. (Figure 1-1b) Therefore, the concept of using renewable energy has been encouraged due to increasing concerns about climate change, environmental pollution, [12] and the depletion of fossil fuels [13] and nuclear fuels. [14] Many

technological developments have recently been developed to improve the cost-effectiveness of renewable energy, rendering the economic prospects more attractive; these developments have included different means by which energy can be generated, distributed, and utilized. [15] The conversion and storage of energy in electrochemical reactions depend heavily on the development of high-efficiency catalysts, [16] supercapacitors, [17] and fuel cells [18].

1.2 Energy Materials

Energy materials include energy conversion, energy generation, energy utilization and energy storage, as listed in Table 1. Energy generation materials [19] include (1) photovoltaic:nano-optimized cells (such as polymers, dyes, quantum dots, thin-films, and anti-reflective coatings), (2) wind power using multifunctional composite materials for lighter and stronger rotor blades, wear and nanocoating, and (3) fossil fuels that require gas drilling equipment that must avoid wear and corrosion. Energy conversion materials [20] include (1) thermoelectrics: nanostructured compounds (interface design, nanorods) for high-efficiency thermoelectrical power generation and (2) fuel cells: nano-optimized membranes and electrodes for efficient fuel cells. Energy distributions include high-voltage transmission, nanofillers for electrical isolation systems, and soft magnetic nanomaterials for efficient current transformers. Superconductors (SC) [21] include the nanoscale interface design of a high-temperature SC for loss-less power. Energy storage devices [22] involve (1) metal ion batteries (MIBs) based on nanostructured electrodes and ceramic separators, (2) supercapacitors: nanomaterials for electrodes (CNTs, metal oxides) and electrolytes for higher energy density, and (3) hydrogen with nanoporous materials application in hydrogen–oxygen fuel cells. Furthermore, nanoporous foams, thermal insulation, gels for thermal insulation, and bright windows, such as nanostructured materials, are used for electrochromic devices. [23] To date, electrocatalysis provides a sustainable process for future energy conversion and storage technologies for different electrochemical reactions and plays a critical role in resolving environmental pollution.

The U.S. Department of Energy has proposed several technical advancements to develop sustainable energy and reduce carbon dioxide emissions. [24] In this section, we briefly describe the energy materials. We then discuss the literature survey of energy storage and conversion applications, which focuses on predicting materials' performances based on modeling design. An electrochemical catalyst is defined as an electrode material that increases the rate of a particular desired chemical reaction without being consumed itself. The electrocatalytic reaction can occur on the gas/solid or liquid/solid surface or interfaces of materials. Recently, a comprehensive review of advanced energy materials in the energy conversion and storage field has been performed, describing the latest literature on the applications of advanced energy materials, such as metal alloys, oxides, intermetallic borides, and carbide nitrides. and The family of graphene has been reported and had a wide application in the energy field. [25] They have been applied in various energy storage and conversion systems depending on the functional energy materials' development (Figure 1-2a), for example, electrochemical energy storage (battery and supercapacitor) and various catalytic reactions (electrochemical reaction). Substantial synergistic effects and surface sensitivity have been used to gain insight into the reaction mechanism and predict the physics and chemistry of catalysts; these excellent properties benefit catalytic activity during electrochemical energy conversion processes. They promote the investigation of noble metal and noble metal-free electrocatalysts in the oxygen reduction reaction (Fuel cell) as well in the carbon dioxide reduction reaction (CO_2RR), which is helpful for reducing carbon dioxide emissions and the nitrogen reduction reaction (NRR) for nitrogen fixation. Advanced energy materials also demonstrate attractive and promising hydrogen evolution and storage applications, such as for supercapacitors and rechargeable batteries. Advanced energy materials generally possess high activity, selectivity, and stability, [26] which has motivated great efforts toward developing and designing related energy

storage devices. In recent decades, with the extensive application of nanomaterials in batteries and electrochemical reaction systems, they have been included in manytypes of battery and electrochemical energy conversion materials due to their excellent ionic conductivity and large specific surface/interface area due to the nanosize effect. [27] Such properties can help determine the differences between electrocatalytic materials and battery materials. The involved materials include various metal oxides, transition metal dichalcogenides (TMDs), single atoms supported on g-CN or graphene, MXene and MBene, and metal-organic framework compounds.

Table. 1. The application of advanced materials in energy technologies [28]

Energy Generation	Energy Conversion	Energy Distribution	Energy Storage	EnergyUtilization
Photovoltaic:optimizedcells(polymeric, dye,quantum dot, thin film,antireflectivecoating).	**GasTurbines:**heatand corrosionprotectionof turbineblades	**High-Voltage Transmission:**nanofiberfo relectricalisolationsystem. Softmagneticnano-materialsforefficientcurren ttransfomer	**Batteries:**LIBbased on nanostructured electrode,ceramicseparator s.	**Thermal Insulation:**nanoporousfoa mesandgelsfor thermalinsulation
Wind power: nano-compositionforlighterandstronggerrotorb lades,wearand corrosionprotection,nanocoating.	**Thermoelectrlcs:**nanostru cturedcompounds(interface design,nanorods)forefficie ntthermoelectricalpowerge neration.	**Superconductor:**nonoscal einterfacedesignof high temperatureSCforloss-lesspowertransmission	**Supercapacitor:**nano electrode material(CNT,metaloxides) andelectrolytesfor higherenergydensity.	**Smartwindows:**nanostruct ured materialforelectrochromicd evicesand transparentheaters
Fossil fuels:wearandcorrosionprotectionof oil andgasdullingequipment,Nanoparticles.	**FuelCells:**nanooptimized menbranesandelectrodes forefficientfuel cells.	**CNI power lines:**SC basedon CNT.	**Hydrogen:**nanoporousmat erialsforapplicationin microfuel cells.	**Lighting:**efficient lighting system usingLED andOLED.
				Lightweight Construction: construction materials using nano-composites

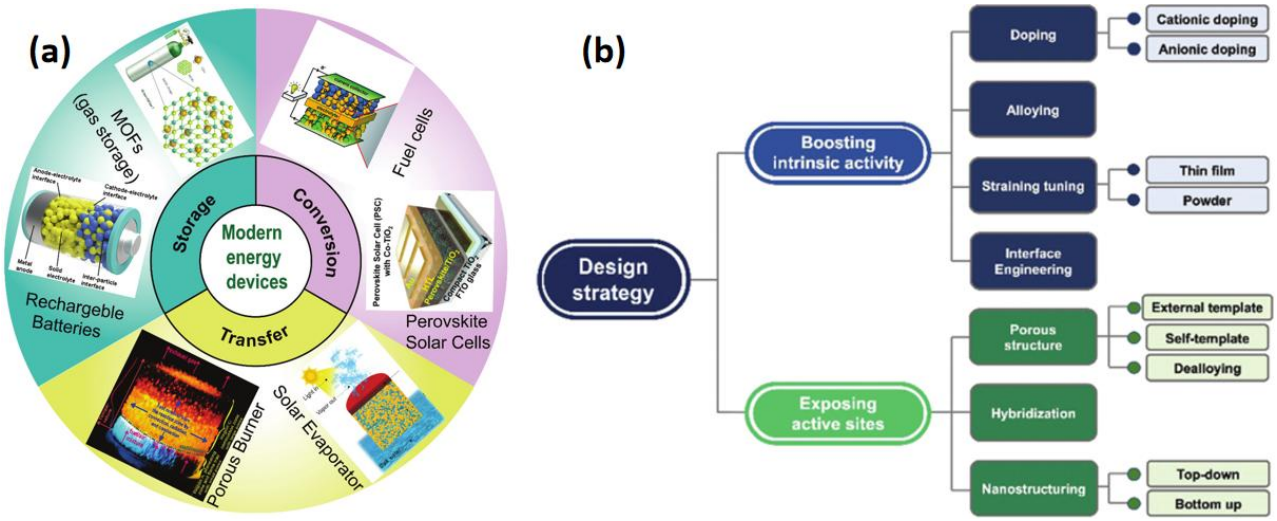

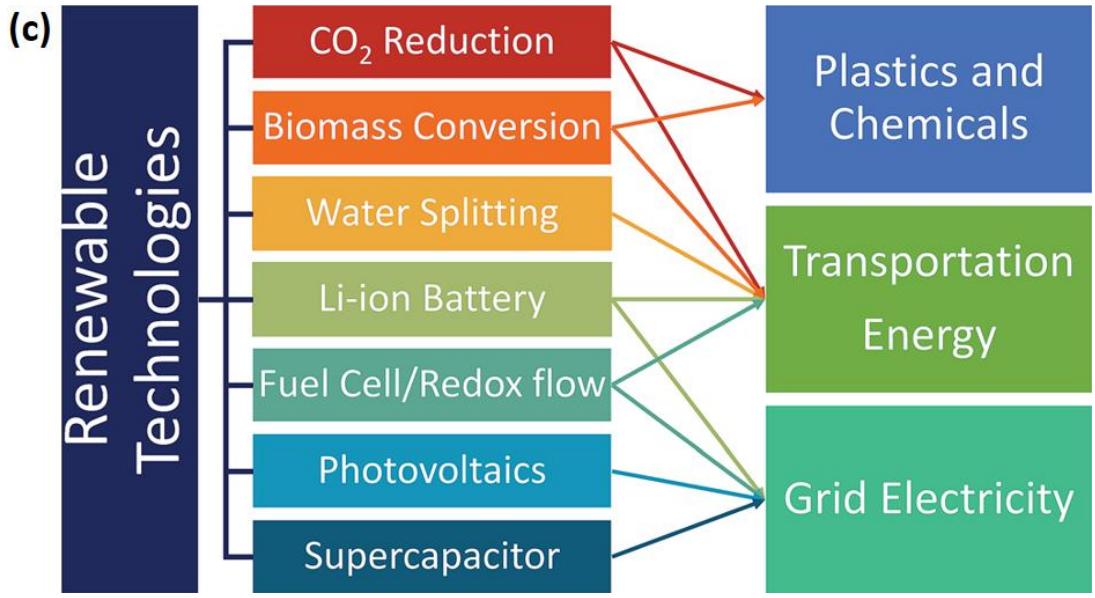

Figure 1-2 (a) Schematics of energy materials for modern energy devices. (Reprinted with permission from the Royal Society of Chemistry, adopted from [29]) (b) Design strategy of the electrocatalyst. (Reprinted with the authorization from the Royal Society of Chemistry, adopted from [30]) (c) Renewable technologies addressing energy issues. (Reprinted with permission from the Royal Society of Chemistry, adopted from [31])

In recent years, many studies have reported on the advantages of metal oxides in many electrochemical applications. For example, the inherent crystalline orderliness in the structural and rich active site and doping defects have been verified to be highly alkali ion diffusion in the lattice with great potential applications in metal ion batteries. The intercalation-type metal oxide (MO) structure can be applied in lithium-ion batteries (LIBs). [32] This type of material could provide a variety of channels for Li-ion intercalation and diffusion, reduce the Li-ion diffusion length, and accommodate the structural evolution during the intercalation and diffusion process. The ab initio molecular dynamics simulations (AIMD) approach has been certified to provide insight into the volume expansion during Li-ion diffusion in the ordered $NiFe_2O_4$ structure. In terms of conversion-type electrode materials, MOs exhibit low activation energy and enhance the reversibility of reactions. As reported for iron oxide (Fe_2O_3), it was applied in lithium-ion storage, as an example of a prototype to elucidate the advantages of MOs. They possess small volume expansion, extra active sites based on defects and chemical modification, and promising ion mobility. These advantages are highly favorable for electrochemical energy storage processes. Furthermore, the synthetic and preparation conditions of MOs are usually under ambient conditions, which is also helpful in tuning the electronic properties to achieve the desired electrochemical behavior. The roles of different prototype MO materials in energy storage applications, which serve as electrode materials in supercapacitors and batteries, and catalysts enhance the efficiency of electrochemical reactions, such as water splitting [33] and those in metal-air batteries [34] and in fuel cells. Due to the high anisotropy and unique crystal structures of transition metal dichalcogenides (TMDs), this type of material can be used in a variety of energy conversion and conversion devices, including those involving photocatalytic water splitting, supercapacitors, rechargeable batteries, and fuel cells, as well as various optoelectronic and electronic applications [35]. Nanotechnology and nanoengineering can tune the morphology, many layers, size, and phase stability. These advantages have made TMDs a hot research topic and provided them as a forward field of study in recent years, aiming to modulate the material properties. Recent reports of their applications in the electrochemical energy field include lithium-ion batteries (LIBs), sodium-ion batteries (SIBs), and pseudocapacitors, [36] as well as in electrocatalytic reactions. TMD materials also possess various physical properties: they can exhibit insulating (e.g., HfS_2), [37] semiconducting (e.g., WS_2 and MoS_2), [38] and metallic (e.g., TiS_2, VS_2, and $NbSe_2$) properties. [39]

Furthermore, the band gaps of TMDs can be tuned by adjusting the number of layers. This type of catalyst usually possesses high activity and selectivity toward the given products and thus has been widely applied in electrocatalytic reactions, such as the hydrogen evolution reaction (HER), oxygen reduction reaction (ORR), CO_2 electroreduction (CO_2RR), and nitrogen reduction reaction (NRR).

Metal-organic frameworks (MOFs), as a new family of energy materials, are quickly growing and arousing great interest among researchers in a wide range of fields. Due to their diversity of organic ligands and metal-containing nodes, more than 20,000 different prototype MOFs were reported by 2013. [40] Their different pore structures and compositions can be achieved by tuning the precursor and synthetic conditions. In addition, MOFs can be synthesized as nanocomposites and nanoparticles with additional experimental conditions and active components. The diversity of the nanostructure and composition can be derived from a variety of tunable functionalities of MOFs. A brief literature survey follows. Férey et al. [41] reported that lithium ions could be inserted into an iron-based MOF, MIL-53(Fe), in 2007, with a specific capacity of 75 $mAhg^{-1}$ based on the Fe^{3+}/Fe^{2+} redox couple. Furthermore, a highly reversible degree can be obtained from metal-organic frameworks (MOFs), as first defined by Yaghi et al. [42] in 1995. A brief introduction of the MOF hybrid micro/nanostructures relates to applications in energy storage and conversion involving lithium-sulfur (Li-S) batteries, lithium-ion batteries (LIBs), metal-oxygen ($M-O_2$) batteries, supercapacitors, and fuel cells. Large tunable pore volumes and porosities can be applied in many fields based on porous materials, including traditional areas, such as magnetism, catalysis, sensors, and proton conduction. Many new energy materials have been successfully synthesized by chemical vapor deposition (CVD). [43] For example, experimental results from Zhang et al. [44] showed that intercalating phosphorus atoms could tune the electrical transport properties of MoS_2. With a chemical characterization approach, [45] the materials structure could be well observed, such as with X-ray diffraction (XRD), high-resolution transmission electron microscopy (HRTEM), and scanning electron microscopy (SEM). The crystal structure information can be obtained from the position of diffraction peaks in the XRD pattern, while HRTEM images can observe the interplanar crystal spacing. (Figure 1-2c)

1.3 2D Materials

2D materials possess unique features compared to other materials, including quantum dots (zero-dimensional, 0D), [46] nanorods or nanowires (one-dimensional, 1D), [47] and networks or bulk (three-dimensional, 3D). Charge carriers [48] are limited by the thickness of 2D materials but can move along the surface, rendering these materials popular and promising candidates for use in condensed matter and electronic devices. Controlling the thickness of 2D nanomaterials allows the precise tuning of their electronic properties, which is impossible to achieve with 0D, 1D, and 3D materials. Furthermore, the thickness of 2D materials can impose both mechanical flexibility and stability, [49] rendering these materials suitable for use in flexible electronic devices. Because a large specific surface area is beneficial for improving surface activity, such materials are helpful for various surface-active applications. 2D materials are particularly sensitive to external stimuli, such as chemical modification, chemical doping, and molecular adsorption. [50] These advantages demonstrate the excellent properties of 2D materials for application in catalysis, [51] electrochemical reactions, [52] energy storage and conversion, [53] optoelectronics, [54] biomedicine, [55] and sensors. [56] 2D nanomaterials have a wide range of possible energy conversion and storage applications based on these unique properties.

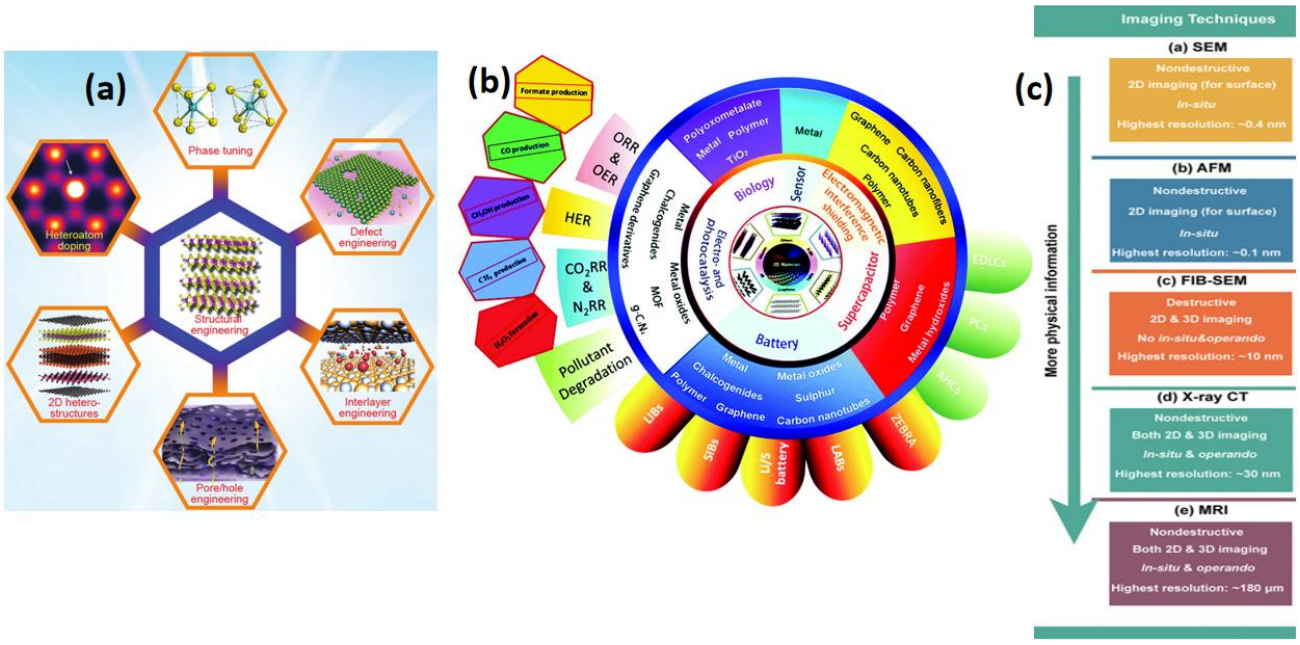

Figure 1-3 (a) Overview of structural engineering strategies for 2D nanomaterials. (Reprinted with permission from Wiley-Blackwell, adopted from [57]) (b) Electrocatalytic applications of 2D materials in energy production. (Reprinted with permission from Royal Society of Chemistry, adopted from [58]) (c) Imaging techniques used to determine more physical information about energy materials. (Reprinted with permission from Elsevier Inc., adopted from [59])

Novel 2D materials have many advantages for electrochemical energy conversion. The large specific surface area on 2D materials can provide various surface-active applications, such as chemical modification, chemical doping, and molecular adsorption. Furthermore, 2D MBene materials can impose both mechanical and flexible stability. They also possess high electrical conductivity due to the high thermal conductivity and promising electron mobility. Thus, the chemical properties of the active sites can be tuned and change the binding mechanism between the active sites and adsorbates. According to previous studies, the metal atoms on the surface can improve their electrocatalytic activity and selectivity properties. Transitional atoms have been widely applied to tune both the electronic structure and chemical properties of MBenes in many electrochemical reactions. In general, three mechanisms have been commonly used in tuning the chemical properties of catalysts. The first is the strain effect, which adjusts the distance through the neighboring metal atoms for the metal ligand effect and changes the electronic structure. The second approach is the chemical modification effect, in which the binding of reaction intermediates results in improved catalytic activity. The last mechanism depends on chemical doping effects that will improve the chemical properties of the active sites. The optimization algorithms applied use high throughput screening and machine learning (ML) [60]. These methods have been widely applied in designing materials and predicting material properties. With the development of a material genomics database, ML has been widely used to further develop electrochemical energy conversion technologies. Meanwhile, the multiscale modeling of electrocatalysis has also played an important role in exploring the electrochemical reaction mechanism and electronic properties to gain insight into the catalytic activity of catalysts.

2D MOF, MXene, and MBene materials, accompanied by their high stability and selectivity, demonstrate interesting behaviors compared to traditional metal catalysts and have recently been introduced as CO_2 electroreduction catalysts. Moreover, the electroreduction of nitrogen (N_2) to ammonia (NH_3) is critical for both agriculture and industry, as NH_3 is an essential source of nitrogen in the fertilizer and chemical industries. However, this process is difficult to realize under ambient conditions owing to the strong, chemically inert N≡N bond. [61] The Haber–Bosch [62] method generally used to produce ammonia is a high temperature and pressure process that is expensive and involves CO_2 gas. The key to solving the challenge of delivering economical and

environmentally sound NRR is the exploration and design of highly efficient catalysts. MBenes are a new type of 2D material that provides new concepts for designing high-efficiency catalysts for the NRR. Finally, NO is a significant pollutant that is produced during the combustion of fossil fuels and leads to many harmful effects via the severe air pollution that is associated with photochemical smog and can lead to severe diseases, such as lung cancer, or environmental problems, such as acid rain, [63] affecting humans, animals, plants, and materials. Therefore, several measures and methods have been developed to reduce NO emissions during combustion. Electrochemical reduction is considered a promising means of reducing NO to yield value-added products, such as NH_3, which is harmless. Thus, a competitive route for the synthesis of ammonia is provided by NORR, and two-dimensional (2D) MBene materials exhibit high selectivity and activity toward the desired products, such as NH_3 and N_2. However, current studies are still mainly focused on conventional metal-based catalysts. In this thesis, our goal is to solve these challenges, including energy storage and conversion in fuel cells, the reduction of CO_2 to hydrocarbon fuels, and the synthesis of ammonia via electrochemical nitrogen fixation, by designing catalysts with surface features (active sites) that can tune the activity and selectivity to these electrochemical reactions.

1.4 Research Objectives (Highlights of 2D Materials for Catalytic Activity Systems)

Furthermore, the burning of fossil fuels leads to environmental pollution due to the emission of exhaust gases, such as CO_2 and nitrogen oxides (NO, NO_2) [64]. The replacement of fossil fuels with other clean and renewable energy sources is becoming increasingly urgent. Based on this, fuel cells have been proposed as promising devices for the stable and efficient storage of energy, and in the exploration and development of more suitable catalysts to replace precious Pt-based electrocatalysts for the ORR, [65] 2D materials have been proposed as promising options for energy storage and conversion technologies because of their unique electronic properties at the atomic scale and their high surface areas, (Figure 1-3b) Furthermore, the greenhouse gas CO_2, which is detrimental to the environment and is emitted in the burning of fossil fuels, can be used to store excess energy in chemical bonds via the electrochemical reduction of CO_2 (CO_2RR), which has been proven effective in reducing excess CO_2 and producing value-added chemical fuels, such as methane and methanol. [66] Catalysts play an essential role in achieving this goal, as they involve many intermediate electrochemical reactions and can convert electrical energy into chemical energy. A catalyst with high catalytic activity and selectivity toward the target products is required to obtain an efficient and stable electrochemical reaction. In this thesis, we focus on electrochemical catalysis relevant to renewable fuel production and the environmental pollution of 2D materials. For example, the conversion of CO_2 into valuable chemical products and the synthesis of ammonia from N_2 focus on insight into material properties and reaction mechanisms during these conversions. Current catalysts exhibit high overpotentials for CO_2 and N_2 electroreduction, which means they have to theoretically require more energy to facilitate the reaction. Thus, it is necessary to explore how electrocatalysts develop stable, more selective, and cheaper novel electrocatalysts. Electrochemical conversions are significant advantages because they only need electricity to run the process under ambient conditions, possibly resulting in a more energy efficient and safer conversion process.

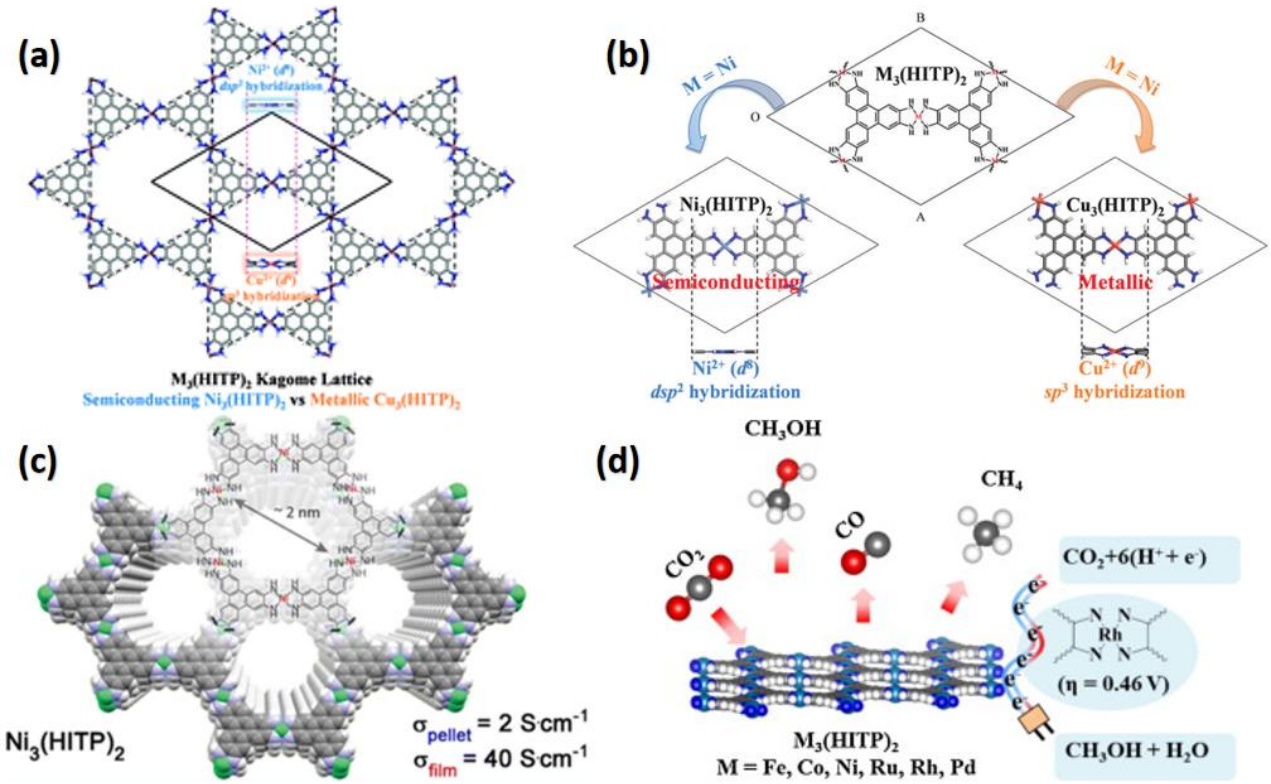

Figure 1-4 (a) A semiconducting metal-organic framework analog metal-organic kagome lattice and (b) crystal model of 2D MOFs $M_3(HITP)_2$ (M=Ni and Cu). [67] (c) A supercell model of $Ni_3(HITP)_2$. (Reprinted with permission from American Chemical Society, adopted from [68]. (d) Metal-organic framework $M_3(HITP)_2$ compound as a highly efficient catalyst for the CO_2RR. (Reprinted with permission from Elsevier, adopted from [69]).

These 2D MOFs could be promising candidates as future excellent heterogeneous electrocatalysts for electrochemical reactions. Due to their high electrical conductivity and high specific surface area making them particularly attractive for use as electrocatalysts, the stacking arrangements of $Ni_3(HITP)_2$ crystals have been analyzed by powder X-ray diffraction (PXRD), and extended X-ray absorption fine structure (EXAFS) experimental techniques have been reported. [68] In this chapter, we describe how MOFs were directly used as carbon dioxide reduction catalysts, and found that CO_2 can be adsorbed onto the active site of the MOF surface; however, these catalysts are generally utilized via physisorption or van der Waals interactions rather than chemisorption, which is caused by the thermodynamically unfavorable nature of CO_2 molecules under ambient conditions. Once CO_2 reacts with the active site on an MOF, CO_2 is hydrogenated by a set of H^+/e^- pairs under an applied potential; this process is known as electrocatalytic reduction. The low heat capacity of MOFs makes them outstanding candidates for carbon reduction; MOF-177 [70] was designed for CO_2 capture and has a low heat capacity of 0.5 J/g K at room temperature. Recently, the experimental synthesis of a new type of 2D metal-organic framework analog, semiconducting M_3(hexaiminotriphenylene)$_2$, has been achieved (Figure 4-4a). According to previous research, Xiao et al. [71] reported that $M_3(HITP)_2$ (where M= Co, Ni, Cu) MOF alloys have continuous electrical conductivity variation attributed to the CO_2RR. Chen et al. [72] found the new types of metal-organic Kagome lattices of $Ni_3(HITP)_2$ and $Cu_3(HITP)_2$ that can be transformed into metals by metal substitution, as shown in Figure 4-4c. This substitution makes excellent changes to the electronic properties of $Ni_3(HITP)_2$. In $Ni_3(HITP)_2$, the Ni atom is a dsp^2 hybridized with organic ligands, leading to perfect 2D conjugation and a distorted 2D $Cu_3(HITP)_2$ sheet. $Cu_3(HITP)_2$ exhibits a metallic character; Cu uses sp^3 hybridization, which is assembled via strong π–π interactions, as shown in Figure 4-4b. Furthermore, these 2D metal-organic frameworks have high thermal stability and catalytic activity. Mao and Xin et al. [73] used a theoretical screening approach to study CO_2 reduction on MN_4 (M=Ti-Cu), where the metal-organic frameworks

depend on a descriptor for the d-band center. It was found that this type of MOF catalyst can be widely used to reduce carbon dioxide, depending on the binding energies of *CO and *OH, which were suggested as descriptors to evaluate the catalytic activity of these materials. Our theoretical study provides a new approach for insights into the electrochemical activity and electronic properties of this type of 2D MOF. In this thesis, we selected the recently synthesized $Ni_3(HITP)_2$ as a model system to explore the physical and chemical characteristics of the $M_3(HITP)_2$ MOF by replacing the coordination metal ions in the MOF 2D sheets. A schematic of the electrochemical reaction mechanism of the CO_2RR on metal-organic framework heterogeneous electrocatalysts is shown in Figure 4-5d.

MXenes are a new type of 2D layered structure that was first synthesized in 2011 [74]. The large specific surface area, stability, excellent hydrophilicity, and conductivity of MXenes have led to these materials receiving significant attention. Many studies have shown that this type of material has broad prospects in electrochemical energy storage. Currently, much attention is focused on the field of catalysis because electrochemical catalysis is promising for the storage and conversion of energy for use in future clean energy technologies, including the hydrogen evolution reaction (HER), carbon dioxide reduction reaction (CO_2RR), nitrogen reduction reaction (NRR) and nitric oxide reduction reaction (NORR). According to the properties mentioned above, MXenes can be employed as catalysts, and it is necessary to summarize and review their application at the atomic scale in electrocatalysis. We underlined the theoretical screening combined with experimental research to explore the most promising candidate catalyst of MXenes to clarify future developments and improvements in this field. MXenes are a family of 2D inorganic materials and are nonmetallic materials consisting of layers of transition metal carbide or nitride structures. Monolayer MXenes can be obtained from a bulk crystal called the MAX phase by HF exfoliation, [75] where M is the transition metal, A is Al or Ga, and X is C or N. 2D MXene layered materials can be derived from the MAX phase via HF etching. Since the first Ti_3C_2 MXene material was synthesized in 2011, [74] this new type of 2D material has attracted widespread attention, and MXenes with different compositions have been rapidly synthesized (Figure 1-5a). The strong interaction between the transition metal and the carbides of 2D MXenes significantly favors the formation of different functional groups during the HF etching process. MXenes can be deduced from three different types of structures obtained from the MAX phases, which have the general formula $M_{n+1}X_n$ (n=1, 2, 3), as shown in Figure 1-5b. MXenes have been given much attention due to their tunable structures and excellent electrochemical properties for various applications. In particular, as some functional groups can terminate the surfaces of MXenes, the terminated MXene chemical formula was defined as $M_{n+1}X_nT_x$, where T represents the functional group, such as O, F, and OH. MXenes have good conductivity and specific surface area with two sides, and based on these conclusions, MXenes have already found applications ranging from energy storage to conversion in electrochemical reactions.

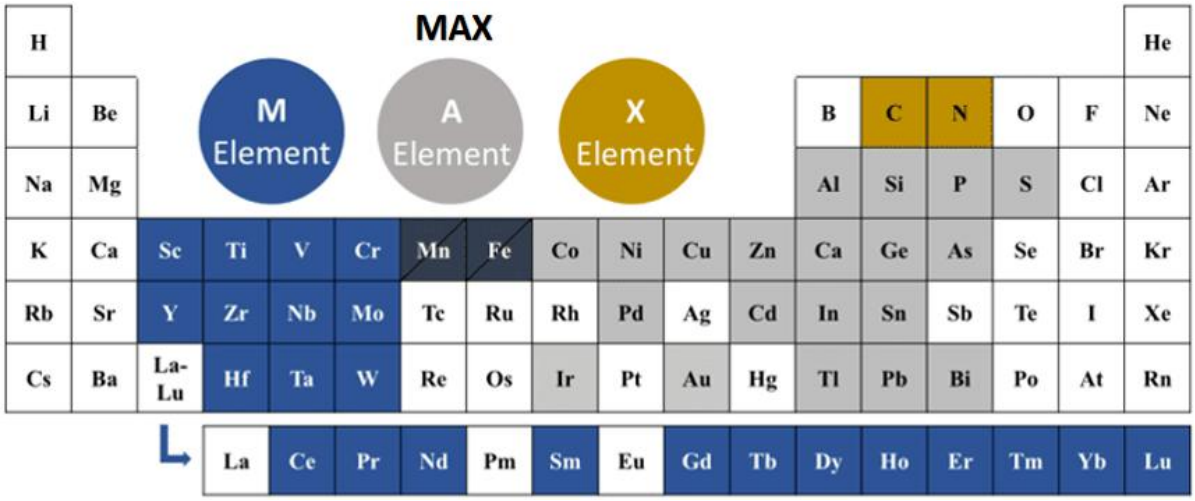

Figure 1-5. Schematic of a periodic table of the elements for the MAX phase compositions (Reprinted with permission from Elsevier, adopted from [76])

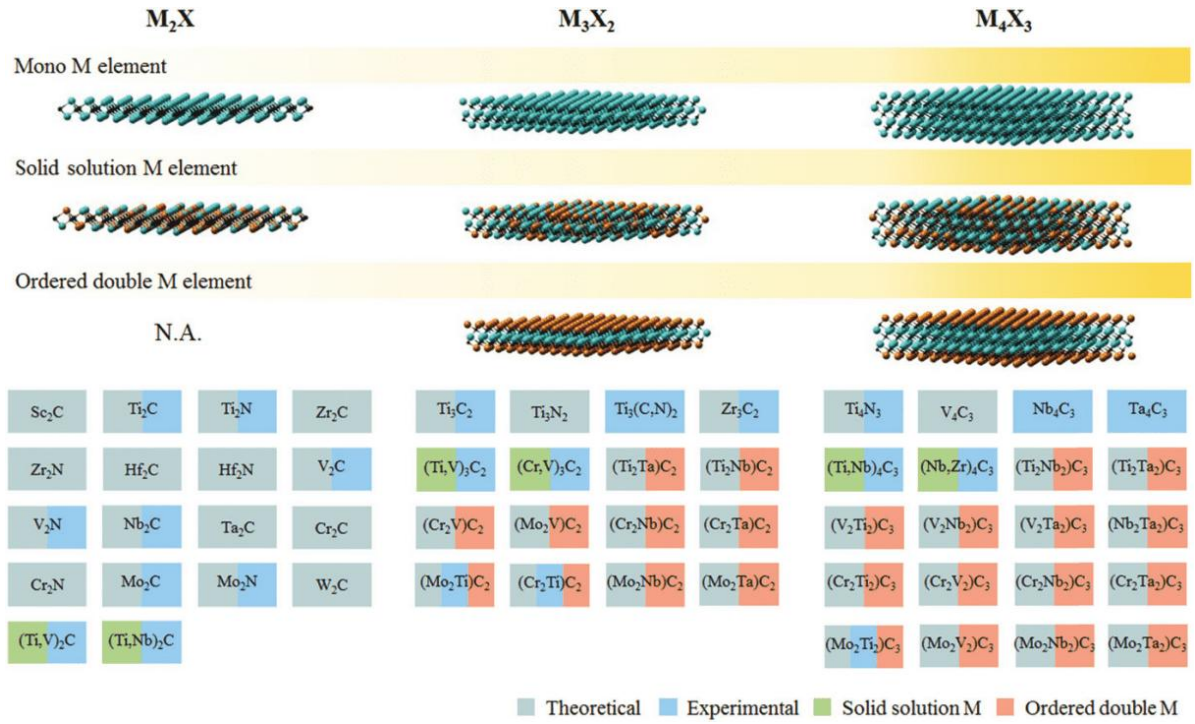

Figure 1-6: 2D transition metal carbide/nitride (MXenes) has been discovered both theoretically and experimentally. (Reprinted with permission from Nature Publishing Group, adopted from [77])

Recently, Handoko et al. [78] established a new linear scaling relationship depending on binding to CO_2RR intermediates, such as *CO and *CHO, and constructed a stability-independent catalytic activity scale on MXene surfaces, indicating that they are suitable as promising electrocatalysts for the electroreduction of CO_2 to CH_4. MXenes, as a new family of 2D metal materials, have also been verified to be highly efficient in catalyzing the CO_2RR via thermodynamics. MXenes are expected to significantly influence the future development and improvement of energy conversion and storage technologies. However, there are still some crucial factors that influence the properties of MXenes, such as problems surrounding the presence of functional groups during the chemical etching process, electron conductivity and interface effects, which require further discussion, and the outstanding electrical conductivity and stability of MXenes, which guarantees the use of these electrocatalysts for the CO_2 reduction reaction (CO_2RR). Overall, the large family of MXenes has various features that serve as an

ideal geometrical configuration used to explore high-efficiency electrocatalysts with broad applicability to CO_2 electrochemical reduction; thus, exploring and screening novel MXene materials and their surface functional group derivative compounds is an urgent challenge for researchers.

Recently, a novel two-dimensional material of transition metal borides (MBene), whose configurations are similar to those of MXene, has been reported both experimentally and theoretically, and MBene monolayers can be achieved by etching A atomic layers (where A is Al or In) from the MAB bulk phases [79]. Mo_2B_2, Ti_2B_2, and Cr_2B_2 MBenes have been synthesized experimentally, and they exhibit metallic behavior. MBenes have diverse structures, such as orthogonal, hexagonal and tetragonal phases with different ratios of metal and boron atoms, producing materials, such as M_2B_2, M_2B, and M_3B_4, as shown in Figure 1-7. Yang et al. [80] reported that the MBenes FeB_2, Ru_2B_4, Os_2B_4, V_3B_4, Nb_3B_4, Ta_3B_4, Cr_2B_2, Mn_2B_2, ZrB, and HfB have outstanding catalytic activity, and their stability was confirmed based on phonon calculations and molecular dynamics simulations. Compared to MXenes, there is no evidence to suggest that functional groups exist on the surfaces of MBenes during the etching process. Because MBenes have novel physical and chemical properties, many potential applications have also been proposed for these materials. For example, Jia and Jun et al. [81] found that monolayer MBenes are suitable as anode materials for lithium-ion and sodium-ion batteries. Guo Z et al. [82] reported that new 2D MBenes could be applied in Li-ion batteries and pointed out that Fe_2B_2 MBene exhibits outstanding activity as a promising electrocatalyst for the HER. Furthermore, Jiang Zhou et al. [83] reported that MnB has a high Curie temperature and is a metallic ferromagnet. MBenes are suitable as efficient catalysts for energy conversion and storage devices because of their outstanding surface and interface roles, such as for the HER, nitrogen fixation (NRR), and the CO_2 reduction reaction (CO_2RR). Thus, Yuan et al. [84] proposed that M_2B_2 MBenes are highly desirable for catalyzing CO_2 electroreduction. In 2017, Sun et al. [85] reported that single-layer and few-layer samples of Mo_2B_2 and Cr_2B_2 MBenes were successfully synthesized, and extensive experimental studies were conducted in 2018, indicating that they are suitable for Li-ion battery electrodes and HER catalysts. In particular, the metal atoms can potentially provide occupied d orbitals to enhance the activation ability of some small molecules, such as N_2 and NO, which is considered essential for the NRR and NORR processes. Even though many MBene structures have been evaluated, the vast MBene composition has yet to be explored.

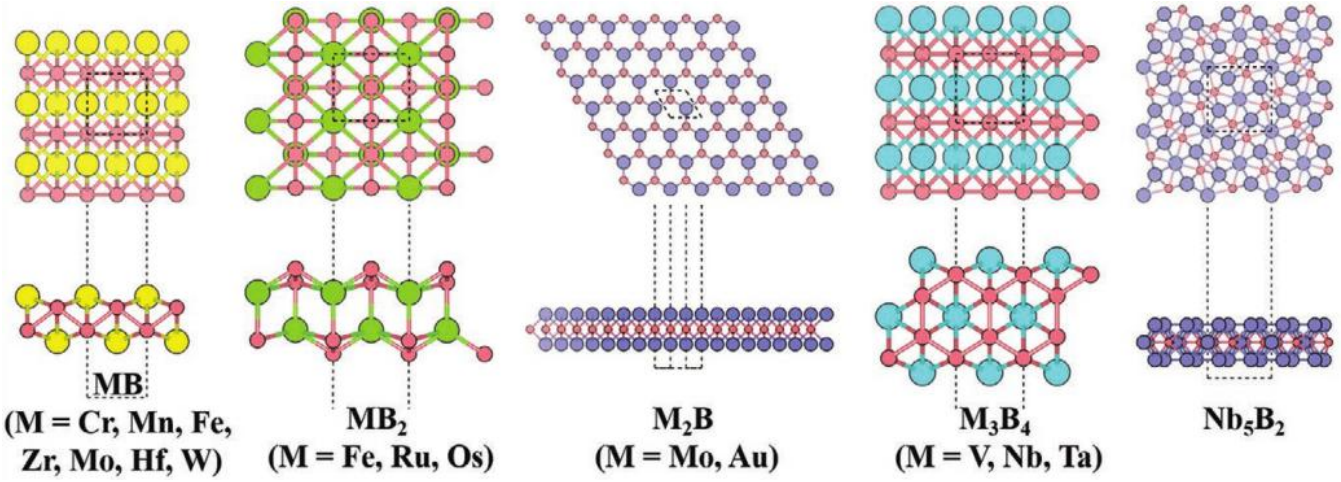

Figure. 1-7 The different MBene structural prototypes that have been reported are listed. (Reprinted with permission from Royal Society of Chemistry, adopted from [98])

To achieve a credible and high-efficiency approach to designing and exploring the optimal reaction mechanism for the electrochemical process, it is essential to identify the surface character of active sites and to

set up suitable and reliable descriptors to evaluate their catalytic properties. Because it is a novel 2D material, the electrochemical properties and possible applications of MBenes require further exploration. Recently, owing to their high catalytic activity and highly competitive hydrogen evolution reaction (HER) side reactions, MBenes, such as Fe_2B_4 and Ru_2B_4, have been widely applied in the CO_2 reduction reaction (CO_2RR) and N_2 fixation (NRR). As boron is a low-abundance nonmetallic element in the Earth's crust, [86], it is primarily used in chemical compounds because of its low valence and high unoccupied p orbitals, leading to significantly improved catalytic efficiency for electrochemical reactions (CO_2RR and NRR). In this regard, to utilize transition metal borides for large-scale applications in electrocatalysis, the large specific surface areas of 2D MBene can provide a variety of active sites and therefore are more preferable than dispersed or doped B-atom catalysts. The electron-deficient feature of boron makes transition metal boride compounds exhibit unsaturated bonding states and provides them with diverse geometrical and electronic properties of MBene materials. Therefore, it is essential to achieve a comprehensive understanding of how to precisely manipulate the catalytic behavior of 2D transition metal borides on exposed surfaces; diverse chemical compositions generated using the formula M_xB_y and x:y ratios set to 1:1, 2:1, 1:2, 3:4, and 5:2 produce well-defined surface structures with both exposed boron and metal sites. These results can provide ideal models for electrochemical reaction mechanism studies for their promising conductivities and large surface areas.

1.5 Screening Principle (Descriptors)

The theoretical screening method based on the density functional theory (DFT) approach was adopted to calculate the desired properties. Theoretical screening involves the development of effective descriptors. Sufficient descriptors can directly describe the stability, activity, and selectivity of materials. Adsorbate binding energy has been applied in the design of catalysts. Binding energy as the primary descriptor was used to gain insight into the intrinsic correlation between the binding energy and activity. A volcano plot was established by using Sabatier's principle. [87] This principle suggests that catalysts interact between adsorbates, and catalysts should neither be too strong nor too weak. As too strong an interaction leads to catalyst poisoning and too weak an interaction may fail to activate the adsorbates, they all will limit the overall reaction rate. Thus, the binding energy is a valid descriptor for catalyst design and discovery. Taking the CO_2RR as an example, the CO_2 reduction reaction is one of the hottest electrocatalytic reactions in this topic. In this reaction, first, the most surface-active site has been identified with the hydrogen adsorption test, and many previous studies suggest that there may be strong intrinsic correlations within the oxygen-bound and carbon-bound species. In this regard, we can successfully correlate the binding energies of the oxygen-bound species E_B[OH] and carbon-bound species to E_B[CO], so the CO and OH binding energies have been used to describe and predict the electrocatalytic activity. [88] Based on this, Xin and coworkers proposed the principle of screening to correlate surface properties with the binding energy. Furthermore, to gain insight into the intrinsic correlation between the adsorption property and structural properties, the electronic properties are used together with machine learning to predict CO and OH binding energies on the catalyst surface, showing that electronegativity, crystal orbital Hamiltonian population (COHP) [89] and d-band center [90] features are critical to describing the CO and OH binding energy. Without DFT calculations, Niu H and coworkers [91] introduced electronegativity (E_{TM}) and the number of TM-d orbital electrons (N_d) as well as adequate coordination numbers for the ORR and OER in TM/g-CN systems, which were not obtained from DFT calculations. These descriptors only relate to material properties. While electronegativity and integrated crystal orbital Hamiltonian population (ICOHP) descriptors have shown good performance in predicting the activity of catalysts, the catalytic activity difference of transition metals is determined by the d-band feature. (Figure 1-8) However, to develop d-band information without DFT calculations, Noh et al. [92]

reported the d-bandwidth of the d-orbital theory and combined it with electronegativity to screen the CO or OH binding energy. This method has suggested several promising catalyst candidates for the CO_2RR.

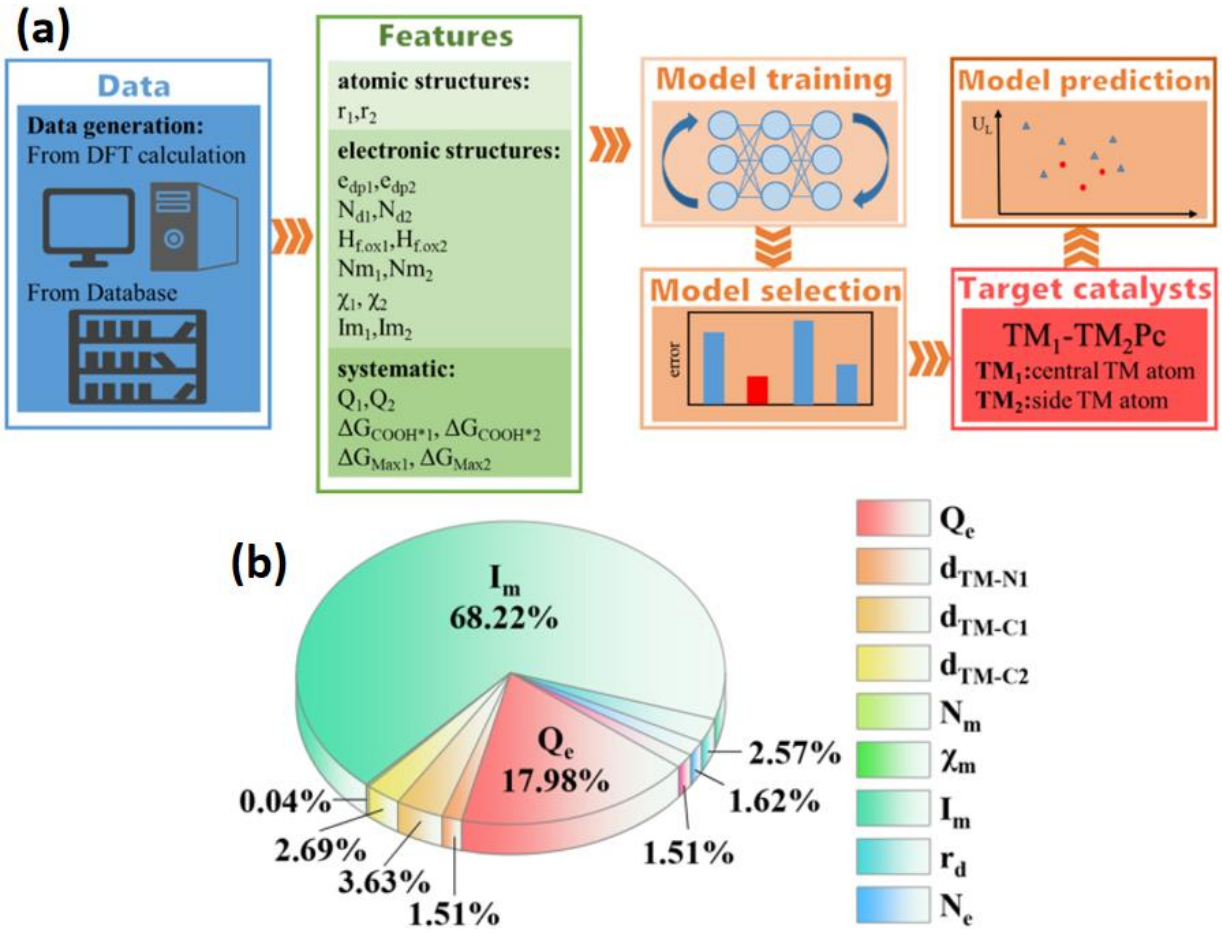

Figure 1-8 (a) Schematic diagrams of the inner procedure of machine learning for catalytic activity prediction. (Reprinted with permission from the American Chemical Society, adopted from [93]) (b) The descriptors of catalytic properties are summarized. (Reprinted with permission from American Chemical Society, adopted from [94])

In the oxygen reduction reaction (ORR), a volcano plot-shaped relationship between the ORR overpotential and ΔG_{*O}, ΔG_{*O} values can serve as a critical descriptor to describe the catalytic activity of the catalyst. Many studies have reported that ΔG_{*O} possesses a linear scaling relationship between ΔG_{*OH} and ΔG_{*OOH}. In addition, because catalytic activity is closely related to the d orbitals of transition metals, by using the d-band center of d states as an activity descriptor for the ORR and the states near the Fermi level (E_F), the states near the Fermi level are mainly contributed by the d electrons of metal atoms. Meanwhile, other electronic structure descriptors induced from the abundance of electronic states near the E_F should be considered. Recently, Huang et al. [95] proposed a weight function to quantify each state's contribution to the bonding properties. Figure 1-8 illustrates that these descriptors are usually selected to describe the intrinsic correlation between materials' electronic and thermochemical properties. These descriptors include the atomic number (Z) and atomic radius (r_d), outer d-electron number (N_d), electronegativity (E_{TM}), ionization energy (I_E), and electron affinity energy (E_A) of TM atoms, which are generated from TM atomic features. In this case, considering these descriptors is beneficial to the underlying correlation between the surface reactivity and the atomic features that can be identified. However, it is challenging to deal with different catalysts generally within only one descriptor, so multiple descriptors have been applied to describe electrocatalytic reactions. More recently, Liu J et al. [96] examined 14 descriptors of the metal-oxygen bond strength depending on the intrinsic ORR activities of 51 perovskites by linear regression models and factor analysis. They confirmed that the number of d electrons and charge-transfer energy play an

essential role in the ORR reactivity of catalysts. Zhang et al. [97] considered the electronegativity of TM and their interaction between N and C atoms coordinated with the active center of single-atom catalysts for the ORR. They proposed a new descriptor to evaluate the activity on TM/g-CN for the ORR, which involved both the electronegativity (E_{TM}) and the number of TM-d orbital electrons (N_d).

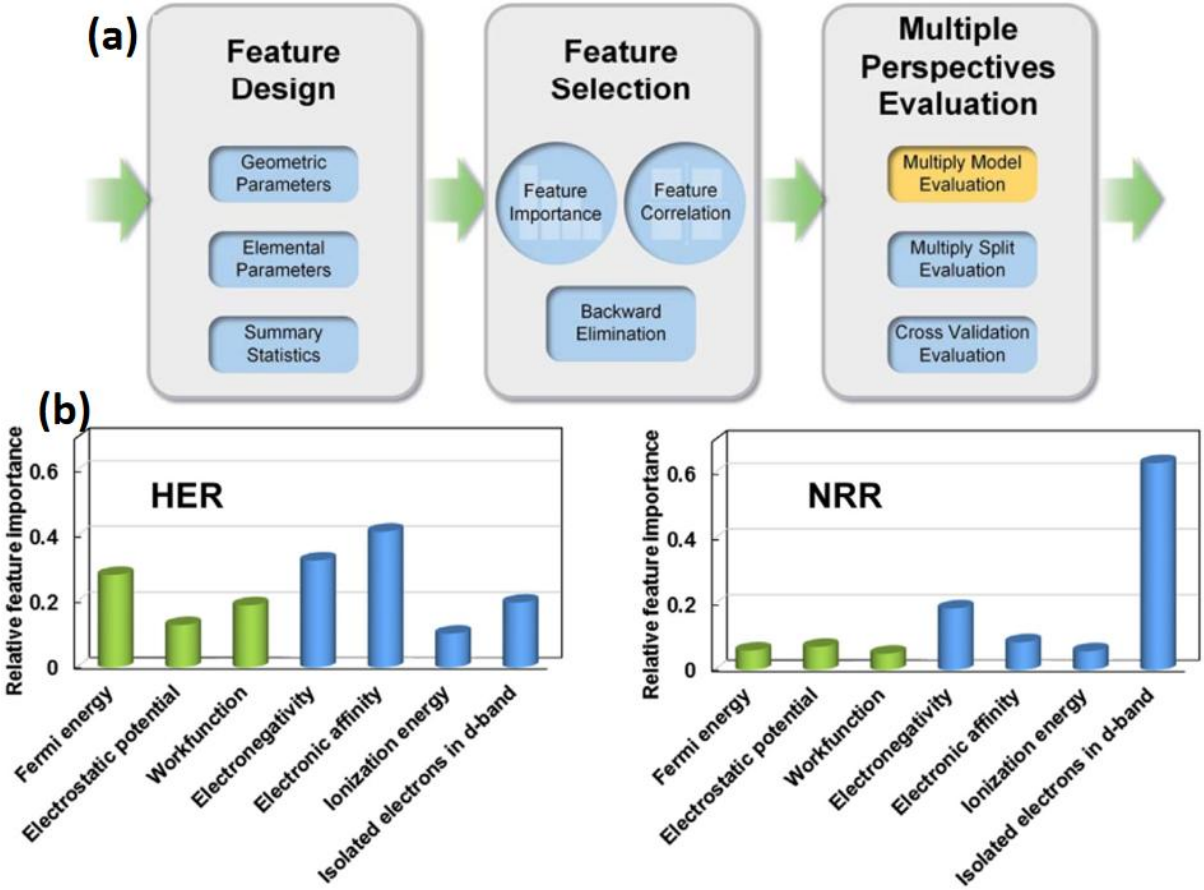

Figure 1-9. (a) Illustration of the machine learning workflow. (b) Relative feature importance for the HER and NRR. (Reprinted with permission from the Royal Society of Chemistry, adopted from [98])

To generate new descriptors to design and screen promising catalysts for the HER, we found reliable descriptors that can be used to predict the catalytic activity for the HER. The ΔG_{*H} and d-band centers are widely used descriptors to evaluate the interaction between adsorbates and catalyst surfaces and have been applied extensively for qualitative evaluation of catalytic activity. In this case, the center of the d-states could provide an excellent way to determine the relationship between material properties and binding energy. Thus, the linear correlation between the d-band center was considered with the coefficient of determination (R^2). The high R^2 suggests that structural property factors beyond the d-band center play a key role in determining ΔG_{*H}. Because the reaction mechanism of the HER is relatively simple, ΔG_{*H} is a very general thermochemical descriptor and works well for many catalysts, including 2D MOF, MXene and MBene materials, and single-atom catalysis, it would be more desirable to examine the mechanism of the HER in future studies. However, it has also been indicated that the charge transfer between the catalyst and adsorbates could also play a crucial role in the catalytic performance of the catalyst. To achieve a good design principle helpful in guiding catalyst exploration, it is essential to identify the feature properties of the active center. The hydrogen binding strength of the intermediate (*H) has been extensively applied to evaluate the catalytic activity of the HER, but there is no universal design principle to describe the intrinsic correlation between the binding energy and structural properties. Therefore, some new types of features have been proposed; the descriptors can be classified as electronic structure features, such as electronegativity (E_f), the first ionization energy of the transition metal (I_e), valence electron number of TM-X (V_{TM}), work

function and the covalent radius of the transition-metal atom (R_{TM}), to establish the intrinsic correlation models. The workflow of machine learning (ML) prediction is based on some input features, including some intrinsic features of electronic properties, such as electrostatic potential, the work function, electronic affinity, electronegativity and ionization energy of the TM atom. These features can be induced directly from databases. To gain insight into how important each feature is used for predicting catalytic activity, Figure 1-9 shows the importance of feature importance in evaluating the catalytic performance of the HER and NRR. The relative importance proportion of features is displayed in Figure 1-9b (Left) for HER and in Figure 1-9b (Right) for NRR. Explicitly, the relative importance of features is different between the HER and NRR. The HER is greatly influenced by the Fermi energy, while the electronic electronegativity and isolated electrons in the d-band features of the TM are more critical than the HER for the NRR. The high feature importance in isolated electrons (N_{ie-d}) in d-bands for NRR is opposite, while the new descriptor of N_{ie-d} indicates a low importance feature for HER. Meanwhile, the different feature importance is beneficial to accommodate the catalytic activity of NRR and HER depending on various features. This result suggests designing an electrochemical catalyst with high activity for NRR but low activity for HER, which could play a crucial role in the selectivity during the NRR process. The high relative feature importance of N_{ie-d} indicates high catalytic activity and further reveals its relation to the electronic structure, a valid descriptor usually covering a wide range of structural and thermochemical properties.

Recently, a high-throughput screening approach based on DFT theory techniques has provided a reliable tool to gain insight into the fundamental understanding of electrochemical reactions. [99] DFT calculations have been used to elucidate reaction mechanisms by identifying the binding strength of the intermediates. A high-throughput screening method that depends on first-principles calculations can be used to design and screen promising materials and gain insight into electrochemical reaction mechanisms due to its low computational cost and high accuracy, which has been widely used to understand electrochemical reactions from the electronic structure from the solution of the Schrodinger equation at the atomic scale within GGA-PBE functional hybrid functionals. This work aims to explore the efficiency of catalysts for electrochemical reactions based on DFT calculations. This plays an important role in the electrocatalytic reaction conversion of water (H_2O), nitrogen (N_2) and carbon dioxide (CO_2) into value-added products, such as NH_3, hydrocarbon fuels, and hydrogen, by utilizing energy from renewable sources, including solar, wind, and biomass energy. The experimental and theoretical investigation combined allows us to explore electrochemical reaction mechanisms and guidelines for developing high-performance electrocatalysts. This thesis aims to address energy shortages and climate change challenges by screening and designing high-performance catalysts with catalytic activity and product selectivity for the four aforementioned electrocatalytic reactions on 2D materials.

1.6 Outline of the Thesis (Comprehensive and Summarizing)

This thesis provides an overview of research electrocatalytic activity systems and will provide insight into the reaction mechanism and address the electrochemical energy conversion of H_2O, CO_2, N_2, and NO into value-added products, such as NH_3, and hydrocarbon fuels, by utilizing sustainable energy from renewable sources, such as solar, wind and biomass energy. With the continuous development of human society, we are facing a series of problems, such as increased energy demands and climate change. Thus, developing sustainable energy could provide an effective way of reducing carbon dioxide emissions. Based on this, electrocatalytic energy conversion plays an integral role in these technologies. It can increase the overall reaction rate, high efficiency, and provide promising selectivity of the given products. However, electrocatalytic reduction reactions (CO_2RR, NRR, and NORR) under acidic aqueous solution conditions are an effective alternative to the Haber−Bosch process. However, electrochemical energy conversion faces many challenges due to both poor reaction kinetics

and increased consumption due to the activation of CO_2 and N_2 molecules. Furthermore, the competitive HER also suppresses the selectivity of electrocatalysts. This is another bottleneck for these electrocatalytic reactions. Thus, developing and designing electrocatalysts with high activity and selectivity for the CO_2RR and NRR are still highly desirable.

To address these significance issues, this doctoral thesis presents six publications in **Chapter 5**, which have all been published in journals; corresponding supplementary information is provided in the online Appendix. The outline of the PhD thesis is organized as follows:

The implementation of the screening on three different structure types of novel two-dimensional (2D) materials has been observed based on DFT calculations, which depended on the investigation of their intrinsic correlation between electrocatalytic activity and material properties, as mentioned in my publications in Chapter 5. The results were combined into a cumulative dissertation, including 6 published papers that were presented in the results and discussions. All the publications are associated with some common keywords, such as 2D materials, electrochemical reactions, DFT calculations, theoretical screening and descriptor. Although they correspond to different catalysts and chemical reactions, they have a common workflow among each publication, and there is a short brief introduction before each publication in **Chapter 4**. It is necessary to note that electrocatalytic activity systems were classified based on different electrochemical reactions on 2D materials that have been adopted in this cumulative dissertation. There are chapters in the main text dedicated to introducing the fundamentals of electrochemical reactions and theoretical background methods, and the specific data generation, data processing and screening techniques are also discussed in each published article.

In Chapter 1, we provide a brief introduction to the background of electrocatalytic energy conversion, our motivation, energy materials, 2D materials for candidate catalysts, research objectives, screening principle (descriptors), and the electrochemical reactions relevant to this thesis.

In Chapter 2, a summary of the theoretical background of density functional theory (DFT) and implementation codes, including VASP and VASPKIT for DFT calculations and Gibbs free energy correction is provided. **Chapter 3** provides a brief introduction on the fundamentals of electrochemical reaction theory and the research methods. It includes the computational hydrogen electrode (CHE) mode, reaction mechanism path, binding energies of the adsorbate, and the d-band model for structural properties. Furthermore, Sabatier's principle was used to predict the catalytic performance of the catalysts.

Chapter 4 describes the electrocatalytic activity systems on different electrocatalytic reactions on some 2D catalytic materials, such as M_2S_2 for the ORR, $M_3(HITP)_2$ MOF and MXenes for the CO_2RR, and MBenes for the CO_2RR, NRR and NORR.

Chapter 5 provides a brief introduction to my publications. It consists of my publications' synopsis and a declaration signed by the doctoral candidate and all coauthors of my publications.

In **Section 5-3-1**, we describe how transition metal sulfide (M_2S_2) monolayers have been investigated as catalysts for the ORR by using the DFT approach, wherein M_2S_2 is considered a promising electrode material for ORR applications in fuel cells. This section topic has been published in *Energy & Fuels*.

In **Section 5-3-2,** we describe the observation that the $M_3(HITP)_2$ prototype of 2D MOF compounds has a high activity for producing C1 hydrocarbon fuels from CO_2 by electroreduction. These results indicate that $Cr_3(HITP)_2$ and $Mn_3(HITP)_2$ were identified to have a high selectivity toward CH_3OH. This section topic has been published in *Electrochimica Acta*. As described in **Section 5-3-3**, M_3C_2 MXenes can serve as efficient catalysts for CO_2 electroreduction to CH_4 hydrocarbon fuels. This section topic has been published in *Nanoscale*.

The topic of **Section 5-3-4** was initially published in the Journal of *Physical Chemistry Letters*, describing a quantum mechanical study for the production of C1 hydrocarbon fuels from CO_2 on 2D MBenes. The study

results provide an effective approach to explore and design high-efficiency electrocatalysts on MBenes for CO_2 reduction to C1 hydrocarbon fuel devices.

In **Section 5-3-5**, a theoretical screening workflow of an efficient catalyst for N_2 reduction to NH_3 on 2D MBenes is presented. This work provides compelling evidence for acting as an NRR electrocatalyst and guidance for the further development and design of high-performance catalysts for some common electrochemical reaction processes. This work has been published in *Chemistry of Materials*.

Section 5-3-6 describes transition-metal borides (MBenes) that can serve as new high-performance electrocatalysts for nitric oxide (NO) reduction to ammonia by DFT calculations. This work is conducive to the development and design of high-performance catalysts for reducing NO emitted from combustion processes and reducing NO to a value-added product (NH_3), facilitating the development of more efficient methods to reduce air pollution. This work has been published in *Small*.

Finally, in **Sections 5-4 and 5-5,** I conclude the thesis's summaries and give an outlook and prospects for my further research based on the already published achievements. The final chapter of the thesis is the list of my publications, acknowledgment, and curriculum vitae. **Chapter 6** provides the bibliography.

2 Fundamentals of Electrochemical Reactions

2.1 Grand Canonical Approach in Heterogeneous Electrocatalysis

The interaction features of solid–liquid interfaces [100] are critical for electrochemical reactions in double-layer systems. Nevertheless, it is a severe challenge that only depends on modeling approaches to reveal such interface interactions at the atomic level, so other tools beyond standard methods should be considered. An atomistic modeling scheme based on quantum mechanical calculations to describe adsorption and chemical reactions assumes that the modeling system is in thermal equilibrium and is under ideal conditions. However, the relevant macroscopic variables in a real experiment involve the temperature, [101] electrode potential, [102] solvent effect and ionization effect [103]. This contribution of variables should also be explicitly included in the double-layer system of the computational model. In this regard, a density functional theory (DFT) framework with fixed ion chemical potentials and electrons under the Grand Canonical ensemble (GC) [104] was developed to simulate electrocatalytic and electrochemical interfaces; it relies on the completely quantum mechanical description of nuclei and electrons in the framework of GC-DFT, including the contribution of DFTs and GC ensembles under the actual experimental conditions, to establish various implicit solvent models based on Poisson-Boltzmann (PB) theory. [105] For a small number of atom systems under the grand-canonical (GC) ensemble, the function $\Omega(\mu, T, V)$ is a general method to deal with a modeling system under fixed electron and ion chemical potentials. [106] Combining the real experimental environment variables with the DFT method and proposing the grand canonical DFT (GC-DFT) approach, it is beneficial to simulate the fixed chemical potentials of ions as performed in an experimental environment. The GC-DFT approach provides a way to study microscopic electrochemical systems via multiscale modeling.

Clearly, the grand canonical DFT (GC-DFT) approach has already provided powerful theoretical merit for modeling practical electrochemical systems [107] and for a specific electrochemical system involving the charge transfer number (N_e). The grand canonical energy Ω includes the $E_{DFT,}$ which can be directly obtained from the DFT calculation, and the electronic potential from fixed electron and ion chemical potentials was evaluated by the following equation:

$$\Omega = E_{DFT} + N_e \mu_e \quad \textbf{(1-1)}$$

where μ_e is the electronic chemical potential when an applied potential (U) is applied to the standard hydrogen electrode (SHE), and the electronic chemical potential is obtained by the equation below:

$$|e|U = -\Phi_{SHE} - \mu_e \quad \textbf{(1-2)}$$

where Φ_{SHE} is defined as the work function of the SHE, which is set to 4.66 eV depending on previous reports. In this case, the Gibbs free energy change (ΔG) of each elementary reaction involves an electron-proton pair transfer, and the chemical potential of an electron-proton pair is expressed as:

$$G(H^+ + e^-) = G(H_2)/2 - |e|U \quad \textbf{(1-3)}$$

Here, ΔG is set to pH=0, electrode potential U=0 V vs. SHE, and at room temperature, T=300 K was generated from the difference in grand canonical energy ΔΩ. Furthermore, the zero-point energy ΔZPE and entropy TΔS are also considered via the following:

$$\Delta G = \Delta\Omega + \Delta ZPE - T\Delta S \quad \textbf{(1-4)}$$

The modeling method was employed to evaluate catalyst performance based on the change in Gibbs free energy (ΔG). Taking the hydrogen evolution reaction (HER) as an example, according to the Sabatier principle for heterogeneous catalysis, optimal activity suggests that depending on the moderate binding energy of a hydrogen atom, $\Delta G_{*H} \approx 0$ eV, a very positive value indicates too weak binding and limits the activation of the hydrogen atom. At the same time, a very negative value indicates binding too strongly so that the hydrogen atom is difficult to desorb from the catalyst surface, the desorption of the intermediate is hindered, and the catalyst is poisoned. To apply the grand-canonical DFT approach to study the competition reaction during electrocatalytic reactions, by comparing the computational hydrogen electrode (CHE) model, we can combine it with the CHE model and grand canonical approach, which is widely used to describe solid–liquid interfaces. Interestingly, the grand-canonical DFT approach can consider the temperature, electrode potential, solvent effect and ion polarization effect. In this approach, the electrode potential and surface charge transfer, which can tune the electrochemical potential, describe the interaction in the double layer via the DFT method, while the solvent, electrolyte, and ion effects are represented by the solution of the linearized Poisson−Boltzmann (PB) equation. In this regard, the grand canonical potential is defined as G(n; U):

$$G(n;U) = F(n) - ne(U_{SHE} - U) \quad \textbf{(1-5)}$$

where G(n;U) represents the grand canonical free energy, which is related to the applied electrode potential U vs. SHE, n is the number of electron transfers, F(n) is the function of total energy depending on the number of electron transfers, and $U_{SHE} = \mu_{e,SHE}/e$ represents the electronic energy vs. the SHE condition, for example, U= 0.1 V corresponds to 0.1 eV/e vs. SHE. Furthermore, the applied potential can tune the Fermi level by changing the occupation or inoccupation of the electronic bands and accommodating the number of electrons by the equation below:

$$\mu_e = \frac{dF(n)}{dn} = e(U_{SHE} - U) \text{ or } \frac{dG(n;U)}{dn} = 0 \quad \textbf{(1-6)}$$

Furthermore, we propose a new descriptor $N_e^{ads,\alpha}$, defined as the absolute surface charge, due to the electrons that were provided from the external potential in a double layer, where eN_e^{ads} is measured depending on the number of electrons in the charge neutral system, $q_\alpha N_\alpha^\alpha$ represents the total charge for ions, and $eN_e^{ads,\alpha}$ is the net electronic surface induced from electrolyte counter charges in the double-layer system. This equation can also be applied to the solvated ionic species (α).

$$N_e^{ads,\alpha} = N_e^{net,\alpha}(:\text{double layer charge}) + \frac{q_\alpha}{e} N_\alpha^\alpha \quad \textbf{(1-7)}$$

$G_{DFT}(\alpha, N_s, N_i, N_e^{ads})$ represents the DFT total energy for surface terminations α, coverages N_i, and $N_e^{ads,\alpha}$ under 0 K conditions. In this regard, the remaining electrons have already been considered to be $\mu_s N_s$ (surface) and $\mu_i N_i$ (interfaces), respectively. This rule can be applied in other electron counting. It allows provides insight into the computational hydrogen electrode (CHE) approach. The chemical potentials of the ions $N_i\mu_i$ in the solid–liquid interfaces should also be evaluated from an experimental or theoretical thermochemical database for an equilibrium electrochemical reaction. For protons, the electrochemical potential is measured under SHE conditions as follows:

$$\frac{1}{2}H_2(g) \leftrightarrow H^+(aq) + e^-(electrode), \quad \textbf{(1-8)}$$

The proton electrochemical potential is expressed by

$$\mu_{SHE}^{ads}(e^-) = -e\cdot\Phi_{SHE}^{ads} = -4.44eV, \quad \textbf{(1-9)}$$

$$\mu_{SHE}^{ads}(H^+@[pH=0]) = \frac{1}{2}\mu[H_2(g)] + 4.44\,eV, \quad \textbf{(1-10)}$$

$$\mu_{SHE}^{ads}[H^+@(pH\neq 0)] = \mu_{SHE}^{ads}[H^+@(pH\neq 0)] - k_B T\ln(10)pH. \quad \textbf{(1-11)}$$

where the energy of gas-phase H_2 can determine $\mu[H_2(g)]$ at 0 K depending on the partition function for an ideal H_2 gas. This is generated from an ideal solution model from Eq. (1-11), where the chemical potential only depends on the contribution of the entropic. Furthermore, the electrochemical solid–liquid interfaces are described by the linearized Poisson-Boltzmann equation implemented in the VASPsol model. [108] In the VASPsol model, the interface is described as a function of the electron density (ρ). The default value of ρ depends on the solvation energies of molecules in a solution, but we did not model it for this thesis due to limitations of computing power.

2.2 Computational hydrogen electrode (CHE) model

The computational hydrogen electrode (CHE) model [109] was proposed by Nørskov et al., which takes the electrochemical oxygen reduction reaction (ORR) on Pt(111) as a reference, leading to significant increase in computational electrocatalytic reactions. Both experiments and theories have proven the feasibility of this method. However, to avoid the complex solvation effect from protons in acidic media, protons and electron pairs couple to gaseous H_2 in equilibrium states at 0 V. From a thermochemical point of view, the CHE model represents a very simple and widely applied electrocatalytic model, and energetic calculations have been performed using the CHE model, which can also be used in thermal corrections and solvent effects. The modeling study of electrochemical processes made significant progress due to applying the CHE approach, which was proposed by Nørskov et al. [110] in 2004. Due to its computational efficiency and conceptual simplicity, the CHE model enabled insights into the reaction mechanism and resulted in a large-scale computational screening investigation. It focused on identifying ideal catalyst materials in electrochemical catalysis. In this case, the CHE model can be applied equally to other electrochemical processes, taking the water-splitting reaction as an example because it is one of the most well-studied chemical reactions in electrocatalysis. In essence, two proton and electron pairs need to be removed from an H_2O molecule and then generate a hydrogen molecule. It includes two half-reactions, namely, water oxidation,

$$H_2O \rightarrow 1/2\,O_2 + 2H^+ + 2e^- \quad \textbf{(2-1)}$$

and hydrogen evolution

$$2H^+ + 2e^- \rightarrow H_2 \quad \textbf{(2-2)}$$

They will react on the anode and cathode of the electrochemical cell. This approach is also feasible for complex electrocatalytic reactions on different catalysts, depending on the assumption of determining reaction pathways based on the energy diagram of each reaction intermediate species. Taking the process of water splitting as an example, such intermediate *OH, *O, and *OOH species formed on the catalyst, and then, this assumed a reaction pathway proceeding through several intermediates, which is determined by the free energy change between different intermediate steps to estimate whether a reaction can continue to its given final state, get stuck along the way or convert to another intermediate products. The contribution of pH to the reaction free energy is defined as the variation in the concentration of protons in the solid–liquid interface. This contribution term is generally calculated from $k_BT \times pH \times \ln 10$ and simply added to the free energy for each intermediate species. Koper [111] suggested that uncoupling the H^+/e^- pair could lead to a more complex free energy dependence on pH. In this case, the pathway commonly employed in the water oxidation half-reaction is as follows:

$$* + H_2O \rightarrow *OH + H^+ + e^- \quad \textbf{(2-3)}$$

$$*OH \rightarrow *O + H^+ + e^- \quad \textbf{(2-4)}$$

$$*O + H_2O \rightarrow *OOH + H^+ + e^- \quad \textbf{(2-5)}$$

$$*OOH \rightarrow * + O_2 + H^+ + e^- \quad \textbf{(2-6)}$$

Therefore, an ideal catalyst should spread the cost across all four steps so that each step requires only 1.23 eV to proceed. The ideal equilibrium potential is set to 1.23 V for each step. However, the electrocatalytic reaction under real conditions is different from the ideal behavior of models, resulting in some steps requiring much more than 1.23 eV, while others require much less. The difference between the required potential and potential is defined as the overpotential, which essentially measures the amount of energy lost due to a suboptimal catalyst. Finally, the CHE model can also be used for the theoretical screening of novel catalyst materials. The CHE model can provide deep insight into the essence of electrochemical reactions. The modeling study assumes that the binding energies on a catalyst surface are related to the structure and different adsorbates, and the Gibbs free energy needed to form an intermediate (ΔG_{rxn}) can be obtained as follows:

$$\Delta G_{rxn} = G_{\text{int}} - G_{slab} - \sum N_i \times \mu_i \quad \textbf{(2-7)}$$

G_{int} is the Gibbs free energy of the intermediate state, and G_{slab} is the Gibbs free energy of a catalyst slab. N_i and μ_i are the numbers and chemical potentials of molecular species (i.e., O_2, CO_2, or N_2 molecules), with the standard hydrogen electrode (SHE) at pH= 7 with the applied potential versus the SHE and the pH of the system:

$$\mu_{H^+} + \mu_{e^-} = \frac{1}{2}\mu_{H_2} - eU_{SHE} - 0.059 \times pH \quad \textbf{(2-8)}$$

In this thesis, we used the CHE model suggested by Nørskov et al. to calculate the binding energies of the intermediates during the electrochemical reaction process. Here, we briefly discuss the standard hydrogen electrode (SHE), similar to the CHE model and used it as a reference electrode for electrochemical reduction. The CHE model is based on the following electrode reaction and is set to zero.

$$H^+ + e^- \rightarrow 1/2\,H_2 \quad \textbf{(2-9)}$$

The standard reduction potential (E^0) is denoted as 0.00 V at T=298.15 K and standard pressure. It is expressed in terms of the chemical potential as follows:

$$\mu_{H+} + \mu_{e-} = 1/2\mu_{H_2(g)} \quad \textbf{(2-10)}$$

When an electrode potential is applied, the chemical potential of an electron-proton pair is added with the term eU as follows:

$$\mu_{H+} + \mu_{e-} = 1/2\mu_{H_2(g)} + eU \quad \textbf{(2-11)}$$

The CHE model assumes that at zero potential and standard conditions (pH = 0, $P(H_2)$ = 1 atm, T=298 K), the electron and proton pairs are in thermodynamic equilibrium with $1/2H_2(g)$, the chemical potential of an electron and proton pair, which is difficult to calculate using the Vienna ab initio simulation package (VASP) [112] under the gas states available. Many common electrochemical reactions, such as the ORR, CO_2RR, NRR, NORR, and competing HER, involve electron-proton pair transfers. Thus, the chemical potential of electrons and proton pairs can be replaced with half the energy of hydrogen in the gas phase, meaning that the binding energies of different adsorbates that involve electron-proton transfer can be calculated directly. Taking the last protonation of the ORR as an example, the reduction of hydroxyl to water occurs at the cathode as the proton migrates through the exchange membrane (PEM) [113] in the fuel cell, as follows:

$$*OH + (H^+ + e^-) \rightarrow H_2O(g) + * \quad \textbf{(2-12)}$$

where * represents the free adsorption sites of the catalyst. Based on the CHE model, the free energy of the reaction can be calculated as follows:

$$\begin{aligned} \Delta G &= G_* + \mu_{H_2O_{(l)}} - G_{*OH} - [\mu(H^+) + \mu(e^-)] \\ &= G_* + \mu_{H_2O_{(l)}} - G_{*OH} - \frac{1}{2}\mu_{H_{2(g)}} \\ &= E^*_{DFT} + E^{H_2O_{(l)}}_{DFT} - E^{*OH}_{DFT} - 1/2E^{H_{2(g)}}_{DFT} + (\Delta ZPE - T\Delta S) \\ &= \Delta E_{DFT} + \Delta ZPE - T\Delta S \end{aligned} \quad \textbf{(2-13)}$$

where μ represents the chemical potential of the H_2 gas molecules, ΔE_{DFT} is the difference in the electronic energies calculated directly using the DFT calculations, ΔZPE is the difference in the zero-point energies calculated from vibrational analyses in the VASPKIT code, [114] and ΔS is the change in entropy under T temperature conditions. Under nonzero electrode potentials, the free energy of the changes involves electron-proton transfer by eU. Furthermore, at nonzero pH values, the difference in the chemical potential of the protons that results from changes in the concentration is

$$\Delta G_{pH} = -k_B T \times In[H^+] = k_B T \times pH \times In10 = 2.303 \times k_B T \times pH \quad \textbf{(2-14)}$$

where ΔG_{pH} is the contribution of the free energy from the concentration variation of $[H^+]$ and k_B is the Boltzmann constant, considering the external electrode potential and pH effects. Taking into account the external electrode potential and pH effects, the Gibbs free energy change of reactions (1-11) was calculated using the following equation:

$$\Delta G = \Delta E_{DFT} + \Delta ZPE - T\Delta S + \Delta G_U + \Delta G_{pH} \quad \textbf{(2-15)}$$

For gas-phase molecules, the entropy correction term can be defined as the sum of the rotational, translational, and vibrational contributions. In contrast, the translational and rotational entropy was not used for the considered adsorbates due to their negligible contributions. Moreover, during these frequency computations, all atoms of the substrate were rigidly constrained so that there were no contributions from additional degrees of freedom. Taking the nitrogen reduction reaction (NRR) as an example, the entropies of gas-phase N_2, H_2, and NH_3 species can be directly obtained from the NIST database. [115] The ΔG between two reaction intermediates involved in the N_2 reduction process can be expressed as follows:

$$*N_{2-m}H_{n-1} + 1/2H_{2(g)} \rightarrow *N_{2-m}H_n \quad \textbf{(2-16)}$$

$$\Delta G = G_{(*N_{2-m}H_n)} - G_{(*N_{2-m}H_{n-1})} - 1/2G(H_2) \quad \textbf{(2-17)}$$

where n (n > 1) is the number of H^+/e^- pairs transferred, while m is the number of NH_3 molecules formed, which equals 0 or 1. For example, the Gibbs free energy change leading to N_2 hydrogenation can be computed when n = 1 and m = 0:

$$* + N_2 + 1/2H_{2(g)} \rightarrow *NNH \quad \textbf{(2-18)}$$

$$\Delta G = G_{*NNH} - G_* - G_{N_2(g)} - 1/2G_{H_{2(g)}} \quad \textbf{(2-19)}$$

Here, * denotes the catalyst that is introduced into the reacting system.

Finally, CHE model studies of electrochemical reactions only depend on limiting potentials obtained from thermodynamic free energy differences. They neglect kinetic barriers between them (activation energy). This might lead to influencing the most favorable reaction pathway that was estimated and may achieve a completely different energy landscape for the reaction. The main reason for the rare consideration of these problems is the computational cost associated with the kinetic calculations required to determine the free energy distribution and the barrier energy of first principles. Recently, several reports of kinetic barrier studies on electrochemical reactions have been put forward, focusing on improvements of the methodologies to effectively analyze standard CHE calculation approaches, such as solvation effects, kinetic barriers and reactive sites. These methodologies are not discussed in this thesis but will be discussed in my future work. However, it is difficult to consider solvation effects due to only calculating the potential of free isolated systems within the CHE model, which overlooks the apparent solvent effects in the energetics of chemical reactions.

2.3 Gibbs Description of Chemical Reactions

The criterion for prediction of reaction spontaneity is based on Gibbs free energy change (ΔG) at constant temperature and pressure. All thermodynamic quantities are constant under standard conditions, whether a process is spontaneous or nonspontaneous. However, ΔG is defined as the energy change during the same process occurring in a reversible reaction if ΔG is equal to zero, and the system is certified at equilibrium conditions, indicating that there will be no net energy change of the overall reaction. What happens when ΔG is not equal to zero? To gain insight into how the sign of ΔG determines the direction of the reaction and predicts spontaneity, the relationship between the entropy and enthalpy change by the system provides the key criterion between the thermodynamic properties of the reaction system. Based on this principle, high exothermic processes ($\Delta H \ll 0$) can increase the disorder of the system and therefore occur spontaneously. Some conclusions for a reaction system are summarized by four laws: when the reaction energy change is less than zero ($\Delta G<0$), the process proceeds spontaneously. When the reaction energy change is equal to zero ($\Delta G=0$), the reaction systems are usually in equilibrium. If $\Delta G>0$, the process is spontaneous in the reverse direction. Calculated values of ΔG^o are helpful in estimating whether a chemical reaction will occur spontaneously or not under standard conditions. However, it cannot confirm whether a specific reaction will occur spontaneously under nonstandard conditions based only on the values of ΔG^o. For example, if the sign of ΔH and TΔS terms for a given reaction is the same, then it may be feasible to reverse by changing the character of ΔG depending on the temperature, converting into a spontaneous reaction. Because the signs of ΔH and TΔS usually do not vary significantly without a phase change, we can directly calculate the values of ΔG° from ΔH° and ΔS° at various temperatures, and no phase transition occurs over the temperature range under consideration for the vaporization of water, as shown in Figure 2-1(a).

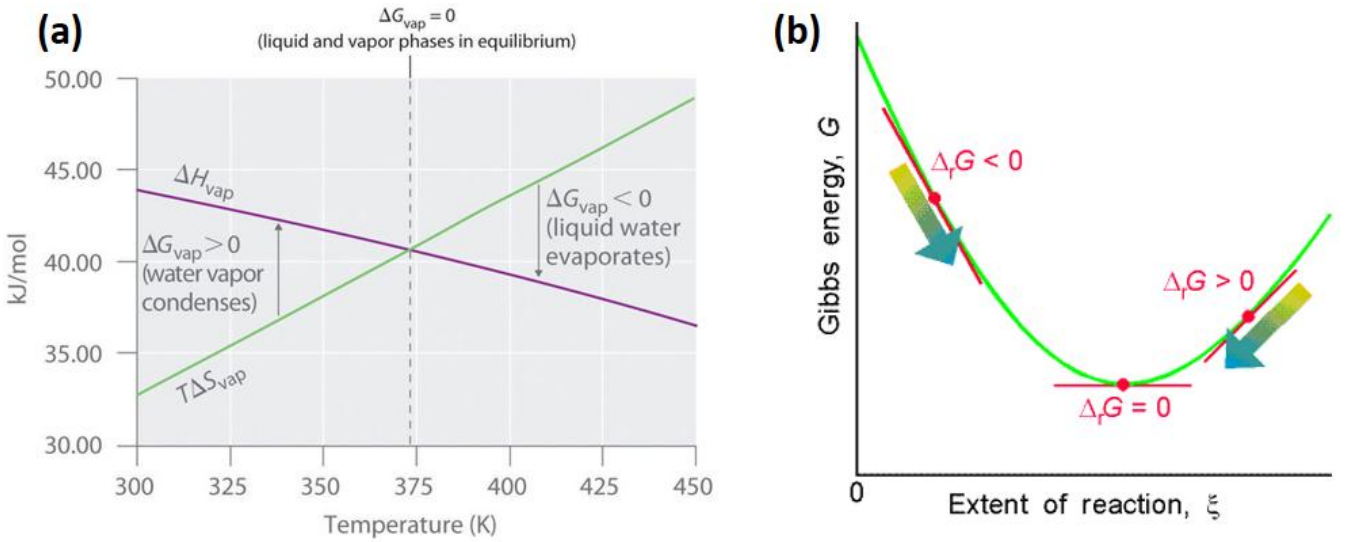

Figure 2-1. (a) Schematic of TΔS and ΔH for the vaporization of water under over-temperature conditions. (Reprinted with permission from [116]) (b) Schematic of the reaction process. (Reprinted with authorization from [117])

The standard ΔG° is defined as the energy change in its standard states. Here, taking $N_2(g)+3H_2(g) \rightleftharpoons 2NH_3(g)$ as an example, the standard entropy change ΔS° is calculated for the reaction between the reactants and the products by using the following rule:

$$\Delta S^0_{rxn} = 2S^0(NH_3) - [S^0(N_2) + 3S^0(H_2)] \quad \textbf{(3-1)}$$

Meanwhile, the standard enthalpy change ΔH° was obtained for the given reaction by using the equation below.

$$\Delta H^0_{rxn} = 2H^0_f(NH_3) - [H^0_f(N_2) + 3H^0_f(H_2)] \quad \textbf{(3-2)}$$

In this reaction, it has a significant influence on the thermodynamic direction of a designated reaction by changing the temperature. The reaction of nitrogen and hydrogen to produce ammonia is spontaneous under standard conditions in theory. However, in practice, it is too slow to be useful industrially due to the sluggishness of the thermodynamics and kinetics of N_2. The formation energies of the standard Gibbs free energy of a reaction can be calculated by using the following rule:

$$\Delta G^0_{rxn} = \sum m\Delta G^0_f(\text{products}) - \sum n\Delta G^0_f(\text{reactants}) \quad \textbf{(3-3)}$$

where m and n represent the stoichiometric coefficients of each product and reactant in the equilibrium chemical reaction. Depending on the second law of thermodynamics, [118] electrochemical reaction systems under ambient conditions have a universal natural tendency to achieve a minimum energy state during the electrochemical process. The change in Gibbs free energy (ΔG) for a chemical reaction in a reversible process can be used to quantitatively measure the favorability of a given reaction under constant pressures and temperatures. In detail, if ΔG presents a positive value in a chemical reaction, it means that sufficient energy has been input to make the reaction possible under constant temperature and pressure. A reaction can only occur when the system's entropy change (ΔS) is either zero or positive. A negative value of ΔG means that the reaction is exothermic. However, if the two chemical reactions are coupled or competing, an endothermic reaction (ΔG > 0) may occur. The energy input of an inherently energy-consuming reaction can be thought of as the coupling of an adverse reaction with a favorable reaction. The entropy variation trend in the entire reaction system is more significant than zero. In this regard, the Gibbs free energy difference associated with the coupled reactions is negative. The description of a given reaction will be more accurate if the limitation in the amount of energy available for nonpressure–volume work is considered.

When the charge in a chemical reaction is passive, a thermodynamic term is produced in the expression equation that is related to the change in the Gibbs free energy, as follows:

$$\partial G = \partial U + P\partial V - T\partial S \quad \textbf{(3-4)}$$

where G and P are the Gibbs energy and pressure, respectively. U and V denote the internal energy and system volume, respectively. S and T describe the entropy and temperature, respectively. The latter term is closely related to the entropy change in chemical reactions and is expressed by the Maxwell relation as follows:

$$(\frac{\partial P}{\partial T})_V = -(\frac{\partial S}{\partial V})_T \quad \textbf{(3-5)}$$

Based on the second law of thermodynamics, the trend in the total Gibbs free energy change is assessed in terms of a closed reaction system as follows:

$$\partial G \leq 0 \quad \textbf{(3-6)}$$

Depending on this criterion, for a closed system that is not in a state of thermodynamic equilibrium, the Gibbs energy will permanently be reduced to achieve equilibrium, which is achieved when the energy of the reaction no longer changes and ΔG tends toward zero. If n moles of electrons are transferred in the reaction, the corresponding charge in the external circuit can be calculated as follows:

$$\Delta Q = -nF \quad \textbf{(3-7)}$$

where n and F are the number of electrons and Faraday constant, respectively. The thermodynamic properties of a given chemical reaction are related to the electron transfer that occurs under ambient conditions (25 °C and 100 kPa), and the standard Gibbs free energy change of formation is expressed as follows:

$$\Delta_f G = \Delta_f^0 G + RT \ln Q_f \quad \textbf{(3-8)}$$

where Q_f is the reaction equilibrium coefficient.

In thermodynamic equilibrium, $\Delta_f G = 0$, and if $Q_f = K$, the equation can be reduced to:

$$\Delta_f G = -RT \ln K_{eq} \quad \textbf{(3-9)}$$

where K_{eq} is the equilibrium constant.

The change in Gibbs free energy (ΔG) is a standard that is often used to measure the scale of a reaction and provides helpful information about the thermodynamic activity to estimate whether a reaction can occur spontaneously under ambient conditions. A simple definition of the standard Gibbs free energy is:

$$\Delta G = G_{Final} - G_{Initial} \quad \textbf{(3-10)}$$

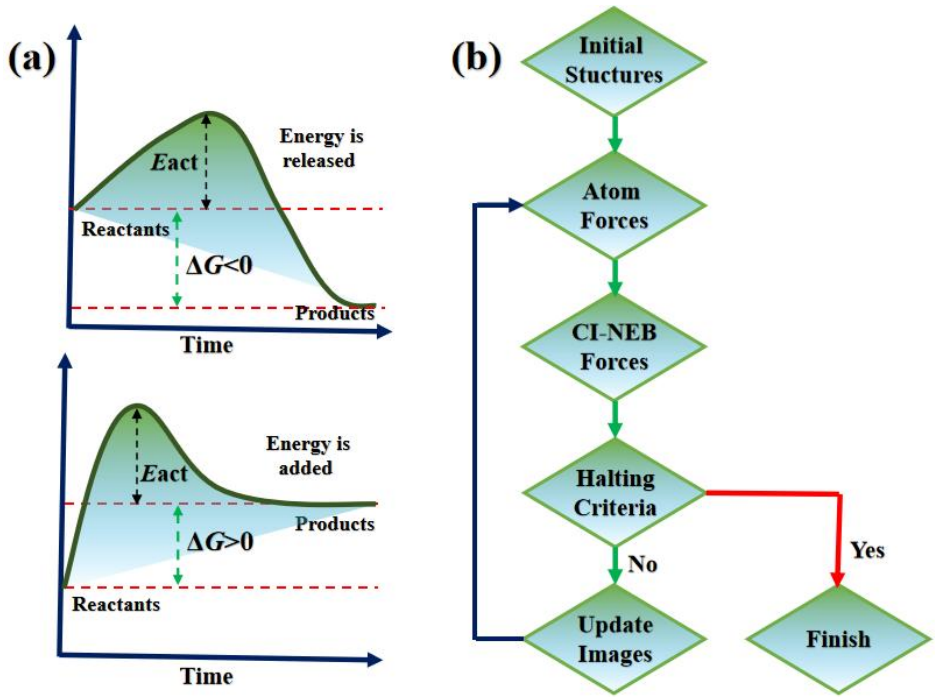

Figure 2-2. (a) Endergonic vs. exergonic reactions and processes. (b) The basic workflow of the CI-NEB technique.

The rate of a chemical reaction depends on the change in energy between the initial and final states. Figure 2-2 shows both exothermic and endothermic reactions, indicating that the thermodynamic trend is only dependent on the initial and final states of a reaction. Furthermore, the activation energy needs to be further considered, which can be achieved by searching for transition states with which the reactive activation of the reaction can be evaluated, followed by the determination of the rate at which the chemical process occurs via the image nudged elastic band (CI-NEB) approach in Figure 2-2b. First, we need to confirm the lattice parameter in the initial and final images and then optimize the first and final images. Second, the intermediate images are set based on the linear interpolation relationship between the initial and final images. Third, the force convergence on the lattice and the energy convergence on the atoms in the intermediate images are calculated until the calculation criteria are met during structural relaxation. Fourth, we calculated the change in the lattice parameters and displacement of atoms based on the CI-NEB forces by using structure optimization. Finally, steps (3)-(4) are repeated until the convergence criteria of relaxation are satisfied.

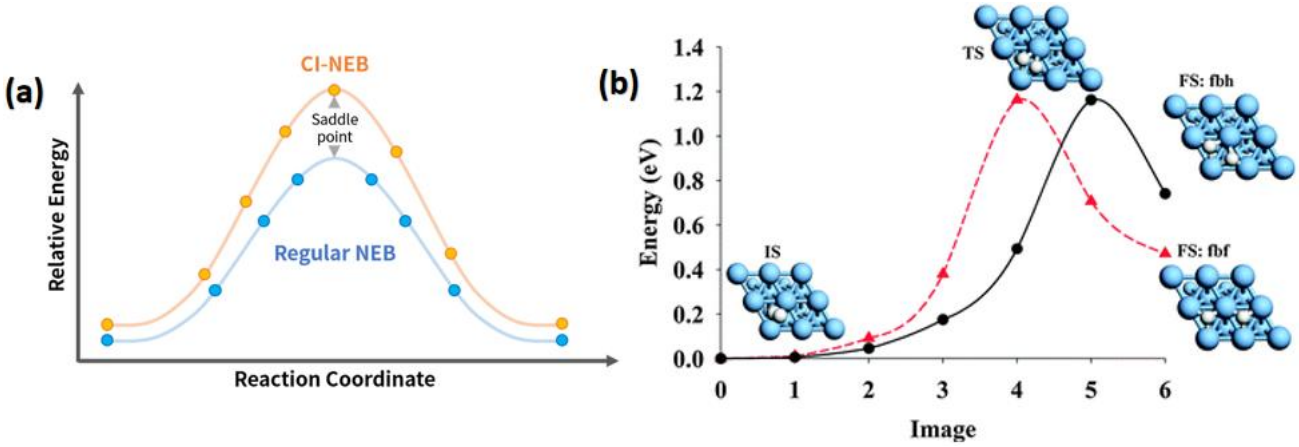

Figure 2-3 (a) Comparison of NEB and CI-NEB. (Reprinted with permission from [119]) (b) The most promising energy path for the diffusion of H_2 on Ag(111) by using CI-NEB. (Reprinted with permission from the Royal Society of Chemistry, adopted from [120])

Another approach can also be used to determine the reaction rate; the transition state (TS) search that is carried out using the climbing CI-NEB is a method that makes the energy at the saddle point the highest energy when determining the reaction path shown in Figure 2-3a. This method effectively confirms the minimum energy path chosen by the saddle point between the reactants and products and depends on optimizing several intermediate configurations along the reaction path to find the lowest energy configuration while maintaining equal distance with neighboring configurations. This constraint optimization is achieved by adding a spring force along with the bands between the intermediate configuration and projecting the force generated by the potential energy in the perpendicular direction to the bands. To summarize, to lower the energy of the transition states and promote the reaction rate, the graph describing this reaction shows an NEB calculation (blue) and a climbing image CI-NEB calculation (red), as presented in Figure 2-3a, which indicates that the CI-NEB energies have been shifted by 0.05 eV so that the two curves are different.

2.4 Rate-Determining Step and Overpotential

The RDS was identified in the previous analysis, and the calculation of the overpotential depends on the limiting potential. However, the most straightforward approach to achieve enhanced reaction rates is to lower the energy of the transition state or find more favorable product and reaction paths, as indicated by the red and black lines in Figure 2-4b. When a thermodynamic reaction step is considered unfavorable, the RDS is called the "thermodynamic bottleneck," or the "kinetic bottleneck." [121] In a simple system, both kinetic and thermodynamic bottlenecks result from the reaction rate, but identifying the thermodynamic bottleneck is a more direct and effective strategy for designing high-performance catalysts. The distinction between thermodynamic and kinetic bottlenecks is also an effective means of understanding the confusion when discussing the RDS in electrochemical processes.

Although predicting the catalytic performance of catalysts is mainly empirical at present, the theoretical screening approach, which depends on density function theory, has gradually become a powerful tool with which the performance of a catalyst can be predicted. For a given chemical reaction, the reaction kinetics are described by the reaction rate constant, which is obtained from the Arrhenius formula as follows:

$$k = Ae^{-\frac{Ea}{RT}} \tag{4-1}$$

where k represents the rate constant (mol.cm^{-2}s^{-1}), R represents the universal gas constant (8.3 J mol^{-1} K^{-1}), and E_a represents the activation energy. Thus, the thermodynamic equilibrium potential of a given redox reaction is an inherent property in all electrochemical reactions, as calculated by Nernst's equation.

$$E_{eq} = E^0 + \frac{RT}{nF}\ln\frac{c_O}{c_R} \tag{4-2}$$

Here, E^0 is the standard equilibrium potential, and C_O and C_R are the oxidation and reduction state concentrations, respectively. However, to efficiently carry out the electrochemical process, a suitable overpotential (η) is required to overcome the kinetic obstacle that provides the energy barrier:

$$\eta = E - E_{eq} \tag{4-3}$$

In this equation, E_{eq} represents the equilibrium potential, and E represents the applied electrode potential. The overpotential can be estimated from the RDS and the current exchange density of the electrochemical reaction, and the fundamental thermodynamic equation can be expressed using the Butler–Volmer equation. [122]

$$j = j_0 = \exp\frac{-a_c nF}{RT}\eta + \exp\frac{a_a nF}{RT}\eta \tag{4-4}$$

Here, j^0 is the current exchange density, α_c is the transfer coefficient at the cathode, and α_a is the transfer coefficient at the anode. Furthermore, an essential descriptor of catalytic activity can be deduced from the calculated Gibbs free energy (ΔG), where for the limiting potential of the RDS with the largest ΔG for the ORR/OER, CO_2RR, NRR, and NORR in consecutive elementary reaction steps, the reaction overpotential is related to the chemical reactions that precede the transfer of the electron and proton pairs, which can be reduced or eliminated with catalysts.

In chemical reactions, the overall rate at which a specific reaction takes is usually determined by the step with the highest energy requirement, known as the rate-determining step (RDS). For a given reaction, it is often possible to simplify the prediction of a corresponding rate equation by using the RDS. Thus, the assumption of a single RDS can significantly streamline the reaction process's basic mathematics and logical analysis. The rate equations associated with mechanisms with a single RDS are usually expressed in a simple mathematical form strongly related to the most favorable reaction path, meaning that the RDS is also evident. The RDS can be identified by predicting each possible reaction path and comparing the different rate results achieved with those obtained via the experiment. The RDS plays a vital role in understanding chemical catalysis. The steps that determine the RDS do not have to correspond to the highest Gibbs energy on the reaction coordinate diagram. Therefore, the RDS has defined a significant energy difference step, which depends on the initial intermediates in the Gibbs free energy diagram. If the reaction intermediate has lower energy than the initial reactants, the activation energy of the transition state (TS) is required to determine and confirm the lower energy intermediate.

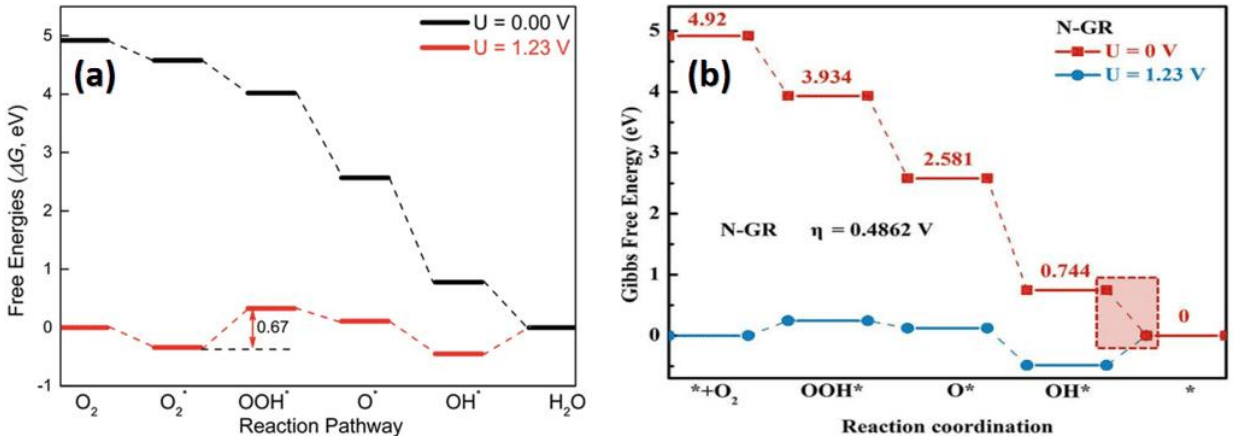

Figure. 2-4 The free energy profile diagram of the ORR. (Reprinted with permission from the Royal Society of Chemistry, adopted from [123]) (a) $Co(acac)_2$ and (b) $Co(acac)_2$/N-doped on graphene. (Reprinted with permission from Frontiers Media S. A, adopted from [124])

Figure 2-4 shows that the energy profile at the zero-electrode potential is marked in black, and the pink line characterizes the limiting potential (U=1.23 V). The figure indicates that the energy profile of all the elementary steps in the ORR catalyzed with $Co(acac)_2$/N-doped graphene under zero potential is downhill. The RDS cannot be confirmed because each step is an exothermic reaction process, and no energy barrier can be observed in the overall reaction. However, some of the ORR elementary reaction steps change to an uphill direction in the energy profile for the equilibrium potential (U = 1.23 V). For example, in Figure 2-4a, the energy associated with reducing $*O_2$ to *OOH and OH* to H_2O is uphill, at 0.67 and 0.45 eV, respectively. Thus, the RDS of the ORR occurs in the second step ($H^+ + e^-$) of the pair transfer ($*O_2 \rightarrow$ *OOH) with an energy barrier of 0.67 eV. The small energy change associated with the RDS means that the ORR process takes place rapidly. The minor energy barrier of the RDS and the fast ORR process is similar to the reaction observed for $Co(acac)_2$ that is supported by N-doped graphene, which also exhibits excellent ORR catalytic performance. The limiting potential of 0.74 eV in the free energy profile of the last hydrogenation step ($*OH \rightarrow *H_2O$) results from the RDS. At the same time,

calculation of the overpotential is based on the limiting potential (U_L) ($\eta = 1.23 - U_L$) of 0.49 V for the ORR and ($\eta = U_L - 1.23$) for the OER in four ($H^+ + e^-$) pair transfer steps. The ORR proceeds through the formation of *OOH from adsorbed $*O_2$, which is then further hydrogenated to O* and OH* by two successive hydrogenation steps and is finally reduced to $*H_2O$.

In contrast, the OER proceeds in the reverse direction. However, to maximize the energy conversion efficiency, an ideal electrochemical catalyst must possess promising thermal kinetics properties. Any additional applied potential beyond the equilibrium potential is described as overpotential. In this case, a lower overpotential can effectively release energy than those at higher overpotentials.

2.5 Scaling Relations Laws

Scaling linear relations is a popular and reliable numerical analysis method used to describe the correlation of material catalytic properties. There are linear relationships between the adsorption energies of related electrochemical reaction intermediates. A linear relationship curve based on adsorption energies has been established, and a linear relationship exists between adsorption energies of the same adsorbates on a similar catalyst structure. [125] Figure 2-5 shows a study of ammonia (NH_3) synthesis on transition metal boride (TMD) materials, suggesting various scaling linear relationships of NH_x species depending on the binding energy as a function of ΔG_{*N}. The catalytic performance was predicted from the binding energies. Furthermore, scaling relationships allow us to predict the adsorption energies of several species on a specific surface based on the adsorption energies of a single species on catalyst surfaces with similar structures. Combining reported experimental data with our own DFT calculations reveals a linear correlation between the adsorption energies of different intermediate species on catalyst surfaces, and a summary of the scaling relation types that have been reported in Table 1. This is an important descriptor of catalytic performance and makes scaling relations a powerful tool for studying electrochemical catalysis. There are some seminal papers on this theory that suggested a formula for the linear relationship between the binding energies of a hydride with the same active central site. The formula of scaling linear relations for the species AH_x (A = C, N, O, or S) is expressed as:

$$E_{ads}(\mathrm{AH_x}) = \gamma E_{ads}(\mathrm{A}) + \zeta \quad \textbf{(5-1)}$$

where γ is the slope, which depends on the valences of A and AH_x. Here, ξ and γ are coefficients of the linear fit to the binding energy data, and γ was calculated by the formula

$$\gamma = \frac{(x_{\max} - x)}{x_{\max}} \quad \textbf{(5-2)}$$

where x_{max} is A-H (here, 4 for C, 3 for N, 2 for O and S). The nitrogen reduction process is shown in Figure 2-5, and γ is the number of bonds in NH_x divided by the total number of bonds that the N atom can form.

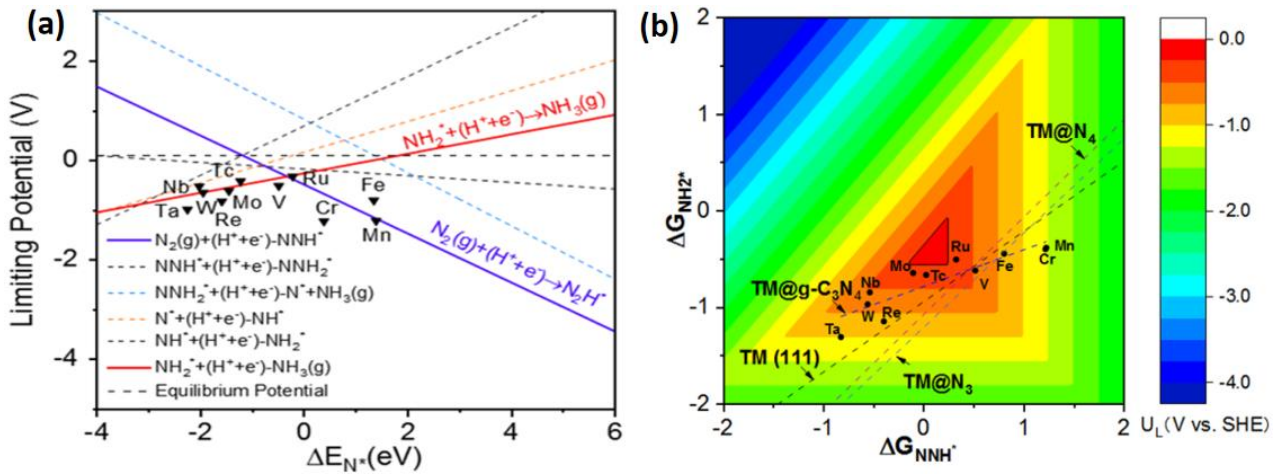

Figure 2-5 (a) The scaling linear relation between different limiting potentials defined as each step as a function of *N (ΔE_{*N}) at 0 V vs. SHE and (b) color-filled contour plots of the limiting potential between *NNH (ΔG_{*NNH}) and *NH_2 (ΔG_{*NH2}). (Reprinted with permission from American Chemical Society, adopted from [126])

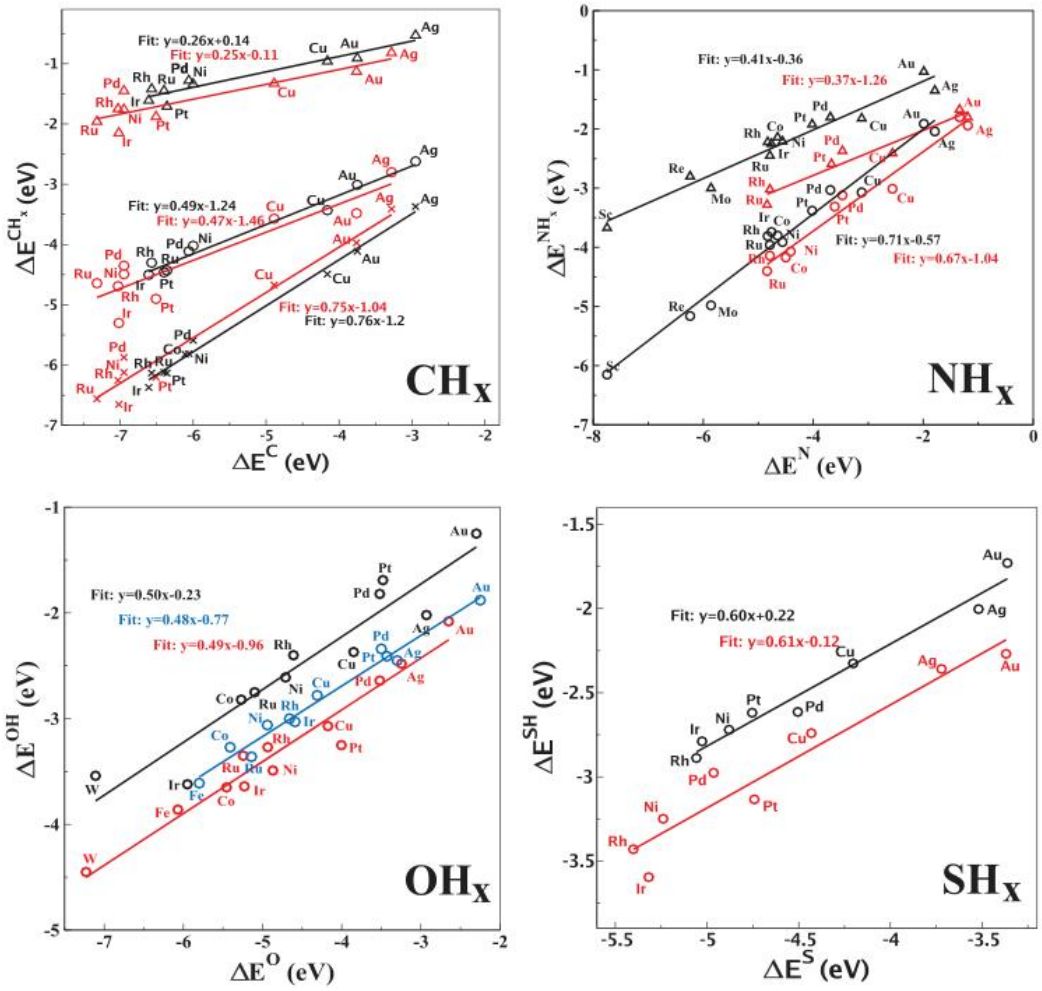

Figure 2-6 The scaling linear relation between different adsorption energies of CH_x, NH_x, OH_x, and SH_x intermediates. (Reprinted with permission from American Physical Society, adopted from [127])

We systematically studied the scaling linear relations of four different groups of molecules (e.g., CH_4, NH_x, OH_x, and SH_x) and found that their slope of the linear relation depends only on the valence of the adsorbate. Insight into the essential origin of this principle may explain the phenomena based on the simple valency or bond-counting arguments. By comparing *CH, *CH_2, and *CH_3 on surfaces, we found that *CH with a valency of 3 prefers the

threefold adsorption configuration, while *CH_2 with a valency of 2 prefers the twofold adsorption configuration, and last, CH_3 has a valency of 1, which tends to choose the one-fold adsorption configuration. These results suggest that these unsaturated bonds of the carbon atom can form bonds with surface metal atoms, indicating that each unsaturated sp^3 orbital hybridization on the central C atom binds independently to the d orbital of the active site metal atoms; therefore, a conventional interpretation for CH, CH_2, and CH_3 is related to the different amounts of hydrogen and adsorption sites. Figure 2-6 summarizes the scaling linear relation between different adsorption energies of CH_x, NH_x, OH_x, and SH_x intermediates based on DFT calculations. This result clarifies that all the considered AH_x intermediates exhibit a linear correlation between the corresponding adsorption energy of atom A and the adsorption energy of molecule AH_x. The different colors of the data points represent the adsorption energies on the stepped (red) and close-packed (black) on various metal surfaces. In addition, the data points marked in blue represent pure metals on the fcc (100) plane for OH_x.

Table 2 Summary of the scaling relations reported in the literature [128]

Scale from	Scale to
C	CH_x, C_2Hx, CHO, HCHO, CHO, HCOOH, CH_3OH
CO	CHO, COOH, CH_xOH, HCHO
CHO	HCHO, CHOH, CH_2OH, COH, CO
O	OH, OOH, CH_3O, HCHO, H
OH	O, OOH, CH_3O, HCOO, HCHO
N	NH_x, N_2Hx, NO, H
H	OH
C, O	HCHO, HCHO, CH_2OH
C, N	CH_xNH_y

In Figure 2-5(a), depending on the scaling relations of the limiting potential, a linear relationship plot is established based on the limiting potential of each elementary reaction as a function of ΔE_{N*}. The different colored solid lines represent the free energy change for each elementary step. The interpretation of these lines corresponds to a given value of ΔE_{N*}, and the lowest line suggests that the limiting potential of the elementary step is defined as the rate-determining step (RDS). As shown in Figure 2-6(b), the scatter plot agrees well with the estimation based on the line description, and the RDS predictive energy based on the scale relation is verified. The interpretation of Figure 6a leads to the following observations. All catalysts have a linear scaling relation between *NNH (ΔG_{*NNH}) and *NH_2 (ΔG_{*NH2}). Linear scaling relationships between binding energies have been observed for many other chemical reactions, as summarized in Table 2. Some studies simply fit a particular scaling relation for every adsorbate they predicted. It also introduces a constant contribution to the scaling relations. This was obtained from the covalent bond interaction between the intermediates and the surface.

2.6 Volcano Plots

Nobel Prize winner Paul Sabatier first proposed a principle for confirming an ideal catalyst, which requires that the binding between adsorbates and catalyst be neither too weak nor too strong. This approach has been extended by constructing activity and stability volcano plots. The promising zone in a volcano plot is determined by the linear proportional relationship between the limiting potential of the RDS and the descriptor function. In this thesis, the underlying principle provides an efficient route for designing and identifying electroreduction catalysts. The adsorbates will fail to bind to the catalyst if the binding is too weak, rendering the reaction unlikely to occur. If the binding is too strong, the adsorbate will fail to desorb. This principle can be illustrated by plotting the reaction rate concerning properties, such as the catalyst's energy binding, to the intermediate product. Such plots can establish a shape similar to that observed in volcano plots, which is generally a linear correlation plot

based on the limiting potential of each elementary step, which is called the volcano surface. Figure 2-7a shows a volcano plot for the NRR that was established based on limiting potential as a function of ΔG_{*N} on novel transition metal borides (MBenes). The colored line denotes the elementary NRR reaction step, which was established using a descriptor of the function of ΔG_{*N} on different transition metals supported on MBenes as catalysts. Each colored dotted line represents an elementary NRR reaction step, and the lowest lines indicate that this elementary step is the RDS for the overall NRR process. A descriptor is a powerful tool for understanding the catalytic activity of materials during electrocatalysis, and the binding energy of an intermediate or d-band center is usually defined as a function of the descriptor. In electrochemical catalysis, different descriptors, such as the d-band center or the binding energy of intermediates, are available, such as ΔG_{*OH} for ORR, ΔG_{*OH} and ΔG_{*CO} for CO_2RR, and ΔG_{*N} for NRR. The descriptors are usually applied based on the underlying reaction, and the formation energy of adsorbed atomic N has been used as a suitable descriptor for the NRR electrochemical reaction.

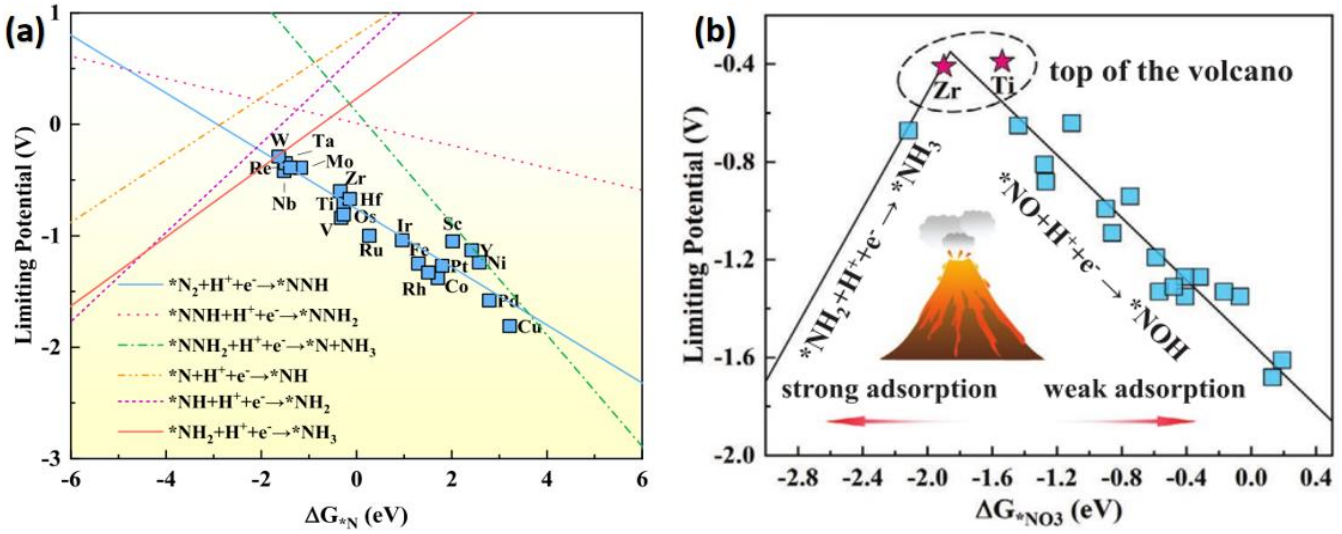

Figure 2-7 (a) Volcano plot for the NRR based on limiting potential as a function of ΔG_{*N}. (Reprinted with permission from American Chemical Society, adopted from [129]) (b) NORR volcano plot of TM/g-CN with a descriptor of ΔG_{*NO3} depending on the rate-determining step. (Reprinted with permission from Wiley-VCH Verlag, adopted from [130])

Figure 2-7a shows that the volcano plot of NRR with a descriptor depends on the binding energy of *N, which indicates that W/g-CN and Ta/g-CN lie near the top of the volcano plot, meaning that the adsorption of N_2 was neither strong nor weak and demonstrating that these catalysts are suitable for NRR. These results suggest that the RDS depends on the step $*NH_2$ to $*NH_3$, which lies on the left leg of the volcano plot. However, weak binding leads to RDS from $*N_2$ to *NNH on the right leg. Specifically, the best U_L ($\approx$ -0.4 V) occurs when $\Delta G(*N)$ is close to -1.1 eV. The optimal binding energy of -1.1 eV ensures that the binding strength of the intermediate species is neither too strong nor too weak, thus helping to achieve an excellent catalyst for NRR. Furthermore, the applied electrode potential can be included in the analysis by conjoining the volcanic curve, which depends on the potential-dependent electrode surface. The activity volcano plot can be used to gain an in-depth understanding of the catalytic performance of catalysts for use in electrochemical reactions.

Furthermore, the Sabatier principle (volcano plot) has been widely applied in thermodynamic interpretation and prediction and in the development of new high-efficiency catalysts. For example, Greeley et al. [131] used the ΔGRI model to screen metal alloy catalysts for the HER and found that Bi-Pt alloys possess higher electrocatalytic activity than pure platinum. Interestingly, Hinnemann et al. [132] reported that MoS_2 nanoparticles could be used as a good HER electrocatalyst based on the Sabatier principle within the

thermodynamic form. Recently, the increase and gradual improvement of the material gene database has promoted the Sabatier principle for materials design and screening. For example, Ulissi et al. [133] proposed a neural network-based model to extensively screen active sites for CO_2 reduction. Furthermore, the Sabatier Principle has been used to screen molecular catalysts and other homogeneous catalysts. The Sabatier principle (volcano plots) was used to predict catalytic activity for various electrocatalytic energy conversion applications. Outstanding electrocatalysts from experiments usually appear close to the peak of the activity volcano plot, suggesting that the Sabatier principle can be helpful in predicting and screening homogeneous catalysts. Furthermore, the Sabatier principle has been extended to the field of lithium-ion battery studies, focusing on the study of lithium-ion intercalation in the spinel lithium titanate crystal structure. However, the Sabatier principle only evaluates and predicts performance by analyzing binding energies, and an activity-stability volcano plot was induced as another criterion to rationalize experiments based on the system's stability. This is why the concept of intermediate bonding strength combined with the volcano concept provides a breakthrough for the screening of electrode materials for metal-ion batteries. Based on these reasons, the concept of activity-stability volcano plots can also be adapted to both the electrocatalytic and battery fields. In summary, volcano plots are a practical approach to predict the activity of catalysts with a descriptor that relates both adsorption and structural properties, with typically the adsorption energy of the intermediate or d-band center of the metal atom as a single descriptor. Nevertheless, the kinetics of complex reactions are not simple.

2.7 D-Band Model

The surface reactivity in electrochemical reactions is determined by the adsorption properties between the intermediate species and the catalyst surface. The binding energies of the intermediates are closely related to the electronic structure of the catalysts in the electrochemical reaction. The d-band center plays an important role in this case, and the d-band center ε_d is expressed as:

$$\varepsilon_d = \frac{\int_{-\infty}^{+\infty} ED(E)dE}{\int_{-\infty}^{+\infty} D(E)dE} \quad \textbf{(7-1)}$$

where D(E) represents the density of states (DOS) of the d states of transition metal atoms and E represents the energy of the d electrons. The d-band model [134] can explain this phenomenon, and the sp-band center is shown in the model in Figure 2-8a. The downward displacement of ε_{sp} is more significant in the sp band states than in the d-band states, meaning that more electrons are transferred and injected into the sp band. This displacement of energies is demonstrated as an increase in the filling (Figure 2-8a), which suggests that the difference $\Delta\varepsilon = \varepsilon_{sp} - \varepsilon_d$ is suitable to describe the activity of the catalyst. The catalytic activity is modulated using the d-band model: one approach is to reduce $\Delta\varepsilon$ by increasing ε_d, while the other is to reduce $\Delta\varepsilon$ by lowering $\Delta\varepsilon_{sp}$. The change in $\Delta\varepsilon_{sp}$ - $\Delta\varepsilon_d$ is easily computed using the d-band center theory, and only the catalytic activity of the catalyst is determined. Note that ε_{sp} - ε_d also has the advantage of being independent of any reference energy selection. The d-band center of the metal can serve as a reliable descriptor for predicting the trend of the binding strength of adsorbates. The volcano plot curve relation is a fundamental principle helpful in describing and predicting the catalytic properties of a given descriptor in electrochemical catalysis. Due to the linear correlation between the d-band center and binding energy, the Brønsted–Evans–Polanyi (BEP) relation [135] based on the linear relationship between binding energy and activation energy can also be used to establish a similar linear relationship between activation energy and d-band centers. More importantly, there is a volcanic relationship

between the overall reactivity and the d-zone center. This suggests that accommodating the d-band center's position improves the performance of a catalyst, leading to the d-band center theory being successfully applied in the reasonable design of outstanding catalysts. However, the d-band center is closely associated with surface chemisorption features and reactivity, but it is not a perfect descriptor in catalyst screening. First, the volcano plots revealed by d-band theory only describe a trend and confirm the data points of the best catalytic performance. The d-band center theory is limited to materials that contain transition metals (d-orbitals), but for nonmetals or metals without d orbitals, it is a failure. Thus, other descriptors must be induced, such as the p-band center or the natural bond orbital approaches. Finally, the d-band center theory cannot provide any spatial modeling information, so it cannot describe the catalytic activity and spatial anisotropy at different active sites. Regardless, the d-band center theory is still an ideal descriptor for dealing with many actual electrochemical reactions.

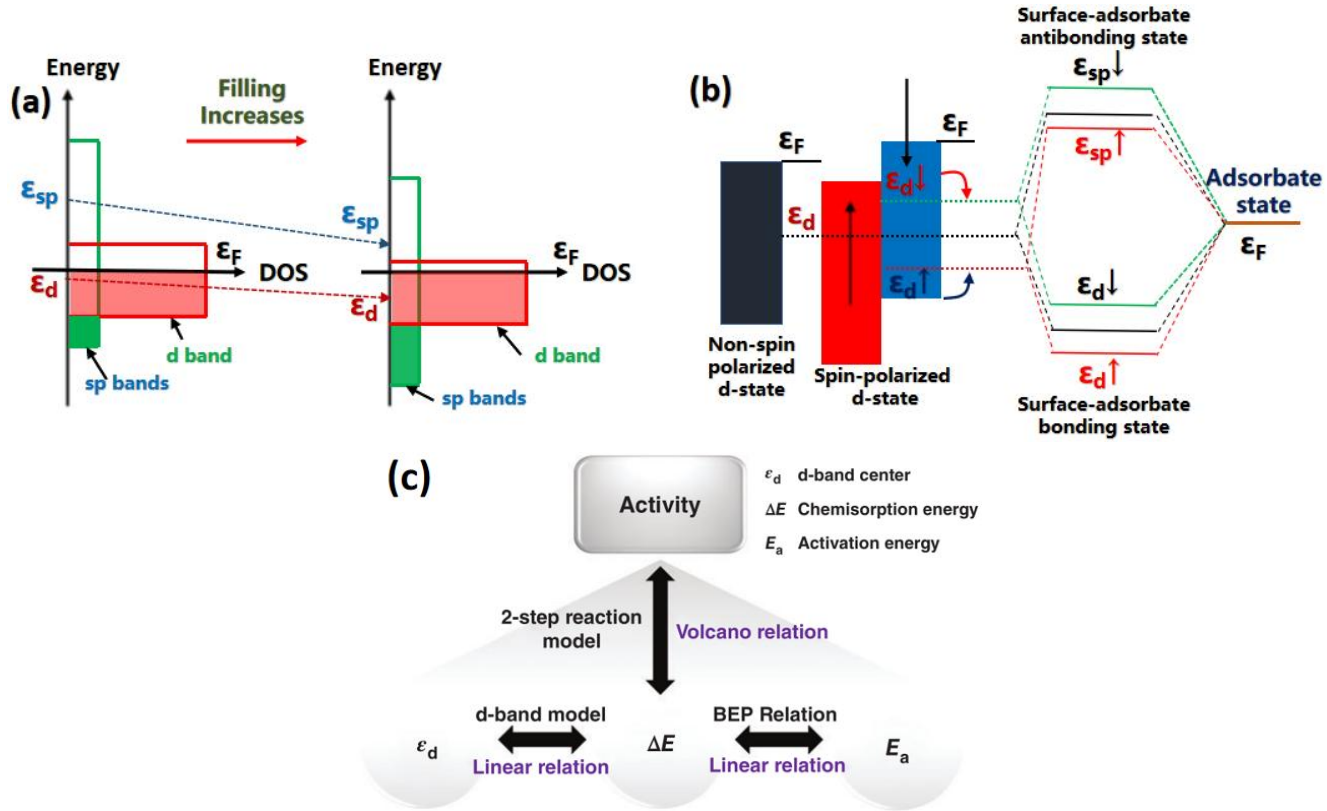

Figure. 2-8. (a) Schematic model demonstrating the interaction mechanism based on the DOS between the sp- and d-bands. (Reprinted with permission from American Institute of Physics, adopted from [136]) (b) Schematic in which the coupling of an adsorbate level is compared using the metal d-band center. (Reprinted with permission from American Institute of Physics, Nature Publishing Group adopted from [137]) (c) Workflow of the linear relationships generated based on the adsorption energy, d-band center and catalytic activity. (Reprinted with permission from American Chemical Society, adopted from [138])

The binding strength of an adsorbate to an active catalytic site is dependent on the occupation of the antibonding state, which is usually located above the Fermi level. The occupation of the antibonding states and the inoccupation of the bonding states were determined by their position relative to the Fermi levels, and several d-band states remain unfilled. The only means of accommodating the electron is to move the center of the d-band, which leads to the occupation of the antibonding states change. The downward movement of the d-band center leads to an increase in the number of unoccupied antibonding states, thus weakening the bond between the adsorbate and the metal atom. Meanwhile, upward movement leads to the opposite effect, resulting in fewer antibonding states between the adsorbed and surface atoms and stronger binding. In this theory, the surface reactivity is strongly correlated to the width of the d-band, which is proportional to the center of the d-band. Thus,

adjusting the width of the d-band can serve as a reliable descriptor to evaluate the surface's reactivity and explore and design new high-efficiency catalysts. In this case, it is essential to understand the influencing factors and the meaning of the width and the center of the d-band. Similarly, the width of the d-band in the transition metal atoms on the surface is determined by the interaction and strong correlation between the d orbital and the neighboring atom. In particular, overlapping d-bands contribute to the orbitals, the bonding distance between the metal atom and its adjacent metal atom, and the intrinsic properties of the metal atom, which are essential factors in determining the d-band width. It is possible to adjust the d-band center by changing the bonding distance between the metal atoms on the surface, altering the overlap between the metal atoms on the surface and the adjacent atoms. Furthermore, replacing adjacent atoms with different metallic elements modifies their electronic structure. This improves the physical-chemical properties of the material, resulting in the production of new d-band centers. Another approach is to change the coordination of the transition metal atoms with the neighboring atoms in a material, such as changing the degree of coupling between the d orbitals. The general relationship between the binding energy of the adsorbates and the d-band centers in electronic systems and changes in the chemisorption energy of a catalyst can be determined by the conventional d-band center model as follows:

$$\delta\Delta E_d = (\frac{\partial\Delta E_d}{\partial\varepsilon_d})_V \delta\varepsilon_d + (\frac{\partial\Delta E_d}{\partial V^2})_{\varepsilon_d} \delta V^2 = \gamma\delta\varepsilon_d + v\delta V^2 \quad \textbf{(7-2)}$$

The first term in Eq. (7-2) represents the covalent interaction contribution between a substrate and its adsorbates, while the second term represents the Pauli repulsion, which depends on the d states of the transition metal and the adsorbate $\gamma = (\frac{\delta\Delta E_d}{\partial\varepsilon_d})_V < 0$ and $v = (\frac{\delta\Delta E_d}{\partial V^2})_{\varepsilon_d} > 0$. ε_d is the d-band center, which can be calculated using a nonspin-polarized calculation; if the second term is ignored, Eq. (7-2) can be reduced to Eq. (7-3) as follows:

$$\delta\Delta E_d = (\frac{\partial\Delta E_d}{\partial\varepsilon_d})_V \delta\varepsilon_d = \gamma\delta\varepsilon_d \quad \textbf{(7-3)}$$

Finally, Eq. (7-3) represents the conventional d-band central model; a positive $\delta\varepsilon_d$ indicates an increase in the binding energy, while a negative $\delta\varepsilon_d$ denotes a decreasing trend in the binding energy. To gain further insight into the linear scaling relationship between adsorption energies and the corresponding d-band center properties of materials, it depends on the change in the d-band model and the adsorption energy across the electrode surfaces. In d-band theory, a higher ε_d shows a decrease in the filling of the unoccupied antibonding states and leads to the stronger binding energy of adsorbates. The regulation of the d-band model can provide a credible reason to explain the origin of the intrinsic correlation between the activity and electronic properties of catalysts.

2.8 Multiscale Modeling and Screening of Electrocatalysis

To date, a series of modern surface science techniques have been used to probe the interaction details of solid-liquid interface regions, such as STM, XPS, SIMS, and SEM experimental techniques [139], which support efforts to gain a deeper understanding of electrochemical phenomena in atomic-scale architecture. However, electrochemistry has not yet fully undergone the atomic revolution enjoyed by other branches of surface science. This section introduces the theoretical methods of multiscale modeling of electrocatalysis, which were considered in the electrochemical reaction. The DFT method is a beneficial and reliable simulation approach at the nanoscale level. It is a tool that depends on first-principles calculations that can study reaction mechanisms and explore promising candidate catalyst materials for electrochemical reactions in terms of both kinetic and thermodynamic properties at a given time and length scale. The DFT method exhibits high efficiency and reliability, which can

explain and predict experimental results. It includes several of the significant categories based on the approximate time and system scales. As shown in Figure 2-9, the purpose of multiscale modeling is to stitch these various aspects into a unified whole. The thermodynamics of molecular systems can be simulated at the atomic scale level by combining molecular dynamics (MD) and first-principles calculations, which are usually defined as ab initio molecular dynamics (AIMD) and have been applied in the field of simulation of complex model systems, such as chemical reactions and electronic property studies. Molecular dynamics (MD) simulations provide an approach for detailed microscopic modeling at the molecular scale for further understanding the electrochemical process and developing and designing applications of electrochemical catalyst materials to obtain desired products. A typical example approach is QM/MM coupling modeling [161] used to describe the reaction process of a specific system. [69]

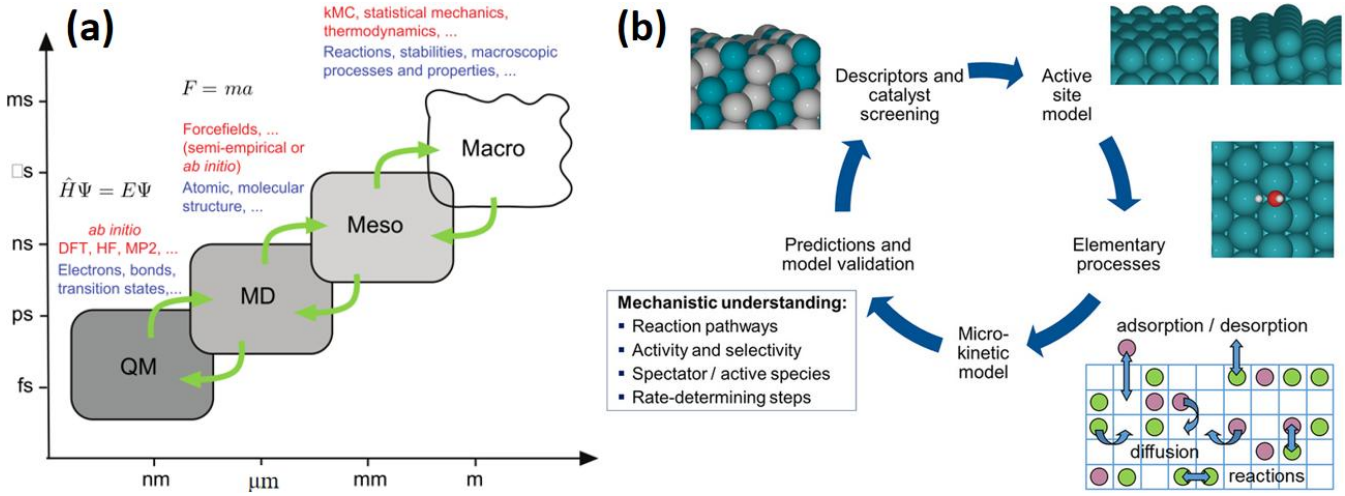

Figure 2-9 (a) Schematic of various multiscale simulation methods by modeling electrocatalysis models. (Reprinted with permission from Springer Publishing Company, adopted from [140) (b) Summary of the various levels of theory involved in the multiscale modeling of electrocatalytic reactions. (Reprinted with permission from [141])

Furthermore, the kinetic Monte Carlo (kMC) method [142] can be applied to describe the chemical process of a given system based on a minimum set of potential energy surfaces. It includes thermodynamics and molecular dynamics simulations, and each multiscale modeling level of theory focuses on the system, as shown in Figure 2-9a. The dynamics of a quantum mechanical system are governed by the time-dependent Schrodinger equation: [143]

$$i\hbar\left(\frac{\partial\psi(r,t)}{\partial t}\right) = \hat{H}\psi(r,t) \quad \textbf{(8-1)}$$

Complete quantum mechanics theory has been widely used in statistical mechanics, quantum chemistry, and chemical kinetics. For multiscale modeling of electrochemical systems, the limit of the system energy means that the ground state has the lowest energy. Multiscale modeling and modern electronic structure theory provide reliable descriptions of electrocatalysis systems. These can be used to link the predicted results to macroscopic electrochemical systems. In Figure 2-9(b), each intermediate's binding energy is calculated based on the most active site models within the DFT approach. All the DFT calculations were performed within the Vienna Ab Initio Simulation Package (VASP) code, and the input and target data were obtained from the microkinetic model, usually constructed using mean-field approximation simulations. Several predictions can be made from the microkinetic model, such as insight into the reaction mechanism and determination of the most favorable pathway among all pathways. The rate-determining step and limiting potential could play an important role in observing the activity and product selectivity of the cover, and descriptors related to both structural and binding

properties can be used to identify the catalytic performance of the catalyst, which facilitates the search for new and improved catalyst materials through theoretical screening applications in heterogeneous catalysis. As discussed above, the formation energy is typically obtained from DFT calculations, while scaling relations between different intermediates can extend the predictions to many electrocatalytic reactions. Thus, most of the multiscale modeling approaches depend on supercomputing power.

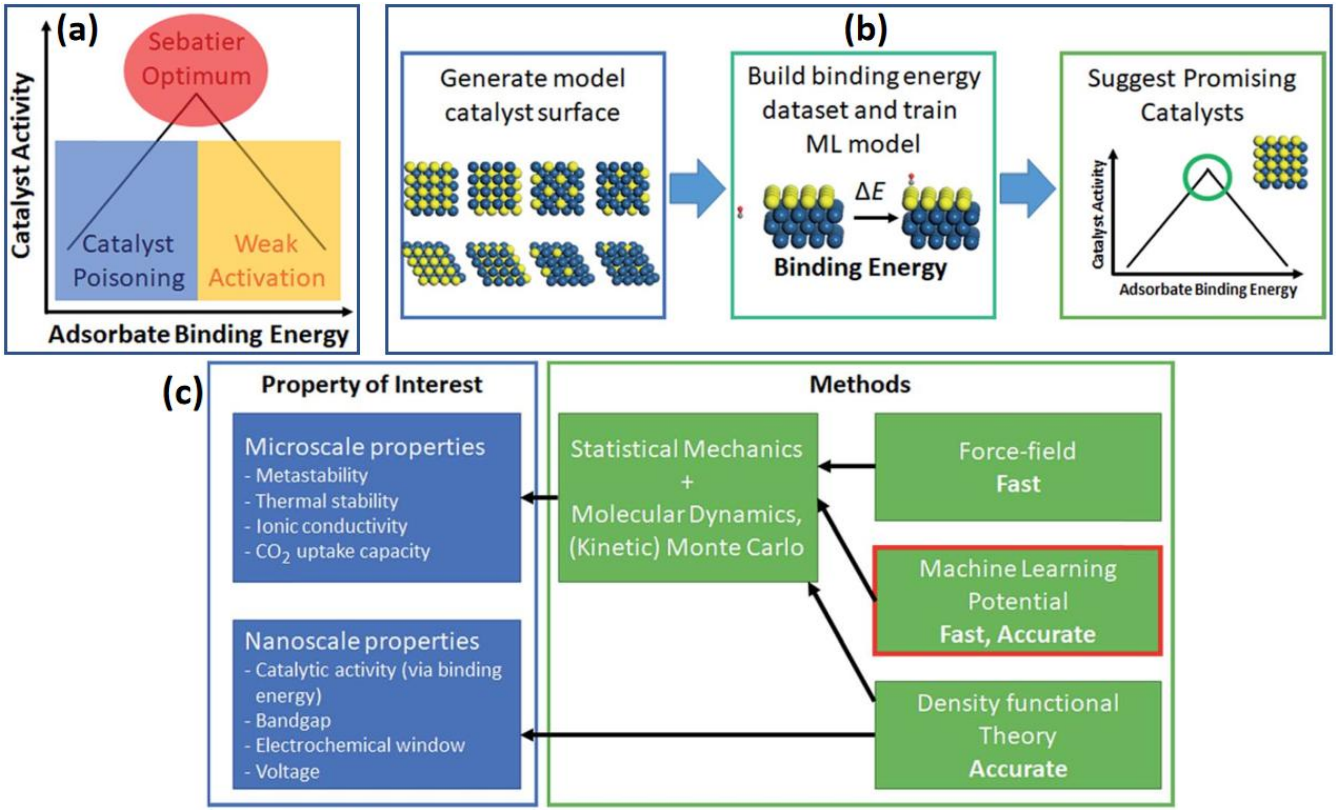

Figure 2-10 (a) Illustration of the Sabatier principle for screening catalysts with optimal activity and (b) workflow of the catalyst screening principle. (c) Microscale modeling simulations to understand the critical properties of materials. (Reprinted with permission from the Royal Society of Chemistry, adopted from [144]).

Theoretical screening and the design of catalysts are based on atomic-scale simulations of thermodynamic stability. Based on this, we can directly understand the structure of intermediates and confirm the reaction mechanism at the atomic level. Using the high-throughput approach with first-principles calculations is an efficient and low-cost way of exploring potential catalyst materials for chemical reactions. Furthermore, machine learning (ML) [145] has recently emerged as a potentially powerful tool for accelerating the discovery of new materials. This type of model has been applied to explore and screen promising catalysts for various electrochemical reactions. However, there are still some challenges and perspectives in using this method. One challenge is that many models include atomic surface state features, such as a central d-band, which require additional DFT calculations to supply sufficient data for machine learning; another is the limitation of input models to only some types of crystal or adsorbate structures, meaning that there is no universal model suitable for probing the large variety of electrochemical catalytic reactions. In addition, the utilization of these ML models for screening in the development and improvement of new technologies has become increasingly urgent to systematically explore and design catalyst materials with ideal properties. In particular, theoretical screening is an efficient and low-cost approach that can establish and develop electrocatalyst materials. The theoretical screening method based on DFT can conduct a systematic study of computational material science. Depending on this

theory, many materials can be evaluated according to the workflows in Figure 2-10a. It shows a workflow based on training models to facilitate the exploration of novel catalysts.

The empirical Sabatier principle indicates that an optimal binding strength exists for catalyst activity; it should provide neither too strong binding nor too weak binding to adsorbates, as shown in Figure 2-10a. In this regard, we propose a "five-step" strategy, which is executed depending on the following criteria: (i) stability, which is estimated using E_b; (ii) the limiting potential (U_L); and (iii) the Faradaic efficiency, which is estimated by (F) or overpotential (η), as shown in Figure 2-10b. An excellent candidate catalyst should possess high thermodynamic stability. To determine possible catalytic descriptors, such as binding energies, limiting potential, or the D band center, it is necessary to decide on the variation trend in the catalytic activity by exploring an excellent and reliable descriptor closely related to the predicted activity. Alternatively, a microdynamic model can develop rate expressions as a function of the given descriptor. We found that this strategy is effective for exploring catalysts. To determine the criterion of the descriptor from DFT calculations, produce the best catalytic activity via microkinetic modeling, and evaluate the practicability of the catalytic descriptors on these catalysts, another approach is to estimate the descriptors via linear interpolation and find promising candidate catalysts with microkinetic modeling, [146] estimating the stability and selectivity of the catalysts under practical reaction conditions and further confirming the optimal candidates experimentally.

3 Theoretical Background

3.1 Many-Body Problem

In physical and chemical systems, many solid properties can be evaluated by solving the Schrödinger equation:

$$H_{tot}\Psi_{tot}(R,r) = E_{tot}\Psi_{tot}(R,r) \tag{1-1}$$

where H_{tot}, $\Psi_{tot}(R,r)$, and E_{tot} represent the total Hamiltonian operator, total wave function, and total system energy, respectively. The Hamiltonian operator contains the following terms:

$$H_{tot} = \frac{\hbar^2}{2m}\sum_{i=1}^{N}\nabla_i^2 - \sum_{i=1}^{N}\frac{Z_I e^2}{|r_i - R_I|} + \frac{1}{2}\sum_{i,j}^{N}\frac{e^2}{|r_i - r_j|} - \frac{\hbar^2}{2m}\sum_{I}^{N}\nabla_i^2 + \frac{1}{2}\sum_{i,j}^{N}\frac{Z_I Z_J e^2}{|R_I - R_J|} \tag{1-2}$$

where the kinetic energy of the electrons (first term) and Coulomb interaction between the electrons and nuclei (second term) are included, while the third term represents the Coulomb interactions between the electrons, the fourth term represents the kinetic energy of the nuclei, and the final term describes the Coulomb interactions between the nuclei. The first three terms focus on describing the electronic parts of the Hamiltonian, while the last two terms describe the nuclei parts. [147] E_{tot} and Ψ_{tot} can be obtained by solving the Schrödinger equation and can directly determine the electronic properties. However, the solution to this equation cannot be obtained directly, except in simple systems with few atoms. Therefore, to study the properties of materials that consist of large numbers of electrons and nuclei, it is necessary to use other approaches and tools to solve the Schrodinger equation.

However, the Born–Oppenheimer approximation may be considered stationary on the electronic timescale. Thus, it is possible to neglect the contribution of nuclear kinetic energy to the system's total energy. It is difficult to solve it at the current level of computation. There are two reasons for this case. The first reason is that a large number of electrons can reach $N\sim10^{28}$ electrons; second, the electron-electron Coulomb interaction leads to the electronic motions being correlated. Thus, the many-body problem is a complicated mathematical issue that contains the effects of electron correlation. Moreover, this interaction is too strong to be regarded as a

perturbation to search for approximations that make the Schrodinger equation easy to solve, and it is necessary to perform numerical calculations while preserving the critical physics quantities as much as possible.

3.2 Density Functional Theory

Over the last few decades, the development and application of quantum mechanics have been some of the most significant scientific milestones in natural science, providing an efficient approach to understanding matter's physical and chemical properties on an atomic and subatomic scale. Quantum mechanics has also been used to identify and design catalysts on an atomic scale. To obtain more effective calculations that can describe the physical properties of matter, high-throughput screening based on density functional theory (DFT) [148] has been widely developed and applied in material design. Thus, many-body theory based on electron density is often used to describe the electronic structure of the ground state of homogeneous systems. Compared with the method based on the wave function, this technique offers a significant reduction in the amount of numerical calculations needed. DFT approaches are based on Hohenberg Kohn and Kohn-Sham [149], which can be used to provide an effective single-particle approximation. At the same time, their exchange-correlation functional is still functional, developing, and improving. In the long term, DFT has been applied to evaluate various physical and chemical properties as distinct materials, providing more accurate descriptions of the different material properties. This thesis introduces the fundamentals of the DFT approach and briefly discusses the theoretical screening workflow. DFT is a powerful tool that can be used to solve the electronic structures of many-body interaction systems. An effective single-particle Schrödinger equation based on the variational principle can be obtained. The fundamentals of DFT have been successfully applied in quantum chemistry and condensed-matter physics. The quantum many-body problems are simplified to a single-particle problem that can be obtained by solving the Schrödinger equation, which depends on the Thomas-Fermi model. [150] P. Hohenberg and W. Kohn [151] proposed the fundamental theories of density functional theory.

Theorem 1. First, we assume that the external electric potential is only a unique function of the charge density. In this regard, the Hamiltonian operator of all ground-state properties is uniquely determined by the electron density as follows

$$F[n(r)] = \langle \psi | (T + V_{ee}) | \psi \rangle \tag{2-1}$$

where T represents the kinetic energy operator, V_{ee} is the electron-electron interaction operator, and F[n(r)] is defined as a universal functional. The system energy of a nondegenerate ground state many-body wave function can be expressed in terms of the ground state as follows

$$E[n(r)] = \langle \psi | H | \psi \rangle \tag{2-2}$$

Proof: We define two potentials $v_1(r)$ and $v_2(r)$, and they further derive different ground state wave functions $\Psi_1(r)$ and $\Psi_2(r)$. Now, we assume that these two ground state wave functions were determined by the same number of ground-state electrons n(r). The energy depends on the variational principle asserted below:

$$E_1 \le \langle \Psi_2 | H_1 | \Psi_2 \rangle = \langle \Psi_2 | H_2 | \Psi_2 \rangle + \langle \Psi_2 | H_1 - H_2 | \Psi_2 \rangle \tag{2-3}$$

$$= E_2 + \int n(r)[\upsilon_1(r) - \upsilon_2(r)]dr \tag{2-4}$$

Equation 2-4 only applies to the ground state; by interchanging 1 and 2, a similar expression can be derived:

$$E_2 \le \langle \Psi_1 | H_2 | \Psi_1 \rangle = \langle \Psi_1 | H_1 | \Psi_1 \rangle + \langle \Psi_1 | H_2 - H_1 | \Psi_1 \rangle \tag{2-5}$$

$$= E_1 + \int n(r)[\upsilon_2(r) - \upsilon_1(r)]dr \tag{2-6}$$

$$E_1 + E_2 \le E_1 + E_2 \tag{2-7}$$

Thus, Theorem 1 is proved.

3.3 Born–Oppenheimer Approximation

In the Born–Oppenheimer approximation, [152] because nuclei are much larger and more massive than electrons, the electrons and the nuclear parts are dealt with separately. However, the nuclei are fixed, the kinetic terms of the nuclei are neglected, and only the electronic part of the Hamiltonian operator remains in the Born–Oppenheimer approximation. This simplifies the Hamiltonian operator and separation of the wave function into two parts, electronic and nuclei, and can be expressed as follows:

$$\Psi_{tot}(R,r) = \Psi_e(R,r)\Psi_n(R,r) \tag{3-1}$$

where $\Psi_e(R,r)$ and $\Psi_n(R)$ correspond to the electronic and nuclear wave functions, respectively. In this regard, the Hamiltonian operator can be divided into two independent Schrödinger equations. Here, the electronic part is as follows

$$H_e\Psi(R,r) = E_e\Psi(R,r) \tag{3-2}$$

where the total Hamiltonian is listed as follows

$$[T_N + T_e + V_{ee}(r) + V_{NN}(R) + V_{eN}(r,R)]\Psi(r,R) = E\Psi(r,R) \tag{3-3}$$

where T_N, T_e, $V_{ee}(r)$, $V_{NN}(R)$, and $V_{eN}(R)$ represent the kinetic energy of the nucleus, electrons and the potential energies from the electron-electron, nucleus-nucleus and the electron-electron, respectively; $V_{eN}(r,R)$ is the external potential of the electrons that move to the nuclei, and H_e is the Hamiltonian for the electronic part,

$$H_e = -\frac{1}{2}\sum_{i=1}^{N}\nabla_i^2 - \sum_{i,I}\frac{Z_I}{r_{Ii}} + \sum_{i>j}\frac{1}{r_{i,j}} \tag{3-4}$$

The electronic Schrödinger equation is as follows

$$H_e\phi_e(r,R) = \left\{-\frac{1}{2}\sum_{i=1}^{N}\nabla_i^2 - \sum_{i,I}\frac{Z_I}{r_{Ii}} + \sum_{i>j}\frac{1}{r_{i,j}}\right\}\phi_e(r,R) = E_e(R)\phi_e(r,R) \tag{3-5}$$

Furthermore, the nuclei Schrödinger equation is described by the nuclear wave function as follows

$$H_N\phi_N(R) = \left\{-\sum_{i=1}^{N}\frac{1}{2M_I}\nabla_I^2 - E_e(R) + \sum_{I>J}\frac{Z_I Z_J}{R_{IJ}}\right\}\phi_N(R) \tag{3-6}$$

However, even considering the simplification of the Born–Oppenheimer approximation, Equation 3-5 cannot be used to solve many-electron systems, and another approximation is needed. A many-electronic system contains N electrons and produces 3N degrees of freedom, making it difficult to solve Equations (3–5). In this regard, two methods can be used to solve the electronic part: one is the Hartree-Fock approximation based on a wave function-based approach, and the other is DFT based on electronic density. In the first strategy, the wave function electron coordination function is used as a variable to solve the Schrödinger equations. However, the electron density $\rho(r)$ depends on the number of electrons present in the density-based approximation. The two theorems were proposed by Kohn and Hohenberg in 1964 [153] and then further developed by Kohn and Sham [154]; they form the basis of DFT. In the next section, we focus on these two theorems. Hartree approximation is the simplest approximation, and its many-body wave function can be expressed as:

$$\Psi_{tot}(\mathrm{r}_1,\mathrm{r}_1,....\mathrm{r}_N) = \psi_1(\mathrm{r}_1)\psi_2(\mathrm{r}_2)...\psi_N(\mathrm{r}_N) \tag{3-7}$$

It assumes that the electrons are independent and can only interact through the Coulomb potential, and the one-electron Schrödinger equation is expressed as:

$$-\frac{\hbar^2}{2m}\nabla^2\psi_i(\mathrm{r})+V(r)\psi_i(\mathrm{r})=\varepsilon_i\psi_i(\mathrm{r}) \quad \textbf{(3-8)}$$

where V(r) represents the exchange-correlation potential function, which includes both the electron-electron interaction and electron-nuclear interaction, and the nuclear-electron interaction potential function is expressed as:

$$V_{nucleus}(r)=-Ze^2\sum_R\frac{1}{|e-R|} \quad \textbf{(3-9)}$$

3.4 Hohenberg-Kohn Theorems

The first theorem illustrates that the Hamiltonian and external potential are uniquely identified by the electron density of the ground state. Therefore, the total energy of many-electron systems can be expressed as a function of the electron density.

$$E[\rho]=\left\langle\Psi[\rho]\left|\hat{H}\right|\Psi_0[\rho]\right\rangle=T[\rho]+V_{ee}[\rho]+V_{ext}[\rho]=F_{HK}[\rho]+V_{ext}[\rho] \quad \textbf{(4-1)}$$

In this regard, the Hohenberg-Kohn functional can be simplified as follows without considering the external potential:

$$F_{HK}[\rho]=\left\langle\Psi[\rho]\left|\hat{T}+\hat{V}_{ee}\right|\Psi[\rho]\right\rangle \quad \textbf{(4-2)}$$

The second theorem proposes a method for solving the wave function that corresponds to the external potential and depends on the ground state density $\rho_0(r)$, which corresponds to the minimum energy density $E[\rho]$. This means that for a specific density, $\rho(r)$, an upper bound exists compared to the energy of the ground state E_0:

$$E_0=E[\rho_0(r)]\le E[\rho(r)] \quad \textbf{(4-3)}$$

In this regard, the minimization problem of the ground state energy is obtained. However, this theoretical basis does not introduce any specific methodology for determining the ground state wave function. Thus, the two theorems need to be applied in combination with each other in large systems based on quantum mechanics.

3.5 Kohn-Sham Equations

Kohn and Sham proposed a feasible route to solving the problem of searching for ground state energy in 1965. [154] The idea behind calculating the electron density of an interacting electronic system assumes that a many-electronic system does not interact, and Kohn-Sham proposed that the electronic density obtained can be assumed to be an effective potential in real interacting electronic systems. In this case, all other contributions to nondirect electron-electron interactions of the interacting system, such as exchange-correlation potential function contributions, are merged into one term, $E_{xc}[\rho]$, including the noninteracting electronic systems. In this form, the Kohn-Sham Hamiltonian is expressed as follows:

$$H_{KS}(r)=-\frac{1}{2}\nabla^2+V_{eff}(r) \quad \textbf{(5-1)}$$

$$V_{ef}f(r)=V_{ext}(r)+V_{Hartree}(r)+V_{xc}(r) \quad \textbf{(5-2)}$$

$V_{ext}(r)$ represents the external potential, and $V_{Hartree,}(r)$ is the classical self-interaction potential function of the interacting electronic systems:

$$V_{Hartree}(r) = \frac{1}{2}\int d^3r d^3r' \frac{\rho(r)\rho(r')}{|r-r'|} \quad \textbf{(5-3)}$$

and $V_{xc}(r)$ is the exchange-correlation potential functional

$$E_{xc}[\rho]:\ V_{xc}(r) = \frac{\delta E_{xc}([\rho],r)}{\delta\rho(r)}|_{\rho=\rho_0} \quad \textbf{(5-4)}$$

V_{eff} is the effective potential functional of the electronic density ρ(r) that is used to calculate the energy of the ground state, and the Schrödinger equation related to the effective potential can be expressed as follows:

$$[\frac{\hbar^2}{2m}\sum_{i=1}^{N}\nabla_i^2 + V_{eff(\rho)}]\phi_i(r) = E_i\phi_i(r) \quad \textbf{(5-5)}$$

The wave functions $\phi_i(r)$ can be calculated from equations (5-5) by solving a self-consistent solution. In this regard, the ground state electronic density of a given electronic system is expressed as

$$\rho(r) = \sum_{i=1}^{N}|\phi_i(r)|^2 \quad \textbf{(5-6)}$$

The crucial issue is how to confirm the effective exchange-correlation potential functional. Several different approaches can be used to obtain the exchange-correlation potential, while the local density approximation (LDA) is the simplest exchange-correlation potential functional [155] that Kohn and Sham proposed. In this case, the homogeneous electronic density system can be approximated as a uniform electron gas:

$$E_{xc}^{LDA}[\rho] = \int \rho(\vec{r})\varepsilon_{xc}^{uni}\rho(\vec{r})d\vec{r} \quad \textbf{(5-7)}$$

Although the LDA approach can perform well in calculating geometrical parameters, it is also often accompanied by overestimated interaction energies. Thus, to develop and improve the LDA potential functional, researchers have proposed using density gradients in a technique that has been denoted the generalized gradient approximation (GGA) [156] method. Finally, the LDA exchange-correlation potential includes both the electron density functional and the density gradient functional, which is expressed as follows:

$$E_{xc}^{GGA}[\rho] = \int \rho(\vec{r})\varepsilon^{GGA}[\rho(\vec{r}),\rho(\vec{r})]d\vec{r} \quad \textbf{(5-8)}$$

Based on GGA theory, several potential functionals have been proposed and developed, such as Perdew-Burke-Ennzerhof (PBE), [157] revPBE [158], and RPBE [159], which have been widely used to calculate the ground state energies of many-electronic systems. Throughout this thesis, the generalized gradient approximation (GGA) has been used in combination with the Perdew-Burke-Ernzerhof (PBE) functional approach to describe the exchange and correlation potentials of electrons and calculate the energies of the ground state.

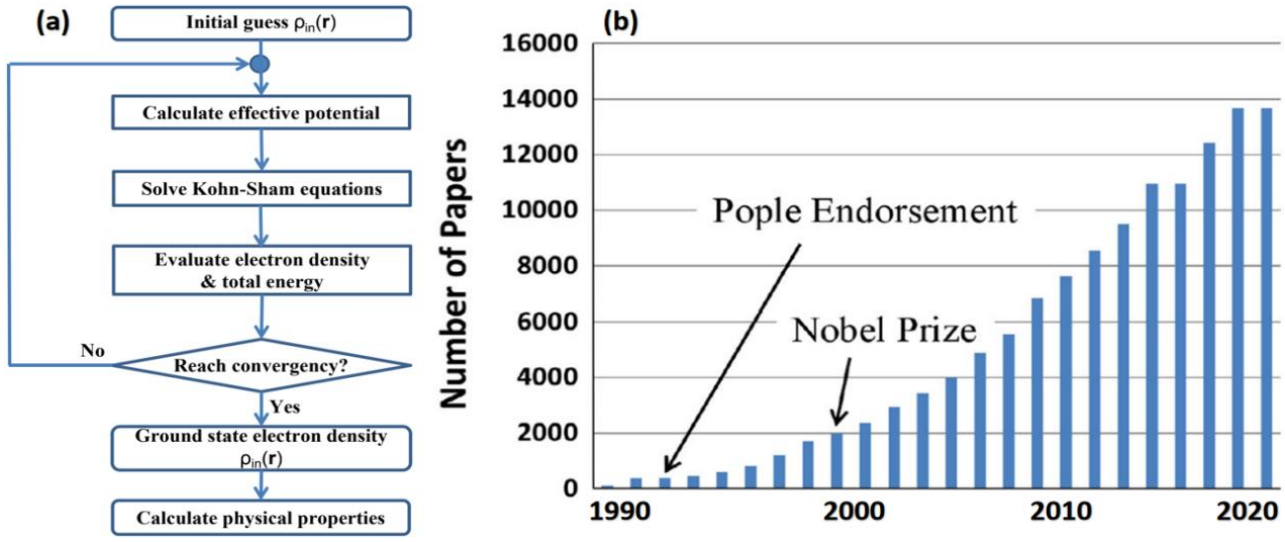

Figure 3-1 (a) Scheme of the workflow procedure for using the Kohn-Sham equations in a self-consistency field for DFT calculations. (b) The number of publications per year depends on the DFT topic, as shown from Web of Science. (Reprinted with permission from [183])

3.6 Exchange-Correlation Functionals

One of the most straightforward and reliable strategies used to construct the exchange-correlation functional of electrons is the homogeneous electron gas (HEG) [160] model hypothesis, where the electrons are defined as a uniform electron density distribution on a positive charge around the nuclei. In practice, the electron density can be divided into exchange and correlation. Jones and Gunarsson suggested modifications to the LDA in which the LDA theory is based on the exchange correlation functional of a physical system and obeys uniform scaling relations. Although the LDA theory can perform moderately well in calculating the lattice parameters, it provides overestimated energies for the ground state.

$$e_{XC}^{HEG}[\rho(r)] = e_{X}^{HEG}[\rho(r)] + e_{C}^{HEG}[\rho(r)] \quad \textbf{(6-1)}$$

For a non-spin-polarized electronic system, the exchange-correlation functional is expressed as follows

$$E_{XC}^{LDA}[\rho(r)] = \int \rho(r) e_{XC}^{HEG}[\rho(r)]dr = \int [(e_{X}^{HEG}\rho(r) + e_{C}^{HEG}\rho(r)]dr = E_{X}^{LDA}\rho(r) + E_{C}^{LDA}\rho(r) \quad \textbf{(6-2)}$$

The exchange-correlation E_{XC}^{LDA} depends only on the local electron density, called the local density approximation (LDA), and is linearly decomposed into exchange and correlation terms. According to the approximate values obtained using LDA, the energy is obtained from a local constant electron density energy. Many approaches can yield local approximations of E_{xc}. Nevertheless, it fails to solve situations in which the electron density undergoes rapid changes. One approach that can be used to improve this is to consider the electron density gradient; this approach is defined as the generalized gradient approximation (GGA). This can be expressed by the following equation:

$$Exc = Exc[\rho(r), \nabla\rho(r)] \quad \textbf{(6-3)}$$

The GGA can significantly improve the accuracy of the LDA results, as LDA only includes one parameterization, while the GGA includes several different parameterizations. General semilocal approximation to the exchange-correlation energy as a function of the electron density (ρ(r)) and its gradient is used to fulfill the maximum number of exact relations. It can be used to systematically calculate the gradient corrections of $|\nabla\rho(r)|$, $|\nabla\rho(r)|^2$ and $|\nabla^2\rho(r)|$, etc., to the local-density approximation (LDA). These functionals can be expressed as follows:

$$E_{xc}^{GGA}[\rho(r)] = \int f^{GGA}[\rho(r), \nabla\rho(r)]dr \quad \textbf{(6-4)}$$

The GGA is especially appropriate for systems with a significantly inhomogeneous electron density. Currently, two concepts are included in the GGA. In this regard, Perdew, Burke, and Ernzerhof developed the so-called PBE functional. In this thesis, the use of the GGA-PBE method for calculating the binding energies is crucial.

3.7 Implementation

Throughout this thesis, all first-principles calculations have been demonstrated in two DFT codes: the Vienna Ab initio Simulation Package (VASP), which was applied to describe the electron exchange-correlation potential during DFT calculations, and the VASPKIT code [161], which was adopted to perform the thermal energy correction calculation of Gibbs free energy. In the following, a brief overview of some of the essential aspects of these two codes is provided.

3.7.1 Pseudopotentials

It is widely known that the electron configuration of an atom is divided into two parts: inner shell core electrons, which are bound by the strong Coulomb attraction of the nucleus, and valence shell electrons. According to the frozen core approximation theory, core-shell electrons are not involved in determining the chemical properties of a material; therefore, the chemical properties are only determined by valence electrons. It is difficult to describe the electron wave function in the core region for implementation in VASP code; to solve this drawback, the core electrons are described using pseudopotentials, [162] a smoother and easier numerical approach for defining the nuclear electrons in atoms for DFT calculations. The pseudopotentials are usually generated by all-electronic calculations during the self-consistent field solution of the all-electron Schrodinger equation as follows:

$$(-\frac{1}{2}\nabla^2 + V)\psi_l^{AE} = \varepsilon_l \psi_l^{AE} \qquad \textbf{(7-1-1)}$$

where ψ_l^{AE} is the wave function of all electrons related to the angular momentum quantum number *l*. The eigenvalues are then substituted back into the Schrödinger equation, and the self-consistent field solution is performed again. The Kohn-Sham equations with this pseudo wave function then yield the pseudopotential to ensure that the valences of all electrons and pseudopotential eigenvalues are consistent.

However, the descriptions of the core electrons are different when this method is implemented in various codes. For example, the ultra-soft pseudopotentials within the VASP code are acquired using the Projected Augmented Wave (PAW) method, an all-electron approach. A smooth pseudo wave function describes the all-electron wave function in the valence domain and a local basis set in the core region. PAW potentials are suitable for all elements in the periodic table except those in the first row. The default energy cutoff for the generated PAW potentials was 250 eV, which VASP from the POTCAR file read. The default energy cutoff can be assumed to work reliably and accurately during the DFT calculations. The distributed PAW potentials were proposed and developed by G. Kresse. PAM's radial cutoffs (core radii), which possess smaller radial cutoffs than ultra-soft pseudopotentials, and valence electron wave functions of all the electrons in the core region have been reconstructed by PAM potentials. Because the core radii of the PAW are smaller than those of ultra-soft pseudopotentials, the basis sets and energy cutoffs are also larger. Furthermore, the older standard pseudopotentials are also reliable when high precision is not needed. In particular, the energy cutoffs for the C, N, and O atoms did not change appreciably when the PAW potentials and standard pseudopotentials were used; therefore, the calculation of model structures that include these elements is no more expensive with PAW potentials than it is with the standard pseudopotentials.

3.7.2 VASP

The Vienna Ab initio Simulation Package (VASP) is a familiar computational simulation program used to study material properties by modeling at the atomic scale, such as electronic structure calculations from first principles. VASP calculates an approximate solution to the many-body Schrödinger equation, which involves solving the Kohn-Sham and Roothaan equations. In VASP, the electron orbitals and electronic charge density can be expressed by the local potential in plane-wave basis sets to obtain the energy of the electronic ground state. Initially, the VASP theoretical basis was based on the code written by Mike Payne and was the basis of the CASTEP code [163] from Materials Studio. It was then transferred to the University of Vienna, Austria, by Jürgen Hafner in 1989. The main program was completed by Jürgen Furthmüller, who joined the group at the Institut für Materialphysik in 1993. [164] VASP is still being improved and developed by Kresse. [165] Currently, VASP is extensively used both in academia and industry worldwide based on software license agreements with the University of Vienna. The primary consideration of VASP is the periodic approach to multidimensional structures; this approach is more suitable for solving the Kohn–Sham equations because of the advantages surrounding the periodic boundary conditions. Therefore, according to the advantage of Bloch's theorem, [166] the wave function can be expressed as the plane wave in the periodicity system within the VASP code:

$$\Psi_{nk}(r) = e^{ik.r} u_{nk}(r) \tag{7-2-1}$$

where r and k represent the position vector and the wave vector, respectively. This indicates that $u_{nk}(r)$ is a periodic function that depends on the same periodicity related to the lattice of the system. Thus, $\mu_{nk}(r)$ can be expanded to the plane waves:

$$\Psi_i(r) = \sum_j C_{ij}\Phi_j(r) = \sum_G C_{i,k+G} e^{i(k+G)r} \tag{7-2-2}$$

G denotes the reciprocal lattice vector; it is required to introduce a vacuum region and impose periodic boundary conditions in all directions due to the limitation of the number of plane wave functions for each k-point in the first billion zone [167]. Therefore, the plane wave cutoff is expressed as follows:

$$(\frac{\hbar^2}{2m})|k + G_{cut}| \le E_{cut} \tag{7-2-3}$$

The 2D bravais lattice Brillouin zones for a 2D crystal lattice were discussed. In solid-state theory, the Bragg plane was bisected by connecting the origin and the reciprocal lattice points. The first Brillouin region is defined as points arriving from the origin without passing through any Bragg plane. The second Brillouin region is a collection of reachable points from the first region through a Bragg plane. In this regard, this definition can be extended, and the nth Brillouin region is defined as the set of points that can be reached from the origin through no less than n Bragg planes. The five different 2D Bravais lattices and their corresponding Brillouin zones are shown in Figure 3-2. In general, the Brillouin region can be constructed by using the rules of strong scattering of incident waves on the lattice with reciprocal lattice vector K, only when

$$k \times K = \frac{1}{2} K^2 \tag{7-2-4}$$

The set of points that satisfy Eq. (2-4) is perpendicular to the vector connecting the origin to K and lying midway between 0 and K. When many such planes are constructed using all possible K values, the origin would be enclosed within a solid region. This is the first Brillouin zone because all points inside are closer to the origin than any reciprocal lattice vector.

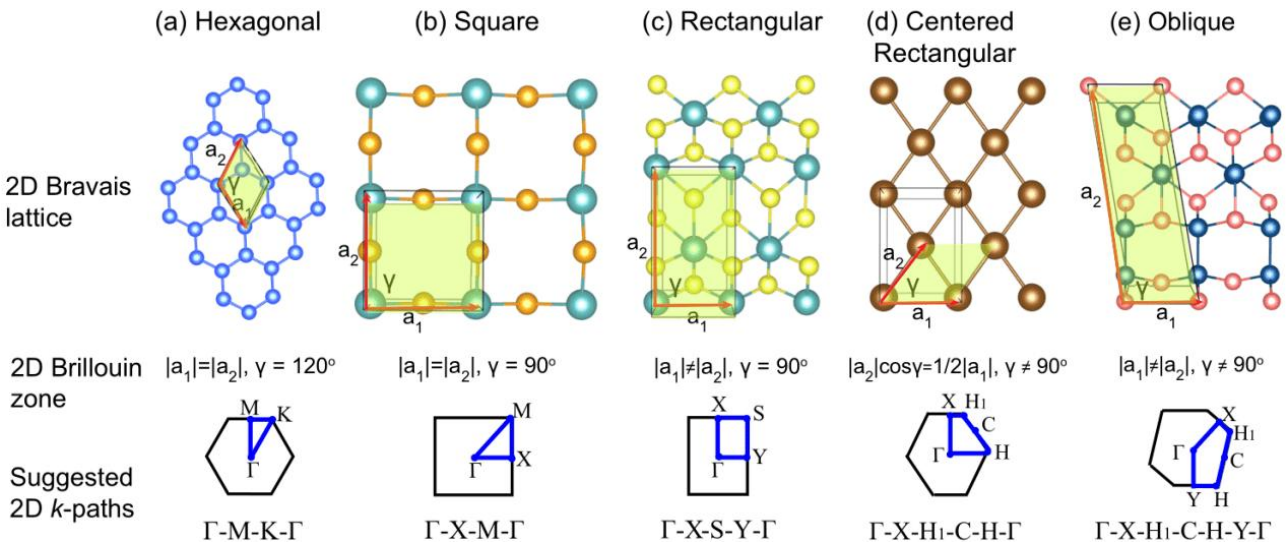

Figure 3-2 A summary of the 2D Bravais lattices and corresponding Brillouin zones (upper). (Reprinted with permission adopted from [168])

There are five different 2D Bravais lattices: square, hexagonal, oblique, rectangular, and centered rectangular. The blue line indicates the suggested k-paths for the band structure. The green box indicates the primitive unit cell. The Brillouin zones and suggested k-paths for the Bravais lattices executed in our DFT calculations are presented in Figure 3-2. Most of the 2D material candidates for use as electrocatalysts focus on rectangular or hexagonal Bravais lattices. Wang and Vei et al. [168] proposed a high-throughput approach based on density functional theory; they screened a sufficient number of two-dimensional materials according to energetic, mechanical, and thermodynamic stability criteria and identified the five regular 2D Bravais lattices shown in Figure 3-2, which show centered rectangular, hexagonal, rectangular, square, and oblique lattices. Thus, the Brillouin zones and k-paths for the materials considered in this study were adopted for the theoretical screening calculations, and the calculated formation energy, energy correction term, and electronic structure (band gap and DOS) for all considered candidates satisfied these criteria.

3.7.3 Numerical Details on Gibbs Energy Correction

Herein, we briefly provide a brief overview of the VASPKIT code, [161] which is based on a Fortran 90 programming language source with compiled versions and has the goal of delivering a powerful and user-friendly interface with which to perform big data analytics and screen the various material properties of raw computational data that are widely used in the VASP code. VASPKIT can perform format correction and pseudopotential checks; it automatically corrects both the INCAR and POSCAR formats in Figure 3-3(b). The module is used to extract and analyze calculated data, such as the band structure postprocess electronic structure, electrostatic potential, charge/spin density, thermal energy correction, and the d-band center in real space. The command-line options of VASPKIT allow high-throughput calculations in combination with the VASP code and bash scripts. VASPKIT is still undergoing improvements and is under development, and it is therefore currently only supported for use with VASP; extending it to work with files from other electronic structure packages is challenging. This application program is compiled in Fortran 90 and can work on Linux platforms. An instruction manual is available at https://vaspkit.com/tutorials.html.

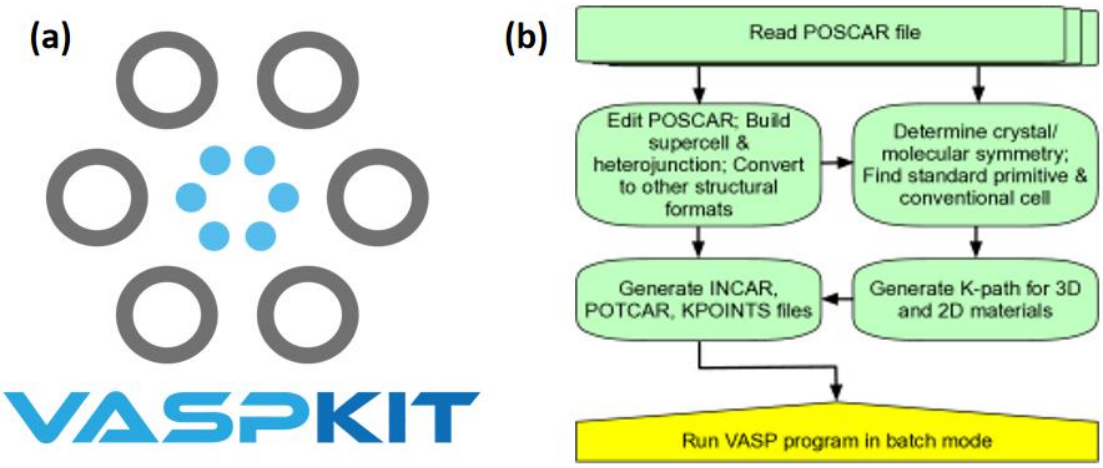

Figure 3-3 (a) The VASPKIT icon. (b) Description of the workflow within the VASPKIT package. (Reprinted with permission from Elsevier, adopted from [161])

As implemented in the VASPKIT package, the postprocessing modules are aimed at extracting and analyzing the original data from DFT calculations, such as electronic properties, electrochemical thermodynamic properties, and molecular dynamics-related properties. VASPKIT also possesses a high-throughput interface to study adsorption energies on solid surfaces, which can be used as part of bash scripts to take full advantage of bash's capabilities to perform pre- and post-processing. For example, thermal energy correction in catalysis is described in the following section, and thermo energy correction can be performed by calculating the free energy change of catalysis, which is crucially important. However, VASP does not have a module that can directly calculate molecular free energy, which means that the free energy corrections in some publications are inconsistent and inaccurate. Furthermore, the computed thermochemical data free energy correction for gas molecules in VASPKIT is calculated in Gaussian. (https://Gaussian.com/thermo/). The partition function can be expressed with the entropy as follows:

$$S = Nk_B + Nk_B \ln(\frac{q(V,T)}{N}) + Nk_B T(\frac{\partial \ln q}{\partial T})_V \quad \textbf{(7-3-1)}$$

Here, $N_A k_B$=R, and the internal thermal energy U can also be calculated based on the following partition function:

$$U = Nk_B T^2(\frac{\partial \ln q}{\partial T})_V = RT^2(\frac{\partial \ln q}{\partial T})_V \quad \textbf{(7-3-2)}$$

The partition functions of translational, electronic, rotational, and vibrational contributions were calculated using the equations (https://gaussian.com/thermo/)

$$U = E_t + E_e + E_n + E_r \quad \textbf{(7-3-3)}$$

$$S = S_t + S_e + S_n + S_r \quad \textbf{(7-3-4)}$$

The degree of vibrational freedom in linear molecules is 3N-5, and VASPKIT neglects the smallest five frequencies. For nonlinear molecules, the degree of vibrational freedom is 3N-6, and VASPKIT does not consider the smallest six frequency modes. VASPKIT also includes zero-point energy (ZPE), which can be obtained from the frequency calculation.

$$ZPE = \frac{hv}{2} \quad \textbf{(7-3-5)}$$

The Gibbs free energy (G) is expressed based on the fundamental thermodynamic relation:

$$G = E_{DFT} + H + ZPE - TS \quad \textbf{(7-3-6)}$$

At room temperature and constant pressure, enthalpy can be expressed in terms of H^0 based on the heat capacity C_p:

$$H = H^0 + \int_0^T C_p dT \quad \textbf{(7-3-7)}$$

Additionally, entropy can be expressed as the sum of the rotational, translational, electronic, and vibrational contribution terms, which are listed as follows:

$$S = S_t + S_r + S_v + S_e \quad \textbf{(7-3-8)}$$

The zero-point energy (ZPE) correction terms can then be included in Eq. (5-9) to finally obtain the following:

$$G = E_{DFT}^0 + \int C_p dT - T(S_r + S_r + S_v + S_e) + ZPE \quad \textbf{(7-3-9)}$$

$$\begin{aligned} \Delta G_{21} &= E_{DFT}^2 + \int C_{P.2} dT - T(S_{t,2} + S_{r,2} + S_{v,2} + S_{e,2}) + \mathrm{ZPE}_2 \\ &- E_{DFT}^1 - \int C_{P.1} dT + T(S_{t,1} + S_{r,1} + S_{v,1} + S_{e,1}) - \mathrm{ZPE}_1 \end{aligned} \quad \textbf{(7-3-10)}$$

or simply:

$$\Delta G_{21} = \Delta E_{21}^0 + \Delta \int (C_P)_{21} dT - T\Delta S_{21} + \Delta ZPE_{21} \quad \textbf{(7-3-11)}$$

$$\Delta G_{21} = \Delta E_{DFT}^0 + \Delta H - (T\Delta S - \Delta ZPE) \quad \textbf{(7-3-12)}$$

When computing the Gibbs free energy variation between two states denoted as 1 and 2, and applying Eqns. (7-3-12) at the atomic scale:

For gases, translational, rotational, and vibrational entropy terms that have contributions that cannot be neglected, therefore,

$$S = S_t + S_r + S_v \quad \textbf{(7-3-13)}$$

For the solid phase and adsorbates, both $S_t = 0$ and $S_r = 0$; therefore, $S = S_v$. As $\int C_p dT$ is almost negligible $\int C_p dT = 0$, and no thermal corrections for the enthalpy have been considered in the calculation of ΔG.

Next, we introduce the adsorbed molecular free energy correction. Unlike molecules in the gas phase, adsorbates bind via chemical bonds to the surface of a catalyst, limiting the adsorbates' rotation and translation. Therefore, the contribution of rotation and translation to entropy is almost negligible, as it is significantly minimal. Consequently, we must fix the substrate and relax the adsorbates. This does not mean that there are no translational or rotational contributions. An approximation approach is used to attribute the translational or rotational component of the vibration, which means that the total contribution of the vibrations of adsorbates does not include the virtual frequency and neglects the contribution of frequencies that are less than 50 cm^{-1}; this approach is used to calculate the correction term for the thermal energy. The slight vibration frequencies may contribute to the entropy; therefore, minimal vibration frequencies are likely to result in anomalous entropies and free energy corrections. This suggests that when the free energy of the surface adsorption molecule is corrected, VASPKIT neglects the electron motion because of its small contribution.

4. Electrocatalytic Reaction Systems

4.1. HER (Hydrogen Evolution Reaction)

The hydrogen evolution reaction (HER) is a dual-step reaction process and generates gaseous hydrogen on a given catalyst. The first step of the HER is called the Volmer, as shown by the blue arrows in Figure 4-1a, in which an electron is coupled with a proton to form an absorbed hydrogen atom. The hydronium cation (H_3O^+)

can serve as the proton source in acidic conditions or the water molecule in alkaline conditions. Subsequently, hydrogen molecules can be generated through two different reaction mechanisms: the Volmer Tafel mechanism and the Volmer Heyrovsky [169] mechanism. The first mechanism, marked by purple arrows in Figure 4-1a, is the electrochemical desorption chemical adsorption mechanism. The second mechanism is electron transfer to the absorbed hydrogen atom coupled with another proton from H_2. This is an electrochemical desorption mechanism.

Furthermore, combining two absorbed hydrogen atoms simultaneously to form H_2 is called the Tafel reaction mechanism (or combination reaction), represented by red arrows in Figure 4-1a. According to the difference in reaction media, the reaction mechanism is also different. In acidic media, the reactions are expressed as:

$$\text{Volmer step: } *+H^+ + e^- \rightarrow *H \quad \textbf{(1-1)}$$

$$\text{Heyrovsky step: } *H + H^+ + e^- \rightarrow *H_2 \quad \textbf{(1-2)}$$

$$\text{Tafel step: } *H + *H \rightarrow *H_2 \quad \textbf{(1-3)}$$

where * is the catalyst. Furthermore, in alkaline media, the proton source is induced from an additional H_2O dissociation step, and the generated intermediate *H in the reactions is as follows:

$$\text{Volmer step: } *+H_2O + e^- \rightarrow *H + OH^- \quad \textbf{(1-4)}$$

$$\text{Heyrovsky step: } *H + H_2O + e^- \rightarrow *H_2 + OH^- \quad \textbf{(1-5)}$$

$$\text{Table step: } *H + *H^+ \rightarrow *H_2 \quad \textbf{(1-6)}$$

Previous studies reported that the adsorption energy of the *H intermediate is closely related to the activity of electrocatalysts for the HER, as shown in Figure 4-1b, which can be evaluated by ΔG_{*H}. When the value of ΔG_{*H} is less than 0, it indicates that if the bonding strength of H is too strong, it makes it difficult for H to desorb on the electrode surface and would lead to a high desorption energy for the Tafel or Heyrovsky step. However, when the value of ΔG_{*H} is more than zero, it causes a high-energy barrier for the Volmer step and limits the overall reaction rate. In addition, if the value of ΔG_{*H} is close to 0, it exhibits the optimal thermodynamic adsorption/desorption performance for hydrogen ions. Nørskov et al. proposed this theory, which is called the volcano plot. The y-axis and x-axis of the volcano plot represent the exchange current density (j_0) and ΔG_{*H}, respectively. A higher value of j_0 indicates higher intrinsic activity. Tuning the value of ΔG_{*H} has been identified as a practical approach to improving the activity of catalysts for the HER. Neither too strong nor too weak binding of *H is conducive to HER performance. A typical volcano curve is based on exchange current density (j_0) [170] with ΔG_{*H}. If binding of *H is too weak and will limit the rate of the overall reaction (Volmer), if the binding is too strong during the desorption of the *H step (Heyrovsky), the rate of the overall reaction will be limited. According to Norskov's assumption, the theoretical exchange current (i_0) was obtained from the following formula. When the proton adsorption process is exothermic ($\Delta G_{*H}<0$), the exchange current (pH= 0) is defined as:

$$i_0 = \frac{-ek_0}{1+\exp(-\Delta G_{*H}/k_B T)} \quad \textbf{(1-7)}$$

If the proton adsorption process is endothermic ($\Delta G_{*H}>0$), i_0 is given by:

$$i_0 = \frac{-ek_0}{1+\exp(\Delta G_{*H}/k_B T)} \quad \textbf{(1-8)}$$

where k_B and k_0 represent the Boltzmann constant and rate constant, respectively.

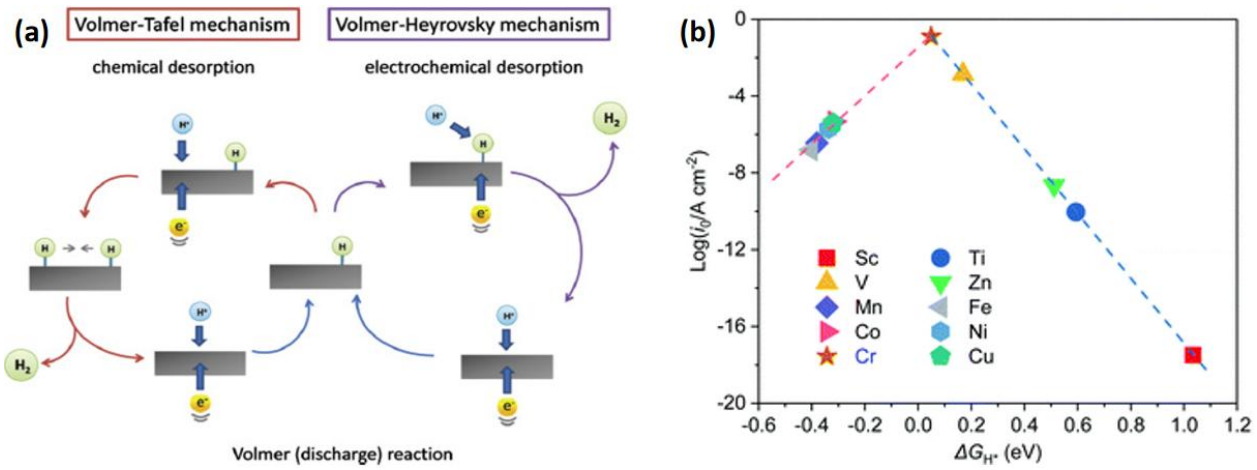

Figure 4-1 (a) Schematic of the hydrogen evolution reaction mechanism. (Reprinted with permission from Elsevier, adopted from [171]) (b) A volcano curve of the HER depending on the exchange current (i_0) on the M@FeS_2 catalysts. (Reprinted with permission from the Royal Society of Chemistry, adopted from [172])

Generally, due to the competitive relation between the adsorption and desorption of H atoms, the Tafel slope value from the volcano plot curve of the HER is considered based on the Sabatier principle, suggesting that an ideal HER electrocatalyst should possess a moderate bond with adsorbed *H to promote the proton-electron pair transfer process to ensure not only adsorption and desorption of *H but also the release of gaseous H_2 from the catalyst surface. The volcano plot of current exchange densities (j0) as a function of ΔG_{*H} shows a volcano shape in Figure 4-1(b), in which Cr metal is at the top of the volcano, indicating that the lowest energy barrier corresponds to the highest activity for the HER, meaning the values of ΔG_{*H} are closer to zero and show higher activity. Based on the Sabatier principle, to the left side of the volcano plot, binding hydrogen atoms are very strong and may fail to desorb hydrogen atoms, whereas to the right side of the volcano plot, binding hydrogen is very weak and may fail to stabilize the hydrogen atoms and limit the rate of reaction due to such a weak interaction. According to quantum mechanics calculations, ΔG_{*H} has been identified to be satisfactorily capable of describing the electrocatalyst activity for the HER. It also plays a vital role in guiding the development and design of high-performance HER electrocatalysts. Furthermore, the kinetics of the hydrogen evolution reaction on a given electrode in an acidic medium and the overall HER can be expressed as

$$2H^+ + 2e^- \rightarrow H_2 \quad \textbf{(1-9)}$$

Hydrogen atoms first desorb on the electrode surface and then recombine with another H ion into molecules:

$$H_{ads} \rightarrow H \quad \textbf{(1-10)}$$

The electrochemical hydrogen desorption (Eq. 1-12) on the electrode surface is the rate-determining step that controls the hydrogen overpotential. The reaction mechanism includes desorption of hydrogen from the electrode surface and hydrogen gas molecule formation.

$$1/2H_2 \leftrightarrow H(Equilibrium) \quad \textbf{(1-11)}$$

$$H \leftrightarrow H^+ + e^-(RDS) \quad \textbf{(1-12)}$$

Since Eq. (1.11) is in equilibrium and Eq. (1.12) is the rate-determining step, the hydrogen atom concentration is defined as:

$$[H] = K[H_2]^{1/2} \quad \textbf{(1-13)}$$

where K represents the rate constant of the equilibrium state. The net reaction rate of H^+ reduction to H_2 molecules is defined as the difference between the rates of the anodic and cathodic reaction steps and is expressed as the current (i) in Eq. (1.14):

$$i = F\left\{k_1^o e^{E/b_a} K[H_2]_b^{1/2} - k_{-1}^o e^{-E/b_c}[H^+]_s\right\} \quad \textbf{(1-14)}$$

where K_1^o and K_{-1}^o are the rate constants of the anodic and cathodic reactions, respectively. When at equilibrium, i=0, and E=E_{eq}; thus,

$$i^o = Fk_1^o e^{E/b_a} K[H_2]_b^{1/2} = Fk_{-1}^o e^{-E/b_c}[H^+]_s \quad \textbf{(1-15)}$$

Finally, the rate constants at equilibrium are listed as follows:

$$k_1^o = i^o e^{-E_{eq}/b_a} / FK[H_2]_b^{1/2} \quad \textbf{(1-16)}$$

$$k_{-1}^o = i^o e^{E_{eq}/b_c} / F[H^+]_s \quad \textbf{(1-17)}$$

where i_o is the current exchange density and [H^+] and [H_2] are hydrogen ion and hydrogen molecule surface concentrations in the equilibrium states, respectively.

4.2. ORR (Fuel Cells)

In recent years, fuel cells have attracted increasing attention because of their high-energy conversion and storage efficiency. In particular, they have high power density, operate at suitable temperatures, and produce almost no pollution as the energy produced is renewable. The development of efficient and stable catalysts will significantly affect the application of fuel cells, and many theoretical and experimental studies have explored promising candidate catalysts for the ORR. In particular, the density functional theory (DFT) approach has been used to design and screen high-efficiency catalysts for application in fuel cells. This approach uses polymer exchange membrane metal-air batteries and fuel cells, and the ORR plays a vital role in the conversion and storage of energy in fuel cells. According to Sabatier's principle, the binding energy of OH can be used as a descriptor of ORR reactivity and can predict the overpotential needed. The entire reaction step of the ORR is defined using two or four proton-electron pair transfer steps, which can be summarized into three mechanism pathways: (i) O_2 dissociation, (ii) H_2O_2 formation, and (iii) H_2O formation. The first reaction mechanism involves the dissociation of O_2 into two adsorption atomic oxygen atoms ($O_2 \rightarrow 2*O$), followed by the formation of a hydroxide ($*O \rightarrow *OH$) and finally water ($*OH \rightarrow H_2O$). In the H_2O formation mechanism, the *OOH intermediate species are proposed as the first hydrogenation step, and the production of H_2O after four proton-electron pair transfer steps, which is a two proton-electron pair transfer step, has been proposed for the formation of H_2O_2.

In fuel cells, the reaction platform catalyst can significantly improve the thermodynamics of the electrochemical reaction at the catalyst interface and affect the service life. In summary, the design and screening of low-cost, highly stable, and active ORR catalysts are of great significance for promoting the large-scale commercial application of fuel cells. Recently, nonmetal and metal atoms confined on graphene, or single-atom catalysts (SACs), have attracted significant attention because they can provide the advantage of maximum atom utilization efficiency while significantly reducing the use of precious metals. Furthermore, because the isolated metal atoms are scattered across two-dimensional boron nitride (2D-BN) and MoS_2 transition metal dichalcogenides (TMDs), which have significant advantages in terms of both thermal stability and electronic conductivity, they have also gained much interest for the ORR compared to precious catalysts, making them promising candidates for use as ORR catalysts. Of these materials, the confined Mo- or S-substituted single atoms on the MoS_2 catalyst possess superior catalytic activity for the ORR. At present, $M_3(HITP)_2$ MOF compounds have been verified to have outstanding and reasonable activity in catalyzing the ORR. The use of confined metals or nonmetals on 2D materials as single-atom catalysts has received significant attention in both

experimental and theoretical research on heterogeneous materials, providing unique ideas and guidance for designing novel catalysts for ORR reactions in fuel cells.

Here, we took the ORR reactions as an example to deduce the thermodynamic process of the ORR. The catalytic activity of the ORR reaction can be described by evaluating the free energy of different elementary steps. The free energy change of each intermediate can be calculated from the formation energies of *O, *OH, and *OOH on the catalyst. When the standard electrode potential is set to -2.46 eV, the equation can be written as:

$$G^0_{H_2O(l)} - 1/2G^0_{O_2(g)} - G^0_{H_2(g)} = -2.46eV \quad \textbf{(2-1)}$$

Thus, we took the standard entropies from the NIST database for gas-phase molecules. The formation process of each intermediate (*OOH, *O, and *OH) on the surface of the catalyst (*) is listed as follows:

$$* + O_2 + H^+ + e^- \rightarrow *OOH \quad \textbf{(2-2)}$$

$$*OOH + H^+ + e^- \rightarrow *O + H_2O \quad \textbf{(2-3)}$$

$$*O + H^+ + e^- \rightarrow *OH \quad \textbf{(2-4)}$$

$$*O + H^+ + e^- \rightarrow * + H_2O(l) \quad \textbf{(2-5)}$$

The oxygen reduction reaction is a downhill reaction in an acidic electrolyte, the inverse of the OER reaction. The change information energy associated with each intermediate can be obtained from the formation energies of *OH, *O, and *OOH. The standard electrode potential has been experimentally confirmed to be -2.46 eV for the standard free energy change in a half-cell, a spontaneous reaction, while a Gibbs free energy change of -4.92/eV occurs over the overall reaction. The following half-reactions occur in the acid:

$$O_{2(g)} + 2H_{2(g)} \rightarrow 2H_2O_{(l)} \qquad E_{re}\text{=-4.92 eV vs. CHE} \quad \textbf{(2-6)}$$

Therefore, the ORR equilibrium potential (U_{eq}) is 1.23 V. The theoretical voltage of 1.23 V indicates how much energy is required for each elementary reaction that drives the electrochemical reaction. This value is usually the kinetic barrier in spontaneous reactions, and the theoretical overpotential is obtained from the difference between the equilibrium potential (1.23 V) and the limiting potential of the rate-determining step.

4.3 CO_2RR (CO_2 capture)

Currently, oil, coal, and natural gas are the primary energy resources. The chemical raw materials from which these resources are composed have extensively promoted both societal and technological development. However, these energy sources produce large quantities of greenhouses (CO_2, CH_4) and harmful gases (NO, NO_3), which are emitted into the atmosphere during fossil fuel burning and are causing rapid changes in the global climate. The situation has become a severe environmental issue from which humankind is suffering in many aspects. Furthermore, fossil fuels are not infinite; they will ultimately run out due to the growth of the global population and the industrialization of developing countries in the future. Therefore, the search for replacements for fossil fuels with other renewable and clean energy resources is becoming increasingly favored. Renewable energy resources require high-energy conversion efficiency and stable storage devices for practical application. In recent years, scientists have found that some greenhouse (CO_2) and harmful (NO) gases can be converted into renewable energy sources to reduce emissions and utilize renewable resources. The excess energy can be stored in chemical bonds in the form of chemical fuels, such as in the reaction in which carbon dioxide is reduced (CO_2RR) to methane and methanol. Nitric oxide is reduced to form ammonia (NORR), which can be accomplished using highly efficient and stable catalysts. It is essential to obtain high-performance catalysts that can play a crucial role in achieving this goal. In principle, these reaction mechanisms are electrochemical processes.

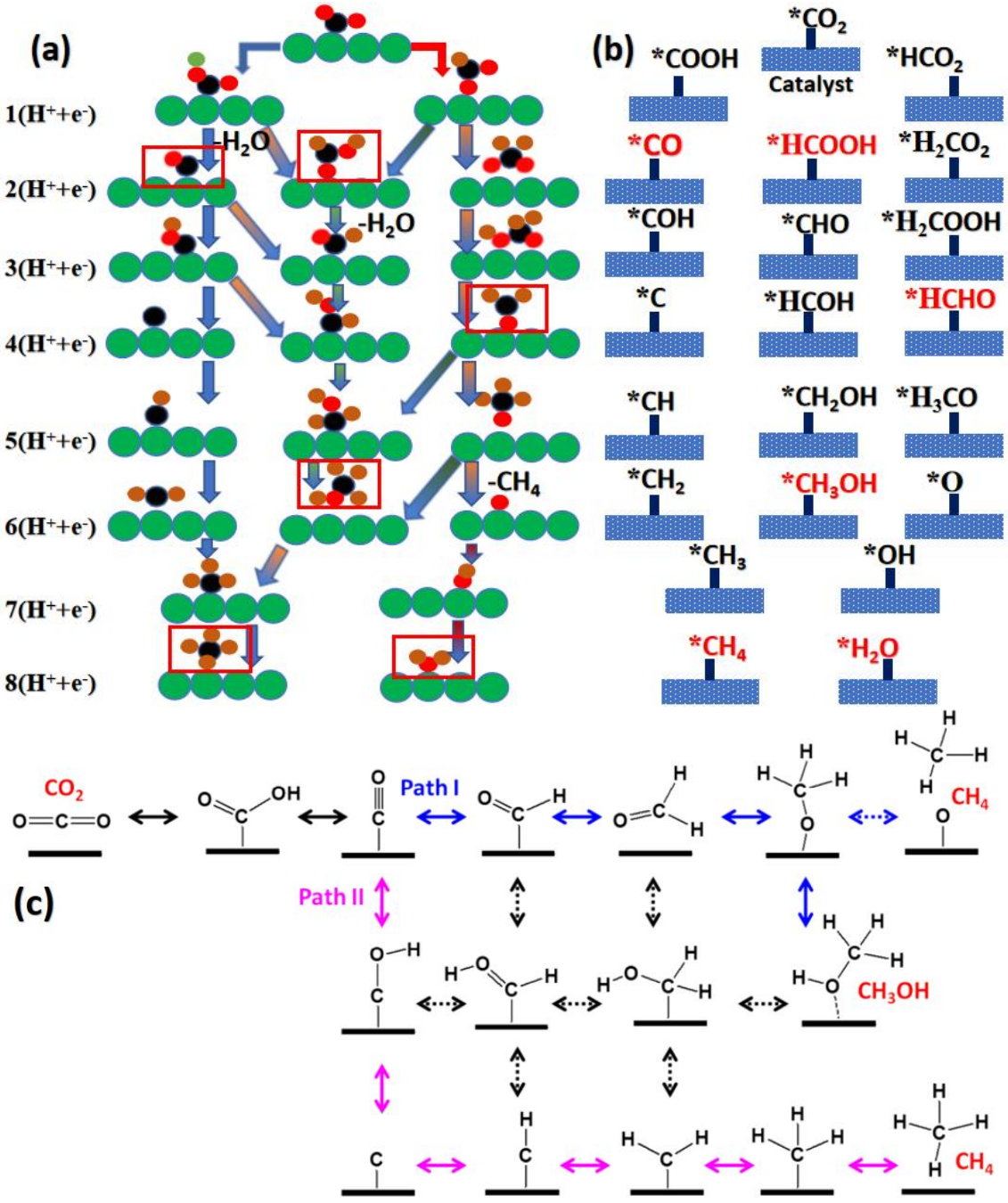

Figure 4-2 Full proposed mechanism path of the electrochemical reaction of CO_2 reduction in an aqueous electrolyte system on MBene model surfaces: (a) atomic models and (b) schematic illustration of a complete CO_2 reduction pathway. (c) A proposed route for a CO_2 reduction mechanism pathway. (Reprinted with permission from Academic Press Inc., adopted from [173])

The elementary steps in the electrochemical reduction of CO_2 to CH_4, with eight transferred proton and electron pairs can be summarized as follows.

$$* + CO_2 + H^+ + e^- \rightarrow *COOH \quad \textbf{(3-1)}$$

$$*COOH + H^+ + e^- \rightarrow *HCOOH \quad \textbf{(3-2)}$$

$$*HCOOH + H^+ + e^- \rightarrow *CHO + H_2O \quad \textbf{(3-3)}$$

$$*CHO + H^+ + e^- \rightarrow *HCHO \quad \textbf{(3-4)}$$

$$*HCHO + H^+ + e^- \rightarrow *CH_3O \quad \textbf{(3-5)}$$

$$*CH_3O + H^+ + e^- \rightarrow *O + CH_4 \quad \textbf{(3-6)}$$

$$*O + H^+ + e^- \rightarrow *OH \quad \textbf{(3-7)}$$

$$*OH + H^+ + e^- \rightarrow *H_2O \quad \textbf{(3-8)}$$

$$* + CO_2 + H^+ + e^- \rightarrow *HCO_2 \quad \textbf{(3-9)}$$

$$*HCO_2 + H^+ + e^- \rightarrow *H_2CO_2 \quad \textbf{(3-10)}$$

$$*H_2CO_2 + H^+ + e^- \rightarrow *H_2COOH \quad \textbf{(3-11)}$$

$$*H_2COOH + H^+ + e^- \rightarrow *HCHO + H_2O \quad \textbf{(3-12)}$$

$$*CH_3O + H^+ + e^- \rightarrow *H_3COH \quad \textbf{(3-13)}$$

$$*CHO + H^+ + e^- \rightarrow *HCOH \quad \textbf{(3-14)}$$

$$*CHOH + H^+ + e^- \rightarrow *H_2COH \quad \textbf{(3-15)}$$

$$*COOH + H^+ + e^- \rightarrow *CO + H_2O \quad \textbf{(3-16)}$$

$$*CH_3O + H^+ + e^- \rightarrow *CH_3OH \quad \textbf{(3-17)}$$

$$*CH_3OH + H^+ + e^- \rightarrow *CH_3 + H_2O \quad \textbf{(3-18)}$$

$$*CH_3 + H^+ + e^- \rightarrow *CH_4 \quad \textbf{(3-19)}$$

$$*COOH + H^+ + e^- \rightarrow *HCOOH \quad \textbf{(3-20)}$$

In particular, CH_4, CH_3OH, CO, and their formation have been reported as the major C1 products of the CO_2RR on Cu-based catalysts. Some metals, such as Pb and Sb, have high selectivity toward producing format from CO_2. Copper is one of the most promising catalysts for CO_2 reduction, as it can directly reduce CO_2 to hydrocarbons and alcohols. The reactions for the major reported products of the CO_2RR are summarized below with the corresponding standard equilibrium potential (E^0) of the reactions compared to the reversible hydrogen electrode (RHE).

$$CO_2 + 2H^+ + 2e^- \rightarrow CO + H_2O \qquad E^0 = -0.11 \text{ V vs. RHE} \quad \textbf{(3-21)}$$

$$CO_2 + 2H^+ + 2e^- \rightarrow HCOOH \qquad E^0 = -0.22 \text{ V vs. RHE} \quad \textbf{(3-22)}$$

$$CO_2 + 6H^+ + 6e^- \rightarrow CH_3OH + 2H_2O \qquad E^0 = 0.02 \text{ V vs. RHE} \quad \textbf{(3-23)}$$

$$CO_2 + 8H^+ + 8e^- \rightarrow CH_4 + 2H_2O \qquad E^0 = 0.17 \text{ V vs. RHE} \quad \textbf{(3-24)}$$

The theoretical voltage E^0 is defined against the corresponding standard potential. However, the limiting potential (U_L), which depends on the RDS, is commonly much higher at the standard potential; thus, it is necessary to overcome the electrode kinetic barrier in each reaction, and the overpotential ($\eta = E^0 - U_L$) is used to describe how much additional potential is required to achieve a reaction. This clearly shows that the reduction of CO_2 to CH_4 is exergonic with equilibrium potentials of 0.17 V and that the production of CO is endogenous with an equilibrium potential of -0.11 V. Therefore, electrocatalysts play an essential role in increasing the rate of electrochemical reactions and reducing the overpotential as much as possible, meaning that the overpotential is lower. The catalytic activity of an electrocatalyst is better.

There are both challenges and prospects for CO_2RR for beyond C1 hydrocarbon fuels on both Cu and non-Cu catalysts, although significant progress has been made in the reduction of CO_2 to multicarbon products on Cu materials, and many challenges remain for non-Cu catalysts. First, due to the low activity for certain C^{2+} products on some non-Cu catalysts, developing high-performance non-Cu catalysts for the CO_2RR to produce multicarbon

products remains a great challenge. Second, the poor reproducibility of low limiting potentials and high Faraday efficiency for CO_2 reduction to multicarbon products on some reported non-Cu catalysts has rarely been reproducible by experiments. Third, the organic solvents used may contaminate the product, such as C_2H_5OH, acetone, ethylene, and glycol, in the CO_2 feedstock. Only Cu catalysts have been verified to be capable of driving CO_2 reduction to multicarbon products with the main activity. Finally, due to the lack of an unclear reaction mechanism of multicarbon products from the CO_2RR, the mechanistic pathways of CO_2 electroreduction to multicarbon products remain unclear. Overall, exploring and gaining high activity and selectivity of non-Cu catalysts for CO_2 reduction to multicarbon products should be the prime objective of my future work.

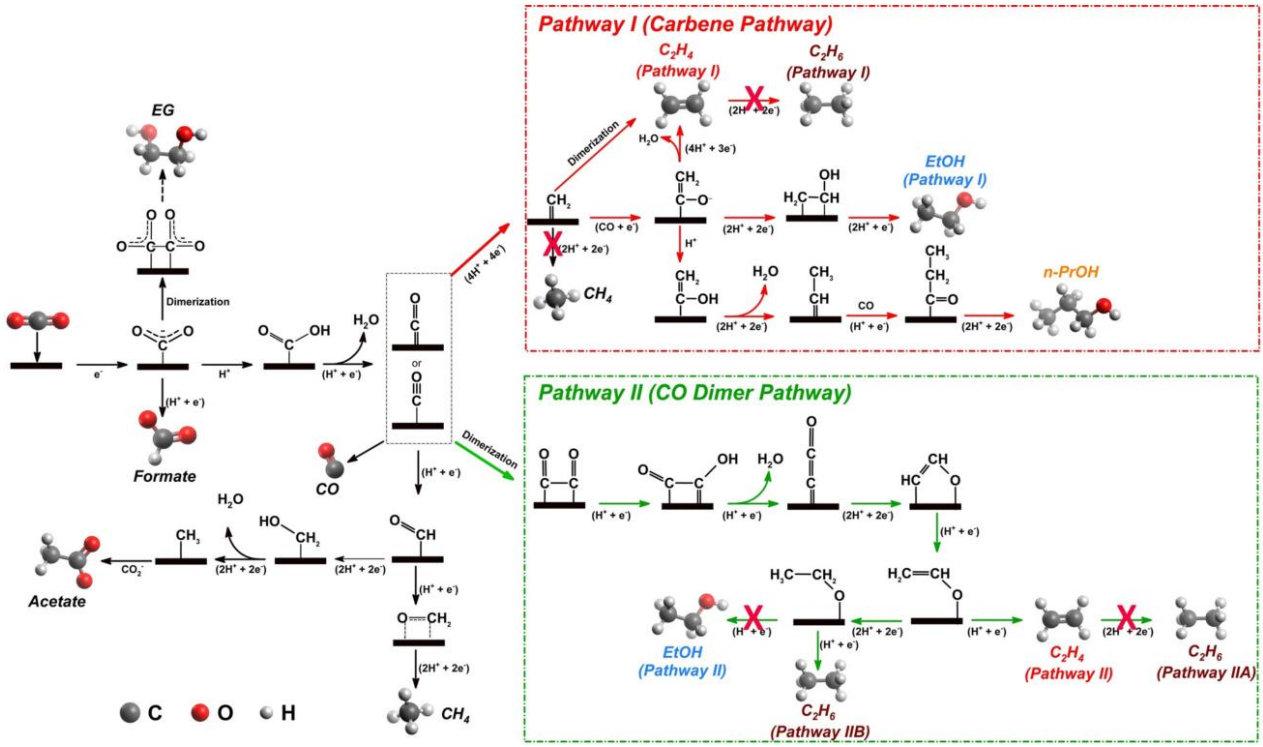

Figure 4-3. Proposed reaction roadmaps of the CO_2RR on Cu catalysts. (Reprinted with permission from John Wiley and Sons Ltd, adopted from [174])

Moreover, CO has been identified as a critical intermediate during the reduction of CO_2 to various C2 hydrocarbon fuels, while C1 hydrocarbon products are easily obtained from carbon dioxide reduction on a Cu catalyst. We shed light on several elusive reduction mechanism pathways widely reported but disputed in the literature, as shown in Figure 4-3. Recently, it was reported that ethane is induced by CO dimerization based on an ethoxy intermediate, suggesting that ethane production is mainly carried out through pathway IIB. At the same time, ethanol would most likely proceed through path EtOH pathway I. These two reaction mechanism pathways involve the formation of an intermediate ($*CH_2CO$) (Pathway I) or CO dimerization (Pathway II), as proposed on a Cu catalyst. Furthermore, it has been reported that ethanol formation is usually suppressed by the ethane mechanism on Cu catalysts, leading to the formation of ethane being more feasible. Generally, the formation of n-PrOH involves an intramolecular reaction between CH_3CH^+ and CO coupling accompanied by hydrogenation to $CH_3CH_2C{=}O^+$, hydrogenation by a proton/electron pair transfer to form propionaldehyde (CH_3CH_2CHO), and further production to n-propanol ($CH_3CH_2CH_2OH$). Of note, the formation of both EtOH and n-PrOH involves carbene species ($*CH_2$), which leads to high overpotentials that produce ethylene with this mechanism. The formation of ethanol, n-PrOH, and ethylene at high overpotentials indicates that these products likely share some common intermediates selectively. Furthermore, by checking another mechanism, pathway II (CO dimer pathway)

was significantly identified by Zhang, G. R et al. [174]; by the comparable Faraday efficiency (FE) of methane on both Cu and ionic liquid (IL) copper foam catalysts, IL copper foam could be employed as a chemical trap to explore the CO_2RR mechanism pathways.

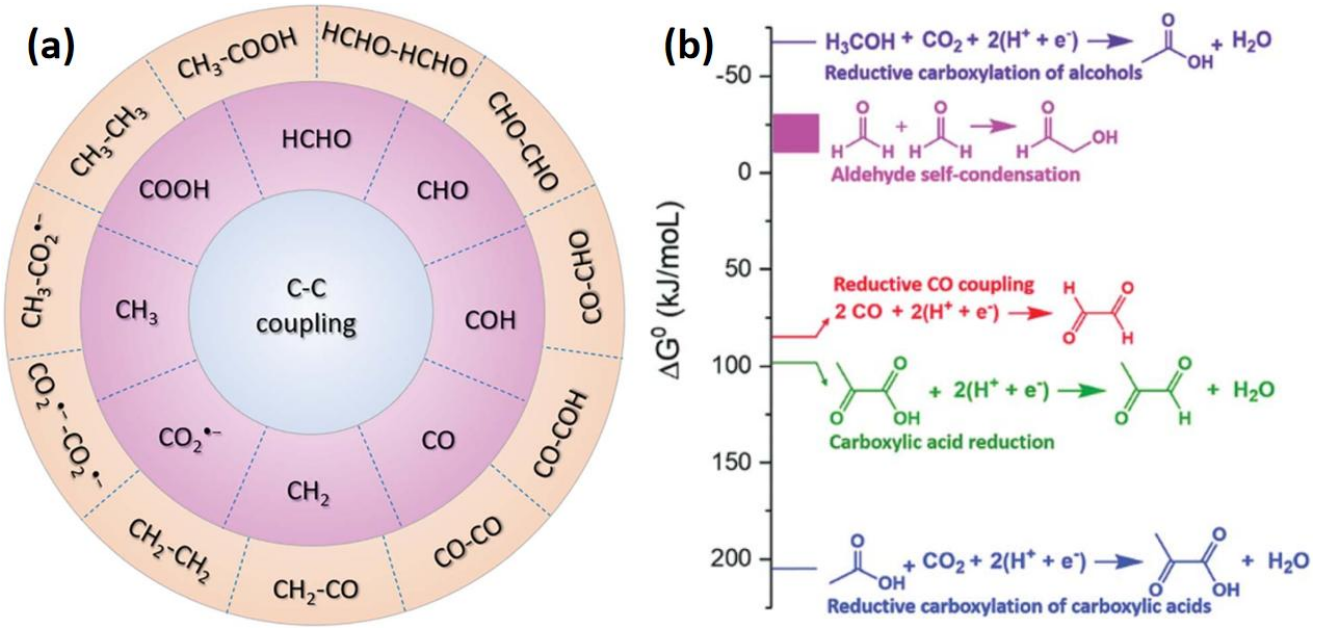

Figure. 4-4 (a) Schematic of all possible C–C coupling reactions for the CO_2RR. (Reprinted with permission from Royal Society of Chemistry, adopted from [175]) (b) Standard Gibbs free energies of some C–C bond formations. (Reprinted with permission from the Royal Society of Chemistry, adopted from [176])

The CO_2RR is a complicated chemical reaction process and involves a multi-electron-proton pair transfer process, leading to the proposal of a definitive reaction mechanism for a given electrochemical reaction. According to Kuhl et al. [177], there are more than 16 possible products, as shown in Figure. 4-4a, which include a wide range of glyoxal, acetate, glycolaldehyde, ethylene glycol, acetaldehyde, ethylene, ethanol, hydroxyacetone, alyl alcohol, acetone, and propanol, which have been identified for the CO_2RR on a Cu catalyst, as listed in Figure 4-3, including the possible C_1 and C_2 pathways. Figure 4-4b shows the proposed reaction pathways for CO_2RR possible products via alkene and alcohol intermediates. It represents a complex reaction network and leads to many products sharing similar reaction intermediates. However, most of these detailed mechanistic elementary steps have yet to be confirmed by experimental studies of possible products, which include ethylene, glycolaldehyde, glycol, hydroxyacetone, glyoxal, and acetone. They are oxygenated beyond the C1 hydrocarbon fuel pathway and have yet to be reported on a catalyst without Cu to the best of our knowledge. If we consider these pathways, some C-C coupling occurs between some C1 species, such as the $*CH_2$ or CO dimerization pathway, at this early stage of CO_2 reduction. In addition, some CO_2RR products are oxygenates, suggesting that the C-C coupling step occurs before two CO dimerizations. These C1 hydrocarbon species can C-C couple to form all of the possibilities beyond C1 products. If the C-C coupling steps are kinetically accessible to explain the C^{2+} products, the enol-like intermediates are a primary conduit by which C2 and C3 products are produced. Further study is needed to fully clarify the CO_2 reduction mechanisms on the Cu catalyst. The proposed C2 and C3 pathway results can help search for C2 and C3 hydrocarbon products, which are involved in C-C coupling based on CO_2 reduction. This thesis summarizes recent reports on the electroreduction of CO_2 beyond C1 hydrocarbon fuels on non-Cu catalysts, focusing on the mechanisms of C-C and the coupling mechanism between the dimerization of two $*CH_2$ or CO intermediates in the CO_2RR. Furthermore, non-Cu data, including that of pure metals, carbon-based materials, metal alloys, metal oxides, and metal complexes, have been reported for the CO_2RR to multicarbon products.

4.4 NRR (N_2 fixation)

As society continues to develop, the growing environmental concerns and increasing population will result in a pressing energy crisis. There is an urgent need to search for sustainable, green strategies that can solve these problems. Ammonia is an essential raw material used both in agriculture and industrial chemicals and is therefore closely involved in human activities. Currently, the fixation of industrial nitrogen depends mainly on technology that uses the Haber–Bosch process. However, nitrogen molecules are highly stable and are particularly difficult to activate with a bond energy of -92.4 kJ/mol, meaning that realization of the Haber–Bosch process requires a high temperature and pressure (300–500 °C and 200–300 atm) environment, which leads to increased energy consumption and environmental pollution. Thus, the search for a sustainable and clean approach to the production of synthetic ammonia is gaining increasing attention from the scientific community. Inspired by the fixation of biological nitrogen with nitrogenase, the electrocatalytic reduction of nitrogen via fixation has been proposed as one of the most attractive and high-efficiency approaches for producing ammonia by weakening but not directly breaking the inert N≡N bond under acidic conditions via multiple successive protonation steps. The electrochemical nitrogen reduction reaction (NRR) has spurred a growing interest because it is more efficient, sustainable, environmentally friendly, and cost-effective than the Haber–Bosch process. In this regard, the exploration and design of suitable catalysts that can lead to sufficient activation to reduce nitrogen to ammonia under ambient conditions during the electrochemical reduction of N_2 to NH_3 are crucial. A simple illustration of the electrocatalytic reaction is the attachment of nitrogen molecules to an electrode surface, reduced by electrons supplied by an external circuit. The process involves the transfer of six proton-electron pairs during ammonia ($N_2 + 6H^+ + e^- \rightarrow 2NH_3$). The main challenge in the electrocatalytic reduction of N_2 to ammonia is determined by the activity and selectivity of the electrocatalysts. Therefore, the practical design of efficient, active, and durable NRR electrocatalysts is still a challenge for practical applications. Some renewable energy sources have been applied to drive N_2 reduction reactions, such as solar and wind power, and have been verified as the most effective strategies for reducing N_2 to NH_3. Furthermore, protons can be obtained from water electrolysis during the electrochemical NRR process.

The elementary steps of the electroreduction of N_2 conversion into NH_3, with six transferred proton and electron pairs, can be summarized as follows.

$$N_2 + 6H^+ + 6e^- \rightarrow 2NH_3 \quad \textbf{(4-1)}$$

$$* + \mathrm{N_2} + \mathrm{H^+} + \mathrm{e^-} \rightarrow * \mathrm{NNH} \quad \textbf{(4-2)}$$

$$* \mathrm{NNH} + \mathrm{H^+} + \mathrm{e^-} \rightarrow * \mathrm{NNH_2} \quad \textbf{(4-3)}$$

$$* NNH_2 + \mathrm{H^+} + \mathrm{e^-} \rightarrow * \mathrm{N} + \mathrm{NH_3} \quad \textbf{(4-4)}$$

$$* \mathrm{N} + \mathrm{H^+} + \mathrm{e^-} \rightarrow * \mathrm{NH} \quad \textbf{(4-5)}$$

$$* \mathrm{NH} + \mathrm{H^+} + \mathrm{e^-} \rightarrow * \mathrm{NH_2} \quad \textbf{(4-6)}$$

$$* \mathrm{NH_2} + \mathrm{H^+} + \mathrm{e^-} \rightarrow * \mathrm{NH_3} \quad \textbf{(4-7)}$$

$$* \mathrm{NH_2} + \mathrm{H^+} + \mathrm{e^-} \rightarrow * \mathrm{NH_3} \quad \textbf{(4-8)}$$

$$* \mathrm{NHNH} + \mathrm{H^+} + \mathrm{e^-} \rightarrow * \mathrm{NHNH_2} \quad \textbf{(4-9)}$$

$$* \mathrm{NHNH_2} + \mathrm{H^+} + \mathrm{e^-} \rightarrow * \mathrm{NH_2NH_2} \quad \textbf{(4-10)}$$

$$* \mathrm{NH_2NH_2} + \mathrm{H^+} + \mathrm{e^-} \rightarrow * \mathrm{NH_2} + \mathrm{NH_3} \quad \textbf{(4-11)}$$

$$*NHNH_2 + H^+ + e^- \rightarrow *NH + NH_3 \quad \textbf{(4-12)}$$

$$*NH_2NH_2 + H^+ + e^- \rightarrow *NH_2 + NH_3 \quad \textbf{(4-13)}$$

The reaction involves the intermediates *NNH, *NNH_2, *N, *NH, *NH_2, *NHNH, *$NHNH_2$, *NH_2NH_2, and *NH_3. The standard potentials vs. reversible hydrogen electrode (RHE) as a reference can be expressed as follows:

$N_2(g) + 6H^+ + 6e^- \rightleftarrows 2NH_3(g)$, $E^0 = +0.55$ V vs. RHE **(4-14)**

$2H^+ + 2e^- \rightleftarrows H_2(g)$, $E^0 = 0$ V vs. RHE at pH = 0 **(4-15)**

$N_2(g) + H^+ + e^- \rightleftarrows N_2H(g)$, $E^0 = -1.10$ V vs. RHE **(4-16)**

$N_2(g) + 2H^+ + 2e^- \rightleftarrows N_2H_2(g)$, $E^0 = -0.36$ V vs. RHE **(4-17)**

Many results for electrochemical N_2 reduction on 2D materials have been reported. A series of 2D nonprecious metal catalysts that have high catalytic performance in producing NH_3 have been found, such as single-atom catalysts in which the transition metal is supported on g-CN, transition metal carbides (MXenes), transition metal borides (MBenes), and transition-metal disulfides (TMDs). Searching and screening new types of highly efficient catalysts that possess high stability, catalytic activity, and selectivity is essential for ammonia production via electrochemical nitrogen reduction reactions. Guo X. et al. [178] reported a computational screening approach to explore catalysts with high selectivity and activity for the NRR of the transition-metal diborides (MBene), and they reported the excellent N_2 capture behavior of 2D MBenes with which N_2 can be activated to convert into NH_3. Furthermore, 2D transition metal carbides (MXenes) are a promising class of 2D materials for electrochemical N_2 fixation; MXenes exhibit an excellent metallic character. Systematically researching the potential application of single-atom embedded defective $Mo_2TiC_2O_2$ for the electrochemical reduction of N_2 to NH_3 suggests that these transition metals exhibit excellent catalytic activity for NRR when supported on insufficient $Mo_2TiC_2O_2$ MXene layers. Recently, Sun et al. [179] found that the edges and defects of 2D MoS_2 transition-metal disulfides (TMDs) play an essential role in N_2 fixation by creating defects and edges that can enhance the Faradaic efficiency and NH_3 yield during the NRR process, as high-efficiency catalysts are suitable for electrochemical nitrogen fixation.

4.5 NORR (nitric oxide pollution)

Due to the increase in the concentration of nitrogen oxide (such as NO_2 and NO) in the environment, nitrogen pollution has become a global problem accompanied by human activities and economic growth, seriously polluting water resources and air and further threatening human health. Some advanced technologies include improving the combustion process and equipment or using catalytic reduction absorption and other nitrogen removal methods. In addition, facilitating the recycling and utilization of nitrogen oxides (NO_x) in exhaust gas or the harmless treatment of NO_x has also been considered; however, finding a solution to the nitrogen oxide pollution problem is still a challenging task. NO is thermodynamically stable under normal conditions. The electrochemical NO reduction reaction (NORR) has been confirmed as a prospective approach for transforming NO into harmless (N_2) products or, even better, into value-added products (NH_3). In particular, it provides a competitive route to synthesize ammonia (NH_3) by electrochemical NO reduction on a given catalyst, accompanied by the transfer of five proton-electron pairs ($NO + 5H^+ + 5e^- \rightarrow NH_3 + H_2O$) during the electrochemical process. This process can be used to synthesize ammonia under ambient conditions using renewable wind and solar power. In this regard, converting NO to NH_3 is a practical strategy to solve the plight

threatening both energy and the environment, and the reduction of NO to NH_3 is considered feasible. NO is an essential accessible form of nitrogen obtained from industrial waste gas, automobile exhaust, the electrochemical oxidation of nitrogen, and the nitrification of bacteria. NO is a significant pollutant produced during the combustion of fossil fuels. Developing more effective methods to reduce NO emissions from combustion is essential to control and reduce NO pollutant emissions that reach the atmosphere. The electrochemical conversion into N_2 or NH_3 is an exothermic process, which suggests that this process is thermodynamically favorable and can be kinetically facilitated under ambient conditions. However, the strong N-O bond (204 $kJmol^{-1}$) is challenging to break directly, meaning that a suitable catalyst and a low applied potential are needed. In electrochemical applications, the selective catalytic reduction of NO to NH_3 is a common process used as a typical technology in practical applications.

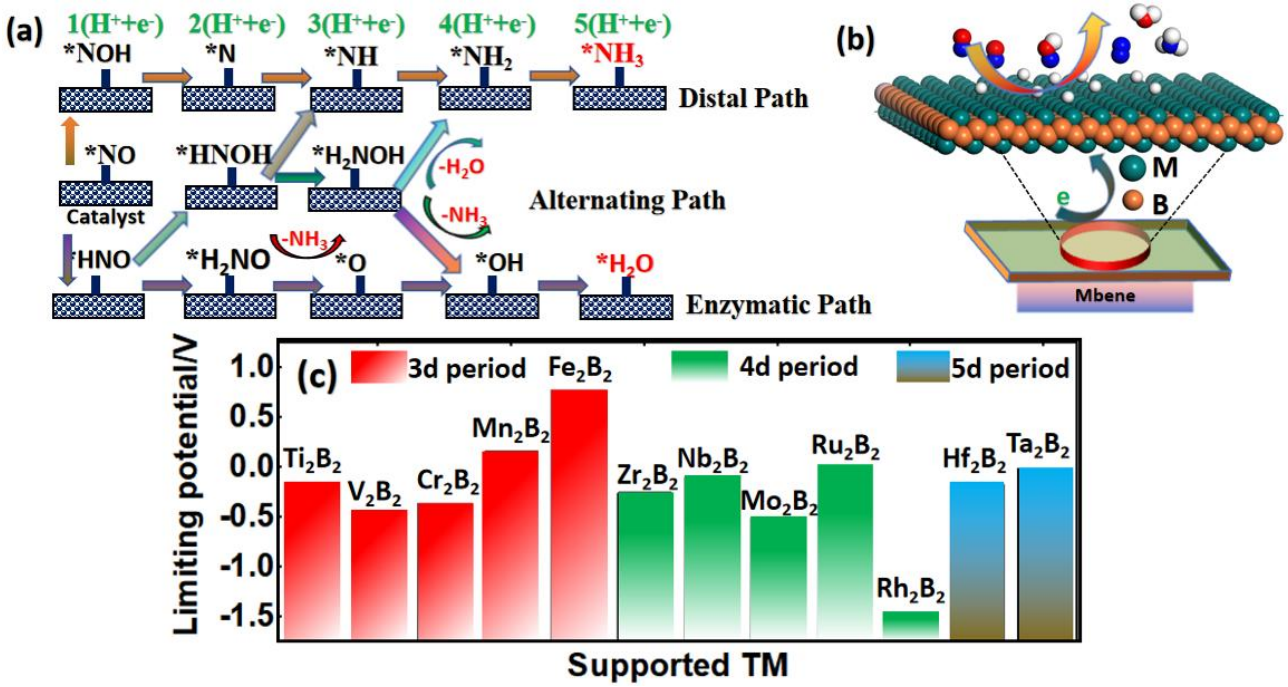

Figure 4-5 (a) Proposed full reaction mechanism for NO reduction to NH_3. (b) Schematic of the NORR on 2D Mo_2B_2. (c) Limiting potentials are summarized for each MBene.

The elementary reaction steps in the NO electrochemical reduction suggest that the formation of NH_3 occurs via five transferred proton and electron pairs. The overall reaction steps are summarized as follows:

$$NO + 5H^+ + 5e^- \rightarrow NH_3 + H_2O \quad \textbf{(5-1)}$$

Nitric oxide reduction (NORR) involves the intermediates *NOH, *N, *NH, *NH_2, *NH_3, *HNO, *H_2NO, *O, *HNOH, *H_2NOH, and *OH. The N-end pathway along the distal pathway is considered the most favorable pathway for MBenes, and the elementary steps are described as follows:

$$* + NO + H^+ + e^- \rightarrow *NOH \quad \textbf{(5-2)}$$

$$*NOH + H^+ + e^- \rightarrow *N + H_2O \quad \textbf{(5-3)}$$

$$*N + H^+ + e^- \rightarrow *NH \quad \textbf{(5-4)}$$

$$*NH + H^+ + e^- \rightarrow *NH_2 \quad \textbf{(5-5)}$$

$$*NH_2 + H^+ + e^- \rightarrow *NH_3 \quad \textbf{(5-6)}$$

$$* + NO + H^+ + e^- \rightarrow *HNO \quad \textbf{(5-7)}$$

$$*HNO + H^+ + e^- \rightarrow *H_2NO \quad \textbf{(5-8)}$$

$$*H_2NO + H^+ + e^- \rightarrow *O + NH_3 \quad \textbf{(5-9)}$$

$$*O + H^+ + e^- \rightarrow *OH \quad \textbf{(5-10)}$$

$$*OH + H^+ + e^- \rightarrow *H_2O \quad \textbf{(5-11)}$$

$$*HNOH + H^+ + e^- \rightarrow *NH + H_2O \quad \textbf{(5-12)}$$

$$*H_2NOH + H^+ + e^- \rightarrow *OH + NH_3(g) \quad \textbf{(5-13)}$$

$$*N + *N \rightarrow *N_2 \quad \textbf{(5-14)}$$

$$*N + NO_{(g)} \rightarrow *N_2O \quad \textbf{(5-15)}$$

Nitric oxide reduction (NORR) involves the intermediates *NOH, *N, *NH, *NH_2, *NH_3, *HNO, *H_2NO, *O, *HNOH, *H_2NOH, and *OH. Furthermore, *N may lead to the production of the byproduct N_2 or N_2O accompanied by the transfer of two proton and electron pairs on the catalyst.

Although the electrochemical reduction method has been widely applied, the catalysts used are usually precious metals with high costs; therefore, the exploration for efficient and inexpensive catalysts is urgently needed. The reduction of NO by protonation via electrocatalysis is a promising feasible method in an acidic environment, as inferred by the results of this thesis. A recent mechanistic study of nitric oxide reduction by Bai, Y., & Mavrikak, M. [180] reported that NO could be reduced to NH_3 on Pt (111) and found that a direct NO dissociation path is preferred to one that includes the intermediates *HNO and *NOH and that the NO dissociation mechanism is indeed more favorable on Pt (111). Saeidi N. [181] also reported that NO's electrochemical reduction is an efficient approach for nitrogen recycling on single-atom catalysis SiN_4-embedded graphene; the authors studied it in depth using the DFT approach. Based on their results, NO can be highly activated via a single-atom electrocatalyst and exhibits excellent activity for NORR molecules with a limiting potential of 0.56 eV on SiN_4-embedded graphene electrocatalysts under ambient conditions. This study provides new insights into the exploration and design of efficient catalysts for the electrochemical reduction of NO molecules.

4.6. Stability and Selectivity (Single-atom Catalysis)

To gain further insight into the stability of catalyst materials in electrocatalytic systems, the formation energy and dissolution potential of surface metal atoms can be studied as they play an essential role in evaluating stability. Several studies have reported the dissolution potential to reduce Pt in nanoparticulates, especially in single-atom catalysis (SAC) systems. The catalytic activity is typically determined by the Pt transition metal atom of the surface and lowering the trend of the dissolution potential is similar to that of all transition metals. Thus, we evaluated the thermostabilities of these M@N_4G single-atom catalysts based on not only the formation energy E_f but also the dissolution potential [182] U_{diss} (Figure 4-6), which were calculated by the following equation:

$$E_f = E_{M@NC} - E_{NC} + 6\mu_C - 4\mu_N - E_M < 0 \quad \textbf{(6-1)}$$

$$U_{diss} = U^o_{diss}(\text{metal,bulk}) - E_f / ne \quad \textbf{(6-2)}$$

where $E_{M@NC}$ and $E_{M@NC}$ are the total energy of the M@NC and NC substrate, respectively, in their ground state. Furthermore, μ_N, μ_C, and μ_M represent the chemical potentials of nitrogen, carbon, and metal atoms, respectively, which can be derived from the total electronic energy of carbon or N_2 molecules. Meanwhile, 6 and 4 are the number of carbon and nitrogen atoms removed from the intrinsic graphene during the construction of a single-atom

catalyst, respectively. U^{o}_{diss}(metal,bulk) is the standard dissolution potential, and n is the number of electrons transferred during dissolution. According to this definition, if the reaction systems have $E_f < 0$ eV, they can be confirmed to be thermodynamically stable systems, while materials with $U_{diss} > 0$ V vs. CHE are considered electrochemically stable. In addition, the binding energy of the metal atom embedded at the SV-G site with vdW correction was adopted by using Grimme's DFT-D3 approach. In this thesis, the adsorption energy is defined as:

$$\Delta E_{ads}^{vdW-DF3} = E_0^{vdW-DF3}[M@SV-G] - E_0^{vdW-DF3}[SV-G] - E_0^{vdW-DF3}[M] \quad \textbf{(6-3)}$$

where E_0 represents the ground state energy of the atom adsorbed on graphene [A@SV-G], the single vacancy of graphene [SV-G], and the isolated metal atom [A], respectively. When Eads is negative, the adsorption is exothermic. We further considered the formation energetics of vacancies, and the vacancy formation energy (E_{vf}) was calculated as:

$$\Delta E_0 = E_0[SV-G] - \frac{n-1}{n} E_0[G] \quad \textbf{(6-4)}$$

where E_0[SV-G] and E_0[G] are the total energies of the vacancy and pristine graphene sheet, respectively, and n represents the number of carbon atoms in the system. The metal-support interaction plays a vital role in heterogeneous catalysis, especially because the catalytic activity of single-atom catalysts directly depends on the electronic properties of the metal atoms. The diffusion and aggregation effect of the metal could decrease the activity and stability of the catalysts. Thus, further evaluation of the binding of g energies (E_b) and cohesive energy in biatom catalysts is needed. Since binding of the metal atom at vacancy graphene sheet sites with N_4-G links is thermodynamically favorable, it is still possible for the metal atoms to aggregate on the support. Thus, we considered the difference in binding energy (E_b) on the supports and the cohesive energies (E_c) of each metal atom in the bulk crystal to confirm that the energy barrier can limit the diffusion and aggregation of metal atoms. The following equations can be used to calculate Eb and Ec:

$$E_b = -E(M@N_4C_x) - E(M_{single}) \quad \textbf{(6-5)}$$

$$E_c = -E(M_{bulk})/N - E(M_{single}) \quad \textbf{(6-6)}$$

where E(M_{bulk}) and E(M_{single}) are the energies of the bulk crystal and the isolated metal atom, respectively, and N is the number of isolated atoms in the bulk crystal.

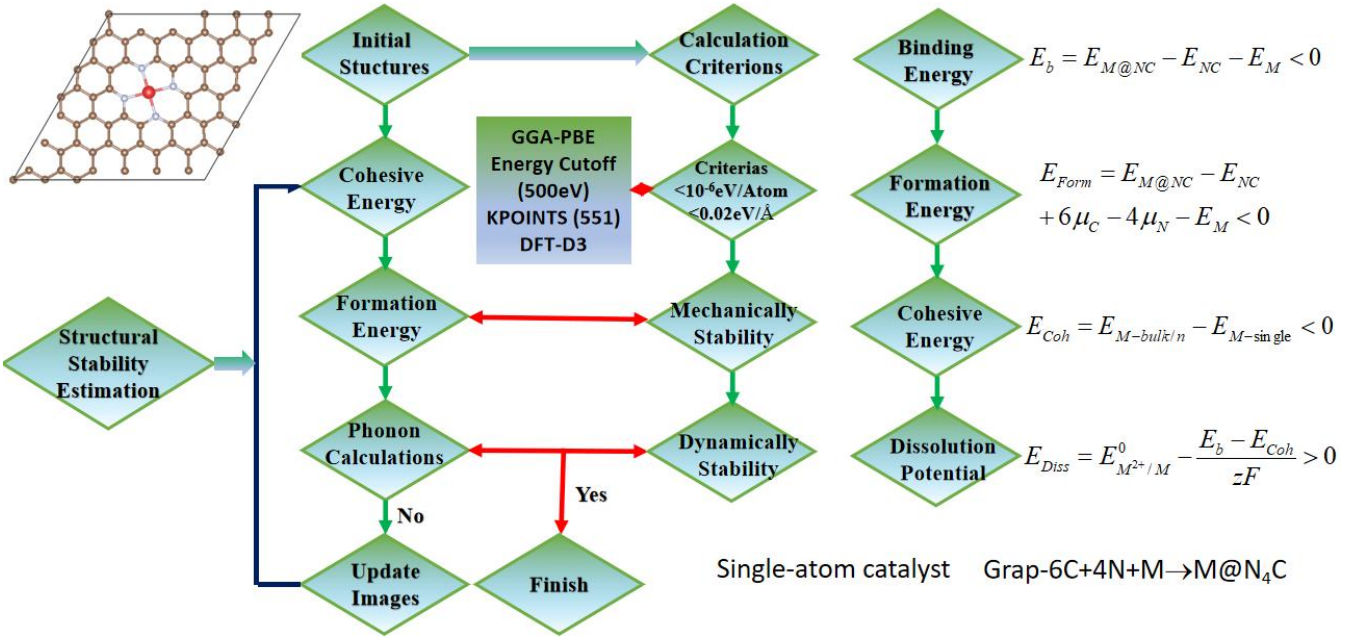

Figure 4-6. Structural stability estimation of 2D single-atom M@N_4G catalyst nanosheets

To understand the thermodynamic stabilities of SACs, we focused on graphene or BN monolayers when $E_b > E_c$, indicating that the binding of metal atoms with the support is thermodynamically more favorable than the aggregation of metal atoms from a thermodynamic point of view. By comparing the values of calculated E_c, E_b-E_c, and experimental E_c, some metal atoms showed negative values of E_b-E_c at specific defect sites, and the differences ($\Delta E_b=E_b-E_{coh}$) between the cohesive energies (E_{coh}) in their bulk crystal phase and binding energy were considered. When ΔE_b is more than zero, TM atoms possess higher stability than in their bulk phase. Otherwise, the opposite is true. In addition to the stability and activity, the selectivity for the electrocatalytic reaction is another significant factor impeding the development of efficient catalysts. To explore the selectivity of electrochemical reactions, competition and side reactions should be considered. The HER is often regarded as a significant competitive reaction. Taking the nitrogen reduction reaction on TM/g-CN as an example, to study the selectivity between the HER and NRR, an important descriptor is proposed, which is named faraday efficiency (FE), due to the strong binding between the H atom and active centers so that the HER competes with the NRR under the same conditions. Interestingly, the selectivity of NRR on a given catalyst should be evaluated for NRR activity. The *H may easily cover the active center and suppress the NRR activity. Thus, the adsorption energy difference between *H (ΔG_{*H}) and *N_2 (ΔG_{*N2}) can be used to investigate the selectivity of the NRR, and the values of ΔG_{*N2}-ΔG_{*H} are closely related to the favorable NRR selectivity.

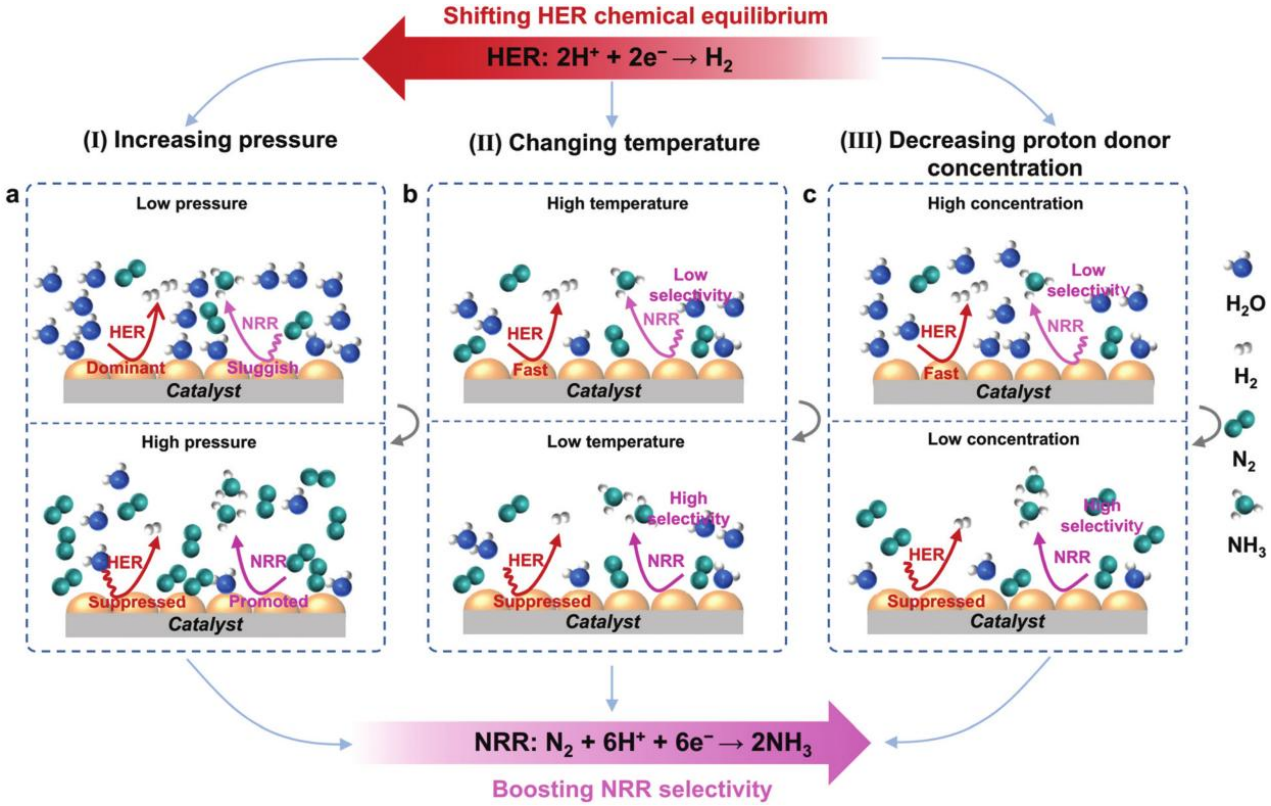

Figure 4-7. Strategies for shifting the chemical equilibrium to suppress the HER in the NRR process; (a) changing pressure, (b) changing temperature, and (c) changing proton donor concentration. (Reprinted with permission from the Royal Society of Chemistry, adopted from [183])

Furthermore, we considered the difference in the limiting potential between the HER and NRR based on rate-determining steps. The values of [U_L(NRR)-U_L(HER)] can be used to estimate the selectivity of catalysts, and the Faradic efficiency (FE) based on the Boltzmann distribution can effectively evaluate the competition between the HER and NRR. Depending on the Boltzmann distribution, [184] the selectivity of the NRR can be obtained from the equation below:

$$f_{\mathrm{NRR}} = 1/[1+\exp(-\Delta G / k_B T)]\times 100\% \quad \textbf{(6-7)}$$

where f_{NRR} is the selectivity toward NRR and T and ΔG represent the temperature and Gibbs free energy difference, respectively. Suppose the equation of FE can reach up to 100%, which means much better, by combining the activity (limiting potential) and selectivity (FE) analysis. In that case, the higher activity and selectivity are more favorable to the potential catalyst for NRR and could be identified by further experiments. Note that the value of [U_L(NRR)-U_L(HER)] with a more positive value shows a higher selectivity toward NRR for a given catalyst. The HER is the primary competing reaction to an electrocatalytic reaction in an acidic medium. Depending on some assumptions, if the proton and electron pair transfer are not the determining factors of the overall rate for both the HER and NRR and if only the HER and NRR are competing reactions, the selectivity of the NRR can be estimated based on Faradaic efficiency, which can be calculated from the Boltzmann distribution. It is widely believed that the HER is the major reaction competing with the NRR in electrochemical processes. The adsorbed *H could cover the active site (*H poisoned) and move toward the HER rather than the NRR, leading to a low FE. Thus, the Gibbs free energy of *H is an essential descriptor of the NRR selectivity, indicating that the competitive HER could be efficiently suppressed. As shown in Figure 4-9, the primary strategies for suppressing the competing HER have focused on the proton and electron-transfer kinetics in the electrocatalytic reaction process. However, the competing HER can also be suppressed by changing its chemical equilibrium, such as increasing the condition pressure, decreasing the concentration of the proton donor, and changing the reaction temperature, as shown in Figure 4-7.

5. Results and Discussions

In this chapter, the specific problems and challenges among those listed previously are addressed via our DFT calculation models, and we calculated them using the first-principles method in the Vienna Ab initio Simulation Package (VASP) software to verify whether these thermodynamically stable MBenes can actually be applied in electrocatalytic reactions. These include the carbon dioxide reduction reaction (CO_2RR), nitrogen reduction reaction (NRR), and nitric oxide reduction reaction (NORR). With these encouraging processes, can 2D transition metal borides (MBenes) enhance catalytic activity and high selectivity. What descriptors can be used to predict and explain the activity trends? What are the specific problems and challenges that are addressed via our high-throughput screening based on DFT calculations?

5.1 Synopsis of Publications

This chapter has been published, and the idea originated from M.Sc. Yi Xiao designed the research. The models were trained by M.Sc. Yi Xiao collected the stable crystal structures and generated the desired structures for DFT calculations by M.Sc. Yi Xiao processed and collected data, analyzed the results, and wrote, revised and submitted the manuscript, while my colleagues reviewed this article and made suggestions to improve it. The statement of the personal contribution of my publications with a declaration signed by the doctoral candidate, all coauthors and the academic supervisor will be attached in the next section (5.2).

5.1.1 ORR (Fuel Cell)

Publication I: High-Throughput Approach Exploitation: Two-Dimensional Double-Metal Sulfide (M_2S_2) of Efficient Electrocatalysts for Oxygen Reduction Reaction in Fuel Cells. This article has been published as **Xiao Y*,** Tang L. High-Throughput Approach Exploitation: Two-Dimensional Double-Metal Sulfide (M_2S_2) of

Efficient Electrocatalysts for Oxygen Reduction Reaction in Fuel Cells[J]. ***Energy & Fuels***, 2020, 34(4): 5006-5015.; following is the overview of publication I.

Overview of publication I: High-Throughput Approach Exploitation: Two-Dimensional Double-Metal Sulfide (M_2S_2) of Efficient Electrocatalysts for Oxygen Reduction Reaction in Fuel Cells. (Highlight of 2D M_2S_2)

In previous research, it has been observed that the oxygen reduction reaction (ORR) plays an important role in energy storage and conversion, such as in fuel cells, lithium-sulfur batteries and metal-air batteries. However, the slow kinetic characteristics of the ORR limit its development in practical applications. Thus, exploring and designing efficient catalysts are becoming increasingly urgent. Fortunately, Pt-based catalysts have been identified to have superior activity and stability among the underlying catalysts. However, the low reserve in Earth's crust results in high prices of Pt-based catalysts at present. Thus, we precluded the possibility of its widespread application in practice, but it provides great motivation to explore nonprecious metal catalysts with high efficiency for the ORR. 2D transition-metal dichalcogenide (TMD) materials have been reported to possess good mechanical stability, active site diversity and a large specific surface area. Therefore, TMDs can serve as a typical 2D traditional representative electrocatalyst and have been applied in hydrogen evolution reactions (HERs) and hydrogenation reactions, which have been reported in both theoretical and experimental studies. In this article, we propose a new type of metal sulfide (M_2S_2) crystal structure that is similar to TMDs (MS_2). We found that this type of M_2S_2 compound can tune the electronic structure to enhance catalytic activity based on the difference in electronegativity between the metal and the sulfur atoms. They can serve as a new TMD family, and the ratio of transition metals and sulfides have different chemical formulas, such as MS, MS_2, M_2S_2 and M_3S_4. The first publication of this PhD dissertation is a comprehensive study focusing on the transition metal sulfide (M_2S_2) nanolayer as a catalyst for ORR by high-throughput approach exploitation. The ORR reaction mechanism on M_2S_2 under acidic conditions (pH = 0) is more preferable via the four-electron transfer than the two-electron transfer pathway, which is illustrated in Figure 5-1e.

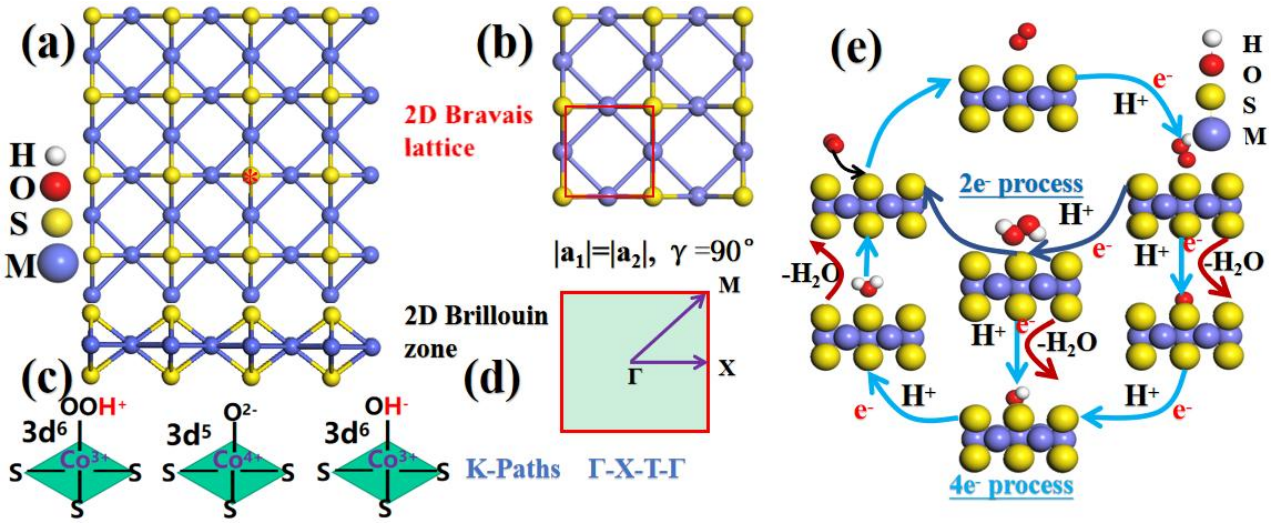

Figure 5-1 (a) Crystal structure of double metal sulfide (M_2S_2), (b) The active center site of M_2S_2 catalysts. (c) Schematic of orbital splitting with ORR intermediate species. (d) Schematic of the Brillouin zone. (e) Entire mechanism for the ORR as proposed.

In the initial stage, one $*O_2$ molecule is adsorbed on M_2S_2 with one H^++e^- coupling pair transfer, leading to the production of *OOH at the first hydrogenation step. Next, one more H^++e^- pair continues hydrogenating to the first H_2O molecule, leaving one atomic *O. Then, the next subsequent two H^++e^- pairs react with *O to form

the second *H_2O molecule. The elementary reaction steps via four $4e^-$ transfer pathways, formation energies for each intermediate (ΔG_{*OOH}, ΔG_{*O}, and ΔG_{*OH}) and the reaction energy of each elementary step can be expressed as follows:

$$*+O_2+H^++e^-\rightarrow *OOH \quad \textbf{(5-1-1)}$$

$$\Delta G_{*OOH}=G_{*OOH}-G_*-(G_{O_2}+1/2G_{H_2})$$

$$\Delta G_1=\Delta G_{*OOH}-4.92$$

$$*OOH+H^++e^-\rightarrow *O+H_2O \quad \textbf{(5-1-2)}$$

$$\Delta G_{*O}=G_{*O}+G_{H_2O}-G_*-(G_{O_2}+G_{H_2})$$

$$\Delta G_2=\Delta G_{*O}-\Delta G_{*OOH}$$

$$*O+H^++e^-\rightarrow *OH \quad \textbf{(5-1-3)}$$

$$\Delta G_{*OH}=G_{*OH}+G_{H_2O}-G_*-(G_{O_2}+3/2G_{H_2})$$

$$\Delta G_3=\Delta G_{*O}-\Delta G_{*OH}$$

$$*O+H^++e^-\rightarrow *+H_2O(l) \quad \textbf{(5-1-4)}$$

$$\Delta G_{*H_2O}=G_{*H_2O}+G_{H_2O}-G_*-(G_{O_2}+2G_{H_2})$$

$$\Delta G_4=-\Delta G_{*O}$$

Furthermore, the elementary reaction step with the lowest downward energy of the ORR is defined as the rate-determining step (RDS). In this regard, the limiting potential was obtained from the rate-determining step, and the overpotential was calculated based on the equilibrium potential (1.23 V), which is a criterion to evaluate the catalytic activity of M_2S2. The ORR overpotential (η_{ORR}) is defined as follows:

$$\eta ORR=\max\{-\Delta G_1,-\Delta G_2,-\Delta G_3,-\Delta G_4\}/e+1.23 \quad \textbf{(5-1-5)}$$

This result indicates that some M_2S_2 compounds are stable and can be successfully synthesized. Remarkably, Zr_2S_2 and Mo_2S_2 exhibited catalytic activity with low overpotentials of 0.22 V and 0.47 V, respectively. These two candidates were considered outstanding catalysts for the ORR. The volcano plots were established based on the scaling relation of limiting potential depending on the reaction energy of the *OOH, *O, and *OH steps. The activity of promising candidates was evaluated by the descriptors of the ΔG_{*O} - ΔG_{*OH} and d-band center, which was performed to understand the ORR activity essence. Furthermore, the linear scaling relationship approach was used to analyze the intrinsic correlation between the activity and the structural features. Our theoretical calculation not only provides a way to generate effective descriptors for screening criteria but also provides guidance for the discovery and design of high-performance catalysts for fuel cells. Moreover, some other important descriptors are also considered, and they can provide more detailed descriptors to reveal the origin of adsorption properties. For example, the charge transfer (Q_e) and crystal orbital Hamilton population (COHP) are more related to the adsorption behavior, with feature relative importance values of 68.22% and 17.98%, respectively. Therefore, the high-throughput screening approach is very helpful for understanding the intrinsic correlation between the catalytic activity and the structural properties of the ORR on M_2S_2-like TMDs.

5.1.2 CO_2RR (CO_2 capture)

CO_2 capture and electroreduction to a series of value-added hydrocarbon fuels have attracted many researchers. CO_2RR has been proposed as a multistep H^+/e^- pair transfer process and involves 16 different

products that have been observed on a pure Cu electrode surface. The process includes many viable reaction pathways. Developing and designing a promising catalyst for the CO_2RR has many challenges, and it not only requires a relatively low overpotential but also needs to enhance selectivity toward a given product. In this thesis, we focus on $M_3(HITP)_2$ prototype 2D MOF compounds. M_3C_2 MXenes and MBenes serve as promising candidate catalysts and can serve as our screening target material. We propose a feasible strategy to explore high-efficiency catalysts for CO_2 electroreduction based on Sabatier's principle in this thesis. The interactions between CO_2RR intermediate species and MXenes have been studied by a theoretical screening approach due to their potential application in CO_2 electrocatalytic reduction reactions. The CO_2RR can serve as a prototype reaction for the search for electrocatalytic reactions for energy conversion because it not only reduces CO_2 emissions but also produces some value-added hydrocarbon fuels and useful chemicals; it can also be representative of several electrochemical energy conversion reactions. It has been reported that the CO_2RR yields several different products, such as CO, HCOOH, CH_3OH and CH_4, and only the hydrogen evolution reaction (HER) is considered a competing process. The reaction intermediate species include carbon-binding species (CO, CHO, COH, CHOH, COOH, and CH_x) and oxygen-binding intermediate species (HCOO, CHO, CH_3O and CH_3OH). However, these reaction mechanism pathways are competitive and coupled during the CO_2RR, and gaining insight into their individual reaction mechanisms and guiding the development and design of high-performance electrocatalysts still involve many challenges.

Some primary elementary reactions of the reaction mechanism for CO_2RR are listed below; they may determine the preferable reaction paths and achieve the desired products.

$$*+CO_2+H^++e^-\rightarrow *COOH/*HCO_2 \quad \textbf{(5-2-1)}$$

$$*COOH+H^++e^-\rightarrow *CO+H_2O \quad \textbf{(5-2-2)}$$

$$*HCO_2+H^++e^-\rightarrow *HCOOH \quad \textbf{(5-2-3)}$$

$$*CO+H^++e^-\rightarrow *CHO \quad \textbf{(5-2-4)}$$

$$*CHO+H^++e^-\rightarrow *HCHO \quad \textbf{(5-2-5)}$$

$$*HCHO+H^++e^-\rightarrow *CH_3O \quad \textbf{(5-2-6)}$$

$$*CH_3O+H^++e^-\rightarrow *O+CH_4 \quad \textbf{(5-2-7)}$$

$$*O+H^++e^-\rightarrow *OH \quad \textbf{(5-2-8)}$$

$$*OH+H^++e^-\rightarrow *H_2O \quad \textbf{(5-2-9)}$$

Publications II, III and IV of this thesis reported that the exposed surface metal atom is most likely to serve as the active site for the CO_2RR, indicating that the primary reaction pathway $*CO+H^++e^-\rightarrow *CHO$ can serve as the rate-determining step of *COOH → *CO → *CHO, leading to either CH_3OH or CH_4 formation under a moderate applied potential. For example, $Cr_3(HITP)_2$ and $Mn_3(HITP)_2$ are both predicted to be most efficient in promoting the CO_2RR toward CH_4 and CH_3OH with a low overpotential. Furthermore, because the binding strengths of *OH and *CO can serve as effective descriptors so that we can identify the activity and selectivity for the CO_2RR on various MBenes, it has been reported that moderate oxyphilic species (OH) and carbophilic species (CO) interact with TM. Thus, these articles highlight the most important aspect of breaking the linear scaling relationships of *OH and *CO' binding at the most active site for evaluating CO_2RR performance. The scaling relationships and volcano plots are established depending on the binding energies of *OH and *CO. To further gain an understanding of the quantum mechanical screening aspects, we calculated the limiting potentials (U_L) for each elementary step during the CO_2RR process as a function of ΔG_{*CO} and ΔG_{*OH}. Because their binding strength is strongly associated with the electronic properties of the active site, they can be used to

evaluate the importance of adsorbate interactions to the active site. Specifically, ΔG_{*CO} plays a significant descriptor role in evaluating the overpotential for producing CH_3OH and CH_4, while ΔG_{*OH} is preferred to estimate the selectivity strength toward CH_4 or CH_3OH, and ΔG_{*OH} is also used as a descriptor to estimate catalytic activity for producing HCOOH. Depending on the descriptor methods, which provide an effective tool to achieve rapid screening of high performance for CO_2RR catalysts, the too strong or too weak binding strengths of oxophilic or carbophilic elements should be avoided, and the moderate binding strengths of oxophilic and carbophilic elements should be perfected. Furthermore, Nørskov et al. proposed d-band center theory to gain insight into the electronic structure of catalysts applied in electrochemical reactions, and it can serve as an effective descriptor that has been successfully applied to identify good catalysts.

Publication II: Mechanistic Study of Efficient Producing CO_2 Electroreduction via 2D Metal Organic Frameworks $M_3(HITP)_2$ Surface, This chapter has been published as **Xiao Y***, Shen C, and Chen R. Mechanistic Study of Efficient Producing CO_2 Electroreduction via 2D Metal Organic Frameworks $M_3(HITP)_2$ Surface[J]. ***Electrochimica Acta***, 2021: 138028. (**Highlight of 2D $M_3(HITP)_2$ MOF Materials).**

Overview of publications II: Mechanistic Study of Efficient Producing CO_2 Electroreduction via 2D Metal Organic Frameworks $M_3(HITP)_2$ Surface:

Publication II describes the study of the application potential of $M_3(HITP)_2$ prototype 2D MOF compounds in CO_2 electroreduction and found that these MOFs possess a high catalytic activity for the CO_2RR production of hydrocarbon fuels under low applied potentials. To achieve a credible and high-efficiency approach to designing and exploring the optimal reaction mechanism for the electrochemical process, it is important to identify the surface character of active sites and to set up suitable descriptors to evaluate their catalytic performance. As emerging 2D materials, the electrochemical properties and possible applications of MBenes require further exploration. Recently, owing to their high catalytic activity and highly competitive hydrogen evolution reaction (HER) side reactions, MBenes, such as Fe_2B_4 and Ru_2B_4, have been widely applied in the CO_2 reduction reaction (CO_2RR). However, the preferable reaction paths and catalytic activity are still hard to confirm during the electroreduction process and only depend on the computational model. The transition metal (TM) coordinated with nitrogen in the active center of $M_3(HITP)_2$ catalysts was identified to have strong M-C bond coupling, leading to a high selectivity toward CH_3OH, $Cr_3(HITP)_2$, and $Mn_3(HITP)_2$.

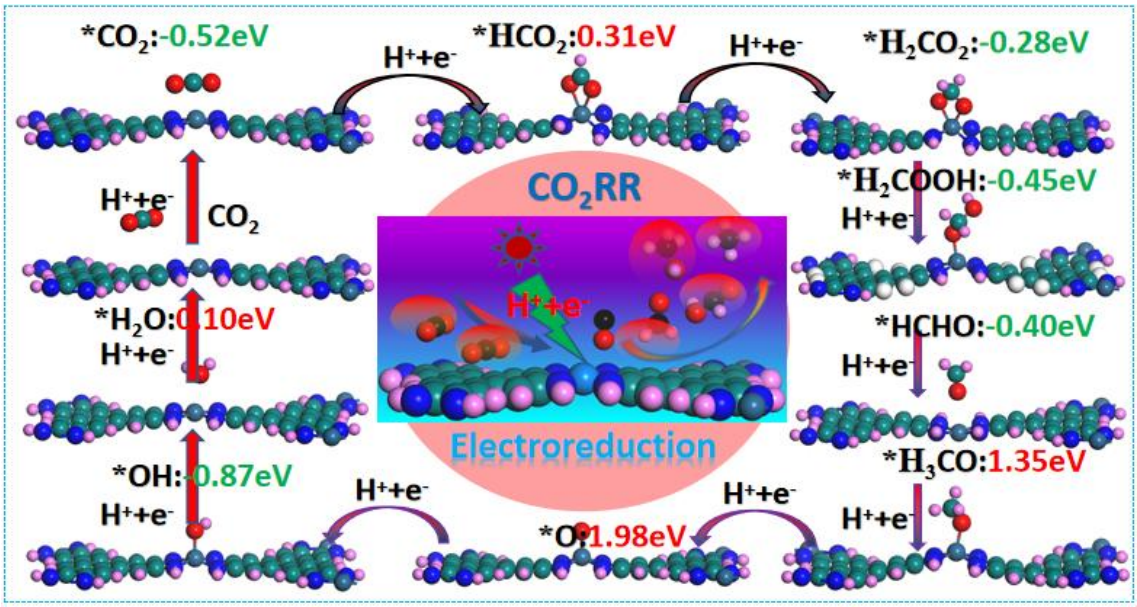

Figure 5-2. Side view of the optimization model based on all possible intermediates of CO_2 reduction to CH_4 via the $Pt_3(HITP)_2$ surface. * denotes the adsorbed states.

To achieve a credible and high-efficiency approach to designing and exploring the optimal reaction mechanism for the electrochemical process, it is important to identify the surface character of active sites and to set up suitable descriptors to evaluate their catalytic performance. As emerging 2D materials, the electrochemical properties and possible applications of MBenes require further exploration. Recently, owing to their high catalytic activity and highly competitive hydrogen evolution reaction (HER) side reactions, Fe_2B_4 and Ru_2B_4 have been widely applied in the CO_2 reduction reaction (CO_2RR). To gain further insight into the optimal reaction mechanism path and obtain targeted products during the CO_2RR, the authors considered all the possible intermediate species. The bonding strength of intermediate species can be determined by the metal-oxygen (M-O) bonds or metal-carbon (M-C) bonds. The catalytic activity depends on the limiting potential, which is calculated from the rate-determining step (RDS) via the most favorable path. Furthermore, the electronic properties of catalysts could also play a key role in the catalytic performance for the CO_2RR. Product selectivity was based on the bonding strength of C-bound or O-bound intermediates. Overall, 2D $M_3(HITP)_2$ MOF are suitable as promising catalysts for the CO_2RR with low limiting potential.

Publication III: High throughput screening of M_3C_2 MXenes for efficient CO_2 reduction conversion into hydrocarbon fuels. This chapter has been published as **Xiao Y***, Zhang W. High throughput screening of M_3C_2 MXenes for efficient CO_2 reduction conversion into hydrocarbon fuels[J]. ***Nanoscale***, 2020, 12(14): 7660-7673. **(Highlight of 2D M_3C_2 MXene Materials).**

Overview of publication III: High-throughput screening of M_3C_2 MXenes for efficient CO_2 reduction conversion into hydrocarbon fuels

This article explores the electrocatalytic conversion mechanism of CO_2 to produce methane (CH_4) as a hydrocarbon fuel, which has attracted intensive attention for producing renewable energies and reducing carbon dioxide emissions. The density functional theory (DFT) calculations combined with the CHE model were applied to study the hydrogenation of CO_2 on the two-dimensional (2D) M_3C_2 transition metal carbide (MXene) surface. It demonstrated that the adsorbed CO_2 is activated and can combine with surface hydrogen to form bicarbonate species, leading to selectivity that is more competitive for the CO_2RR than the HER. However, there are many challenges in designing catalysts while regulating the selectivity and activity during the electroreduction of CO_2, which is accompanied by the hydrogen evolution reaction (HER). 2D MXenes are new 2D materials that can catalyze the production of CH_4 from CO_2 with high Faraday efficiency and low limiting potential, indicating that MXene materials are attractive for producing clean hydrocarbon energy sources and chemical products from CO_2. At present, exploring the catalytic activity and kinetic stability of Mo_2CT_x and $Ti_3C_2T_x$ (MXenes) to catalyze CO_2 electroreduction to CH_4 has led to reports indicating that MXenes may be a new class of 2D candidate catalyst materials for producing CO_2. W_2CO_2 and Ti_2CO_2 have been identified as the most promising MXene candidates with low overpotential and excellent selectivity for CO_2 electroreduction.

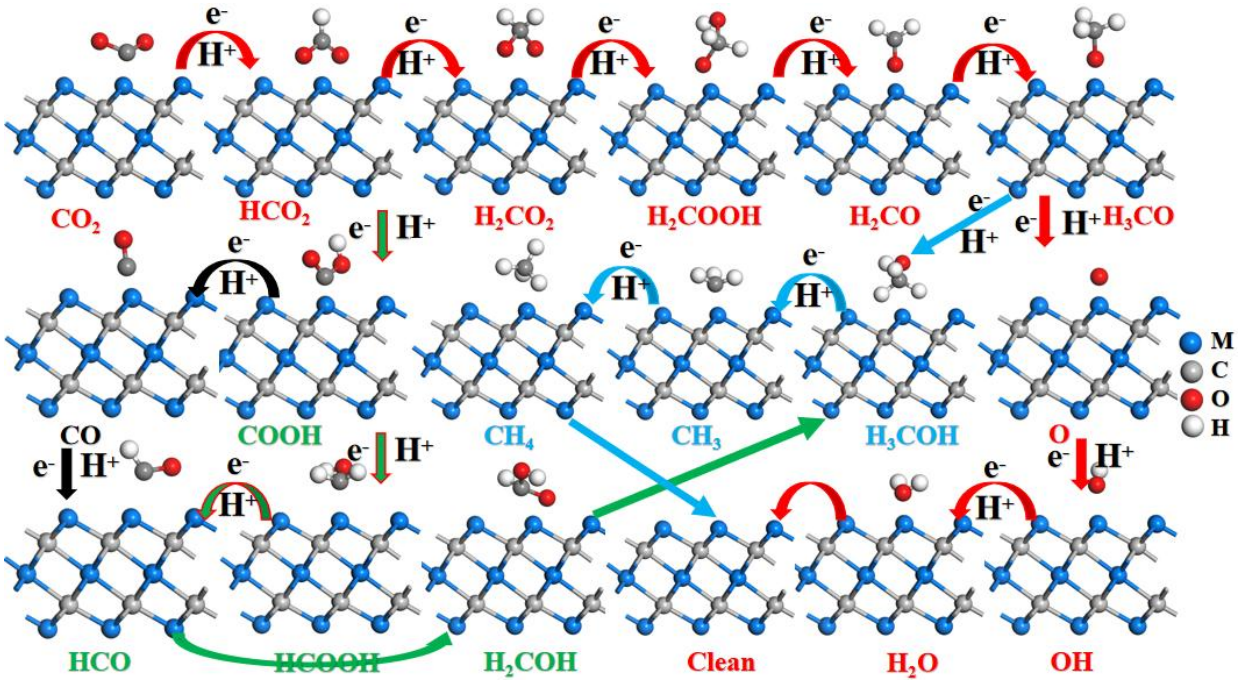

Figure 5-3. CO_2RR reaction mechanism to reduce C1 hydrocarbon products on M_3C_2 MXenes

Many complex elementary reaction steps may be involved during the conversion of electrical energy into chemical energy, meaning that electrochemistry plays a primary role in this field. To render the electrochemical reaction rate efficient and the mechanism path apparent, high catalytic activity and selectivity toward favorable reaction products of the catalyst are needed, accompanied by the possibility of converting CO_2 into renewable energy sources and other chemical products to enhance the carbon cycle. The selectivity for the product and the activity in terms of the reaction efficiency of a given catalyst are determined by the chemical properties at the surface-active site. Recent theoretical screening and electrochemical techniques have been carried out using DFT calculations within the VASP, which provides an atomic-scale approach for exploring the fundamental understanding of electrochemical reactions. The electroreduction of CO_2 to hydrocarbon fuels and other valuable chemical products is attractive for electrochemical applications in energy conversion and storage while also improving the climate from the carbon cycle perspective. DFT calculations have been used to evaluate the electrochemical reaction mechanism depending on the intermediates' binding energy and verify their catalytic activity and selectivity.

Publication IV: Quantum Mechanical Screening of 2D MBenes for the Electroreduction of CO_2 to C1 Hydrocarbon Fuels. This chapter has been published as **Yi Xiao***, Chen Shen, and Niloofar Hadaeghi. Quantum Mechanical Screening of 2D MBenes for the Electroreduction of CO_2 to C1 Hydrocarbon Fuels. ***Journal of Physical Chemistry Letters***. 2021, 12, 6370−6382. **(Highlight of 2D MBene Materials)**

Overview of publications IV: Quantum Mechanical Screening of 2D MBenes for the Electroreduction of CO_2 to C1 Hydrocarbon Fuels

This article presents quantum mechanical screening for producing C1 hydrocarbon fuels (such as CO, HCOOH, CH_3OH, and CH_4) from CO_2. We propose a new family of two-dimensional (2D) transition metal borides (MBenes) to design and explore new high-efficiency catalysts for CO_2 electroreduction using the density functional theory (DFT) approach. The reduction of CO_2 to C1 hydrocarbon compounds, such as carbon monoxide (CO), formic acid (HCOOH), methane (CH_4) and methanol (CH_3OH), was extensively studied.

Because methane is the main component of natural gas with high energy density and combustion heat, it is desirable to researchers.

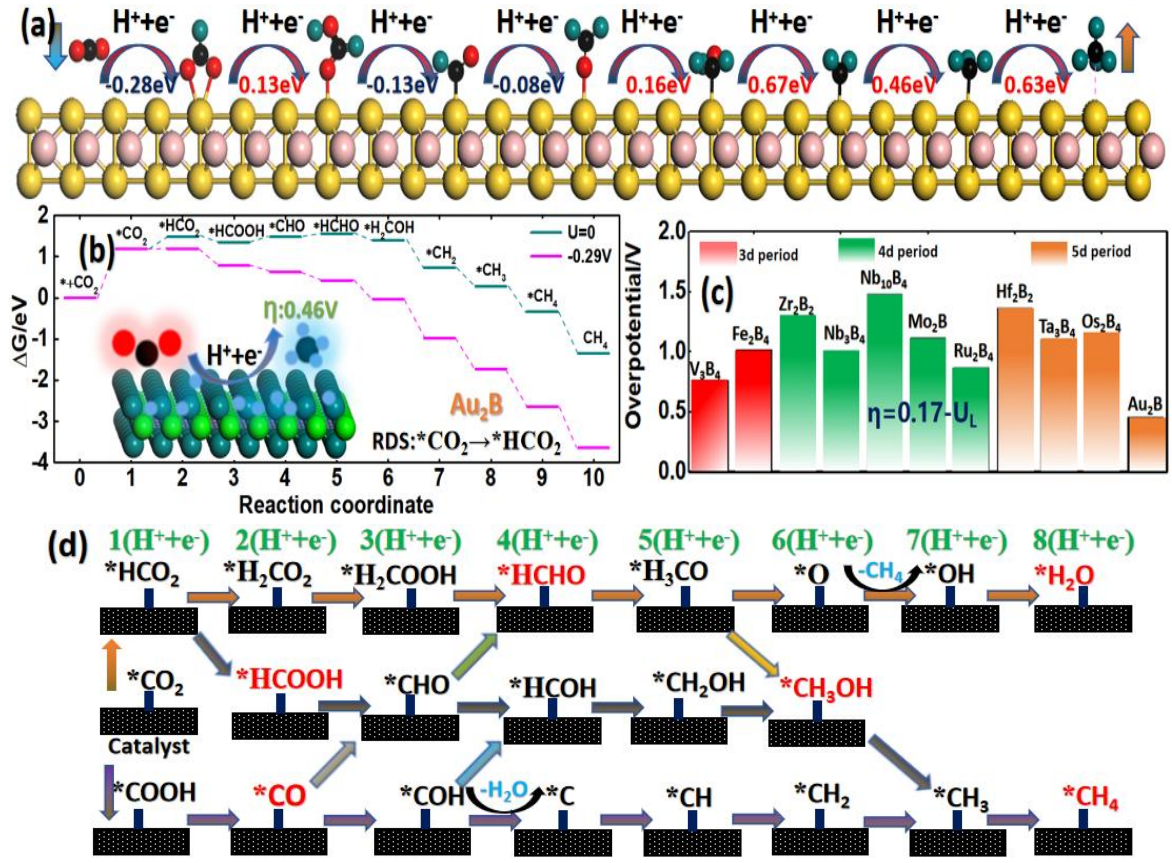

Figure 5-4 (a) Side view of the optimization structure for the CO_2RR catalyzed by Au_2B MBene, (b) Gibbs free energy diagrams of the CO_2RR under an electrode potential on Au_2B. (c) Summary of overpotentials for the CO_2RR on all considered MBenes. (d) A full reaction mechanism for the CO_2RR to C1 products.

We explored this new family of MBenes. Transition-metal diborides (MBenes) may also be a new family of two-dimensional catalysts, meaning that exploring and designing high-efficiency catalysts for the electroreduction of CO_2 on MBenes is expected to develop the field beyond the use of precious metal catalysts in the future. In addition, C_3N_4 is another 2D electrocatalyst that can be used for the catalysis of CO_2 to CH_4 and is therefore highly desirable for electroreduction. Experimental studies have demonstrated that nonmetal doping (with elements such as B, O, N, P, and S) can dramatically improve the electrocatalytic performance of g-C_3N_4. However, multiple reaction pathways and different intermediate species are involved, and the selectivity of the product is still a challenging goal for the high-efficiency carbon dioxide reduction reaction (CO_2RR). Furthermore, the final product of CO_2 electroreduction is also determined by the applied electrode potential, which depends on the difference in the binding energy of the intermediate species, or the limiting potential, which is also an essential factor influencing product selectivity. MBenes have been verified experimentally and theoretically to catalyze CO_2 electroreduction to CH_4 on pure transition-metal catalyst platforms. However, owing to the high theoretical overpotential of the Cu electrode, it is not attractive for practical application. In recent years, some studies have found that 2D materials can provide a multifunctional platform for reducing carbon dioxide to hydrocarbon chemical products, and a great deal of research has been conducted in this field.

5.1.3 NNR (N_2 fixation)

Publication V: Theoretical Establishment and Screening of an Efficient Catalyst for N_2 Electroreduction on

Two-Dimensional Transition Metal Borides (MBenes). This chapter has been published as **Xiao Y***, Shen C, and Long T. Theoretical Establishment and Screening of an Efficient Catalyst for N_2 Electroreduction on Two-Dimensional Transition-Metal Borides (MBenes) [J]. ***Chemistry of Materials***, 2021 33 (11), 4023-4034.

(Highlights of 2D MBene Materials)

Overview of publication V: Theoretical Establishment and Screening of an Efficient Catalyst for N_2 Electroreduction on Two-Dimensional Transition Metal Borides (MBenes).

In this article, we propose a transition-metal boride (MBene) electrocatalyst, and all MBene systems were verified to be energetically stable with high-throughput screening via DFT calculations. First, the stability of all MBenes was considered by phonon calculations to ensure the availability experimentally, and then we evaluated the selectivity between NRR and HER, indicating that most of those catalysts have higher selectivity over HER during the NRR process. The activity was examined by limiting the potential depending on the rate-determining step. The rate-determining steps are always the first hydrogenation step ($*N_2 \rightarrow *N_2H$) and the last hydrogenation step ($*NH_2 \rightarrow *NH_3$), which are suggested to stabilize $*N_2H$ and destabilize $*NH_2$. Based on our calculation results, we observed that Nb_3B_4 (-0.50 V), Ta_3B_4 (-0.39 V), and Mo_2B_2 (-0.43 V) have a low limiting potential and high selectivity toward the NRR and HER competing processes, respectively. These MBene catalysts are promising electrocatalysts for the NRR with low limiting potential. Therefore, these promising candidates for the electrochemical nitrogen fixation production of ammonia under ambient conditions need further experimental verification. However, the long-range van der Waals (vdW) interactions cannot be described within the nonlocal electron correlation exchange, so the DFT-D3 method was applied to consider the dispersion corrections in Grimme's scheme. The Gibbs free energy profile diagram is one of the most important indicators for electrochemical catalysis and depends on the energy change for each elementary step during the electrochemical reaction process. The energy barrier between the two steps can directly be used to determine the thermodynamics of the reaction and obtain the corresponding limiting potential. In summary, the Gibbs free energy profile diagram, density of states, and charge density distribution are all effective indicators for evaluating catalysts and estimating their performance. Furthermore, the bond length between the active site, d-band center (ε_d), and the number of TM-d electrons could be descriptors for the catalytic activity. In addition, some multiple-level effective descriptors, such as ΔG_{*N}, which relates to binding properties, and the crystal orbital Hamilton population (COHP), which relates to the electronic structure, were used to reveal the nature of NRR activity on MBenes. They shed light on the essential relationship between the electrocatalytic activity and the electronic properties.

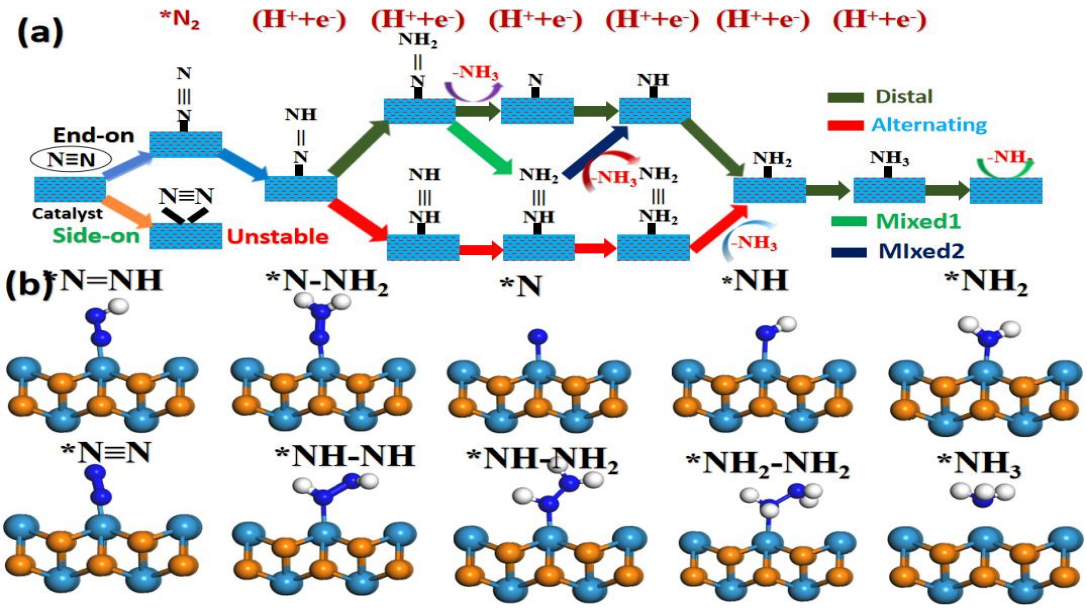

Figure 5-5. (a) Proposed reaction mechanism for the NRR. (b) Side view computational models of NRR on M_2B MBene.

In this chapter, we consider the possibility that the reaction follows this reaction mechanism. Considering the different adsorption configurations of N_2, it includes the end-end and side-end as the possible pathways of NRR reduction to NH_3, as shown in Figure 1. (*represents the activation state):

$$*+N\equiv N+6(H^++e^-)\rightarrow *+2NH_3 \quad \textbf{(5-3-1)}$$

$$*+N\equiv N\rightarrow *N\equiv N \quad \text{(End-on binding configuration)} \quad \textbf{(5-3-2)}$$

$$*+N\equiv N\rightarrow *N\equiv *N \quad \text{(Side-on binding configuration)} \quad \textbf{(5-3-3)}$$

Distal path:

$$*N\equiv N+6(H^++e^-)\rightarrow *N=NH+5(H^++e^-) \quad \textbf{(5-3-4)}$$

$$*N=NH+5(H^++e^-)\rightarrow *N\text{-}NH_2+4(H^++e^-) \quad \textbf{(5-3-5)}$$

$$*N\text{-}NH_2+4(H^++e^-)\rightarrow *N+*NH_3+3(H^++e^-) \quad \textbf{(5-3-6)}$$

$$*N+3(H^++e^-)\rightarrow *NH+2(H^++e^-) \quad \textbf{(5-3-7)}$$

$$*NH+2(H^++e^-)\rightarrow *NH_2+(H^++e^-) \quad \textbf{(5-3-8)}$$

$$*NH_2+(H^++e^-)\rightarrow *NH_3 \quad \textbf{(5-3-9)}$$

$$*NH_3\rightarrow *+NH_3 \quad \textbf{(5-3-10)}$$

Alternating path:

$$*N\equiv N+6(H^++e^-)\rightarrow *N=NH+5(H^++e^-) \quad \textbf{(5-3-11)}$$

$$*N=NH+5(H^++e^-)\rightarrow *NH\text{-}NH+4(H^++e^-) \quad \textbf{(5-3-12)}$$

$$*NH\text{-}NH+4(H^++e^-)\rightarrow *NH\text{-}NH_2+3(H^++e^-) \quad \textbf{(5-3-13)}$$

$$*NH\text{-}NH_2+3(H^++e^-)\rightarrow *NH_2\text{-}NH_2+2(H^++e^-) \quad \textbf{(5-3-14)}$$

$$*NH_2\text{-}NH_2+2(H^++e^-)\rightarrow *NH_2+NH_3+(H^++e^-) \quad \textbf{(5-3-15)}$$

$$*NH_2+(H^++e^-)\rightarrow *NH_3 \quad \textbf{(5-3-16)}$$

$$*NH_3\rightarrow *+NH_3 \quad \textbf{(5-3-17)}$$

The hydrogen evolution reaction (HER) is a major competing reaction of the NRR. Herein, to investigate the selectivity of the NRR, some assumptions are given

1) Only HER is the competing reaction of NORR;

2) The proton and electron transfer are not the rate-determining factors of either HER or NRR;

3) The selectivity of the NRR in comparison to the HER can be estimated by the Boltzmann distribution.

5.1.4 NORR (NO pollution)

Publication **VI:** Transition-Metal Borides (MBenes) as New High-efficiency Catalysts for Nitric Oxide Electroreduction to Ammonia by a High-Throughput Approach. This chapter has been published as Xiao Y*, Shen C. Transition-Metal Borides (MBenes) as New High-Efficiency Catalysts for Nitric Oxide Electroreduction to Ammonia by a High-Throughput Approach[J]. *Small*, 2021: 2100776. **(Highlight of 2D MBene Materials)**

Overview of publication VI: Transition-Metal Borides (MBenes) as New High-efficiency Catalysts for Nitric Oxide Electroreduction to Ammonia by a High-Throughput Approach.

As described in this article, the reaction conversion mechanism of nitric oxide (NO) reduction to NH_3 has led to widespread concern and discussion and involves various reactions and final byproducts, such as NO_2, NO, N_2O, and N_2. Figure 4-5a presents the proposed routes for the conversion of NO to various byproducts. An understanding of the interaction mechanism during the process of nitric oxide reduction by hydrogenation (NORR) is shown in Figure 5-6, showing that a double covalent bond is present in nitrogen and oxygen. Nitrogen lacks one electron in the p orbital, which renders it highly reactive. The mechanism that depends on the formation energies of the intermediate production of NO to NH_3 was also investigated. The different adsorption configurations include the O-end, N-end, and NO-side as possible pathways of NORR reduction to NH_3. Meanwhile, the path to N_2 demands the formation of NH_3, and all intermediate species were considered, providing insight into the details of the mechanism leading to the (H^++e^-) pair transfer during each elementary step.

We considered the possibility that the reaction follows a reaction mechanism, where the nitrogen molecules are hydrogenated by protons, analogous to the mechanism in the enzyme (* represents the activation state):

$$*+NO \rightarrow *NO \quad \textbf{(5-4-1)}$$

NORR path:

$$*NO+5(H^++e^-) \rightarrow *NOH+4(H^++e^-) \quad \textbf{(5-4-2)}$$

$$*NOH+4(H^++e^-) \rightarrow *N+H_2O+3(H^++e^-) \quad \textbf{(5-4-3)}$$

$$*N+3(H^++e^-) \rightarrow *NH+2(H^++e^-) \quad \textbf{(5-4-4)}$$

$$*NH+2(H^++e^-) \rightarrow *NH_2+(H^++e^-) \quad \textbf{(5-4-5)}$$

$$*NH_2+(H^++e^-) \rightarrow *NH_3 \quad \textbf{(5-4-6)}$$

$$*NO+5(H^++e^-) \rightarrow *HNO+4(H^++e^-) \quad \textbf{(5-4-7)}$$

$$*HNO+4(H^++e^-) \rightarrow *H_2NO+3(H^++e^-) \quad \textbf{(5-4-8)}$$

$$*H_2NO+3(H^++e^-) \rightarrow *O+NH_3+2(H^++e^-) \quad \textbf{(5-4-9)}$$

$$*O+2(H^++e^-) \rightarrow *OH+(H^++e^-) \quad \textbf{(5-4-10)}$$

$$*OH+(H^++e^-) \rightarrow *H_2O \quad \textbf{(5-4-11)}$$

$$*NOH+4(H^++e^-) \rightarrow *HNOH+3(H^++e^-) \quad \textbf{(5-4-12)}$$

$$*HNO+4(H^++e^-) \rightarrow *HNOH+3(H^++e^-) \quad \textbf{(5-4-13)}$$

$$*HNOH+3(H^++e^-) \rightarrow *NH+H_2O+2(H^++e^-) \quad \textbf{(5-4-14)}$$

$$*HNOH+3(H^++e^-) \rightarrow *H_2NOH+2(H^++e^-) \quad \textbf{(5-4-15)}$$

$$*H_2NOH+2(H^++e^-) \rightarrow *NH_2+H_2O+(H^++e^-) \quad \textbf{(5-4-16)}$$

NO dimer path:

$$*NO+NO \rightarrow *N_2O_2 \quad \textbf{(5-4-17)}$$

$$*N_2O_2+4(H^++e^-) \rightarrow *N_2O_2H+3(H^++e^-) \quad \textbf{(5-4-18)}$$

$$*N_2O_2H+3(H^++e^-) \rightarrow *N_2O+H_2O+2(H^++e^-) \quad \textbf{(5-4-19)}$$

$$*N_2O+2(H^++e^-)\rightarrow *N_2OH+(H^++e^-) \quad \textbf{(5-4-20)}$$

$$*N_2OH+(H^++e^-)\rightarrow *N_2+H_2O \quad \textbf{(5-4-21)}$$

NO oxidization path:

$$*NO+1/2O_2\rightarrow *NO_2 \quad \textbf{(5-4-22)}$$

$$*NO_2+1/2O_2\rightarrow *NO_3 \quad \textbf{(5-4-23)}$$

$$*NO_3+(H^++e^-)\rightarrow *HNO_3 \quad \textbf{(5-4-24)}$$

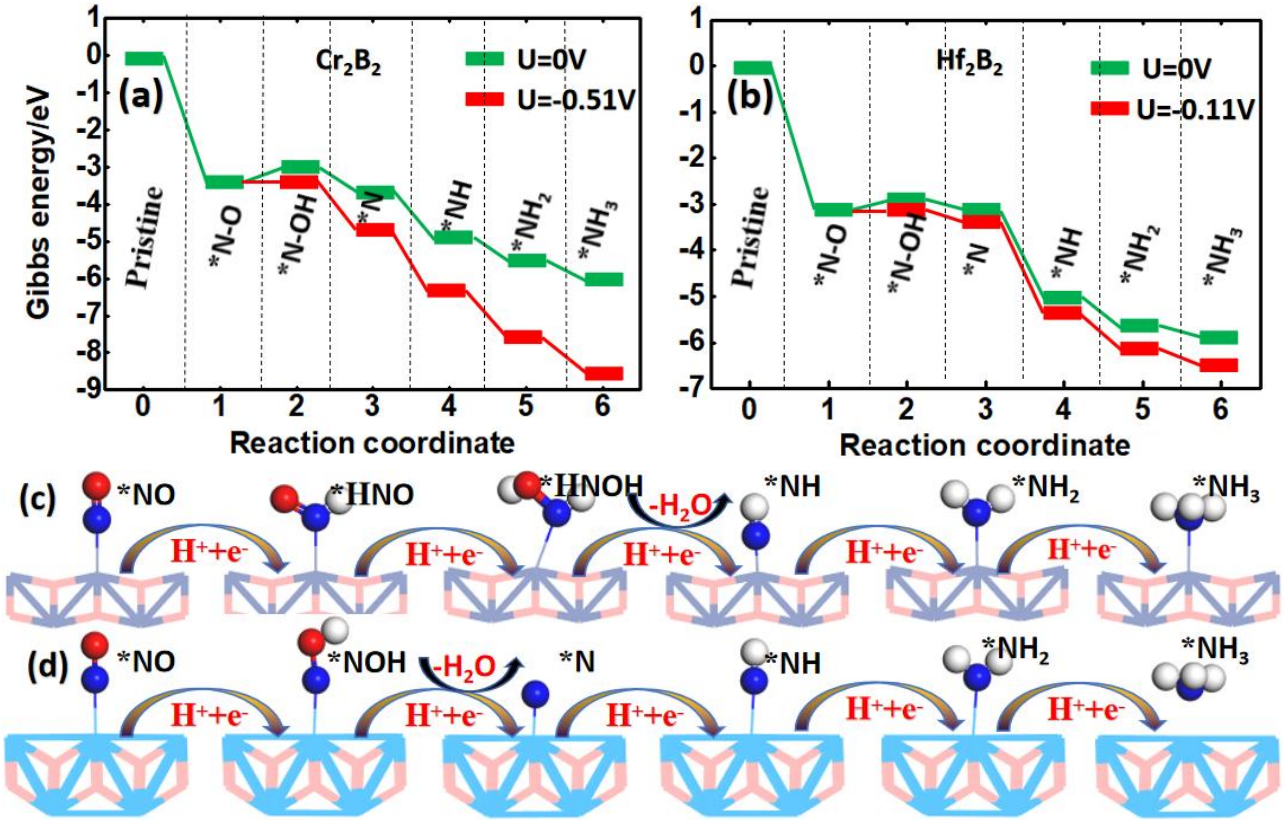

Figure 5-6. Gibbs free energy landscape of NO reduction to NH_3. (a) Cr_2B_2, (b) Hf_2B_2, and the optimization model (side view) of each intermediate species. (c) Cr_2B_2 and (d) Hf_2B_2.

To explore effective and reliable descriptors that can identify promising nitric oxide electroreduction (NORR) to ammonia catalysts on the 2D MBenes, we first calculated the binding energies of all possible intermediates involved in NORR on the 19 candidate MBenes materials. The limiting potential of each elementary reaction exhibits excellent linear scaling relationships as a function of ΔG_{*N}. Based on this principle, the binding energy of N* can serve as an effective descriptor to screen high-efficiency catalysts for the NORR. Furthermore, because the NO on these MBene surfaces prefers to hydrogenate to form *NOH in the first elementary step with a H^+/e^- pair transfer and the hydrogenation of $*NH_2$ to form $*NH_3$ molecules is also determined by the binding strength of NO, it has been reported that the first hydrogenation step (*NOH formation) or the last hydrogenation step ($*NH_3$ formation) is always the rate-determining step of the NORR. Thus, ΔG_{*NO} can serve as an effective descriptor. In addition, the d-band center (ε_d) and crystal orbital Hamilton population (COHP) for electronic properties could be descriptors to evaluate the catalytic activity of MBenes. These descriptors are helpful for exploring and designing high-performance catalysts for the NORR and reveal the essential relationship between activity and electronic properties.

5.2. Declaration of Contribution and Summarizing to the Publications

Statement of Personal Contribution:

High-Throughput Approach Exploitation: Two-Dimensional Double-Metal Sulfide (M_2S_2) of Efficient Electrocatalysts for Oxygen Reduction Reaction in Fuel Cells.

Xiao Y*, Tang L.
Energy & Fuels. Reprinted with permission from Energy & Fuels, @ 2020, American Chemical Society.

The idea was originated by M.Sc. Yi Xiao, the research was designed by Yi Xiao. The models are trained by M.Sc. Yi Xiao and my colleague M.Sc. Li Tang. Yi Xiao collected the stable crystal structures and generation of desired structures for DFT calculations. The processed and collection of data, analyzed the results, wrote, revised and submitted manuscript by Yi Xiao alone.

The first author Yi Xiao recognized the contribution of Yi Xiao in "Xiao Y, Tang L. High-throughput approach exploitation: two-dimensional double-metal sulfide (M_2S_2) of efficient electrocatalysts for oxygen reduction reaction in fuel cells[J]. Energy & Fuels, 2020, 34(4): 5006-5015."

Signature:

Yi Xiao	Li Tang	Hongbin Zhang (supervisor)

Statement of personal contribution

Mechanistic Study of Efficient Producing CO_2 Electroreduction via 2D Metal Organic Frameworks $M_3(HITP)_2$ Surface.

Xiao Y*, Chen D, Chen R*.
Electrochimica Acta. Reprinted with permission from Electrochimica Acta, @ 2021, Elsevier Ltd.

The idea was originated by M.Sc. Yi Xiao, the research was designed by Yi Xiao. The models are trained by M.Sc. Yi Xiao and my colleague PhD. Rui Chen and Prof. Dazhu Chen. Yi Xiao collected the stable crystal structures and generation of desired structures for DFT calculations. The processed and collection of data, analyzed the results, wrote, revised and submitted manuscript by Yi Xiao alone, my colleague PhD. Rui Chen and Prof. Dazhu Chen for reviewing this article and making suggestions to improve it.

The first author Yi Xiao recognized the contribution of Yi Xiao in "Xiao Y, Chen D, Chen R. Mechanistic study of efficient producing CO_2 electroreduction via 2D metal-organic frameworks M_3(2, 3, 6, 7, 10, 11-hexaiminotriphenylene)$_2$ surface[J]. Electrochimica Acta, 2021, 378: 138028."

Signature:

Yi Xiao	Dazhu Chen	Rui Chen	Hongbin Zhang (supervisor)

Statement of personal contribution

High throughput screening of M_3C_2 MXenes for efficient CO_2 reduction conversion into hydrocarbon fuels.

Xiao Y*, Zhang W
Nanoscale, 2020, 12(14): 7660-7673. Reprinted with permission from Nanoscale, @ 2020,Royal Society of Chemistry.

The idea was originated by M.Sc. Yi Xiao, the research was designed by Yi Xiao. The models are trained by M.Sc. Yi Xiao and my colleague PhD.Weibin Zhang. Yi Xiao collected the stable crystal structures and generation of desired structures for DFT calculations. Yi Xiao processed and collection of data, analyzed the results, wrote, revised and submitted manuscript by alone.

The first author Yi Xiao recognized the contribution of Yi Xiao in "**Xiao Y***, Zhang W. High throughput screening of M_3C_2 MXenes for efficient CO_2 reduction conversion into hydrocarbon fuels[J]. ***Nanoscale***, 2020, 12(14): 7660-7673."

Signature:

Yi Xiao	Weibin Zhang	Hongbin Zhang (supervisor)

Statement of personal contribution

Quantum Mechanical Screening of 2D MBenes for the Electroreduction of CO_2 to C1 Hydrocarbon Fuels.

Xiao Y*, Shen C, Hadaeghi N.
Journal of Physical Chemistry Letters, 2021, 12: 6370-6382**.** Reprinted with permission from Journal of Physical Chemistry Letters, @ 2021, American Chemical Society.

The idea was originated by M.Sc. Yi Xiao, the research was designed by Yi Xiao. The models are trained by M.Sc. Yi Xiao and my colleague M.Sc. Chen Shen, Niloofar Hadaeghi. Yi Xiao collected the stable crystal structures and generation of desired structures for DFT calculations. The processed and collection of data, analyzed the results, wrote, revised and submitted manuscript by Yi Xiao alone, my colleague M.Sc. Chen Shen, Niloofar Hadaeghi. for reviewing this article and making suggestions to improve it.

The first author Yi Xiao recognized the contribution of Yi Xiao in "Xiao Y, Shen C, Hadaeghi N. Quantum Mechanical Screening of 2D MBenes for the Electroreduction of CO_2 to C1 Hydrocarbon Fuels[J]. The Journal of Physical Chemistry Letters, 2021, 12: 6370-6382."

Signature:

Yi Xiao	Chen Shen	Niloofar Hadaeghi	Hongbin Zhang (supervisor)

Statement of personal contribution

Theoretical Establishment and Screening of an Efficient Catalyst for N_2 Electroreduction on Two-Dimensional Transition-Metal Borides (MBenes).

Xiao Y*, Shen C*, Long T.
Chemistry of Materials, 2021 33 (11), 4023-4034**.** Reprinted with permission from Chemistry of Materials, @ 2021, American Chemical Society.

The idea was originated by M.Sc. Yi Xiao, the research was designed by Yi Xiao. The models are trained by M.Sc. Yi Xiao and my colleague M.Sc. Chen Shen and Teng Long. Yi Xiao collected the stable crystal structures and generation of desired structures for DFT calculations. The processed and collection of data, analyzed the results, wrote, revised and submitted manuscript by Yi Xiao alone, my colleague M.Sc. Chen Shen and Teng Long for reviewing this article and making suggestions to improve it.

The first author Yi Xiao recognized the contribution of Yi Xiao in "Xiao Y*, Shen C, Long T. Theoretical Establishment and Screening of an Efficient Catalyst for N_2 Electroreduction on Two-Dimensional Transition-Metal Borides (MBenes)[J]. Chemistry of Materials, 2021 33 (11), 4023-4034."

Signature:

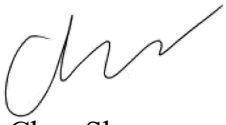
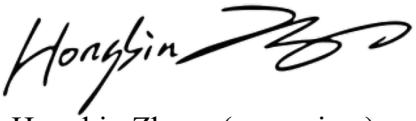

Yi Xiao Chen Shen Teng long Hongbin Zhang (supervisor)


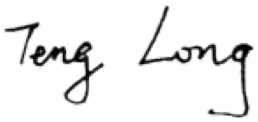

Statement of personal contribution

Transition - Metal Borides (MBenes) as New High - Efficiency Catalysts for Nitric Oxide Electroreduction to Ammonia by a High-Throughput Approach.

Xiao Y*, Shen C.
***Small*,** 2021: 2100776. Reprinted with permission from Small, @ 2021, Wiley-VCH Verlag.

The idea was originated by M.Sc. Yi Xiao, the research was designed by Yi Xiao. The models are trained by M.Sc. Yi Xiao and my colleague M.Sc.Chen Shen. Yi Xiao collected the stable crystal structures and generation of desired structures for DFT calculations. Yi Xiao processed and collection of data, analyzed the results, wrote, revised and submitted manuscript by alone.

The first author Yi Xiao recognized the contribution of Yi Xiao in "Xiao Y, Shen C. Transition-Metal Borides (MBenes) as New High-Efficiency Catalysts for Nitric Oxide Electroreduction to Ammonia by a High-Throughput Approach[J]. Small, 2021: 2100776."

Signature:


Yi Xiao Chen Shen Hongbin Zhang (supervisor)

5.3 Publications (I, II, III, IV and VI)

energy&fuels

pubs.acs.org/EF Article

High-Throughput Approach Exploitation: Two-Dimensional Double-Metal Sulfide (M_2S_2) of Efficient Electrocatalysts for Oxygen Reduction Reaction in Fuel Cells

Yi Xiao* and Li Tang

Cite This: *Energy Fuels* 2020, 34, 5006−5015 Read Online

ACCESS | Metrics & More | Article Recommendations | Supporting Information

ABSTRACT: A transition-metal sulfide (M_2S_2) nanolayer as a catalyst for the oxygen reduction reaction (ORR) has been investigated by the density functional theory (DFT) method to explore the underlying mechanisms of the elementary reaction steps for the ORR process. Both the O_2 dissociation and O_2 hydrogenation paths are probably possible in the ORR on the M_2S_2 surface. All of the possible intermediate reaction steps of the ORR are exothermic for O_2 hydrogenation. This indicates that the four-electron reaction path ($4e^-$ ORR) process is the most favorable path, and it is preferred over the two-electron path ($2e^-$ ORR) process. The changes in the reaction free energy diagrams were determined, and these diagrams showed that oxygen hydrogenation (OOH) is the rate-determining step. Meanwhile, different working potentials for our studied catalysts were also considered, and we observed that the double-transition-metal sulfide catalysts are energetically favorable (exothermic) catalysts via a 4e transfer mechanism of the ORR processes. According to the formation energies of the ORR intermediates (*O, *OH, *OOH) and the scaling relations between them on different slabs, the volcano plot for the overpotential of the catalyst is also an important index of the catalytic activities, and we found that a smaller overpotential is appropriate to determine better catalytic activities for the ORR process.

INTRODUCTION

Double-transition-metal sulfide nanostructures are becoming more and more attractive for their superior catalytic activity in the oxygen reduction reaction (ORR) and their application in the fuel cells. The transition-metal dichalcogenides (TMDs) have been widely studied due to their high physical properties and excellent electrochemical behavior.[1,2] The MoS_2 pristine surface has defects; thus, it always requires large overpotentials (>1.0 V), making the MoS_2 surface unfavorable for the ORR.[3,4] The two-dimensional (2D) materials of metal sulfides (M_2S_2) are now being developed as a new fuel cell battery cathode material after pure metals[5] and metal oxides.[6] This type of compound could tune the charge distribution and hence change its catalytic activity due to the difference in the electronegativity between the contiguous metal and the sulfur atoms. As a significant class in the TMD family, transition-metal sulfides with different chemical formulas (MS, MS_2, M_2S_2, and M_3S_4) have been investigated for use in supercapacitors,[7,8] metal-ion batteries,[9,10] and catalysis.[11,12] Currently, they are mainly used as reliable energy storage or energy conversion devices,[13,14] and the main challenges need to be overcome are mainly related to the storage of O_2 and the energy conversion efficiency.[15] Here, 2D metal sulfide (M_2S_2) layer structures have attracted attention; due to their high catalytic activity, these may be used as power sources for electric vehicles.[16] For example, there have been considerable studies that reveal that metal sulfide compounds exhibit similar catalytic activity to that of metallic N-doped graphene.[17,18] Recently, Tang et al.[19] found that the heterostructures of TMDs have potential in the application of sodium-ion batteries (SIBs) and sodium−air batteries. The lowest overpotential values are 0.55:0.20 V for η_{ORR}/η_{OER}. Thus, the SIBs exhibit high electrocatalytic activity for MoS_2/Mo_2C heterogeneous systems. Tan et al.[20] examined the catalytic properties of class IIIA−VIA and IVA−VIA 2D layered metal sulfides and found that GaSe and GeS have an electrochemical impact as well as a role in the catalysis of the ORR. Thulasi et al.[21,22] found the catalytic activity of ReS_2 for the ORR by a density functional theory (DFT) study, indicating a higher energy density and stability comparable with those of the platinum catalyst. Xinyi et al.[23,24] found that the 2D layered transition-metal sulfide, MX_2, exhibits favorable electrochemical properties and provided a summary of the related articles they reviewed.[25,26]

In the calculations for this study, we established the standard conditions, meaning that the temperature was constant at 298.15 K with $pO_2 = 0.1$ bar.[27] Thus, changes in the Gibbs free energy that are caused by the temperature, phase state, solvation, and H-bond effects need corrections.[28] To further explore the most favorable pathway for the elementary reaction of the ORR process, we needed to search for the most favorable reaction mechanism and obtain the lowest energy path by the relative free energy.[29,30] There are two reaction mechanisms for O_2 production; one is that O_2 can directly protonate to form an OOH species in which the oxygen molecules are hydrogenated. Another is O_2 dissociation into

Received: January 28, 2020
Revised: March 20, 2020
Published: March 22, 2020

https://dx.doi.org/10.1021/acs.energyfuels.0c00297
Energy Fuels 2020, 34, 5006−5015

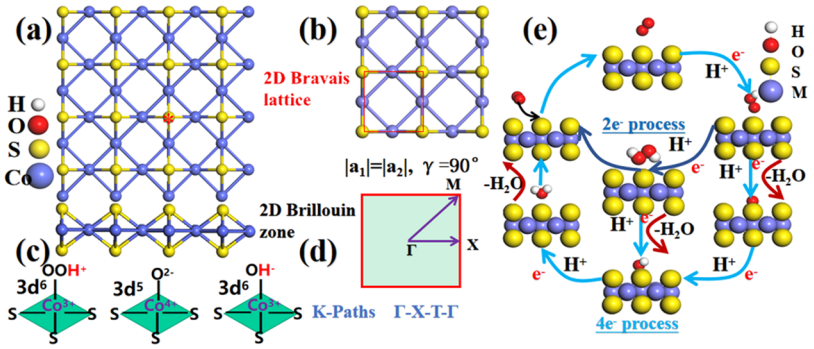

Figure 1. (a) Geometric structure of double-metal sulfide (M_2S_2) in a 4 × 4 × 1 supercell. (b) Local part of the supercell in the catalytic activity site. (c) Schematic diagram of band splitting for the Co atom with three sulfur atoms. (d) Schematic diagram of the Brillouin zone and K-path. (e) Full mechanism for the O_2 reduction to H_2O on the transition-metal macrocycle is proposed.

two atomic O's. Both occur during the oxygen evolution reaction (OER) and ORR processes.[29]

COMPUTATIONAL DETAILS

In this work, all of the periodic DFT calculations of the geometry and energy were performed using the Vienna ab initio simulation program (VASP) code.[31] A periodic (4 × 4 × 1) supercell of double-metal sulfide (M_2S_2) structures, as shown in Figure 1a, was used, and the structure parameters of the unit cells were obtained from the crystal database (Materials project). The electronic exchange−correlation interactions were determined with the Perdew−Burke−Ernzerhof (PBE) function, and the generalized gradient approximation (GGA)[32] method was used to describe the exchange−correlation potential in all our calculations. The spin was polarized at the DFT + U level[33] for electronic structure calculations to more accurately describe the transition metal. The cutoff energy of planewave basis was set to 500 eV, and the convergence for the structure optimization was set to 10^{-6} eV/Å. All our theoretical models were fully relaxed when the maximum energy exerted on each atom was less than 0.005 eV/Å. The K-point sampling of the Brillouin zone integration was implemented on a 5 × 5 × 1 grid for relaxation calculations, and a denser 11 × 11 × 1 Monkhorst−Pack mesh with a cutoff energy of 600 eV was used for the electronic structure calculations.

Meanwhile, the van der Waals (vdW) density functional (DFTD3) of IVDW = 11 in INCAR was calculated for all simulations, so there was a weak electrostatic repulsion between the like-charged ions. The formation energies of intermediates were calculated using the method that was proposed by Nørskov.[24] The change in the Gibbs free energy for an elementary reaction is calculated by the following equation: $\Delta G = \Delta E_{DFT} + \Delta H + \Delta ZPE - T\Delta S$, and it needs correction for H-bonds and phase states. Here, ΔE_{DFT} is the binding energy of intermediates that can be obtained from the DFT calculations, ΔH is the enthalpic temperature correction, and ΔZPE is the correction of zero-point energy. The addition of the entropic change ($T\Delta S$) under the standard conditions at 298.15 K was performed using the VASPKIT code (Supporting Information).[34]

RESULTS AND DISCUSSION

Various ORR-Involved Species. To conduct a thoughtful study of the mechanism of the ORR (O_2) in acidic media on an M_2S_2 surface, we needed to analyze the adsorption energy of the various intermediate species and the possible molecular adsorption configurations of the various species in the reaction mechanism, including O_2, O, OH, OOH, and H_2O.[35,36] The formation energies for some selected stable molecular configurations are summarized in Figure 4 The free energy profile diagrams of ΔG(*H) for the hydrogen evolution reaction (HER) are used to explore the competitive relationship between the HER and ORR, indicating a lower reactive activation in the same reaction medium than that for the ORR. Due to the weak binding energy of the key intermediate, *H, the HER impedes the reaction for reducing O_2 and is a competing reaction. Therefore, we concluded that HER is dominant over ORR and portended that M_2S_2 is a good candidate catalyst for the ORR. This determines the selectivity and whether HER or ORR is dominant during the entire process of electroreduction. Figure 2b indicates the difference

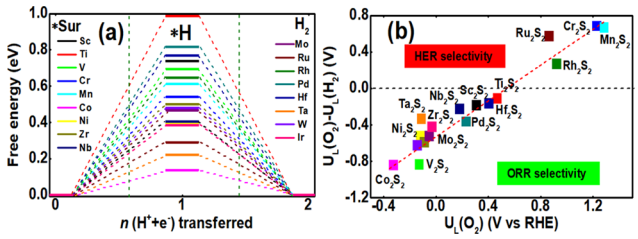

Figure 2. (a) Free energy diagrams for the HER at the zero electrode potential on M_2S_2 catalysts, with n as a function of protons and electrons transferred during the HER. The asterisk represents a clean surface, while *H represents the hydrogen binding to the surface. (b) Tendency of limit potential of the ORR (O_2) compared to HER (H_2) molecules in M_2S_2 materials with transition metals.

in the limit potential (U_L) between the HER and ORR. This figure can explain that U_L (O_2) − U_L (H_2) is a crucial factor to identify the selectivity toward H_2O final products for ORR catalysts. A higher U_L (O_2) − U_L (H_2) implies a higher selectivity for the ORR over the HER.[37,38] Figure 2b illustrates that the M_2S_2 compound has a similar selectivity toward H_2O but not H_2 as the final product catalyst. It is well known that the physical absorption of O_2 is the prerequisite for the ORR to proceed via the 4e transfer process. The intermediate species are influenced by chemisorption, which involves the adsorption energy of O, OH, and OOH, and their adsorption energy is much greater than that of the H_2O and O_2 molecules. Therefore, the most stable adsorption configuration of O_2 is

https://dx.doi.org/10.1021/acs.energyfuels.0c00297
Energy Fuels 2020, 34, 5006−5015

first determined and then the corresponding adsorption energy values are calculated by the following equation

$$\Delta E_{ads} = E_{adsorbate/sub} - E_{sub} - E_{adsorbate} \quad (1)$$

Eq 1 above indicates that the total energy of the adsorbed configurations is obtained by subtracting the total energy values of the substrate (M_2S_2 surface) and the H_2O or O_2 molecule. Meanwhile, stable adsorption systems and the corresponding binding energies for intermediate products are obtained by the following formulas.[39,40]

In Figure S2 (Supporting Information), energetically favorable adsorption configurations of the intermediates (O, OH, and OOH) for coadsorption are shown. For example, we found that OH prefers to stay on top of the upper sulfur atom (S) site and O prefers to stay at the metal (hollow) site when they coadsorb. The ΔE values of OH in the adsorption configurations were 2.09, 1.90, 1.54, 1.52, and 0.75 eV for Sc_2S_2, Ti_2S_2, V_2S_2, Mn_2S_2, and Co_2S_2, respectively. Meanwhile, the ΔE values of *O were 2.88, 2.75, 2.02, 1.70, and 1.36 eV, respectively. The ΔE values of *OOH were much higher than those of *O and *OH, which correspond to 5.62, 5.42, 5.10, 5.69, and 4.42 eV. It should be noted that H_2O has a small adsorption energy value (less than 0.17 and greater than 0.04 eV) due to the weak interactions between the surface and the H_2O molecules, indicating that water can be easily released from the surface as the final product of the ORR process. This is different from the calculation method of adsorption energy for molecules (O_2 and H_2O) and intermediates (*O, *OH, and *OOH), which must be inferred from the relationship of the $H_2O(l)$ and $H_2(g)$ molecules and are defined in the following formulas

$$M_2S_2 + H_2O(l) \leftrightarrow M_2S_2 - O + H_2(g)$$
$$\Delta E_O = E_{M_2S_{2-O}} - E_{M_2S_2} - (E_{H_2O} - E_{H_2}) \quad (2)$$

$$M_2S_2 + H_2O(l) \leftrightarrow M_2S_2 - OH + 1/2H_2(g)$$
$$\Delta E_{OH} = E_{M_2S_{2-OH}} - E_{M_2S_2} - (E_{H_2O} - 1/2E_{H_2}) \quad (3)$$

$$M_2S_2 + 2H_2O(l) \leftrightarrow M_2S_2 - OOH + 3/2H_2(g)$$
$$\Delta E_{OOH} = E_{M_2S_{2-OOH}} - E_{M_2S_2} - (2E_{H_2O} - 3/2E_{H_2}) \quad (4)$$

Here, M_2S_2 stands for a metal−N codoped active site on the graphene surface. Meanwhile, E_O, E_{OH}, and E_{OOH} are the adsorbed-state energies of the O, OH, and OOH intermediate species, respectively. Moreover, we set them for the $4e^-$ ORR path processes and are shown in the following 5−8 reactions. The whole ($O_2 + 4H^+ + 4e^+ \rightarrow 2H_2O$) process comprises four stages that follow the following formulas, and the Gibbs free energy calculation corresponding to the intermediate reaction is given by

$$O_2(g) + (H^+ + e^-) + M_2S_2 \rightarrow M_2S_2 - OOH$$
$$\Delta G_1 = \Delta G_{*OOH} + 2\Delta Gw - eU \quad (5)$$

$$M_2S_2 - OOH + (H^+ + e^-) \rightarrow M_2S_2 - O + H_2O$$
$$\Delta G_2 = \Delta G_{*O} - \Delta G_{*OOH} + eU \quad (6)$$

$$M_2S_2 - O + (H^+ + e^-) \rightarrow M_2S_2 - OH$$
$$\Delta G_3 = \Delta G_{*O} - (\Delta G_{*OH} - eU) \quad (7)$$

$$M_2S_2 - OH + (H^+ + e^-) \rightarrow M_2S_2 - H_2O$$
$$\Delta G_4 = eU - \Delta G_{*OH} \quad (8)$$

Meanwhile, there are some small additional effects on the ORR adsorbates, such as solvation phases and hydrogen bonds that will be stabilized when the transfer solution medium is solvated, so the Gibbs free energy values need to be corrected. In this study, we set $\Delta G_O = \Delta E_O + G(T)$, $\Delta G_{OH} = \Delta E_{OH} + G(T)$, and $\Delta G_{OOH} = \Delta E_{OOH} + G(T)$, corresponding to the adsorbed species;[41,42] the $G(T)$ values are shown in Tables S1 and S2 (Supporting Information). The term ΔG_W is equal to −2.96 eV for the H_2O molecule form. The total Gibbs free energy ($\Delta G_1 + \Delta G_2 + \Delta G_3 + \Delta G_4$) of the full reaction is obtained from the reaction $O_2 + 2H_2 \rightarrow 2H_2O$, which is −4.92 eV at a temperature of 298.15 K and a pressure of 0.035 bar.[43]

Figure 4 shows that the central activated atom (the sulfur atom site) serves as the catalytic activity site and is the most stable adsorption site for all of the ORR intermediate species.[44] For Co_2S_2, the first-stage O_2 tends to be adsorbed on top of the upper sulfur atom and forms a S−O bond with a distance of 2.01 Å and an adsorption energy of −0.36 eV, while the H_2O is adsorbed on top of the S atom with adsorption energy (0.12 eV) that is larger than that of the O_2 molecule, as shown in Figure 4c. This figure shows the schematic reaction pathway for the oxygen reduction reaction on Co_2S_2 materials with descriptors of the intermediates. We calculated the free energy diagram for the ORR process of O_2 catalyzed by the M_2S_2 structure. It is well known that the calculation of overpotentials has been widely applied in theoretical research. In this work, first, we calculated the free energy at zero potential (U = 0 V) and then deduced the equilibrium potential (U_{eq} = 1.23 V), oxidation potential ($U = \Delta E_{*O} - \Delta E_{*OH}$), and reduction potential ($U = \Delta E_{*OOH} - \Delta E_{*O}$), as shown in Figure 3. U_{ORR}

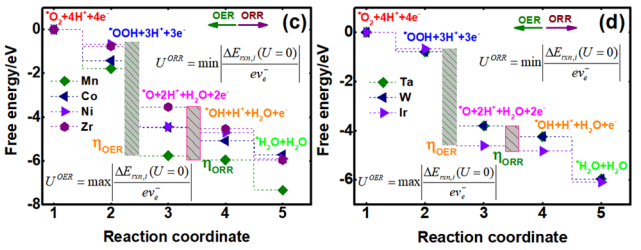

Figure 3. Free energy diagrams of the corresponding reaction steps on the M_2S_2 surface: (a) Sc_2S_2, Ti_2S_2,V_2S_2, and Cr_2S_2; (b) Nb_2S_2, Mo_2S_2, Rh_2S_2, and Hf_2S_2; (c) Mn_2S_2, Co_2S_2, Ni_2S_2, and Zr_2S_2; and (d) Ta_2S_2, W_2S_2, and Ir_2S_2. The most favorable free energy profile for the ORR to H_2O is at zero electrode potential (U = 0 V).

denotes the lowest change in energy that makes the free energies of the ORR process go uphill, while the U_{OER} is the highest energy change that makes the free energies of the OER process go downhill. For an ORR/OER catalyst, we set the equilibrium potential at 1.23 V based on the experimental observations. To further evaluate the catalytic performance of the M_2S_2 catalysts, the overpotentials (η) for the ORR and OER processes were calculated by the following equations: $\eta_{OER} = U_{OER} - U_{eq}$ and $\eta_{ORR} = U_{eq} - U_{ORR}$, respectively. By definition, η_{ORR} means the η_{ORR} overpotential and η_{OER} is the η_{OER} overpotential. The calculated OER potential of Co_2S_2 was 3.06 V and that of ORR was 0.61 V (Pt, 0.34V).[45] This indicates that the potential of the catalyzed OER (3.06 V) is much higher than that of the ORR (0.61 V). It is worth noting

https://dx.doi.org/10.1021/acs.energyfuels.0c00297
Energy Fuels 2020, 34, 5006−5015

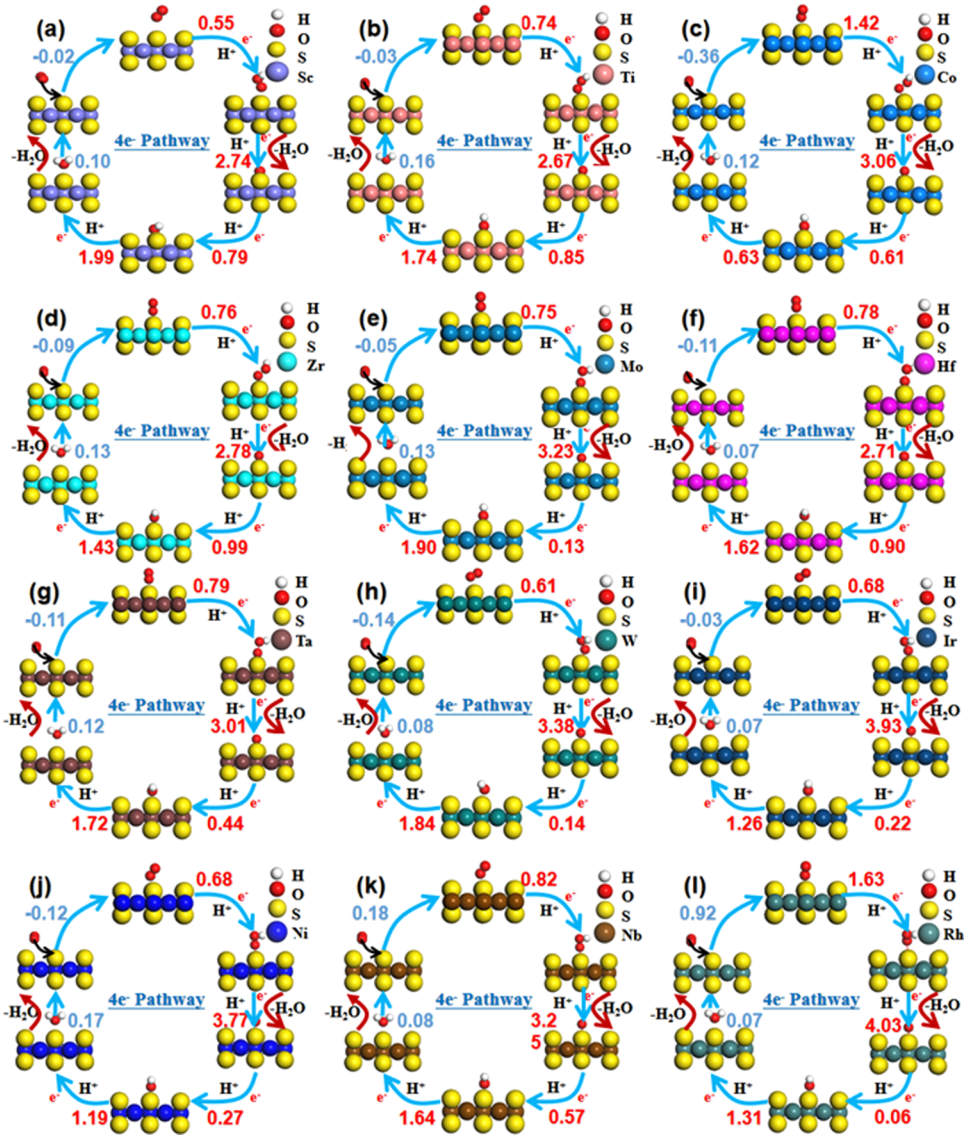

Figure 4. (a) Schematic reaction pathway for the oxygen reduction reaction on M_2S_2 materials with descriptors of intermediates, while the numbers represent the reaction energy in eV for the related species: (a) Sc_2S_2, (b) Ti_2S_2, (c) Co_2S_2, (d) Zr_2S_2, (e) Mo_2S_2, (f) Hf_2S_2, (g) Ta_2S_2, (h) W_2S_2, (i) Ir_2S_2, (j) Ni_2S_2, (k) Nb_2S_2, and (l) Rh_2S_2.

that the ORR overpotential is much less than that of the OER. From the calculation results, we can see that the low overpotential of the ORR makes Co_2S_2 an ideal candidate as a catalyst in the ORR process. Our study can offer meaningful insight into the promising role of M_2S_2 compounds in future fuel cell devices.

ORR Mechanism. It is reflected from our calculations of the adsorption of intermediates and the DFT results that the catalytic activity of the double-metal sulfide is comparable to that of 2D d^3–d^5 (M_2S_2) transition-metal electrocatalysts.[46] The detailed data on all potential reaction steps and barrier energies are summarized in Figures 4 and S2. According to the calculated barriers energy alone the reaction pathway (shown as the red line in Figure S2). According to the elementary reactions that are presented in Figure S2, there are four possible stages of the ORR process in which four proton–electron couples ($H^+ + e^-$) are defined. The first reaction step with the highest reaction energy corresponds to the hydrogenation process of the O_2 molecule with one atomic H to form the final species.

We performed the DFT calculations for the active sites; the entire possible elementary reaction steps were calculated and are illustrated in Figure S2. This task involved the investigation of the dissociative and formative pathways. It is seen from all of the possible reaction pathways that for O_2 dissociation the most favorable pathway is the following process. It should be noted that $*O_2 \rightarrow *O + *O$ (O_2 dissociation) has a reaction energy of −3.11 eV for Co_2S_2. Meanwhile, $*O_2 \rightarrow *OOH$ has a higher reaction energy (−1.42 eV). This indicates that the $4e^-$ and $2e^-$ pathways are competitive. Nonetheless, we also noted that the OOH hydrogenation to form H_2O_2 has the highest reaction energy (1.71/eV), which means that it is an endothermic process. On the other hand, O_2 hydrogenation is the process of O_2 hydrogenation → *OOH dissociation → atomic *O and OH → then *O hydrogenation → *OH hydrogenation → H_2O form with the rate-determining step of *O hydrogenation preferred due to having the smallest reaction energy (−0.62/eV) than that of the other steps for the Co_2S_2 compound.[47] In summary, the dissociation of O_2 during the entire possible elementary reaction steps is a

https://dx.doi.org/10.1021/acs.energyfuels.0c00297
Energy Fuels 2020, 34, 5006−5015

difficult reaction due to the large reaction energy. Meanwhile, the direct hydrogenation of O_2 is much easier as examined in our calculations for Sc_2S_2, Ti_2S_2, and Mo_2S_2. The hydrogenation of the atomic O occurs easily to form OH species with a small reaction energy (less than 0.12/eV). The formed OH species is located on top of the upper sulfur atom. Subsequently, the OOH species dissociates into an atomic O adsorbed on top of the S atom and an OH species adsorbed on the hollow site of the metal atom in the square ring. Meanwhile, the rate-limiting stage of the O_2 dissociation mechanism that has a higher reaction rate than that of hydrogenation corresponds to the O_2 change into two atomic O's. As shown in Figure 4, the protonation process was performed by adding a hydrogen and an electron to the surface and then binding them with an adsorbed intermediate species. Adding one hydrogen form per OOH (ads) or O−O bond breaks are promoted by the proton transfers from coadsorbed. In summary, O_2 adsorption on M_2S_2 (M for 3d−5d of a transition metal) is endothermic, while O_2 dissociation is facile on transition metals; it becomes exothermic with *O and *OH coadsorbtion that lowers the free energy of coadsorbed atomic oxygen upon the 4e pathway, which is energetically favorable.[48]

As shown in Figure 5a, ΔG_{*OOH} and ΔG_{*O} have a linear relationship with ΔG_{*OH}, displaying a strong scaling relation-

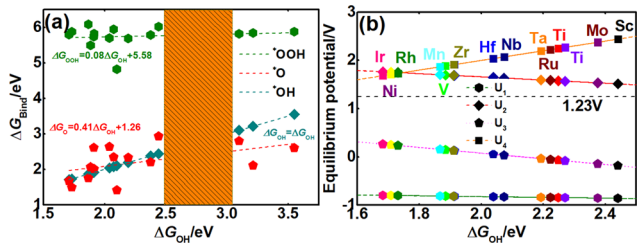

Figure 5. (a) Scaling relations between the binding energies of the ORR intermediate species. (b) Thermodynamic activity volcano curves. Each point displayed in a different color represents the highest ΔG_i (i = 1, 2, 3, 4) step. The dark dashed line indicates the standard equilibrium potential (1.23 V) for the overall ORR.[49]

ship between them. In fact, the trend of change originates from the difference in *OOH and *O and the activities of the catalysts relative to *OH. However, for *O as the primary species adsorbed on the top site of the sulfur atom that is similar to the adsorption sites for *OOH and *OH, the linear correlations of ΔG_{*OOH} versus ΔG_{*OH} and ΔG_{*O} versus ΔG_{*OH} are obvious. Meanwhile, the catalytic activity of the ORR on certain electrocatalysts can also be strengthened from the relationships between the Gibbs free energies of the intermediate species. Moreover, a volcano plot curve correlation between ΔG_{*OH} and equilibrium potential using the approach of chemical equilibrium theory at the highest ratio was discussed (see in Figure 5a), and the equilibrium potential of each elementary reaction could be calculated based on the linear relationships between the Gibbs free energies of each intermediate species. Hence, we obtained a linear relationship among them, $\Delta G_{*OOH} = 0.08\Delta G_{*OH} + 5.58$ and $\Delta G_{*O} = 0.41\Delta G_{*OH} + 1.26$. As shown in Figure 5b, the equilibrium potential curve is defined by the region of *OH binding, with the linear relationships as $U_1 = -0.08\Delta G_{*OH} - 0.66$ (U_1 versus ΔG_{*OH}), $U_2 = -0.33\Delta G_{*OH} + 2.32$ (U_2 versus ΔG_{*OH}), $U_3 = -0.59\Delta G_{*OH} + 1.26$ (U_3 versus ΔG_{*OH}), and $U_4 = \Delta G_{*OH}$ (U_4 versus ΔG_{*OH}). The positive values of ΔG_{*OH} for all of the 2D M_2S_2 monolayers indicate that the *OH desorption step is an exergonic process. This result shows strong adsorption for intermediate species via an O atom, which is ideal for a good catalyst.

The surface free energy diagrams of the limiting potentials (U_L) for each of the elementary proton-transfer steps of the complete ORR process for both of the 4e⁻ and 2e⁻ paths are shown in Figure 6. The difference in the U_L values between the

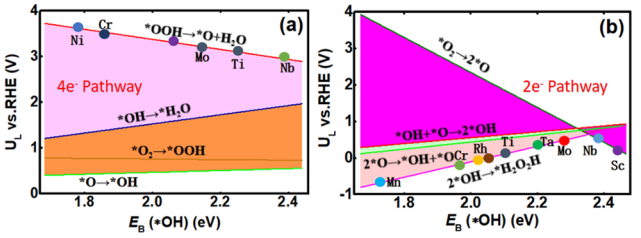

Figure 6. Possible ORR for the 4e⁻ path (a) and 2e⁻ path (b) on 2D M_2S_2; free energy profiles for the ORR pathway (a, b) and OER pathway (c, d) on the 2D double-metal sulfide (M_2S_2) surface for complete O_2 reduction at different potentials.

ORR and HER, which means the value of U_L (O_2) − U_L (H_2), is an accurate descriptor to identify the trend in selectivity toward oxygenated products for ORR catalysts. The higher value of U_L (O_2) − U_L (H_2) implies a higher selectivity for the ORR over the HER reaction mechanism. In the aggregate, the U_L lines correspond to the potential determinate steps (PDSs) of the 4e⁻ path for the various catalysts, as shown in Figure 6a,b, representing $*O_2(g) \rightarrow *OOH$ and $*O_2(g) \rightarrow 2*O$ reaction mechanisms, respectively. Obviously, the *OOH → *O transformation is generally the PDS for the overall ORR, whereas *OOH → *O of Ni and Cr transformations have to overcome the limiting potentials (U_L) of *O → *OH. Note that $*O_2(g) \rightarrow *OOH$ and *O → *OH are located at the lowermost U_L line of ORR(g) and *OOH → *O is located at the top of the the uppermost curve. Meanwhile, this indicates that $*O_2 \rightarrow *OOH$ and *OH → $*H_2O$ are still different than the 4e⁻ path process, $*O_2 \rightarrow *OOH$ downhill and uphill *O → *OH, respectively. In addition, Figure 6b shows that O_2 dissociation on Sc_2S_2 and Nb_2S_2 is unfavorable because the binding energy is much smaller than the $E_{B(*O_2)}$. Thus, Sc_2S_2 and Nb_2S_2 cannot radically change the ORR electroreduction pathway, the $*O_2 \rightarrow 2*O$ and 2*O → *OH + *O; Mo_2S_2 and Nb_2S_2 have the uppermost values, ranging from 2.28 to 2.33 eV. This means that 2*OH + $*H_2O_2$ over $*O_2 \rightarrow 2*O$ of Mo_2S_2 and Nb_2S_2 is at the U_L line of *OH + *O → 2*OH near the top of the volcano plot relationship. The protonation of *OH + *O to form 2*OH is thus the PDS rather than *OH + *O → $*H_2O_2$ owing to its strong binding ability for *OH. This is a prerequisite to this type of subsequent protonation of *OH to form $*H_2O$. However, the atomic-scale mechanisms of the ORR with the HER-concerted reaction are complicated and the thermodynamics of the reaction needs to be further explored; this can be calculated using the approach developed by Nørskov.

Thermodynamic Analysis. We conducted a thermodynamic analysis to further explore the reaction mechanism of the ORR process; we converted the free energy into Gibbs free energy using corrections. Figure 7 shows a constant separation catalytic activity of 0.6 eV between the energy differences of ΔG_{*OH}, ΔG_{*OOH}, and ΔG_{*OH}, and it shows a similar

https://dx.doi.org/10.1021/acs.energyfuels.0c00297
Energy Fuels 2020, 34, 5006−5015

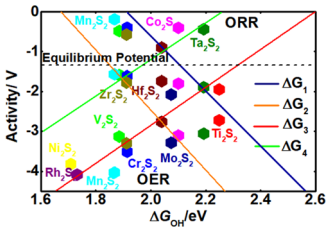

Figure 7. Theoretical predictions of volcano plots for the ORR/OER on different sites of the M_2S_2 surface, resulting from the thermodynamic analysis.

relationship to the difference between ΔG_{*OH} and each elementary reaction step. However, from our calculations, we cannot identify whether these materials should be efficient electrocatalysts for the oxygen reduction reaction under acidic environments. The volcano plot (see in Figure 7) of the catalytic activity shows some particular types of catalysts; the lines represent a linear correlation among the Gibbs free energy values of each step in the 4e$^-$ path mechanism of the ORR, at the top for ORR and at the bottom for OER resulting from the intersection of these lines. It was found that the former will be efficiently catalyzed by M_2S_2 with Mn, Co, and Ta and the Gibbs free energy values of reactions 5−8 can be calculated. For the ORR, the method used to determine the overpotentials is as follows

$$\Delta G_{\mathrm{rxn},i}(U = 0) = \max\{\Delta G_1, \Delta G_2, \Delta G_3, \Delta G_4\} \tag{9}$$

$$U^{\mathrm{ORR}} = \min\left|\frac{\Delta G_{\mathrm{rxn},i}(U = 0)}{ev_e^-}\right| \tag{10}$$

$$\eta_{\mathrm{ORR}} = 1.23 - U_{\mathrm{ORR}}/e \tag{11}$$

In (9), ΔG_1, ΔG_2, ΔG_3, and ΔG_4 are the Gibbs free energies of elementary reaction steps 5−8, respectively. $\Delta G_{\mathrm{rxn,i}}$ for each elementary reaction step is the result in energy changes of ORR. The M_2S_2 toward the mechanism of the ORR process has been explored to determine the interaction between the intermediates, calculating the corresponding overpotential for the ORR, an ideal catalyst for ORR ($\eta_{\mathrm{ORR}} = 1.23 - U_{\mathrm{ORR}}$) needing a value below the equilibrium potential (1.23 eV). However, it is unreliable to obtain the overpotential directly because the free energy values of the intermediates are needed to be correlated and changed into Gibbs free energies; in this case, the lower overpotential indicates the better catalyst. Figure 8a,b exhibits a trend similar to the linear plots, which means the overpotential for various active sites, and this identified to have a small ORR overpotentials of 0.23 V and comparison N-doped MoS_2 with 0.67 V.[50] Meanwhile, the

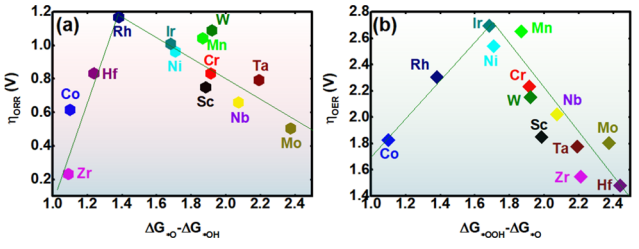

Figure 8. Volcano plots of the overpotential with the difference between the formation energies of *O and *OH and *OOH and *O, respectively: (a) ORR and (b) OER.

lowest OER overpotential for the catalyst was 1.42 V. We note the best ORR performance based on the estimate from the volcano plot, pointing to M_2S_2 catalysts with transition metals.

As shown in Figure 8a, we presented the scaling relationship between the Gibbs energy of the ORR intermediates, as a function of ΔG_{OH}, presenting the potential-dependent surface phase diagram at T = 298 K and pO_2 = 0.1 bar, corresponding to the electron transfer steps of the Gibbs free energy between the overpotentials of the ORR intermediates. We observed a small overpotential for Zr_2S_2 of approximately 0.22 V with the difference between *O and *OH and for Hf_2S_2 of approximately 1.43 V with the difference between *OOH and *O for OER.[53−60] As a guide to our research, we marked a dotted area between 1 and 2.4 eV in the x-axis of Figure 8. This value is expected from the analysis of the scaling relationships, and it has been recognized in the study on M_2S_2. It should be noted that both the volcano plots and the Gibbs free energy diagrams (see in Figure 9) have the same results as those obtained from our calculations. For each step, the total Gibbs free energy of the reaction is defined as follows

$$O_2 + 4H^+ + 4e^- \rightarrow 2H_2O$$

$$\Delta G_1 + \Delta G_2 + \Delta G_3 + \Delta G_4 = -4.92 \tag{12}$$

This similarity was determined not only by the Gibbs free energy of the binding catalytic sites but also by the intermediate species. In this case, all intermediates have binding available only at the top of the S atoms, resulting in similar relationships between the different intermediates. However, the 2D double-metal sulfide (M_2S_2) materials were usually more suitable for use as an ORR catalyst than as an OER catalyst in our calculations. On the basis of these abundant results, this study fully summarizes and analyzes the ORR/OER process on the M_2S_2 surface in Figure 9. For O_2 hydrogenation, the most favorable pathway was the process of O_2 hydrogenation.

In Figure 9, the Gibbs free energy diagram is shown exactly along the 4e$^-$ path. It can be seen that the associative mechanism has gradually become lower and the free energy change between elementary reaction steps of the ORR was uphill. When the electrode potential was at U = 1.23 V, the 4e$^-$ path of the ORR is downhill at 0 V. For Co_2S_2, the minimum (ΔG_{ORR}) potential was set to be 0.61 V, 1.23−0.61 = 0.62 V is the overpotential, and the *O to *OH transformation is the rate-determination step. Meanwhile, the maximum (ΔG_{OER}) potential was set to be 3.06 V, 3.06−1.23 = 1.83 V is the overpotential for this catalyst, and the transformation of *O to *OOH is the rate-determination step of the OER process. It is well established that the 4e$^-$ path mechanism is the more favorable compared to the 2e$^-$ path mechanism for O_2 reduction on the M_2S_2 catalyst surface. The calculated free energy diagrams of the ORR intermediates binding on the active site at 1.23 V as the equilibrium potential for ORR catalytic site of top S atom.[51] Meanwhile, the ORR pathway on active sites with M_2S_2 has been calculated for comparison. The DFT calculations reveal that the Gibbs free energies of intermediates on Mn_2S_2, Co_2S_2, Ni_2S_2, and Zr_2S_2 moieties have smaller negative values than those of the other compounds for the ORR. By a comprehensive analysis, it is seen that the free energies of each elementary step of the ORR on 2D double-metal sulfide (M_2S_2) are downhill. This means that they are all exothermic reactions, but for the two-electron path, these are not always downhill. Therefore, this shows that the four-

https://dx.doi.org/10.1021/acs.energyfuels.0c00297
Energy Fuels 2020, 34, 5006−5015

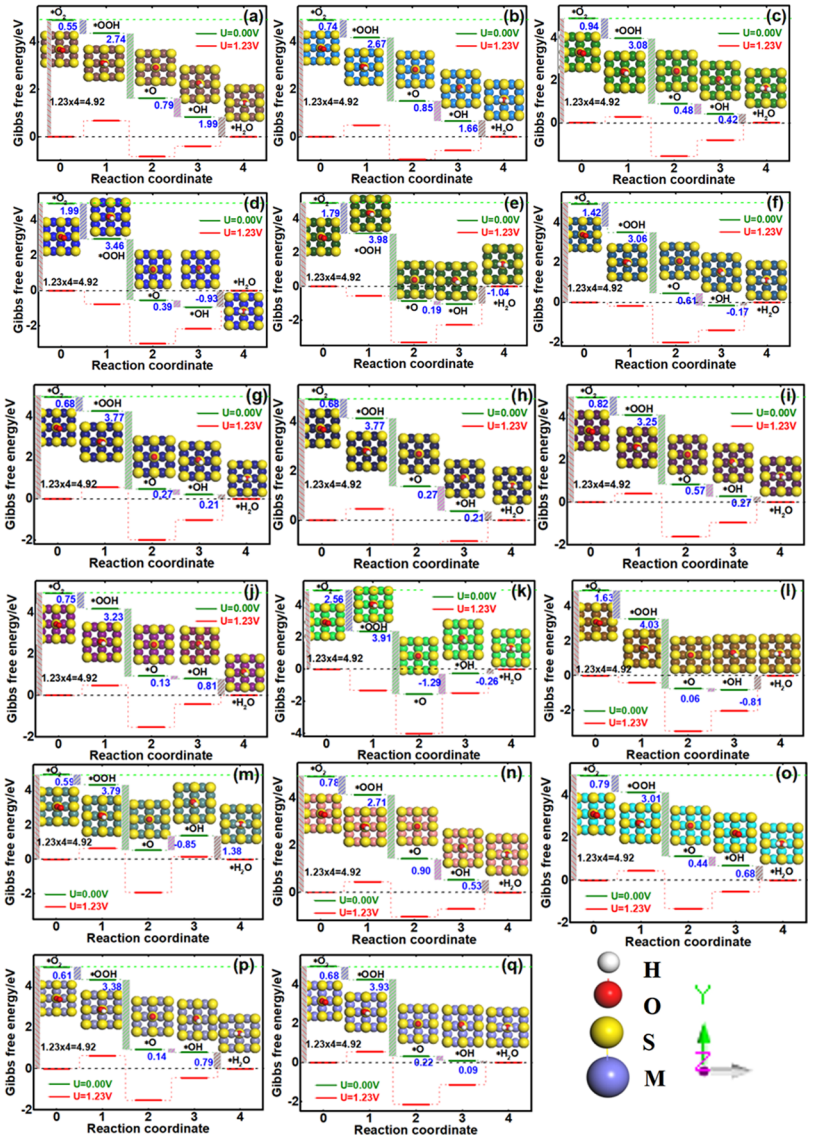

Figure 9. Gibbs free energy diagrams of ORR on 2D M_2S_2 monolayers: (a) Sc_2S_2, (b) Ti_2S_2, (c) V_2S_2, (d) Cr_2S_2, (e) Mn_2S_2, (f) Co_2S_2, (g) Ni_2S_2, (h) Zr_2S_2, (i) Nb_2S_2, (j) Mo_2S_2, (k) Rh_2S_2, (l) Hf_2S_2, (m) Ta_2S_2, (n) W_2S_2, and (o) Ir_2S_2.

electron ORR pathway was more favorable than the two-electron pathway at the zero electrode potential for both catalysts. As the reaction continues, the overall reactions become more exothermic and some intermediate species become stabilized and are energetically downhill. There exists an electrode potential to keep each elementary reaction exothermic, which is defined as the working potential of the electron catalyst for the ORR. Our results show that the electrode potentials, U_{ORR}, were above 0.79 V for Sc_2S_2 and 0.85 V for Ti_2S_2. Meanwhile, the working potentials were 0.48 V and 0.39 V for V_2S_2 and Cr_2S_2, respectively. The formation of *OOH is the most uphill with the increase of the electron transfer steps for both catalysts (Figure 10).[52]

The four-electron transfer process of the ORR mechanism has been further confirmed, and it is also predicted to be more active for the ORR. To understand the reason behind this, we have analyzed the clean surface of an electronic structure, as shown in Figure S10 (Supporting Information), wherein a band state is presented in which the valence band edge is across the Fermi level surface, so the surface is metallic. Other remarkable feature of the charge density difference plot curves and band splitting for the metal ion with two sulfur atoms in a square-planar orientation with ORR intermediates are shown in Figures S6 and S7 (Supporting Information), respectively. There is a strong energy overlap between the electronic states of this clean surface. In conclusion, accurate spin-polarized calculations are also performed with the generalized gradient approximation (GGA) and the effect of d-band electron correlation is described by the on-site Coulomb (U) and exchange (J) interactions. We use U_{eff} = 3.5 eV; although this value leads to an adequate reproduction of the experimental oxidation energies of d metals, it may predict the band gap as well. We have shown that 2D M_2S_2 is determined from the linear response. The electronic distribution of a Ni atom is $3d^8 4s^2$, and it has Co^{2+} as a clean surface. The orbital splitting would be that of a d^8 orbital. Meanwhile, for Co^{3+}, the orbital splitting would be that of a d^7 orbital distribution. Our spin-polarized calculations show that in the presence of *O, S = 2.5, whereas in the presence of *OH and *OOH, S = 0. The different possibilities in each case correspond to low-spin, intermediate-spin, and high-spin states. The ground-state spin corresponds to the arrangement with energy change, indicating

https://dx.doi.org/10.1021/acs.energyfuels.0c00297
Energy Fuels 2020, 34, 5006−5015

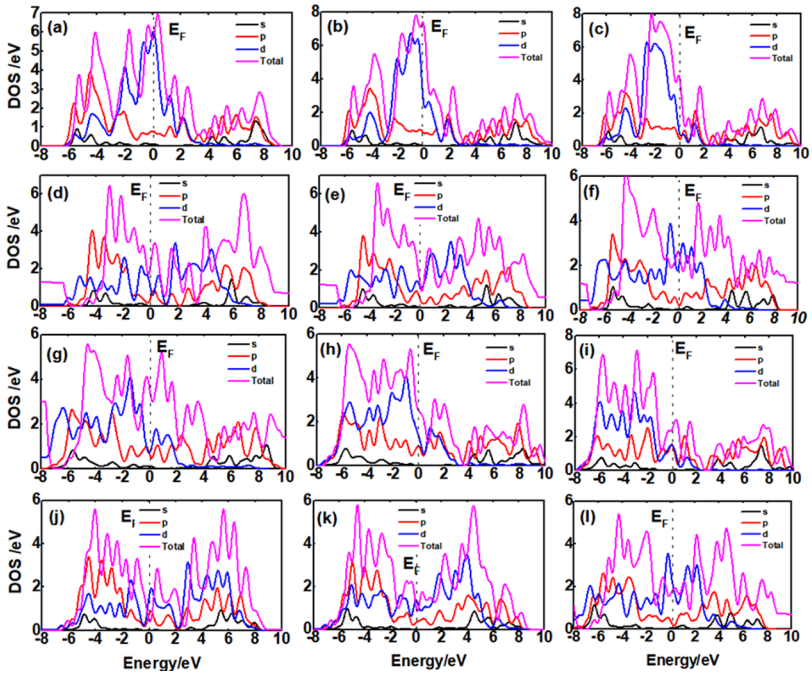

Figure 10. Projected density of states for the 2D M_2S_2 surface; the energy zero is set at the Fermi energy for the DOS: (a) Sc_2S_2, (b) Ti_2S_2, (c) V_2S_2, (d) Cr_2S_2, (e) Mn_2S_2, (f) Co_2S_2, (g) Ni_2S_2, (h) Zr_2S_2, (i) Nb_2S_2, (j) Mo_2S_2, (k) Rh_2S_2, and (l) Hf_2S_2.

that the ion present in the complex has a low-spin ordering of its d-state band, as shown in Figures S5 and S6. Figure S7 shows the charge density difference plots for a metal atom as a feature in both 2D M_2S_2 compounds. It can be seen that, electronically, the electron transfer for different ORR intermediate species is noticeably different from that on the surface. This difference arises from the electronic hybridization with sulfur atoms, which results in opening a gap between the occupied and unoccupied states near the Fermi energy level, indicating that the d-band center of the metal in the M_2S_2 sheets is the most energy-demanding part when forming ORR intermediates on the active sites.

CONCLUSIONS

Our calculations showed that the 2D metal sulfide (M_2S_2) layer structures exhibit good catalytic activity for the ORR process. The intermediate species always chemisorbed on top of the S atom site on the M_2S_2 surface, implying that sulfur and the transition-metal atom, coembedded, play an important role in the ORR process. The active site for all of the possible elementary reactions of the ORR is located at the square center. This can happen spontaneously with negative reaction energy values, which plays an extremely important role in the ORR on these catalyst. The Gibbs energy diagram of the ORR exhibits different working potentials for a small overpotential for ORR and a large overpotential for OER along the most favorable $4e^-$ ORR path, respectively. The volcano plot shows a linear correlation between different intermediate species; the thermodynamic analysis demonstrates that the formation of H_2O is easier than that of H_2O_2. Further, the electronic properties of the four-electron transfer process show no band gaps toward the ORR, indicating excellent conductivity. These results will be useful for designing M_2S_2-supported transition-metal catalysts that have high efficiency for the ORR. Our theoretical research can be helpful to probe the application and design of high-efficiency catalysts for fuel cells.

ASSOCIATED CONTENT

Supporting Information

The Supporting Information is available free of charge at https://pubs.acs.org/doi/10.1021/acs.energyfuels.0c00297.

Thermochemistry analysis; zero-point energy corrections and entropy contributions to the free energies under the standard conditions (298.15 K, 1 bar) (Table S1); Gibbs free energies at 298.15 K, in eV, corresponding to the isolated O_2, H_2, OOH, O, OH, H_2O_2, and H_2O species (Table S2); scaling relations in formation energies of the ORR intermediates in 2D double-metal sulfide materials with active sites composed of M_2S_2 with d-transition metals (Figure S1); and DFT study of the ORR on the 2D double-metal sulfide (M_2S_2) surface in acid solutions (Figure S2) (PDF)

AUTHOR INFORMATION

Corresponding Author

Yi Xiao − *Institute of Materials Science, TU Darmstadt, 64287 Darmstadt, Germany;* orcid.org/0000-0001-6318-8010; Email: yixiao@tmm.tu-darmstadt.de

Author

Li Tang − *Chongqing Hongyu Precision Industrial Co., Ltd., 402760 Chongqing, China*

Complete contact information is available at: https://pubs.acs.org/10.1021/acs.energyfuels.0c00297

Notes

The authors declare no competing financial interest.

ACKNOWLEDGMENTS

Financial support from the China Scholarship Council (CSC, 201808440416) of China and Research and the Arts (HMWK) of the Hessen State in Germany is acknowledged. The

Lichtenberg high-performance computer is gratefully acknowledged, and we are also thankful to TU Darmstadt.

REFERENCES

(1) Zhang, H.; Tian, Y.; Zhao, J.; et al. Small dopants make big differences: Enhanced electrocatalytic performance of MoS_2 monolayer for oxygen reduction reaction (ORR) by N−and P−doping. *Electrochim. Acta* **2017**, *225*, 543−550.
(2) Lv, K.; Suo, W.; Shao, M.; et al. Nitrogen doped MoS_2 and nitrogen doped carbon dots composite catalyst for electroreduction CO_2 to CO with high Faradaic efficiency. *Nano Energy* **2019**, *63*, No. 103834.
(3) Hao, Y.; Gong, P. L.; Xu, L. C.; et al. Contrasting Oxygen Reduction Reactions on Zero-and One-Dimensional Defects of MoS_2 for Versatile Applications. *ACS Appl. Mater. Interfaces* **2019**, *11*, 46327−46336.
(4) Tan, Y.; Liu, P.; Chen, L.; et al. Monolayer MoS_2 films supported by 3D nanoporous metals for high-efficiency electrocatalytic hydrogen production. *Adv. Mater.* **2014**, *26*, 8023−8028.
(5) Koh, S.; Toney, M. F.; Strasser, P. Activity−stability relationships of ordered and disordered alloy phases of Pt_3Co electrocatalysts for the oxygen reduction reaction (ORR)[J]. *Electrochim. Acta* **2007**, *52*, 2765−2774.
(6) Su, H. Y.; Gorlin, Y.; Man, I. C.; et al. Identifying active surface phases for metal oxide electrocatalysts: a study of manganese oxide bifunctional catalysts for oxygen reduction and water oxidation catalysis. *Phys. Chem. Chem. Phys.* **2012**, *14*, 14010−14022.
(7) Chen, Z.; Wan, Z.; Yang, T.; et al. Preparation of nickel cobalt sulfide hollow nanocolloids with enhanced electrochemical property for supercapacitors application. *Sci. Rep.* **2016**, *6*, No. 25151.
(8) Shen, L.; Yu, L.; Wu, H. B.; et al. Formation of nickel cobalt sulfide ball-in-ball hollow spheres with enhanced electrochemical pseudocapacitive properties. *Nat. Commun.* **2015**, *6*, No. 6694.
(9) Yang, W.; Chen, L.; Yang, J.; et al. One-step growth of 3D $CoNi_2S_4$ nanorods and cross-linked $NiCo_2S_4$ nanosheet arrays on carbon paper as anodes for high-performance lithium ion batteries. *Chem. Commun.* **2016**, *52*, 5258−5261.
(10) Wang, J. G.; Jin, D.; Zhou, R.; et al. One-step synthesis of $NiCo_2S_4$ ultrathin nanosheets on conductive substrates as advanced electrodes for high-efficient energy storage. *J. Power Sources* **2016**, *306*, 100−106.
(11) Nelson, A.; Fritz, K. E.; Honrao, S.; et al. Increased activity in hydrogen evolution electrocatalysis for partial anionic substitution in cobalt oxysulfide nanoparticles. *J. Mater. Chem. A* **2016**, *4*, 2842−2848.
(12) Singh, Y.; Back, S.; Jung, Y. Activating Transition Metal Dichalcogenides by Substitutional Nitrogen Doping for Potential ORR Electrocatalysts. *ChemElectroChem* **2018**, *5*, 4029−4035.
(13) Cui, Y.; Zhou, C.; Li, X.; et al. High performance electrocatalysis for hydrogen evolution reaction using nickel-doped CoS_2 nanostructures: experimental and DFT insights. *Electrochim. Acta* **2017**, *228*, 428−435.
(14) Voiry, D.; Yang, J.; Chhowalla, M. Recent strategies for improving the catalytic activity of 2D TMD nanosheets toward the hydrogen evolution reaction. *Adv. Mater.* **2016**, *28*, 6197−6206.
(15) Woo, J.; Sim, E. S.; Je, M.; et al. Theoretical dopant screening and processing optimization for vanadium disulfide as cathode material for Li-air batteries: a density functional theory study. *Appl. Surf. Sci.* **2020**, No. 145276.
(16) Ferrero, G. A.; Fuertes, A. B.; Sevilla, M.; et al. Efficient metal-free N-doped mesoporous carbon catalysts for ORR by a template-free approach. *Carbon* **2016**, *106*, 179−187.
(17) Ding, W.; Wei, Z.; Chen, S.; et al. Space-Confinement-Induced Synthesis of Pyridinic-and Pyrrolic-Nitrogen-Doped Graphene for the Catalysis of Oxygen Reduction. *Angew. Chem.* **2013**, *125*, 11971−11975.
(18) Jiang, S.; Sun, Y.; Dai, H.; et al. Nitrogen and fluorine dual-doped mesoporous graphene: a high-performance metal-free ORR electrocatalyst with a super-low HO_2—yield. *Nanoscale* **2015**, *7*, 10584−10589.
(19) Tang, C.; Min, Y.; Chen, C.; et al. Potential Applications of Heterostructures of TMDs with MXenes in Sodium-Ion and Na−O_2 Batteries. *Nano Lett.* **2019**, *19*, 5577−5586.
(20) Tan, S. M.; Chua, C. K.; Sedmidubský, D.; et al. Electrochemistry of layered GaSe and GeS: applications to ORR, OER and HER. *Phys. Chem. Chem. Phys.* **2016**, *18*, 1699−1711.
(21) Alves, H. J.; Junior, C. B.; Niklevicz, R. R.; et al. Overview of hydrogen production technologies from biogas and the applications in fuel cells. *Int. J. Hydrogen Energy* **2013**, *38*, 5215−5225.
(22) Li, Y.; Gong, M.; Liang, Y.; et al. Advanced zinc-air batteries based on high-performance hybrid electrocatalysts. *Nat. Commun.* **2013**, *4*, No. 1805.
(23) Qu, K.; Zheng, Y.; Dai, S.; et al. Graphene oxide-polydopamine derived N, S-codoped carbon nanosheets as superior bifunctional electrocatalysts for oxygen reduction and evolution. *Nano Energy* **2016**, *19*, 373−381.
(24) Chia, X.; Eng, A. Y. S.; Ambrosi, A.; et al. Electrochemistry of nanostructured layered transition-metal dichalcogenides. *Chem. Rev.* **2015**, *115*, 11941−11966.
(25) Christensen, R.; Hansen, H. A.; Dickens, C. F.; et al. Functional independent scaling relation for ORR/OER catalysts. *J. Phys. Chem. C* **2016**, *120*, 24910−24916.
(26) Tripković, V.; Skúlason, E.; Siahrostami, S.; et al. The oxygen reduction reaction mechanism on Pt(1 1 1) from density functional theory calculations. *Electrochim. Acta* **2010**, *55*, 7975−7981.
(27) Bai, X.; Zhao, E.; Li, K.; et al. Theoretical insights on the reaction pathways for oxygen reduction reaction on phosphorus doped graphene. *Carbon* **2016**, *105*, 214−223.
(28) Liang, W.; Chen, J.; Liu, Y.; et al. Density-functional-theory calculation analysis of active sites for four-electron reduction of O2 on Fe/N-doped graphene. *ACS Catal.* **2014**, *4*, 4170−4177.
(29) Xiao, Y.; Zhang, W. Mechanism of Electrocatalytically Active Precious Metal (Ni, Pd, Pt and Ru) Complexes in the Graphene Basal Plane for ORR Applications in Novel Fuel Cells. *Energy Fuels* **2020**, *34*, 2425−2434.
(30) Xiao, Y.; Zhang, W. DFT analysis elementary reaction steps of catalytic activity for ORR on metal-, nitrogen-co-doped graphite embedded structure. *SN Appl. Sci.* **2020**, *2*, 194.
(31) Kresse, G.; Furthmüller, J. Efficient iterative schemes for ab initio total-energy calculations using a plane-wave basis set. *Phys. Rev. B* **1996**, *54*, 11169.
(32) Nørskov, J. K.; Rossmeisl, J.; Logadottir, A.; et al. Origin of the overpotential for oxygen reduction at a fuel-cell cathode. *J. Phys. Chem. B* **2004**, *108*, 17886−17892.
(33) Tripković, V.; Skúlason, E.; Siahrostami, S.; et al. The oxygen reduction reaction mechanism on Pt (1 1 1) from density functional theory calculations. *Electrochim. Acta* **2010**, *55*, 7975−7981.
(34) Ho, J. C. K.; Piron, D. L. Active surface area in oxide electrodes by overpotential deposited oxygen species for the oxygen evolution reaction. *J. Appl. Electrochem.* **1996**, *26*, 515−521.
(35) Grillo, M. E.; Finnis, M. W.; Ranke, W. Surface structure and water adsorption on Fe_3O_4 (111): Spin-density functional theory and on-site Coulomb interactions. *Phys. Rev. B* **2008**, *77*, No. 075407.
(36) Mott, N. F. Conduction in non-crystalline materials: III. Localized states in a pseudogap and near extremities of conduction and valence bands. *Philos. Mag.* **1969**, *19*, 835−852.
(37) Henkelman, G.; Uberuaga, B. P.; Jónsson, H. A climbing image nudged elastic band method for finding saddle points and minimum energy paths. *J. Chem. Phys.* **2000**, *113*, 9901−9904.
(38) Sheppard, D.; Xiao, P.; Chemelewski, W.; et al. A generalized solid-state nudged elastic band method. *J. Chem. Phys.* **2012**, *136*, No. 074103.
(39) Kresse, G.; Furthmuller, J. Efficiency of Ab-Initio Total Energy Calculations for Metals and Semiconductors Using a Plane-Wave Basis Set. *Comput. Mater. Sci.* **1996**, *6*, 15−50.
(40) Perdew, J.; Burke, K.; Ernzerhof, M. Generalized Gradient Approximation Made Simple. *Phys. Rev. Lett.* **1996**, *77*, 3865−3868.

https://dx.doi.org/10.1021/acs.energyfuels.0c00297
Energy Fuels 2020, 34, 5006−5015

(41) Shin, H.; Choi, W.; Choi, J. Y.;et al. Doped Graphene, Method of Manufacturing the Doped Graphene, and a Device Including the Doped Graphene. U.S. Patent US98870202018.
(42) Wang, V.; Xu, N. *VASPKIT: A Pre-and Post-processing Program for the VASP Code*, 2013.
(43) Makov, G.; Payne, M. C. Periodic boundary conditions in ab initio calculations. *Phys. Rev. B* **1995**, *51*, 4014.
(44) Fomine, S.; Vargas, S. M.; Tlenkopatchev, M. A. Molecular modeling of ruthenium alkylidene mediated olefin metathesis reactions DFT study of reaction pathways. *Organometallics* **2003**, *22*, 93−99.
(45) Tripković, V.; Skúlason, E.; Siahrostami, S.; et al. The oxygen reduction reaction mechanism on Pt (1 1 1) from density functional theory calculations. *Electrochim. Acta* **2010**, *55*, 7975−7981.
(46) Xiao, Y.; Wang, J.; Wang, Y.; et al. A new promising catalytic activity on blue phosphorene nitrogen-doped nanosheets for the ORR as cathode in nonaqueous Li−air batteries. *Appl. Surf. Sci.* **2019**, *488*, 620−628.
(47) Simón, L.; Goodman, J. M. How reliable are DFT transition structures? Comparison of GGA, hybrid-meta-GGA and meta-GGA functionals. *Org. Biomol. Chem.* **2011**, *9*, 689−700.
(48) Vittadini, A.; et al. "Formic acid adsorption on dry and hydrated TiO_2 anatase (101) surfaces by DFT calculations.". *J. Phys. Chem. B* **2000**, 1300−1306.
(49) Xiao, Y.; Zhang, W. Adsorption Mechanisms of Mo_2CrC_2 MXenes as Potential Anode Materials for Metal-ion Batteries: A First-Principles Investigation. *Appl. Surf. Sci.* **2020**, No. 145883.
(50) Hao, L.; Yu, J.; Xu, X.; et al. Nitrogen-doped MoS2/carbon as highly oxygen-permeable and stable catalysts for oxygen reduction reaction in microbial fuel cells. *J. Power Sources* **2017**, *339*, 68−79.
(51) Calle-Vallejo, F.; Martínez, J. I.; Rossmeisl, J. Density functional studies of functionalized graphitic materials with late transition metals for oxygen reduction reactions. *Phys. Chem. Chem. Phys.* **2011**, *13*, 15639−15643.
(52) Greeley, J.; Stephens, I. E. L.; Bondarenko, A. S.; et al. Alloys of platinum and early transition metals as oxygen reduction electrocatalysts. *Nat. Chem.* **2009**, *1*, 552.
(53) Fazio, G.; Ferrighi, L.; Di Valentin, C. Boron-doped graphene as active electrocatalyst for oxygen reduction reaction at a fuel-cell cathode. *J. Catal.* **2014**, *318*, 203−210.
(54) Li, L.; Wei, Z. D.; Zhang, Y.; et al. DFT study of difference caused by catalyst supports in Pt and Pd catalysis of oxygen reduction reaction. *Sci. China, Ser. B: Chem.* **2009**, *52*, 571−578.
(55) xiong, W.; Zhang, J.; Xiao, Y.; et al. Oxygen-rich nanoflakes-interlaced carbon microspheres for potassium-ion battery anodes. *Chem. Commun.* **2020**, No. 3433.
(56) Lu, F.; Zhang, Y.; Liu, S.; et al. Surface proton transfer promotes four-electron oxygen reduction on gold nanocrystal surfaces in alkaline solution. *J. Am. Chem. Soc.* **2017**, *139*, 7310−7317.
(57) Deng, C.; He, R.; Wen, D.; et al. Theoretical study on the origin of activity for the oxygen reduction reaction of metal-doped two-dimensional boron nitride materials. *Phys. Chem. Chem. Phys.* **2018**, *20*, 10240−10246.
(58) Zhang, J.; Zhao, Z.; Xia, Z.; et al. A metal-free bifunctional electrocatalyst for oxygen reduction and oxygen evolution reactions. *Nat. Nanotechnol.* **2015**, *10*, 444.
(59) Xiao, Y.; Zhang, W. High Throughput Screening of M_3C_2 MXenes for Efficient CO_2 Reduction Conversion into Hydrocarbon Fuels. *Nanoscale* **2020**, No. 10598.
(60) He, F.; Li, K.; Yin, C.; et al. Single Pd atoms supported by graphitic carbon nitride, a potential oxygen reduction reaction catalyst from theoretical perspective. *Carbon* **2017**, *114*, 619−627.

https://dx.doi.org/10.1021/acs.energyfuels.0c00297
Energy Fuels 2020, 34, 5006−5015

Electrochimica Acta 378 (2021) 138028

Contents lists available at ScienceDirect

Electrochimica Acta

journal homepage: www.elsevier.com/locate/electacta

Mechanistic study of efficient producing CO_2 electroreduction via 2D metal-organic frameworks M_3(2,3,6,7,10,11-hexaiminotriphenylene)$_2$ surface

Yi Xiao[a,*], Dazhu Chen[b], Rui Chen[b,c,**]

[a] Institute of Materials Science, TU Darmstadt, Darmstadt 64287, Germany
[b] College of Materials Science and Engineering, Shenzhen University, Shenzhen 518061, China
[c] College of Physics and Optoelectronic Engineering, Shenzhen University, Shenzhen 518060, China

ARTICLE INFO

Article history:
Received 10 November 2020
Revised 23 January 2021
Accepted 18 February 2021
Available online 24 February 2021

Keywords:
High throughput calculation
Metal-organic frameworks
Co_2 electroreduction
Overpotential
Thermodynamics

ABSTRACT

M_3(HITP)$_2$ prototype 2D MOFs compounds possess a high catalytic activity for CO_2 electroreduction to hydrocarbon fuels at low overpotentials. However, the mechanism path selectivity is still a huge challenge during the production of final product species at low potentials. The transition metal coordinated nitrogen active center of M_3(HITP)$_2$ catalysts is identified to strong M-C bound coupling, leading to a high selectivity towards CH_3OH, Cr_3(HITP)$_2$, and Mn_3(HITP)$_2$. Further, it also demonstrates a high efficiency catalytic performance for generating CH_4. In addition, linear scaling relations and volcano plot of thermodynamic stability are also investigated and compared, suggesting that some M_3(HITP)$_2$ compounds have effective selectivity performance to CO_2 reduction reaction (CO_2RR). Furthermore, linear scaling relationships and volcano plots between different intermediate species are common descriptors used to identity an excellent catalyst for CO_2 electroreduction. In order to get a further exploration of the reaction mechanism pathway and final products for the CO_2RR, authors considered all the intermediates. It showed that the most favorable reaction pathway and intermediate species can be determined by the metal-carbon (M-C) or metal-oxygen (M-O) bounds. The reduction of CO_2 into CH_4 with a high overpotential depends on the thermodynamic rate-determining step (RDS) of the largest limiting potential along the minimum energy path, the electronic structure of these catalysts also plays an important role in the selective CO_2RR.

Introduction

To further control the emission of carbon dioxide greenhouse gases mainly from the combustion of fossil energy [1,2], the development of high-performance catalysts to capture and reduce CO_2 to hydrocarbon fuels [3] can help energy-saving and emission reduction to resolve environmental issues. Carbon dioxide, one of the main components of greenhouse gases and mainly produced from the combustion of fossil fuels, it has attracted the primary concern of today's environmental issues. Developing high-performance catalysts to capture and reduce CO_2 into hydrocarbon fuels has been considered as an economic and effective way to help energy-saving and emission reduction and pursued by numerous researchers during last several decades [4]. However, regarding energy storage and conversion the reduction mechanism of CO_2 is still met with significant challenges [5], like the poor efficiency of catalysts and the selectivity of the product is not clear [6]. So many materials have been tested as catalysts to produce hydrocarbon fuels from CO_2 thus far. Hori and co-workers [7], tested various precious metals and metal oxides as CO_2 reduction catalysts depending on the observed product selectivity. As summary, Pb, Hg, In, Sn, Cd, and Tl produce formate as the final product; Zn, Ag, Pd, and Au are easier to form CO as the final product [8]. Most of the catalysts were carried out by experiments within polycrystalline or heterostructure materials [9], which is often costly and time-consuming. Therefore, density functional theory (DFT) calculation as a powerful tool is becoming and popular for studying catalytic mechanism and developing new high efficiency catalysts for CO_2 reduction. Theoretical predictions have been done using crystal with (1) Metal-nitrogen-doped carbon catalysts [10], (2) Nanostructured gold, copper, and metal alloy materials [11], (3) Au- and Cu-based materials: Au, Zn, and CuAu alloy nanoclusters [12], (4) 2D materials (such as TMDs, MXenens, and MOFs) [13,14], (5) Pt-based alloy nanoparticle catalysts [14,15], and (6) Grain boundary surface [16]. It can provide some qualitative conclusions to gain an insight into the reaction

* Corresponding author.
** Corresponding author.
E-mail addresses: yixiao@tmm.tu-darmstadt.de (Y. Xiao), ruichen@szu.edu.cn (R. Chen).

https://doi.org/10.1016/j.electacta.2021.138028
0013-4686/

mechanism that is difficult to obtain by experiments. Up to now the modeling method is still undergoing rapid development due to the fact that the CO_2 reduction reaction process is complex. In addition to considering the electronic properties of materials of catalyst, the formation energy of intermediates and thermodynamic stability of each elementary steps on the catalyst surface is also important to consider. The strength of O-bound and C-bound between intermediates and the catalyst surface plays a very important role in controlling the reaction pathway and the product selectivity of the CO_2RR [17,18]. Nørskov and co-workers [19] proposed that the linear scaling relations and volcano relationship of the formation energy of intermediates can determine the catalytic activity as well as the thermodynamic stability.

Some recent experimental and theoretical works have identified a new class of 2D $M_3(HITP)_2$ metal-organic frameworks (MOFs) which have been studied as the catalysts for CO_2 reduction [20]. $Co_3(HITP)_2$ and $Rh_3(HITP)_2$ demonstrate an excellent catalytic activity for the reduction of CO_2 to CH_3OH, with small overpotentials of 0.67 and 0.46 V, respectively. Sun and Chen [21], found that Ni_3 $(HITP)_2$ exhibits a high catalytic activity for oxygen reduction reaction (ORR). Dou et al. [22], found that $M_3(HIB)_2$ (M = Ni, Cu; HIB = hexaiminobenzene) are insulators with quite low conductance by experiments. Tian et al. [23], through theoretical insights into the catalytic mechanism for the ORR on $M_3(HITP)_2$, found that the hydrogenation steps are kinetically favorable and explained that $M_3(HITP)_2$ (M = Ni, Cu) are promising catalysts for the ORR. In this work, a comprehensive theoretical study of a number of $M_3(HITP)_2$ (M = Cr, Mn, Fe, Co, Ni, Cu, Rh, Os, Ir, Pt, and Au) surfaces for high efficiency electroreduction of CO_2 is presented and various intermediate products are estimated under different applied potential. DFT is used to calculate the formation energy and estimate the limiting potential (overpotential) along the most favorable pathway for each proton-electron transferred step. Firstly, the structure optimization was performed on $M_3(HITP)_2$ unit-cell surfaces using conjugate gradient method to determine their selectivity between CO_2RR and hydrogen evolution reaction (HER) from the change of binding energies. $U_L(CO_2)$-$U_L(H_2)$, a useful descriptor for CO_2RR and the competing HER processes, apart from the interference of HER on those catalysts, the electronic properties are also observed to understand catalytic efficiency for this class of MOF CO_2RR catalysts. Authors found that the d-band center [24] can rationalize these activity trends, specifically due to its correlation to the binding energy of adsorbates, which can be used to describe the strongly correlated catalytic activity by the localized d electronic structures of transition metal. Through the theoretical evaluation of CO_2RR catalysts undertaken, we plot a volcano plot to establish a linear scaling relation of intermediates, depending on the Gibbs energy profiles of CO_2RR. The $M_3(HITP)_2$ (M = Cr, Mn, and Ru) catalysts revealed a high catalytic efficiency for CO_2RR with their low overpotential [25,26]. The low costs, high efficiency, and high selectivity of metal organo-inorganic hybrid catalysts for CO_2 reduction motivates us to further progress [27].

Computational detail

All calculations were carried out by a DFT method within spin-polarized wave functions using a VASP code [28]. The Perdew–Burke–Ernzerhof (PBE) functional within the generalized gradient approximation (GGA) was employed to describe the electron exchange correlation interactions [29], and the DFT-D3 scheme [30] was utilized for the dispersion correction of the van der Waals interactions with the most stable adsorption configurations of all the CO_2RR intermediates. A basis set cutoff energy of 500 eV as the plane-wave (PAW) was used to describe the core electrons [31], while a vacuum space of 20 Å was set to avoid interactions being repeated between periodic images along the *z* direction. The monolayer $M_3(HITP)_2$ computing modes were built by replacing a Ni atom from $Ni_3(HITP)_2$, and a Monkhorst–Pack of 5 × 5 × 1 k-point mesh for all during geometry optimizations in the Brillouin zone was sampled. The convergence criteria for energy was set to 1.0 × 10^{-5} eV for each atom relaxed. Further, the electronic properties calculation, including the density of states (DOS) and charge density, was also considered for various catalysts. The DFT+U method [32] was used to overcome the strongly correlated localized d electronic structures of transition metal, and a cutoff energy of 600 eV with a U_{eff} = 3 eV and 11 × 11 × 1 k-point mesh was considered in the electronic properties calculation. The Gibbs free energy change (ΔG) of each elementary reaction for CO_2RR involved a proton and an electron (H^++e^-) pair transfer, and the computational hydrogen electrode model proposed by Nørskov et al. [33] was used to calculate the formation energy of intermediates. On the basis of this model, the free energy of (H^++e^-) pair is defined to half of the potential of isolated hydrogen H_2(g) versus CHE [34] at pH = 0. The variation of ΔG is the relative energy of intermediate formation (see details from the supporting information) in each step based on the chemical reaction of the 2D MOFs. The Gibbs free energy can be corrected using the following expression: $\Delta G = \Delta E_{DFT} + \Delta ZPE + \Delta H - T\Delta S + \Delta GpH + \Delta G_U$, where ΔE_{DFT} is obtained from DFT calculations and a relaxed structure is proposed, it depends on the chemical reaction process for each CO_2RR intermediate species formation, $\Delta ZPE + \Delta H$ is the zero-point energies and enthalpy correction terms, ΔS is the entropy correction term, and *T* is a specific temperature. ΔG_U and ΔGpH are the contribution of electrode potential U and the correction of hydrion (H^+) energy to the Gibbs free energy. They can be obtained from ΔG_U = -neU and $\Delta G_{pH} = -k_B T \ln[H^+] = pH \times k_B T \ln 10$, ne represents the number of electrons transferred that correspond to each elementary steps, while U is the electrode potential. Furthermore, ΔZPE and TΔS can be calculated from the frequencies data using the VASPKIT code [35], in which only the vibrational modes of the adsorbates' modes were considered while the slab was fixed. Limiting potential (U_L) [36] was defined to the maximum energy change (ΔGmax) along the minimum energy reaction pathway. It is known as a RDS from maximal limiting potential, following this descriptor: $U_L = -\Delta Gmax/e$. Theoretical overpotential [36] was deduced using the formula $\eta = U_0 - U_L$, where U_0 is the equilibrium potential (Table S3) corresponding to a final product of a specific reaction pathway.

Results and discussion

The2D $M_3(HITP)_2$ (M = Cr, Mn, Co, Ni, Cu, Rh, Ir, Os Pt and Au) metal-organic frameworks based on transition metals as catalytic active centers have been validated by experimental data, as multi-functional catalyst has been synthesized successfully through chemical reforming (see Fig. 1a,b) [37]. In order to evaluate whether our selected 2D $M_3(HITP)_2$ MOFs structures are suitable for electroreduction CO_2, we calculated the electronic properties of single-layer $M_3(HITP)_2$, including $M_3(HITP)_2$ monolayers that have excellent conductivity properties. So far, their catalytic activities in CO_2 electroreduction to hydrocarbon products provide inadequate evidence to support their application in practice. We found that these coupling organometallic hybrid structure $M_3(HITP)_2$ layers can prove the electron properties, and they can find the best catalytic activity by changing the hybridization form of central atomic orbital of coordinated metal state. For example, the nickel and cobalt coordination are dsp^2 hybridization (semiconducting) as shown in Fig. 1c, indicating the high tunability electronic properties of $M_3(HITP)_2$ by transition metal substitution. We can see that the Co, and Ni-based $M_3(HITP)_2$ are all metallic and have good electrical conductivity. The high conductivities can en-

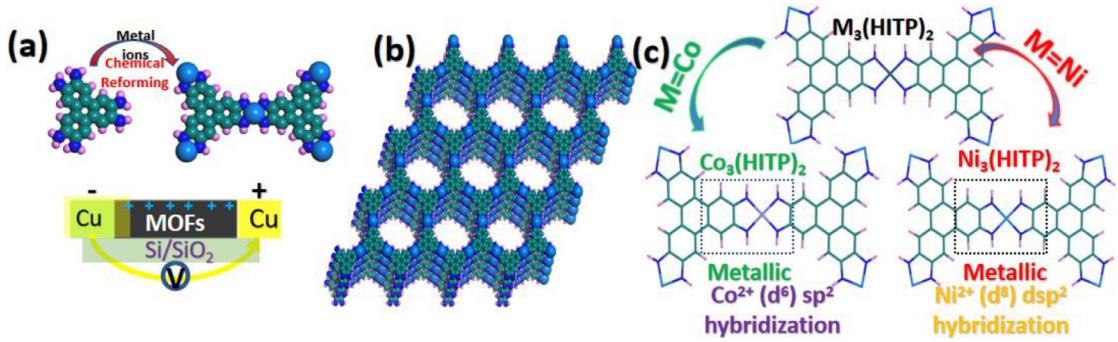

Fig. 1. (a) Synthesis of M_3(2,3,6,7,10,11-hexaiminotriphenylene)$_2$ diagram and schematic illustration of the Cu-MOF fuel cell systems, (b) 3D coordination supercell structure of $Co_3(HITP)_2$, (c) Illustration of 2D MOFs $M_3(HITP)_2$ (*M*=Co and Ni) geometry within the 2D plane.

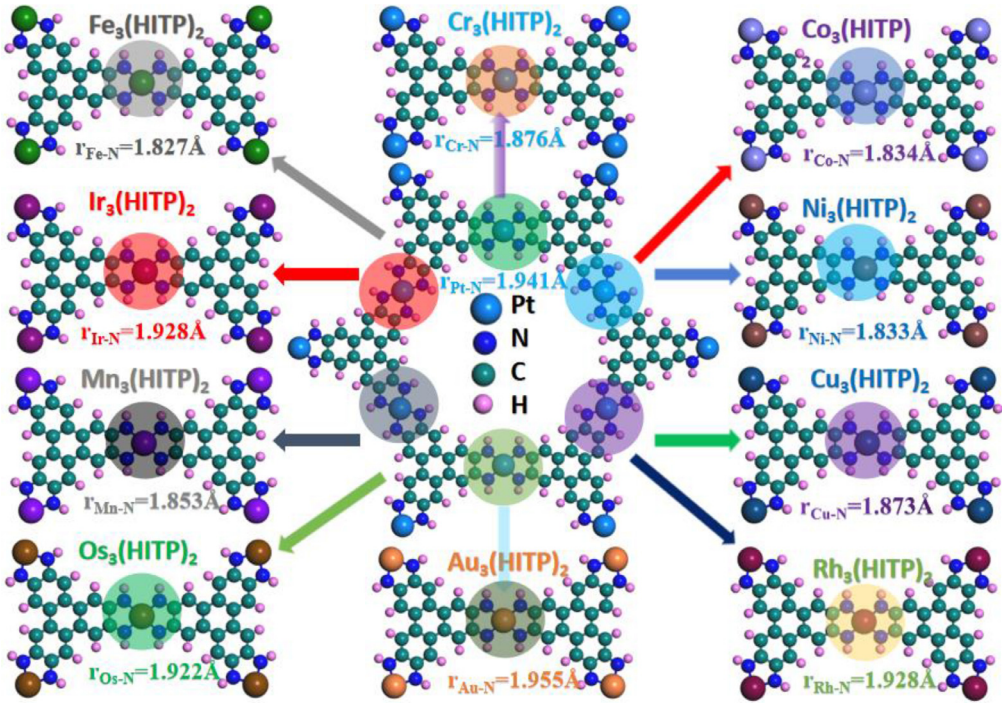

Fig. 2. Side views of 2D $M_3(HITP)_2$ sheets and r_{M-N} indicate the bond length are taken from the most stable optimized configurations (Å).

sure fast electron transfer during the process of electroreduction reaction. According to this criterion, we constructed a series of $M_3(HITP)_2$ structures with metal (M = Cr, Mn, Co, Ni, Cu, Rh, Ir, Os Pt, and Au) substitution [38]. The calculation results, involving geometrical parameters of these structures, were shown in Fig. 2. In order to obtain the best electrocatalysis performance, more detailed data is shown in Table S2 and S3.

To further investigate the geometry of in-plane network and the geometrical parameters that could be achieved from the structural relaxation, 2D $M_3(HITP)_2$ sheets are modified, as shown in Fig. 2. It displays the stable configurations, and the primary structural parameters are considered. It shows that a transition metal form a coordinating ligand with four equivalent nitrogen atoms, indicating the MN_4 as a metal active centre of catalyst. In the $Cr_3(HITP)_2$ site, the Cr−N lengths are 1.876, and the Cu−N lengths of $Cu_3(HITP)_2$ are 1.873 Å. Meanwhile, the bond of Co−N (with a length of 1.834 Å) and Ni−N lengths are 1.833. On the basis of the shorter the more stable, s they are obviously stronger than the other M-N bonding. In the $Au_3(HITP)_2$ and $Rh_3(HITP)_2$ site, the Au-N lengths are 1.955 Å and the Rh-N lengths are 1.928 Å. From the length comparison, it can also be clearly seen that $Fe_3(HITP)_2$ and $Ir_3(HITP)_2$ are much stronger than Au in terms of metal and nitrogen binding. It demonstrates the possibility that these organic and inorganic hybrid compounds may possess an excellent electrocatalytic performance for CO_2RR. In addition to a well-studied topic between non-metal and metal atoms, it also involves the CO_2 reduction reaction. The metal-atom substitution $M_3(HITP)_2$ catalysts obtain their high activity from the reaction sites. To explore the overall catalytic performance of the transition metals based $M_3(HITP)_2$ 2D MOF as a catalyst for the conversion of CO_2 reduction to CH_4, the free energy diagram on $M_3(HITP)_2$ sheets was shown in Figs.S3 and 4. In this work, authors took advantage of those great unique catalytic properties of transition metals, which have been investigated according to previous literature, and focused on the different intermediate products reduced to CH_4 from CO_2 along all possible reaction paths. Furthermore, authors illustrated the minimal energy reaction paths of each catalyst, identified different final products, and then calculated the limiting potential of each elementary reaction step and overpotential based on the rate-determining steps (RDSs) [39–40].

Furthermore, authors considered both reactions of COOH, going to HCOOH or CO – which path was more likely to react. Although the COH and CHO intermediates were found to be unstable on the transition metals-nitrogen active center, it was found that these in-

termediates were much less stable than the HCHO and CH_3O intermediates on the $Ni_3(HITP)_2$ surfaces (see Fig. 5a). Every reaction pathway involved eight proton–electron pairs transferred from CO_2 reduction to CH_4. Herein, it need to be pointed out that authors did not consider electrode potential, because the formation energy of each reaction steps is calculated at zero voltage and 298.25 K without taking the effect of applied potential into account. According to the computational standard hydrogen electrode model, the variation of Gibbs free energy (ΔG) is the relative energy of intermediate formation in each elementary reaction step. The limiting potential (U_L) is estimated as the change of the variation of Gibbs free energy (ΔG), while the overpotential depends on the equilibrium potential (Table S3) which is obtained using $\eta = U_0 - U_L$. This means that under the applied electrode potential, each step of the overall reaction pathway becomes an exothermic process [41–42]. It assumes that the energy required to carry out a reaction step for proton transfers is small and easily feasible under room temperature. In summary, there are six alternative reaction paths during CO_2 reduction to CH_4. Due to the HER, there are competitive relationships with CO_2RR. *H binding energies, a HER free energy diagram, and change limiting potentials for the CO_2RR and HER of $U_L(CO_2)$-$U_L(H_2)$ are also included in Figs.S2a and b.

The 2D $M_3(HTIP)_2$ exhibit a significant change in the electronic properties for different transition metals substitution, as shown in Fig. 3 (PDOS) and Figure S1 (TDOS). The $Cr_3(HTIP)_2$ sheet is a semiconductor with a band-gap of 0.663 eV (Fig. S1a), while the $Ni_3(HTIP)_2$ and $Cu_3(HTIP)_2$ sheet (Figure S1e, 1f) are still semimetal, with a small band-gap of 0.179 eV and 0.191 eV, respectively. Fig. 3 shows that the 3d orbitals of transition metal are major contributors to the DOS. Our analysis focuses on the distribution of the PDOS of the 2D $M_3(HITP)_2$ MOF in the energy range from −1 to 1 eV at the Fermi level, underlying the formation of the valence shell orbital hybridization and forming M-N metal-nitrogen bonds. In Fig. 3a, the main PDOS distribution of $Cr_3(HITP)_2$ HITP is localized in the range from −0.9 to 0 eV below Fermi level (0 eV), indicating the formation of dsp^2 hybridization and presenting a semiconductor feature. This indicates a significant difference in the electronical properties of $M_3(HTIP)_2$ sheet between metals and nitrogen, and overlaps the valence d orbitals of metal versus p orbitals of nitrogen under relatively high energy levels. N atom tends to utilize all three of its valence 2p orbitals, resulting in dsp^2 hybridization formation, four valence p orbitals of nitrogen with d orbitals of metal to form to dsp^2 (semiconducting), and sp^3 (metallic and semimetal) orbital hybridization. So, here are some issues, for the upper valance bands, there is an obvious admixture orbital hybridization [43] that is dominated by d and p-states (between −0.2 and 0.2 eV) and forms a covalent bonding contribution in $Mn_3(HITP)_2$. HITP? As a result of hybridization, the metal s-states and p-states of N and C atoms contribute to the valance bands. The higher conduction band is governed by d states of metal by examination, the PDOS exhibited the band gap presence between the occupied (conduction band) and unoccupied (valance bands) states [44], respectively.

The calculations exhibited an excellent catalytic performance based upon the evaluation of the free energy of each proton–electron pairs transferred step. It showed good performance of electro-catalytic reduction for CO_2. The final product from CO_2 reduction to CH_4 can be defined as follows: $CO_2+8H^++8e^-\rightarrow CH_4+2H_2O$, which involves eight proton electron transfer steps. Meanwhile, CO_2 reduction to carbon monoxide (CO) and formic acid (HCOOH) involves two proton electron transfer steps: $CO_2+2H^++2e^-\rightarrow CO+H_2O$ and $CO_2+2H^++2e^-\rightarrow HCOOH$. For detailed analysis, the first protonation reaction step of CO_2 reduction forms the intermediate *COOH or HCO_2 which M-O or M-C binding coupling has a stronger bonding to catalyst surface. For the second protonation step, there are two possibilities that intermediate products may be generated. CO and HCOOH, as final products from COOH production, were considered. The CO formation is familiar to these transition metal $M_3(HITP)_2$ MOFs catalysts, where the protonation occurs at the OH segment of the *COOH to yield *CO. Water is formed and released from the catalyst surface. The small reaction energy ($\Delta G = -0.75$ eV) of COOH was formed on the $Cr_3(HITP)_2$ surface, indicating that this pathway is the most optimum catalyst along the reaction pathway: the lowest free energy pathway alone $*CO_2\rightarrow *HCO_2\rightarrow *H_2CO_2\rightarrow *H_2COOH\rightarrow *HCHO\rightarrow *H_3CO\rightarrow *O\rightarrow *OH\rightarrow *H_2O$ compared to the other MOF catalysts. Meanwhile, the lowest overpotential pathway alone, $*CO_2\rightarrow *COOH\rightarrow *CO\rightarrow *CHO\rightarrow *HCHO\rightarrow *H_2COH\rightarrow *H_3COH\rightarrow *CH_3\rightarrow *CH_4$, is the most possible through which *COOH is easier formed in $Cr_3(HITP)_2$ (η: 0.62 V) and $Mn_3(HITP)_2$ (η: 0.69 V) by the strong O–H coupling with hydrogen to the OH atom of *COOH. It was found to be significantly more favorable. Proceeding along the third pathway, it indicated that the lowest energy path CO_2 reduction to CH_4 on $Ir_3(HITP)_2$ is $*CO_2\rightarrow *HCO_2\rightarrow *H_2CO_2\rightarrow *H_2COOH\rightarrow *HCHO\rightarrow *H_3CO\rightarrow *CH_3OH\rightarrow *CH_3\rightarrow *CH_4$. It is worth mentioning that the binding of the intermediates on the catalyst surface (*COOH, *CHO, and $*CH_2OH$) to the $Mn_3(HITP)_2$ MOFs surface are through the strong M-C coupling, while the other intermediates, such as $*HCO_2$, $*H_3CO$, and *HCOOH, bind to the MOFs surface through the strong M-O coupling.

Figs. 4 and S9 calculated the relative Gibbs free energy diagram for CO_2 reduction to CH_4 of each intermediate on $Pt_3(HITP)_2$ MOFs surface. The corresponding free energy profiles and their geometric configurations were also discussed and are presented in Fig. 4. The most favorable reaction pathway of CO_2RR strongly depends on how the successive protonation step was. The first protonation of CO_2 forms the HCO_2 and COOH intermediate species; the reaction energy is 1.75 eV of $*HCO_2$ and 1.24 eV of *COOH, respectively. However, the Pt-C coupling is more thermodynamically preferred than hydrogenation of Pt-O coupling. It implies that *COOH formation would be easier than $*HCO_2$ formation, which is followed by the third H^+/e^- transfer to form the *HCOOH intermediate species with −0.72 eV. As a result, the fourth H^+/e^- of *CHO is formed (0.59 eV), although the release of this captured *HCHO and formation of *HCOH require an amount of reaction energy (−1.68 and −0.72 eV, respectively) due to the strong interactions between adsorbates and catalyst surface. Further, the CO_2 conversion into CH_4 catalyzed by $Pt_3(HITP)_2$ MOFs follows a common route reaction pathway and involves successive hydrogenations on the M-C or M-O terminate coupling of intermediate species to reach $*H_2COH$ (−0.07 eV), *O (−0.12 eV), *OH (−1.67 eV), *C(1.26 eV), *CH (−0.76 eV), and $*CH_3$ (0.27 eV), since the reaction energy of $*CH_3O$ is more thermodynamically preferred than $*H_2COH$ along the first path. Furthermore, our results predict some common products towards the formation of CO, HCHO, and CH_3OH as final products that are favored with respect to the electroreduction hydrogenation on $Pt_3(HITP)_2$. The lower reaction energy ($\Delta G_{reactant} - \Delta G_{product}$) of each step indicates a higher reactivity [45], as shown by the exothermic reaction process in the seventh and eighth hydrogenation to form the *OH and H_2O species along path 1, which have a larger reaction energy corresponding to the *OH and H_2O formation of −1.67 and −1.96 eV, respectively. That indicates our proposed catalysts present a different thermodynamics model with an electrochemical feature. $*H_2O$ and $*CH_4$, reaction energy values of −1.67 and −1.44 eV, are defined as the best final products alternatives for the catalytic reduction of CO_2 based on M_3(2,3,6,7,10,11-hexaiminotriphenylene)$_2$ MOF during our present study. For comparison, Cu surface (Zhang et al. [46], CO_2 to CH_4, limiting step of 0.74 eV) or graphene/MoS_2 (Xiao et al. [47], CO_2 reduction to CO, overpotential of 0.54 eV).

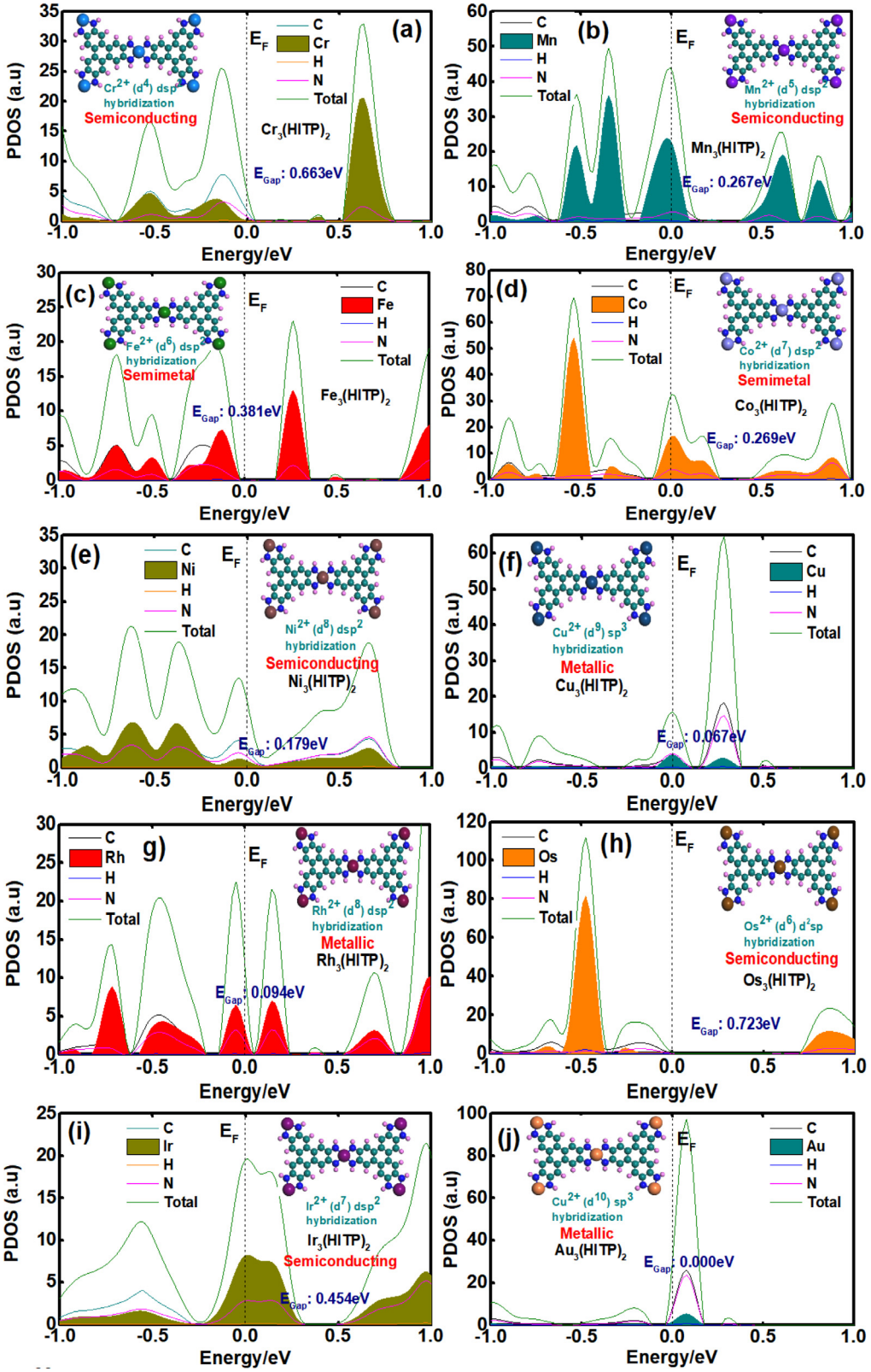

Fig. 3. Density of states (DOS) (above) and projected density of states (PDOS) (below) of the (a) $Cr_3(HITP)_2$, (b) $Mn_3(HITP)_2$,(c)$Fe_3(HITP)_2$,(d)$Co_3(HITP)_2$,(e)$Ni_3(HITP)_2$ (f)$Cu_3(HITP)_2$,(g)$Rh_3(HITP)_2$(h)$Os_3(HITP)_2$(i)$Ir_3(HITP)_2$ and (j)$Au_3(HITP)_2$, respectively. Which are obtained from the GGA-PBE D3 calculation, the Fermi energy is referenced at 0 eV.

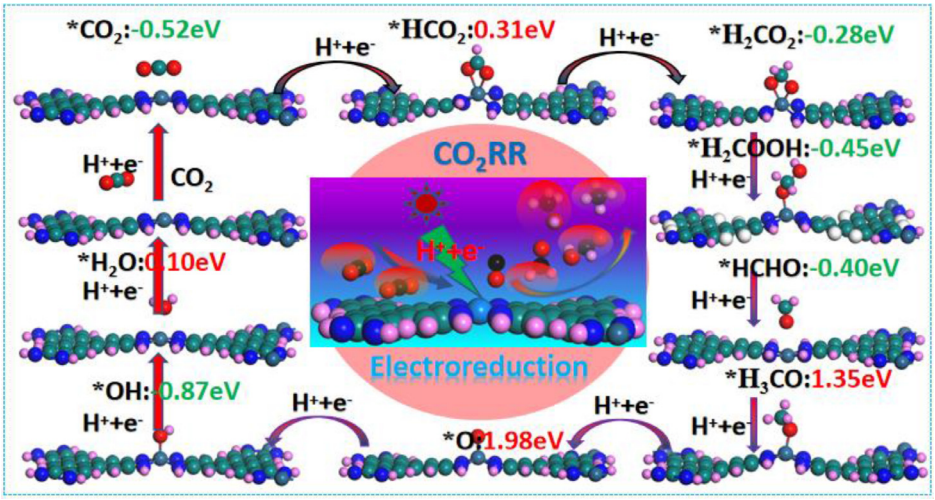

Fig. 4. Side view of all intermediates at each hydrogenation step of CO_2 reduction mechanism to CH_4 via $Pt_3(HITP)_2$ sheets. The reaction energies are labeled in eV with red (endothermic) and dark cyan (exothermic) by reactions, respectively. * represents the adsorbed species.

Figs.5 and S7 show the comparison of Gibbs free energy diagrams are calculated under zero and an applied potentials. Considering that in our DFT calculations there is no influence by the factors, such as temperature and solvation, it is the same for all the elementary steps after correction. The considered pathway at all the catalyst surfaces shows the optimal reaction pathway. Under U = 0 (Cyan solid lines) and applied potentials (red solid lines), the RDSs are marked by purple solid lines. The free energy diagrams for the reduction of CO_2 to CH_4 on $Cr_3(HITP)_2$ and $Mn_3(HITP)_2$ are shown in Fig. 5a–b, the free energies change are uphill by 1.09 eV (*OH→*H_2O) of $Cr_3(HITP)_2$ and 1.45 eV (*COOH→*CO) of $Mn_3(HITP)_2$, respectively. This step is the RDSs, and the corresponding overpotentials are only 0.62 V $Cr_3(HITP)_2$ and 0.69 V $Mn_3(HITP)_2$, which are much lower than those of other transition metal catalyst surfaces (such as the Cu surface with a theoretical overpotential of 0.91 V) in Fig. 8. Furthermore, the RDSs of $M_3(HITP)_2$ (M= Fe, Rh and Os) are *CHO→*HCHO, while the corresponding overpotentials are 1.16, 1.13, and 1.13 V, respectively. In the subsequent hydrogenation step, *CHO can hydrogenate, forming *HCHO or *HCOH, corresponding to *CHO+H^++e^-→*HCHO and *CHO+H^++e^-→*HCOH. In the next hydrogenation reaction, *H_3CO and *H_2COH will be formed at the top of the transition metal. The next proton-electron transfer results in the formation of methanol and the production of CH_4. The introduction of $Cr_3(HITP)_2$ and $Mn_3(HITP)_2$ 2D MOFs surface lower the limiting potential during the *CO→*CHO reaction process. As shown in Figures S3 and S4, it is well established that the hydrogenation of *COOH species produces *CO in $M_3(HITP)_2$, (M=Cr, Mn, Fe, and Co), which can easily form at the catalyst surface (*COOH→*CO+H_2O), or beyond protonate to CHO* or COH*. When the CO_2 reduction proceeds along, the *HCO_2 is formed. Further, *HCO_2 can be hydrogenated to *HCOOH and H_2CO_2 from the $M_3(HITP)_2$ catalysts. Fig. 6 and Figure S4 and S5 show the Gibbs free energy diagram reduction of CO_2 to CO at 0 and −0.11 V versus RHE, and the HCHO reduction at 0 and −0.25 V versus RHE, respectively. the Gibbs free energy diagram for the reduction of CO_2 to CH_3OH at 0 V and 0.02 V versus RHE and the calculated minimum energy Gibbs free energy pathway for CO_2 reduction on $M_3(HITP)_2$ MOFs surface are shown in Figure S6. As a result, the overpotential of intermediate species of methane formation is the highest compared to the formation of other products.

Fig. 6 (a-d) illustrates that there are only three elementary reaction steps from CO_2 reduction to CO. The CO_2 molecule was firstly activated and hydrogenated to *COOH, then further hydrogenation was catalyzed by $M_3(HITP)_2$ sheets and produced the final product *CO. Fig. 6 (e-h) illustrates the Gibbs free energy diagram of CO_2 reduction to HCOOH. The formaldehyde (HCHO) was considered to be the difference in formation energy at zero and limiting potentials versus SHE at room temperature. The calculated RDS for the various products (such as HCOOH, HCHO, and CH_3OH) is shown in Fig. 6 and Figure S4-S6, respectively. Considering our DFT calculations contain no experimental adjustable parameters, so these results of the Gibbs free energy are the same for all the elementary steps at zero and applied potential. The formation energy of intermediates with H^+/e^- transfer steps is dependent on the applied potential, focusing on the formation of *H_3COH from *H_2COH and were shown in Figure S6. The rate-limiting step is expected to be the minimal energy barrier pathway of *CO→*CHO preceding intermediate. For $Cr_3(HITP)_2$ and $Cr_3(HITP)_2$, the reaction barrier energy for the rate-limiting step in *CO→*CHO are −0.44 and −0.52 eV, respectively. This step hydrogenation is an endothermic process. Meanwhile, $Ni_3(HITP)_2$ and $Cu_3(HITP)_2$ need to overcome the reaction barrier energy of *CO_2→*COOH (−1.61 and −1.57 eV, respectively). What is more, the $Os_3(HITP)_2$ also shows the need to overcome a small reaction energy barrier of −0.45 eV for the protonation step of the *H_2CO_2→*H_2COOH in the $Rh_3(HITP)_2$ system, indicating that the lowest the energy barrier of the RDS of *CHO→*HCHO to −0.96 eV makes it become more stabilized relative to *HCHO compared to *CHOH intermediate species. This implies that the $M_3(HITP)_2$ (M=Cr, Mn, Rh, and Os) system can be applied for improving the energy efficiency of the electroreduction of CO_2 due to a relatively low energy barrier [47]. To further explore the relationship between different intermediate species for these $M_3(HITP)_2$ surfaces, it has been confirmed that linear scaling relations [49] play a significant role and descriptor in high catalytic efficiency for CO_2RR as shown in Fig. 7. In addition, the volcano plot are based on limiting potential of different intermediate species on the $M_3(HITP)_2$ surfaces. The scaling of these limiting potential has similar correlations and exhibits strong thermodynamic activity; the different systems between the U_L relations for ΔG(*OH) is about 0.75 eV at high kinetic activity (*OH→H_2O) as shown in Fig. 7b, the limiting potential of *O→*OH on $M_3(HITP)_2$ catalysts are approximately 0.64 eV, Fig. 7a show the linear scaling relations of *COOH→ *CO relative to the binding of *CO with a more pronounced effect on strong carbon and metal coupling, showing that CO production may be kinetically difficult as well [48]. As shown in Fig. 7c, *COOH →*HCOOH are bound differently to the $M_3(HITP)_2$ catalysts surface. This indicates the binding en-

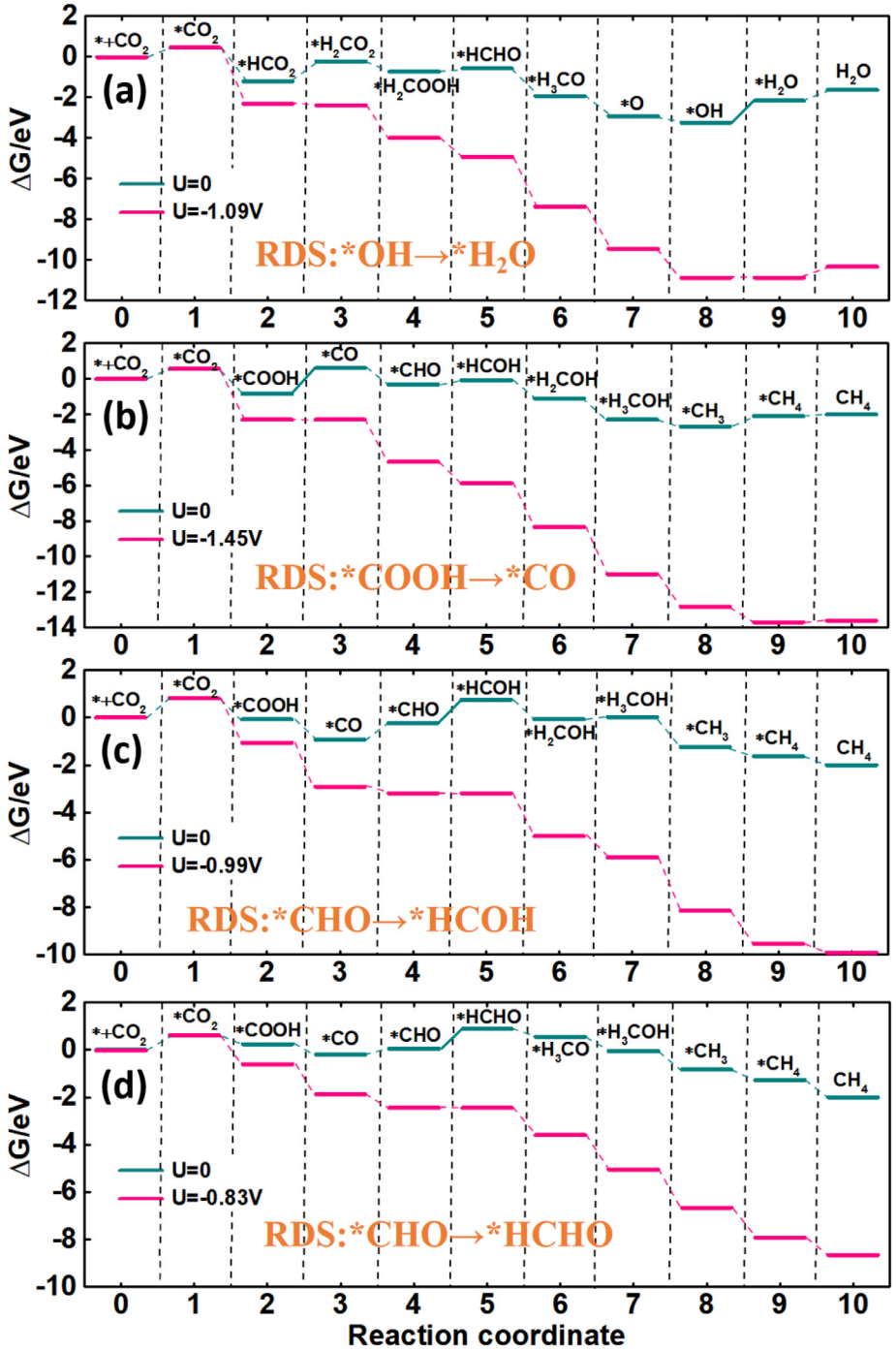

Fig. 5. Gibbs free energy diagram for the reduction of CO_2 to CH_4 on $M_3(HITP)_2$ sheets along the lowest energy pathways at 0 V and under an applied potential) versus reversible hydrogen electrode (RHE), the rate determining steps and limiting potential (violet number) of proton electron transfer have been highlighted.(a)$Cr_3(HITP)_2$, (b)$Mn_3(HITP)_2$, (c)$Fe_3(HITP)_2$, and (d)$Co_3(HITP)_2$, respectively.

ergies of C-bonded or O-bonded intermediates are independent, the linear scaling relations of limiting potential derived from the reaction trend are quantitatively calculated, such as $COOH^* \rightarrow CO^*$ and $CO^* \rightarrow CHO^*$ reduction. To evaluate the catalytic efficiency of the selected catalyst, the theoretical overpotentials were compared by calculating limiting potentials combination analysis from scaling correlation [50]. It is an effective and easy method as for theoretical consideration. Fig. 8 illustrates the overpotentials in predicting the final product formation trends in CO_2RR mechanism pathway selectivity. After screening enough number of 2D $M_3(HITP)_2$ MOF materials, which could be used as potential high-efficient catalysts in CO_2RR applications, linear scaling relationships could potentially be established between the different elementary reaction steps. Those relationships can be applied for the description of the relative stability of a final product. Theoretical limiting potential is relative to the catalytic activity and is used to create volcano plots onset. These relations only describe the electronic effects of the system, and the corrections for such effects should be considered in the future. Under CO_2/CO reducing conditions, as was shown in Fig. 8b, the $M_3(HITP)_2$ (M=Cr, Mn Ir, and Fe) surfaces are more suitable for CO formation. The high limiting potentials close to the top of the volcano implies that these

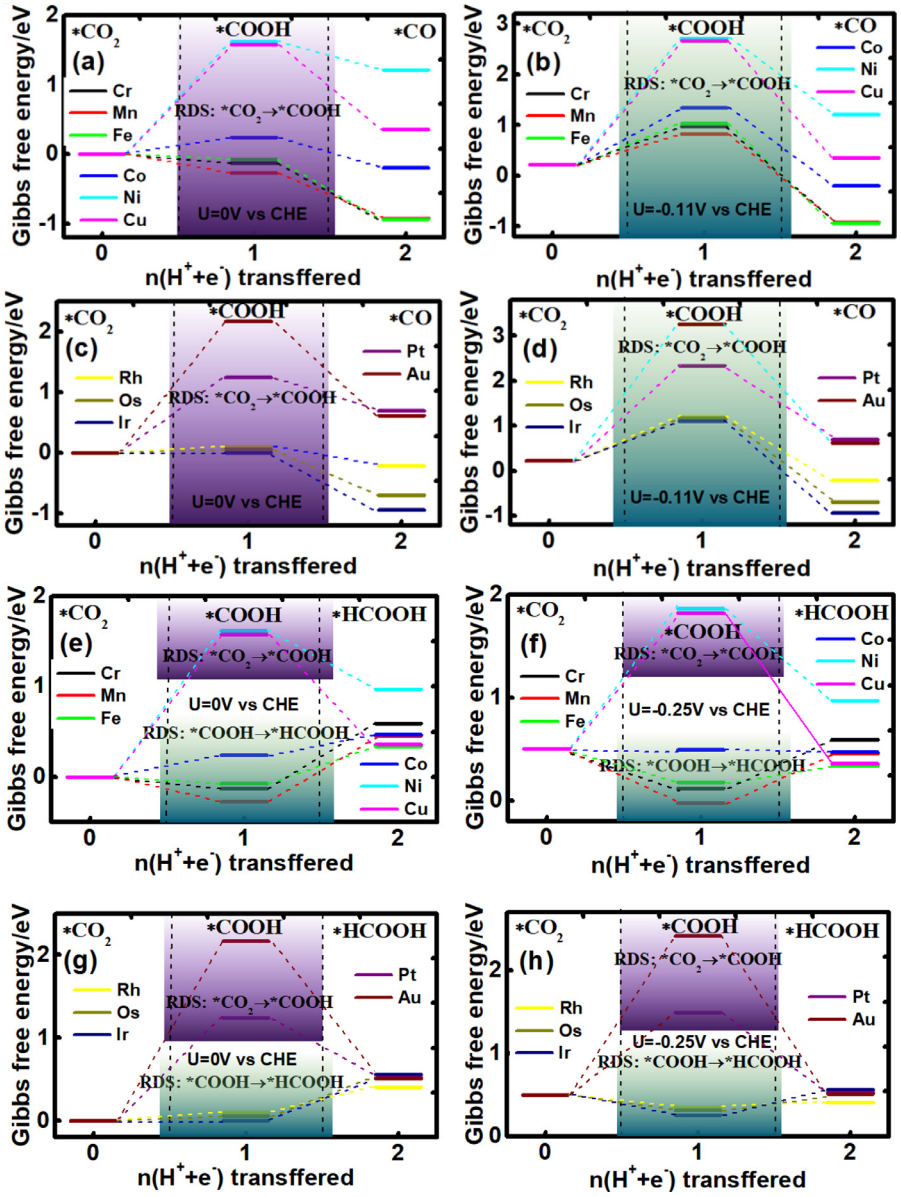

Fig. 6. Gibbs free energy diagram for the reduction of CO_2 to CO on $M_3(HITP)_2$ sheets at 0 V (a, c) and −0.11 V (b, d) (equilibrium potential) versus RHE, and the reduction of CO_2 to HCOOH at 0 V (e, g) and −0.25 V (f, h) (equilibrium potential) versus RHE, respectively. the rate determining steps of proton electron transfer have been highlighted under different colors.

catalysts have a correlation between their catalytic activity and stability.

The theoretically predicted limiting potentials of some main reaction steps (shown in Fig. 9) in the process of electroreduction CO_2 corresponds to different products (CH_4, CO, HCOOH, and CH_3OH) [51-52]. The RDS [53] is determined by the most negative U_L. In Fig. 7c, there are two downhill limiting potential lines corresponding to $*CO_2+H^++e^-\rightarrow *COOH$ and $*HCOOH+H^++e^-\rightarrow *CHO+H_2O$ for producing HCOOH as the final product, representing how *COOH is easier to be formed. Obviously, the formation of *HCHO on $Cu_3(HITP)_2$ and $Au_3(HITP)_2$ are generally difficult due to the high limiting potential of PDS for the $*CHO+H^++e^-\rightarrow *HCHO$ overall CO_2RR, as they have to overcome a large barrier energy. $*CH_4$ is favorably desorb from $M_3(HITP)_2$ (M=Ni, Au, and Pt) because of the smaller binding energy than the other intermediates. The bottom left corner sites on $Cu_3(HITP)_2$ (M=Cr, Mn, and Ir) have a large $\Delta G(*CH_4)$, ranging from −0.45 to 0.54 eV. It is close to the 0.58 eV of Cu(211), the $*H_3CO$ and *O to form $*H_2O$, the PDS are $*O + H^++e^-\rightarrow *OH$ and $*OH+H^++e^-\rightarrow *H_2O$ due to the strong binding of $M_3(HITP)_2$ (M=Co, Cu, Ni, and Au). Overall, for CO_2 reduction, the small limiting potential is usually accompanied by a low reaction barrier and overpotential [54,55]. This provides further evidence that scaling relations is an effective approach to obtain lower reaction energy. We evaluated the catalytic performance of $M_3(HITP)_2$ for the CO_2RR by calculating the limiting potential profiles diagram of the entire pathways towards different products, such as: CO, HCOOH, HCHO, CH_3OH, and CH_4. The production mechanism of CO occurs through the path $*CO_2\rightarrow *COOH\rightarrow *CO$ accompanied by two proton-electron pairs transferred, while the desorption of CO is found to be difficult because it is strongly bound to metal atoms. Meanwhile, the HCOOH production, CO_2, is hydrogenated by the first proton-electron pair forming *COOH, and then a second proton-electron pair transfers generate to *HCOOH. The rate limiting step is the $*COOH\rightarrow *HCOOH$ because of uphill limiting potential lines (Fig. 7c). Furthermore, the RDSs in the formation of beyond re-

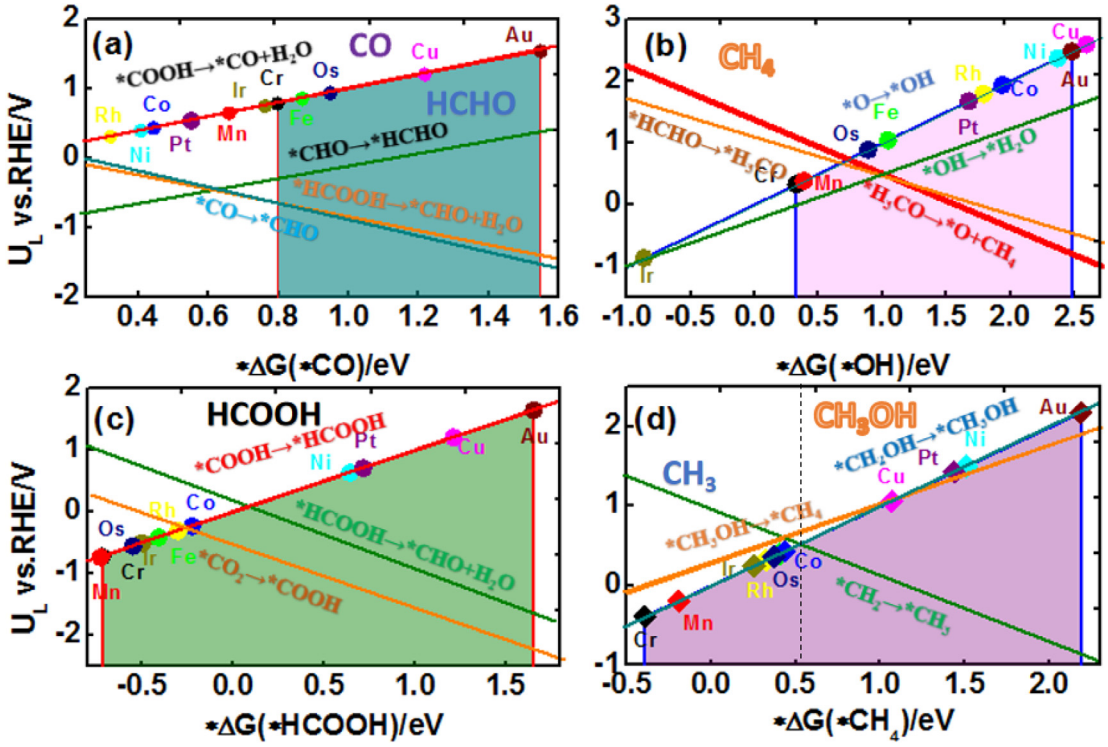

Fig. 7. Theoretical volcano plot of catalytic activity from different final products, each line is for one electron proton transfer pair step, volcano plot of limiting potential as a function of formation energy of different final products (a) *CO, (b) $^*CH_4$, (c) *HCOOH and (d) CH_3OH, respectively. The symbols match the different colors of data points represent different catalysts.

duction hydrocarbon products (HCHO, CH_3OH, and CH_4) with more than four proton-electron pair transfers usually is the hydrogenation of the *CO to form *CHO [56]. However, due to the strength of $^*H_2COH \rightarrow ^*CH_3OH$ is uphill limiting potential lines, the hydrogenation of *CO to *CHO is not always the rate limiting step from thermodynamic limiting potentials. The $M_3(HITP)_2$ (M=Cr, Mn, Rh and It) exhibit much lower required potential towards CH_4, indicating higher efficiency and selectivity in generating CH_4. The uphill limiting potential lines toward H_2O products of $^*H_3CO \rightarrow CH_4 + ^*O$ is relatively low. The similar limiting potentials towards different products suggest complex selectivity, and the competition relation between the CO_2RR and HER is further analyzed using the difference in the limiting potentials, and was shown in Figure S1b by using the change of $U_L(CO_2)$-$U_L(H_2)$. The higher the $U_L(CO_2)$-$U_L(H_2)$, the higher the selectivity for CO_2 reduction over H_2 evolution [57].

Microscopic thermodynamic simulations are useful to predict reaction kinetic activity on a complex reaction mechanism. $M_3(HITP)_2$ (M=Cr, Mn and It) surfaces are suitable for $^*CO_2 \rightarrow ^*HCO_2$ as the first hydrogenation step, reaching limiting potentials of more than 0.17 V (equilibrium potential). This step is usually taken as the RDS for most $M_3(HITP)_2$ catalysts. Any data points reveal a linear relation for each elementary reaction step on the activity map. When two different chemical reactions are compared, such as $^*CO_2 \rightarrow ^*COOH$ vs. $^*CO_2 \rightarrow ^*HCO_2$, they are identical to the activity with the strong binding towards weaker binding due to the energy of hydrogen ion interactions. [58] theoretical calculations are carried out for a deeper insight into the kinetics of these reactions, the role of proton-electron (H^+/e^-) transfer reduction reactions, and the reduction of CO_2. Theoretical prediction is used to define surfaces that will provide an understanding of the atomic-scale phenomena involved in chemical interaction. In general, the smaller limiting potentials (only up to 0.17 V) shows the high activity for CO_2 reduction to CH_4. Linear scaling relations of reaction kinetic activity illustrates the variation tendency between the intermediates, and the lines describing the reaction energy change between two continuous intermediates in the electrocatalytic process. This implies that the increase of bonding strength reduces limiting potential and increases catalytic activity, it binds substrates $^*OH \rightarrow ^*H_2O$ is potential determining (wine line) and when substrates are strongly under $^*H_3CO \rightarrow ^*O$ is RDS for $M_3(HITP)_2$ without Pt and Ir, the RDSs are usually defined as the strong binding interaction.

As illustrated in Fig. 9, several $M_3(HITP)_2$ (M= Cr, Mn, Fe, or Rh) catalysts were proposed via the minimum energy path for CO_2 reduction to methane. The overpotentials are 0.62 V ($Cr_3(HITP)_2$) and 0.69 V ($Mn_3(HITP)_2$), corresponding to the RDSs of $^*CO \rightarrow ^*CHO$, respectively. Meanwhile, the RDS for forming CO is $^*COOH \rightarrow ^*CO$ and the corresponding overpotentials are only −0.91 V ($Cr_3(HITP)_2$), −0.77 V ($Mn_3(HITP)_2$) and −0.87 V ($Os_3(HITP)_2$), which are much lower than the other $M_3(HITP)_2$ catalysts. Furthermore, when CO_2 is reduced to methanol, the overpotentials are the same to form methane [59], In general, the maximum value of limiting potentials is determined by the energy barrier which must be overcome during the rate-limiting reaction, The overpotential is used as a crucial indicator of catalytic performance [60]. It is investigated according to the change in equilibrium potential and limiting potential versus the computational hydrogen electrode (CHE) are listed in table S3. The equilibrium potential of the reaction $^*CO_2 \rightarrow ^*CH_4$ is about 0.17 V, $^*CO_2 \rightarrow ^*CH_3OH$ is about 0.01 V, and $^*CO_2 \rightarrow ^*HCOOH$ and $^*CO_2 \rightarrow ^*CO$ are −0.25 V and −0.11 V, respectively. Generally, a lower overpotential indicates a better catalytic performance for the CO_2RR. The overpotentials of CO forming are in the range from −1.32 V ($Cu_3(HITP)_2$) to 1.50 V ($Ni_3(HITP)_2$), the overpotentials of CH_3OH forming are in the range from 0.47 V to 1.63 V, respectively. The proposed mechanism of product selectiv-

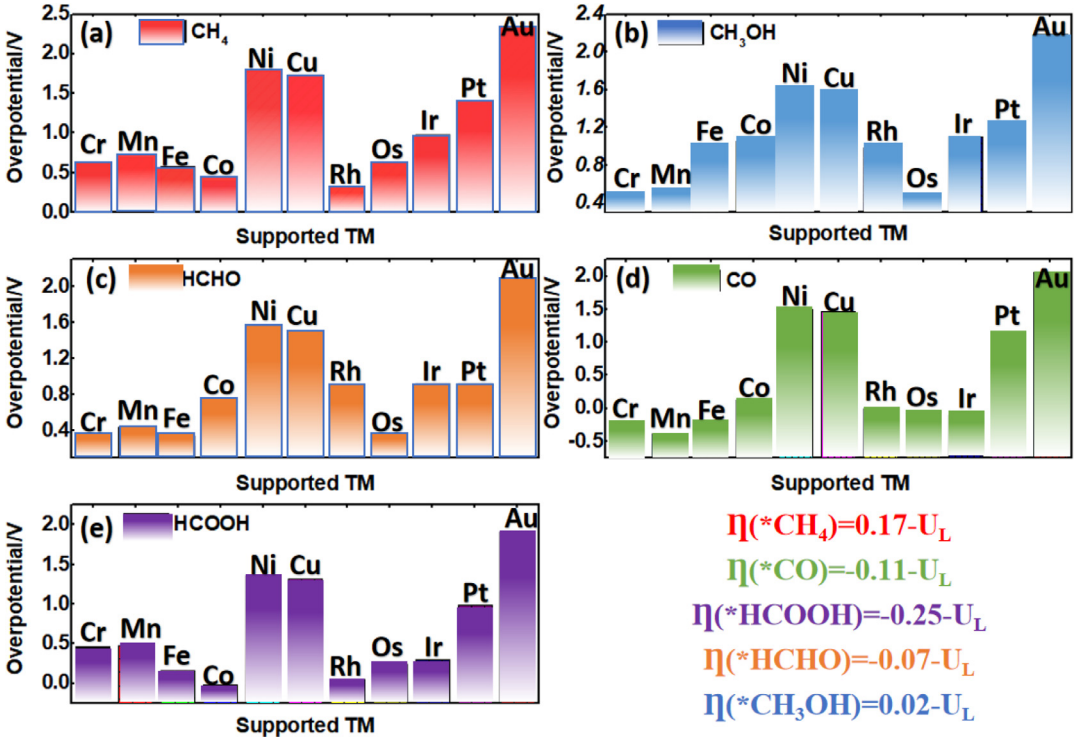

Fig. 8. Illustration for combined volcano plot correspond to different final products depend on thermodynamic analysis, the calculated CO_2RR overpotentials versus the RHE.

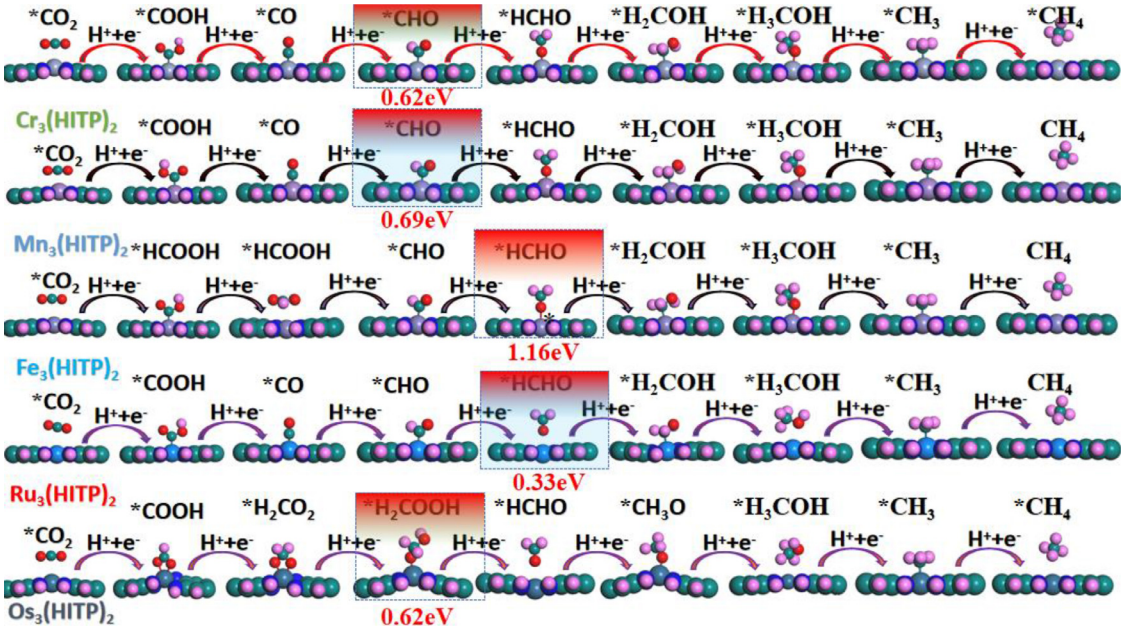

Fig. 9. Side views of the intermediates at each hydrogenation step via the minimum energy path mechanisms of the CO_2RR. The RDS and their corresponding overpotential are labeled in different color boxes with red number text, respectively. * represents the chemisorbed species.

ity shown in Fig. 10 can be explained from the trend of strong or weak bound by the M–C and M–O coupling. If the intermediates were observed at small overpotential, this demonstrates a C-bound configuration, such as *COOH, *CO and *COH. This suggests that M-C bound are hydrogenated to oxygen form *CO, *COH and *C, respectively. However, we can estimate the final product from the intermediate species (M-O bound vs M-C bound); O-bound intermediates generally produce HCO_2, CHO, HCHO, H_3CO, CH_4 and CH_3OH hydrocarbons, whereas the hydrogenation process with M-O bound is more likely to happen with an oxygen atom, while C-bound intermediates are easier to produce. The CO intermediates have been deserved to be C-bound intermediates which can be further reduced to CHO via two subsequent hydrogenation processes. Moreover, we found it difficult to form COH due to the strong M-O coupling, which indicated that the COH is difficult to form from CO reduction with hydrogenation. The coupling of C-bound intermediates in the weaker binding indicates M-O rather than M-C coupling, which further supports O-bound intermediates. Therefore, HCOOH and CH_3OH may be hard to form via our proposed reaction pathways.

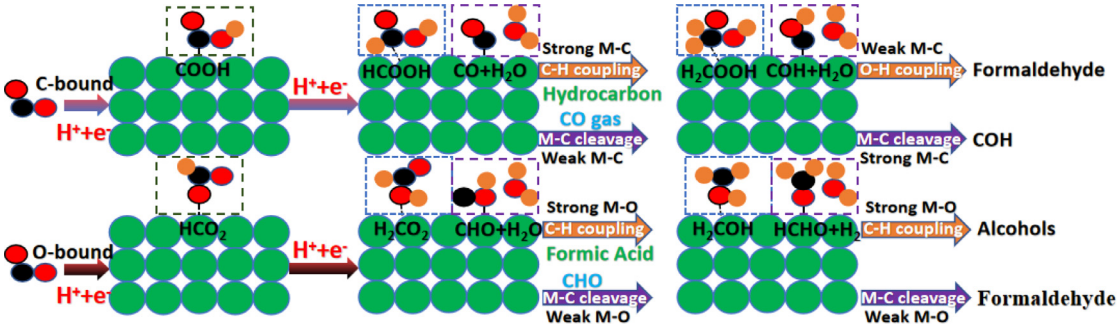

Fig. 10. A proposed reaction network for intermediates selectivity determineed by the strength of the C-bound and O-bound species.

Conclusions

In this work, 2D $M_3(HITP)_2$ MOF as the catalysts for efficient electroreduction of CO_2 were systemically studied by DFT calculations. Through high throughput screening of catalytic performance based on the linear scaling relations of formation energy for different intermediates, there are eleven stable candidates that are considered for electroreduction of CO_2 to different final products, such as CO, HCHO, HCOOH CH_3OH, and CH_4. The free energy diagram of all the reduction mechanisms toward CH_4 at zero and equilibrium potential were considered, the RDSs were also highlighted. $Cr_3(HITP)_2$ and $Mn_3(HITP)_2$ exhibit the best catalytic performance with very low overpotentials (0.62 V and 0.69 V, respectively) toward to CH_4 production. Authors examined whether these different $M_3(HITP)_2$ MOF have different bounds for M-C bound and M-O bound adsorbates, which plays an important role in the formation of intermediates during the CO_2RR process. DFT calculations were applied to establish final product selectivity for the CO_2RR. $M_3(HITP)_2$ (M=Cr or Mn) are found to produce CO with low overpotentials (−0.24 V and −0.38 V, for Cr and Mn, respectively), as well as production of CH_3OH with potentials of 0.47 V and 0.54 V, respectively. Furthermore, HCHO is produced during CO_2RR on $M_3(HITP)_2$ (M=Cr, Mn, Fe or Os) with potentials of 0.38 V, 0.45 V, 0.34 V and 0.38 V, respectively. Those products are accompanied by the coupling strength of O-bound or C-bound. Product selectivity depends on whether C-bound or O-bound intermediates were stronger. The metallic 2D $M_3(HITP)_2$ MOF can be used as an efficient catalyst for the CO_2RR with low overpotential and small energy barrier for future energy storage and conversion applications.

Declaration of Competing Interest

The authors declare that they have no conflict of interest.

Credit authorship contribution statement

Yi Xiao: Conceptualization, Data curation, Formal analysis, Funding acquisition, Investigation, Methodology, Writing - original draft, Project administration, Resources, Data curation, Formal analysis, Funding acquisition, Software, Validation, Visualization. **Dazhu Chen:** Writing - review & editing. **Rui Chen:** Conceptualization, Data curation, Formal analysis, Funding acquisition, Investigation, Methodology, Writing - original draft, Project administration, Resources, Data curation, Formal analysis.

Acknowledgments

Financial support comes from the China Scholarship Council (CSC:201808440416) of China. Research and the Arts (HMWK) of the Hessen state in Germany; The Lichtenberg high performance computer is gratefully acknowledged, and we are also thankful to TU Darmstadt.

Supplementary materials

Supplementary material associated with this article can be found, in the online version, at doi:10.1016/j.electacta.2021.138028.

References

[1] M. Rastogi, S. Singh, H. Pathak, Emission of carbon dioxide from soil, Curr. Sci. 82 (5) (2002) 510–517.
[2] J. Karlsson, R. Giesler, J. Persson, et al., High emission of carbon dioxide and methane during ice thaw in high latitude lakes, Geophys. Res. Lett. 40 (6) (2013) 1123–1127.
[3] X. Chen, Y. Zhou, Q. Liu, et al., Ultrathin, single-crystal WO_3 nanosheets by two-dimensional oriented attachment toward enhanced photocatalystic reduction of CO_2 into hydrocarbon fuels under visible light, ACS Appl. Mater. Interfaces 4 (7) (2012) 3372–3377.
[4] D. Gao, R.M. Arán-Ais, H.S. Jeon, et al., Rational catalyst and electrolyte design for CO_2 electroreduction towards multicarbon products, Nat. Catal. 2 (3) (2019) 198–210.
[5] A. Bagger, W. Ju, A.S. Varela, et al., Single site porphyrine-like structures advantages over metals for selective electrochemical CO_2 reduction, Catal. Today. 288 (2017) 74–78.
[6] Y. Ouyang, L. Shi, X. Bai, et al., Breaking scaling relations for efficient CO_2 electrochemical reduction through dual-atom catalysts, Chem. Sci. (2020) 1807–1813.
[7] N. Hoshi, M. Kato, Y. Hori, Electrochemical reduction of CO_2 on single crystal electrodes of silver Ag (111), Ag (100) and Ag (110), J. Electroanal. Chem. 440 (1–2) (1997) 283–286.
[8] Y. Hori, H. Wakebe, T. Tsukamoto, et al., Electrocatalytic process of CO selectivity in electrochemical reduction of CO_2 at metal electrodes in aqueous media, Electr. Acta 39 (11–12) (1994) 1833–1839.
[9] S. Cao, B. Shen, T. Tong, et al., 2D/2D heterojunction of ultrathin MXene/Bi_2WO_6 nanosheets for improved photocatalytic CO_2 reduction, Adv. Funct. Mater. 28 (21) (2018) 1800136.
[10] A.S. Varela, W. Ju, P. Strasser, molecular nitrogen–carbon catalysts, solid metal organic framework catalysts, and solid metal/nitrogen-doped carbon (MNC) catalysts for the electrochemical CO_2 reduction, Adv. Energy Mater. 8 (30) (2018) 1703614.
[11] C. Kim, F. Dionigi, V. Beermann, et al., Alloy nanocatalysts for the electrochemical oxygen reduction (ORR) and the direct electrochemical carbon dioxide reduction reaction (CO_2RR), Adv. Mater. 31 (31) (2019) 1805617.
[12] M. Bernal, A. Bagger, F. Scholten, et al., CO_2 electroreduction on copper-cobalt nanoparticles: size and composition effect, Nano Energy 53 (2018) 27–36.
[13] C.B. Hiragond, H. Kim, J. Lee, et al., Electrochemical CO_2 reduction to CO catalyzed by 2D nanostructures, Catalysts 10 (1) (2020) 98.
[14] Y. Li, Z. Dong, L. Jiao, Multifunctional transition metal-based phosphides in energy-related electrocatalysis, Adv. Energy Mater. 10 (11) (2020) 1902104.
[15] L. Gan, M. Heggen, C. Cui, et al., Thermal facet healing of concave octahedral Pt–Ni nanoparticles imaged in situ at the atomic scale: implications for the rational synthesis of durable high-performance ORR electrocatalysts, ACS Catal. 6 (2) (2016) 692–695.
[16] Z. Chen, T. Wang, B. Liu, et al., grain-boundary-rich copper for efficient solar–driven electrochemical CO_2 reduction to ethylene and ethanol, J. Am. Chem. Soc. 142 (15) (2020) 6878–6883.
[17] Q. Cui, G. Qin, W. Wang, et al., Mo-based 2D MOF as a highly efficient electrocatalyst for reduction of N_2 to NH_3: a density functional theory study, J. Mater. Chem. A 7 (24) (2019) 14510–14518.
[18] Y. Katayama, F. Nattino, L. Giordano, et al., An in situ surface-enhanced infrared absorption spectroscopy study of electrochemical CO_2 reduction: selectivity dependence on surface C-bound and O-bound reaction intermediates, J. Phys. Chem. C 123 (10) (2018) 5951–5963.

[19] C. Shi, H.A. Hansen, A.C. Lausche, et al., Trends in electrochemical CO_2 reduction activity for open and close-packed metal surfaces, Phys. Chem. Chem. Phys. 16 (10) (2014) 4720–4727.
[20] Y. Tian, Y. Wang, L. Yan, et al., Electrochemical reduction of carbon dioxide on the two–dimensional M_3(Hexaiminotriphenylene)$_2$ sheet: a computational study, Appl. Surf. Sci. 467 (2019) 98–103.
[21] F. Sun, X. Chen, Oxygen reduction reaction on Ni_3(HITP) $_2$: a catalytic site that leads to high activity, Electrochem.Commun. 82 (2017) 89–92.
[22] J.H. Dou, L. Sun, Y. Ge, et al., Signature of metallic behavior in the metal–organic frameworks M3(hexaiminobenzene)2 (M= Ni, Cu), J. Am. Chem. Soc. 139 (39) (2017) 13608–13611.
[23] Y. Tian, Z. Zhang, C. Wu, et al., Theoretical insights into the catalytic mechanism for the oxygen reduction reaction on M_3(hexaiminotriphenylene)$_2$ (M= Ni, Cu), Phys. Chem. Chem. Phys. 20 (3) (2018) 1821–1828.
[24] N. Acerbi, S.C.E. Tsang, G. Jones, et al., Rationalization of interactions in precious metal/ceria catalysts using the D-band center model, Angew. Chem. Int. Ed. 52 (30) (2013) 7737–7741.
[25] C. Li, K. Wang, J. Li, et al., Recent progress in stimulus-responsive two-dimensional metal-organic frameworks, ACS Mater. Lett. (2020).
[26] X. Duan, J. Xu, Z. Wei, et al., Metal-free carbon materials for CO_2 electrochemical reduction, Adv. Mater. 29 (41) (2017) 1701784.
[27] C. Shi, H.A. Hansen, A.C. Lausche, et al., Trends in electrochemical CO_2 reduction activity for open and close-packed metal surfaces, Phys. Chem. Chem. Phys. 16 (10) (2014) 4720–4727.
[28] G. Kresse, J. Furthmu ¨ller, Efficiency of ab-initio total energy calculations for metals and semiconductors using a plane-wave basis set, Comput. Mater. Sci. 6 (1) (1996) 15–50.
[29] G. Kresse, J. Furthmu ¨ller, Efficient iterative schemes for ab initio total-energy calculations using a plane-wave basis set, Phys. Rev. B 54 (16) (1996) 11169.
[30] S. Ehrlich, J. Moellmann, W. Reckien, et al., System-dependent dispersion coefficients for the DFT-D3 treatment of adsorption processes on ionic surfaces, Chem. Phys. Chem. 12 (17) (2011) 3414–3420.
[31] B.D. Dunnington, J.R. Schmidt, Generalization of natural bond orbital analysis to periodic systems: applications to solids and surfaces via plane-wave density functional theory, J. Chem. Theory Comput. 8 (6) (2012) 1902–1911.
[32] M. Cococcioni, S. De Gironcoli, Linear response approach to the calculation of the effective interaction parameters in the LDA+ U method, Phys. Rev. B 71 (3) (2005) 035105.
[33] J.K. Nørskov, T. Bligaard, J. Rossmeisl, et al., Towards the computational design of solid catalysts, Nat. Chem. 1 (1) (2009) 37.
[34] H. Reiss, A. Heller, The absolute potential of the standard hydrogen electrode: a new estimate, J. Phys. Chem. 89 (20) (1985) 4207–4213.
[35] wang V., Xu N., Liu J.C., et al. VASPKIT: a pre-and post-processing program for VASP code. arXiv preprint arXiv:1908.08269, 2019.
[36] X. Zheng, Y. Ji, J. Tang, et al., Theory-guided Sn/Cu alloying for efficient CO_2 electroreduction at low overpotentials, Nat. Catal. 2 (1) (2019) 55–61.
[37] Y. Cui, J. Yan, Z. Chen, et al., synthetic route to a triphenylenehexaselenol-based metal organic framework with semi-conductive and glassy magnetic properties, Iscience 23 (1) (2020) 100812.
[38] J. Wang, Y. Fan, S. Qi, et al., Bifunctional HER/OER or OER/ORR catalytic activity of two-dimensional TM_3(HITP)$_2$ with TM= Fe–Zn, J. Phys. Chem. C 124 (17) (2020) 9350–9359.
[39] J. Hussain, H. Jónsson, E. Skúlason, Calculations of product selectivity in electrochemical CO_2 reduction, ACS Catal. 8 (6) (2018) 5240–5249.
[40] A.D. Handoko, K.H. Khoo, T.L. Tan, et al., Establishing new scaling relations on two-dimensional MXenes for CO_2 electroreduction, J. Mater. Chem. A, 6 (44) (2018) 21885–21890.
[41] W. Zhang, Y. Xiao, Mechanism of electrocatalytically active precious metal (Ni, Pd, Pt, and Ru) complexes in the graphene basal plane for ORR applications in novel fuel cells, Energy Fuels 34 (2) (2020) 2425–2434.
[42] Y. Xiao, W. Zhang, High throughput screening of M_3C_2 MXenes for efficient CO_2 reduction conversion into hydrocarbon fuels, Nanoscale 12 (14) (2020) 7660–7673.
[43] Y. Meng, X. Qu, K. Li, et al., rhodium and nitrogen codoped graphene as a bifunctional electrocatalyst for the oxygen reduction reaction and CO_2 reduction reaction: mechanism insights, J. Phys. Chem. C 123 (9) (2019) 5176–5187.
[44] S. Chen, J. Dai, C Zeng X, Metal–organic Kagome lattices M_3(2, 3, 6, 7, 10, 11-hexaiminotriphenylene)$_2$ (M= Ni and Cu): from semiconducting to metallic by metal substitution, Phys. Chem. Chem. Phys. 17 (8) (2015) 5954–5958.
[45] Y. Xiao, L. Tang, High-throughput approach exploitation: two-dimensional double-metal sulfide (M_2S_2) of efficient electrocatalysts for oxygen reduction reaction in fuel cells, Energy Fuels, 34 (4) (2020) 5006–5015.
[46] W.B. Zhang, X. Xiao, F. Wu Q, et al., Facile synthesis of novel Mn-doped $Bi_4O_5Br_2$ for enhanced photocatalytic NO removal activity, J. Alloy. Compd. 826 (2020) 154204.
[47] Y. Xiao, J. Wang, Y. Wang, et al., A new promising catalytic activity on blue phosphorene nitrogen-doped nanosheets for the ORR as cathode in nonaqueous Li–air batteries, Appl. Surf. Sci. 488 (2019) 620–628.
[48] N. Vonrüti, U. Aschauer, The role of metastability in enhancing water-oxidation activity, Phys. Chem. Chem. Phys. 21 (44) (2019) 24354–24360.
[49] C. Ren, Y. Zhang, Y. Li, et al., Whether corrugated or planar vacancy graphene–like carbon nitride (g-C_3N_4) is more effective for nitrogen reduction reaction? J. Phys. Chem. C 123 (28) (2019) 17296–17305.
[50] Y. Xiao, W. Zhang, High-throughput calculation investigations on the electrocatalytic activity of codoped single metal–nitrogen embedded in graphene for ORR mechanism, Electrocatalysis (2020) 1–12.
[51] S. Siahrostami, K. Jiang, M. Karamad, et al., Theoretical investigations into defected graphene for electrochemical reduction of CO_2, ACS Sustain. Chem. Eng. 5 (11) (2017) 11080–11085.
[52] Y. Xiao, W. Zhang, DFT analysis elementary reaction steps of catalytic activity for ORR on metal-, nitrogen-co-doped graphite embedded structure, SN Appl. Sci. 2 (2) (2020) 194.
[53] Y. Hori, in: Electrochemical CO_2 Reduction On Metal Electrodes[M]//Modern Aspects of Electrochemistry, Springer, New York, NY, 2008, pp. 89–189.
[54] X. Chen, F. Sun, F. Bai, et al., DFT study of the two dimensional metal–organic frameworks X_3(HITP)$_2$ as the cathode electrocatalysts for fuel cell, Appl. Surf . Sci. 471 (2019) 256–262.
[55] S. Tang, X. Zhou, S. Zhang, et al., Metal-free boron nitride nanoribbon catalysts for electrochemical CO_2 reduction: combining high activity and selectivity, ACS Appl. Mater. Interfaces 11 (1) (2018) 906–915.
[56] J.Y. Lee, O.K. Farha, J. Roberts, et al., Metal–organic framework materials as catalysts, Chem. Soc. Rev. 38 (5) (2009) 1450–1459.
[57] J.L. White, M.F. Baruch, III J E Pander, et al., Light-driven heterogeneous reduction of carbon dioxide: photocatalysts and photoelectrodes, Chem. Rev. 115 (23) (2015) 12888–12935.
[58] N. Austin, S. Zhao, J.R. McKone, et al., Elucidating the active sites for CO_2 electroreduction on ligand-protected Au 25 nanoclusters, Catal. Sci. Technol. 8 (15) (2018) 3795–3805.
[59] W. Bi, X. Li, R. You, et al., Surface immobilization of transition metal ions on nitrogen-doped graphene realizing high-efficient and selective CO_2 reduction, Adv. Mater. 30 (18) (2018) 1706617.
[60] Y. Meng, X. Qu, K. Li, et al., rhodium and nitrogen codoped graphene as a bifunctional electrocatalyst for the oxygen reduction reaction and CO_2 reduction reaction: mechanism insights, J. Phys. Chem. C 123 (9) (2019) 5176–5187.

Nanoscale

PAPER

View Article Online
View Journal | View Issue

Cite this: *Nanoscale*, 2020, **12**, 7660

High throughput screening of M_3C_2 MXenes for efficient CO_2 reduction conversion into hydrocarbon fuels†

Yi Xiao *[a] and Weibin Zhang[b]

Received 15th December 2019,
Accepted 15th March 2020

DOI: 10.1039/c9nr10598k

rsc.li/nanoscale

The electrocatalytic reduction conversion of CO_2 to produce methane (CH_4) as a fuel has attracted intensive attention for renewable energy. Density functional theory (DFT) calculations with a computational hydrogen electrode (CHE) model are applied to study the hydrogenation of CO_2 on the two-dimensional (2D) M_3C_2 transition metal carbide (MXenes) surface. It is demonstrated that the adsorbed CO_2 is activated and can combine with surface hydrogen to form bicarbonate species, thus leading to more competitive selectivity for the CO_2RR than the HER. All possible conversion pathways for carbon dioxide to methane are explored, and it is found that the formation of the bicarbonate (HCO_2) species is energetically the most favourable reaction pathway, whereas the main intermediate of the CO_2RR is HCHO. Detailed characterization of the initial activation, scaling relationships, protonation steps and electrode overpotential, together with the evaluation of the limiting potentials for several reaction mechanisms, reveals that MXene M_3C_2 exhibits a high catalytic performance for CO_2, providing novel fuel cells.

Introduction

Over the past few years, increasing attention has been paid to fuel cells for energy storage and conversion due to their high efficiency, high power density, and low pollution.[1,2] To develop and explore highly efficient and low-cost components, a cathode catalyst is a novel concept.[3,4] For example, 2D materials such as titanium-based (TiO_2) semiconductors,[5] functionalized graphene oxide,[6] and graphite-like carbon nitride (g-C_3N_4)[7,8] are good candidates for the application of renewable energy sources.[9] The carbon dioxide reduction reaction (CO_2RR) into high-value hydrocarbons (*e.g.*, CH_4, CH_3OH or HCHO) is an appealing approach to generate fuels.[10,11] It presents a viable approach to CO_2 mitigation with great promise due to its excellent chemical reaction rate and stability. Recently, 2D transition metal carbide materials (MXenes) have been used to gain insights into the CO_2 capture and energy conversion. Such systems can be obtained by etching from the MAX phases,[12,13] and they possess excellent chemical activity and electronic conductivity for the electrocatalytic CO_2 reduction reaction (CO_2RR) as catalysts. MXenes have also been thought to be excellent candidates for high efficiency catalysts.[14,15]

However, carbon dioxide is chemically inert, and there is a weak interaction that exists between it and the catalyst carrier. In particular, the CO_2RR reaction mechanism under standard conditions can be a complicated process, and it requires a large number of elementary reactions along with coupled proton–electron pairs to be transferred for producing diverse products. In addition, the reaction intermediates generated can lead to the determination of various products by different limiting potentials, indicating that it is difficult to obtain a single product. Moreover, the reversible reduction potential of products in the CO_2RR is close to 0 V, which means that the reaction potential of $2H^+ + 2e^- \rightarrow H_2$ is set to zero ($E^\circ = 0$ V), and the hydrogen evolution reaction (HER)[19] is the most competitive secondary reaction during the entire CO_2RR process.[20] Due to these issues, the electrocatalytic reduction of CO_2 can be fundamentally challenging. The most favourable pathway of the subsequent protonation steps for producing methane alone is $*CO_2 \rightarrow *HCO_2 \rightarrow *H_2CO_2 \rightarrow *H_2COOH \rightarrow *HCHO \rightarrow *CH_3OH \rightarrow *O \rightarrow *OH \rightarrow *H_2O$, and it is found that $*H_2COOH + H^+ + e^- \rightarrow *HCHO + H_2O$ is the potential determining step (PDS). According to previous theoretical studies by Li *et al.*[21] indicating that 2D transition-metal carbides with the formula M_3C_2 (MXenes) can catalyse the reduction of CO_2 into a variety of hydrocarbons, the results and methods for the study of the CO_2RR catalytic mechanism with M_3C_2 (MXenes) are reviewed. In addition, Siahrostami S *et al.*[22] theoretically studied the

[a]*Institute of Materials Science, TU Darmstadt, 64287 Darmstadt, Germany. E-mail: yixiao@tmm.tu-darmstadt.de*
[b]*School of Physics and Optoelectronic Engineering, Yangtze University, Jingzhou, 434023, P. R. China*

†Electronic supplementary information (ESI) available. See DOI: 10.1039/c9nr10598k

CO_2RR with single atom catalysts (SAC) on carbon-based materials and demonstrated that metallic carbon-based materials can significantly enhance the catalytic activity of the CO_2RR towards the CO formation. Furthermore, C_2N–graphene-supported single-atom catalysts have also been widely applied as an efficient cathode catalytic material for the CO_2RR,[23] and they have been regarded as efficient, selective and competitive cathode catalysts. The reaction mechanism and activity scale relationships have also been systematically expounded. However, for many catalysts used as CO_2RR cathodes, the HER catalytic activity is more facile than that of the CO_2RR, thus resulting in the inefficiency of the selectivity towards the CO_2RR and the target product, as well as requiring a lower overpotential.[24] The distribution of the intermediate species and final products of the CO_2RR is greatly influenced by the catalytic material. Therefore, scientific researchers have performed a great deal of theoretical exploration and experimental studies on them to find the optimal catalyst for the reduction of CO_2. For example, when the selectivity of a catalyst for the HER is higher than that for the CO_2RR and the main product is H_2, this means that it needs a higher overpotential for the CO_2RR. According to the reaction thermodynamics of each elementary reaction, diverse intermediates and products should be formed under different potentials.[24,25]

Inspired by both previous experimental and theoretical studies, we performed DFT calculations together with computational hydrogen electrode (CHE) model[16,17] analysis to study the CO_2 reduction and energy conversion. According to each step of the transfer of H^+/e^- couples throughout the reaction, a series of intermediate species and diverse hydrocarbon compound products were generated, such as formic acid (HCOOH), methanol (CH_3OH), carbon monoxide (CO), formaldehyde (HCHO), and methane (CH_4).[18] Among all of the transition metals screened, we discovered that M_3C_2, with M = Sc, V, Mn, Zr, Nb, Hf, Hf, Mo, and W, is strongly bonded with CO_2. Mo_3C_2 and Zr_3C_2 were identified as the best candidates for catalysing the CO_2RR. Due to their superior catalytic activity, selectivity and stability, they were regarded as efficient catalysts and exhibited a distinct selectivity for the CO_2RR. Here, to further explore these issues, we have systematically investigated the electroreduction of CO_2 to CH_4 by using DFT calculations for investigation on M_3C_2 MXenes. We performed high throughput calculation approach[26–28] investigations on stable structures, elementary reaction pathways, CO_2RR kinetics and reaction mechanisms, and the most favourable pathways and free-energy diagrams of the CO_2RR have also been considered. We found that there are five possible reaction conversion products (CO, HCOOH, HCHO, CH_3OH, and CH_4). In addition, there are four favourable reaction mechanism pathways by which the CO_2RR can proceed through on MXenes that have been investigated, and transition-metal carbide (MXene) compounds have been shown to be very highly efficient catalysts for the electroreduction of CO_2. Thus, they have emerged as an excellent platform for enhancing the catalytic performance not only for the ORR, but also for the CO_2RR.[29] On the basis of these results, we used transition-metal carbides with the formula of M_3C_2 as CO_2 capture agents for electroreduction conversion. In our plan, a very reliable scaling relationship was established for different intermediates bound to the MXene surface, and the first protonation state of either *COOH or through $*HCO_2$ plays a very important role. Unlike carbon-based materials for single atom catalysts (SAC)[30] and precious metals,[31] the limiting potential of the MXene catalyst is determined by the binding energy of *COOH or *HCOOH, which can be independently regulated. Comparing the limiting potential of $U_L(CO_2)$ with the $U_L(H_2)$ of the reversible hydrogen electrode (RHE),[32] the theoretical overpotentials for the CO_2RR are significantly lower than those for the HER. In this work, we studied the electrocatalytic HER on MXenes by studying the adsorption properties of hydrogen on supported MXene surfaces, and the most favourable configuration for each MXene was identified by placing hydrogen atoms on the MXene surface.

Computational details

All of the DFT calculations and hydrogen electrode computations were performed using the Vienna *ab initio* simulation package (VASP).[33,34] The exchange correlation interactions were described by the generalized gradient approximation (GGA) parameterized by the Perdew–Burke–Ernzerhof (PBE) method.[35] The van der Waals (vdW) interactions are accounted for by using the DFT-D3 schemes.[36,37] The energy cut-off for the plane-wave basis was set to 500 eV, and a $5 \times 5 \times 1$ *k*-point mesh was sampled by the Monkhorst–Pack method,[38] which can provide sufficient accuracy for the Brillouin zone integration. All structures were fully relaxed until the forces were smaller than 0.005 eV $Å^{-1}$ and the energy change was less than 10^{-6} eV by using the conjugate gradient (CG) algorithm. To model MXene (M_3C_2), where M = Sc, Ti, V, Cr, Mn, Y, Zr, Nb, Mo, MoTi, Hf, Ta, and W, we employed $3 \times 3 \times 1$ monolayer supercells (Fig. 1a), and a vacuum region in the *z*-direction was set to 20 Å to avoid interactions between the layers. All of the free energies of the CO_2RR intermediate species in electrochemical reaction pathways were calculated by using the computational hydrogen electrode (CHE) model proposed by Nørskov *et al.*[39] The Gibbs free energy of the reaction for each elementary step involving the transfer of the H^+/e^- pair was calculated to evaluate the zero point energy (ZPE) and the thermal correction terms (TS). For each elementary step, the reaction Gibbs free energy of intermediates at zero potential is calculated using $\Delta G = \Delta E_{DFT} + \Delta H + \Delta ZPE - T\Delta S + \Delta G_U + \Delta G_{pH}$, where ΔE_{DFT} is the change in the total energy between reactants and products obtained by calculation and ΔZPE and ΔH are the zero-point energy correction ($1/2h\Delta\nu$) and the thermal correction, respectively. $T\Delta S$ is the vibrational entropy change at a certain temperature. $\Delta G_U = -eU$, where e is the elementary charge and U is the electrode overpotential, and ΔG_{pH} is the correction of the H^+ free energy. For correcting the Gibbs free energy data, we needed additional calculations at the Γ point, and they were carried out in the VASPKIT code.[40]

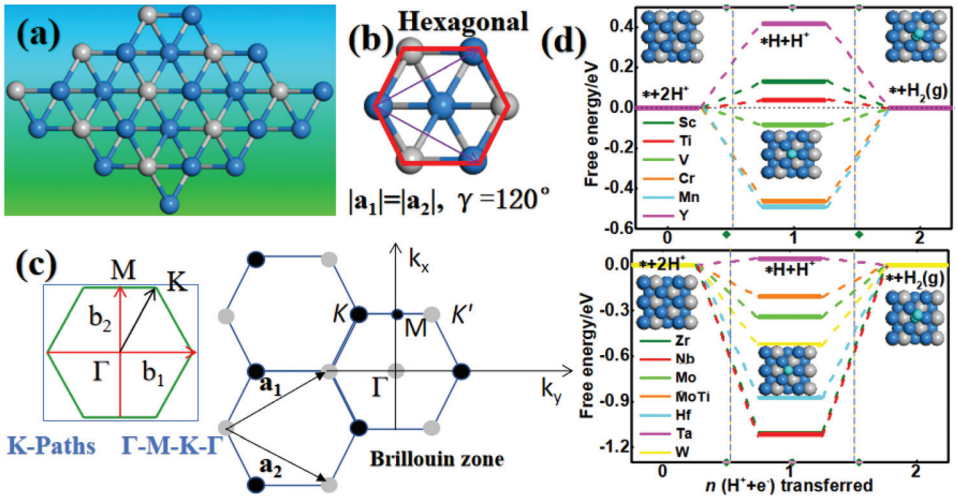

Fig. 1 (a) Schematic structure of type M_3C_2 MXene, (b) a local area of hexagonal unit and lattice parameter, (c) Brillouin region and *k*-point path of two-dimensional materials, a_1 and a_2 are the unit vectors of real space and b_1 and b_2 are the reciprocal lattice vectors. (d) HER at zero electrode potential at the top of the transition metal site on the M_3C_2 MXene surface, it means the binding energy change (ΔE) of atomic H to the surface, *n* represents the number of proton electron pairs transferred during the HER process.

The limiting potential (U_L) of each reaction mechanism pathway was obtained from the maximum free energy change (ΔG_{max}) among each elementary step along the most favourable energy pathway by using the relation $U_L = -\Delta G_{max}/e$.[41] In addition, the overpotential can be evaluated from the Gibbs free energy differences of each step by the formula η = Max $\{\Delta G_1, \Delta G_2, \Delta G_3, \Delta G_4, \Delta G_5, \Delta G_6, \Delta G_7, \Delta G_8\}/e - 0.17$, where ΔG_n (n = 1, 2, ... 8) are the Gibbs free energies of each elementary reaction.[42,43] The reaction energy ($\Delta E = E_{FS} - E_{IS}$) was set to the difference between the reactants and products. The energy barrier ($\Delta E = E_{TS} - E_{IS}$) was calculated by using the climbing-image nudged elastic band (CI-NEB) method,[44] and it is also employed to search the transition states (TS) for each elementary reaction of the CO_2RR on the surfaces of both Mo_3C_2 and Mo_2TiC_2 catalysts. All of the forces were converged to less than 0.005 eV Å^{-1} on the climbing image, and the cut-off energy, functional, and calculator parameters were the same as those used in adsorbate structure optimizations.

Results and discussion

Various species involved in the CO_2RR

We first studied the various CO_2RR mechanism pathways involving diverse intermediate species of the electrocatalytic CO_2RR on the M_3C_2 MXenes. The most favourable reaction pathway and all involved species for each MXene were considered. After fully relaxing the structure, we found that transition metal carbide (MXene) materials can capture CO_2 and reduce it to hydrocarbons. We first study the factors that affect the reaction mechanism with regards to the kinetic analysis of the CO_2RR, and the result indicates that the adsorption of CO_2 and CH_4 on MXenes is physisorption by the spontaneous binding energies,[45] suggesting that it is promising for CO_2 capture.

Our simulation system has shown a strong competitiveness and overcome some major secondary reactions such as H^+/H_2 (HER) conversion, thus showing promising applications in catalysis for the CO_2RR. As summarized in Fig. 1d, the limiting potential of the HER reaction mechanism is characterized as being between −1.12 and 0.42 eV, which means that the MXenes of M_3C_2 (here M = Y, Sc, Ti and Ta) seem to be more active towards the CO_2RR than the HER, showing that the small overpotential for the CO_2RR originates from the correlation between different mechanistic pathways and intermediate species. The simulation results show that the dispersion interaction has a great impact on the catalytic efficiency through our calculations by considering the van der Waals (vdW) interactions *via* the PBE/DFT-D3 method.[37] It is shown that the catalytic selectivity of the structure for the CO_2RR is higher than that for the HER, as the selectivity between the CO_2RR and HER is crucial and depends on the catalytic efficiency of the catalyst. In this regard, our calculations employing the free energy profiles are presented to explore the feasibility of the formation of the intermediate hydrocarbons. In addition, the limiting overpotential for the HER is usually lower than that for the CO_2RR through weakly binding hydrogen under the same conditions.[46] Nevertheless, we cannot come to the conclusion that these MXenes are good candidates for the CO_2RR, as the reduction of CO_2 and the evolution of $^+$H jointly determine the selectivity in the electroreduction process. The change in the limiting potential (U_L) between the CO_2RR and HER means that $U_L(CO_2)$–$U_L(H_2)$ plays an important role in the trend in selectivity towards carbonaceous products for reducing CO_2 catalysts. A higher $U_L(CO_2) - U_L(H_2)$ implies a higher selectivity for the CO_2RR over the HER. Our DFT calculations putting forward the possible reaction mechanism path and the intermediate product of each reaction mechanism (see Fig. 2) are discussed. The

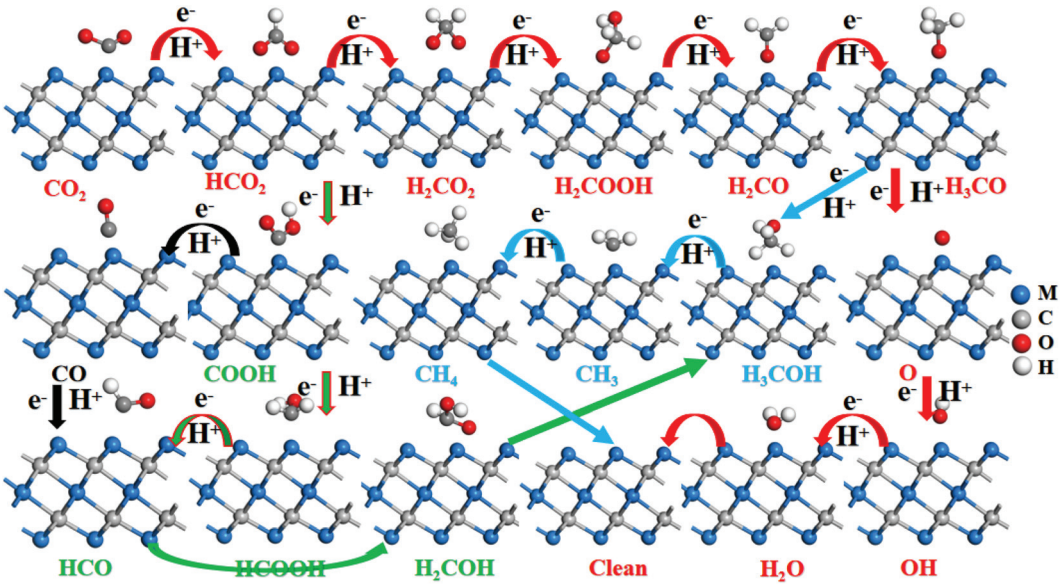

Fig. 2 Proposed CO_2RR possible mechanism pathways to different products on transition-metal carbides (MXenes) with the formula M_3 C2 as high efficiency catalysts, the blue colored numbers are formation energy (in eV) of CO_2RR intermediates.

potential determining steps (PDS), limiting potentials (U_L) and overpotentials (η) for the production of CH_4 and CH_3OH are also considered.[47]

Furthermore, during the electrocatalysis of fuel cells, the adsorption and desorption of reactants and products from the surface of the catalyst is an important step for the entire chemical process, and the different mechanistic pathway for the elecrocatalytic reduction of CO_2 to CH_4 is examined by first-principles DFT calculations. In summary, there are four alternative reaction paths leading to a slightly smaller overall reaction energy, and mechanism I (red line in Fig. 2) was set to go along with the intermediate species of $CO_2 \rightarrow HCO_2 \rightarrow H_2CO_2 \rightarrow H_2COOH \rightarrow H_2CO \rightarrow H_3CO \rightarrow O \rightarrow OH \rightarrow H_2O$ as the most favourable pathway in our current work. In addition, mechanism II (blue line in Fig. 2) went along $CO_2 \rightarrow COOH \rightarrow HCOOH \rightarrow HCO \rightarrow H_2CO \rightarrow H_2COH \rightarrow H_3COH \rightarrow CH_3 \rightarrow CH_4$. For mechanism III, the different reaction steps compared to mechanism I are $CH_3O \rightarrow CH_3OH \rightarrow CH_3 \rightarrow CH_4$ (cyan line in Fig. 2), and the last reaction mechanistic path is similar to the first mechanism $CO_2 \rightarrow COOH \rightarrow CO \rightarrow HCO \rightarrow H_2CO \rightarrow H_2COH \rightarrow H_3COH \rightarrow CH_3 \rightarrow CH_4$ (black line in Fig. 2).[48] The other alternative paths have much higher reaction energies than the previous step, and the lowest free energy path for CO_2 reduction is the primary concern in this work. It would make the energies of all intermediate steps more negative so that it can occur more easily. In all cases, the kinetic energy for CO_2 adsorption is negative at the applied zero potential (U = 0 eV). It occurs in the elementary step of H_2CO formation and corresponds to the potential determining steps (PDS) for the CO_2RR process on the M_3C_2 (MXene) surface. It demands the minimum energy path and can provide the best CO_2RR catalytic performance. The CO_2 can be reduced to the following five substances: HCHO, CH_3OH, CH_4, CO, and HCOOH products, and the catalytic activity of MXene has higher selectivity for the CO_2RR than for the HER.[49]

The overall kinetic energies required to carry out a reaction step for the hydrogenation of CO_2 to CH_4 along mechanism I on the Sc_3C_2 and Ti_3C_2 (Fig. 3a and b) are highly favourable with values of 1.82 eV ($H_2COOH \rightarrow H_2CO$) and 1.88 eV ($H_2CO_2 \rightarrow H_2COOH$) for the potential determining steps (PDS),[50] respectively. In addition, the calculated reaction energies (Fig. 3e and f) imply that the Mo_3C_2 (0.47 eV) and W_3C_2 (0.63 eV) are more easily capable of spontaneously reducing CO_2 than the other MXene catalysts. Our calculations indicate that the Mo_3C_2 MXene capture energy of H_2O is −0.10 eV and predict that it is a slightly endothermic process. In addition, it is always less negative than those for CO_2 reaction kinetics (Fig. 3e) with CO_2 over H_2O. Our system appears to be able to overcome some secondary reactions of CO_2 conversion into CH_4 *via* the transfer of 8 e^-/H^+ electron pairs from the MXene surface. In the following experiment, we use the configurations of W_3C_2 resulting from the conversion of CO_2 to CH_4 to study the adsorption performance and mechanism of MXene. For example, the first structure represents the configuration of CO_2 adsorption on the W_3C_2 surface, and the last structure represents the configuration of H_2O adsorption on the W_3C_2 surface. Adsorbed CO_2 (E_{ads} = −0.06 eV) on the top of the transition metal is in the form of carbonate (HCO_2) with a formation energy −1.40 eV, and then, carbonate (H_2CO_2) and (H_2COOH) form with formation energies of −0.30 eV and −0.22 eV, respectively. The corresponding potential determining step (PDS) is ($H_2COOH \rightarrow H_2CO$), and it resulted in very different adsorption structures and energies, with a 0.63 eV energy nonspontaneously formed by reactions, which is higher than the other steps.

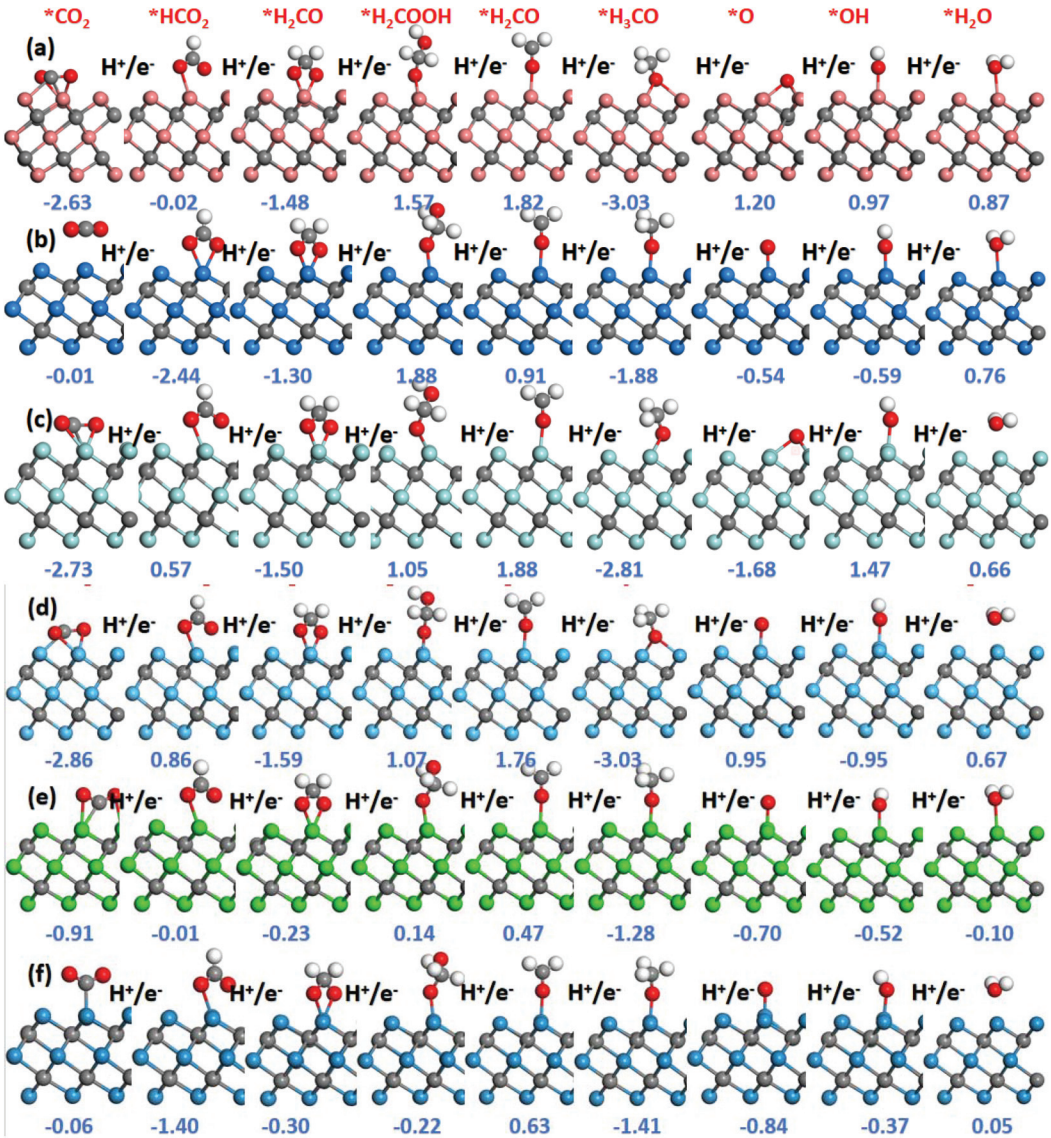

Fig. 3 Side view of the most favorable reaction path followed for CO_2 conversion into CH_4 and H_2O. The change in energy of CO_2RR intermediates for the mechanism I on (a) Sc_3C_2, (b) Ti_3C_2, (c) Zr_3C_2, (b) Hf_3C_2, (e) Mo_3C_2, and (f) W_3C_2 MXene, respectively. The blue colored numbers represent the reaction energy for each elementary step (in eV).

To provide a desire for us to further study the CO_2RR pathways and free-energy diagrams, our calculations showed that the relative free energy profile for the most favourable CO_2RR is energetically preferred for intermediate carbonate atoms (shown in Fig. 4). It is demonstrated that the CO_2RR includes an eight $(H^+ + e^-)$ pair transfer step in the CO_2 reduction pathway, and it induces the production of a CO_2 intermediate in an acid environment. In the free energy diagram of the CO_2RR at the zero potential ($U = 0$ V),[51] the free energies of all elementary reaction steps are downhill (exothermic) except for the third and fourth (endothermic) steps (shown in Fig. 4a and b), which are the endothermic steps associated with the high reaction energies of the H_2COOH and H_2CO formation. These exothermic steps can arise from the stability of carbonate intermediate species on the MXene surface. In addition, in the free-energy diagrams of mechanism II, the adsorption energy of *COOH is much higher than that of $*CO_2$, indicating that it is an endothermic process with a weak interaction between *COOH and the surface. It corresponds to the maximum thermodynamic pathway (shown in Fig. 4c and d) of the MXene electrode applied in a fuel cell, and the free energy in the $(H^+ + e^-)$ transfer step 4 (*HCO → *HCHO) is uphill for the $(H^+ + e^-)$ pair transfer step.[52] The rate-determining step lies in the middle $(H^+ + e^-)$ transfer step with high energy changes of 1.33 eV and 0.51 eV for *HCO → *HCHO or $*H_2COOH$ → *HCHO, respectively; it is defined as the maximum energy required for the CO_2RR on the Cr_3C_2 surface. The preceding results indicate the strong binding of HCHO intermediates for CO_2 activation in the fourth reaction process. As shown in Fig. 4e and f, CO_2 prefers to bind on the

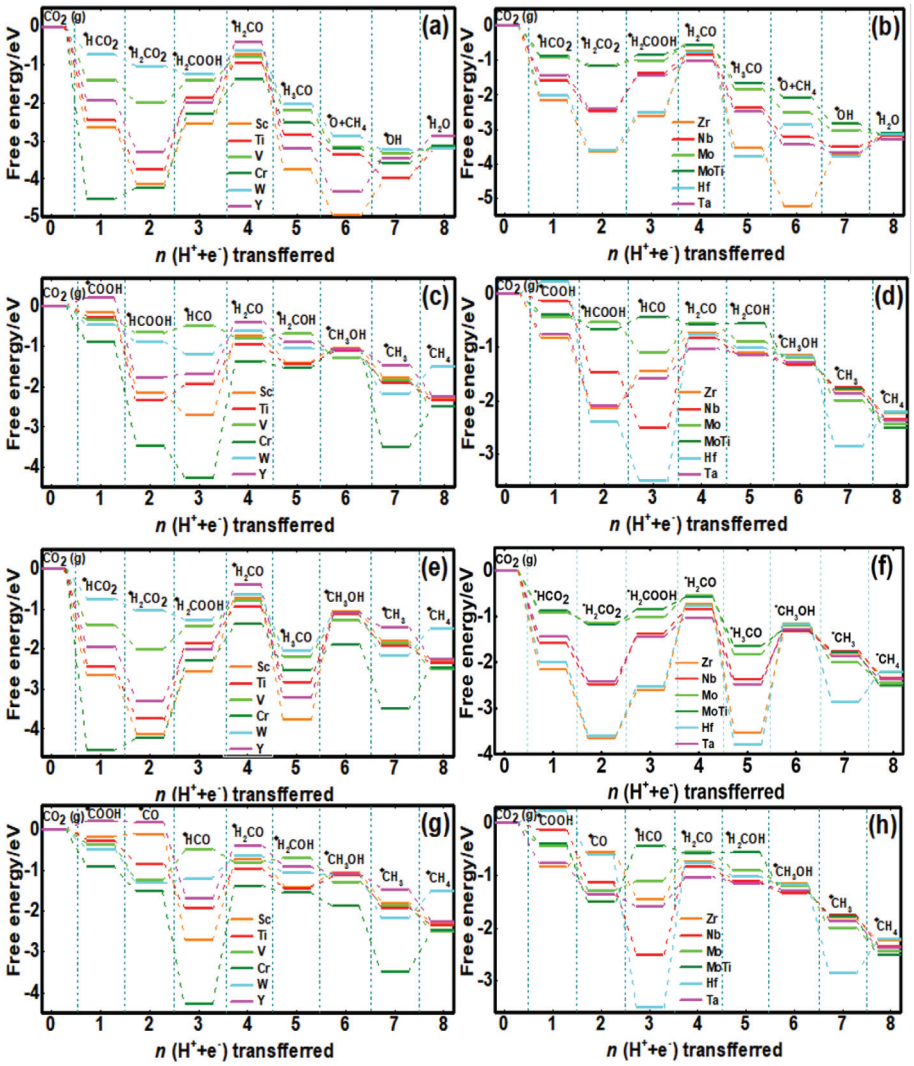

Fig. 4 Free energy diagrams of the overall CO_2RR for different reaction mechanisms on M_3C_2 (MXene) at 0 V *vs.* the RHE, *n* is the number of protonation steps during the CO_2RR. (a–b) Path 1 (c–d) path 2 (e–f) path 3 and (g–h) path 4 of all possible reaction mechanisms, respectively.

top of the metal, and CH_4 also easily releases from the catalyst surface with a small adsorption energy. The adsorption energy of CH_4 is 0.48 eV for Cr_3C_2, which is higher than that of 0.33 eV on Nb_3C_2, and it is also 2.46 eV and 2.18 eV higher than that of *COOH on Sc_3C_2 and Y_3C_2. However, the reaction step of $*H_3CO \rightarrow *H_3COH$ for path 3 with 3.026 eV on the Sc_3C_2 surface is mostly the same as that for Hf_3C_2 with a value of 3.027 eV. The energy comparison indicates that $*CO_2$ is −2.63 eV for Sc_3C_2, which is higher than −2.86 eV for Hf_3C_2, respectively. Furthermore, we predicted that for obtaining CO and CHO, $*COOH \rightarrow *CO \rightarrow *CHO$ is the primary reaction pathway (shown in Fig. 4g and h), supplemented by $*HCHO \rightarrow *H_2COH$ as the secondary pathway in comparison with path 2, and they mainly lead to CH_4 as the final product at zero potential. Our results suggest that the $*CO \rightarrow *CHO$ rather than $*CO \rightarrow *COH$ step is the primary reaction step in the fourth path for all MXenes, and thus, $*CO \rightarrow *CHO$ protonation is most likely the rate-determining step (RDS) for both path 2 and path 4.

As shown in Fig. 5, according to the subsequent protonation steps towards HCOOH, CH_3OH, CO and the final CH_4 production, using different electrode potentials showed that either the reduction of $*CO_2$ to *COOH or the reduction of $*CO_2$ to HCO_2 is likely to be a competitive relationship.[53] The linear relationships of the changes in the limiting potential (U_L) for the primary elementary reactions are a strong correlation between various surface reactions catalysed by M_3C_2-type MXenes, and they have imposed the ultimate deciding role in enhancing the catalytic activity and selectivity for either the CO_2RR or HER process. To obtain high-efficiency catalysts in catalysing the CO_2RR, it is desirable to describe the limiting potential (U_L) relationships of hydrogenated derivatives. We examined the linear relationships of $*CO_2 \rightarrow *COOH$, $*HCO \rightarrow *HCHO$, $*COOH \rightarrow *CO$ and $*CO_2 \rightarrow *HCO_2$ in Fig. 5a and $*H_3CO \rightarrow *H_3COH$, $*H_3CO \rightarrow *CH_4 + *O$ in Fig. 5b. Clearly, the formation of $*CO_2 \rightarrow *HCO_2$ over $*CO_2 \rightarrow *COOH$ is generally the potential determining step (PDS) for the overall CO_2RR in

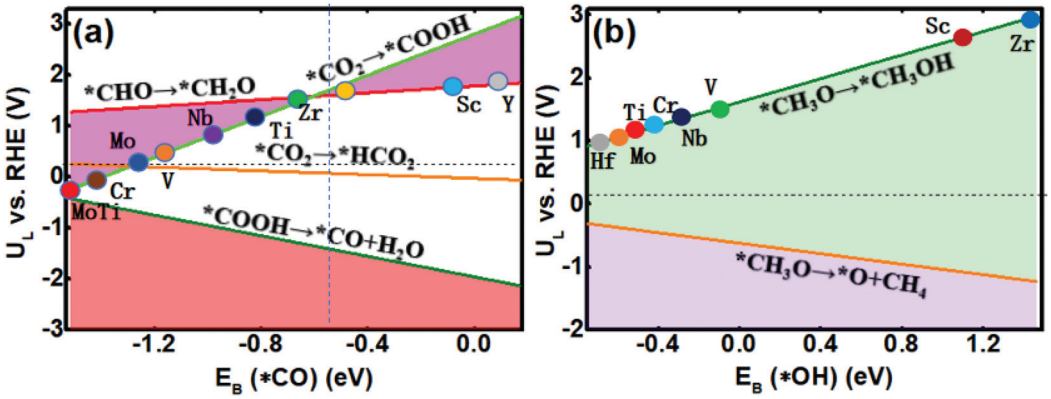

Fig. 5 Schematic illustration of the primary protonation steps of CO_2RR by predicted limiting potentials (U_L) for binding energy of the intermediate as a function through (a) E_B(*CO) and (b) E_B(*OH).

Fig. 5a. Considering that $*CH_3O \rightarrow *CH_4 + *O$ is the primary PDS for all mechanism I studies, as shown in Fig. 5, it is implied that the similarity of detailed configurations of the adsorbed intermediates determines the scaling relationships between the binding energies of the CO_2RR adsorbates,[54] and this suggests that altering the selectivity reaction mechanism of *COOH and $*HCO_2$ intermediates can be challenging for all MXene catalysts. The linearity difference can be attributed to the discrepancies in the reaction mechanism of $*CH_4 + *O$ or $*CH_3OH$, which leads to some overlapping elementary reaction steps between path 1 and path 3 or path 2 and path 4, respectively. Furthermore, the predicted trend of CO_2RR activity based on calculated thermodynamics is expected to be valid for all M_3C_2 (M = Sc, V, Mn, Zr, Nb, Mo, Hf, Ta, and W) MXenes. The first protonation step of the CO_2RR can form either carboxyl (*COOH) or formate (*OCHO), which played a crucial role in the overall reaction, followed by further reduction steps towards the products HCOOH, HCHO, CH_3OH and the final product CH_4. According to the criterion, the more negative reaction energy (ΔE) values are more favoured, and thus, we examined the reaction thermodynamics for each protonation step *via* $*HCO_2$ and *COOH intermediates to form the final product of CH_4(g). For example, when one elementary reaction step over another is mainly determined by their limiting potential, it then forms more reduced intermediates, such as *OCHO *vs.* *COOH, *CO *vs.* $*CH_2O$ *vs.* *HCOH and *HCOOH, and *CHO *vs.* *COH.[1] However, it should be noted that in addition to the formed *CO, *HCOOH, and $*CH_2O$, we also took into account the distribution of the final products in the gas and liquid phases. It is for this reason that gas molecules CO(g), HCOOH(g), CH_3OH(g) and HCHO(g) have their weak binding strengths with the catalyst surface, indicating that *CO and *HCHO can also act as intermediates for further protonation steps to *CHO and $*H_2COH$. In addition, $*CH_3OH$ (l) is likely to weakly desorb as a liquid product and then undergo further protonation steps to $*CH_4$ with weaker binding strengths (ΔE: −0.13 eV to −0.41 eV) on the M_3C_2 MXene studied. According to the linear correlation plot of thermodynamic analysis shown in Fig. 6, it exhibited a linear relationship by representing the Gibbs free energies of each elementary reaction step in the lowest energy pathway, and the upper equilibrium potential for the CO_2RR (at −0.17 V) results from the main text, as we have considered. The lowest CO_2RR overpotentials are achieved with highly active catalysts containing Cr_3C_2, Sc_3C_2, Ti_3C_2, Hf_3C_2, Y_3C_2, and Zr_3C_2 for the first protonation step, whereas the lowest reaction Gibbs free energies, similar to the second protonation step, of Mo_2TiC_2, V_3C_2 and Mo_3C_2 are not beneficial for the ($H^+ + e^-$) pair being transferred. In addition, the third protonation step $*H_2CO_2 \rightarrow *H_2COOH$ is difficult to spontaneously react through the same active sites of MXenes.

The free energies of ΔE_{*CO} and *CO for hydrocarbon intermediate species from the scaling relationships for different M_3C_2 MXene surfaces can be seen, indicating that Sc_3C_2 and Y_3C_2 candidates have much lower limiting potential (U_L) values for the potential determining steps (PDS), which is shown in Fig. 6a. All limiting potentials included in CO_2 reduction are lower than those of the HER. In addition, Mo_2TiC_2 and Ta_3C_2 candidates have low limiting potentials (U_L) *vs.* RHE for the potential determining step (*CHO → *HCHO), as shown in Fig. 6b. We expected these surfaces to be selective for CO_2 reduction, as the same ΔE_{*CO} with much lower $*CO_2 \rightarrow$ *COOH could be covered by hydrogen. Fig. 7 indicates the ΔE_{*CO} activity for binding critical intermediates in the PDS on M_3C_2 (M = Sc, V, Mn, Zr, Nb, Mo, Hf, Ta, and W). Generally, the smaller ΔE_{*CO} corresponds to the more efficient activity for these potential determining steps in the process of CO_2 protonation, and the smaller *CO favours the further protonation of *CHO to produce HCHO to CH_3OH, while $*CH_4$ is more stable. Along the potential determining steps of path 2, the PDS for Sc_3C_2 and W_3C_2 is *CO → *CHO instead of *CO → *COH. The calculated U_L of this PDS for Sc_3C_2 (−0.47 V) is smaller than that for Hf_3C_2 (−0.23 V), indicating that Sc_3C_2 not only has high catalytic activity for the CO_2RR but also lowers the overpotential required for further reduction, as shown in Fig. 6d.

As shown in Fig. 8, according to the dashed diagonal line, which mostly lies on the diagonal line, this is predicted to be

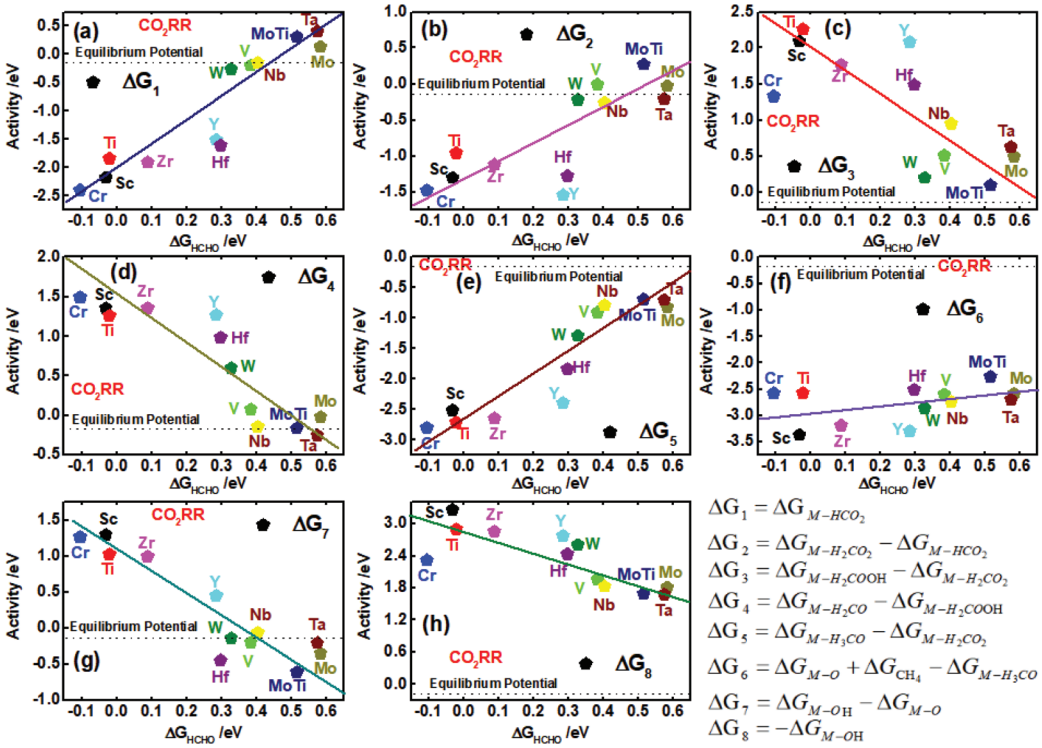

Fig. 6 Combined volcano plot of the catalytic activity for each intermediate reaction step of CO_2RR (up) (equilibrium potential: −0.17 V), resulting from the thermodynamic analysis, ΔG_n (n = 1, 2, 3, 4, 5, 6, 7, 8) corresponding to 8 ($H^+ + e^-$) transferred, respectively.

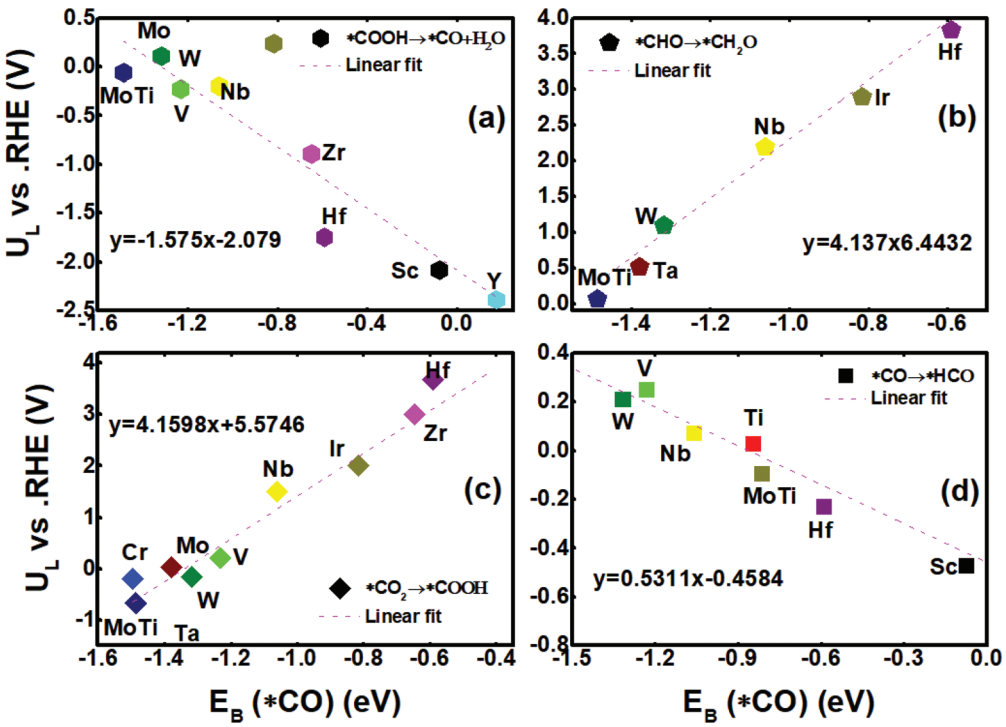

Fig. 7 The limiting potential (U_L) *vs.* RHE relationship of hydrocarbon derivatives, the U_L *vs.* RHE vs ΔE_{*CO} binding energy were obtained with different catalysts under the same conditions. The potential determining steps (PDS) for the overall CO_2RR. Considering that (a) *COOH → *CO + *O (b) *CHO → *HCHO (c) $*CO_2$ → *COOH (d) *CO → *CHO are the primary PDS mechanisms in this work for the CO_2RR.

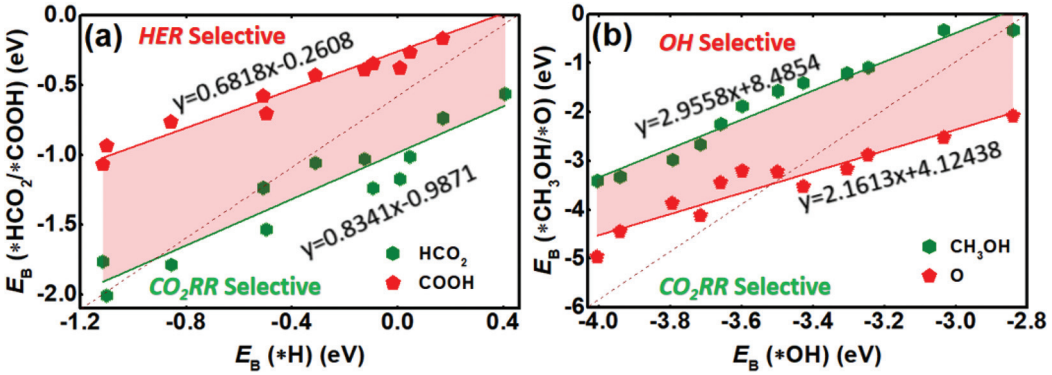

Fig. 8 Binding energy changes (ΔE_B) for (a) the first protonation step of $*CO_2 \rightarrow *HCO_2$ and $*CO_2 \rightarrow *COOH$ *vs.* HER, (b) the protonation step of $*CH_3O \rightarrow *CH_3OH$ and $*CH_3O \rightarrow *CH_4 + *O$ *vs.* HER. Data points lie below the dashed diagonal are more selective towards the CO_2RR than the HER or OH formation at $U = 0$ V (*vs.* RHE).

more selective preferring the CO_2RR rather than the HER and forming $*HCO_2$ rather than *COOH along mechanism I at the applied zero potential ($U = 0$ eV) in Fig. 8a. In addition, it is more selective for $*CH_3O \rightarrow *CH_4 + *O$ rather than $*CH_3O \rightarrow *CH_3OH$ as shown in Fig. 8b, demonstrating their feasibility as cathodes for forming $*CH_4 + *O$ rather than $*CH_3OH$ along the favourable pathway. The calculated ΔE values of $*HCO_2$ range from −0.74 eV to −2.01 eV, and those for *COOH are −0.16 eV to −1.07 eV, respectively. As shown in Fig. 3, the changes in difference adsorbate substrate configurations along mechanism I can be clearly seen on Sc_3C_2, Ti_3C_2, Zr_3C_2, Hf_3C_2, Mo_3C_2, and W_3C_2 MXenes. Those below the dashed diagonal except for Nb_3C_2 have the potential limiting step determined by $*CO_2 \rightarrow *HCO_2$. Both $*CO_2 \rightarrow *HCO_2$ and $*CH_3O \rightarrow CH_4 + *O$ are more selective for the CO_2RR compared to the HER below the dashed diagonal area, and as the potential determining steps (PDS) of mechanism I, they are more favourably reduced at the zero applied potential. On the other hand, in Fig. 8 below the diagonal, such as for Zr_3C_2, Hf_3C_2 Cr_3C_2, V_3C_2, Ta_3C_2, and Ti_3C_2, the $*CO_2 \rightarrow *HCO_2$ and $*CH_3O \rightarrow CH_4 + *O$ are the thermodynamic limiting steps. This indicates that more negative potentials are required to reduce the CO_2RR compared with that of OH reduction, and it is unlikely for OH reduction to H_2O to form below the CO_2RR potentials.[54] These six candidate MXenes are taken into account in the next section to further investigate the CO_2RR reaction kinetics. As shown in Fig. 8, the first hydrogenation step of CO_2 is binding with an energy of −2.01 eV in Zr_3C_2. The different colour solid lines have a linear relationship with a series of intermediates, with the slope and coefficient marked on the plot place, producing a mixture of products. M_3C_2 MXenes, as extremely valuable candidates for the CO_2RR, should exhibit high catalytic activity and selectively at a low overpotential, and has a low activity towards competing processes with the HER under the reaction conditions. In contrast to hydrocarbon formation, the CO_2 reduction to CO only requires the transfer of two electrons with two protons,[9] and *HCHO is formed in the next protonation of *CHO for all MXene surfaces that have been studied. The competitive binding between C–M and O–M may result in the formation of $*CH_3O$ through O–M binding or $*CH_2OH$ through C–M binding, and this is associated with the relative strengths of carbophilicity or oxophilicity on top of the different transition metals. This has further implications for the primary intermediates to the two possible products, $*CH_3O$ for CH_4 and $*CH_2OH$ for $*CH_3OH$ and finally forming CH_4.[55]

As shown in Fig. 9, we predicted the rate-determining step (RDS) with limiting potentials ($U_L = -\Delta E_{max}/e$), and the overpotential (η) was deduced using the formula $\eta = U_0 - U_L$. Here U_0 is the equilibrium potential (0.17 V for methane formation) of a specific reaction (see Table S5†).[56] It is based on these calculated results from the primary potential rate-determining step for different reaction mechanisms. Then, it is predicted that the overpotential along mechanism I for CH_4 formation is in the order of Mo_2TiC_2 ($\eta = 0.18$ V) and Hf_3C_2 ($\eta = 2.91$ V) (shown in Fig. 9c). In addition, the overpotentials of CH_3OH formation are in the order of Mo_2TiC_2 ($\eta = 0.32$ V) < Fe ($\eta = 1.56$ V) > Nb_3C_2 ($\eta = 1.02$ V) < Ta_3C_2 ($\eta = 1.19$ V) < Cr_3C_2 ($\eta = 0.89$ V), as shown in Fig. 8a. We noted that our calculated overpotential (η) of Mo_2TiC_2 is −0.38 V and that with Cr_3C_2 is −0.13 V for CO formation, where $*COOH \rightarrow *CO + H_2O$ is predicted to be the potential determining step (PDS) (in Fig. 8b). In addition, these results agree reasonably well with those ($\eta = 0.11$ V, PDS: $*COOH \rightarrow *CO$) obtained from the CO_2RR on the Nb_3C_2 surface and ($\eta = 0.23$ V, $*COOH \rightarrow *CO$) those obtained from the CO_2RR on the Ta_3C_2 surface, which is shown in Fig. 8b. Another observed reaction mechanism path is that $*CO_2 \rightarrow *COOH \rightarrow *HCOOH$ is the primary competitive relationship with $*CO_2 \rightarrow *HCO_2 \rightarrow *H_2CO_2$ for the overall CO_2RR. Furthermore, Ti_3C_2 encounters an overpotential (η) of 0.66 V more from the PDS $*COOH \rightarrow *HCOOH$ compared with those (0.37 V and 0.59 V) from the PDS $*CO_2 \rightarrow *COOH$ on Cr_3C_2 and V_3C_2, respectively. Hf_3C_2 and Mo_3C_2 are predicted to be excellent in catalysing the CO_2RR from PDS, and $*CHO \rightarrow *HCHO$ encounters overpotentials (η) of 0.80 V and 0.62 V along mechanism IV. Nevertheless, the most stable intermediates (*HCHO or $*CH_2OH$) on Mo_3C_2 and Mo_2TiC_2 free reaction energies and reaction energy barriers will decide the catalytic

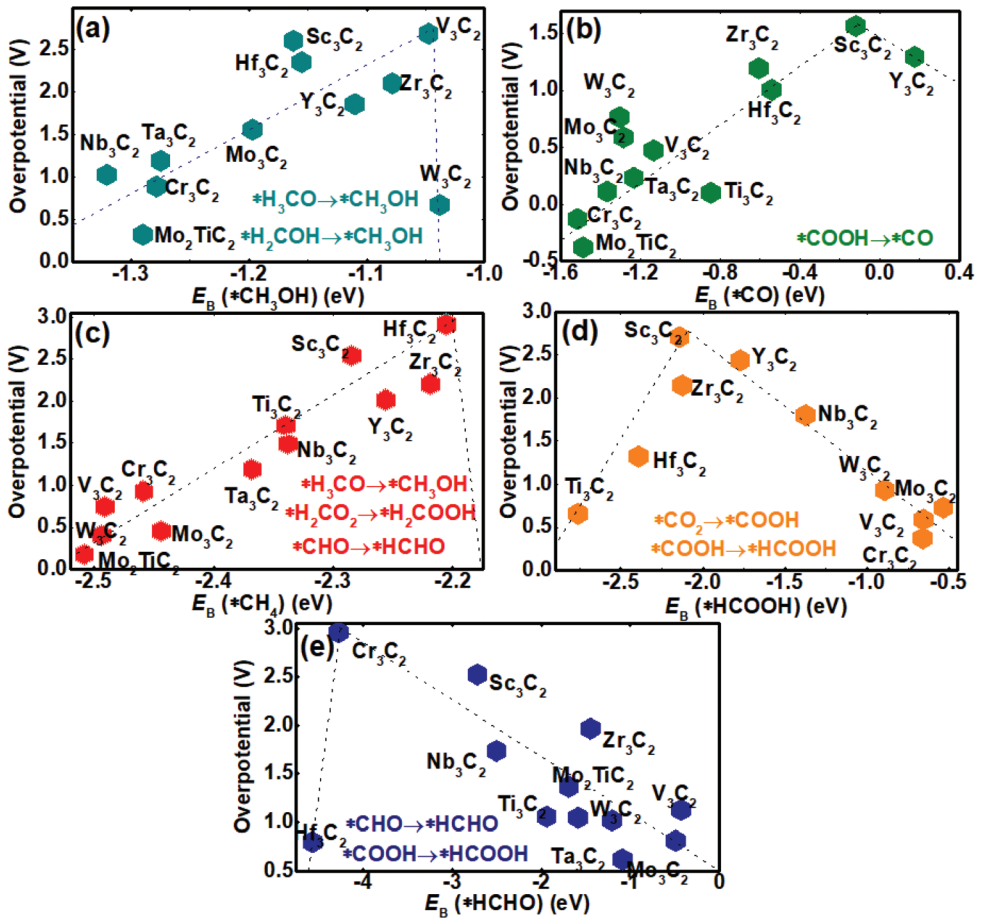

Fig. 9 Volcano relation of overpotentials as a function of binding energy (ΔE) for different intermediate species, (a) E_B(*CH_3OH) (b) E_B(*CO), (c) E_B(*CH_4), (d) E_B(*HCOOH), and (e) E_B(*HCHO), open symbols are for M = Sc, Mn, Zr, V, Mo, Nb, Hf, Ta, and W in M_3C_2 for production of CH_4, CO, HCHO, HCOOH, and CH_3OH.

activity of the catalyst, and they contributed to the observed CO_2RR activity. Our calculations observed that for obtaining the final product CH_4, *CO_2 → *HCO_2 → *H_2CO_2 → *H_2COOH → *H_2CO → *H_3CO → *H_4C + *O → *O → *OH → *H_2O is the most favourable overall reaction pathway. In addition, for *CO_2 → *COOH → *HCOOH → *CHO → *H_2CO → *H_2COH → *CH_3OH → *CH_3 → *CH_4 as the secondary reaction pathway, these two reaction mechanisms mainly lead to liquid HCHO as the key intermediate product at a zero potential, as mechanism II suggests that *CHO is more stable than *COH as the primary intermediate in the third protonation step for all M_3C_2-type MXenes that have been studied. We also compared the competition between *CH_2O → *CH_3O and *CH_2O → *H_2COH, and *CH_2O → *CH_3O may be more likely to occur under low potentials. Our calculations show that the CO_2RR is favoured over *H_3CO → H_4C + *O on M_3C_2 MXenes. Actually, the first hydrogenation of CO_2 to form HCO_2 demands a large energy output, and in this case for MXenes, we observed exothermic reaction energies of −0.91 eV for Mo_3C_2 and −0.87 eV for Mo_2TiC_2. In addition, much more exothermic reaction energies of −2.65 eV for Sc_3C_2 and −2.45 eV for Ti_3C_2 were observed.

Our work has also identified the barrier of activation[57] for each intermediate reaction by searching for transition states (TSs) and their reaction energies[58] (shown in Fig. 10 and Fig. S10†), indicating a reaction energy of −0.05 eV for the first transition state in the representative candidate and an activation barrier of 0.06 eV for the first transition state (TS) in Zr_3C_2, where the first hydrogenation step of CO_2 is from CO_2 adsorption to the HCO_2 form. For example, the transition state (TS) of the second hydrogenation step of the CO_2RR leading to the H_2CO_2 intermediate species forms with a reaction energy of 0.05 and an activation barrier of 0.36 eV. It exhibits a high activation barrier of 0.36 eV and is an endothermic process. In addition, the third hydrogenation step for which the reduction reaction is H_2CO_2 to H_2COOH is interesting and it was found to have an increased energy barrier (0.11 eV), and then, it spontaneously transformed into H_2CO with an energy barrier of 0.01 eV. However, *CO_2 → *COOH would exhibit a higher activation barrier of 0.24 eV than *CO_2 → *HCO_2 for the first hydrogenation step. Through simulation for transition-metal carbides M_3C_2,[59] we predicted that Mo_3C_2 and Zr_3C_2 are the two best candidates for reducing CO_2 into CH_4, as high activities are obtained under the same conditions. Based on our

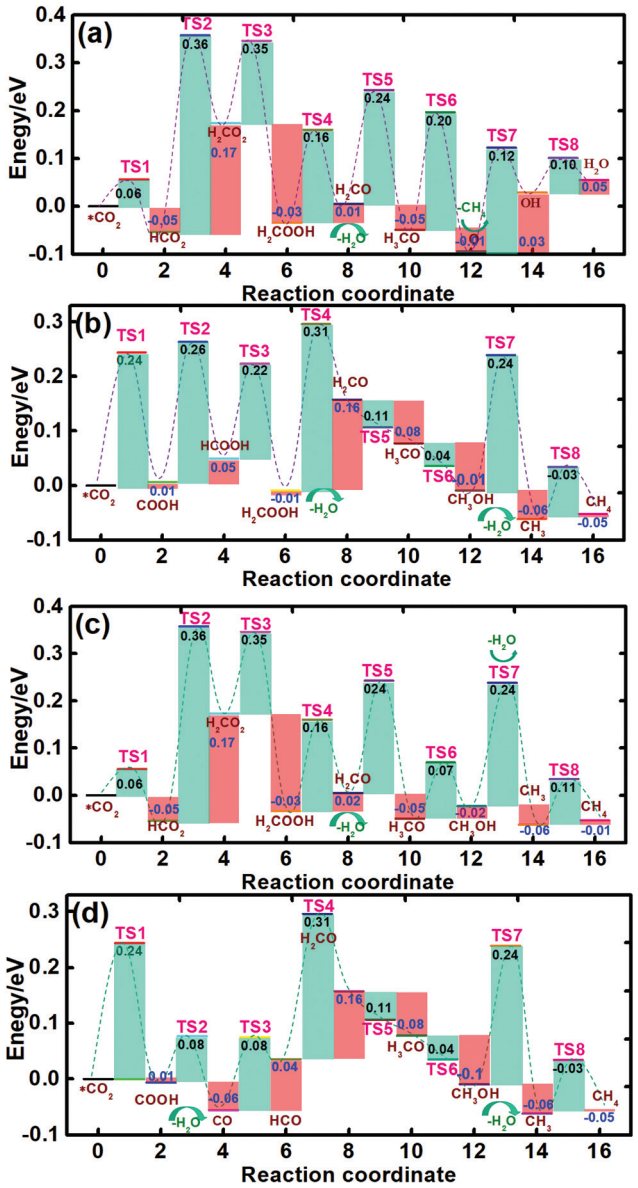

Fig. 10 All energy reaction mechanism paths for CO_2 conversion into $*CH_4$ in catalysis on the Zr_3C_2 MXene surface by using the DFT-D3 scheme. (a) Path 1, (b) path 2, (c) path 3, and (d) path 4. The intermediates and transition state (TS) are observed. Free energies for reaction (blue number) and activation (black number) are shown in eV for each reaction.

data, we hypothesize that a good catalytic activity for the CO_2RR can be obtained, and the catalytic mechanism was also described for M_3C_2 (M = Sc, V, Mn, Zr, Nb, Mo, Hf, Ta, and W) MXenes. They exhibited a common route along the minimum energy path involving successive hydrogenation steps.[60,61] On the basis of Fig. 10, there are four reduced intermediate products, HCHO, CO, CH_3OH, and HCHO, which exhibit weak binding. Since the CH_3O radical is more thermodynamically stable than the H_2COH along mechanism III with one H^+/e^- pair, our results have also shown that the route towards the formation of CH_3OH and HCHO as the final products is not favoured. As happened in the different reaction mechanism pathway of HCHO formation, we observed that producing O···CH_4 is the preferred spontaneous process from H_3CO. Finally, the *O moiety on the surface appears to be highly reactive after CH_4 release from the surface, and it corresponds to energy barriers of 0.02 eV and −0.05 eV for CH_4 release, respectively. As shown in Fig. 10b, a highly spontaneous reaction occurs in the seventh hydrogenation step from *O to *OH and further generation of H_2O, which has the lowest release of energy of all of the elementary reactions, even less than the earlier CO_2 adsorption process. M_3C_2-type MXenes, as a new material, have been increasing significantly in fuel cells,[62,63] and the rate-determining step[64] is usually imposed by the first hydrogenation step. However, our analysis presented different conclusions; the limiting step may be the release of H_2O or CH_4, as the final H^+/e^- transfer plays an important role, which is hypothesized as the best alternative for the catalytic reduction of CO_2 based on transition-metal carbides (MXenes) in this work.[65,66]

Conclusions

In summary, the systematically investigated 2D M_3C_2-type MXenes (M = Sc, V, Cr, Mn, Zr, Nb, Mo, Mo_2Ti, Hf, Ta, and W) towards the CO_2 reduction reaction to CH_4 with combined electrocatalytic technologies are discussed. We found that the transition metal plays an important role in the active site of the CO_2RR for each protonation step, producing diverse hydrocarbon products, such as CO, CH_3OH, HCHO and HCOOH, along the different mechanistic pathways of CO_2 conversion into hydrocarbons (CH_4). By analysing the changes in the limiting potential (U_L) between the CO_2RR and HER, it indicates that the CO_2RR is the dominant competing reaction over the HER, and it is predicted to be more selective for the CO_2RR forming HCO_2 than COOH as the first protonation step. This indicates that formic acid (HCOOH) is unlikely to be implemented as the intermediate product for the successive protonation steps because it may easily desorb as a liquid product from the MXene surface under the standard conditions. To produce methane as the final product, $*HCO_2 \rightarrow *H_2CO_2 \rightarrow *H_2CO_2 \rightarrow *H_2COOH \rightarrow *H_2CO \rightarrow *H_3CO \rightarrow *O \rightarrow *OH \rightarrow *H_2O$ (mechanism I) is predicted to be the primary pathway except for Ta_3C_2 and W_3C_2, and they are supplemented with $*COOH \rightarrow *HCOOH \rightarrow *CHO \rightarrow *HCHO \rightarrow *H_2COH \rightarrow *H_3COH \rightarrow *CH_3 \rightarrow *CH_4$ (mechanism II) as the most favourable pathway, resulting in $*HCHO \rightarrow *H_2COH$ being the potential determining step with limiting potentials of −2.10 eV and −0.89 eV, which are much lower than those of mechanism I (−1.43 eV and −0.74 eV) for the majority of the Ta_3C_2 and W_3C_2 studied, respectively. We identified the scaling relationships of the limiting potential (U_L) *vs.* RHE and the CO_2RR selectivity compared to the HER. The $*HCO_2$ and *COOH binding features may be determined by the intermediates, such as M–O–C and M–C–O binding, which are comparable to the relative strengths of the carbophilicity or oxophili-

city with the transition metal, and this plays an important role in determining the primary pathway to the two major reaction mechanisms, not only $*HCO_2 \rightarrow *H_2CO_2$ but also $*COOH \rightarrow *HCOOH$. Among all of the transition metal carbides (MXenes) considered, Ti_3C_2, Ta_3C_2 and Sc_3C_2 can greatly reduce CO_2 to CH_4. This work is likely to further guide the design of CO_2RR catalysts to produce high efficiency fuel cells, and V_3C_2, Mo_3C_2, Mo_2TiC_2 and W_3C_2 are certainly predicted to be promising CO_2RR catalysts for reducing methane (CH_4) under lower overpotentials of 0.74 V, 0.45 V, 0.17 V and 0.41 V, respectively.

Conflicts of interest

The authors declare that they have no conflict of interest.

Acknowledgements

Financial support comes from the China Scholarship Council (CSC: 201808440416) of China, Research and the Arts (HMWK) of the Hessen state in Germany, The Lichtenberg high-performance computer is gratefully acknowledged, and the authors are also thankful to TU Darmstadt. They also thank Elsevier Author Services (https://webshop.elsevier.com) for its linguistic assistance during the preparation of this manuscript.

References

1 E. V. Kondratenko, G. Mul, J. Baltrusaitis, *et al.*, Status and perspectives of CO_2 conversion into fuels and chemicals by catalytic, photocatalytic and electrocatalytic processes, *Energy Environ. Sci.*, 2013, **6**(11), 3112–3135.

2 Y. G. Kim, J. H. Baricuatro, A. Javier, *et al.*, The evolution of the polycrystalline copper surface, first to Cu (111) and then to Cu (100), at a fixed CO_2RR potential: A study by operando EC-STM, *Langmuir*, 2014, **30**(50), 15053–15056.

3 J. H. Wee, Applications of proton exchange membrane fuel cell systems, *Renewable Sustainable Energy Rev.*, 2007, **11**(8), 1720–1738.

4 Y. Jiao, Y. Zheng, M. Jaroniec, *et al.*, Design of electrocatalysts for oxygen-and hydrogen-involving energy conversion reactions, *Chem. Soc. Rev.*, 2015, **44**(8), 2060–2086.

5 G. Liu, N. Hoivik, K. Wang, *et al.*, Engineering TiO2 nanomaterials for CO_2 conversion/solar fuels, *Sol. Energy Mater. Sol. Cells*, 2012, **105**, 53–68.

6 H. C. Hsu, I. Shown, H. Y. Wei, *et al.*, Graphene oxide as a promising photocatalyst for CO_2 to methanol conversion, *Nanoscale*, 2013, **5**(1), 262–268.

7 W. J. Ong, L. L. Tan, Y. H. Ng, *et al.*, Graphitic carbon nitride ($g\text{-}C_3N_4$)-based photocatalysts for artificial photosynthesis and environmental remediation: are we a step closer to achieving sustainability?, *Chem. Rev.*, 2016, **116**(12), 7159–7329.

8 T. R. Karl and K. E. Trenberth, Modern global climate change, *Science*, 2003, **302**(5651), 1719–1723.

9 S. H. Jensen, P. H. Larsen and M. Mogensen, Hydrogen and synthetic fuel production from renewable energy sources, *Int. J. Hydrogen Energy*, 2007, **32**(15), 3253–3257.

10 A. S. Varela, N. Ranjbar Sahraie, J. Steinberg, *et al.*, Metal-doped nitrogenated carbon as an efficient catalyst for direct CO_2 electroreduction to CO and hydrocarbons, *Angew. Chem., Int. Ed.*, 2015, **54**(37), 10758–10762.

11 Y. Zhou, F. Che, M. Liu, *et al.*, Dopant-induced electron localization drives CO_2 reduction to C2 hydrocarbons, *Nat. Chem.*, 2018, **10**(9), 974.

12 A. D. Handoko, K. H. Khoo, T. L. Tan, *et al.*, Establishing new scaling relations on two-dimensional MXenes for CO_2 electroreduction, *J. Mater. Chem. A*, 2018, **6**(44), 21885–21890.

13 A. D. Handoko, S. N. Steinmann and Z. W. Seh, Theory-guided materials design: two-dimensional MXenes in electro-and photocatalysis, *Nanoscale Horiz.*, 2019, **4**(4), 809–827.

14 J. Peng, X. Chen, W. J. Ong, *et al.*, Surface and heterointerface engineering of 2D MXenes and their nanocomposites: insights into electro-and photocatalysis, *Chem*, 2019, **5**(1), 18–50.

15 X. Zhu and Y. Li, Review of two-dimensional materials for electrochemical CO_2 reduction from a theoretical perspective, *Wiley Interdiscip. Rev.: Comput. Mol. Sci.*, 2019, **9**(6), e1416.

16 A. Rendon-Calle, S. Builes and F. Calle-Vallejo, A brief review of the computational modeling of CO_2 electroreduction on Cu electrodes, *Curr. Opin. Electrochem.*, 2018, **9**, 158–165.

17 W. J. Durand, A. A. Peterson, F. Studt, *et al.*, Structure effects on the energetics of the electrochemical reduction of CO_2 by copper surfaces, *Surf. Sci.*, 2011, **605**(15–16), 1354–1359.

18 A. J. Garza, A. T. Bell and M. Head-Gordon, Mechanism of CO_2 reduction at copper surfaces: Pathways to C_2 products, *ACS Catal.*, 2018, **8**(2), 1490–1499.

19 J. D. Benck, T. R. Hellstern, J. Kibsgaard, *et al.*, Catalyzing the hydrogen evolution reaction (HER) with molybdenum sulfide nanomaterials, *ACS Catal.*, 2014, **4**(11), 3957–3971.

20 R. Daiyan, X. Lu, Y. H. Ng, *et al.*, Highly Selective Conversion of CO_2 to CO Achieved by a Three-Dimensional Porous Silver Electrocatalyst, *ChemistrySelect*, 2017, **2**(3), 879–884.

21 N. Li, X. Chen, W. J. Ong, *et al.*, Understanding of electrochemical mechanisms for CO_2 capture and conversion into hydrocarbon fuels in transition-metal carbides (MXenes), *ACS Nano*, 2017, **11**(11), 10825–10833.

22 S. Siahrostami, Designing Carbon-Based Materials for Efficient Electrochemical Reduction of CO_2, *Ind. Eng. Chem. Res.*, 2018, **58**(2), 879–885.

23 X. Cui, W. An, X. Liu, *et al.*, C_2N-graphene supported single-atom catalysts for CO_2 electrochemical reduction reaction: mechanistic insight and catalyst screening, *Nanoscale*, 2018, **10**(32), 15262–15272.

24 Z. Wang, L. Wu, K. Sun, *et al.*, Surface Ligand Promotion of Carbon Dioxide Reduction through Stabilizing Chemisorbed Reactive Intermediates, *J. Phys. Chem. Lett.*, 2018, **9**(11), 3057–3061.
25 M. R. Singh, E. L. Clark and A. T. Bell, Thermodynamic and achievable efficiency for solar-driven electrochemical reduction of carbon dioxide to transportation fuels, *Proc. Natl. Acad. Sci. U. S. A.*, 2015, **112**(45), E6111–E6118.
26 W. Setyawan and S. Curtarolo, High-throughput electronic band structure calculations: Challenges and tools, *Comput. Mater. Sci.*, 2010, **49**(2), 299–312.
27 X. Li, Z. Zhang, Y. Yao, *et al.*, High throughput screening for two-dimensional topological insulators, *2D Mater.*, 2018, **5**(4), 045023.
28 H. K. Singh, Z. Zhang, I. Opahle, *et al.*, High-throughput screening of magnetic antiperovskites, *Chem. Mater.*, 2018, **30**(20), 6983–6991.
29 C. Zhan, W. Sun, Y. Xie, *et al.*, Computational Discovery and Design of MXenes for Energy Applications: Status, Successes, and Opportunities, *ACS Appl. Mater. Interfaces*, 2019, **11**(28), 24885–24905.
30 X. F. Yang, A. Wang, B. Qiao, *et al.*, Single-atom catalysts: a new frontier in heterogeneous catalysis, *Acc. Chem. Res.*, 2013, **46**(8), 1740–1748.
31 S. Mou, T. Wu, J. Xie, *et al.*, Boron Phosphide Nanoparticles: A Nonmetal Catalyst for High-Selectivity Electrochemical Reduction of CO_2 to CH_3OH, *Adv. Mater.*, 2019, **31**(36), 1903499.
32 C. Kim, F. Dionigi, V. Beermann, *et al.*, Alloy nanocatalysts for the electrochemical oxygen reduction (ORR) and the direct electrochemical carbon dioxide reduction reaction (CO_2RR), *Adv. Mater.*, 2019, **31**(31), 1805617.
33 Y. Cai and A. B. Anderson, The reversible hydrogen electrode: potential-dependent activation energies over platinum from quantum theory, *J. Phys. Chem. B*, 2004, **108**(28), 9829–9833.
34 G. Kresse and J. Furthmüller, Efficient iterative schemes for ab initio total-energy calculations using a plane-wave basis set, *Phys. Rev. B: Condens. Matter Mater. Phys.*, 1996, **54**(16), 11169.
35 L. Ji, L. Chang, Y. Zhang, *et al.*, Electrocatalytic CO2 Reduction to Alcohols with High Selectivity over a Two-Dimensional Fe2P2S6 Nanosheet, *ACS Catal.*, 2019, **9**(11), 9721–9725.
36 P. E. Blöchl, Projector augmented-wave method, *Phys. Rev. B: Condens. Matter Mater. Phys.*, 1994, **50**(24), 17953.
37 M. C. Payne, M. P. Teter, D. C. Allan, *et al.*, Iterative minimization techniques for ab initio total-energy calculations: molecular dynamics and conjugate gradients, *Rev. Mod. Phys.*, 1992, **64**(4), 1045.
38 J. Moellmann and S. Grimme, DFT-D3 study of some molecular crystals, *J. Phys. Chem. C*, 2014, **118**(14), 7615–7621.
39 J. K. Nørskov, J. Rossmeisl, A. Logadottir, *et al.*, Origin of the overpotential for oxygen reduction at a fuel-cell cathode, *J. Phys. Chem. Biophys.*, 2004, **108**(46), 17886–17892.
40 S. Grimme, J. Antony, S. Ehrlich and H. Krieg, A Consistent and Accurate Ab initio Parametrization of Density Functional Dispersion Correction (DFT-D) for The 94 Elements H-Pu, *J. Chem. Phys.*, 2010, **132**, 154104.
41 S. Liu, J. Xiao, X. F. Lu, *et al.*, Efficient Electrochemical Reduction of CO_2 to HCOOH over Sub-2 nm SnO_2 Quantum Wires with Exposed Grain Boundaries, *Angew. Chem., Int. Ed.*, 2019, **58**(25), 8499–8503.
42 J. P. Perdew, J. A. Chevary, S. H. Vosko, *et al.*, Atoms, molecules, solids, and surfaces: Applications of the generalized gradient approximation for exchange and correlation, *Phys. Rev. B: Condens. Matter Mater. Phys.*, 1992, **46**(11), 6671.
43 W. J. Durand, A. A. Peterson, F. Studt, *et al.*, Structure effects on the energetics of the electrochemical reduction of CO_2 by copper surfaces, *Surf. Sci.*, 2011, **605**(15–16), 1354–1359.
44 V. Wang, N. Xu and J. C. Liu, *et al.*, VASPKIT: A Pre-and Post-Processing Program for VASP code, arXiv preprint arXiv:1908.08269, 2019.
45 M. R. Singh, J. D. Goodpaster, A. Z. Weber, *et al.*, Mechanistic insights into electrochemical reduction of CO_2 over Ag using density functional theory and transport models, *Proc. Natl. Acad. Sci. U. S. A.*, 2017, **114**(42), E8812–E8821.
46 F. Li, H. Shu, C. Hu, *et al.*, Atomic mechanism of electrocatalytically active Co–N complexes in graphene basal plane for oxygen reduction reaction, *ACS Appl. Mater. Interfaces*, 2015, **7**(49), 27405–27413.
47 C. Dong, J. Fu, H. Liu, *et al.*, Tuning the selectivity and activity of Au catalysts for carbon dioxide electroreduction via grain boundary engineering: a DFT study, *J. Mater. Chem. A*, 2017, **5**(15), 7184–7190.
48 G. Henkelman, B. P. Uberuaga and H. Jónsson, A climbing image nudged elastic band method for finding saddle points and minimum energy paths, *J. Chem. Phys.*, 2000, **113**(22), 9901–9904.
49 X. Cui, W. An, X. Liu, *et al.*, C_2N-graphene supported single-atom catalysts for CO_2 electrochemical reduction reaction: mechanistic insight and catalyst screening, *Nanoscale*, 2018, **10**(32), 15262–15272.
50 A. D. Handoko, K. H. Khoo, T. L. Tan, *et al.*, Establishing new scaling relations on two-dimensional MXenes for CO_2 electroreduction, *J. Mater. Chem. A*, 2018, **6**(44), 21885–21890.
51 Y. Meng, X. Qu, K. Li, *et al.*, Rhodium and Nitrogen Codoped Graphene as a Bifunctional Electrocatalyst for the Oxygen Reduction Reaction and CO_2 Reduction Reaction: Mechanism Insights, *J. Phys. Chem. C*, 2019, **123**(9), 5176–5187.
52 A. S. Varela, W. Ju and P. Strasser, Molecular Nitrogen–Carbon Catalysts, Solid Metal Organic Framework Catalysts, and Solid Metal/Nitrogen-Doped Carbon (MNC) Catalysts for the Electrochemical CO_2 Reduction, *Adv. Energy Mater.*, 2018, **8**(30), 1703614.

53 J. Huang, N. Hörmann, E. Oveisi, *et al.*, Potential-induced nanoclustering of metallic catalysts during electrochemical CO_2 reduction, *Nat. Commun.*, 2018, **9**(1), 1–9.
54 L. Feng, Y. Liu and J. Zhao, Iron-embedded boron nitride nanosheet as a promising electrocatalyst for the oxygen reduction reaction (ORR): a density functional theory (DFT) study, *J. Power Sources*, 2015, **287**, 431–438.
55 H. Fei, J. Dong, Y. Feng, *et al.*, General synthesis and definitive structural identification of MN_4C_4 single-atom catalysts with tunable electrocatalytic activities, *Nat. Catal.*, 2018, **1**(1), 63.
56 H. Zhang, Y. Tian, J. Zhao, *et al.*, Small dopants make big differences: Enhanced electrocatalytic performance of MoS_2 monolayer for oxygen reduction reaction (ORR) by N–and P–doping, *Electrochim. Acta*, 2017, **225**, 543–550.
57 X. Zhu and Y. Li, Review of two-dimensional materials for electrochemical CO_2 reduction from a theoretical perspective, *Wiley Interdiscip. Rev.: Comput. Mol. Sci.*, 2019, **9**(6), e1416.
58 L. M. Azofra, D. R. MacFarlane and C. Sun, A DFT study of planar vs. corrugated graphene-like carbon nitride (gC_3N_4) and its role in the catalytic performance of CO_2 conversion, *Phys. Chem. Chem. Phys.*, 2016, **18**(27), 18507–18514.
59 A. S. Nair, A. Mahata and B. Pathak, Multilayered Platinum Nanotube for Oxygen Reduction in a Fuel Cell Cathode: Origin of Activity and Product Selectivity, *ACS Appl. Energy Mater.*, 2018, **1**(8), 3890–3899.
60 J. Heß, Y. Wang and K. Hutter, Thermodynamically consistent modeling of granular-fluid mixtures incorporating pore pressure evolution and hypoplastic behavior, *Continuum Mech. Thermodyn.*, 2017, **29**(1), 311–343.
61 E. Gracia-Espino, X. Jia and T. Wågberg, Improved oxygen reduction performance of Pt–Ni nanoparticles by adhesion on nitrogen-doped graphene, *J. Phys. Chem. C*, 2014, **118**(5), 2804–2811.
62 S. Ma, W. Song, B. Liu, *et al.*, Facet-dependent photocatalytic performance of TiO_2: A DFT study, *Appl. Catal., B*, 2016, **198**, 1–8.
63 D. H. Lim and J. Wilcox, Mechanisms of the oxygen reduction reaction on defective graphene-supported Pt nanoparticles from first-principles, *J. Phys. Chem. C*, 2012, **116**(5), 3653–3660.
64 X. X. Xue, S. Shen, X. Jiang, *et al.*, Tuning the Catalytic Property of Phosphorene for Oxygen Evolution and Reduction Reactions by Changing Oxidation Degree, *J. Phys. Chem. Lett.*, 2019, **10**(12), 3440–3446.
65 L. Wang, H. Dong, Z. Guo, *et al.*, Potential application of novel boron-doped graphene nanoribbon as oxygen reduction reaction catalyst, *J. Phys. Chem. C*, 2016, **120**(31), 17427–17434.
66 K. Teramura, K. Hori, Y. Terao, *et al.*, Which is an intermediate species for photocatalytic conversion of CO_2 by H2O as the electron donor: CO_2 molecule, carbonic acid, bicarbonate, or carbonate ions?, *J. Phys. Chem. C*, 2017, **121**(16), 8711–8721.

THE JOURNAL OF PHYSICAL CHEMISTRY LETTERS
A JOURNAL OF THE AMERICAN CHEMICAL SOCIETY

pubs.acs.org/JPCL

Letter

Quantum Mechanical Screening of 2D MBenes for the Electroreduction of CO_2 to C1 Hydrocarbon Fuels

Yi Xiao,* Chen Shen, and Niloofar Hadaeghi

Cite This: *J. Phys. Chem. Lett.* 2021, 12, 6370–6382

Read Online

ACCESS | Metrics & More | Article Recommendations | Supporting Information

ABSTRACT: In this work, we propose a new family of two-dimensional (2D) transition metal borides (MBenes) to design and explore new high-efficiency catalysts for CO_2 electroreduction according to the Density Functional Theory (DFT) approach. The recently reported MBenes have been synthesized experimentally and have been found to have high electrical conductivities and stability, so they are promising candidates for the development of CO_2 electrocatalytic reduction (RR) catalysts. However, tuning the reaction mechanism such that the production of hydrocarbon species occurs at a low overpotential remains a challenge. Only C1 hydrocarbon products such as CH_4, CH_3OH, HCHO, CO, and HCOOH were identified, indicating that these MBenes have high stability, catalytic activity, and selectivity toward CO_2 reduction and overcome the competing hydrogen evolution reaction (HER). These MBenes possess a metallic feature that can be tuned as a new catalyst for CO_2RR, depending on the ability to control their selectivity and catalytic activity.

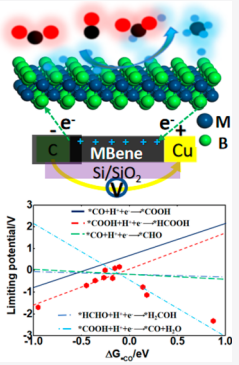

Carbon dioxide storage and recycling is a process involving the capture of CO_2. Researchers have devoted increasing amounts of attention to this process because of the sharp increase in greenhouse gas emissions from fossil fuels, which leads to serious global environmental problems.[1] Thus, CO_2 electrocatalytic reduction (CO_2RR) to useful hydrocarbon fuels, which have economic benefits, occurs via renewable sources, such as sunlight and electricity.[2−4] Transition metal borides (MBenes) are a new family of unique metallic character materials generated in the formula of M_xB_y, where *x*:*y* ratios can be set to 1:1, 1:2, 2:1, 3:4, and 5:2, and M denotes transition metals such as V, Fe, Mo, Ru, Os, Au, Ta, Nb, and Hf atoms. MBenes feature a mix of metallic and covalent bonding between the transition metal and boron. This new type of two-dimensional (2D) MBene material has been synthesized experimentally.[5,6] High-throughput screening was executed by Jiang et al.,[7] who reported 11 MBenes, Zr_2B_2, Hf_2B_2, Au_2B, Mo_2B,[9] Fe_2B_4,[15] Ru_2B_4, Os_2B_4, V_3B_4, Ta_3B_4, Nb_3B_4, and Nb_4B_{10}, with MXene-like family derivatives. This new type of 2D MBene material demonstrates excellent electronic, mechanical, and magnetic properties. The common MBenes are usually obtained by selective etching from the Al-containing group from the MAB phase under acidic solution conditions of HF or HCl, suggesting that they can be exfoliated into the 2D MBene layered structure. Recently, by using topochemical deintercalation from MoAlB phase crystals with NaOH alkaline solution under room-temperature conditions, a stable 2D Mo_2B_2 MBene monolayer was identified.[8] The given MBene monolayers exhibited high stability and selectivity for carbon dioxide electroreduction; however, the reaction mechanism and catalytic activity of MBenes remain unknown. Their electronic and chemical reactivity properties are implemented in first-principles calculations, and promising applications of MBenes as a high-efficiency catalyst to CO_2RR and the hydrogen evolution reaction (HER) have been proposed. As far as we know, some 2D MBene materials applied in CO_2 electrocatalytic reduction have been reported either experimentally or theoretically. Guo et al.[9] reported that 2D Mo_2B_2 and Fe_2B_2 MBenes are suitable for use in lithium-ion batteries and HER electrocatalysis applications due to their excellent metallic features and electronic conductivity. Yuan et al.[10] proposed MB_2 MBene monolayers with high catalytic activity for selective production of CO_2 to CH_4, Fe_2B_4, and Mn_2B_4 monolayers with very low limiting potential for CH_4 production in practical applications. Moreover, a type of Ti_2B_2 monolayer with electronic metallic properties and excellent catalytic activity has been applied in HER,[11] and Mo_2B as a new type of MBene material has been proven to be applicable in lithium-ion batteries because of its high electrical and thermal conductivities.[12] Furthermore, Fe_2B_2 has been reported to be a promising candidate catalyst for hydrogen evolution through theoretical study and experimental analysis, and Ti_2B_2 may be a candidate anode material for LIBs and SIBs.[13] Recently, Zhang et al. reported that HCl solution can selectively etch Al layers from Cr_2Al2B_2 to obtain 2D Cr_2B_2.[14]

Received: May 10, 2021
Accepted: June 25, 2021

https://doi.org/10.1021/acs.jpclett.1c01499
J. Phys. Chem. Lett. 2021, 12, 6370–6382

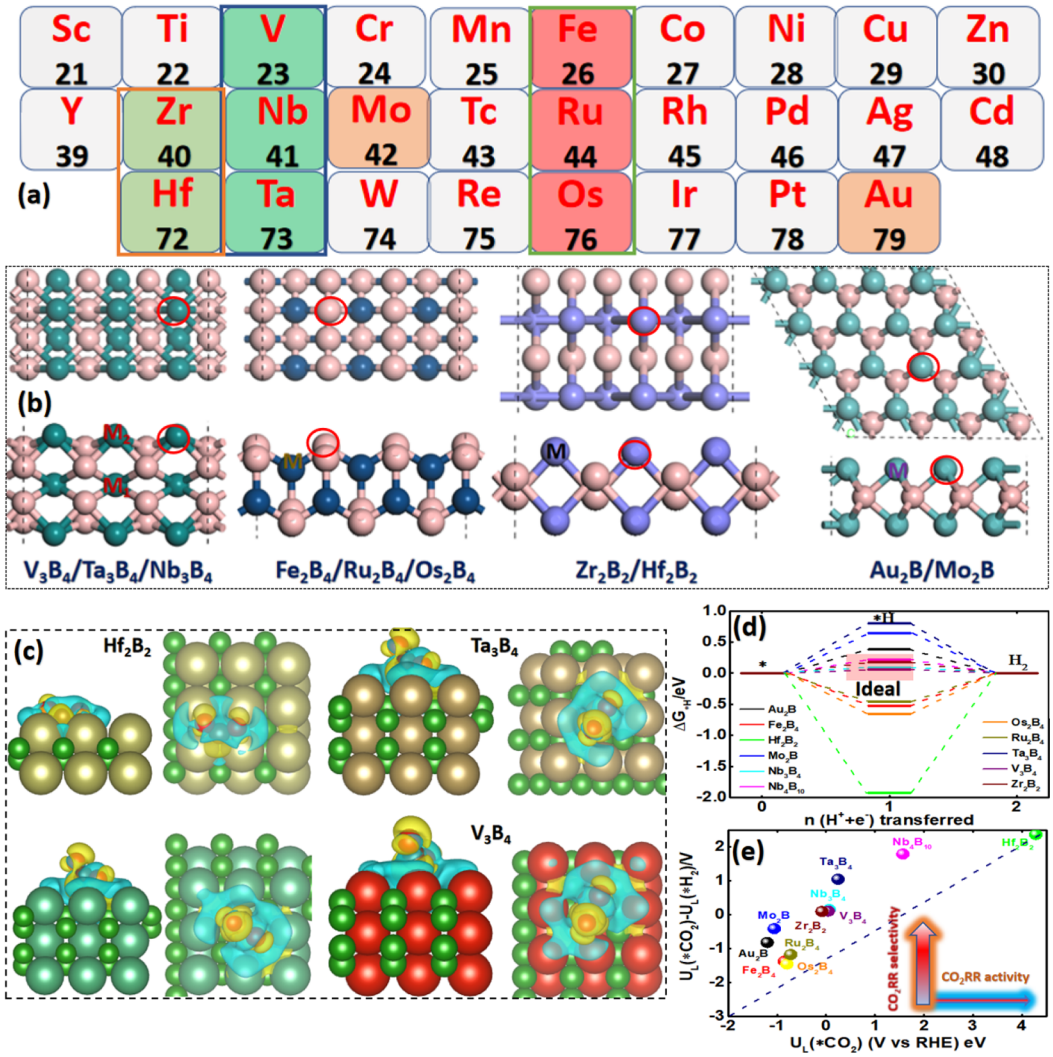

Figure 1. (a) Eleven transition metals in the periodic table of the elements are taken into account in this work. (b) Top views (upper) and side views (lower) of different types of MBene structures, the red circles represent the active sites for CO_2 adsorption and intermediate production. (c) The differential charge density distribution of the most stable CO_2 molecules adsorption configurations Hf_2B_2, Ta_3B_4, Nb_3B_4, and V_3B_4, surfaces, respectively. Side views on configuration (left): top views (right). The yellow and cyan colors represent electron accumulation and depletion regions, respectively, with an isosurface value of 0.001 e/Å^3. (d) Gibbs free energy diagrams for HER at zero electrode potential. (e) Difference of $U_L(CO_2) - U_L(H_2)$ plotted as a descriptor of $U_L(CO_2)$ at 0 V vs RHE on various models surfaces, respectively.

The electrochemical performance of Cr_2B_2 and Mo_2B_2 has been further explored to contribute to the design of a novel catalyst for CO_2 reduction.[15]

In this work, we explore this new family of MBenes, which have been proven to have a stable structure by a theoretical approach[16] and can be exfoliated from layered MAB phases.[8] Here, we investigate 11 new kinds of MBenes from ref 7 for a catalytic platform of CO_2 reduction to C1 product within ab initio calculations. Furthermore, we find that 2D Au_2B and V_3B_4 MBenes are more suitable for applications as a platform in electrocatalysts for CO_2 electroreduction to a CH_4 product with a relatively low working potential among these MBenes. Moreover, Au_2B, Os_2B_4, and Ru_2B_4 are more suitable for the production of CH_3OH with small overpotentials of 0.31, 0.48, and 0.35 V than are other MBenes, respectively. Moreover, these novel 2D compound materials have unique advantages for electrocatalysis, including large surface area and excellent electrical conductivity. The reaction mechanism and catalytic activity in CO_2RR on different types of MBene surfaces and the selectivity related to the competitive reaction of HER were also fully considered. The binding energies of *OH and *CO are two valuable descriptors for the catalytic performance of MBenes. Volcano plots related to limiting potential and overpotential were also used to explore the catalytic properties. The electronic structure and density of states of MBenes were calculated, and the 2D MBene layer structure with a metallic character showed promising electronic conductivity. These theoretical results provide an effective method to design and screen high-performance catalysts based on MBenes for CO_2 electroreduction applications.

COMPUTATIONAL METHODS

All density functional theory (DFT) calculations were executed within application code using the Vienna ab initio simulation package (VASP).[16] A first-principles approach was used to screen 11 2D MBenes as promising candidate electrocatalysts for CO_2RR. The reaction mechanism and catalytic activity of CO_2 electroreduction to C1 hydrocarbon products were explored on several periodic supercells of the 2D MBene surface. The supercells were generated by a 2 × 2 MBene unit

https://doi.org/10.1021/acs.jpclett.1c01499
J. Phys. Chem. Lett. 2021, 12, 6370−6382

cell with a vacuum space set to 20 Å to avoid interactions between periodic boundaries. The GGA-PBE exchange-correlation functional method was used to describe the electron exchange-correlation with a cutoff energy set to 500 eV.[17,18] The Monkhorst−Pack mesh of 5 × 5 × 1 k-points was applied within the sampled Brillouin zone to optimize the geometric structure, and 10 × 10 × 1 k-points were chosen for electronic property calculations. The convergence tolerance was set to 10^{-6}/eV in energy and −0.02 eV/Å in force for both geometric optimization and electronic calculations. To consider the van der Waals interactions between CO_2 reduction intermediates and catalysts, the DFT+D3 correction within Grimme's scheme was executed in all calculations.[19] It is important to point out that the GGA-PBE method might not agree with real experimental results and even compared to other computational methods, such as the PBE+D3 method which has been verified, tends to overestimate the binding energy in contrast to PBE+D3; thus, it might be more suitable to study surface phenomena in electrochemistry reactions. However, due to the computational limitations, our GGA-PBE method is without inevitable errors, but the overall trend between the two methods is similar.[20] The formation energy of the CO_2RR intermediates was obtained from the computational hydrogen electrode model (CHE). The standard hydrogen electrode (SHE) was used as a reference electrode for all proton−electron pair transfer processes and was defined as zero ($2H + 2e^- \rightarrow H_2$). The chemical potential of each proton−electron step contribution was determined under zero potential, pH = 0, T = 298.15 K, and 1 atm. The applied potential with $U_{RHE} = U_{SHE} + k_B T\text{pH} = U_{SHE} + 0.059$ pH was measured at room temperature (k_B is the Boltzmann constant).[21] The binding energies of CO_2RR intermediates were calculated according to the chemical reaction ($* + CO_2 + nH^+ + ne^- \rightarrow *CH_nO_2$). Thus, $\Delta E = E_{total} - E_{catalyst} - E_{adsorbate} - n/2E_{H2}$, where E_{total}, $E_{catalyst}$, and $E_{adsorbate}$ are the total energies of the adsorbate configurations, catalyst, and isolated CO_2RR species (such as CO2, H_2, and CH_4),[22] respectively. Thus, the Gibbs free energy change (ΔG) could be obtained from the binding energies according to the formula $\Delta G = \Delta E + \Delta\text{ZPE} + \Delta H - T\Delta S + \Delta G_U + \Delta G\text{pH}$, where ΔE is the binding energy obtained directly from DFT calculations, ΔZPE is the zero-point energy, ΔH is the enthalpy change, ΔS is the entropy change under applied temperature, ΔG_U is the contribution of the applied electrode potential (U), which is equal to neU with the number of electrons transferred. $\Delta G_{pH} = k_B T \ln[H^+]$ was determined by the concentration of H^+. ΔZPE and ΔS of the CO_2RR intermediate species were calculated depending on the vibrational frequencies within the fixed slabs.[23,24] The vibrational frequency calculations of adsorbate configurations were performed using the VASPKIT code.[25] According to the depiction of the volcano curve of limiting potential (U_L) and overpotential proposed by Nørskov et al., U_L was obtained from the equilibrium potential as $U_L = -\max[\Delta G_1, \Delta G_2, \Delta G_3, \Delta G_4, \Delta G_5, \Delta G_6, \Delta G_7, \Delta G_8]/e$, $\eta_{CORR} = U_{eq} - U_L$, where ΔG_n (n = 2, 4, 6, or 8) is the reaction energy of each elementary reaction step during the CO_2 electroreduction process.[26,27]

A high-throughput scanning approach has been executed to explore the candidate stable and high-efficiency catalysts from the 2D MBenes (M_xB_y) phase, where M denotes transition metals, and the x:y ratios can be defined as 2:2, 2:4, 1:2, 3:4, and 10:4. In this study, we considered 11 2D MBenes that have been successfully theoretically studied or synthesized experimentally (Supporting Information, Figure S1a. Depending on the ratio of metal and B atoms, these MBenes can be divided into four types: Zr_2B_2/Hf_2B_2, Au_2B/Mo_2B, $Fe_2B_4/Ru_2B4/Os_2B_4$, and $V_3B_4/Ta_3B_4/Nb_3B_4$. Their geometric structures after full structure relaxations are displayed in Figure 1b. The stability structure of the M_3B_4 MBene monolayer consists of three atomic metal layers with four atomic boron layers, resembling a sandwich. Each metal atom is coordinated to eight boron atoms, and each boron atom is bonded to four metal atoms. The unit cell of the M_2B_4 structural framework contains three M-B bonds of each metal atom, and two atomic metal layers are coordinated with two atomic boron layers (see Figure 1b). The M_2B configurations are similar to those of 2D transition metal carbides (MXenes), as shown in Figure 1d, which can be generated by two metal atomic layers interleaved with one boron atomic layer, forming a rhomboid structure. Similarly, as a CO_2 electrochemical reduction catalyst, the type of M_2B_2 single-layer MBene with exposed metal atomic layers on the surface (Figure 1c) is expected to have high surface state reactivity. In this work, several derivative final products (such as CO, HCOOH, HCHO, CH_3OH, and CH_4)[28] are considered, depending on the overpotential on these MBene single layers. We considered only the most energy-preferred adsorption sites, which are marked in red circles in Figure 1b (red circle), including the top sites of both metal and boron layers. The most stable adsorption energies are listed in Table S3. Because of the electron deficiency of boron, the M−B bonds are slightly weaker than the M−C and M−N bonds.[29,30] The proposed 2D MBenes are similar to MXenes and exhibit superior electrochemical properties for electroreduction of CO_2. To gain further insight into the adsorption of carbon dioxide, we calculated the charge density difference under an isosurface value of 0.001 e/Å^3. The electron accumulation and depletion regions are represented in different colors in Figure 1c. The charge transfer to CO_2 from the MBene surface and the electron transfer from transition metal to boron further contribute to the stability of the adsorption configurations.[31,32] For the M_3B_4-type MBene substrate, the favorable adsorption site is on top of the metal atom with adsorption energies of −0.06 eV, −0.25 eV, and −0.05 eV, corresponding to Nb_3B_4, Ta_3B_4, and V_3B_4, respectively. Furthermore, for Hf_2B_2 and Zr_2B_2, the sites of boron also provide an energetically preferred adsorption energy for CO_2 reduction. The adsorption energies of Hf_2B_2 are lower (−4.29 eV) than those of Zr_2B_2(0.08 eV), suggesting a strong chemical interaction on Hf_2B_2, while the CO_2 can easily bind onto the Ti_2B_2 surface of −3.22 eV. The metal atom is also the preferred adsorption site for CO_2 on the Os_2B_4 and Ru_2B_4 substrate, and its corresponding adsorption energies are 0.80 and 0.72 eV, respectively. In addition, the secondary reaction HER has much higher overpotential than that of CO_2RR in the vast majority of catalysts, indicating that the CO_2 electroreduction can overcome HER during competitive reactions (Figure 1d,e).[43]

To explore the interaction mechanism of CO_2 molecules on MBene surfaces, we calculated the charge density difference and charge density between the absorbed CO_2 molecule and the catalysts, which are shown in Figure 1c and Figure S13, respectively. The charge density of the CO_2 molecule closest to the MBene surface indicates a charge gain (yellow regions) of the CO_2 molecule and a charge reduction on the catalyst. The transfers of charge are determined by the size of the charge cloud and can be quantified depending on the binding strength of CO_2 with the MBene surfaces. The top of the metal

https://doi.org/10.1021/acs.jpclett.1c01499
J. Phys. Chem. Lett. 2021, 12, 6370−6382

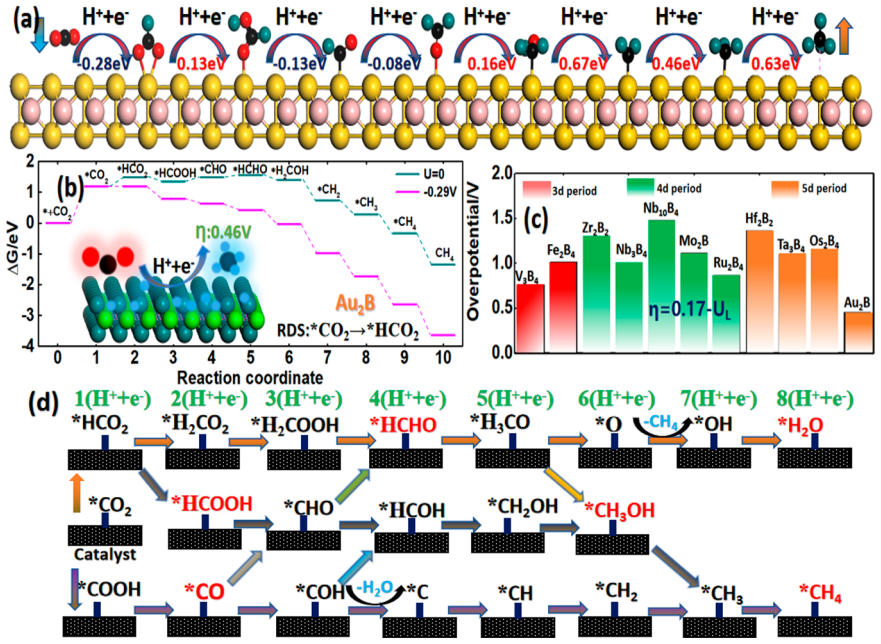

Figure 2. (a) Side view of the minimum reaction energy path for the CO_2 reduction to $*CH_4$ catalyzed by Au_2B MBene with PBE (DFT-D3) calculations, (b) Gibbs free energy diagrams of the CO_2 reduction to CH_4 under different applied potentials along with the most favorable pathway via Au_2B. (c) Summary of overpotentials on MBenes for CO_2RR via the most favorable pathway at 0 V vs RHE, (d) A entire reaction route for CO_2RR to C1 products. The possible final products are shown in red and arrows in different colors denote a single proton−electron transferred.

adsorption site configuration has the most obvious charge exchange due to the strong interaction with the MBene surfaces. The energetically high negativity leads to strong activation on Hf_2B_2, and the CO_2 molecule forms a highly bent O−C−O angle of 118.71° on the hollow site. The carbon atom is located above the boron atom on the subsurface, and the two oxygen atoms are bonded to the surface Hf atoms, as shown in Figure 1e. The stable adsorption configurations of all CO_2RR intermediate configurations and the Gibbs free-energy diagram of the most favorable pathway of CO_2 electroreduction to CH_4 on the Au_2B subsurface are displayed in Figure 2a,b. First, the CO_2 adsorbed on Au_2B demonstrates a nonspontaneous physical absorption process of Gibbs free energy at 298.15 K of 1.20 eV, which is larger than that on Hf_2B_2 (−4.29 eV) and Ta_3B_4 (−0.25 eV). This implies that on Hf_2B_2 and Ta_3B_4, MBenes will exhibit CO_2 chemisorption. In Figure 2a, the first protonation step ($*CO_2 \rightarrow HCO_2$) reveals a nonspontaneous reaction energy of −0.28 eV on the Au_2B surface, which is smaller than that on Hf_2B_2 (−1.02 eV). The first hydrogenation step is the rate-determining step, corresponding to the largest step ΔG_{max} in the free energy diagram of −0.29 eV. The applied potential is shown in Figure 2b. The reaction energies of *HCOOH, $*CH_2OH$, $*CH_2$, $*CH_3$, and CH_4 exhibit a spontaneous process with 0.13, 0.16, 0.67, 0.46, and 0.63 eV, respectively. Once the CO_2 molecule is adsorbed, the formation energies of some final products such as *HCOOH, *CO, $*CH_3OH$, *HCHO, and $*CH_4$ along the subsequent hydrogenation reaction step are 1.26, 1.05, 0.88, 1.57, and 0.35 eV, respectively. The final product is CH_4 after the eighth hydrogenation step with desorption energy of 0.59 eV. Moreover, for Hf_2B_2, a CO_2 molecule is adsorbed with adsorption energy of −3.26 eV to form *COOH during the first hydrogenation step (Figure S2c). Furthermore, the energy profile change indicates that the most favorable path of $CO_2(g) \rightarrow *COOH \rightarrow *CO \rightarrow *CHO \rightarrow *HCHO \rightarrow *H_3CO \rightarrow *O \rightarrow *OH \rightarrow *H_2O(l)$ was energetically favorable for the CO_2RR. The formation of intermediate products, such as *CO, *HCHO, $*CH_4$, and $*H_2O$ along the second, fourth, and sixth steps, are all exothermic processes. The second hydrogenation step of the production of *CO was the rate-determining step with a Gibbs free energy change of 1.20 eV. Moreover, Ru_2B_4 can also be a promising candidate for CO_2RR The rate-determining step located at the reaction of $*CH_3 \rightarrow *CH_4$ with a Gibbs free energy change of 0.70 eV (Figure S2h) reveals a much lower overpotential (0.87 V) than that on Hf_2B_2 (1.37 V) and a much higher one on Au_2B (0.46 V) (Figure 2c). In summary, Au_2B (0.46 V), V_3B_4(0.76 V), Ru_2B_2(0.87 V), and Fe_2B_4(1.02 V) reveal a capability to produce methane from CO_2 due to their relatively low overpotential. A histogram plotted with overpotential[33] as a function of CH_4 binding energy is shown in Figure 2c. This demonstrates the feasibility of CO_2RR on our proposed Au_2B and Hf_2B_2 MBene catalysts. For the other MBenes, the first hydrogenation step of $*CO_2$ on the catalysts is always the rate-determining step of CO_2 electroreduction. Under general conditions, CO_2 can be activated by electron transfer from the MBene slab surface, which is always accompanied by the decrease in the O−C−O bond angle and forms chemical bonds between the metal and the oxygen. Figure 2d illustrates an entire reaction route for CO_2RR to C1 products (CO, HCOOH, HCHO, CH_3OH, and CH_4). The possible final products are shown in red, and the arrows in different colors denote a single proton−electron transfer.

The theoretical predictions of the proposed branching and competing reaction in CO_2RR on the 2D MBene surface are shown in Figure 3e−h, which has great significance in confirming the reaction pathway depending on the intermediates species during the hydrogenation process. The intermediate species and reaction mechanism path of CO_2RR on MBene are very complicated processes. As mentioned above, the reaction pathway of CO_2RR is determined by the binding strength of the MBene surface with various

https://doi.org/10.1021/acs.jpclett.1c01499
J. Phys. Chem. Lett. 2021, 12, 6370−6382

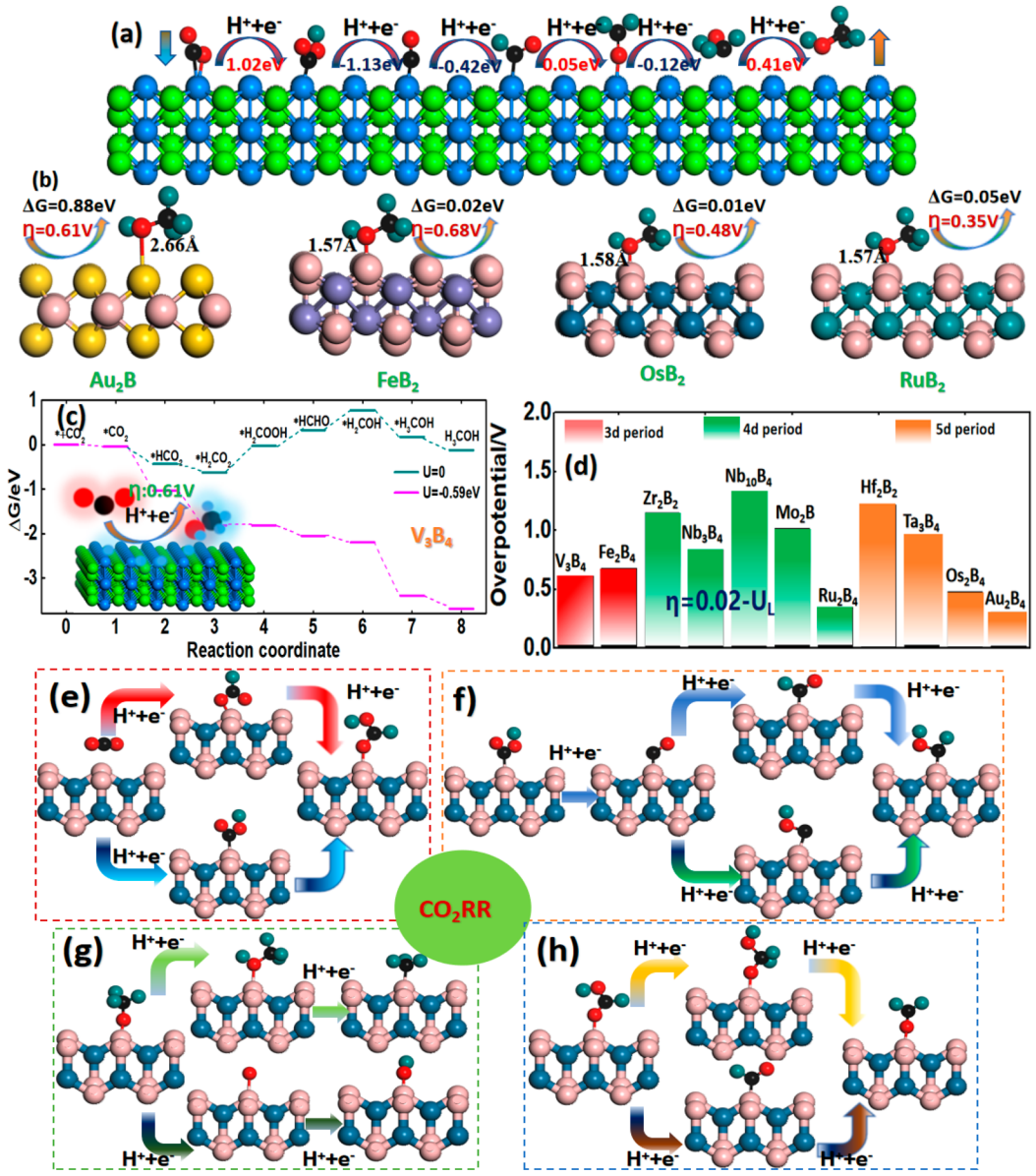

Figure 3. (a) Side view of geometric configurations along the lowest energy path followed for the CO_2 conversion into CH_3OH catalyzed by V_3B_4, the red numbers represent an energy exothermic process, while the dark blue numbers represent the endothermic process for a reaction step, respectively. (b) Some promising candidates for producing CH_3OH with a relative small overpotential; black numbers are the formation energy of CH_3OH; dark red numbers are overpotentials and bond length of M-O in Å, respectively. (c) Gibbs free energy diagrams of the CO_2 reduction to CH_3OH under applied potentials along with the most favorable pathway via V_3B_4. (d) Summary of overpotentials on MBenes for CO_2RR reduction to CH_3OH via the most favorable pathway. (e–h) Schematic illustration of possible electrochemical branch reaction steps during the hydrogenation of CO_2 to CH_4 on M_2B_4: (e) *CO_2 to *HCOOH; (f) *CO to *HCOH; (g) *H_3CO to *CH_3OH or *O; and (h) *COOH to HCHO on Os_2B_4, respectively.

intermediates. Thus, we are designing a high-performance electrocatalyst for CO_2 reduction depending on the formation energy of intermediates. For example, Au_2B, Nb_4B_{10}, and V_3B_4 MBenes are more favorable for producing the energy of *HCO_2 and are suitable for producing HCOOH or H_2CO_2. The other MBenes are preferred to form *COOH and further generate CO. In addition, C–H coupling or O–H coupling can determine the intermediates species of CO_2 reduction to methane.[34,35] The third proton-coupled electron transfer step is the reduction to *CHO or *COH from *CO, which should be considered (Figure 3e) (*CO + H^+ + e^- → *CHO/*COH). If the catalyst could stabilize O, the formation of *CHO or *COH could be adjusted. The *COH pathway is favored over *CHO on Mo_2B, indicating that the binding strengthens *COH over *CHO. The next successive hydrogenations on the C or O atoms of *COH form HCOH or *C, and *CHO can transform to *HCHO and *H_2COH following a sequential hydrogenation step. Since the *CH_3O species is preferred over H_2COH during the fifth H^+/e^- pair transferred, the route toward the formation of the CH_4 on Hf_2B_2 as a product is favored over other MBenes during the sixth hydrogenation step. It is established that the third hydrogenation step on the HCOOH* species will produce *CHO or H_2COOH and further protonate to *HCHO. Furthermore, once the *HCHO reduction proceeds along the *CH_3O pathway, it may be hydrogenated to *CH_3OH or *O. As

https://doi.org/10.1021/acs.jpclett.1c01499
J. Phys. Chem. Lett. 2021, 12, 6370–6382

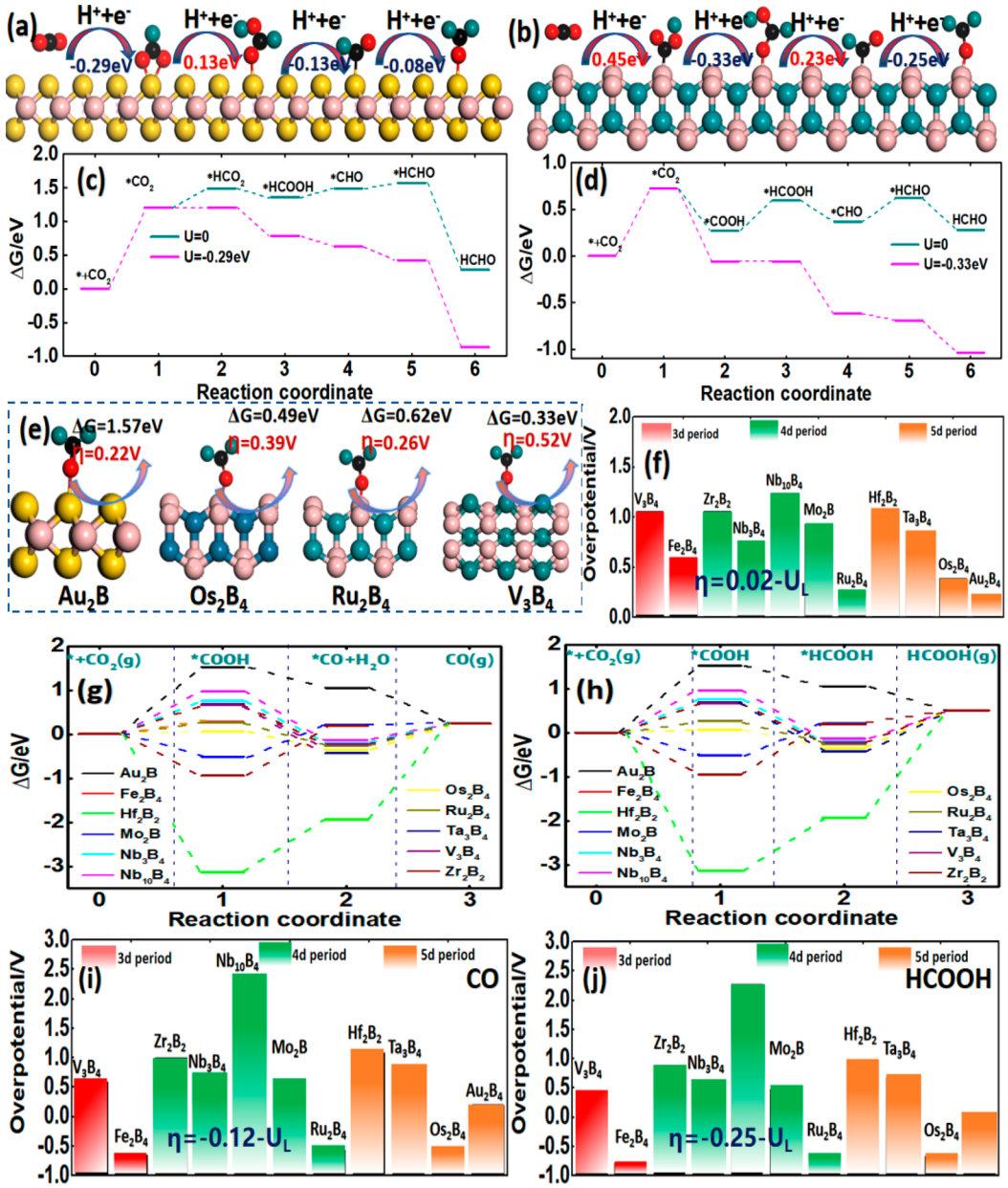

Figure 4. (a,b) Side view of geometric configurations along the lowest energy path followed for the CO_2 conversion into HCHO catalyzed by Au_2B and Ru_2B_4, respectively. Here, the red numbers represent an energy exothermic process, while the dark blue numbers represent the endothermic process for a specific reaction step. (c,d) Gibbs free energy diagrams of the CO_2 reduction to HCHO under applied potentials along with the most favorable pathway via Au_2B and Ru_2B MBenes, respectively. (e) Some promising candidates for producing HCHO with a relative small overpotential, black numbers are the formation energy of HCHO, dark red numbers are overpotentials, respectively. (f) Summary of overpotentials on MBenes for CO_2RR reduction to HCHO via the most favorable pathway. (g,h) Gibbs free energy diagrams of the CO_2 reduction to CO under zero potentials, and Gibbs free energy diagrams of the CO_2 reduction to HCOOH under zero potentials via MBenes, respectively. (i,j) Summary of overpotentials on MBenes for CO_2RR reduction to *CO and *HCOOH via the reaction pathway, respectively.

shown in Figure S2c, Hf_2B_2 has obvious spontaneous reactions during the seventh hydrogenation to form the *OH species. Finally, the rate-determining step becomes the formation of $*H_2O$, which has the largest energy barrier of 0.97 eV among all elementary reactions and is a relatively strongly adsorbed H_2O molecule of 2.18 eV once released from the surface. These hydrogenation steps should be further investigated for producing various hydrocarbon products to determine the most favorable pathway and confirm the final product. The favorable reaction pathway, intermediate species, and final products were determined by the Gibbs free energy profile and their limiting potential of each elementary reaction step. The theoretical overpotentials are very large for the Nb_4B_{10} and Zr_2B_2 catalysts, and the calculated overpotentials are 1.48 and 1.30 V, respectively. In addition, the overpotentials of Au_2B, Ru_2B_4, and V_3B_4 are 0.46, 0.87, and 0.76 V, respectively, indicating that the catalytic performance of CO_2RR on these MBene catalysts are more favorable than those of other MBenes.[9]

Figure 3 shows the CO_2 reduction to CH_3OH along with six hydrogenation steps on the catalyst. The formation of *HCHO is the crucial intermediate species to determine the entire reaction pathways. It can be formed from $*H_2COOH$ or *CHO in the fourth hydrogenation step. For the $*CH_3OH$

https://doi.org/10.1021/acs.jpclett.1c01499
J. Phys. Chem. Lett. 2021, 12, 6370−6382

species on Zr_2B_2 displayed in Figure 3a, the following pathway is preferred: $*CO_2 \rightarrow *COOH \rightarrow *CO \rightarrow *CHO \rightarrow *HCHO \rightarrow *H_2COH \rightarrow *H_3COH$. The CH_3OH molecule prefers physisorptions with a release energy of 0.29 eV. The *COOH formation is an exothermic process of −1.13 eV, while the *CO formation is endothermic by −0.42 eV, suggesting that the formation of *COOH is favorable to that of HCO_2, and the formation of *CO is also favorable to that of HCOOH in the second hydrogenation step, indicating that the *CO species can be hydrogenated to form the CHO* species, and the *HCHO species can be hydrogenated to form the $*CH_2OH$ species with an electron proton pair transferred. $*CHO + H^+ + e^- \rightarrow *HCHO$ and $*CH_2OH + H^+ + e^- \rightarrow *CH_3OH$ are exothermic processes that are uphill in the free energy profile by 0.05 and 0.41 eV, respectively. In Figure 3b, Au_2B, Fe_2B_4, Os_2B_4, and Ru_2B_4 are energetically favorable formations of $*CH_3OH$, corresponding to overpotentials of 0.61, 0.68, 0.48, and 0.35 V, respectively. In Figure S3, the rate-limiting step is the reduction of the first hydrogenation step $*CO_2 \rightarrow *COOH/*HCO_2$, while the reduction of $*H_2COH$ to *HCHO on Fe_2B_4 and V_3B_4 is against the other MBene systems. For the Hf_2B_2, the kinetic activity of the reaction is determined by *COOH → *CO. For V_3B_4, the limiting potential step located at $*H_2COH \rightarrow *HCHO$ makes all reaction steps downhill under an applied potential of −0.59 V on this step (Figure 3c). This indicates that smaller overpotentials are required to reduce *CHO than that of *COH reduction. For Ru_2B_4, the first transfer of H^+/e^- coupling to the $*CO_2$ intermediate to form *COOH is defined as the rate-determining step, because this step is the most exergonic with a value of 0.74 eV downhill in the free energy profile diagram. After a potential of −0.46 V is applied, the energy profile change of all elementary reaction steps are downhill, and CO_2RR occurs more easily than under zero electrode potential. Figure 3d shows that the overpotential was described by the binding energy of $\Delta G(*CH_3OH)$, and the rate-determining step was determined by the highest overpotentials of Au_2B (0.31 V), Os_2B_4 (0.48 V), Ru_2B_4 (0.45 V), and V_3B_4 (0.61 V) located on the bottom left corner of the volcano. This means that these MBene catalysts require relatively high reaction energy to overcome the limiting potential of the rate-determining step. Previously studied 2D materials, such as Cr_3C_2 (−1.05 V) and Mo_3C_2 (−1.31 V) MXenes,[37,38] based on Mn_2B_4 and Fe_2B_4 also exhibit a limiting potential of 0.59 and 0.76 eV, respectively;[39,40] this is comparable to the limiting potential of 0.74 V on Cu.[41]

In the next section, we will examine the formation of the HCHO reaction pathway along with the $4(H^+ + e^-)$ coupling on the MBene surface to identify the minimum energy path followed for the CO_2 conversion mechanism into *HCHO catalyzed by Au_2B and Ru_2B_4, as shown in Figure 4 panels a and b, respectively. Furthermore, we examine the three branched reaction pathways $*HCOOH \rightarrow *CHO$, $*CO_2 \rightarrow *COOH$, and $*COOH \rightarrow *HCOOH$,[36] which require lower limiting potentials than $*CO_2 \rightarrow *HCO_2$ and $*HCO_2 \rightarrow *H_2CO_2$ steps because of the stronger formation of O−H bound intermediates. In Au_2B and Ru_2B_4, the maximum limiting potentials (U_L) are determined by the reaction steps $*CO_2 \rightarrow *HCO_2$ and $*COOH \rightarrow *HCOOH$ corresponding to −0.29 eV and −0.33 eV, respectively. Thus, under applied potentials of −0.29 V and −0.33 V, the Gibbs energy profile diagram of all elementary reaction steps are downhill. This means that the CO_2 electroreduction can happen spontaneously under the applied electrode potential. According to the Gibbs free energy profile change of each elementary step at zero potential, our results revealed that the $*CO_2 \rightarrow *HCO_2 \rightarrow *HCOOH \rightarrow *H_2COOH \rightarrow *HCHO$ path is the most favorable for Au_2B with a small overpotential of 0.22 V (Figure 4e), and the pathway $CO_2 \rightarrow *COOH \rightarrow *HCOOH \rightarrow *CHO \rightarrow *HCHO$ is the most favorable for Au_2B with the smallest overpotential of 0.26 V among all MBenes. The catalytic performance of these MBene catalysts depends on the volcano plot of the overpotential as a descriptor of the formation energy of *HCHO (Figure 4f). Taking Nb_4B_{10} and Zr_2B_2 as examples, the limiting potentials of −0.88 eV and −1.13 eV are so negative that the formation of *HCHO is difficult, leading to high overpotentials corresponding to 0.81 and 1.07 V, respectively. This indicates that they are not suitable for CO_2 electroreduction under normal conditions. Similarly, *HCHO and $*CH_3OH$ share the same intermediate species during the reduction reaction. The volcano plots of overpotential for all MBenes are the same except for the equilibrium potential, which shifts to −0.07 V for *HCHO from 0.02 V for $*CH_3OH$.

For the whole $2H^+/e^-$ transfer process, the final products are *CO and *HCOOH, which share the first hydrogenation step of $*CO_2 \rightarrow *COOH$ in Figure 4g,h. The preferential reaction pathways for the formation of both *CO and *HCHO are the same on all MBene surfaces via the following pathway: $*CO_2 \rightarrow *COOH \rightarrow *CO$ or *HCOOH, and the formation of the *COOH species is the rate-determining step for Au_2B, Nb_3B_4, and Ta_3B_4. For both *CO and *HCHO production, the Gibbs free energy diagram of each elementary reaction step becomes downhill under an applied potential. As shown in Figures S7 and S8, the entire reaction step is exothermic. The smaller overpotential means a lower energy expenditure. Therefore, Fe_2B_4 exhibits higher catalytic activity for CO_2 reduction to CO than on the Au_2B surface. On the MBene surface, the obvious strong binding *O makes M−O breakage more difficult and leads to HCOOH formation, while the M−C bond strong coupling leads to CO formation.[42] We considered the free energy of the hydrogenation of *COOH to *CO since it is the rate-determining step on Mo_2B, Hf_2B_2, and Zr_2B_2. The overpotentials of these MBene catalysts are 0.61, 1.08, and 1.01 V, respectively, which are all larger than those on Ru_2B_4 (−0.57 V), Os_2B_4 (−0.54 V), and Fe_2B_4 (−0.65 V) (see Figure 4i). This means that the formation of CO can spontaneously generate without external voltage on these MBene catalysts. Furthermore, the overpotential for the production of CO is much higher than that for the production of HCOOH, with η_{CO} of 0.20 V and η_{HCOOH} of 0.07 V on Au_2B. The catalytic activity is comparable to that of Pd, 0.15 V,[43] and the overpotential of V_3B_4 for producing HCOOH is 0.46 V, which is comparable to that of the $CuSn_3$ topological insulator catalysts (0.39 V).[44]

To further explore the catalytic activity and product selectivity of the CO_2RR on MBene catalysts, we computed the binding energies of all possible intermediates for producing CO_2 to CH_4 and found that a scaling linear correlation forms between the binding energies of two adjacent intermediates (Figures S10 and S11). Recently, the CHE model was used to study the linear correlation between different intermediates. A series of calculations shows that the production of *CO to form *CHO or *COH is the rate-determining step in CO_2RR. Thus, the linear correlations of ΔG_{*CO} vs ΔG_{*COOH}, ΔG_{*CO} vs ΔG_{*CHO}, and ΔG_{*CO} vs ΔG_{*HCHO} have been verified. The

https://doi.org/10.1021/acs.jpclett.1c01499
J. Phys. Chem. Lett. 2021, 12, 6370−6382

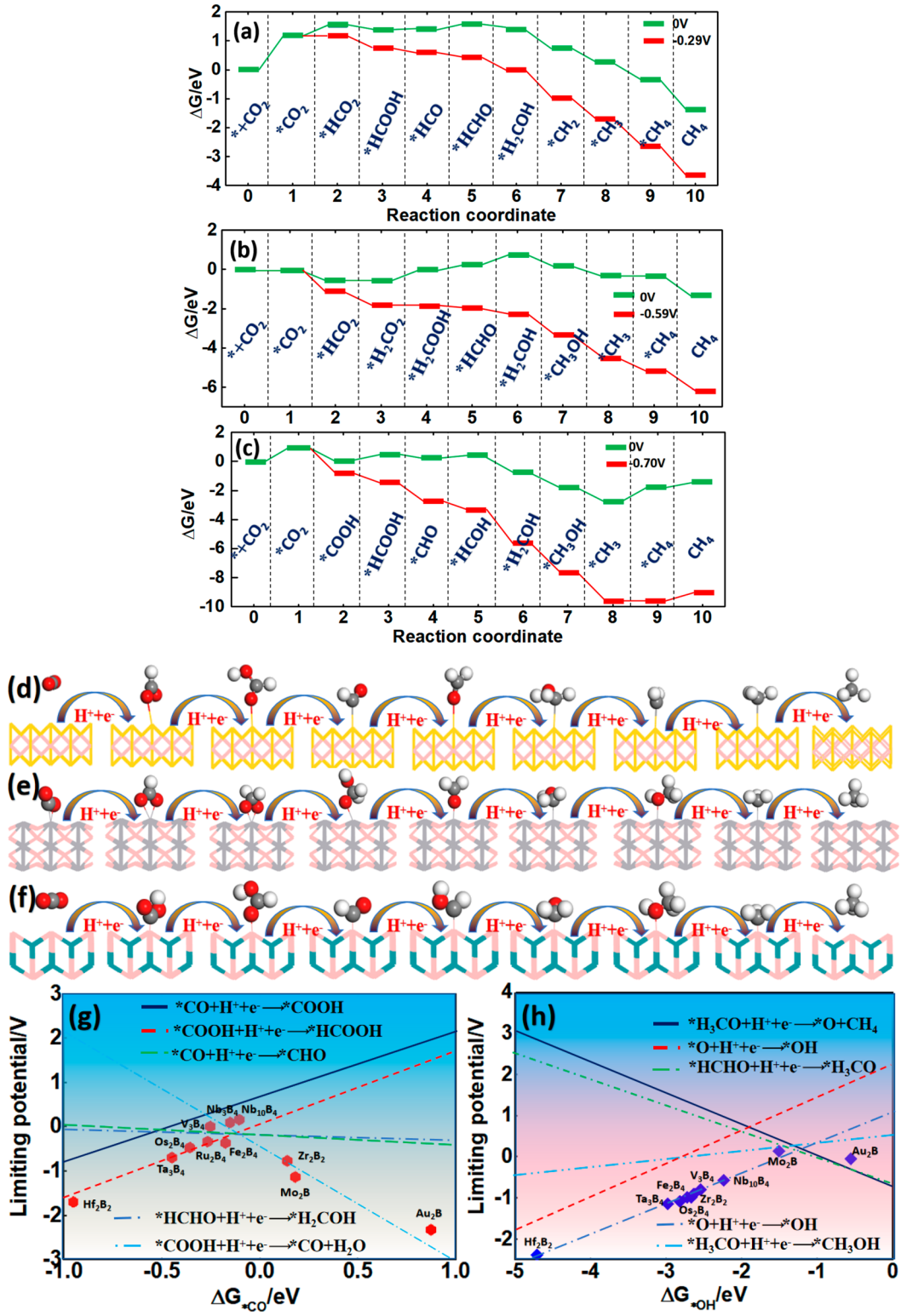

Figure 5. (a–c) Gibbs free energy diagrams for CO_2 reduction through the most favorable mechanisms paths on Au_2B, V_3B_4, and Ru_2B_4 at a zero potential (green line) and under an applied potential (red line). (d–f) The structures of each intermediate via the reaction paths. (g,h) Limiting potentials for each elementary reaction step as a function depending on the formation energy of ΔG_{*CO} and ΔG_{*OH}, respectively.

colored lines represent the linear regressions of line correlation. We find that ΔG_{*O} vs ΔG_{*OH}, ΔG_{*H3CO} vs ΔG_{*OH}, and ΔG_{*CH3OH} vs ΔG_{*OH} on these MBene surfaces are highly correlated, so their binding energies are highly correlated to catalytic activity and selectivity for CO_2RR, when the *O binds too strongly to the MBene surfaces, it leads to the formation of $*CH_4$ rather than reduction to $*CH_3OH$. We note that the scaling linear correlation between ΔG_{*H3CO} and ΔG_{*OH} is sensitive to the binding free energy of *OH. The linear fitting line of ΔG_{*H3CO} vs ΔG_{*OH} has a slope 0.99, indicating that the binding of *OH and the binding of $*H_3CO$ intermediate species exhibited an ideal correlation among these MBene

https://doi.org/10.1021/acs.jpclett.1c01499
J. Phys. Chem. Lett. 2021, 12, 6370−6382

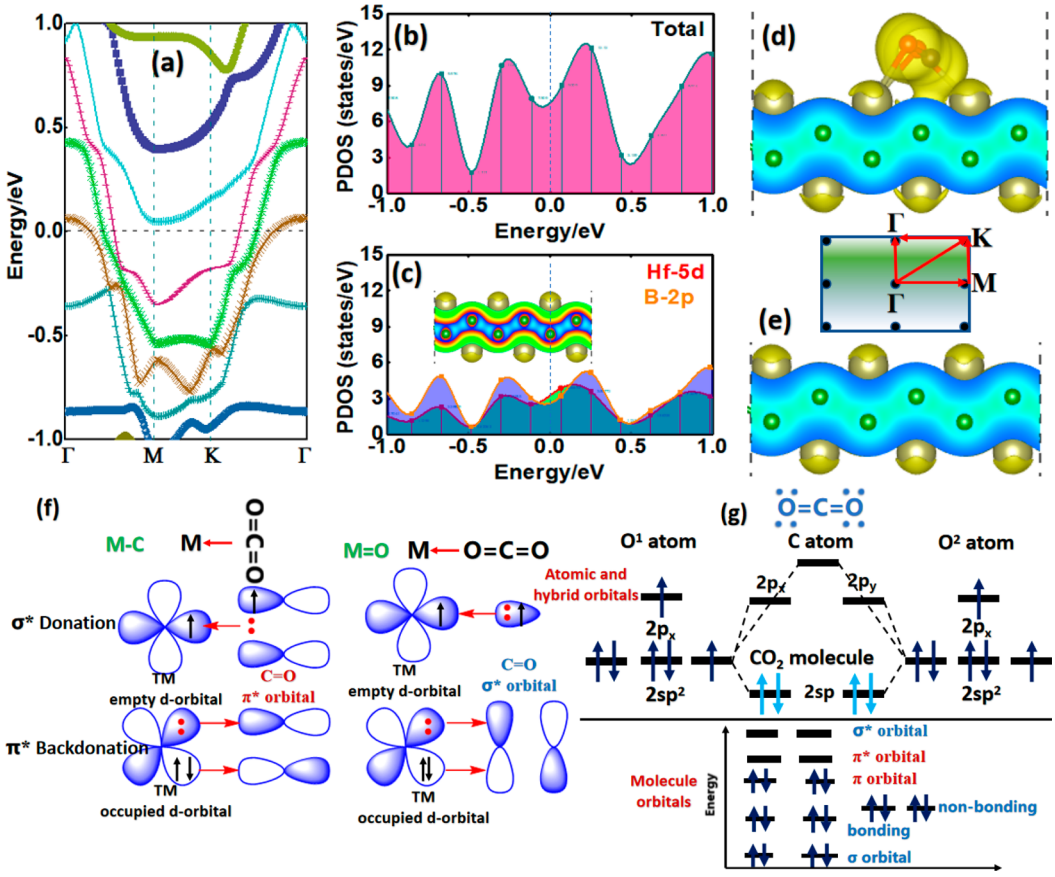

Figure 6. (a) Electronic band structure of Hf_2B_2. (b) Total density of states of Hf_2B_2. (c) Partial density of states (PDOS) of Hf 5d and B 2p contribution. (d) Side views of the charge density distribution of the most stable CO_2 molecules adsorption configurations for Hf_2B_2. (e) Side views of the charge density distribution on Hf_2B_2 clean surface with the Brillouin region K point path. The yellow and light blue colors represent positive and negative charge regions with an isosurface value of 0.001 e/Å^3. The Fermi level is set to zero, K presents the high symmetry *k*-points (1/3, 1/3, 0) were generated by VASPKIT in the Brillouin zone. Inset figure is charge density of Hf_2B_2 with an isosurface value of 0.001 e/Å^3. (f) Schematic illustration of the interaction mechanism of CO_2 adsorption on MBenes. (g) The atomic and hybrid orbitals and molecular orbital energy level diagram of CO_2 molecule.

surfaces. Regarding the linear relations for each final product, such as H_2, HCOOH, CO, CH_3OH, and CH_4, it shows the binding energy of ΔG_{*HCOOH} that scales with ΔG_{*COOH}, ΔG_{*HCHO}, and ΔG_{*H2COH}, which reveals the elementary steps that scale with HCOOH and CO reduction. Scaling linear relationships among CO_2RR intermediates can help guide us in the exploration and design of new high-efficiency CO_2 reduction catalysts. As shown in Figure S10, the linear correlations for the binding energy of key intermediates are investigated; $\Delta G_{*HCHO} = 1.08\Delta G_{*CO} + 0.64$, and $\Delta G_{*H3CO} = 0.99\Delta G_{*OH} + 1.98$ (Figure S10c,e). The coefficients of determination (R^2) are 0.93 and 0.99, respectively, which reveals that there is a strong linear relationship between these intermediate species. Moreover, there are also strong scaling relationships between ΔG_{*HCHO} and ΔG_{*HCOOH} and between ΔG_{*H3COH} and ΔG_{*HCOOH}: $\Delta G_{*HCHO} = 1.09\Delta G_{*OH} - 0.18$, with an R^2 of 0.96 (Figure S11d), and $\Delta G_{*H3COH} = 0.97\Delta G_{*OH} - 0.45$, with an R^2 of 0.98 (Figure S11e), respectively. To describe the correlation of catalytic activity on different MBene catalysts, the limiting potential relationship is displayed on volcano plots, which can visualize the evolution relationship of the catalytic activity on various MBene catalysts. Norskov et al. proposed that the binding energy of *OH is a key descriptor for catalytic activity of MBene catalysts. Thus, the volcano plots were generated by limiting the potential of each elementary reaction based on the *OH species as the descriptors. The descriptors of *OH are shown in Figures S10d−f, indicating the bonding strength of the final products' interaction with the catalyst. The negative values of CO and OH (in the left leg) indicate stronger interaction, and positive values (right side of the volcano plot) indicate weaker interaction between the intermediate product and catalyst.[45] The volcano plot of the limiting potential shows the smallest reaction energy required to drive the entire reaction reduction to form our desired product. According to this principle, the ideal catalysts are located at the peak of the volcano plot. Their binding energy corresponds to the value along the *x*-axis, which represents the perfect bond strength depending on the descriptor and gives the maximum reaction rate.

The screening strategy can be seen in Figure 5c, for example: At first (1) CO_2 should be activated ($\Delta E_{ads} < 0$ eV), (2) at a higher selectivity of CO_2RR process than that of the competing HER. (3) To guarantee low energy cost, the limiting steps should be as low as possible with -0.60 V $< U_L < -0.29$ V (the best catalyst Au_2B). Finally a guarantee that the overpotential is less than 0.80 V finds that Au_2B and V_3B_4 MBenes are ideal candidate catalysts for the CO_2RR process. The volcano plots were determined by limiting the potential of each elementary reaction step as a function of ΔG_{*OH}. The negative value of the limiting potential point region means the rate of reaction and

https://doi.org/10.1021/acs.jpclett.1c01499
J. Phys. Chem. Lett. 2021, 12, 6370−6382

overpotential of these candidate materials can be determined. There are two types of bonds: one is the C−O bond, the corresponding intermediate species of which are *CO, *CHO, and *COOH with MBene materials, and the other is the O−C bond, the corresponding intermediate species of which are *OH, *CH_3O, *CH_3OH, *HCHO, *HCOOH, and *H_2COOH. When we focus only on the overpotential for CO_2 reduction, it seems that Au_2B and V_3B_4 electrocatalysts are suitable for CO_2 reduction to CH_4, while Au_2B, Fe_2B_4, Ru_2B_4, and V_3B_4 are all good for producing CO_2 to CH_3OH. However, when we consider the competitive HER reaction, the different limiting potential (U_L) change between $U_L(CO_2RR)$ and $U_L(HER)$ on these MBene catalysts can be used to explore their catalytic performance during CO_2 reduction (Figure 1e). The more positive value of $U_L(CO_2RR)-U_L(HER)$[45] means greater selectivity and activity of CO_2RR than of the HER process, which allows the CO_2 to more easily form *HCO_2 or *COOH and means that the formation of the final product is more favorable on the MBenes electrode. An example is shown in Figure 5h. At first, the protonation of *CO_2 to *COOH has a low saddle point until a crossover occurs at 0.12 V with the binding energy of *CO. The next protonation is *COOH reduction to *CO with higher limiting potentials than for *COOH + $H^+ + e^- \rightarrow$ *HCOOH, which means that is much easier to reach the respective reactants. For *CO + $H^+ + e^- \rightarrow$ *CHO, an intersection occurs at ΔG_{*HCOOH} of 0.89 eV for CO_2 reduction to HCOOH. In Figure 5g, the evolution of rate-determining steps is determined by ΔG_{*OH}. When ΔG_{*OH} reaches −3.47 eV, the rate-determining steps change into *CH_3O + $H^+ + e^- \rightarrow$ *O + CH_4 from *HCHO + $H^+ + e^- \rightarrow$ *CH_3O as an intersection point appears on the peaks, and the optimum catalytic activity for CO_2RR appears. Au_2B and Mo_2B are clearly the candidates with the limiting potential of −0.11 and 0.60 eV. For a strong binding of *CH_4 ($\Delta G_{*CH4} < -0.41$ eV), the rate-determining step is *HCHO + $H^+ + e^- \rightarrow$ *CH_2OH, while it changes to *H_2COH + $H^+ + e^- \rightarrow$ *CH_3OH with relatively weak *CH_4 bonds. As the ΔG_{*OH} and ΔG_{*CO} increase, the limiting potential decreases at the beginning and then increases upon reaching the intersections of lines and forces the overpotential to the lowest value. Compared with MXene single-atom catalysts, the MBene catalysts show better catalytic activity due to their relatively low overpotentials.[46,47]

We investigated the electronic properties of these 2D single-layer MBene catalysts. The band structures are shown in Figure 6 and Figure S14 (Supporting Information). Figure 6a shows an obvious occupied energy band from the conduction band across the Fermi level to the valence band in Hf_2B_2, indicating the metallic character of the Hf_2B_2 monolayer. The projected density of states (PDOS) is also demonstrated, which comprises mainly states contributed by the d electrons of transition metals. The occupied states around the Fermi level are clearly driven by the surface Hf 5d to the electronic properties of the Hf_2B_2 layer, while the unoccupied states in the valence band below the Fermi level are mainly attributed to the orbital hybridization of Hf 5d and B 2p states.[47] This means the formation of strong Hf−B chemical bonds, which make the Hf_2B_2 layer more stable. In addition, the charge density distribution map (Figure S13) shows that the charge cloud is delocalized above the surface and the CO_2 activated molecule on the Hf_2B_2, Nb_3B_4, Ta_3B_4 and V_3B_4 monolayer. This may be caused by the p−d orbital coupling between metal and boron atoms. The free state charge is usually located in an unoccupied state and must shift to the Fermi level to achieve charge transfer to adsorbates. In particular, the charge transfer is rather easy between the surface Hf atom and the CO_2 because of their strong Hf−O bond on the surface. These results may help explain the high catalytic activity of the Hf_2B_2 for CO_2 electroreduction to hydrocarbon products. Figure 6f presents the occupied and unoccupied orbital states between metal and CO_2 molecule adsorption, the unoccupied orbitals can accept the lone pair electrons from the s orbital of C and O atoms, while the occupied orbitals act as back-donate electrons to the antibonding orbital of CO_2.[48] Figure 6g shows a $2sp^2$ hybrid orbital on O1 combined with a 2sp orbital on C to make a sigma bonding and a sigma antibonding molecular orbital. The other 2sp orbital on C combines with a $2sp^2$ orbital on O^2 to make another set of sigma bonding and sigma antibonding molecular orbitals.[49] The $2p_y$ of O^2 combines with the $2p_y$ of C to make another set of π bonding and π antibonding molecular orbitals. The remaining $2sp^2$ from the oxygen atoms become nonbonding molecular orbitals. The O^1 $2p_x$ combines with the C $2p_x$ to make a π bonding and π antibonding molecular orbital.

Figure S14 displays the band structures and PDOS of various 2D MBene materials, such as the electronic structures of Ta_3V_4 compared with V_3B_4 (Figure S14g,h), which have a similar structure. The two materials have a metallic character with bands across the Fermi level at the K and M points in the Brillouin zone. However, the band structures are quite different between Ta_3V_4 and V_3B_4. The Os_2B_4 and Ru_2B_4 exhibit metallic features, and their band structures are similar. To further probe into the band structures and their density-of-states contribution to each MBene system,[50,51] we also present the band structures of Au_2B and Mo_2B monolayer sheets. Figure S14 shows that these also demonstrate metallic features with significant contributions to states at the Fermi level. Their good electrical conductivity is critical to the promising mobility of electron transfer during the CO_2 reduction process.[52−54] It is necessary to point out that the boron site at the catalytic active surfaces, such as Fe_2B_4, Ru_2B_4, and Os_2B_4 MBenes, is due to the exposed B atom surface and leads to a substantial DOS contribution to the Fermi level. There obviously are several bands crossing the Fermi levels that form some sharp peaks near the Fermi level,[55] and there is significant hybridization between M-d and B-p orbitals in the ranges of −4 to −3 eV for Fe_2B_4, −5 to −3 eV for Nb_3B_4, and −6 to −4 eV for Os_2B_4 and Ru_2B_4 in the valence band. This indicates a strong hybridization of orbital interaction between metal and B atoms at this energy level range. Analysis of the PDOS near the Fermi level site clearly shows that the main DOS comprises the d electrons of metal, while the p electrons of B 2p make a small contribution to the Fermi levels in the range of −1 to 2 eV in most of the MBene materials. Several slight peaks can be seen in the conduction band.[56] The excellent conductivity of the MBene materials can provide advantages in CO_2 electro-reduction catalysts.

In this work, we used DFT methods to study the stability and electronic properties of MBenes. We considered a series of MBenes with the formula of M_3B_4 (M = V, Ta, and Nb), MB_2 (M = Fe, Ru, and Os), and M_2B (M = Au and Mo), which were synthesized by experiment. These materials exhibited promising CO_2RR catalytic activity. The competition with HER was also studied on the basis of the change in $U_L(CO_2)-U_L(H_2)$. This work extends the family of MBene applications in the field of catalysis and offers highly promising candidates

https://doi.org/10.1021/acs.jpclett.1c01499
J. Phys. Chem. Lett. 2021, 12, 6370−6382

for CO_2 electroreduction catalysts. We focused on the catalytic properties for producing CO_2 to C1 hydrocarbon products, such as CH_4, CH_3OH, HCHO, CO, and HCOOH. Full optimization of these structures showed that our considered MBenes were stable and demonstrated a moderate binding of CO_2RR intermediate species. All possible reaction mechanism paths were determined by the binding energy of intermediates on these MBene catalysts. When the most favorable reaction pathway was constructed on the basis of the Gibbs energy profile diagram, the applied potential was set depending on the minimum limiting potential, which required that all reaction steps be made downhill in the free energy profile. Linear scaling appeared between the binding energies of the intermediate species, which provided guidance to obtain the target product. The binding energies of ΔG_{*OH} and ΔG_{*CO} were two key descriptors used to determine the catalytic activity of MBene catalysts, and an activity volcano plot of limiting potential was presented between different elementary reaction steps. Au_2B had a higher overpotential production of CH_4 (0.46 V) than CH_3OH (0.31 V), and the first hydrogenation of $*CO_2$ to $*HCO_2$ was identified as the rate-determining step with the limiting potential of −0.29 V. We identified Au_2B and V_3B_4 as promising candidates with high catalytic activity and selectivity for the reduction of CH_4, while Au_2B, Fe_2B_4, Ru_2B_4, and V_3B_4 are expected to be promising candidates for the reduction of CH_3OH with lower overpotential along six proton−electron transfers. Fe_2B_4 and Ru_2B_4 were identified as promising catalysts for the reduction of CO with a lower overpotential of 0.15 and 0.14 eV, respectively. The 2D MBene monolayers exhibited metallic features depend on the band structure and PDOS, with the main density-of-state contribution from the p−d orbital coupling between metal and boron atoms. Charge transfer mainly occurred within the adsorbates and the catalyst, which featured strong mobility, conductivity, and thermal kinetic stabilities. The electronic performance of MBenes exhibited a prominent metallic character. Our results provide a guide to extend 2D MBene system applications in CO_2 electroreduction catalysts with a theoretical approach and promote the development of 2D materials in the design and development of new high-performance catalysts for CO_2RR in the future.

■ ASSOCIATED CONTENT

Supporting Information

The Supporting Information is available free of charge at https://pubs.acs.org/doi/10.1021/acs.jpclett.1c01499.

Gibbs free energies and diagrams; binding energies; scaling linear relations diagrams; charge density distribution diagrams; electronic band structures (PDF)

■ AUTHOR INFORMATION

Corresponding Author

Yi Xiao − *Institute of Materials Science, TU Darmstadt, 64287 Darmstadt, Germany;* orcid.org/0000-0001-6318-8010; Email: yixiao@tmm.tu-darmstadt.de

Authors

Chen Shen − *Institute of Materials Science, TU Darmstadt, 64287 Darmstadt, Germany;* orcid.org/0000-0002-8538-9873

Niloofar Hadaeghi − *Institute of Materials Science, TU Darmstadt, 64287 Darmstadt, Germany*

Complete contact information is available at: https://pubs.acs.org/10.1021/acs.jpclett.1c01499

Notes

The authors declare no competing financial interest.

■ ACKNOWLEDGMENTS

Financial support comes from the China Scholarship Council (CSC:201808440416) of China and the Research and the Arts (HMWK) of the Hessen State in Germany. The Lichtenberg high performance computer is gratefully acknowledged, and we are also thankful to TU Darmstadt.

■ REFERENCES

(1) Olah, G. A.; Prakash, G. K. S.; Goeppert, A. Anthropogenic Chemical Carbon Cycle for a Sustainable Future[J]. *J. Am. Chem. Soc.* **2011**, *133* (33), 12881−12898.

(2) Jhong, H.-R.; Ma, S.; Kenis, P. J. Electrochemical Conversion of CO_2 to Useful Chemicals: Current Status, Remaining Challenges, and Future Opportunities[J]. *Curr. Opin. Chem. Eng.* **2013**, *2* (2), 191−199.

(3) Wang, W.; Wang, S.; Ma, X.; Gong, J. Recent Advances in Catalytic Hydrogenation of Carbon Dioxide[J]. *Chem. Soc. Rev.* **2011**, *40* (7), 3703−3727.

(4) Benson, E. E.; Kubiak, C. P.; Sathrum, A. J.; Smieja, J. M. Electrocatalytic and Homogeneous Approaches to Conversion of CO_2 to Liquid Fuels[J]. *Chem. Soc. Rev.* **2009**, *38* (1), 89−99.

(5) Khazaei, M.; Wang, J.; Estili, M.; Ranjbar, A.; Suehara, S.; Arai, M.; Yunoki, S. Novel MAB Phases and Insights into Their Exfoliation into 2D MBenes[J]. *Nanoscale* **2019**, *11* (23), 11305−11314.

(6) Ozdemir, I.; Kadioglu, Y.; Aktürk, O. Ü.; Yuksel, Y.; AkÑncÑ, Ü.; Aktürk, E. A New Single-layer Structure of MBene Family: Ti_2B[J]. *J. Phys.: Condens. Matter* **2019**, *31* (50), 505401.

(7) Jiang, Z.; Wang, P.; Jiang, X.; Zhao, J. MBene (MnB): a New Type of 2D Metallic Ferromagnet with High Curie Temperature[J]. *Nanoscale Horizons* **2018**, *3* (3), 335−341.

(8) Zha, X. H.; Xu, P.; Huang, Q.; Du, S.; Zhang, R. Q. Mo_2B, an MBene Member with High Electrical and Thermal Conductivities, and Satisfactory Performances in Lithium Ion Batteries[J]. *Nanoscale Advances* **2020**, *2* (1), 347−355.

(9) Yuan, H.; Li, Z.; Yang, J. Transition-metal diboride: A New Family of Two-dimensional Materials Designed for Selective CO_2 Electroreduction[J]. *J. Phys. Chem. C* **2019**, *123* (26), 16294−16299.

(10) Guo, Z.; Zhou, J.; Sun, Z. New Two-dimensional Transition Metal Borides for Li Ion Batteries and Electrocatalysis[J]. *J. Mater. Chem. A* **2017**, *5* (45), 23530−23535.

(11) Li, F.; Tang, Q. First-Principles Calculations of TiB MBene Monolayers for Hydrogen Evolution[J]. *ACS Applied Nano Materials* **2019**, *2* (11), 7220−7229.

(12) Xiao, Y.; Shen, C. Predicted Electrocatalyst Properties on Metal Insulator $MoTe_2$ for Hydrogen Evolution Reaction and Oxygen Reduction Reaction Application in Fuel Cells[J]. *Energy Fuels* **2021**, *35* (9), 8275−8285.

(13) Bo, T.; Liu, P.-F.; Xu, J.; Zhang, J.; Chen, Y.; Eriksson, O.; Wang, F.; Wang, B.-T. Hexagonal Ti_2B_2 Monolayer: a Promising Anode Material Offering High Rate Capability for Li-ion and Na-ion batteries[J]. *Phys. Chem. Chem. Phys.* **2018**, *20* (34), 22168−22178.

(14) Zhang, H.; Xiang, H.; Dai, F. Z.; Zhang, Z.; Zhou, Y. First Demonstration of Possible Two-dimensional MBene CrB Derived from MAB Phase Cr_2AlB_2[J]. *J. Mater. Sci. Technol.* **2018**, *34* (11), 2022−2026.

(15) Alameda, L. T.; Moradifar, P.; Metzger, Z. P.; Alem, N.; Schaak, R. E. Topochemical Deintercalation of Al from MoAlB: Stepwise Etching Pathway, Layered Intergrowth Structures, and Two-dimensional MBene[J]. *J. Am. Chem. Soc.* **2018**, *140* (28), 8833−8840.

(16) Sun, G.; Kürti, J.; Rajczy, P.; Kertesz, M.; Hafner, J.; Kresse, G. Performance of the Vienna ab Initio Simulation Package (VASP) in Chemical Applications[J]. *J. Mol. Struct.: THEOCHEM* **2003**, *624* (1−3), 37−45.
(17) Kresse, G.; Furthmuller, J. Efficient Iterative Schemes for ab initio Total-energy Calculations Using a Plane-wave Basis Set. *Phys. Rev. B: Condens. Matter Mater. Phys.* **1996**, *54*, 11169−11186.
(18) Perdew, J. P.; Burke, K.; Ernzerhof, M. Generalized Gradient Approximation Made Simple[J]. *Phys. Rev. Lett.* **1996**, *77* (18), 3865.
(19) Grimme, S. Semiempirical GGA-type Density Functional Constructed with a Long-range Dispersion Correction[J]. *J. Comput. Chem.* **2006**, *27* (15), 1787−1799.
(20) Ha, M.; Kim, D. Y.; Umer, M.; et al. Tuning metal single atoms embedded in N_xC_y moieties toward high-performance electrocatalysis[J]. *Energy Environ. Sci.* **2021**, *14* (6), 3455−3468.
(21) Oberhofer, H. Electrocatalysis Beyond the Computational Hydrogen Electrode[J]. *Handbook of Materials Modeling: Applications: Current and Emerging Materials* **2020**, 1505−1537.
(22) Chase, M. W. NIST-JANAF Thermochemical Tables for Oxygen Fluorides[J]. *J. Phys. Chem. Ref. Data* **1996**, *25* (2), 551−603.
(23) Barone, V. Vibrational Zero-point Energies and Thermodynamic Functions Beyond the Harmonic Approximation [J]. *J. Chem. Phys.* **2004**, *120* (7), 3059−3065.
(24) Gardiner, S J. *Harmonic Approximation[M]*; Cambridge University Press, 1995.
(25) Wang, V.; Xu, N.; Liu, J. C.; Tang, G.; Geng, W. T. VASPKIT: A Pre-and Post-processing Program for VASP Code[J]. *arXiv*, May 6, 2021, 1908.08269, ver. 6. https://arxiv.org/abs/1908.08269 (accessed 2021-07-06).
(26) Li, N.; Chen, X.; Ong, W. J.; MacFarlane, D. R.; Zhao, X.; Cheetham, A. K.; Sun, C. Understanding of Electrochemical Mechanisms for CO_2 Capture and Conversion into Hydrocarbon Fuels in Transition-metal Carbides (MXenes)[J]. *ACS Nano* **2017**, *11* (11), 10825−10833.
(27) Peterson, A. A.; Abild-Pedersen, F.; Studt, F.; Rossmeisl, J.; Nørskov, J. K. How Copper Catalyzes the Electroreduction of Carbon Dioxide into Hydrocarbon Fuels[J]. *Energy Environ. Sci.* **2010**, *3* (9), 1311−1315.
(28) Meng, Y.; Yin, C.; Li, K.; et al. Improved Oxygen Reduction Activity in Heteronuclear FeCo-Co doped Graphene: A Theoretical Study[J]. *ACS Sustainable Chem. Eng.* **2019**, *7* (20), 17273−17281.
(29) Tang, S.; Zhou, X.; Zhang, S.; Li, X.; Yang, T.; Hu, W.; Jiang, J.; Luo, Y. Metal-free Boron Nitride Nanoribbon Catalysts for Electrochemical CO_2 Reduction: Combining High Activity and Selectivity-[J]. *ACS Appl. Mater. Interfaces* **2019**, *11* (1), 906−915.
(30) Zhang, W.; Xiao, Y. Mechanism of Electrocatalytically Active Precious Metal (Ni, Pd, Pt, and Ru) Complexes in the Graphene Basal Plane for ORR Applications in Novel Fuel Cells[J]. *Energy Fuels* **2020**, *34* (2), 2425−2434.
(31) Liu, S.; Huang, S. Size Effects and Active Sites of Cu Nanoparticle Catalysts for CO_2 Electroreduction[J]. *Appl. Surf. Sci.* **2019**, *475*, 20−27.
(32) Zhao, Y.; Zhou, S.; Zhao, J. Selective C- C Coupling by Spatially Confined Dimeric Metal Centers[J]. *Iscience* **2020**, *23*, 101051.
(33) Wang, Y.; Tian, Y.; Yan, L.; Su, Z. DFT Study on Sulfur-doped g-C3N4 Nanosheets as a Photocatalyst for CO_2 Reduction Reaction-[J]. *J. Phys. Chem. C* **2018**, *122* (14), 7712−7719.
(34) Deng, C.; Li, W.; He, R.; Shen, W.; Li, M. Understanding and Breaking the Scaling Relations in the Oxygen Reduction Reaction on Pd_xCu_{4-x} Subnanoclusters Supported by Defective Two-Dimensional Boron Nitride Materials[J]. *J. Phys. Chem. C* **2020**, *124* (36), 19530−19537.
(35) Guo, X.; Lin, S.; Gu, J.; Zhang, S.; Chen, Z.; Huang, S. Establishing a Theoretical Landscape for Identifying Basal Plane Active 2D Metal Borides (MBenes) toward Nitrogen Electroreduction[J]. *Adv. Funct. Mater.* **2021**, *31*, 2008056.
(36) Liang, Z.; Luo, M.; Chen, M.; Qi, X.; Liu, J.; Liu, C.; Peera, S. G.; Liang, T. Exploring the Oxygen Electrode Bifunctional Activity of Ni−N−C-doped Graphene Systems with N, C Co-ordination and OH Ligand effects[J]. *J. Mater. Chem. A* **2020**, *8* (39), 20453−20462.
(37) Zhao, Z.; Chen, Z.; Lu, G. Computational Discovery of Nickel-based Catalysts for CO_2 Reduction to Formic Acid[J]. *J. Phys. Chem. C* **2017**, *121* (38), 20865−20870.
(38) Shin, D. Y.; Jo, J. H.; Lee, J. Y.; Lim, D. H. Understanding Mechanisms of Carbon Dioxide Conversion into Methane for Designing Enhanced Catalysts from First-principles[J]. *Comput. Theor. Chem.* **2016**, *1083*, 31−37.
(39) Zhao, Z.; Chen, Z.; Zhang, X.; Lu, G. Generalized Surface Coordination Number as an Activity Descriptor for CO_2 Reduction on Cu Surfaces[J]. *J. Phys. Chem. C* **2016**, *120* (49), 28125−28130.
(40) Zhou, S.; Yang, X.; Shen, Y.; King, R. B.; Zhao, J. Dual Transition Metal Doped Germanium Clusters for Catalysis of CO Oxidation[J]. *J. Alloys Compd.* **2019**, *806*, 698−704.
(41) Luo, W.; Wang, H.; Wang, Z.; Liu, G.; Liu, S.; Ouyang, C. First-principles Study of χ 3-borophene for Charge-modulated Switchable CO_2 Capture[J]. *Phys. Chem. Chem. Phys.* **2020**, *22* (16), 8864−8869.
(42) Xiong, J.; Di, J.; Li, H. Atomically thin 2D Multinary Nanosheets for Energy-related Photo, Electrocatalysis[J]. *Advanced Science* **2018**, *5* (7), 1800244.
(43) Xing, M.; Guo, L.; Hao, Z. Theoretical Insight in Electrocatalytic Reduction of CO_2 in Metal Ratio and Reaction Mechanism on Palladium-Copper Alloys. *Dalton Transactions* **2019**, *48*, 1504.
(44) Yang, Z.; Oropeza, F. E.; Zhang, K H L. P-block Metal-based (Sn, In, Bi, Pb) Electrocatalysts for Selective Reduction of CO_2 to Formate[J]. *APL Mater.* **2020**, *8* (6), 060901.
(45) Fernandez, E. M.; Balbas, L. C. Theoretical Study of CO Adsorption on Au/alumina Substrates[J]. *Phys. Status Solidi A* **2006**, *203* (6), 1277−1283.
(46) Li, X.; Cui, H.; Zhang, R. First-principles Study of the Electronic and Optical Properties of a New Metallic MoAlB[J]. *Sci. Rep.* **2016**, *6* (1), 1−10.
(47) Luo, W.; Xie, W.; Mutschler, R.; Oveisi, E.; De Gregorio, G. L.; Buonsanti, R.; Züttel, A. Selective and Stable Electroreduction of CO_2 to CO at the Copper/indium Interface[J]. *ACS Catal.* **2018**, *8* (7), 6571−6581.
(48) Mao, X.; Kour, G.; Zhang, L.; He, T.; Wang, S.; Yan, C.; Zhu, Z.; Du, A. Silicon-doped Graphene edges: An Efficient Metal-free Catalyst for the Reduction of CO_2 into Methanol and Ethanol[J]. *Catal. Sci. Technol.* **2019**, *9* (23), 6800−6807.
(49) Ziegler, T.; Rauk, A. Carbon monoxide, Carbon monosulfide, Molecular nitrogen, Phosphorus Trifluoride, and Methyl Isocyanide as Sigma. Donors and. pi. Acceptors. A theoretical Study by the Hartree-Fock-Slater transition-state Method[J]. *Inorg. Chem.* **1979**, *18* (7), 1755−1759.
(50) Zhang, Z.; Ahmad, F.; Zhao, W.; Yan, W.; Zhang, W.; Huang, H.; Ma, C.; Zeng, J. Enhanced Electrocatalytic Reduction of CO_2 via Chemical Coupling between Indium Oide and Reduced Graphene Oxide[J]. *Nano Lett.* **2019**, *19* (6), 4029−4034.
(51) Zhang, X.; Wang, W.; Yang, Z. CO_2 Reduction on Metal-and Nitrogen-Codoped Graphene: Balancing Activity and Selectivity via Coordination Engineering[J]. *ACS Sustainable Chem. Eng.* **2020**, *8* (15), 6134−6141.
(52) Li, H.; Calle-Vallejo, F.; Kolb, M. J.; Kwon, Y.; Li, Y.; Koper, M. T. Why (1 0 0) Terraces Break and Make Bonds: Oxidation of Dimethyl ether on Platinum Single-crystal Eectrodes[J]. *J. Am. Chem. Soc.* **2013**, *135* (38), 14329−14338.
(53) Kim, D. Y.; Ha, M.; Kim, K. S. A universal screening strategy for the accelerated design of superior oxygen evolution/reduction electrocatalysts. *J. Mater. Chem. A* **2021**, *9* (6), 3511−3519.
(54) Chu, S.; Ou, P.; Ghamari, P.; Vanka, S.; Zhou, B.; Shih, I.; Song, J.; Mi, Z. Photoelectrochemical CO_2 Reduction Into Syngas with the Metal/oxide Interface[J]. *J. Am. Chem. Soc.* **2018**, *140* (25), 7869−7877.
(55) Liu, S.; Wang, X.-Z.; Tao, H.; Li, T.; Liu, Q.; Xu, Z.; Fu, X.-Z.; Luo, J.-L. Ultrathin 5-fold Twinned sub-25 nm Silver Nanowires Enable Highly Selective Electroreduction of CO_2 to CO[J]. *Nano Energy* **2018**, *45*, 456−462.

https://doi.org/10.1021/acs.jpclett.1c01499
J. Phys. Chem. Lett. 2021, 12, 6370−6382

(56) Zafari, M.; Nissimagoudar, A. S.; Umer, M.; Lee, G.; Kim, K. S. First principles and machine learning based superior catalytic activities and selectivities for N 2 reduction in MBenes, defective 2D materials and 2D π-conjugated polymer-supported single atom catalysts. *J. Mater. Chem. A* **2021**, *9* (14), 9203−9213.

https://doi.org/10.1021/acs.jpclett.1c01499
J. Phys. Chem. Lett. 2021, 12, 6370−6382

CHEMISTRY OF MATERIALS

pubs.acs.org/cm

Article

Theoretical Establishment and Screening of an Efficient Catalyst for N_2 Electroreduction on Two-Dimensional Transition-Metal Borides (MBenes)

Yi Xiao,* Chen Shen,* and Teng Long

Cite This: *Chem. Mater.* 2021, 33, 4023−4034

Read Online

ACCESS | Metrics & More | Article Recommendations | Supporting Information

ABSTRACT: Electrochemical nitrogen reduction reactions (NRRs) produce ammonia under ambient conditions, and it is necessary and efficient to explore a high-activity and -selectivity catalyst for NRR activity from the view of the energy change profile and electrical structure. Herein, we utilized a theoretical screening approach to systematically design two-dimensional (2D) transition-metal borides (MBenes) as promising electrocatalysts for NRRs. Density functional theory (DFT) calculation results reveal that Ta_3B_4, Nb_3B_4, $CrMnB_2$, Mo_2B_2, Ti_2B_2, and W_2B_2 MBenes have an excellent catalytic activity to reduce N_2 to NH_3 under ambient conditions. These materials strongly attract N_2 and H around the metal activity center, while the competing hydrogen evolution reaction (HER) can be well suppressed. NRRs occur along the favorite pathway with a low limiting potential of −0.24 V on W_2B_2, indicating that the W_2B_2 monolayer provides a new candidate catalyst for NRRs. In addition, the low limiting potentials of Nb_3B_4 (0.50 eV), Ta_3B_4 (0.39 eV), and Ti_2B_2 (0.37 V) are suitable for NRRs due to strong backdonation between the hybridized d orbital of the metal atom and the 2p orbital in N_2. The improved catalytic activity of NRRs, with limiting potentials ranging from $-0.7\ V < U_L < -0.2\ V$, depends on theoretical screening criteria: the descriptor ΔG_{*N} is proposed to establish the relationship between the different NRR intermediates, and the rate-determining step (PDS) was confirmed by the limiting potential of the volcano plot. The energy barrier for reducing O*/OH* to $*H_2O$ is defined as the redox potential, and the difference in $U_R - U_L$ values acts as a descriptor to study the catalytic activity. Theoretical screening work can provide a highly effective approach to investigate the reaction mechanism and can aid in designing novel catalysts for the reduction of N_2 to NH_3 on MBenes.

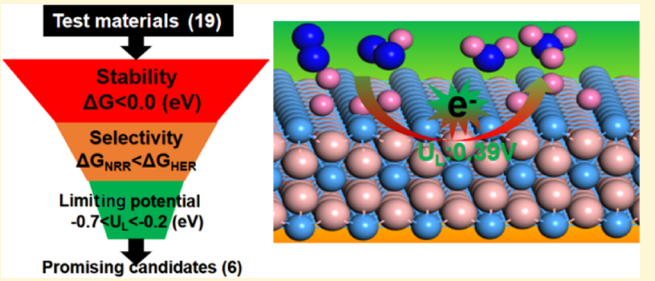

INTRODUCTION

Currently, ammonia is one of the most important feedstocks for synthesizing chemicals and fertilizers,[1,2] and the synthesis of ammonia has enormous significance for both industrial development and global agricultural production.[3] In nature, the nitrogenase of rhizobia can efficiently convert N_2 into NH_3 under ambient conditions using adenosine triphosphate, and this process is called biological nitrogen fixation.[4,5] However, industrial nitrogen fixation depends on the Haber−Bosch process[6,7] under high temperatures and high pressures (500 °C and 20 MPa), which is an energy-intensive and inefficient process. Therefore, the exploration of more efficient catalysts or the development of new alternative technologies is urgently demanded,[8] so the nitrogen reduction reaction (NRR) via electrochemical reduction could be a promising strategy to replace the traditional Haber−Bosch process, as it can be carried out under ambient environmental conditions powered by renewable wind and solar energy.[9,10] However, this electrochemical process is commonly limited by poor reaction kinetics and high overpotential due to the slow activation of chemically inert N≡N triple bonds.[11] Furthermore, the poor selectivity of current electrocatalysts is another bottleneck of NRR due to the competing hydrogen evolution reaction (HER) process under aqueous conditions, and efficient electrocatalysts should have high activity and selectivity toward NRR.[12] To date, large amounts of 2D materials have been used as electrocatalytic platforms for HER,[13] O_2 reduction (ORR),[14] CO_2 reduction,[15] and N_2 reduction.[16] Recently, a series of 2D transition-metal borides, which are boron analogues of MXenes and termed as "MBenes", have been discovered and synthesized experimentally.[16] In 2017, Sun and co-workers reported that Mo_2B_2 and Fe_2B_2 MBenes are suitable for Li-ion battery electrodes,[17] which attracted intensive attention for this novel 2D transition-metal borides. After that, Jiang et al.[18] reported 12 MBenes, MnB, HfB, ZrB,

Received: February 5, 2021
Revised: May 13, 2021
Published: May 26, 2021

https://doi.org/10.1021/acs.chemmater.1c00424
Chem. Mater. 2021, 33, 4023−4034

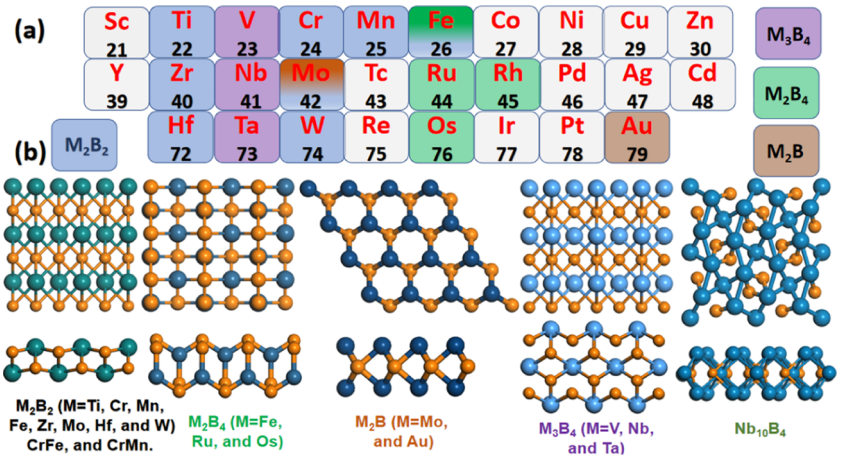

Figure 1. (a) All MBenes for which both experimental and theoretical studies have been proposed are listed in the periodic table of elements. The stable structural prototypes of MBenes are indicated in different colors. (b) Top and side views of calculation models for different MBene structural prototypes that were built.

Au_2B, Mo_2B, Nb_5B_2, Nb_3B_4, Ta_3B_4, V_3B_4, Os_2B_4, Fe_2B_4, and Ru_2B_4, based on systematic high-throughput screening. These theoretical studies encouraged extensive experimental evaluations; among them, 2D MoB and CrB were successfully fabricated by exfoliation of the aluminum layer from their bulk phases.[19]

To systematically study the physical and chemical properties of these MBenes toward nitrogen electroreduction, it is important to identify the catalytic activity and selectivity. Theoretical screening of different MBenes could provide broad prospects in the search for candidate materials for NRR electrocatalysts. Therefore, to find reliable descriptors to evaluate the catalytic performance of MBenes, a valid descriptor is needed as a criterion for judging the activity and selectivity of the catalyst. In this regard, we propose the following strategy: (i) MBenes should possess thermodynamic stability and feasibility; (ii) N_2 can be sufficiently adsorbed; (iii) to achieve low energy cost, the limiting potential of likely rate-determining steps (RDSs) should be as low as possible; and (iv) there should be high selectivity between NRR and HER, and the limiting potential for N_2 adsorption should be much greater than that of H_2.[20] Therefore, are these MBenes suitable for NRR catalysts? What is the difference between MBenes and MXenes? What descriptor can be used to evaluate the catalytic performance of these MBene catalysts for NRR? To settle these questions, we carried out theoretical establishment and screening using a density functional theory (DFT) approach to evaluate the energy change profile of intermediates during the NRR process. By considering stability, activity, and selectivity, we find that some MBenes can effectively activate N_2 molecules and hydrogenate, while the competing HER process can be suppressed.[21] Encouragingly, the common surface oxidation problem that has a great influence on the catalytic performance of catalysts for NRR can be resolved by the potential difference between the redox potential (U_R)[22] and the limiting potential (U_L)[23] in this work. In particular, W_2B_2, Mo_2B_2, and Ta_3B_4 act as promising candidate catalysts for the NRR with limiting potentials of −0.24, −0.43, and −0.39 V, respectively. This theoretical screening work not only provides compelling evidence for acting as NRR electrocatalysts but also provides principles and guidance to further design high-performance catalysts for some common electrochemical reaction processes.

COMPUTATIONAL DETAILS

All structure relaxations and electronic property calculations within spin-polarized density functional theory (DFT) were executed in the Vienna ab initio simulation package (VASP).[24,25] The electron exchange−correlation interactions were described by the Perdew−Burke−Ernzerhof (PBE) functional within the generalized gradient approximation (GGA).[26] A cutoff energy of 500 eV was adopted for the Perdew−Burke−Ernzerhof (PBE) exchange−correlation functional, and[27] this functional was performed to consider the van der Waals (vdW) interactions.[28] To avoid the interlayer interaction introduced by the periodic boundary condition, a sufficient 20 Å vacuum was applied in the z direction.[29] The Brillouin zone was sampled by a 5 × 5 × 1 Monkhorst−Pack (MP) grid for structural relaxation, and a denser 10 × 10 × 1 MP grid was used for electronic property calculations. The convergence criteria for energy and force were set to 10^{-5} eV and 0.02 eV/Å, respectively. Visualization of the charge density difference distribution and Bader charge transfer between NRR adsorbates and MBenes was executed in the VESTA code.[30] Charge transfer and quantitative descriptions are effective approaches to investigate the interaction mechanism and can obtain the electron flow between two fragments. The HSE06 hybrid functional[31] was executed to calculate the band structures and the partial density of states (PDOS) for pristine MBenes, the crystal orbital Hamilton population (COHP) was applied to analyze the bonding/antibonding population between metal active centers and intermediates within the LOBSTER code.[32] According to the computational hydrogen electrode (CHE) model, which was proposed by Nørskov et al.,[33] the formation energy of the NRR intermediate species was determined using the concept of the electron−proton pair ($H^+ + e^-$). The change in free energy for each elementary step can be calculated as follows: $\Delta G = \Delta E_{DFT} + \Delta ZPE - T\Delta S + \Delta G_U + \Delta GpH$, where ΔE_{DFT} is the energy change that can be obtained from DFT calculations, ΔZPE and $T\Delta S$ represent the zero-point energy and enthalpy correction terms at a specific temperature (T = 298.15 K). The ΔZPE and $T\Delta S$ correction terms were obtained from vibration analysis using the VASPKIT code.[34] The energies of gas molecules (such as H_2, N_2, and NH_3) were taken from the NIST database,[35] and the computational methods are given in detail in the Supporting Information.

https://doi.org/10.1021/acs.chemmater.1c00424
Chem. Mater. 2021, 33, 4023−4034

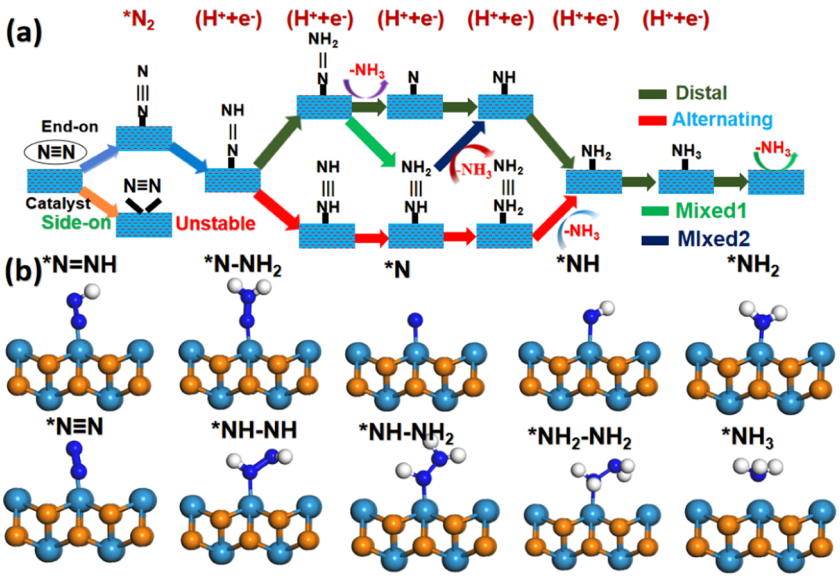

Figure 2. (a) Schematic illustration of NRR mechanisms, including the distal, alternating, and mixed pathways, is also considered for NRR for different MBene structural prototypes. (b) Side view of initial calculation models of M_2B MBene structural prototypes is presented according to the hypothesized NRR intermediate species.

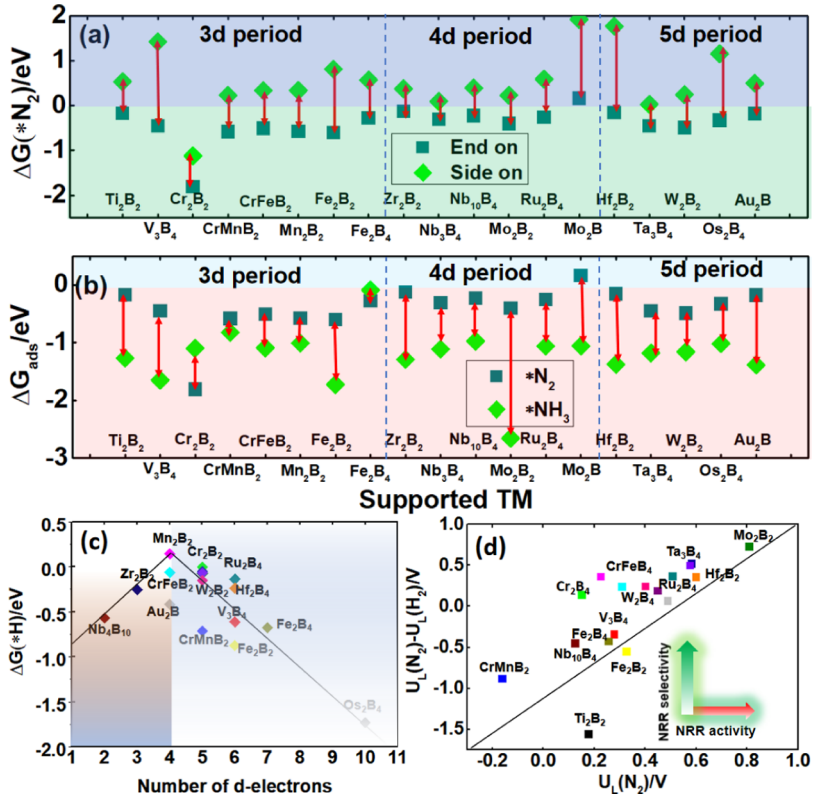

Figure 3. (a) Adsorption energy of end-on and side-on binding configurations of N_2 on the Mbene surfaces. (b) Adsorption energies of N_2 and NH_3 on our consideration MBene surfaces. (c) Volcano plots for the binding Gibbs energy of H^+ vs the number of d electrons of metal on various MBene model surfaces at zero electrode potential (U = 0 V) vs RHE. (d) Limiting potentials difference $[U_L(N_2) - U_L(H_2)]$ between the N_2RR and HER as a function of $U_L(N_2)$ on various MBene model surfaces.

RESULTS AND DISCUSSION

The current study suggested that many transition-metal atoms can combine with boron atoms to form a rather large number of monolayer 2D materials. Through systematic evaluation, catalytic performance and theoretical screening of all possible MBenes is possible. We focus on investigating the catalytic activity for producing nitrogen to ammonia on MBenes. The reliability and stability of MBenes can be verified by theoretical screening tests. Using the five target prototypes, all the transition metals including 3d,4d, and 5d periods (as shown in Figure 1a) are considered in this work. Our results reveal that 19 stable MBenes are considered for N_2 electroreduction

https://doi.org/10.1021/acs.chemmater.1c00424
Chem. Mater. 2021, 33, 4023−4034

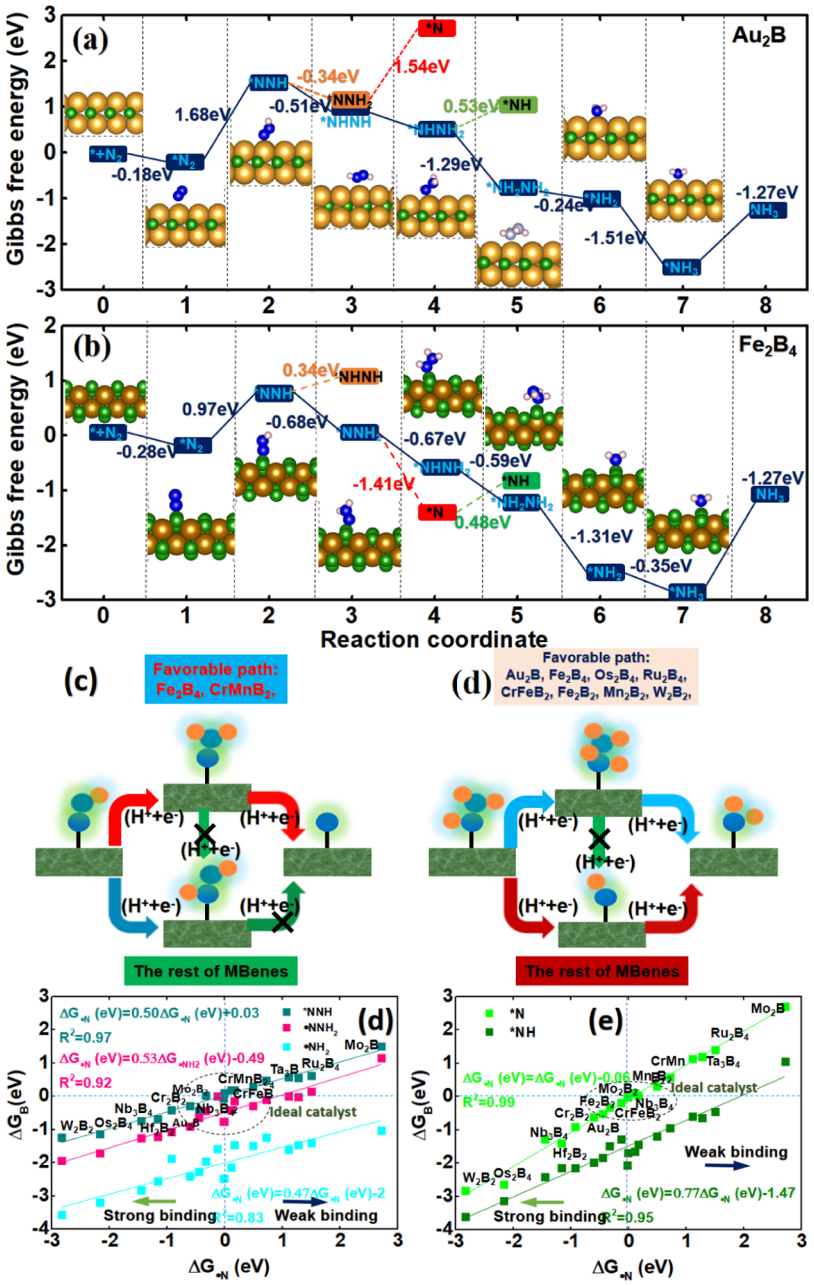

Figure 4. Gibbs free energy profile diagrams of NORR via the end-on binding configuration on Au_2B (a) and Fe_2B_4 (b). The minimum energy reaction pathways are highlighted with a red solid line, and the lowest energy barrier (dark blue solid line) pathway are also highlighted with arrows. All of the energy barriers during each elementary reaction step (in eV) are also plotted for comparison. (c) Possible branch reaction of N_2 electroreduction reaction to confirm the selectivity and priority of chemical reactions. (d, e) Scaling linear relation between binding energies of intermediate species and ΔG_{*N} as a key descriptor.

catalysts, as shown in Figure 1b. These MBene structures are stable without an imaginary frequency and depend on the phonon spectrum calculation, as summarized in Figure S7. Herein, 19 stable MBene structures with different metal/boron ratios were selected as N_2 reduction to NH_3 electroreduction catalysts, including M_2B (M = Mo and Au), M_2B_2 (M = Ti, Cr, Mn, Fe, Zr, Mo, Hf, W, CrMn, and CrFe), M_2B_4 (M = Fe, Ru, and Os), M_3B_4 (M = V, Nb, and Ta), and the inner layer of Nb_5B_2 (Figure 1b).[36] Due to the high kinetic energy required to drive N_2 dissociation under ambient conditions, we excluded the dissociative pathway. Depending on the calculated adsorption energies of different activation sites, the top sites of both metal and boron atoms via the side-on binding mode for N_2 are more favorable than other sites. To explore reaction mechanisms during the production of N_2 to NH_3, the two different binding configurations of N_2 (end on and side on) and all possible reaction pathways of NRR are considered, as seen in Figure 2a, because N_2 can be activated more efficiently via the end-on than side-on pattern on MBene surfaces, as seen in Figure 3a. Therefore, N_2 activation and production of NH_3 via an end-on pattern are considered in the next section. It includes distal, alternating, and mixed reaction paths (Figure 2a). Depending on the end-on binding configurations, N_2 can be reduced to NH_3 either through distal, alternating or following a mixed mechanism with a six-electron-transfer reaction ($N_2 + 6H^+ + 6e^- \rightarrow 2NH_3$) in the

https://doi.org/10.1021/acs.chemmater.1c00424
Chem. Mater. 2021, 33, 4023−4034

subsequent hydrogenation steps.[38] To obtain the most favorable NRR pathway on our candidate MBene surfaces, the initial adsorption configurations of different NRR intermediate species are listed in Figure 2b. The calculated energy change of each elementary step is listed in the Supporting Information.

Next, we investigated the adsorption energy difference between the end-on and side-on configurations on the 19 kinetically stable MBenes, which can be divided into three periods, 3d, 4d, and 5d, depending on the d orbital of the transition metal. N_2 can be adsorbed on Au_2B after overcoming an adsorption energy of −0.18 eV via end-on and side-on configurations, and 0.50 eV is not absorbed. Two MBenes, Cr_2B_2 and Fe_2B_2, are identified to be promising NRR catalysts with limiting potentials $\Delta G(*N_2)$ of −1.81 and −0.60 V, respectively. Furthermore, the comparison for adsorption energies of $*NH_3$ and $*N_2$ on MBenes is shown in Figure 3a,b. Gibbs free energy range of −1.81 to −0.12 eV is observed for the adsorption energy of $*N_2$, while for the adsorption energy range of $*NH_3$, the free energy range is from −2.66 to −0.09 eV. The $\Delta G*NH_3$ values are more negative than $\Delta G*N_2$ for most MBene surfaces except Cr_2B_2, suggesting that the ammonia oxidation reaction (NOR) is a more favorable competitor with NRR. However, acid electrolytes can be beneficial to dissolve $*NH_3$ species ($*NH_3/[NH_4]^+$) and make the final product NH_3 readily desorb from these catalyst surfaces.[37] In addition, the adsorption energy (0.16 eV) of nitrogen on Mo_2B is very small. Actually, the catalytic activity of MBenes for N_2 electroreduction to NH_3 would be determined based on the hydrogenated ability instead of NH_3 desorption. It is necessary to point out that the adsorption strength of N_2 becomes lower under an applied electrode potential, while the binding energy of *H becomes more negative. The adsorption energies of *H are summarized in Figure 3c, and the binding energies of H* (ΔG_{*H}) were applied to evaluate the HER activity. Negative ΔG_{*H} values were observed for all MBenes, and a volcano plot was established between the binding energy and d electrons of the transition metal, as shown in Figure 3c. The ΔG_{*H} values for Mn_2B_2 (−0.07 eV) and $CrMnB_2$ (−0.06 eV) indicated that the top of the volcano plot was closer to that of the highly efficient Pt catalyst (−0.09 eV), indicating that these MBenes preferred the HER process. We compared the limiting potential (U_L) difference between HER and NRR, as plotted in Figure 3d. The values of $U_L(*N_2) - U_L(*H_2)$ are observed to be positive for most metals excluding Ti_2B_2 and Fe_2B_2, indicating that the hydrogen evolution reaction (HER) can be suppressed on MBenes. Thus, the NRR selectivity is significantly enhanced by suppressing HER, while some indication of greater NRR activity can be obtained from $U_L(*N_2)$ values. $U_L(*N_2) - U_L(*H_2)$ can be a valid descriptor of the selectivity of NRR vs HER: a more positive value indicates a more selective catalyst toward NRR. In this regard, the limiting potential of N_2 [$U_L(*N_2)$] is found to remain stronger than that of HER on Mo_2B_2, and Ta_3B_4 and Hf_2B_2 exhibit good selectivity between the HER and NRR with $U_L(*N_2) - U_L(*H_2)$ values of 0.73.[38] Thus, high-selectivity NRR toward NH_3 can be confirmed on Mo_2B_2, Ta_3B_4, and Hf_2B_2 MBenes. Although the selectivity requires consideration of reaction kinetic barriers, the difference in the limiting potentials has been confirmed to be consistent with trends in NRR vs HER selectivity on MBene surfaces. The promising candidates for NRR catalysts are observed the top right-hand corner of Figure 3d, and these catalysts were identified as having greater $U_L(*N_2)$ and $U_L(*H_2)$ values, which means that NRR activity is more positive than the HER activity. In this case, the selectivity of MBenes can be evaluated by the U_L difference, and MBenes with more positive $U_L(*N_2) - U_L(*H_2)$ values suggest higher selectivity for NRR.

To explore the optimum reaction path toward NRR in our 19 MBene candidate catalysts, we systematically calculated the energy change profile diagram associated with all four reaction mechanisms. Based on the free energy diagrams shown in Figures 4a,b, S1, and S2 (Supporting Information), N_2 fixation is the initial step of N_2 adsorption. Due to the highly delocalized free electrons of transition-metal atoms on MBene surfaces, N_2 can be activated and adsorbed on the MBene with adsorption energies between −1.81 eV (Cr_2B_2) and −0.06 eV ($CrMnB_2$), and there is no additional energy input for N_2 adsorption on MBenes with the exception of Mo_2B (0.16 eV). For the whole reaction, the first hydrogenation step can proceed on N atoms via an end-on pattern to form *NNH, which binds to MBene via one N atom. *NNH is preferred with negative binding energy values of −0.06, −1.11, and −0.30 eV on the Ta_3B_4, Cr_2B_2, and W_2B_2 surfaces, respectively, with an energy barrier of at least 0.2 eV for the first hydrogenation step on all MBenes. After *NNH, the second hydrogenation step can occur on either N to form $*NNH_2$ or *NHNH, as shown in Figure 4c. $*NNH_2$ binds to MBenes via one N atom, while *NHNH may bind via one or two of the N atoms (Figure S8). $*NNH_2$ will produce the first $*NH_3$ and then release one NH_3 molecule. The remaining *N atom will be further produced via three consecutive hydrogenation steps to form the final NH_3 molecule (distal path), which is the most favorable N_2 to NH_3 pathway. However, the *NHNH reacts with the third ($H^+ + e^-$) pair to form $*NHNH_2$, and the next hydrogenation step can react either on two N atoms to form $*NH_2NH_2$ (alternating) or *NH to form $*NH_2$ (mixed 4) (Figure 4c). Then, via two consecutive hydrogenations to form final $*NH_3$ on the MBenes surfaces, the free energy profile diagram in each hydrogenation step is nether uphill or downhill, and the most favorable reaction pathway of reducing N_2 to NH_3 on different MBenes may be different. In Figure 4a,b, we focus on Au_2B and Fe_2B_4 as an example to verify the binding energy of all possible NRR intermediates. As shown in Figure 4a, in the first hydrogenation step, which leads to a large uphill in the free energy (1.68 eV), the energy barrier of *NHNH will lead to a downhill of −0.51 eV, and the next hydrogenation of $*NHNH_2$ forms is an exothermic process of 0.48 eV. Compared with the energy barrier of $*NNH_2$ formation (−0.34 eV) and because *N via the distal path is less favorable than the alternating path (−0.51 eV), the third hydrogenation step occurs on the end N atom to form $*NHNH_2$, which leads to a downhill of the free energy profile by 1.29 eV, while the formation of *NH will lead to a free energy uphill of 0.53 eV. The formation of $*NH_2$ and $*NH_3$ are both exothermic processes of 0.24 and 1.51 eV, respectively. Compared with the energy increase (0.97 eV) of the *NNH form and energy decrease (−0.68 eV) for the $*NNH_2$ formation, as shown in Figure 4b, the formation of the first $*NH_3$ molecule in the fourth hydrogenation step is thermodynamically more favorable (−1.41 eV) than $*NHNH_2$ formation (−0.67 eV). This molecule can be further reduced to $*NH_2NH_2$ with a free energy downhill profile of −0.59 eV or to $*NH_2$ (−1.31 eV). Both Au_2B and Fe_2B_4 have a chance to produce $*NH_3$ with energy reductions of −1.51 and −0.35

https://doi.org/10.1021/acs.chemmater.1c00424
Chem. Mater. 2021, 33, 4023−4034

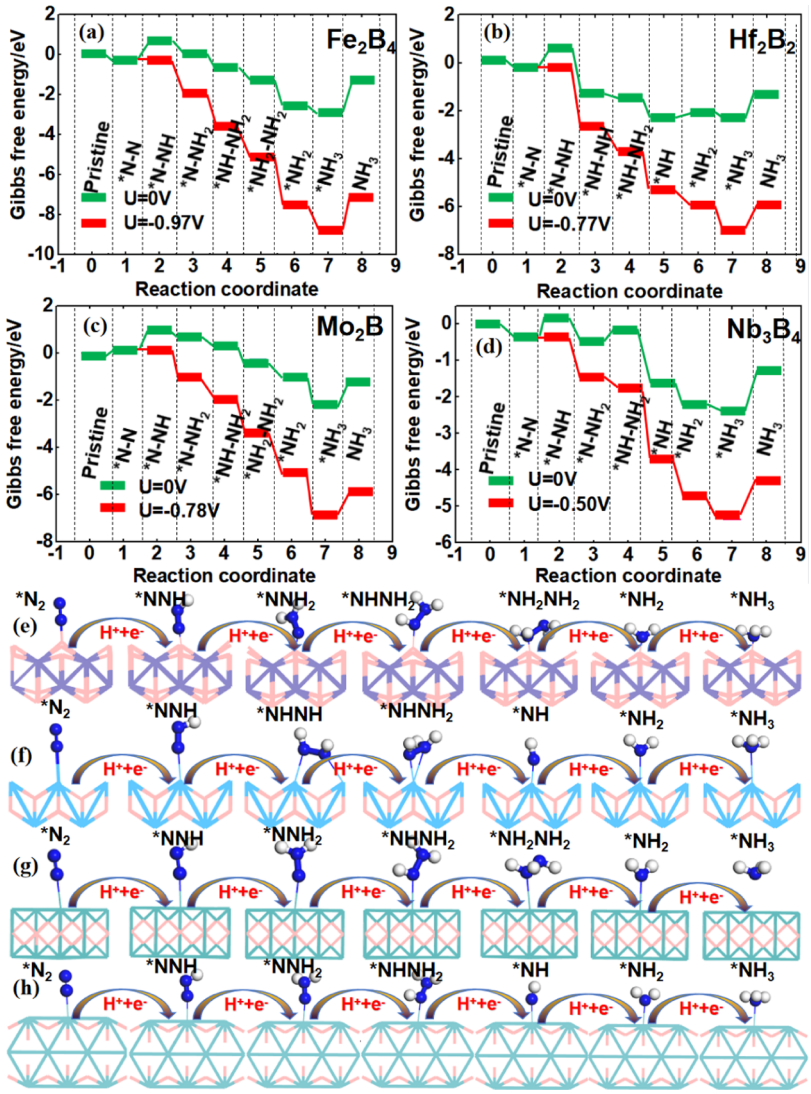

Figure 5. Gibbs free energy profiles for the most favorable reaction mechanism for NRR on MBenes. The colored solid line represents the minimum free energy electrochemical reaction pathway for zero potential ($U = 0$) (blue) and for an applied bias (red). (a) Fe_2B_4, (b) Hf_2B_2, (c) Mo_2B, and (d) Nb_3B_4. The binding configurations (top view) of the corresponding NRR intermediates on (e) Fe_2B_4, (f) Hf_2B_2, (g) Mo_2B, and (h) Nb_3B_4. The H, B, and N atoms are shown in white, pink, blue, respectively, and the other colors represent metal atoms. The symbol * denotes adsorbed states on the MBenes.

eV during the last hydrogenation steps. Considering all of these intermediates, the most favorable pathway for producing NH_3 from N_2 is via the alternating path on both Au_2B and Fe_2B_4: the limiting potentials are −1.68 V and −0.97 eV in the first protonation step during the whole process, respectively. Next, we studied the relationships between ΔG*N and the Gibbs free energy change (ΔG) of the NRR intermediate species, as shown in Figure 4d,e. All of the ΔG values are strongly linearly related to ΔG*N, which can be a descriptor of the catalytic activity for different MBene catalysts. A simple correlation of the catalytic performance between various MBene structures was observed, and a strong linear correlation existed between the binding energies of these intermediates, leading to a low overpotential.[39] The interactions between the d-orbitals of the metal and p-orbitals of nitrogen are reliable for the formation of *N; thus, ΔG*N is assumed to connect to the strength of the binding interaction. The value of ΔG*N for the right side is related to weak interactions. To obtain a promising candidate catalyst for NRR, linear relationships were also found between ΔG*NNH, ΔG*NNH_2, ΔG*NH, and ΔG*NH_2, as shown in Figure 4d,e. We examined the connection between ΔG*N and the free energy changes of N_2 hydrogenation ΔG(*NNH) and desorption ΔG(*N) for most MBenes.

As an important descriptor of NRR catalytic performance, the maximum Gibbs free energy change ΔG_{max} can be obtained from the rate-determining step, and the limiting potential (U_L) can be calculated by $U_L = -\Delta G_{max}/e$. In Figure 5d, for the Nb_3B_4 surface ($U_L = -0.50$ V), which has the highest activity among the four MBene catalysts, our goal is to find MBenes with a limiting potential value range of $-0.7 < U_L < -0.2$. In this regard, we found that six MBenes, namely, Nb_3B_4, Ta_3B_4, $CrMnB_2$, Mo_2B_2, Ti_2B_2, and W_2B_2, exceeded the metal-based catalyst criterion for NRR with U_L values ranging from −0.70 to −0.20. Furthermore, we considered the solvation effect on these MBene surfaces. The solvation-induced energy difference in the potential limiting step is rather small (0.15 eV), which is similar to 3D systems and is much smaller for 2D systems.

https://doi.org/10.1021/acs.chemmater.1c00424
Chem. Mater. 2021, 33, 4023−4034

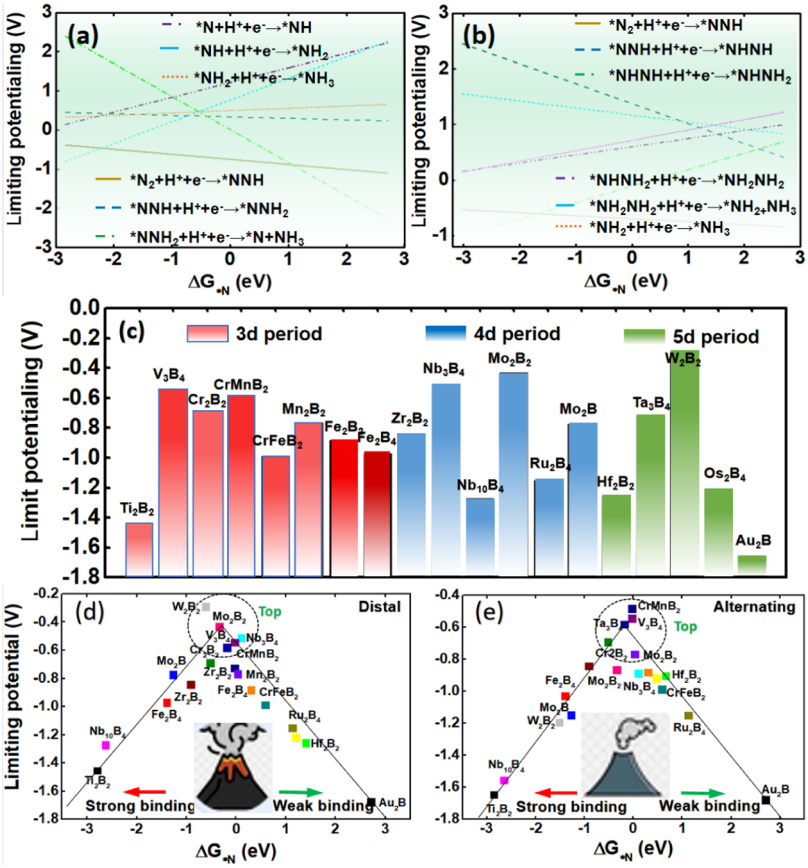

Figure 6. (a, b) Volcano plot for the NRR limiting potential of each elementary step as a function of the binding energy of *N. Each colored line denotes an elementary NRR reaction step. (c) Summary of limiting potentials on different MBenes for N_2 electroreduction to NH_3 along the most favorable reaction pathway. (d) NRR volcano plot of MBenes with a descriptor of ΔG_{*N} via the distal path, (e) NRR volcano plot of MBenes with a descriptor of ΔG_{*N} via the alternating path; the data points that stand near the top of the volcano plot are highlighted. The arrows to left presented strong adsorption of *N, and the arrows to right mean weak adsorption of *N.

Solution effects appear to strongly depend on the thickness of the 2D materials, so there are almost no contributions to the 2D materials studied in this work due to their relatively high thickness.[40] In Figure 5, the Gibbs free energy profile diagrams for N_2 electroreduction to NH_3 on Fe_2B_4, Hf_2B_2, Mo_2B, and Nb_3B_4 surfaces at zero potential and under an applied potential (U_L) are denoted by blue and red solid lines, respectively. Details of the free energy change of each elementary step on the MBenes are shown in Figures S1 and S2 (Supporting Information).

It is necessary to point out that $*NH_3$ can be further hydrogenated to NH_4^+ in an acidic environment; because the explicit solvation model has a large amount of calculation, it is difficult to obtain the reaction free energy for further hydrogenation of $*NH_3$ to be released to solution in the form of NH_4^+. Thus, suggesting that $*NH_3$ on the MBene surface may also be considered easily by forming NH_4^+ in solution, the experiments under acidic media would be helpful to production of $*NH_3$ to NH_4^+. Thus, NH_3 desorption may not be a problematic obstacle in NRR and it is not considered in our DFT calculations. The initial state (zero value) of the free energy profile is referenced to N_2 and H_2 in the gas phase, and the final state is referenced to NH_3 in the gas phase. The rate of the protonation step can be obviously influenced by the applied electrode potential due to electron−proton pair transfer. Thus, after potential is applied to the electrode, the Gibbs free energy change profile will significantly decrease, while the $*N_2$ and $*NH_3$ adsorption energies have no influence on the applied potential due to the lack of charge transfer in this process. In Figure 5, presenting the most favorable pathway on Fe_2B_4, Hf_2B_2, Mo_2B, and Nb_3B_4 as examples, the limiting potentials in the free energy diagram are −0.97 V, −0.77 eV, −0.78 V, and −0.50 eV, respectively. For Hf_2B_2, the $*N_2$ is adsorbed via a side-on binding configuration, the N−N bond is broken during the fourth protonation step ($*NH-NH_2$), and the *NH intermediate, the Hf_2B_2 MBene with an Hf metal active center, is formed. The RDS is the hydrogenation of $*N_2 \rightarrow *NNH$. For Mo_2B_2, Ti_2B_2, W_2B_2, and Nb_3B_4 with metal active centers, the limiting potentials are −0.43 V, −0.37 eV, −0.24 V, and −0.50 eV, respectively. For Mo_2B_2, Ti_2B_2, and Nb_3B_4, the rate-determining step is the first protonation step, and the protonation of $*NNH_2$ to yield $*NHNH_2$ for W_2B_2. Figure S3c,h illustrates an alternating pathway on Ru_2B_4 and $CrFeB_2$ as representatives. The breaking of the N−N bond occurs during the protonation of the $*NH_2-NH_2$ intermediate, and the rate-determining step is located at the first protonation step producing *NNH, involving limiting potentials of −1.15 and −0.99 V for TRu_2B_4 and $CrFeB_2$, respectively. The geometric structures (top views) of the corresponding NRR intermediates on Fe_2B_4, Hf_2B_2, Mo_2B, and Nb_3B_4 are displayed in Figure 5e−h.

Figure 6 presents a volcano plot of the limiting potential of the rate-determining step for the NRR,[42] which depends on the limiting potential of each elementary step as a descriptor of

https://doi.org/10.1021/acs.chemmater.1c00424
Chem. Mater. 2021, 33, 4023−4034

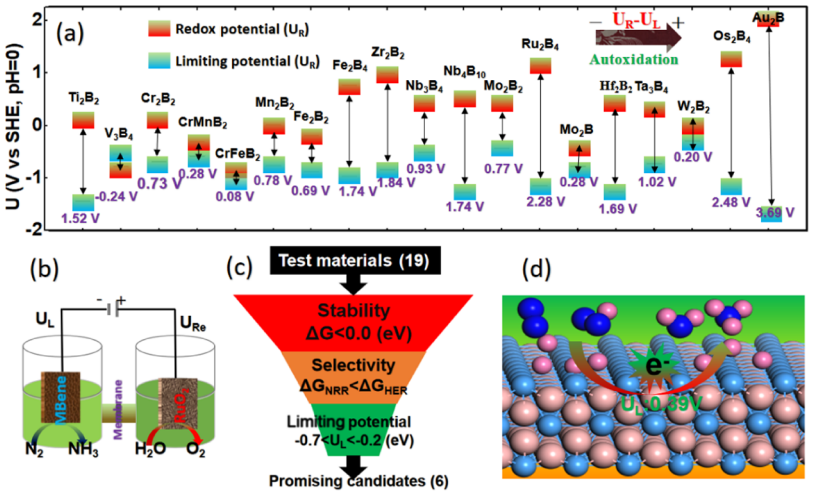

Figure 7. (a) Energy levels and their energy differences between the limiting potential (U_L) and redox potential (U_R) among 19 MBenes. (b) Illustration of the full electrochemical cell for NRR (cathode: MBenes) and OER (anode: RuO_2, as a reference electrode). (c) Illustration of the fully theoretical scanning process to search for high-activity and -selectivity catalysts for the NRR process. (d) Atomic structure schematic of the reaction process during N_2 reduction to NH_3.

ΔG_{*N} on all of the MBene systems. Fe_2B_4, Ru_2B_4, and Os_2B_4 MBenes with active boron centers have high limiting potentials (U_L) of −0.97 to −1.15 V and −0.88, while the other MBenes with active metal centers have larger U_L values of −0.78 to −0.20 V. In particular, $CrFeB_2$ and Au_2B have a U_L of less than −0.90 V. For comparison, previous work proposed single-atom catalysts, such as Mo atoms anchored on an h-BN monolayer (−0.35 V)[41] and the interfacing of graphene with hexagonal boron-nitride (h-BN) possessed with the low overpotential of 0.42 V for the NRR.[42] Herein, a volcano plot between the limiting potential of each elementary step and ΔG_{*N} can be established, as shown in Figure 6a,b. The different colored lines denote an elementary NRR, and the lowest lines (dark yellow) represent that this elementary step is the rate-determining step of the NRR process. Thus, this provides a clear explanation for the first hydrogenation step ($*N_2 \rightarrow *NNH$) or the third hydrogenation step (*N or $*NHNH_2$ formation) always being the rate-determining step for NRR. The optimal ΔG_{*N} is approximately −0.52 eV, where the liming potential is approximately −0.69 V, which indicates that NRR activity may be evaluated by ΔG_{*N}, and ΔG*N can further provide a new route to design catalysts. Cr_2B_2 (−0.69 V), Mo_2B_2 (0.43 V), Ta_3B_4 (−0.39 V), and Zr_2B_2 (0.84 V) are close to the top of the volcano plot, and such low limiting potentials suggest that these MBenes can be promising candidates for NRR. As seen in Figure 6c, the U_L maximum values from the left to right in 3d period V_3B_4 (−0.54 V), 4d period Mo_2B_2 (−0.43 V), and 5d period W_2B_2 (−0.24 V) exhibit high catalytic activity for NRR. In addition, a volcano plot of the limiting potential on MBenes is established in Figure 6d (distal) and Figure 6e (alternating), where Mo_2B_2, V_3B_4, and W_2B_2 stand near the top of the volcano peak via the distal path, while $CrMnB_2$, V_3B_4, and Ta_3B_4 are located on top of the volcano peak via the alternating path. Furthermore, the excessively strong binding of *N leads to the large limiting potential for the step from $*N_2$ to *NNH, whereas weak binding leads to a rate-determining step (PDS) from $*NH_2$ to $*NH_3$, and the candidates are located near the promising zone ($-0.70\ V < U_L < 0.20\ V$). As a result, the weak adsorption of *N ($\Delta G_{*N} > 1.20$ eV) leads to the PDS of $*NNH_2 + H^+ + e^- \rightarrow *N + *NH_3$ (green line) with low limiting potentials, the excessively strong binding of *N ($\Delta G_{*N} < -2.10$ eV) leads to the PDS of $*NH + H^+ + e^- \rightarrow *NH_2$ (cyan line) with low limiting potentials, and the moderate ΔG*N value of ($-0.90\ V < U_L < 0.58\ V$) can guarantee that the binding strength of *N is neither too strong nor too weak and helps obtain high activity toward NRR on the MBene surfaces. Among these 19 MBenes, W_2B_2 has the highest limiting potential.

In Figure 7a, under an applied electrode potential, the water oxidation reaction (WOR) is gradually favorable on the anode (taking RuO_2 as the reference electrode), and the redox potential (U_R) is defined as the potential required to remove the surface O*/OH* species, which suggests the following order: $Au_2B > Os_2B_4 > Ru_2B_4 > Zr_2B_2 > Fe_2B_4 > Nb_4B_{10} > Nb_3B_4 > Hf_2B_2 > Mo_2B_2 > Ta_3B_4 > Ti_2B_2 > Cr_2B_2 > W_2B_2 > Fe_2B_2 > CrMnB_2 > Cr_2B_2 > Mo_2B > V_3B_4 > Cr_{Fe}B_2$. Thus, when considering the redox potential in the reaction potential, the potential difference between $U_R(+)$ and $U_L(-)$ can be used as a descriptor to evaluate the N_2 reduction activity of these 19 MBenes. A more positive value of $U_R - U_L$ suggests a higher ability to promote surface reduction. The computed $U_R - U_L$ values for all MBene monolayers are positive without V_3B_4, suggesting that our candidate MBenes could facilitate surface reduction. The desired NRR with the MBene cathode in the whole electrochemical cell is illustrated in Figure 7b. NRR occurs at the cathode and is accompanied by OER at the anode. A fully theoretical screening workflow process (Figure 7c) depends on the following three criteria: (i) structural stability ($\Delta G < 0$ eV), (ii) selectivity ($\Delta G_{NRR} < \Delta G_{HER}$), and (iii) limiting potential (RDS). Nineteen MBene materials with negative formation energies, which were confirmed by phonon band structures, are shown in Figure S7 and should possess high thermodynamic stability and feasibility. The next criterion is $\Delta G_{NRR} < \Delta G_{HER}$, which guarantees the suppression of HER during the NRR process with the high selectivity of NRR, and the $\Delta G(*N_2)$ values should be much lower than the ΔG(*H) values of the competing hydrogen evolution reaction (HER), and N_2 should be sufficiently activated with $\Delta G(*N_2) < -0.20$ eV. By examining the 19 MBenes, Fe_2B_4, Mo_2B, Ru_2B_4, Os_2B_4, Zr_2B_2, and Ti_2B_2 have negative ($\Delta G_{NRR} - \Delta G_{HER}$) values, indicating their low selectivity toward NRR, whereas the other 12 MBenes have positive ($\Delta G_{NRR} - \Delta G_{HER}$) values.

https://doi.org/10.1021/acs.chemmater.1c00424
Chem. Mater. 2021, 33, 4023−4034

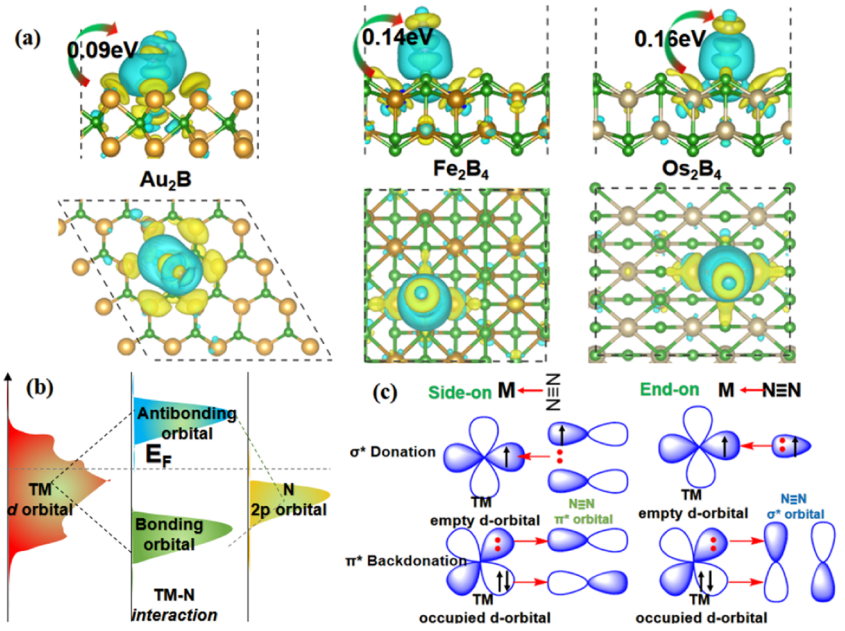

Figure 8. (a) Charge density differences and the values of Bader charge transfer of N_2 adsorbed on Au_2B, Fe_2B_4, and Os_2B_4 via the end-on pattern. The isosurface value is set to 0.005 e/Å^3. (b) Schematic illustrating the transition-metal centers of MBenes how interact with *N. (c) Schematic of the N_2 molecule activation mechanism to transition metals for both side-on and end-on binding configurations.

Furthermore, the last criterion is the limiting RDS potential. With a greater limiting potential and better catalytic activity (-0.7 V < U_L < -0.2 V), to guarantee low energy cost, the U_L of the rate-determining step should be as low as possible (the best catalyst is W_2B_2 MBene). Based on these criteria, Nb_3B_4, Ta_3B_4, $CrMnB_2$, Mo_2B_2, Ti_2B_2, and W_2B_2 are singled out as candidate catalysts for NRR. Figure 7d suggests that the Ta_3B_4 monolayer has promising catalytic activity to reduce N_2 to NH_3 with a limiting potential value of -0.39 eV. The Ta transition-metal atom is the catalytic activity center and acts as a reaction generator, and the Ta metal atom exchanges electrons with N_2 as the acceptance−donation pattern.[43]

The interaction mechanism between MBenes and N_2 can be evaluated depending on the differential charge density distribution shown in Figures 8a and S5 (Supporting Information). The differential charge density is calculated using the following equation[44]

$$\Delta\rho = \rho(\text{MBene@N}_2) - \rho(\text{MBene}) - \rho(\text{N}_2)$$

the yellow color indicates electron accumulation on the MBene, and the cyan color represents electron depletion of the N_2 molecule, which means electron transfer (donation) from the s orbital of N_2 to the d orbital of metal on MBenes, while electrons are transferred from the s orbital of the MBene metal to the antibonding p* orbital of N_2 (backdonation), exhibiting electron accumulation on the N_2 molecule and depletion on the catalytic active sites (Au_2B). By Bader charge analysis, 0.09e$^-$ is transferred from Au_2B to *N_2, and Au atoms exhibit a positive charge, which leads to N_2 adsorption being preferred. Bader charge analysis revealed that the positive charges were +0.14e$^-$ and +0.16e$^-$ for Ru_2B_4 and Os_2B_4, respectively. However, the active boron surface induces a significant charge transfer between the adjacent metal atoms and the active catalytic active site (B) upon N_2 adsorption (Fe_2B_4 and Os_2B_4), and the amount and direction of charge transfer between the nitrogen and MBenes in the N_2 adsorption process are also shown in Figures 8a and S5. The electron-transfer processes would be more favorable on active boron surfaces than active metal surfaces, and the outermost B and metal atoms can cooperatively act as electron donors, which enhances the adaptability for accepting or donating with the NRR intermediates. It is beneficial to reduce the applied potential of the NRR. In Figure 8b, taking *N as an example, the d orbital of the transition metals interacts with the 2p orbital of *N intermediates, and the d orbital of the transition-metal energy levels split into two groups with the 2p orbital of *N: one group is the antibonding orbital (above the Fermi level) and the other group is the s bonding orbital (below the Fermi level) with the bonding states occupied below the Fermi level (E_F) and the antibonding orbital above E_F.[46] *N interacts with the MBenes via the so-called acceptance−donation process, the unoccupied d orbitals of the metal atom accept the lone-pair electrons from the *N intermediate, and the occupied d orbitals of the metal atoms simultaneously backdonate electrons into the π^* antibonding orbitals of N_2, which is termed as π backdonation. Generally, a greater degree of electron transfer from active sites to N_2 results in better N_2 activation, and strong d−π^* coupling can activate the adsorbed N_2 for hydrogenation. The lone-pair electrons of the N atom lead to special orbital occupation overlap between the N_2 and d orbitals of the metal, which leads to strong head-to-head overlap on the MBene, as shown in Figure 8c. For the side-on N_2 adsorption configuration, the occupied σ bonding orbital of N_2 molecules interacts with the empty d−d orbital of the metal and then forms π bonds between N_2 and metal to act as π donations. In general, π bonding is stronger than σ bonding such that π bonding between N_2 and MBene can activate the N≡N triple bond.[45] For the end-on N_2 binding configuration, only one N atom interacts with transition-metal atoms to form a strong σ bond that acts as σ donation. Because the σ bond is stronger than the π bond, N_2 end-on adsorption is stronger than N_2 side-on adsorption.

To further explore the reaction mechanism, we established the electronic structure and PDOS of the MBenes, and these

https://doi.org/10.1021/acs.chemmater.1c00424
Chem. Mater. 2021, 33, 4023−4034

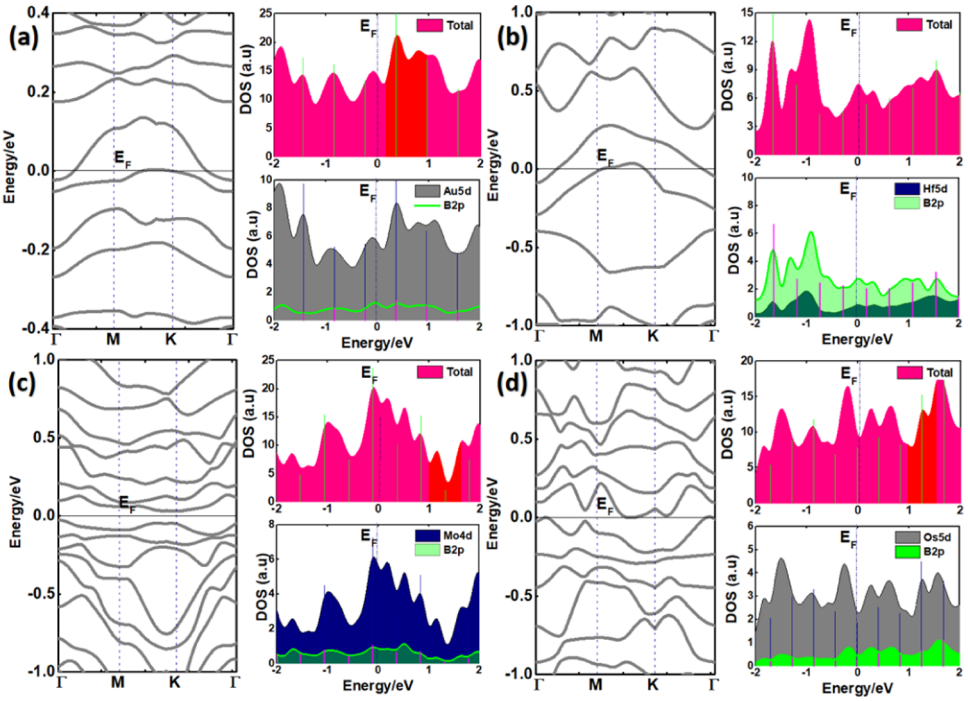

Figure 9. Calculated band structure and PDOS of MBenes (a) Au_2B, (b) Hf_2B_2, (c) Mo_2B, and (d) Os_2B_4. The solid black and blue dashed lines indicate the Fermi level and high-symmetry points in the Brillouin zone, respectively.

are shown in Figures 9 and S6 (Supporting Information).[46] We present the electronic band structures and corresponding partial density of states (PDOS) of the four MBene ground states that were used to investigate the electronic structure in more detail. Our calculations demonstrate that all MBenes have metallic features without band gaps, the band structures are significantly different, and the major contributions are dominated by the d orbital band states of transition-metal atoms.[47] In Figure 9d, the contribution of B 2p orbitals between −2 and 2 eV is very small for Os_2B_4, which shows that the metallic feature is derived from metal d states and boron p states overlapped by orbital hybridization near the Fermi energy. In more detail, the valence band below the Fermi level is mainly attributed to the hybridization of the occupied metal d orbital with unoccupied B p orbital states and represents the formation of TM-B chemical bonds. While the conduction bands above the Fermi level are primarily composed of unoccupied M s states and occupied B p orbital states, an antibonding orbital (π* orbital) is formed, and the metallic and strong electron donation features of MBene are beneficial for designing electrocatalysts for NRR.[48] The PDOS of Au_2B in Figure 9a shows that the bonding combinations of hybridized B 2p orbitals overlapped with Au 5d orbitals is very small, which leads to a weak polar covalent. These orbitals contribute weakly to the π orbital of $*N_2$. The band structures and partial density of states (PDOS) suggest that the chemical bonding between metal and boron atoms is a mixture of covalent and metallic features.[49] The superior conductivity of the catalyst will be crucial to guarantee electron-transfer efficiency during electrochemical reactions. In this case, the electronic properties of Ta_3B_4 (Figure S6b) and V_3B_4 (Figure S6c) are shown. The total density of states (TDOS) and projected density of states (PDOS) of Ta_3B_4 and V_3B_4 exhibit metallic conductivity with a continuum of energy states across the Fermi energy.[50] Hybridized B 2p states overlap with Ta 4d states dramatically in the Fermi level, leading to a strong polar covalent, which contributes weakly to the π orbital of $*N_2$ by E_{ads} of 0.45 eV. Furthermore, Mo_2B, Ru_2B_4, and V_3B_4 are metallic, and the metallic conductivity of these studied MBene materials is mainly contributed by the d orbitals of the transition metal near the Fermi levels. Because the binding energy of the intermediate is strongly dependent on the occupied and unoccupied d band states of surface transition-metal atoms. Thus, the density of states (DOS) combined with the crystal orbital Hamilton population (COHP) analysis showed that under $*N_2$ adsorption, the strongly polarized d orbitals of the metal atom can provide a great contribution to the binding energy of $*N_2$ (Figure S9), shifting the molecular orbitals of $*N_2$ to the lower energy level and resulting in strong bonding, which leads to the different couplings with the NRR intermediate species (Figure S10).[35] So, as the d orbitals shift toward the Fermi level, the metal atoms can provide more unoccupied d band states to accept the electrons transferred from *NNH, which facilitates the *NNH adsorption and further hydrogenation. Furthermore, we also considered the strong spin−orbit coupling (SOC) effect of 2D MBenes, indicating that $\Delta G(*N_2)$ with the SOC effect is greater than the value without the SOC effect for some special 2D catalysts that contain heavy elements and have less effect on the M−N bond (Figure S11);[51] this also provides some guidelines for the further design of ideal 2D catalysts.

CONCLUSIONS

In summary, a theoretical screening approach was implemented to evaluate the catalytic activity of transition-metal boride (MBene) in electrochemical NRR, and the activity and selectivity for NRR depend on a high positive U_L ($*N_2$−$*H_2$) value with a low limiting potential (U_L) at PDS. Based on three criteria for the screening strategy, Ta_3B_4, Nb_3B_4, $CrMnB_2$, Mo_2B_2, Ti_2B_2, and W_2B_2 exhibit the lowest limiting potential

https://doi.org/10.1021/acs.chemmater.1c00424
Chem. Mater. 2021, 33, 4023−4034

among the 19 MBene systems, and N_2 is more activated via the end-on than side-on pattern, which suggests that these MBenes can be promising candidate catalysts for NRR and can activate N_2 molecules to protonate. Furthermore, enzymatic and mixed mechanism paths are found to be more favorable. The limiting potential for NRR on MBenes ranges from −0.7 to −0.2 V, which can guarantee low energy costs, such as in the case of Nb_3B_4 (−0.50 V), Ta_3B_4 (0.39 V), and Mo_2B_2 (−0.43 V). W_2B_2 has a low energy cost and high selectivity in the NRR/HER competing process, and the limiting potential for NRR is as low as −0.24 V. According to the volcano plot, the strong binding energy of *N leads to an RDS from $*N_2$ to *NNH, while weak binding leads to an RDS from the last hydrogenation step ($*NH_2$ to $*NH_3$). In this regard, moderate binding of *N and interaction with MBenes act as electron donation. The redox potential (U_R) is defined as the potential that reduces O*/OH* to H_2O, which suggests that a more positive $U_R - U_L$ value results in a greater ability to arrest surface oxidation, making NRR favorable on our considered MBene surfaces. Analysis of the charge density difference distribution and charge transfer indicated significant charge transfer between the metal atoms (active site) and N_2 molecules. According to the interaction mechanism between MBene and *N, the bonding states occupy below the Fermi level and the antibonding orbital occupy above the Fermi level, making the bound N_2 more favorable and leading to large overlap states between the transition metal and $*N_2$. Our study provides an effective approach to design high-performance catalysts for NRR under simulated environmental conditions and provides guidance for experiments in designing and developing catalysts for N_2 fixation.

■ ASSOCIATED CONTENT

Supporting Information

The Supporting Information is available free of charge at https://pubs.acs.org/doi/10.1021/acs.chemmater.1c00424.

Gibbs free energy diagrams of intermediate species NRR pathways (Figures S1 and S2), Gibbs free energy profiles along the most favorable reaction mechanism for NRR on MBenes (Figures S3 and S4), calculated charge-transfer process for MBenes (Figure S5), electronic band structure of MBenes (Figure S6), calculated phonon band structures of given MBenes (Figure S7), possible surface configurations for adsorbates (Figure S8), DOS and COHP for N_2H* adsorption (Figure S9), calculated adsorption free energy of $*N_2$($\Delta G*N_2$) and bond length (M−N) with and without consideration of SOC (Figure S10), free energy correction terms (Table S1), and Gibbs free energies at 298.15 K of the different states (Table S2) (PDF)

■ AUTHOR INFORMATION

Corresponding Authors

Yi Xiao − *Institute of Materials Science, TU Darmstadt, 64287 Darmstadt, Germany;* orcid.org/0000-0001-6318-8010; Email: yixiao@tmm.tu-darmstadt.de

Chen Shen − *Institute of Materials Science, TU Darmstadt, 64287 Darmstadt, Germany;* orcid.org/0000-0002-8538-9873; Email: chenshen@tmm.tu-darmstadt.de

Author

Teng Long − *Institute of Materials Science, TU Darmstadt, 64287 Darmstadt, Germany*

Complete contact information is available at: https://pubs.acs.org/10.1021/acs.chemmater.1c00424

Notes

The authors declare no competing financial interest.

■ ACKNOWLEDGMENTS

This work received financial support from the China Scholarship Council (CSC, 201808440416) of China and Hessen State Ministry of Higher Education, Research and the Arts (HMWK) in Germany; the Lichtenberg high performance computer is gratefully acknowledged, and the authors are also thankful to TU Darmstadt.

■ REFERENCES

(1) Saadatjou, N.; Jafari, A.; Sahebdelfar, S. Ruthenium nanocatalysts for ammonia synthesis: a review. *Chem. Eng. Commun.* **2015**, *202*, 420−448.

(2) Van der Ham, C. J. M.; Koper, M. T. M.; Hetterscheid, D. G. H. Challenges in reduction of dinitrogen by proton and electron transfer. *Chem. Soc. Rev.* **2014**, *43*, 5183−5191.

(3) Bouwman, A. F.; Boumans, L. J. M.; Batjes, N. H. Estimation of global NH_3 volatilization loss from synthetic fertilizers and animal manure applied to arable lands and grasslands. *Global Biogeochem. Cycles* **2002**, *16*, 8-1−8-14.

(4) Vitousek, P. M.; Cassman, K. E. N.; Cleveland, C. et al. Towards an Ecological Understanding of Biological Nitrogen Fixation. In *The Nitrogen Cycle at Regional to Global Scales*; Springer: Dordrecht, 2002; pp 1−45.

(5) Dixon, R.; Kahn, D. Genetic regulation of biological nitrogen fixation. *Nat. Rev. Microbiol.* **2004**, *2*, 621−631.

(6) Erisman, J. W.; Sutton, M. A.; Galloway, J.; et al. How a century of ammonia synthesis changed the world. *Nat. Geosci.* **2008**, *1*, 636−639.

(7) Soloveichik, G. Electrochemical synthesis of ammonia as a potential alternative to the Haber−Bosch process. *Nat. Catal.* **2019**, *2*, 377−380.

(8) Smith, C.; Hill, A. K.; Torrente-Murciano, L. Current and future role of Haber−Bosch ammonia in a carbon-free energy landscape. *Energy Environ. Sci.* **2020**, *13*, 331−344.

(9) Peng, P.; Chen, P.; Schiappacasse, C.; et al. A review on the non-thermal plasma-assisted ammonia synthesis technologies. *J. Cleaner Prod.* **2018**, *177*, 597−609.

(10) Sánchez, A.; Martín, M. Optimal renewable production of ammonia from water and air. *J. Cleaner Prod.* **2018**, *178*, 325−342.

(11) Ling, C.; Niu, X.; Li, Q.; et al. Metal-free single atom catalyst for N_2 fixation driven by visible light. *J. Am. Chem. Soc.* **2018**, *140*, 14161−14168.

(12) Xue, Z.; Zhang, X.; Qin, J.; et al. High-throughput identification of high activity and selectivity transition metal single-atom catalysts for nitrogen reduction. *Nano Energy* **2021**, *80*, No. 105527.

(13) Ao, K. L.; Shao, Y.; Chan, I. N.; et al. Design of novel pentagonal 2D transitional-metal sulphide monolayers for hydrogen evolution reaction. *Int. J. Hydrogen Energy* **2020**, *45*, 16201−16209.

(14) Jain, A.; Wang, Z.; Nørskov, J. K. Stable two-dimensional materials for oxygen reduction and oxygen evolution reactions. *ACS Energy Lett.* **2019**, *4*, 1410−1411.

(15) Xiao, Y.; Zhang, W. High throughput screening of M_3C_2 MXenes for efficient CO_2 reduction conversion into hydrocarbon fuels. *Nanoscale* **2020**, *12*, 7660−7673.

(16) Li, L.; Wang, X.; Guo, H.; et al. Theoretical screening of single transition metal atoms embedded in MXene defects as superior electrocatalyst of nitrogen reduction reaction. *Small Methods* **2019**, *3*, No. 1900337.

(17) Guo, Z.; Zhou, J.; Sun, Z. New two-dimensional transition metal borides for Li ion batteries and electrocatalysis. *J. Mater. Chem. A* **2017**, *5*, 23530−23535.
(18) Jiang, Z.; Wang, P.; Jiang, X.; et al. MBene (MnB): a new type of 2D metallic ferromagnet with high Curie temperature. *Nanoscale Horiz.* **2018**, *3*, 335−341.
(19) Jiang, Z.; Wang, P.; Xing, J.; et al. Screening and design of novel 2D ferromagnetic materials with high Curie temperature above room temperature. *ACS Appl. Mater. Interfaces* **2018**, *10*, 39032−39039.
(20) Ling, C.; Ouyang, Y.; Li, Q.; et al. A General two-step strategy−based high-throughput screening of single atom catalysts for nitrogen fixation. *Small Methods* **2019**, *3*, No. 1800376.
(21) Yang, T.; Song, T. T.; Zhou, J.; et al. High-throughput screening of transition metal single atom catalysts anchored on molybdenum disulfide for nitrogen fixation. *Nano Energy* **2020**, *68*, No. 104304.
(22) Chen, H.; Cai, R.; Patel, J.; et al. Upgraded bioelectrocatalytic N_2 fixation: from N_2 to chiral amine intermediates. *J. Am. Chem. Soc.* **2019**, *141*, 4963−4971.
(23) Zhang, Z. M.; Yao, X.; Lang, X. Y.; et al. W-N3 center supported on blue phosphorus as a promising efficient electrocatalyst with ultra-low limiting potential for nitrogen fixation. *Appl. Surf. Sci.* **2021**, *536*, No. 147706.
(24) Sun, G.; Kürti, J.; Rajczy, P.; et al. Performance of the Vienna ab initio simulation package (VASP) in chemical applications. *J. Mol. Struct.: THEOCHEM* **2003**, *624*, 37−45.
(25) Kresse, G.; Joubert, D. From ultrasoft pseudopotentials to the projector augmented-wave method. *Phys. Rev. B* **1999**, *59*, 1758−1775.
(26) Perdew, J. P.; Burke, K.; Ernzerhof, M. Generalized gradient approximation made simple. *Phys. Rev. Lett.* **1996**, *77*, 3865−3868.
(27) Siddiqui, O.; Dincer, I. A new solar energy system for ammonia production and utilization in fuel cells. *Energy Convers. Manage.* **2020**, *208*, No. 112590.
(28) Ehrlich, S.; Moellmann, J.; Reckien, W.; et al. System-Dependent Dispersion Coefficients for the DFT-D3 Treatment of Adsorption Processes on Ionic Surfaces. *ChemPhysChem* **2011**, *12*, 3414−3420.
(29) Kannike, K. Vacuum stability conditions from copositivity criteria. *Eur. Phys. J. C* **2012**, *72*, 1−7.
(30) Pinna, F. In *VESTA Toolkit: A Software to Compute Transition and Stability of Boundary Layers*, 43rd AIAA Fluid Dynamics Conference, San Diego, CA, USA, 24−27 June 2013; AIAA 2013-2616.
(31) Deák, P.; Aradi, B.; Frauenheim, T.; et al. Accurate defect levels obtained from the HSE06 range-separated hybrid functional. *Phys. Rev. B* **2010**, *81*, No. 153203.
(32) Maintz, S.; Deringer, V. L.; Tchougréeff, A. L.; et al. LOBSTER: A tool to extract chemical bonding from plane-wave based DFT. *J. Comput. Chem.* **2016**, 1030−1035.
(33) Hammer, B.; Nørskov, J. K. Electronic factors determining the reactivity of metal surfaces. *Surf. Sci.* **1995**, *343*, 211−220.
(34) Watson, C. I.; Wilson, C. L. NIST special database 4. *Fingerprint Database, Natl. Inst. Stand. Technol.* **1992**, *17*, 5.
(35) Guo, X.; Lin, S.; Gu, J.; et al. Establishing a Theoretical Landscape for Identifying Basal Plane Active 2D Metal Borides (MBenes) toward Nitrogen Electroreduction. *Adv. Funct. Mater.* **2020**, No. 2008056.
(36) Niu, H.; Wang, X.; Shao, C.; et al. Computational Screening Single-Atom Catalysts Supported on g-CN for N_2 Reduction: High Activity and Selectivity. *ACS Sustainable Chem. Eng.* **2020**, *8*, 13749−13758.
(37) Choi, C.; Back, S.; Kim, N. Y.; et al. Suppression of hydrogen evolution reaction in electrochemical N_2 reduction using single-atom catalysts: a computational guideline. *ACS Catal.* **2018**, *8*, 7517−7525.
(38) Huang, C. X.; Li, G.; Yang, L. M.; et al. Ammonia Synthesis Using Single-Atom Catalysts Based on Two-Dimensional Organo-metallic Metal Phthalocyanine Monolayers under Ambient Conditions. *ACS Appl. Mater. Interfaces* **2021**, *13*, 608−621.
(39) Guo, H.; Li, L.; Wang, X.; et al. Theoretical investigation on the single transition-metal atom-decorated defective MoS2 for electrocatalytic ammonia synthesis. *ACS Appl. Mater. Interfaces* **2019**, *11*, 36506−36514.
(40) Qian, Y.; Liu, Y.; Zhao, Y.; et al. Single vs double atom catalyst for N_2 activation in nitrogen reduction reaction: A DFT perspective. *EcoMat* **2020**, *2*, No. e12014.
(41) Ma, Z.; Cui, Z.; Xiao, C.; et al. Theoretical screening of efficient single-atom catalysts for nitrogen fixation based on a defective BN monolayer. *Nanoscale* **2020**, *12*, 1541−1550.
(42) Huang, Y.; Yang, T.; Yang, L.; et al. Graphene−boron nitride hybrid-supported single Mo atom electrocatalysts for efficient nitrogen reduction reaction. *J. Mater. Chem. A* **2019**, *7*, 15173−15180.
(43) Li, M.; Cui, Y.; Zhang, X.; et al. Screening a Suitable Mo Form Supported on Graphdiyne for Effectively Electrocatalytic N_2 Reduction Reaction: From Atomic Catalyst to Cluster Catalyst. *J. Phys. Chem. Lett.* **2020**, *11*, 8128−8137.
(44) Zheng, S.; Li, S.; Mei, Z.; et al. Electrochemical nitrogen reduction reaction performance of single-boron catalysts tuned by MXene substrates. *J. Phys. Chem. Lett.* **2019**, *10*, 6984−6989.
(45) Zhang, W.; Xiao, Y. Mechanism of electrocatalytically active precious metal (Ni, Pd, Pt, and Ru) complexes in the graphene basal plane for ORR applications in novel fuel cells. *Energy Fuels* **2020**, *34*, 2425−2434.
(46) Ma, B.; Peng, Y.; Ma, D.; et al. Boron-doped InSe monolayer as a promising electrocatalyst for nitrogen reduction into ammonia at ambient conditions. *Appl. Surf. Sci.* **2019**, *495*, No. 143463.
(47) Chen, R.; Chen, D.; Xiao, Y. Theoretical Scanning of Bimetallic Alloy for Designing Efficient N_2 Electroreduction Catalyst. *Mater. Today Energy* **2021**, No. 100684.
(48) Nazemi, M.; Panikkanvalappil, S. R.; El-Sayed, M. A. Enhancing the rate of electrochemical nitrogen reduction reaction for ammonia synthesis under ambient conditions using hollow gold nanocages. *Nano Energy* **2018**, *49*, 316−323.
(49) Xiao, Y.; Tang, L. High-throughput approach exploitation: Two-dimensional double-metal sulfide (M_2S_2) of efficient electrocatalysts for oxygen reduction reaction in fuel cells. *Energy Fuels* **2020**, *34*, 5006−5015.
(50) Xiao, Y.; Chen, D.; Chen, R. Mechanistic Study of Efficient Producing CO_2 Electroreduction via 2D Metal-Organic Frameworks M_3(2, 3, 6, 7, 10, 11-hexaiminotriphenylene)$_2$ Surface. *Electrochim. Acta* **2021**, No. 138028.
(51) Wang, Y.; Zhu, X.; Li, Y. Spin−orbit coupling-dominated catalytic activity of two-dimensional bismuth toward CO_2 electroreduction: not the thinner the better. *J. Phys. Chem. Lett.* **2019**, *10*, 4663−4667.

https://doi.org/10.1021/acs.chemmater.1c00424
Chem. Mater. 2021, 33, 4023−4034

NANO · MICRO small
www.small-journal.com

Transition-Metal Borides (MBenes) as New High-Efficiency Catalysts for Nitric Oxide Electroreduction to Ammonia by a High-Throughput Approach

Yi Xiao and Chen Shen*

Here, the authors performed density functional theory calculations to study the catalytic performance of the nitric oxide reduction reaction (NORR) via a series of transition metal borides (MBenes). This work screened the M_2B_2 type MBenes from the IVB to V transition metals from the periodic table and systematically probed the catalytic activity and selectivity for the NORR process. It has been reported that Fe_2B_2, Mn_2B_2, and Rh_2B_2 can be high-performance catalysts for converting NO to NH_3 with smaller limiting potentials than other MBenes, and Nb_2B_2 and Hf_2B_2 have low limiting potentials of −0.11 V and −0.17 V for the NO production of NH_3. The binding energy of ΔG*N can be a good descriptor of catalytic performance and is determined by the volcano plot of the rate-determining step. The reaction mechanisms for NO reduction to NH_3, N_2, and N_2O have been studied in detail, atomic *N can interact with another *N or one *NO molecule to form N_2 and N_2O via two successive hydrogenations. In this regard, *NO hydrogenation to *NOH has a lower formation energy than *HNO, and the MBenes have high selectivity for promoting the NORR and suppressing the hydrogen evolution reaction competition process.

1. Introduction

Recently, nitric oxide (NO) has been a common pollutant produced in the emitted waste gases of vehicles and fossil fuel combustion.[1,2] An increased concentration of nitrogen oxides in the atmosphere will lead to a series of serious environmental problems, including water pollution and air contamination, and cause severe human health problems.[3,4] Thus, limiting the emission of NO and environmental cleaning have become the most important tasks in contemporary society. The development of highly efficient, economical, and environmentally friendly catalysts for NO conversion to pollution-free products has become increasingly urgent, and it has recently been confirmed that the efficient performance of ammonia formation can be achieved via the NO electroreduction reaction (NORR).[5,6] Moreover, the NORR is identified as an effective method to convert NO into harmless (NH_3) sources or pollution-free products (N_2) during the nitrogen cycle.[7,8] Recently, Bo et al.[9] expected that Ti_2B_2 MBene is thermally stable and has excellent electronic conductivity as an anode material for Li-ion and Na-ion batteries. Yuan et al.[10] reported that FeB_2 and MnB_2 have a low limiting potential for the selective conversion of CO_2 to CH_4. Recent work reported that TiB monolayers have been synthesized experimentally, suggesting that TiB can be a promising catalyst for the hydrogen evolution reaction (HER).[11] A competitive route to the production of ammonia (NH_3) from the NORR has been extensively studied. Currently, some renewable energy sources (such as NH_3 or N_2) are formed after five proton–electron pairs are transferred via new 2D MBene materials. These MBenes are constructed between the transition metal and boron because boron is an electron-deficient atom and can form a stabilized structure with transition metals via covalent bonds.[12,13] As an emerging new type of 2D material, MBene is similar to transition metal carbide or nitride (MXene), but these MBenes have many unknown physical and chemical properties when used as efficient and highly selective NO electroreduction catalysts.[14] A high-throughput screening approach provides a high-efficiency and economical platform to study NO reduction to NH_3 or N_2 reaction pathways after the high-throughput screening of all transition metals and verification of twelve stable 2D M_2B_2 type MBenes.[15] All stable M_2B_2 monolayers display excellent activation of NO molecules and selectivity toward the production of NH_3. Although some MBene compounds have not yet been synthesized experimentally, theoretical predictions have verified that some MBenes can be electrochemical catalysts by theoretical studies.[16] Therefore, a large number of theoretical studies have reported that Pt(100) is suitable for the reaction of NO reduction to NH_3, which is more difficult than N_2 and N_2O formation.[17] However, NORR studies are mainly focused on metal-based catalysts and single atom catalysts, but these catalysts usually face poor stability and require a high working potential during the NORR process. To further explore the feasible catalytic mechanism of the NORR on M_2B_2 MBenes, density functional theory (DFT) calculations were carried out, and our study showed considerable feasibility for the NORR via the MBene surface.[18]

Dr. Y. Xiao, Dr. C. Shen
Institute of Materials Science
TU Darmstadt
64287, Darmstadt Germany
E-mail: yixiao@tmm.tu-darmstadt.de

The ORCID identification number(s) for the author(s) of this article can be found under https://doi.org/10.1002/smll.202100776.

DOI: 10.1002/smll.202100776

Our theoretical calculation results reveal that a highly efficient NORR toward NH_3 can be achieved on Hf_2B_2, Nb_2B_2, Ta_2B_2, Ti_2B_2, and Zr_2B_2, with relatively low limiting potentials of –0.17, –0.11, –0.01, –0.16, and –0.25 eV, respectively. Furthermore, they also demonstrated small limiting potentials for the formation of byproducts (such as N_2O and N_2) on other MBene compounds. This work provides a new route to screening high-efficiency catalysts for the development of NORR. A volcano plot provides an efficient approach to explore promising candidate catalysts and reaction mechanisms,[19,20] and volcano plots can be constructed by limiting the potential and determining the rate determining step (RDS). For example, the formation of different intermediates and establishment of the most preferable reaction path have been obtained from DFT studies. Yao et al. reported that Re and Os embedded into $Mo_2B_2O_2$ MBene for the electrocatalytic conversion of N_2 to NH_3 possess promising catalytic activity with relatively low potential determining steps (PDSs) of 0.29 and 0.32 eV, respectively.[21] First-principles DFT with a computational hydrogen electrode (CHE) model was executed to explore the catalytic activity and selectivity of transition metals for NORR.[22,23] These results indicate that the M_2B_2 MBene monolayer can efficiently promote NO activation and reduction to NH_3 and N_2 through distal, alternating, and enzymatic pathways. First, we assume the entire route reaction network, considering the detailed binding properties of intermediate species and the corresponding limiting potentials of elementary reaction steps, and then, the most favorable pathway and RDS will be confirmed.[24] The competitive HER was also considered and compared on the MBene catalysts, and it was found that most of these MBene candidates have high selectivity for the NORR except for Ti_2B_2, V_2B_2, and Zr_2B_2. We also evaluated the electronic properties, studied the electron transfer processes of this new class of 2D materials for NORR and compared them with 2D MXenes.

2. Computational Details

All first principles DFT calculations were executed within the Vienna ab initio simulation package (VASP).[25,26] The projector augmented-wave (PAW) potentials were adopted to describe the electron correlation interactions,[27] and the Perdew, Burke, and Ernzerhof (PBE) within the generalized gradient approximation (GGA) approach was employed.[28] The MBene surface was modeled by a supercell with a (2 × 2) unit cell, and a vacuum of 20 Å along the *z*-direction was used to avoid the interactions between the periodic boundary conditions. The stabilities of the M_2B_2 monolayers were authenticated by their phonon band structures within the Phonopy code.[29] On the plane-wave basis of electron convergence with an energy cutoff of 500 eV, the convergence criteria for force and energy were set to 0.02 eV $Å^{-1}$ and 10^{-6} eV of the total energy with respect to the calculation accuracy, respectively.[30] The Brillouin zone (BZ) of the supercell was sampled with a 5 × 5 × 1 Monkhorst Pack and 10 × 10 × 1 k-point meshes for structure optimization self-consistency and electronic property calculations, respectively.[31] Charge density differential distribution[32] analysis was applied to investigate the electron transfer between NORR adsorbates and MBenes, and the visualization of the charge density difference was executed in VESTA code.[33] To consider the van der Waals (vdW) interactions, the DFT-D3 approach was executed to correct the dispersion interaction.[34] The correction term of the Gibbs free energy change (ΔG) under standard conditions (298.15 K and 0.1 MPa) was employed in the computational hydrogen electrode (CHE) model suggested by Nørskov et al.[35,36] In this regard, the Gibbs free energy change of each NORR step was obtained by the equation: $\Delta G = \Delta E_{DFT} + \Delta ZPE + \Delta H - T\Delta S + \Delta G_U + \Delta G\text{pH}$, where ΔE_{DFT} is the free energy change that can be obtained from DFT calculations, ΔZPE and ΔH are zero-point energy and enthalpy correction terms, and $T\Delta S$ represents the contribution of the entropy change under temperature T (T = 298.15 K). These correction terms can be obtained from vibration analysis of the NORR intermediate adsorbed species performed using the VASPKIT code.[37] For the computational procedure, the catalyst slab was fixed, and only the adsorbate was allowed to relax. The vibration frequency contribution of the adsorbate is very likely to lead to free energy correction. ΔG_U is the contribution of the applied electrode potential U, and ΔGpH is the correction of the H^+ free energy calculated by using $\Delta G\text{pH} = 2.303 \times k_B T \times \text{pH}$. k_B is the Boltzmann constant, and this correction term was assumed to be zero in the DFT calculation.[38,39] The free energies of gas molecules, such as NO, NH_3, H_2, and N_2, are obtained from the NIST database.[40] The applied potential (U) was defined as the maximum Gibbs free energy change ($-\Delta G_{max}/e$) along the reaction path, and to ensure that each elementary reaction step was exergonic, it was determined by the RDS.[41]

3. Results and Discussion

All of our considered transition metal diboride (M_2B_2) monolayers are a square structure lattice containing two transition metal atoms and two boron atoms within a unit cell (**Figure 1**a). The BZ of these M_2B_2 systems is depicted in Figure 1b, clearly showing that a central unit cell (yellow area) is surrounded by the nearest neighbor unit cells in the periodic structure of a 2D square. Furthermore, the stabilities of these M_2B_2 monolayers have been verified by their phonon band structures (Figure 1c). Thirteen of the M_2B_2 (marked in green) are stable, as their phonon band structures have no imaginary frequency. These stable and unstable M_2B_2 monolayer structures are summarized in a simple periodic table. The phonon band structures of our considered transition metal diboride (M_2B_2) monolayers have shown stability and excellent capability to capture NO molecules due to their adsorption energy (≈–2 to –5 eV). We will focus on the NORR mechanism to investigate the production of final products (such as NH_3, N_2, and N_2O) depending on the activity of the catalyst. Furthermore, the adsorption energies of *NO, $*NH_3$, and *H on MBenes are shown in Figure 1e. It is observed that the ΔG_{*NO} values are more negative than the ΔG_{*NH3} and ΔG_{*H} values on MBenes, except for Mn_2B_2, Fe_2B_2, and Rh_2B_2, suggesting that the NORR is more favorable than ammoxidation and the HER. Figure 1f illustrates the energy difference between ΔG_{*NOH} and ΔG_{*HNO} during the first hydrogenation step on the 12 stable MBenes. The corresponding competitor performance can be

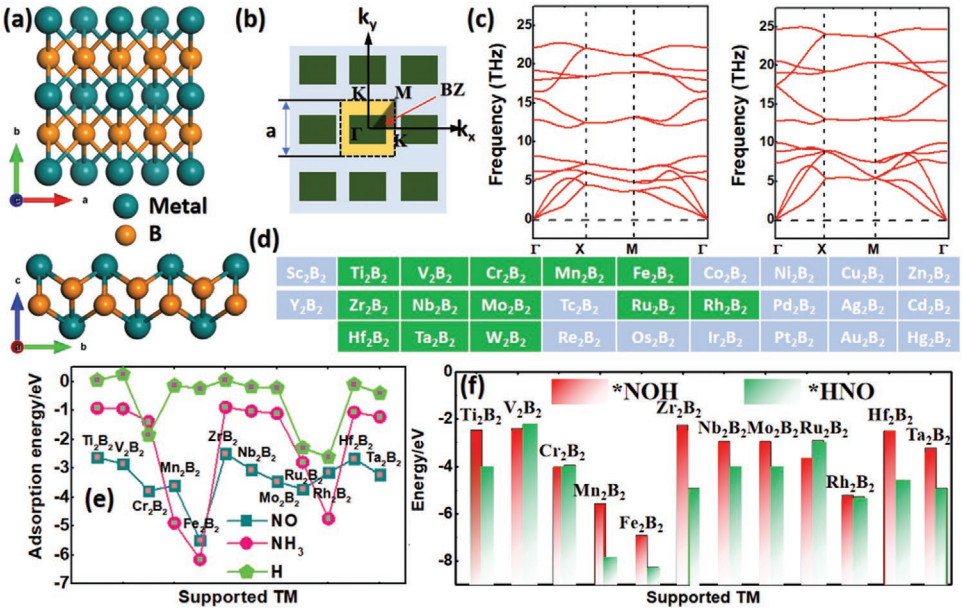

Figure 1. a) Top views (upper) and side views (lower) of the M_2B_2 MBene monolayers. The metal and boron atoms are marked by cyan and orange spheres, respectively. b) Brillouin region in the periodic structure of the 2D square. c) Phonon structure of the Cr_2B_2 and Fe_2B_2 monolayers from left to right. d) Our screened M_2B_2 monolayers, including 3d, 4d, and 5d transition-metal boride compounds. Green and light blue represent stable and unstable M_2B_2, respectively, which were verified from phonon spectrum calculations. e) Comparison of the adsorption energies of NO, NH_3, and H protons on M_2B_2 MBenes. f) Comparison of the Gibbs free energy changes (ΔG) for the formation of *NOH and *HNO on M_2B_2 MBenes.

easily predicted, as the $\Delta G_{*NOH} - \Delta G_{*HNO}$ values are well above zero, indicating the more preferable competition of HNO over the NOH pathway except for V_2B_2 and Ru_2B_2 under ambient conditions. In this work, we focus on these stable MBene compounds. NO electroreduction to ammonia involves the transfer of five successive ($H^+ + e^-$) pairs, and the entire reaction network is presented in **Figure 2**a, including twelve intermediate species. All of the elementary reaction steps are summarized in the Supporting Information.[42] In general, there are three different reaction mechanism paths for producing NO to NH_3 that can be hydrogenated: the HNO-mediated path, NOH-mediated path, and HNOH-mediated path mechanism of the ammonia formation pathway. We calculated the binding energies of all of the NORR intermediate species adsorption configurations along the different reaction mechanism paths mentioned previously, and their corresponding Gibbs free energy profile diagrams are shown in **Figure 3** and Figure S2, Supporting information. In the NOH-mediated route, hydrogenation always takes place preferentially on oxygen atoms during the transfer of the first two successive ($H^+ + e^-$) pairs until the formation of *N and then forms the final product (NH_3).[43] The first hydrogenation step of NO is proposed to form two different intermediates, *HNO and *NOH, which are isomers between *HNO and *NOH. *HNO and *NOH have been reported in the presence of NO reduction reactions in experiments and have been suggested as possible rate determining reaction steps. For the alternative routes, the second hydrogenation step to form *HNOH after the first hydrogenation step will occur along the NOH- or HNO-mediated path, respectively. We find that the adsorbed *NO molecule forms an M...N—O bond, which is important for the activation of the N—O bond, and thus, it is more favorable for the stable adsorption of NOH compared with HNO on the catalyst after the first hydrogenation occurs.

To further explore the stable configurations of all NORRs, intermediate species are catalyzed by M_2B_2 monolayers. In general, the NORR involves five electron–proton coupled pair transfer reactions, and it may proceed via enzymatic, distal, alternating, and hybrid mechanisms. Due to the strong M...N bound coupling between NO molecular orbitals and the metal, the electrons can ensure preferable electron transfer; thus, the N-end binding configuration is more likely to occur and further to form NH_3 than other proceeding paths. Thus, we only considered the N-end path but not O-end binding configuration in which the NORR proceeds initially from the hydrogenation of gas-phase NO to form *NOH. Furthermore, N_2 and N_2O formation are also considered in this investigation with the transfer of two successive ($H^+ + e^-$) pairs (*NO → *NOH → *N), and then, the formation of N_2 occurs from two atomic *N species, while the formation of N_2O occurs between one atomic *N and one NO gas molecule. The reaction of *N + *N → $*N_2$ is the most favorable and widely verified reaction mechanism by experiment. The reaction paths for the formation of N_2 and N_2O are very similar to each other. Meanwhile, we further explored some of the different possible reaction channels (Figure 3 and Figure S2, Supporting information) for the NORR to form NH_3, depending on the ΔG profile, and ensured that the priority elementary reaction step was confirmed, as illustrated in Figure 3a, which shows the first hydrogenation elementary step selectivity between NOH or HNO. NOH and HNO can transform, and we found that NOH is less preferable than HNO during the first hydrogenation step among most MBene materials. The first hydrogenation of NO to form NOH or HNO is the crucial step to influence the entire reaction pathway. It is

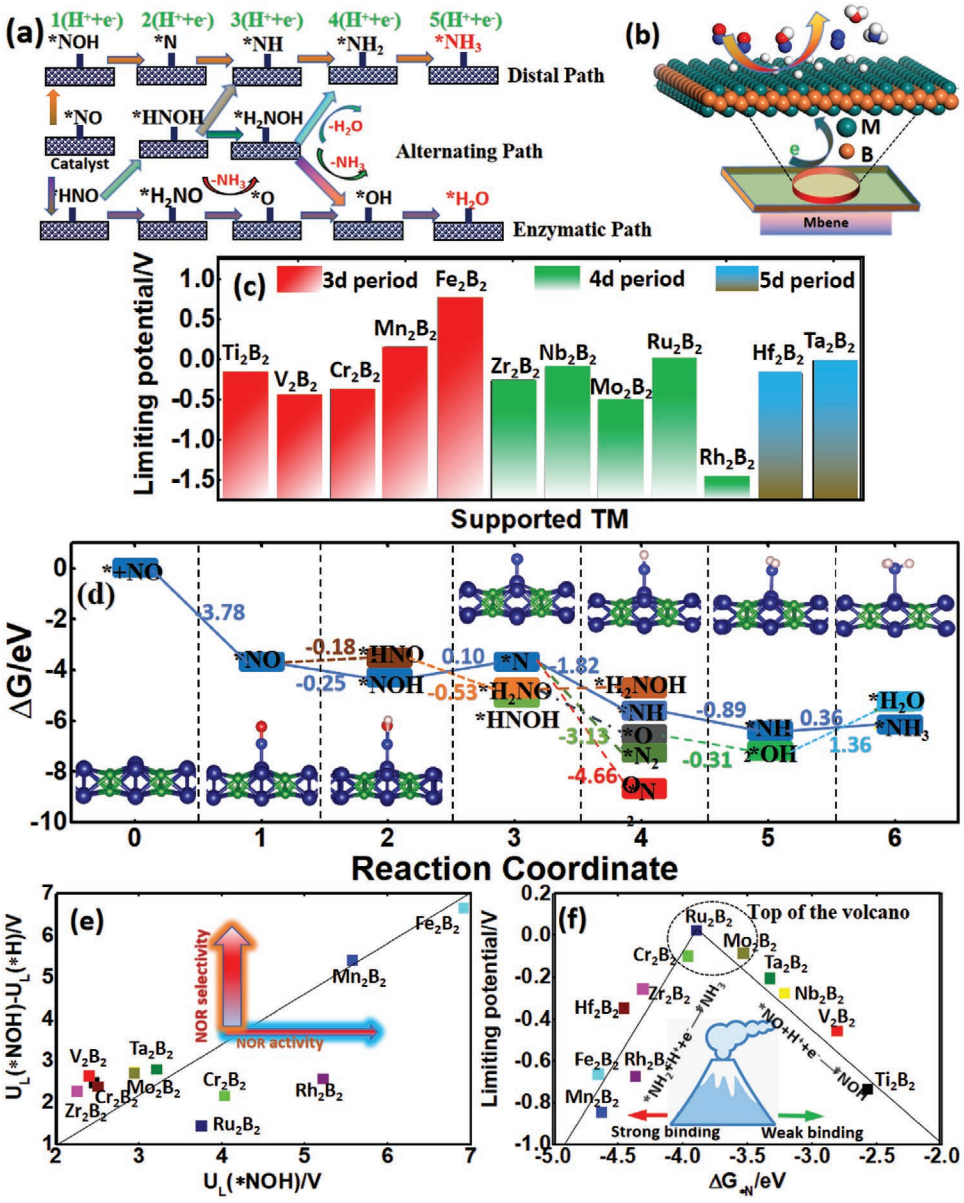

Figure 2. a) Proposed whole reaction network for NO reduction to ammonia with five hydrogenation steps indicated by atomic models (Mo_2B_2) (the numbers represent the reaction energy in eV). b) Schematic diagram of the reaction flow diagram for the electroreduction of NO corresponding to different reaction paths marked by different colored arrows on 2D M_2B_2 MBenes. The adsorbate species in red denote the final products of the NORR, and each intermediate was connected by proton–electron pair transfer. c) Summary of limiting potentials on M_2B_2 MBenes for NORR via the most favorable N-end mechanism. d) Gibbs free energy profile diagrams of the NORR on Cr_2B_2. The pathways to the formation of NH_3, N_2, and N_2O are also considered for comparison. e) The difference limiting potentials between the first hydrogenation step of NORR and HER (U_L(*NOH)-U_L(*H)) versus as descriptor of U_L(NOH). f) NORR volcano plot of M_2B_2 MBenes with a descriptor of ΔG_{*N}.

clearly established that the hydrogenation of *N species will produce $*N_2$ or *NH within two reaction channels. In addition, the HNO-mediated path can be further protonated from $*H_2NO$ (enzymatic path) or *HNOH (hybrid path)/OH* (path 1b) on the MBene catalyst surface. Once H_2NO forms along the enzymatic pathway, the adsorbed H_2NO species can be further hydrogenated to $*H_2NOH$ or dissociated atomic *O and form NH_3 gas molecules because the NH_3 gas molecule is more likely to desorb from the catalyst surface; thus, the H_2NO dissociation mechanism could be more likely to hydrogenate along the expected channel.[44] Comparing this Gibbs free energy change, we find that N—O bond breaking becomes much easier in HNOH than in H_2NOH. Taking Mo_2B_2 as an example, the first hydrogenation of *NOH formed has a reaction energy of –0.51 eV (endothermic process) along the distal path, which is in good agreement with a previously reported value of –0.50 eV on clean Pt(100), while the formation of *HNO has a reaction energy of 0.65 eV with an exothermic reaction, indicating that the limiting potential of the distal path is as low as –0.51 It is worth noting that the formation of H_2NO and H_2O with

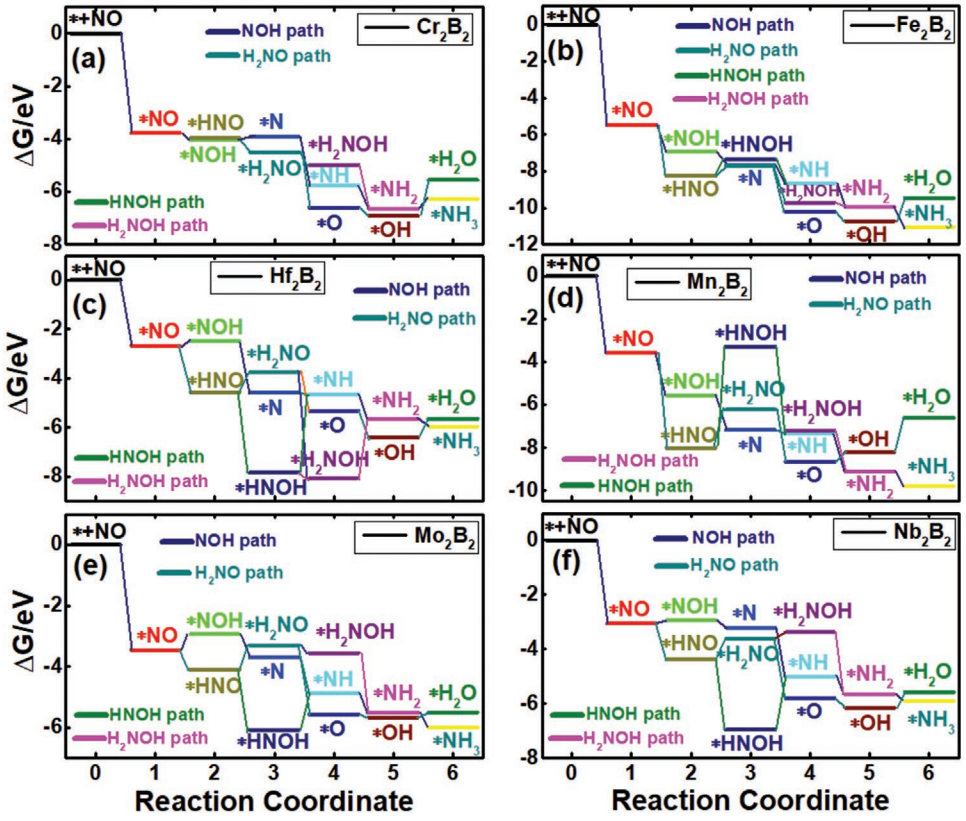

Figure 3. Gibbs free energy profile diagram for NO electroreduction to ammonia on the M_2B_2 (M = Cr, Fe, Hf, Mn, Mo, and Nb) monolayer. All possible reaction pathways for converting NO to ammonia are considered: a) Cr_2B_2, b) Fe_2B_2, c) Hf_2B_2, d) Mn_2B_2, e) Mo_2B_2, and f) Nb_2B_2.

enzymatic paths are endothermic reactions of –0.80 and –0.16 eV, respectively.

We analyzed the NORR catalytic performance of MBene monolayers depending on the Gibbs free energy profile diagram of all possible intermediates to determine the reaction mechanism path. We assume that the NOH, H_2NO, HNOH, and H_2NOH paths in Figure 2a include distal, enzymatic, and alternate mechanisms. An atomic structure schematic display of the reaction mechanism process during NO reduction to NH_3 is shown in Figure 2b. We first considered the adsorption mode of NO on these MBene monolayers. The N atom bound to NO with the top transition-metal atom is the most stable mode, and the adsorption energies of NO on various MBenes range from –2.5 to –5.5 eV; thus, we focused on the M—O bond bound adsorption mode. Taking Cr_2B_2 as an example in Figure 2d, the calculated adsorption energy of *NO is –3.78 eV, which is very close to that calculated by Ge et al.[45,46] It can be clearly found that for the (ΔG) profile of the first step of hydrogenation, the change in the reaction free energy is 0.25 eV along the NOH path and 0.18 eV along HNO. This means that the NOH path is more beneficial than the HNO path on Cr_2B_2 MBene. Then, the second H^+ attacks the NOH intermediates and *N to form with a small upward energy change of –0.10 eV. The next two subsequent hydrogenations have downward energy changes until NH_2 is formed. The last hydrogenation step is the formation of NH_3. This step exhibits an upward energy change of 0.36, which means that this step is the RDS along the NOH path and makes the subsequent reaction much easier than other paths. For other reaction paths, we can find that *OH reduction to $*H_2O$ is the RDS of the entire alternating path, with the highest ΔG = –1.26 eV. A summary of the limiting potential is shown in Figure 2c. The U_L values are negative in each period except for Fe_2B_2, Mn_2B_2, and Ru_2B_2, which exhibit U_L values of 0.78, 0.17, and 0.03 V, respectively. They are spontaneous processes for NO production to NH_3. All of the U_L values are greater than –0.5 V, while Rh_2B_2 demonstrates excellent electrocatalysts for the NORR to produce NH_3 by a U_L of –1.46. Meanwhile, the HER can jointly determine the selectivity in the process of NO reduction to NH_3. The selectivity was described by the limiting potential (U_L) between the NORR and HER, which depends on the difference of U_L(*NO) – $U_L(H_2)$. It is a valid descriptor to identify the catalytic performance and selectivity trend toward NO reduction to NH_3 on MBene catalysts.[47] The primary competing reaction (HER) is also considered in Figure S1a, Supporting information, and Figure 2e shows it. The HER procedure includes two steps: one step is the adsorption of H^+, and the other step is the formation of H_2. The (ΔG) of the reaction is set to zero, starting from hydrogen atom adsorption on the catalyst accompanied by charge transfer, and then, two adsorbed hydrogen atoms combine to form molecular hydrogen. ΔG_{*H} is the key descriptor to evaluate the catalytic performance for HER catalysts. The better HER catalytic performance corresponds to a smaller absolute value of ΔG_{*H}, which means a lower overpotential (η) of the HER ($\eta = \Delta G_{*H}/e$).[48] In this regard, $|\Delta G_{*H}/e|$ is smaller than 0.2 V and is suitable for HER catalysts; thus, Ti_2B_2 and Zr_2B_2 lead to a positive $\Delta G_{*H}/e$ less than 0.2 V, while for

Hf_2B_2, Mn_2B_2, and Nb_2B_2, the $\Delta G_{*H}/e$ values are negative, and their absolute values of ΔG_{*H} are also less than 0.2 V. In theory, these 2D MBene materials can be used as HER catalysts.[49,50] By comparing their limiting potentials, we chose Nb_2B_2 as an outstanding candidate catalyst for the NORR and will discuss it in detail in **Figure 4**. The Gibbs energy profile diagram of the complete catalytic reaction pathway and that under an applied potential are shown in **Figure 5** in the next section. Figure 2e shows the change of limiting potentials between the formation of NOH and HER (U_L(*NOH) − U_L(*H)) versus as function of U_L(*NOH), showing a linear relationships among our consideration MBene systems. Figure 2f shows the calculate volcano plots which created by the limiting potential for the RDS on each MBene. The data points are much closer to the top of the volcano plot, and the reaction activity of the NORR as a function of ΔG(*N) is more beneficial to this reaction mechanism. In this regard, it has been proposed that for the right side of the volcano plot, the second proton transfer process (*NO → *NOH) is the RDS for the distal mechanism. On the left side, $*NH_2 \rightarrow *NH_3$ and *HNO → *HNOH are the rate determining reaction steps. A reasonable conclusion was obtained by the linear relationship of ΔG(*N) on MBene surfaces to verify the lowest energy barrier reaction path from **Figure 6**a.

We plotted the Gibbs free-energy profile diagram for all possible mechanisms to facilitate a clear explanation of the reaction mechanism. Here, we defined five paths (see the Supporting Information), and their optimized configurations of each NORR intermediate on Nb_2B_2 are inset in Figure 5. Both M...O and M...N bond bounds of NO hydrogenated configurations have been proposed. Our calculated adsorption energy on Nb_2B_2 is −3.05 eV, and the simulation results are basically anastomotic with a value of −2.04 eV obtained by Perez-Ramirez et al.[51] The binding energy of *NOH on Nb_2B_2 is −2.94 eV, while *HNO is −4.36 eV; it binds on top of the Nb atom site through M...O bonds. The reported binding energy of NOH* on Pt(100) is −1.76 eV. Furthermore, Yang et al.[52] found binding energies of −3.91 and −4.14 eV for HNO* and NOH* on Pt(111), respectively. Our calculation revealed that the binding energies of *HNOH and $*H_2NO$ on Nb_2B_2 were −6.96 and −3.63 eV, respectively. Therefore, in the second hydrogenation step *HNOH is more stable than H_2NO on Nb_2B_2, and ΔG_{*N}, as a key descriptor to evaluate the catalytic performance for NORR catalysts, is −3.20 eV. The calculated binding energy of the final products of $*NH_3$ on Nb_2B_2 is −5.91 eV. Similar to NH_3, we find that when N_2 and N_2O are possible final products in NO reduction by protonation, the calculated binding energies of N_2 and N_2O are −8.37 and −5.74 eV, respectively. The formation of *NOH is a small endothermic step (−0.11 eV), which is higher than the HNO* formation of a small exothermic step (1.32 eV), indicating that the hydrogenation of *NO to form *HNO is more energetically favorable than *NOH. Such a favorable reaction pathway due to such a small limiting potential (−0.11 V) of the RDS is different from other paths on the Nb_2B_2 surface (Figure 5b). *HNOH can further hydrogenate to

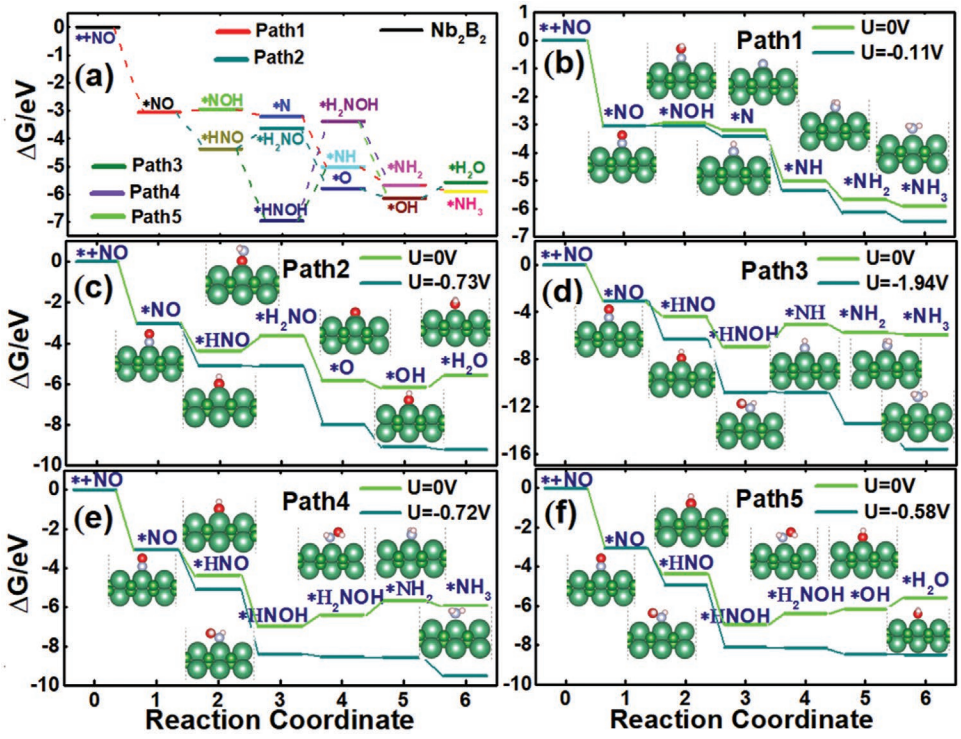

Figure 4. Gibbs free energy diagram for the reduction of NO to NH_3 on Nb_2B_2. a) Gibbs free energies of all intermediate binding energies were obtained by DFT calculations. Gibbs free energy profile diagrams via the different reaction mechanisms under their corresponding working potentials. b) The NOH pathway, c) H_2NO pathway, d) HNOH direct dissociation and reduction to H_2O pathway, e) H_2NOH direct dissociation and reduction to H_2O pathway, and f) H_2NOH direct dissociation and production of NH_3 pathway. The symbol * denotes an intermediate adsorbed on the MBene. Gibbs free energy profile diagrams with dashed lines in (a) and solid lines in (b–f) under zero applied potential. Inset: the optimized NORR intermediates with adsorbed atomic structures on Nb_2B_2 are shown.

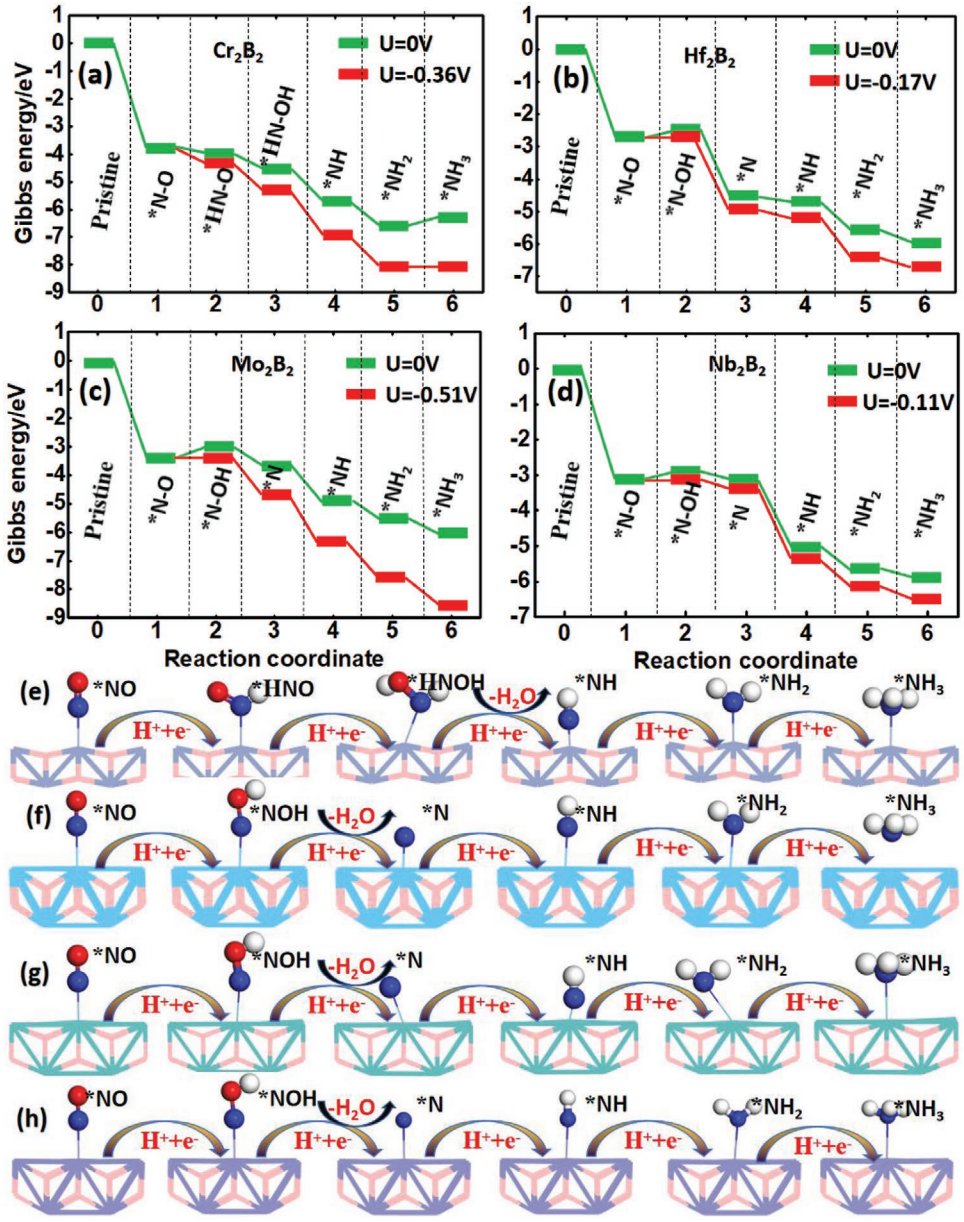

Figure 5. Gibbs free energy profile diagrams of NO reduction to NH_3 via the most favorable reaction path under different applied potentials. a) Cr_2B_2, b) Hf_2B_2, c) Mo_2B_2, and d) Nb_2B_2. The symbol * denotes adsorbates on the MBene surfaces. Inset: the optimized structures (side view) of the corresponding reaction intermediates are shown.

*H_2NOH or break the N—O bond to form H_2O (path 3). The hydrogenation of *HNOH to *NH is the RDS because this step has the lowest limiting potential (U_L = –1.94 Furthermore, the further hydrogenation of *H_2NOH to *NH_2 or *OH has energy barriers of 0.72 (Figure 5e) and 0.24 eV (Figure 5f), respectively. This indicates that *H_2NOH further hydrogenation to NH_3 and *OH is more preferable than the formation of H_2O and *NH_2.

To determine the most preferable NORR reaction pathway, we generated the lowest Gibbs free energy diagram for the NORR, which is shown in Figure 6 and Figure S3, Supporting Information. Here, we only focus on Cr_2B_2, Hf_2B_2, Mo_2B_2, and Nb_2B_2, and the optimized structures of the intermediates are also displayed in Figure 6. In the reaction, five hydrogenation steps are considered, and the formation of ammonia molecules occurs by NO + 5(H^+ + e^-) → NH_3 + H_2O, with uphill Gibbs free energies of 0.36, 0.17, and 0.51 eV for Cr_2B_2, HfB_2, and Mo_2B_2, respectively. The comparison of the Gibbs free energies of *NOH and *HNO determines whether the hydrogenation step goes along the distal or enzymatic pathway. In Figure 4a, the free energy values of *NOH on Cr_2B_2 and Rh_2B_2 are higher than those of *HNO for other MBene compounds. The established pathway is as follows: *NO → *HNO → *HNOH → *NH → *NH_2 → *NH_3; *NH_2 → *NH_3 is an endothermic step (0.36 eV) for the formation of NH_3. This step is also the RDS of the reaction pathway on Cr_2B_2, while *NH → *NH_2 is the RDS with an endothermic step of (1.46 eV) on Rh_2B_2. For the

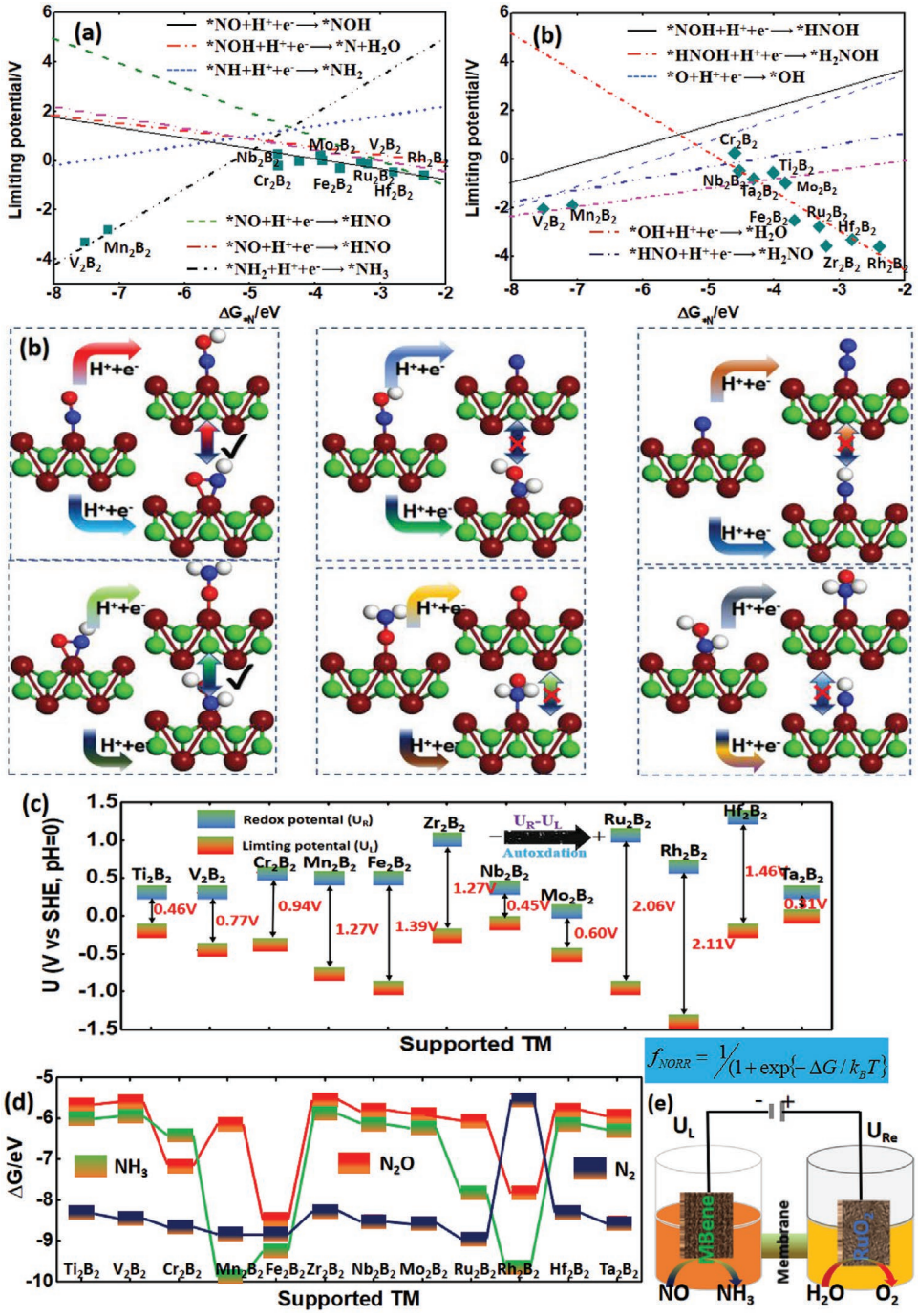

Figure 6. a) Volcano plot of the RDS in NO electroreduction to ammonia on transition-metal boride (MBene) surfaces depending on the limiting potentials plotted as a function of the ΔG_{*N} descriptor. Some data points of promising MBene catalyst candidates for the NORR are presented. b) Schematic illustration of bifurcation reaction steps during the hydrogenation of NO to NH_3 on V_2B_2 MBenes. c) Different theoretical limiting potential (U_L) and redox potential (U_R) values of 12 M_2B_2 MBenes. The calculated values of $U_R - U_L$ are also presented. d) Computed binding energies of $*NH_3$, N_2O, and $*N_2$ on 12 MBene surfaces. e) A schematic diagram of the desired electrochemical cell for the NORR (cathode: MBene) and OER (anode: RuO_2, for reference electrode).

other MBenes, they prefer the formation of *NOH. This step is an endothermic process and RDS, and there is an energy hill for Hf_2B_2 of 0.17 eV, while for Mo_2B_2 and Ti_2B_2, it is 0.51 and 0.16 eV, respectively. The next step is *NOH → *N + H_2O with endothermic energy changes of 0.13, –0.41, and 2.07 eV for Ti_2B_2, V_2B_2, and Zr_2B_2, respectively. The energetically favorable pathway for these is considered to be *NO → *NOH → *N → $*NH_2$ → $*NH_2$ → $*NH_3$. We can conclude that the RDS for Cr_2B_2, HfB_2, Mo_2B_2, Ti_2B_2, V_2B_2, and Zr_2B_2 is the first hydrogenation step *NO → *NOH, and for Cr_2B_2 and Rh_2B_2, the

last hydrogenation step $*NH_2 \rightarrow *NH_3$ is the RDS with limiting potentials of 0.36 and 1.46 V. As an example of concrete analysis, by comparison with other reaction paths on Zr_2B_2, the $*NO \rightarrow *HNO$ reaction step is an exothermic process by 2.42 eV, while $*HNO \rightarrow *HNOH$ has a reaction energy of 2.27 eV. The hybrid reaction path for $*HNOH \rightarrow *NH + H_2O$ is endothermic by −2.78 eV, and $*H_2NOH \rightarrow *NH_2 + H_2O$ is exothermic by 2.65 eV. Furthermore, atomic N* can combine with another adsorbed *NO to form $*N_2O$ (Figure S6f, Supporting Information). The formation energy of $*N + *NO \rightarrow *N_2O$ is −5.43 eV, while the formation energy of $*N + *N \rightarrow *N_2$ is −8.17 eV, which is ≈2.74 eV higher than that of N_2 formation, and they are exothermic processes with limiting potentials of 1.11 and 3.85 V, respectively. Their reaction mechanism paths for $*N_2O$ and $*N_2$ formation are very similar as follows: $*NO \rightarrow *NOH \rightarrow *N \rightarrow *N_2$ or $*NO \rightarrow *NOH \rightarrow *N \rightarrow *N_2O$ with two subsequent hydrogenations, while all of the hydrogenation steps are exothermic. Only the final hydrogenation step is different from the two preceding hydrogenations.

In general, when enough of the same type of catalyst is screened for a particular reaction, it establishes linear scaling relationships depending on the binding energies of the intermediates;[51] these scaling relationships can describe the relative catalytic activity and selectivity of a particular chemical reaction. Considering the most crucial *N intermediates for the entire NORR reaction pathway, it goes to determine the formation of the final product in the entire NORR reaction path, and both the formation of NH_3 and N_2 are investigated. The binding energy of ΔG_{*N} can be used as the descriptor of the NORR catalytic activity on MBene monolayer catalysts, and a scaling relationship can be constructed between different NORR intermediates depending on the ΔG_{*N}. It revealed that most of the binding energies of NORR intermediates demonstrate reasonable linear correlations as a function of ΔG_{*N}, although the transition-metal borides (M_2B_2) are different systems. For the first hydrogenation step species, such as *NOH and *HNO, their linear scaling relationships are plotted separately in Figures S4a and S4f, Supporting Information. As shown in Figure S4, Supporting Information, a strong linear scaling relationship exists between ΔG(*NOH) and ΔG(*NO) ($R^2 = 0.93$); therefore, in terms of $\Delta G(*NOH) = 1.55\Delta G(*NO) + 1.74$, a linear scaling relationship exists between ΔG(*HNO) and ΔG(*NO) with a correlation coefficient of ($R^2 = 0.83$), which can explain the correlation of catalytic activity properties for different MBene catalysts. However, $*NO \rightarrow *NOH$ shows a stronger correlation with ΔG(*NO) than $*NO \rightarrow *HNO$, which may indicate that the first hydrogenation is more beneficial for the formation of *NOH than *HNO, which also explains the binding strength of the TM…N−O bond. The linear scaling relationships of the binding energies of different NORR intermediates are relative to the reaction path and final products.[52] In general, the slope of the linear fitting demonstrates similar bond patterns between the adsorbates and catalyst, and similar correlations are also shown between ΔG(*N) and ΔG(*NH) (Figure S4c, Supporting Information, $R^2 = 0.92$), ΔG(*NH) and $\Delta G(*NH_2)$ (Figure S4d, Supporting Information, $R^2 = 0.92$), and $\Delta G(*NH_2)$ and $\Delta G(*NH_3)$ (Figure S4e, Supporting Information, $R^2 = 0.95$).

Based on the above scaling relationships of binding energies for NORR intermediates, we can also plot scaling relationships depending on the limiting potential (U_L) as a descriptor of ΔG(*N), as shown in Figure 4a, which can determine the reaction path evolutionary trends and selectivity. ΔG(*N), as a descriptor, is based on the product stability and selectivity between NH_3 and N_2 via a thermodynamic reaction under zero potential. Using linear scaling relationships between the limiting potential of the various elementary reaction steps of NO reduction and the NH_3 or N_2 mechanism, depending on the tendency to change of all elementary reaction steps, a volcano plot was built. These plots can describe the five proton electron transfer steps of the mechanism of NO reduction to NH_3 from a full volcano plot. The values of ΔG(*N) are exothermic on all MBene surfaces, the binding energies of *N on Fe_2B_2 and Mn_2B_2 are −7.69 and −7.18 eV, respectively, and the two reaction steps involve low energy barriers of 0.78 and 1.61 eV on those candidates. The effective selectivity of $NO \rightarrow *NOH$ and $NO \rightarrow *HNO$ was reported, as the correlation coefficients (R^2) of $NO \rightarrow *NOH$ and $NO \rightarrow *HNO$ were 0.91 and 0.93 by exothermic processes, respectively. In general, ΔG*N values less than −5 eV indicate that the bonds between *N and the catalyst are too strong to desorb. The next hydrogenation step ($*NOH \rightarrow *N + H_2O$) may become the RDS, such as on Hf_2B_2, Mo_2B_2, V_2B_2, and Zr_2B_2, while ΔG_{*N} values greater than −5 eV mean that *N is moderate and include the rest of the MBene candidate catalysts. Furthermore, for the distal path NORR intermediates NH, NH_2, and NH_3, the correlation coefficients (R^2) of the linear scaling relationships are 0.87, 0.93, and 0.93, the trend of linear fitting for $*N \rightarrow *NH$ is upward and the trends for $*NH \rightarrow *NH_2$ and $*NH_2 \rightarrow *NH_3$ are downward, which depend on the binding energies of *N. A scaling relationship between the limiting potential of $*NO \rightarrow *HNO$ along the H_2NO (enzymatic) path for the NORR also exists, it can be seen that the RDS is determined by the lowest limiting potentials, and the catalytic activity of different MBene catalyst is be decided by the strength of linear correlation relationship. Most MBenes as NORR candidate catalysts fall in the range of −5 to −2 eV as a function of ΔG(*N), indicating a moderate energy barrier and relatively high kinetics for the NORR on these MBene surfaces. Figure 4b shows the two possible paths to break the N−O bond in HNOH, and the other is further hydrogenated to H_2NOH. Therefore, the N−O bond breaking path between HNOH and H_2NOH leads to *NH and $*NH_2$ + *OH, and these channel paths are defined as hybrid paths. Figure 4c shows the selectivity of the NORR evaluated by the Boltzmann distribution, which is defined as $f_{NORR} = 1/(1 + \exp\{-\Delta G/k_BT\})$ and depends on the Gibbs free energy difference between the two competitive reaction steps in Figure 4e. Herein, the potential difference between the redox potential (U_R) anode and limiting potential (U_L) cathode as a descriptor can be used to estimate the oxidation trend on these 12 MBenes, and a more positive value of $U_R - U_L$ suggests a stronger ability to promote surface reduction. The calculated $U_R - U_L$ values are positive for all of the MBene monolayers (Figure 4c), suggesting that these materials could suppress surface oxidation. In this work, we defined the redox potential (U_R) as the anode electrode potential needed to suppress the ORR process. The redox potential is equal to the energy barrier of *OH formed and follows the order of $Rh_2B_2 > Ru_2B_2 > Hf_2B_2 > Fe_2B_2 > Zr_2B_2 > Mn_2B_2 > Cr_2B_2 > V_2B_2 > Mo_2B_2 > Ti_2B_2 > Nb_2B_2 > Ta_2B_2$. When the electrode

potential shifts to the redox potential, the surface ORR can be suppressed. As shown in Figure 4d, the ΔG*N_2 values are more negative than those of ΔG*NH_3 and ΔG*N_2O on most of the MBene surfaces, except for Mn_2B_2, Fe_2B_2, and Rh_2B_2, suggesting that these three MBenes are more favorable for ammonia formation, thus revealing that the formation of *N_2 is a more favorable competitor product with *NH_3 and *N_2O.

For exploration and design of a high-performance catalyst for NO reduction to NH_3 under ambient conditions, a high-throughput screening approach could promote the discovery of a new type of transition metal boride (MBene) material for NORR depending on which volcano plot can confirm the RDS and how much limiting potential is required to be applied during the reaction path. Figure 4a shows the volcano plot of *NO → *NOH, *NOH → *N + H_2O and *N → *NH as a functional of ΔG(*N). The binding energy of *N is neither too strong nor too weak. When it has too strong of a binding strength, the strong interaction between the MBenes and *N is limited to *N reduction to *NH or *N_2. Taking Fe_2B_2 as an example, it has a large binding energy of –6.91 eV for *NOH formation. Since the large spin-polarization 3d orbital of Fe could strongly bind Fe...N—O, the unpaired electron of the nitrogen atom becomes more active for hydrogenation than other MBene systems. In this regard, Fe_2B_2 is identified as a promising candidate catalyst for NO reduction to NH_3. In recent years, a number of different types of 2D materials have been reported to interact with NORR adsorbates in a similar way, such as transition metal dichalcogenides, MXene, MBene, C_3N_4, and graphene. A high-throughput screening approach is beneficial to discover and design high-performance catalysts from fewer calculations and experimental work. High-throughput screening provides a model for the clustering and optimization of catalytic activity and selectivity trends depending on the parameters described, which is an essential prerequisite for customizing surfaces with specific catalytic properties. In general, some key parameters can be used to describe the reaction kinetics features for a given reaction, such as the binding energies of all possible intermediates and the limiting potential of each elementary reaction step. Since the reaction kinetics of the NORR are determined by multiple reaction paths and intermediates, the detailed reaction mechanism and catalytic activity trends will be systematically evaluated, and the optimal reaction path and limiting potential will be identified during the entire reaction under an applied potential. All of the elementary steps of both distal and hybrid path pathways shown in Figure 2a were considered, and the Gibbs free energy profile change trend shows that NORR processes preferably adopt the distal pathway as follows: *NO → *NOH → *N → *NH → *NH_2 → *NH_3 for Cr_2B_2, Hf_2B_2, Mo_2B_2, Nb_2B_2, Rh_2B_2, Ti_2B_2, Ta_2B_2, V_2B_2, and Zr_2B_2. Meanwhile, Fe_2B_2 and Ru_2B_2 preferably adopt the alternating pathway as follows: *NO → *HNO → *HNOH → *H_2NOH → *NH_2 → *NH_3. The last hydrogenation step is identified as the RDS of limiting potential at –0.89 and –0.99 eV, respectively, which is different from the other MBene catalysts displaying that the RDS is usually determined by the first hydrogenation step. Furthermore, the negative value limiting potential of the γ-intercepts for the linear scaling relationships between *NO → *HNO and *O → *OH as well as *HNO → *HNOH and *OH → *H_2O indicate that these next hydrogenation steps have significantly lower reaction energies, which may drive the reaction toward completion. According to the Gibbs energy profile diagram, Fe_2B_2, Mn_2B_2, and Ru_2B_2 are expected to have no thermodynamic barrier through the distal reaction path because each step is an exothermic process. Volcano plots are used to determine the RDS, the value of the γ-intercept with the most negative or least positive ΔG(RDS) is defined as the RDS, ΔG(RDS) is $U_L = -\max(\Delta G_1, \Delta G_2, \Delta G_3, \Delta G_4, \text{and } \Delta G_5)/e$ with five successive ($H^+ + e^-$) transfers, and Nb_2B_2 and Zr_2B_2 are located close to the peak of the volcano plot. In this regard, volcano plots based on linear scaling relationships of the limiting potential could become a reliable and effective tool for high-performance catalyst screening.

4. Electronic Structures

Figure 7 displays the total density of states (TDOS) with and without NO adsorbed on the Hf_2B_2 single layer. Significant peaks are created in the TDOS after NO adsorption, which are mainly located in the energy level range from 0 to 4 eV below the Fermi level. The Fermi level is set to zero, as represented by the cyan dashed line. Compared to Hf_2B_2 without NO adsorption, Hf_2B_2 exhibits large differences. These differences mainly reflect the energy level shift of the peaks, and new peaks appear in the TDOS of Hf_2B_2. Furthermore, the changes in energy and peak shifts or the appearance in these state bands can significantly influence the electron transport properties of the MBene catalyst,[53] which can be useful for designing and exploring high-performance catalysts in NO electroreduction to NH_3 processes. The large change before and after NO adsorption in the density of states shows that the NO molecule formed a chemical bond bound to the Hf atom of Hf_2B_2. The projected density of states (PDOS) of the Hf_2B_2 single layer is shown in Figure 7g,h, and the PDOSs for the B2p interaction with the Hf4d and their orbit splitting are also displayed, which displays a small overlap of band states between the TDOS and NO molecules. It is obvious that the B2p and Hf4d states concentrate from 1 to 2 eV above the Fermi energy (E_F), and the Hf4d states dominate from 4 to 6 eV in the conduction band. The PDOS of orbit splitting into five orbitals for Hf4d and three for B2p are shown in Figure 7i,j. Near the Fermi level, dz^2 and dxz provide the main contributions over a wide range of –4 to –1 eV, while the PDOS of dxy and dx^2 contribute slightly to the total DOS, leading to the splitting of the Hf4d orbitals into higher bands beyond 3 eV after NO adsorption, which also indicates a shifting of the PDOS of the Hf5d atom to a higher energy level. By analyzing the charge transfer depending on charge density difference distribution during the NO adsorption process, the isosurfaces of the charge density difference for NO adsorption on the MBene surfaces have been shown in Figure 7a–d and Figure S8, Supporting Information. The value of isosurfaces was set to 0.002 e A^{-3}, and the number of charges transferred was obtained from the formula $\Delta\rho = {}_{\text{MBene+adsorbate}} - \rho_{\text{MBene}} - \rho_{\text{adsorbate}}$, where $\rho_{\text{MBene+adsorbate}}$, ρ_{MBene}, and $\rho_{\text{adsorbate}}$ are the total charge density of the adsorption configuration, pristine MBene, and isolated adsorbed molecule, respectively. The yellow region represents charge depletion, and the cyan region represents charge accumulation. It is clear that charges accumulate on the

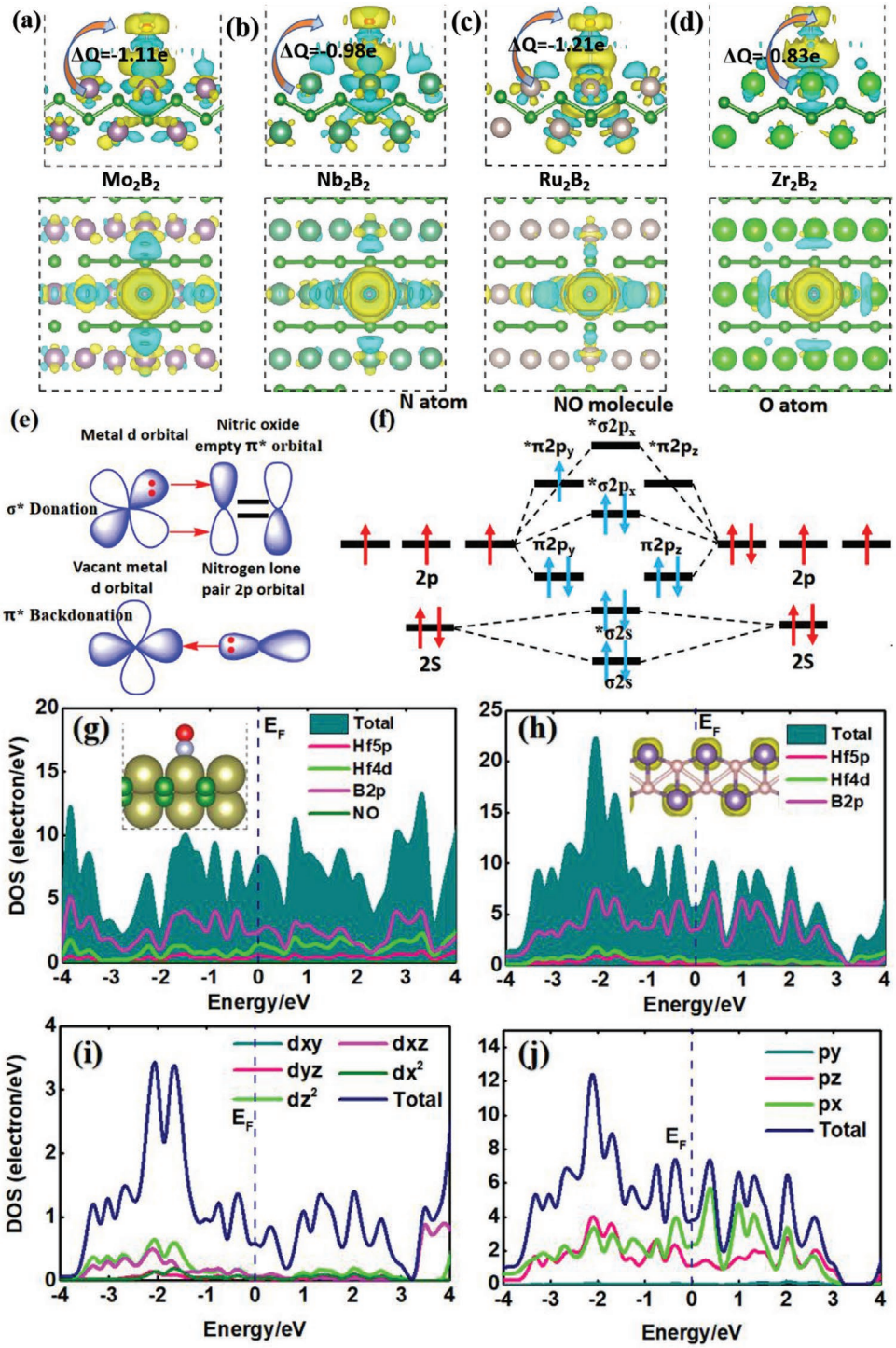

Figure 7. Top and side views of the charge density difference induced by the adsorption of one NO molecule on MBenes. Isosurfaces of differential charge density (yellow: depletion; cyan: accumulation) (isovalue = 0.002 e A^{-3}). a) Mo_2B_2, b) Nb_2B_2, and c) Ru_2B_2, d) Zr_2B_2 and e) A schematic of NO bonding and the activation mechanism to transition metals. f) The orbital hybridization diagram for the NO molecule. g,h) The TDOS and PDOS with and without NO adsorbed as well as the charge density maps of the pristine Hf_2B_2 single layer. i,j) The PDOS from all three orbitals of B2p and the PDOS from all five orbitals of Hf4d on the Hf_2B_2 single layer are presented.

adsorbed NO molecules, and the charge density of the MBene monolayer accumulates, representing the formation of chemical bonds between NO molecules and metal atoms. Covalent bonds are formed, confirming that strong chemisorption occurs in these systems and that the charge density distribution plays an important role in the NO gas adsorbed complex.

This explains why these MBenes give larger adsorption energies of NO gas (−3.78, −2.67, and −3.60 eV for Cr_2B_2, Hf_2B_2, and Mn_2B_2, respectively) than (−2.62, −2.84, and −2.50 eV for Ti_2B_2, V_2B_2, and Zr_2B_2, respectively), as mentioned above. The Bader charge transfer analysis shows net charges of −1.11, −0.98, and −1.21e from the Mo_2B_2, Nb_2B_2, and Ru_2B_2 surface transfer to *NO molecules, respectively. In Figure 7c, according to the coordinate system, the t2g orbitals have dxz, dxy, and d$y^2 - z^2$ character (with respect to the unoccupied orbital), and the eg orbitals contain dx^2 and dyz, while the d$y^2 - z^2$ and dxz orbitals are the most stable and fully occupied. In this regard, the Hf5d unoccupied orbitals couple with the occupied B2p orbitals. The transition metal borides of Mo_2B_2, Nb_2B_2, and Ru_2B_2 have both occupied and unoccupied d orbitals, and they are suitable for the NORR because of the acceptance–donation of charge mechanism. The unoccupied d-orbitals of the transition metal can accept lone-pair electrons from the N atom of NO, and the occupied d-orbitals of the transition metal can donate charge to the antibonding p-orbitals of NO, leading to a strong interaction between the MBene and NO molecule. Revealing that significant charge transfer occurs around the adsorbed NO and metal atom (the most active site for the NORR), charge transfer is also validated by the Bader charge analysis result that Fe_2B_2 transfers 1.83 e to the adsorbed NO molecule.

To further explore the interaction between the MBene catalyst and NO molecule, we described the NO molecule activation index depending on Bader charge transfer ($\Delta\rho$), where a higher charge transfer implies a higher activated NO molecule and shows the charge difference before and after NO adsorbed states. The yellow and blue regions represent positive and negative charge transfer between the MBene substrates and NO molecules. It is obvious that the NO molecule is surrounded by a region of charge accumulation;[54] this indicates some charge transfer to the *NO from the areas of depletion around the metal atoms, while there are also some small depletion and accumulation charge regions near the metal atoms.[55] For the Mo_2B_2 system, the charge density donated to the s orbital is taken not only from the Mo atom but also from the B atom, and some part is charged from the region between the Mo and B atoms. The charge is usually transferred to the electronegative N or O atoms. The activation index of NO adsorption is much higher, and hydrogenation is much easier. The d orbitals of Ti, Zr, and Hf are unfilled, which makes the filling of the 2p orbital of NO decrease. The Bader charge analysis[56] indicates that −0.71, −0.83, and −0.89 e were transferred to the *NO molecule on top of the metal active site, which can be comparable to the binding energy and make the N=O bonding, stronger, shorter, and more easily hydrogenated. The value of the charge transfer is closely related to bonding strength of NO.

5. Conclusions

In summary, we used a high-throughput approach to screen transition metal borides (MBenes) as high-efficiency electrocatalysts. The purpose of this study was to verify and show the function of the model and its usefulness for exploring high-performance catalysts in the future. Our DFT calculations presented high catalytic activity and selectivity for NO reduction to NH_3. These results revealed that MBenes can be promising candidate catalysts for NO electroreduction and that the distal path is the most favorable path via *NO → *NOH → *N → *NH → *NH_2 → *NH_3 for most MBene candidates. The binding energy of *N can be a descriptor of activity and selectivity for the final products, and it assesses linear scaling relationships and the ability of volcanic maps to reproduce known catalytic trends. The formation of *N_2 has a lower energy barrier than NH* and N_2O formation, the NORR prefers to react along the distal pathway with small limiting potentials of 0.17, 0.11, 0.01, and 0.16 V for Hf_2B_2, Nb_2B_2, Ta_2B_2, and Ti_2B_2, respectively, and these selected MBene candidates have exhibited excellent catalytic activities with working potentials less than 0.2 V. Our calculations revealed that Nb_2B_2 and Zr_2B_2 were located close to the volcano plot with moderate binding energies of −3.20 and −4.31 eV, respectively. The limiting potentials corresponding to the formation of NH_3, N_2, and N_2O are 0.25, 5.16, and 2.53 V on Nb_2B_2, respectively. In addition, NO exhibits strong binding strengths on Ti_2B_2 (−2.62 eV), V_2B_2 (−2.85 eV), and Zr_2B_2, (−2.50 eV) MBenes compared with the small binding energies of *H on Ti_2B_2 (0.04 eV), V_2B_2 (0.25 eV), and Zr_2B_2, (0.05 eV), indicating that these MBenes are more favorable for NORRs than the HER. Thus, our theoretical study shows that Fe_2B_2, Mn_2B_2, and Rh_2B_2 are promising electrocatalysts for converting NO to NH_3 with high activity and selectivity. This study provides new ideas for nitrate degradation and ammonia synthesis. Volcano plots depending on the limiting potential can be used as an important descriptor of catalytic activity by the theoretical screening of attractive candidate catalysts. Furthermore, the electronic properties of MBenes are mainly determined by the d unoccupied orbitals of the metal couple with the occupied B2p orbitals near the Fermi level and demonstrate a metallic character for each MBene.

Supporting Information

Supporting Information is available from the Wiley Online Library or from the author.

Acknowledgements

Financial support comes from the China Scholarship Council (CSC:201808440416) of China. Research and the Arts (HMWK) of the Hessen state in Germany; The Lichtenberg high performance computer is gratefully acknowledged, and we are also thankful to TU Darmstadt.

Conflict of Interest

The authors declare no conflict of interest.

Data Availability Statement

Research data are not shared.

Keywords

catalytic activity descriptor, electronic properties, no electroreduction, successive hydrogenation, theoretical screening, transition-metal borides (MBene)

Received: February 5, 2021
Revised: March 25, 2021
Published online:

[1] K. C. Taylor, *Catal. Rev.: Sci. Eng.* **1993**, *35*, 457.
[2] J. N. Armor, *Appl. Catal., B* **1992**, *1*, 221.
[3] V. I. Pârvulescu, P. Grange, B. Delmon, *Catal. Today* **1998**, *46*, 233.
[4] R. Burch, J. P. Breen, F. C. Meunier, *Appl. Catal., B* **2002**, *39*, 283.
[5] S. Roy, M. S. Hegde, G. Madras, *Appl. Energy* **2009**, *86*, 2283.
[6] S. M. Cho, *Chem. Eng. Prog.* **1994**, *90*, 39.
[7] T. Fink, J. P. Dath, M. R. Bassett, R. Imbihl, G. Ertl, *Surf. Sci.* **1991**, *245*, 96.
[8] M. Iwamoto, H. Hamada, *Catal. Today* **1991**, *10*, 57.
[9] T. Bo, P. F. Liu, J. Xu, J. Zhang, Y. Chen, O. Eriksson, F. Wang, B.-T. Wang, *Phys. Chem. Chem. Phys.* **2018**, *20*, 22168.
[10] H. Yuan, Z. Li, J. Yang, *J. Phys. Chem. C* **2019**, *123*, 16294.
[11] F. Li, Q. Tang, *ACS Appl. Nano Mater.* **2019**, *2*, 7220.
[12] Z. Jiang, P. Wang, X. Jiang, J. Zhao, *Nanoscale Horiz.* **2018**, *3*, 335.
[13] H. Zhang, H. Xiang, F. Dai, Z. Zhang, Y. Zhou, *J. Mater. Sci. Technol.* **2018**, *34*, 2022.
[14] I. Ozdemir, Y. Kadioglu, O. Ü. Aktürk, Y. Yuksel, Ü. Akıncı, E. Aktürk, *J. Phys.: Condens. Matter* **2019**, *31*, 505401.
[15] X. Guo, S. Lin, J. Gu, S. Zhang, Z. Chen, S. Huang, *Adv. Funct. Mater.* **2021**, *31*, 2008056.
[16] X. Yang, C. Shang, S. Zhou, J. Zhao, *Nanoscale Horiz.* **2020**, *5*, 1106.
[17] H. J. Chun, V. Apaja, A. Clayborne, K. Honkala, J. Greeley, *ACS Catal.* **2017**, *7*, 3869.
[18] S. Qi, Y. Fan, L. Zhao, W. Li, M. Zhao, *Appl. Surf. Sci.536*, 147742.
[19] S. Zhou, X. Yang, W. Pei, Z. Jiang, J. Zhao, *J. Phys.: Energy* **2021**, *3*, 012002.
[20] S. Xu, G. Qin, Q. Jiang, Q. Cui, A. Du, C. Zhao, Q. Sun, *Int. J. Quantum Chem.* **2021**, *121*, e26548.
[21] M. Yao, Z. Shi, P. Zhang, W.-J. Ong, J. Jiang, W.-Y. Ching, N. Li, *ACS Appl. Nano Mater.* **2020**, *3*, 9870.
[22] M. Rafti, J. L. Vicente, *Phys. Rev. E* **2007**, *75*, 061121.
[23] P. Bera, K. C. Patil, V. Jayaram, G. N. Subbanna, M. S. Hegde, *J. Catal.* **2000**, *196*, 293.
[24] H. S. Pillai, H. Xin, *Ind. Eng. Chem. Res.* **2019**, *58*, 10819.
[25] G. Kresse, J. Furthmu, *Phys. Rev. B: Condens. Matter Mater. Phys.* **1996**, *54*, 11169.
[26] J. P. Perdew, K. Burke, M. Ernzerhof, *Phys. Rev. Lett.* **1996**, *77*, 3865.
[27] G. Kresse, D. Joubert, *Phys. Rev. B: Condens. Matter Mater. Phys.* **1999**, *59*, 1758.
[28] W. Tang, E. Sanville, G. Henkelman, *J. Phys.: Condens. Matter* **2009**, *21*, 084204.
[29] A. Carreras, A. Togo, I. Tanaka, *Comput. Phys. Commun.* **2017**, *221*, 221.
[30] H. J. Monkhorst, J. D. Pack, *Phys. Rev. B* **1976**, *13*, 5188.
[31] B. Hahn, D. G. Ravenhall, R. Hofstadter, *Phys. Rev.* **1956**, *101*, 1131.
[32] M. Kłusek-Gawenda, A. Szczurek, *Phys. Rev. C* **2010**, *82*, 014904.
[33] F. Corbett P, D. G. Feitelson, *ACM Trans. Comput. Syst.* **1996**, *14*, 225.
[34] L. Goerigk, *J. Chem. Theory Comput.* **2014**, *10*, 968.
[35] D. R. Alfonso, D. N. Tafen, D. R. Kauffmann, *Catalysts* **2018**, *8*, 424.
[36] B. Hammer, J. K. Nørskov, *Adv. Catal.* **2000**, *45*, 71.
[37] V. Wang, N. Xu, J. C. Liu, G. Tang, W. T. Geng, *arXiv* **2019**.
[38] A. A. Peterson, F. Abild-Pedersen, F. Studt, J. Rossmeisla, J. K. Nørskov, *Energy Environ. Sci.* **2010**, *3*, 1311.
[39] J. K. Nørskov, J. Rossmeisl, A. Logadottir, L. Lindqvist, J. R. Kitchin, T. Bligaard, H. Jónsson, *J. Phys. Chem. B* **2004**, *108*, 17886.
[40] E. W. Lemmon, M. L. Huber, M. O. McLinden, NIST Reference Fluid Thermodynamic and Transport Properties (REFPROP), version, **2010**, 9.
[41] X. Chen, X. Zhao, Z. Kong, Z. Kong, W.-J. Ong, N. Li, *J. Mater. Chem. A* **2018**, *6*, 21941.
[42] Y. Xiao, W. Zhang, *Nanoscale* **2020**, *12*, 7660.
[43] Y. Bai, M. Mavrikakis, *J. Phys. Chem. B* **2017**, *122*, 432.
[44] Y. Ying, K. Fan, X. Luo, J. Qiao, H. Huang, *Mater. Adv.* **2020**, *1*, 1285.
[45] H. Yuan, Z. Li, J. Yang, *J. Phys. Chem. C* **2019**, *123*, 16294.
[46] L. Chen, J. Li, M. Ge, *Environ. Sci. Technol.* **2010**, *44*, 9590.
[47] Y. Xiao, W. Zhang, *Electrocatalysis* **2020**, *11*, 393.
[48] L. Li, B. Li, Q. Guo, B. Li, *J. Phys. Chem. C* **2019**, *123*, 14501.
[49] X. Lv, W. Wei, F. Li, B. Huang, Y. Dai, *Nano Lett.* **2019**, *19*, 6391.
[50] M. Yao, Z. Shi, P. Zhang, W.-J. Ong, J. Jiang, W.-Y. Ching, N. Li, *ACS Appl. Nano Mater.* **2020**, *3*, 9870.
[51] J. Pérez-Ramírez, C. H. Christensen, K. Egeblad, C. H. Christensen, J. C. Groen, *Chem. Soc. Rev.* **2008**, *37*, 2530.
[52] J. Yang, *Phys. Chem. Chem. Phys.* **2019**, *21*, 6112.
[53] W. Zhang, Y. Xiao, *Energy Fuels* **2020**, *34*, 2425.
[54] Y. Xiao, L. Tang, *Energy Fuels* **2020**, *34*, 5006.
[55] L. Liu, Y. Xiao, *Comput. Mater. Sci.* **2021**, *187*, 110082.
[56] X. Xu, X. Hou, J. Lu, P. Zhang, B. Xiao, J. Mi, *J. Phys. Chem. C* **2020**, *124*, 24156.

5.4 Conclusions

The conclusion of this doctoral thesis is focused on novel 2D crystal structures. This thesis aimed to screen and design high-performance catalysts for electrochemical reactions, investigate their electronic structure and propose reaction mechanism pathways to understand the activity and stability of catalysts. To achieve this goal, four different classes of 2D crystal structures (TMDs, MOFs, MXenes, and MBenes) were considered for this purpose, and a summary of important findings for each of the publications is listed below.

2D Double Metal Sulfide (M_2S_2) for the ORR in Fuel Cells. Our theoretical study reported that the 2D metal sulfide layer structure (M_2S_2) possesses promising activity for ORR applications in fuel cells. The most preferable reaction mechanism of the ORR is determined by the Gibbs free energy landscape based on the formation energy, while the limiting potential is determined by the rate-determining step and the overpotential is calculated based on the equilibrium potential. The Gibbs energy change landscape of the ORR displays a low external working potential corresponding to a small overpotential via $4e^-$ transfer for the ORR, and the opposite exhibits a large bottleneck for the OER via the $4e^-$ transfer pathway. This indicates that Mo_2S_2 and Zr_2S_2 catalysts are more suitable for the ORR with low overpotentials of 0.22 V and 0.47 V, respectively. Furthermore, the electronic structure of these M_2S_2 catalysts exhibits outstanding electrical conductivity without band gaps, which means excellent conductivity and charge mobility during the ORR process. These conclusions will be helpful for developing and designing high-efficiency catalyst applications in fuel cells.

CO_2 Electroreduction via a 2D Metal-Organic Framework Surface. In this article, describing that 2D $M_3(HITP)_2$ MOF can serve as a candidate catalyst for the electroreduction of CO_2 to CH_4, we systemically investigated the catalytic activity by high-throughput screening via DFT calculations. By analyzing the catalytic performance based on the linear scaling relations of limiting potential for each elementary reaction on different catalyst surfaces, eleven stable 2D $M_3(HITP)_2$ candidates were studied for CO_2 reduction to different C1 hydrocarbon fuel products. The results indicated that $Cr_3(HITP)_2$ and $Mn_3(HITP)_2$ MOFs possess promising catalytic performance with relatively low overpotentials (0.62 V and 0.69 V, respectively) for the production of CH_4 fuel cells. Furthermore, by further examining these 2D $M_3(HITP)_2$ prototype MOFs, they were found to have two types of M-C and M-O bonds between the adsorbates and surface metal atoms, which determines the formation of M-C or M-O bond intermediates during the CO_2RR process. In summary, $Cr_3(HITP)_2$ and $Cr_3(HITP)_2$ produce CO with low overpotentials of 0.24 V and 0.38 V, respectively, as well as CH_3OH with overpotentials of 0.47 V and 0.54 V, respectively.

M_3C_2 MXenes for Efficient CO_2 Reduction. The systematically investigated 2D M_3C_2-type MXene toward the CO_2 reduction reaction to CH_4 was discussed. Analyzing the change in limiting potential (U_L) between the CO_2RR and HER indicated that the CO_2RR over the HER is a dominant competing reaction for the selectivity of the CO_2RR. To produce methane as the final product, Ta_3C_2 and W_3C_2 were used with limiting potentials of -2.10 eV and -0.89 eV, respectively. The M-O-C and M-C-O binding is comparable to the relative strengths of carbophilicity or oxophilicity with transition metals. This work is likely to further guide the design of CO_2RR catalysts to produce high-efficiency fuel cells.

2D MBenes for the Electroreduction of CO_2 to C1 Hydrocarbon. In this work, we considered a series of MBenes as highly promising candidates for CO_2 electroreduction catalysts, and the binding energies of ΔG_{*OH} and ΔG_{*CO} were two key descriptors used to determine the catalytic activity of MBene catalysts. We identified Au_2B and V_3B_4 as promising candidates with high catalytic activity and selectivity for the reduction of CH_4, while Au_2B, Fe_2B_4, Ru_2B_4 and V_3B_4 are expected to be promising candidates for the reduction of CH_3OH. Fe_2B_4 and Ru_2B_4 were identified as promising catalysts for the reduction of CO with lower overpotentials of 0.15 and 0.14 eV, respectively.

N_2 Electroreduction on 2D MBenes. Then, a theoretical screening approach was implemented to evaluate the catalytic activity of transition metal boride (MBene) in the electrochemical NRR. These results indicate that Ta_3B_4, Nb_3B_4, $CrMnB_2$, Mo_2B_2, Ti_2B_2, and W_2B_2 exhibit the lowest limiting potential, and N_2 is more activated via the end-on than side-on pattern. The low limiting potential for NRR on MBenes can guarantee low energy costs, such as in the case of Nb_3B_4 (-0.50 V), Ta_3B_4 (-0.39 V), and Mo_2B_2 (-0.43 V). W_2B_2 has a low energy cost and high selectivity in the NRR/HER competing process. Our study provides an effective approach to designing high-performance catalysts for NRR and provides guidance for experiments in designing and developing catalysts for N_2 fixation.

MBenes High-efficiency Catalysts for NO Electroreduction to Ammonia. In summary, we used a high-throughput approach to screen transition metal borides (MBenes) as high-efficiency electrocatalysts. Our theoretical study shows that Fe_2B_2, Mn_2B_2, and Rh_2B_2 are promising electrocatalysts for converting NO to NH_3 with high activity and selectivity. This study provides new ideas for nitrate degradation and ammonia synthesis and found promising candidate catalysts via theoretical screening.

All publications show that this doctoral work involved three different types of 2D materials, showing that some M_2S_2 (TMDs-like) can serve as outstanding electrocatalysts for ORR applications in fuel cells, while some of the 2D $M_3(HITP)_2$ MOF compounds and M_3C_2 MXenes are suitable for CO_2RR, which is not only helpful in reducing carbon dioxide emissions but also producing value-added hydrocarbon fuel products. The majority of this thesis is focused on the application of a new novel 2D material, named transition-metal borides (MBenes), which will serve as the topic of my defense. MBene monolayers possess outstanding electrocatalytic activity for electrochemical energy conversion. 2D MBenes exhibit tunable electrochemical features and distinctive electronic structures, making them excellent candidates for optical, magnetic and spintronics devices and can serve as future research fields. As a new family of 2D materials, MBenes have recently been used in electrocatalytic reactions and have a significant influence on the application of sustainable energy storage and conversion. However, the electrocatalytic study of MBenes is still in its primary stage, and although theoretical calculations have verified that some MBene structures can be promising efficient catalysts for many energy conversion and storage reactions, their experimental investigation is still insufficient. For example, the mechanisms by which these materials act in the ORR, CO_2RR, and NRR remain to be explored. Thus, we have reasons to expect MBenes to have more remarkable activity performances in terms of electrochemical reactions. For example, MBenes are predicted to exhibit favorable N_2 adsorption by acting as nitrogen reduction electrocatalysts, which play an important role in the production of HER, OER, ORR, CO_2RR, and NRR, and MBenes are the focus of investigations based on high-throughput screening. To date, several different types of MBenes have been reported, both theoretically and experimentally, and the exploration of different types of 2D metal boride components and their catalytic activity will lead to many interesting applications and results. We expect that the unique properties of MBenes means that they can be used as CO_2RR, NRR, and NORR catalysts, owing to their excellent reaction activity and selectivity. We also expect new combinations of MBenes with other semiconductor materials to accelerate the development and design of catalysts for photocatalytic reactions. In general, 2D metal boride compounds as electrochemical catalysts are still a relatively unexplored field, and there are still challenges and difficulties in designing catalysts for electrochemical synthesis at the atomic scale. However, we believe that under the guidance of theory, material design is expected to result in major breakthroughs in the study of clean energy in the near future.

5.5 Prospects and outlook

5.5.1 Perspectives

2D material electrocatalysts play an important role in the catalytic electrochemical process. Due to the favorable action of charge carriers in transferring along a plane, these materials have a highly flexible, large, planar area and a highly specific surface area, which makes them suitable for application in electronic devices. The 2D materials studied work as highly active catalysts for the ORR, CO_2RR, NRR, and NORR electrochemical processes while also suppressing the competing HER process and being highly selective toward the target product. Furthermore, the initial molecule can be allowed to adsorb onto the active sites, and the structure of the catalyst plays a crucial role in the transport and activation of molecules on the catalyst layer. However, the low adsorptive capacities of CO_2 and N_2 are also major disadvantages that limit the mass transport of molecules. In fact, several studies have shown that using 2D material catalysts in electronic devices can lead to much higher current densities in comparison with traditional metal materials. The theoretical screening approach provides a more reliable and systematic review of the catalytic performance of a given material for CO_2RR, NRR, and NORR at an atomic scale. Electrocatalytic ammonium synthesis on 2D metal borides (MBenes) has attracted great attention and interest from researchers and industry owing to the following advantages: (i) electrochemical nitrogen fixation for NH_3 synthesis can be achieved using abundant N_2 as raw materials under ambient conditions, not only reducing the cost but also alleviating the energy crisis; (ii) NRR without carbon emissions can effectively alleviate environmental problems, such as the global warming caused by carbon dioxide; and (iii) 2D metal borides (MBenes) can also provide a promising route to producing clean and renewable energy that depends on electrochemical energy storage and conversion, hydrocarbon fuel (CO_2 electroreduction), and chemical raw materials (NH_3). However, the heterogeneous catalysis used in CO_2RR and NRR technology faces some technical bottlenecks, such as the weak binding strength of CO_2 and N_2 molecules to heterogeneous catalysts, and ammonia synthesis is usually accompanied by the generation of hydrazine, leading to a low selectivity toward NH_3. Current exploration of the fundamental mechanisms of N_2 electroreduction is still limited experimentally because of the complexity of the reaction process.

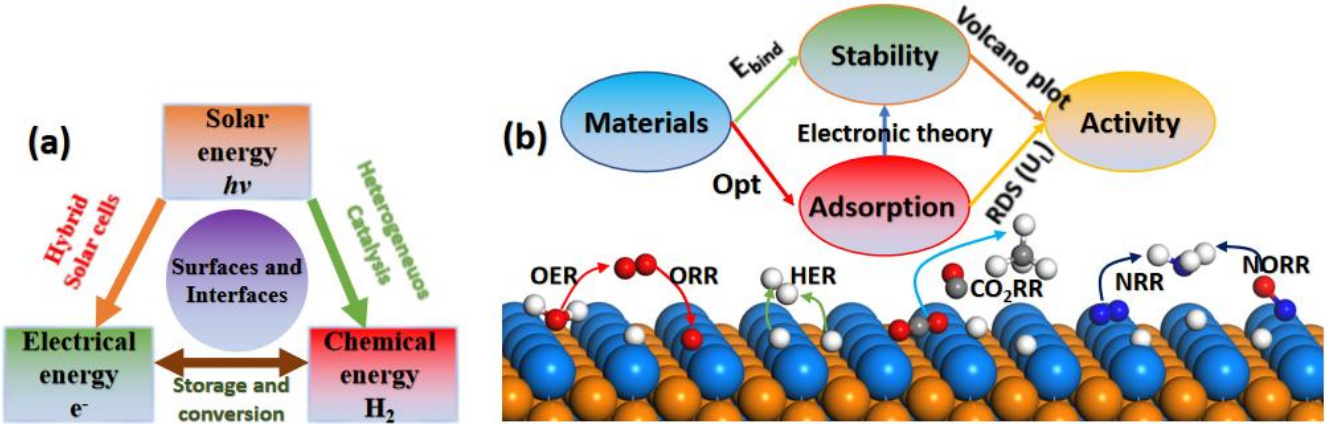

Figure 5-7. (a) Energy materials - surfaces and interfaces for conversion and storage. (b) An energy-integrated-based descriptor used in the theoretical screening of transition metal catalysts for electrochemical reaction.

To date, 2D materials have attracted extensive attention owing to their excellent physicochemical properties, such as high activity, high selectivity, and high conductivity in electrocatalyst materials. For example, 2D metal-organic frameworks (MOFs), 2D transition metal carbides (MXenes), and 2D metal borides (MBenes) have been systematically studied for their electronic structure, which might reveal particularly intriguing electrochemical reduction applications in energy conversion and storage devices. For the exploration of 2D MBene applications in electrocatalysis, more in-depth and systematic studies detailing the evolution of the surface state as related to the

reactive conditions are needed, including studies of the reactive phase and ionic, solvent, and electrode potentials. To accelerate the design and exploration of these catalysts for electrochemical catalysis, a theoretical screening approach can provide insight into the interaction mechanism, which can then be used to evaluate the catalytic activity of materials depending on the energy change profile analysis. To gain an in-depth understanding of the excellent catalytic performance of MBenes in electrocatalysis, the external potential and the electrolyte effect also require consideration. The adsorption of water molecules at the catalyst surface has been confirmed to significantly change the reactivity of the catalyst, and the surface properties of the catalyst are expected to depend on the essential features of the MBene materials and their surface states, which may open the door to more active and selective catalysts in comparison to the known catalysts that are difficult to react with traditional catalysts for common electrochemical reactions.

In particular, as strategies for how to suppress the competing HER and enhance the electrochemical reaction selectivity, the perspective of thermodynamics and reaction kinetics have been considered based on catalyst engineering. For example, based on the mechanism of the electrochemical reaction, limiting the transfer of proton-electron pairs from the electrolyte on the electrode surface or changing the equilibrium state through the external potential can effectively suppress the kinetics toward HER to achieve the goal of enhanced NRR selectivity. However, it needs to be noted that excessively restricting the transitivity of proton-electron pairs may influence and limit the overall conversion efficiency of the electrochemical energy conversion, and the balance of selectivity and conversion efficiency should be taken into consideration in actual applications while considering the corresponding energy consumption. For sustainable and clean energy applications, highly efficient and stable electrocatalysts have been widely studied, especially 2D materials, which are an independent hot research topic in the field of electrocatalysis and have achieved great development in recent decades. The high surface area of 2D materials can facilitate adsorption and electron transport, such as metal and nitrogen codoped graphene, g-C_3N_4, TMDs, LDH (layered double hydroxide), MXene, and MBenes. Some analysis and experimental techniques, such as XRD, TEM, STM and XPS, have been widely applied to 2D materials. These newly developed 2D materials possess high stability and selectivity toward electrochemical energy conversion applications and suggest promising activity for electrocatalytic reactions.

5.5.2 Outlook (Future work)

The combined analysis of all the publications highlights the potential of some novel 2D materials, which are all further research in my future work. In fact, the possibilities of 2D MBene materials show broad prospects for practical applications, especially the synergies generated from the different ratios of multiple metals with boron atoms, which can produce excellent physical and chemical properties. Some of my future research directions related to this dissertation are listed here in brief. The systematic exploration and design of heterogeneous catalysts is useful for electrochemical energy conversion and storage electronic devices, such as fuel cells, CO_2 capture, and N_2 fixation, and to solve the pollution of NO_x under ambient conditions. In this thesis, we propose some perspectives on the design and screening of high-performance catalysts. The materials should meet the requirements of being more efficient, cost-effective, and environmentally friendly. Because the composition and morphology of nanomaterials are different, it is essential to develop new synthesis technologies for 2D materials to enhance their catalytic performance. Optimization of the catalyst performance can be carried out by controlling the surface engineering, chemical modification, and interface control, all of which significantly influence catalytic performance. Compared to 1D and 3D materials, 2D material surfaces have rich low-coordination sites and possess a larger active surface area, leading to greatly enhanced catalytic activity.

For insight into the design and screening of promising electrocatalysts in my future research:

1. The free energies for the electrode materials can be calculated using the VASP code for a more realistic study with high-throughput calculations.
2. The physical and chemical properties of materials can be obtained by first-principles calculations (DFT) for the specific electrochemical reaction of a given material.
3. The structure of 2D material active surfaces can be reconstructed using theoretical models, which can be extremely useful for the design and optimization of catalysts.

The crystal and electronic structures of metallic boride compounds, due to the metalloid nature of boron, can generate rich bonding schemes between metal and boron atoms, leading to boron atoms playing an important role in the electrocatalytic process on metallic boride surfaces. The applications of metallic borides can extend to energy storage and conversion devices, including electrochemical catalysis, metal-ion batteries, electrochemical catalysis, and supercapacitors. Although great achievements have been reported both on the synthesis and theoretical research of metallic boride compounds, there are still several challenges and issues that should be addressed in practical applications. Some issues are classified as follows, which I need to focus on in my future work:

(i) Due to the lack of low specific surface areas and uncontrollable morphology of crystallized metal boride compounds, which site is the most favorable active center cannot be guaranteed in the modeling. Thus, further research can focus on controlling the particle size, and surface characterization of the morphology of metal borides is necessary.

(ii) The different ratios of metal to boron can form several metal boride crystal structures, but it prefers to form the most stable structure during the chemical synthesis process. Therefore, it is necessary to strengthen and improve the reaction route for forming the target product.

(iii) The material properties of metal boride compounds play a vitally important role in electrocatalytic applications, especially when considering the effects of solvation when working on the electrolyte. However, there are few reports about this, and further research is needed.

(iv) Current studies of metal borides mainly focus on structural features, but studies on electrochemical mechanisms and activity are deficient. It is necessary to investigate their catalytic properties in practical applications.

(v) The 2D MBenes considered in this doctoral thesis have not been sufficiently explored. Further studies exploring the catalytic mechanism on 2D metal borides are needed.

5.5.3 Appendices

Supplementary material

Supplementary information for chapter. 5.3.1

A High Throughput Approach Exploitation: 2D Double Metal Sulfide (M_2S_2) of Efficient Electrocatalysts for ORR in Fuel Cell

Yi Xiao*, and Li Tang

Supporting Information

The Supporting Information is available free of charge at https://pubs.acs.org/doi/10.1021/acs.energyfuels.0c00297

Supplementary information for chapter. 5.3.2

Mechanistic study of efficient producing CO_2 electroreduction via 2D metal-organic frameworks M_3(2,3,6,7,10,11-hexaiminotriphenylene)$_2$ surface

Xiao Y*, Chen D, Chen R.

Supporting Information

Supplementary material associated with this article can be found, in the online version, at doi: 10.1016/j.electacta.2021.138028 .

Supplementary information for chapter. 5.3.3

High throughput screening of M_3C_2 MXenes for efficient CO_2 reduction conversion into hydrocarbon fuels

Xiao Y*, Zhang W.

Supporting Information

Electronic supplementary information (ESI) available. See DOI: 10.1039/ c9nr10598k.

Supplementary information for chapter. 5.3.4

Quantum Mechanical Screening of 2D MBenes for the Electroreduction of CO_2 to C1 Hydrocarbon Fuels

Xiao Y*, Shen C, Hadaeghi N.

Supporting Information

The Supporting Information is available free of charge at https://pubs.acs.org/doi/10.1021/acs.jpclett.1c01499.

Supplementary information for chapter. 5.3.5

Theoretical Establishment and Screening of an Efficient Catalyst for N_2 Electroreduction on Two-Dimensional Transition-Metal Borides (MBenes)

Xiao Y*, Shen C, Long T.

Supporting Information

The Supporting Information is available free of charge at https://pubs.acs.org/doi/10.1021/acs.chemmater.1c00424.

Supplementary information for chapter. 5.3.6

Transition-Metal Borides (MBenes) as New High-Efficiency Catalysts for Nitric Oxide Electroreduction to Ammonia by a High-Throughput Approach

Xiao Y*, Shen C.

Supporting Information

The Supporting Information is available free of charge at https://onlinelibrary.wiley.com/doi/full/10.1002/smll.202100776.

6.Bibliography

1. Dincer I, Rosen M A. A worldwide perspective on energy, environment and sustainable development[J]. International journal of energy research, 1998, 22(15): 1305-1321.
2. Trombetta M J. Environmental security and climate change: analysing the discourse[J]. Cambridge Review of International Affairs, 2008, 21(4): 585-602.
3. Owusu P A, Asumadu-Sarkodie S. A review of renewable energy sources, sustainability issues and climate change mitigation[J]. Cogent Engineering, 2016, 3(1): 1167990.
4. BloombergNEF. (Bloomberg New Energy Finance). 19 January 2021. Archived from the original on 19 January 2021.
5. Seh Z W, Kibsgaard J, Dickens C F, et al. Combining theory and experiment in electrocatalysis: Insights into materials design[J]. Science, 2017, 355(6321).
6. Wirth T E, Gray C B, Podesta J D. The future of energy policy[J]. Foreign Affairs, 2003: 132-155.
7. Herbert G M J, Iniyan S, Sreevalsan E, et al. A review of wind energy technologies[J]. Renewable and sustainable energy Reviews, 2007, 11(6): 1117-1145.
8. Faaij A. Modern biomass conversion technologies[J]. Mitigation and adaptation strategies for global change, 2006, 11(2): 343-375.
9. Barbier E. Geothermal energy technology and current status: an overview[J]. Renewable and sustainable energy reviews, 2002, 6(1-2): 3-65.
10. Kreider J F, Kreith F. Solar energy handbook[J]. 1981.
11. Momirlan M, Veziroglu T N. Current status of hydrogen energy[J]. Renewable and sustainable energy reviews, 2002, 6(1-2): 141-179.
12. Holdgate M W. A perspective of environmental pollution[M]. Cambridge University Press, 1979.
13. Höök M, Tang X. Depletion of fossil fuels and anthropogenic climate change—A review[J]. Energy policy, 2013, 52: 797-809.
14. Olander D. Nuclear fuels–present and future[J]. Journal of Nuclear Materials, 2009, 389(1): 1-22.
15. Singh M, Khadkikar V, Chandra A, et al. Grid interconnection of renewable energy sources at the distribution level with power-quality improvement features[J]. IEEE transactions on power delivery, 2010, 26(1): 307-315.
16. Batista M S, Santos R K S, Assaf E M, et al. High efficiency steam reforming of ethanol by cobalt-based catalysts[J]. Journal of Power Sources, 2004, 134(1): 27-32.
17. Zhang S, Pan N. Supercapacitors performance evaluation[J]. Advanced Energy Materials, 2015, 5(6): 1401401.
18. Kordesch K, Simader G. Fuel cells and their applications[J]. 1996.
19. MacFarlane D R, Forsyth M, Howlett P C, et al. Ionic liquids and their solid-state analogues as materials for energy generation and storage[J]. Nature Reviews Materials, 2016, 1(2): 1-15.
20. Arico A S, Bruce P, Scrosati B, et al. Nanostructured materials for advanced energy conversion and storage devices[J]. Materials for sustainable energy: a collection of peer-reviewed research and review articles from Nature Publishing Group, 2011: 148-159.
21. Little W A. Possibility of synthesizing an organic superconductor[J]. Physical Review, 1964, 134(6A): A1416.
22. Wang X, Lu X, Liu B, et al. Flexible energy-storage devices: design consideration and recent progress[J]. Advanced materials, 2014, 26(28): 4763-4782.
23. Granqvist C G. Electrochromic devices[J]. Journal of the European Ceramic Society, 2005, 25(12): 2907-2912.
24. Williams M C, Strakey J P, Surdoval W A. The US department of energy, office of fossil energy stationary fuel cell program[J]. Journal of power sources, 2005, 143(1-2): 191-196.
25. Khanafer K, Vafai K. A review on the applications of nanofluids in solar energy field[J]. Renewable Energy, 2018, 123: 398-406.
26. Li Q, Cao R, Cho J, et al. Nanocarbon electrocatalysts for oxygen reduction in alkaline media for advanced energy conversion and storage[J]. Advanced Energy Materials, 2014, 4(6): 1301415.
27. Xue X, Ji W, Mao Z, et al. Raman investigation of nanosized TiO_2: effect of crystallite size and quantum confinement[J]. The Journal of Physical Chemistry C, 2012, 116(15): 8792-8797.
28. http://www.ee.ui.ac.id/epes/research-group/energy-materials.
29. Niu Z, Pinfield V J, Wu B, et al. Towards the digitalisation of porous energy materials: evolution of digital approaches for microstructural design[J]. Energy & Environmental Science, 2021, 14(5): 2549-2576.
30. Wang J, Gao Y, Kong H, et al. Non-precious-metal catalysts for alkaline water electrolysis: operando characterizations, theoretical calculations, and recent advances[J]. Chemical Society Reviews, 2020.
31. Gu G H, Noh J, Kim I, et al. Machine learning for renewable energy materials[J]. Journal of Materials Chemistry A, 2019, 7(29): 17096-17117.

32. Zai J, Qian X. Three dimensional metal oxides–graphene composites and their applications in lithium ion batteries[J]. RSC Advances, 2015, 5(12): 8814-8834.
33. Wang F, Shifa T A, Zhan X, et al. Recent advances in transition-metal dichalcogenide based nanomaterials for water splitting[J]. Nanoscale, 2015, 7(47): 19764-19788.
34. Xiao Y, Wang J, Wang Y, et al. A new promising catalytic activity on blue phosphorene nitrogen-doped nanosheets for the ORR as cathode in nonaqueous Li–air batteries[J]. Applied Surface Science, 2019, 488: 620-628.
35. Yu X, Marks T J, Facchetti A. Metal oxides for optoelectronic applications[J]. Nature materials, 2016, 15(4): 383-396.
36. Lu Q, Chen J G, Xiao J Q. Nanostructured electrodes for high-performance pseudocapacitors[J]. Angewandte Chemie International Edition, 2013, 52(7): 1882-1889.
37. Lai S, Byeon S, Jang S K, et al. HfO_2/HfS_2 hybrid heterostructure fabricated via controllable chemical conversion of two-dimensional HfS 2[J]. Nanoscale, 2018, 10(39): 18758-18766.
38. Nayeri M, Moradinasab M, Fathipour M. The transport and optical sensing properties of MoS_2, $MoSe_2$, WS_2 and WSe_2 semiconducting transition metal dichalcogenides[J]. Semiconductor Science and Technology, 2018, 33(2): 025002.
39. Nohara S, Namatame H, Matsubara H, et al. Angle-resolved inverse photoemission spectra of layered 1T-VSe_2, 1T-TiS_2, 1T-TaS_2, 2H-$NbSe_2$ and 2H-$TaSe_2$[J]. Journal of the Physical Society of Japan, 1991, 60(11): 3882-3892.
40. Gallucci F, Fernandez E, Corengia P, et al. Recent advances on membranes and membrane reactors for hydrogen production[J]. Chemical Engineering Science, 2013, 92: 40-66.
41. Millange F, Guillou N, Medina M E, et al. Selective sorption of organic molecules by the flexible porous hybrid metal− organic framework MIL-53 (Fe) controlled by various host− guest interactions[J]. Chemistry of Materials, 2010, 22(14): 4237-4245.
42. Rowsell J L C, Yaghi O M. Metal–organic frameworks: a new class of porous materials[J]. Microporous and mesoporous materials, 2004, 73(1-2): 3-14.
43. Creighton J R, Ho P. Introduction to chemical vapor deposition (CVD)[J]. Chemical vapor deposition, 2001, 2: 1-22.
44. Ye L, Chen S, Li W, et al. Tuning the electrical transport properties of multilayered molybdenum disulfide nanosheets by intercalating phosphorus[J]. The Journal of Physical Chemistry C, 2015, 119(17): 9560-9567.
45. Schulte F, Lingott J, Panne U, et al. Chemical characterization and classification of pollen[J]. Analytical chemistry, 2008, 80(24): 9551-9556.
46. Loss D, DiVincenzo D P. Quantum computation with quantum dots[J]. Physical Review A, 1998, 57(1): 120.
47. Hurst S J, Payne E K, Qin L, et al. Multisegmented one-dimensional nanorods prepared by hard-template synthetic methods[J]. Angewandte Chemie International Edition, 2006, 45(17): 2672-2692.
48. Latil S, Henrard L. Charge carriers in few-layer graphene films[J]. Physical Review Letters, 2006, 97(3): 036803.
49. Chen W, Gui X, Yang L, et al. Wrinkling of two-dimensional materials: methods, properties and applications[J]. Nanoscale horizons, 2019, 4(2): 291-320.
50. Guo Y, Xu K, Wu C, et al. Surface chemical-modification for engineering the intrinsic physical properties of inorganic two-dimensional nanomaterials[J]. Chemical Society Reviews, 2015, 44(3): 637-646.
51. Shifa T A, Wang F, Liu Y, et al. Heterostructures based on 2d materials: a versatile platform for efficient catalysis[J]. Advanced Materials, 2019, 31(45): 1804828.
52. Zagal J H. Metallophthalocyanines as catalysts in electrochemical reactions[J]. Coordination Chemistry Reviews, 1992, 119: 89-136.
53. Xiong P, Sun B, Sakai N, et al. 2D superlattices for efficient energy storage and conversion[J]. Advanced Materials, 2020, 32(18): 1902654.
54. Tan T, Jiang X, Wang C, et al. 2D material optoelectronics for information functional device applications: status and challenges[J]. Advanced Science, 2020, 7(11): 2000058.
55. Ma L, Song X, Yu Y, et al. Two-Dimensional Silicene/Silicon Nanosheets: An Emerging Silicon-Composed Nanostructure in Biomedicine[J]. Advanced Materials, 2021: 2008226.
56. Choi S J, Kim I D. Recent developments in 2D nanomaterials for chemiresistive-type gas sensors[J]. Electronic Materials Letters, 2018, 14(3): 221-260.
57. Zhu Y, Peng L, Fang Z, et al. Structural engineering of 2D nanomaterials for energy storage and catalysis[J]. Advanced Materials, 2018, 30(15): 1706347.
58. Khan K, Tareen A K, Aslam M, et al. Recent advances in two-dimensional materials and their nanocomposites in sustainable energy conversion applications[J]. Nanoscale, 2019, 11(45): 21622-21678.
59. Peng J, Chen X, Ong W J, et al. Surface and heterointerface engineering of 2D MXenes and their nanocomposites: insights into electro-and photocatalysis[J]. Chem, 2019, 5(1): 18-50.
60. Herbst J. A machine learning approach to workflow management[C]//European conference on machine learning. Springer, Berlin, Heidelberg, 2000: 183-194.
61. Walawalkar M G. Boron: the first p-block element to fix inert N_2 all the way to NH 3[J]. Dalton Transactions, 2021, 50(2): 460-465.
62. Kandemir T, Schuster M E, Senyshyn A, et al. The Haber–Bosch process revisited: on the real structure and stability of “ammonia iron” under working conditions[J]. Angewandte Chemie International Edition, 2013, 52(48): 12723-12726.
63. Likens G E, Bormann F H, Johnson N M. Acid rain[J]. Environment: Science and Policy for Sustainable Development, 1972, 14(2): 33-40.

64. Hu X, Zhang J J, Mukhnahallipatna S, et al. Transformations and destruction of nitrogen oxides—NO, NO_2 and N_2O—in a pulsed corona discharge reactor [J]. Fuel, 2003, 82(13): 1675-1684.
65. Zhang C, Shen X, Pan Y, et al. A review of Pt-based electrocatalysts for oxygen reduction reaction[J]. Frontiers in Energy, 2017, 11(3): 268-285.
66. Hu B, Guild C, Suib S L. Thermal, electrochemical, and photochemical conversion of CO_2 to fuels and value-added products[J]. Journal of CO_2 Utilization, 2013, 1: 18-27.
67. Dou J H, Sun L, Ge Y, et al. Signature of metallic behavior in the metal–organic frameworks M_3 (hexaiminobenzene)$_2$ (M= Ni, Cu)[J]. Journal of the American Chemical Society, 2017, 139(39): 13608-13611.
68. Sheberla D, Sun L, Blood-Forsythe M A, et al. High electrical conductivity in Ni_3(2, 3, 6, 7, 10, 11-hexaiminotriphenylene)$_2$, a semiconducting metal–organic graphene analogue[J]. Journal of the American Chemical Society, 2014, 136(25): 8859-8862.
69. Tian Y, Wang Y, Yan L, et al. Electrochemical reduction of carbon dioxide on the two–dimensional M_3 (Hexaiminotriphenylene)$_2$ sheet: A computational study[J]. Applied Surface Science, 2019, 467: 98-103.
70. Gaikwad S, Kim Y, Gaikwad R, et al. Enhanced CO_2 capture capacity of amine-functionalized MOF-177 metal organic framework[J]. Journal of Environmental Chemical Engineering, 2021, 9(4): 105523.
71. Xiao Y, Chen D, Chen R. Mechanistic study of efficient producing CO_2 electroreduction via 2D metal-organic frameworks M_3(2, 3, 6, 7, 10, 11-hexaiminotriphenylene)$_2$ surface[J]. Electrochimica Acta, 2021, 378: 138028.
72. Chen S, Dai J, Zeng X C. Metal–organic Kagome lattices M_3(2, 3, 6, 7, 10, 11-hexaiminotriphenylene)$_2$ (M= Ni and Cu): from semiconducting to metallic by metal substitution[J]. Physical Chemistry Chemical Physics, 2015, 17(8): 5954-5958.
73. Mao X, Tang C, He T, et al. Computational screening of MN_4(M= Ti–Cu) based metal organic frameworks for CO_2 reduction using the d-band centre as a descriptor[J]. Nanoscale, 2020, 12(10): 6188-6194.
74. Naguib M, Kurtoglu M, Presser V, et al. Two-dimensional nanocrystals produced by exfoliation of Ti_3AlC_2[J]. Advanced materials, 2011, 23(37): 4248-4253.
75. Högberg H, Hultman L, Emmerlich J, et al. Growth and characterization of MAX-phase thin films[J]. Surface and Coatings Technology, 2005, 193(1-3): 6-10.
76. Lin Z, Shao H, Xu K, et al. MXenes as high-rate electrodes for energy storage[J]. Trends in Chemistry, 2020, 2(7): 654-664.
77. Anasori B, Lukatskaya M R, Gogotsi Y. 2D metal carbides and nitrides (MXenes) for energy storage[J]. Nature Reviews Materials, 2017, 2(2): 1-17.
78. Handoko A D, Khoo K H, Tan T L, et al. Establishing new scaling relations on two-dimensional MXenes for CO 2 electroreduction[J]. Journal of Materials Chemistry A, 2018, 6(44): 21885-21890.
79. ZHANG H, Wang J, Khazaei M, et al. Phase Diagram Exploration of Tc-Al-B: from Bulk Tc_2AlB_2 to Two-dimensional Tc_2B_2[J]. Physical Chemistry Chemical Physics, 2021.
80. Yang X, Shang C, Zhou S, et al. MBenes: emerging 2D materials as efficient electrocatalysts for the nitrogen reduction reaction[J]. Nanoscale Horizons, 2020, 5(7): 1106-1115.
81. Jia J, Li B J, Duan S, et al. Monolayer MBenes: prediction of anode materials for high-performance lithium/sodium ion batteries[J]. Nanoscale, 2019, 11(42): 20307-20314.
82. Guo Z, Zhou J, Sun Z. New two-dimensional transition metal borides for Li ion batteries and electrocatalysis[J]. Journal of Materials Chemistry A, 2017, 5(45): 23530-23535.
83. Jiang Z, Wang P, Jiang X, et al. MBene (MnB): a new type of 2D metallic ferromagnet with high Curie temperature[J]. Nanoscale horizons, 2018, 3(3): 335-341.
84. Yuan H, Li Z, Yang J. Transition-metal diboride: a new family of two-dimensional materials designed for selective CO2 electroreduction[J]. The Journal of Physical Chemistry C, 2019, 123(26): 16294-16299.
85. Sun X, Zheng J, Gao Y, et al. Machine-learning-accelerated screening of hydrogen evolution catalysts in MBenes materials[J]. Applied Surface Science, 2020, 526: 146522.
86. Evans C M, Sparks D L. On the chemistry and mineralogy of boron in pure and in mixed systems: A review[J]. Communications in Soil Science and Plant Analysis, 1983, 14(9): 827-846.
87. Laursen A B, Varela A S, Dionigi F, et al. Electrochemical hydrogen evolution: Sabatier's principle and the volcano plot[J]. Journal of Chemical Education, 2012, 89(12): 1595-1599.
88. Ananthaneni S, Smith Z, Rankin R B. Graphene supported tungsten carbide as catalyst for electrochemical reduction of CO_2[J]. Catalysts, 2019, 9(7): 604.
89. Deringer V L, Tchougréeff A L, Dronskowski R. Crystal orbital Hamilton population (COHP) analysis as projected from plane-wave basis sets[J]. The journal of physical chemistry A, 2011, 115(21): 5461-5466.
90. Acerbi N, Tsang S C E, Jones G, et al. Rationalization of interactions in precious metal/ceria catalysts using the d-band center model[J]. Angewandte Chemie, 2013, 125(30): 7891-7895.
91. Niu H, Wan X, Wang X, et al. Single-Atom Rhodium on Defective g-C_3N_4: A Promising Bifunctional Oxygen Electrocatalyst[J]. ACS Sustainable Chemistry & Engineering, 2021, 9(9): 3590-3599.
92. Gu G H, Choi C, Lee Y, et al. Progress in computational and machine-learning methods for heterogeneous small-molecule activation[J]. Advanced Materials, 2020, 32(35): 1907865.

93. Wan X, Zhang Z, Niu H, et al. Machine-Learning-Accelerated Catalytic Activity Predictions of Transition Metal Phthalocyanine Dual-Metal-Site Catalysts for CO_2 Reduction[J]. The Journal of Physical Chemistry Letters, 2021, 12(26): 6111-6118.
94. Niu H, Wan X, Wang X, et al. Single-Atom Rhodium on Defective g-C_3N_4: A Promising Bifunctional Oxygen Electrocatalyst[J]. ACS Sustainable Chemistry & Engineering, 2021, 9(9): 3590-3599.
95. Ying Y, Fan K, Luo X, et al. Unravelling the origin of bifunctional OER/ORR activity for single-atom catalysts supported on C_2N by DFT and machine learning[J]. Journal of Materials Chemistry A, 2021, 9(31): 16860-16867.
96. Liu J, Liu H, Chen H, et al. Progress and challenges toward the rational design of oxygen electrocatalysts based on a descriptor approach[J]. Advanced Science, 2020, 7(1): 1901614.
97. Zhang J, Yang H, Liu B. Coordination Engineering of Single-Atom Catalysts for the Oxygen Reduction Reaction: A Review[J]. Advanced Energy Materials, 2021, 11(3): 2002473.
98. Wang X, Wang C, Ci S, et al. Accelerating 2D MXene catalyst discovery for the hydrogen evolution reaction by computer-driven workflow and an ensemble learning strategy[J]. Journal of Materials Chemistry A, 2020, 8(44): 23488-23497.
99. Zafari M, Kumar D, Umer M, et al. Machine learning-based high throughput screening for nitrogen fixation on boron-doped single atom catalysts[J]. Journal of Materials Chemistry A, 2020, 8(10): 5209-5216.
100. Klebes J, Finnigan S, Bray D J, et al. The Role of Chemical Heterogeneity in Surfactant Adsorption at Solid–Liquid Interfaces[J]. Journal of Chemical Theory and Computation, 2020, 16(11): 7135-7147.
101. Sakaushi K, Kumeda T, Hammes-Schiffer S, et al. Advances and challenges for experiment and theory for multi-electron multi-proton transfer at electrified solid–liquid interfaces[J]. Physical Chemistry Chemical Physics, 2020, 22(35): 19401-19442.
102. Zagar C, Griffith R R, Podgornik R, et al. On the voltage-controlled assembly of nanoparticle arrays at electrochemical solid/liquid interfaces[J]. Journal of Electroanalytical Chemistry, 2020, 872: 114275.
103. Yahya M. Insights into structural, solvent effect, molecular properties and NLO behavior of hemithioindigo-photoisomerization: A DFT study[J]. Journal of Molecular Liquids, 2021: 116944.
104. Ströker P, Meier K. Classical statistical mechanics in the grand canonical ensemble[J]. Physical Review E, 2021, 104(1): 014117.
105. Su M, Wang Y. A brief review of continuous models for ionic solutions: the Poisson–Boltzmann and related theories[J]. Communications in Theoretical Physics, 2020, 72(6): 067601.
106. Baricuatro J H, Kwon S, Kim Y G, et al. Operando Electrochemical Spectroscopy for CO on Cu (100) at pH 1 to 13: Validation of Grand Canonical Potential Predictions[J]. ACS Catalysis, 2021, 11(5): 3173-3181.
107. Hartmann G, Hwang G S. First-principles description of electrocatalytic characteristics of graphene-like materials[J]. The Journal of Chemical Physics, 2020, 153(21): 214704.
108. Oğuz I C, Vassetti D, Labat F. Assessing the performances of different continuum solvation models for the calculation of hydration energies of molecules, polymers and surfaces: a comparison between the SMD, VASPsol and FDPB models[J]. Theoretical Chemistry Accounts, 2021, 140(8): 1-13.
109. Oberhofer H. Electrocatalysis beyond the computational hydrogen electrode[J]. Handbook of Materials Modeling: Applications: Current and Emerging Materials, 2020: 1505-1537.
110. Peterson A A, Abild-Pedersen F, Studt F, et al. How copper catalyzes the electroreduction of carbon dioxide into hydrocarbon fuels[J]. Energy & Environmental Science, 2010, 3(9): 1311-1315.
111. Koper M T M. Theory of multiple proton–electron transfer reactions and its implications for electrocatalysis[J]. Chemical science, 2013, 4(7): 2710-2723.
112. Sun G, Kürti J, Rajczy P, et al. Performance of the Vienna ab initio simulation package (VASP) in chemical applications[J]. Journal of Molecular Structure: THEOCHEM, 2003, 624(1-3): 37-45.
113. Xu J, Sheng G P, Luo H W, et al. Fouling of proton exchange membrane (PEM) deteriorates the performance of microbial fuel cell[J]. Water research, 2012, 46(6): 1817-1824.
114. Wang V, Xu N, Liu J C, et al. VASPKIT: a user-friendly interface facilitating high-throughput computing and analysis using VASP code[J]. Computer Physics Communications, 2021: 108033.
115. Watson C I, Wilson C L. NIST special database 4[J]. Fingerprint Database, National Institute of Standards and Technology, 1992, 17(77): 5.
116. https://chem.libretexts.org/Bookshelves/General_Chemistry/Map%3A_Chemistry.
117. https://es.paperblog.com/interpretacion-de-la-energia-libre-de-gibbs-1780312/
118. Boltzmann L. The second law of thermodynamics[M]//Theoretical physics and philosophical problems. Springer, Dordrecht, 1974: 13-32.
119. http://theory.cm.utexas.edu/vtsttools/neb.html.
120. Jiang B, Guo H. Six-dimensional quantum dynamics for dissociative chemisorption of H_2 and D_2 on Ag (111) on a permutation invariant potential energy surface[J]. Physical Chemistry Chemical Physics, 2014, 16(45): 24704-24715.
121. http://doye.chem.ox.ac.uk/jon/PhD2/node40.html
122. Dickinson E J F, Wain A J. The Butler-Volmer equation in electrochemical theory: Origins, value, and practical application[J]. Journal of Electroanalytical Chemistry, 2020, 872: 114145.
123. Wang N, Liu Y, Zhao J, et al. DFT-based study on the mechanisms of the oxygen reduction reaction on Co(acetylacetonate)$_2$ supported by N-doped graphene nanoribbon[J]. RSC advances, 2016, 6(83): 79662-79667.

124. Ma J, Gong L, Shen Y, et al. Detrimental effects and prevention of acidic electrolytes on oxygen reduction reaction catalytic performance of heteroatom-doped graphene catalysts[J]. Frontiers in Materials, 2019, 6: 294.
125. Pegis M L, Wise C F, Koronkiewicz B, et al. Identifying and breaking scaling relations in molecular catalysis of electrochemical reactions[J]. Journal of the American Chemical Society, 2017, 139(32): 11000-11003.
126. Liu X, Jiao Y, Zheng Y, et al. Building up a picture of the electrocatalytic nitrogen reduction activity of transition metal single-atom catalysts[J]. Journal of the American Chemical Society, 2019, 141(24): 9664-9672.
127. Abild-Pedersen F, Greeley J, Studt F, et al. Scaling properties of adsorption energies for hydrogen-containing molecules on transition-metal surfaces[J]. Physical review letters, 2007, 99(1): 016105.
128. Andersen M, Levchenko S V, Scheffler M, et al. Beyond scaling relations for the description of catalytic materials[J]. ACS Catalysis, 2019, 9(4): 2752-2759.
129. Niu H, Wang X, Shao C, et al. Computational Screening Single-Atom Catalysts Supported on g-CN for N_2 Reduction: High Activity and Selectivity[J]. ACS Sustainable Chemistry & Engineering, 2020, 8(36): 13749-13758.
130. Niu H, Zhang Z, Wang X, et al. Theoretical Insights into the Mechanism of Selective Nitrate-to-Ammonia Electroreduction on Single-Atom Catalysts[J]. Advanced Functional Materials, 2021, 31(11): 2008533.
131. Greeley J, Jaramillo T F, Bonde J, et al. Computational high-throughput screening of electrocatalytic materials for hydrogen evolution[J]. Nature materials, 2006, 5(11): 909-913.
132. Hinnemann B, Moses P G, Bonde J, et al. Biomimetic hydrogen evolution: MoS2 nanoparticles as catalyst for hydrogen evolution[J]. Journal of the American Chemical Society, 2005, 127(15): 5308-5309.
133. Tran K, Ulissi Z W. Active learning across intermetallics to guide discovery of electrocatalysts for CO_2 reduction and H_2 evolution[J]. Nature Catalysis, 2018, 1(9): 696-703.
134. Nørskov J K, Abild-Pedersen F, Studt F, et al. Density functional theory in surface chemistry and catalysis[J]. Proceedings of the National Academy of Sciences, 2011, 108(3): 937-943.
135. Bligaard T, Nørskov J K, Dahl S, et al. The Brønsted–Evans–Polanyi relation and the volcano curve in heterogeneous catalysis[J]. Journal of catalysis, 2004, 224(1): 206-217.
136. Mammen N, de Gironcoli S, Narasimhan S. Substrate doping: A strategy for enhancing reactivity on gold nanocatalysts by tuning sp bands[J]. The Journal of chemical physics, 2015, 143(14): 144307.
137. Bhattacharjee S, Waghmare U V, Lee S C. An improved d-band model of the catalytic activity of magnetic transition metal surfaces[J]. Scientific reports, 2016, 6(1): 1-10.
138. Van Santen R A, Neurock M, Shetty S G. Reactivity theory of transition-metal surfaces: a Brønsted− Evans− Polanyi linear activation energy− free-energy analysis[J]. Chemical reviews, 2009, 110(4): 2005-2048.
139. Somorjai G A. Modern concepts in surface science and heterogeneous catalysis[J]. Journal of physical chemistry, 1990, 94(3): 1013-1023.
140. Mueller J E, Fantauzzi D. Multiscale modeling of electrochemical systems[J]. Electrocatalysis, 2013, 4.
141. Reuter K, Andersen M, Plaisance C. First principles multiscale kinetic modelling of catalytic reactions[C]//High Performance Computing. 80.
142. Chatterjee A, Vlachos D G. An overview of spatial microscopic and accelerated kinetic Monte Carlo methods[J]. Journal of computer-aided materials design, 2007, 14(2): 253-308.
143. Tal-Ezer H, Kosloff R. An accurate and efficient scheme for propagating the time dependent Schrödinger equation[J]. The Journal of chemical physics, 1984, 81(9): 3967-3971.
144. Gu G H, Noh J, Kim I, et al. Machine learning for renewable energy materials[J]. Journal of Materials Chemistry A, 2019, 7(29): 17096-17117.
145. Raschka S, Mirjalili V. Python Machine Learning: Machine Learning and Deep Learning with Python[J]. Scikit-Learn, and TensorFlow. Second edition ed, 2017.
146. Motagamwala A H, Dumesic J A. Microkinetic modeling: a tool for rational catalyst design[J]. Chemical Reviews, 2020, 121(2): 1049-1076.
147. Dreizler R M, Gross E K U. Density functional theory: an approach to the quantum many-body problem[M]. Springer Science & Business Media, 2012.
148. Hohenberg P, Kohn W. Density functional theory (DFT)[J]. Phys. Rev, 1964, 136: B864.
149. Sahni V. The Hohenberg-Kohn Theorems and Kohn-Sham Density Functional Theory[M]//Quantal Density Functional Theory. Springer, Berlin, Heidelberg, 2004: 99-123.
150. Myers W D, Swiatecki W J. Nuclear properties according to the Thomas-Fermi model[J]. Nuclear Physics A, 1996, 601(2): 141-167.
151. Hohenberg P, Kohn W. Inhomogeneous electron gas[J]. Physical review, 1964, 136(3B): B864.
152. Combes J M, Duclos P, Seiler R. The born-oppenheimer approximation[M]//Rigorous atomic and molecular physics. Springer, Boston, MA, 1981: 185-213.
153. Hohenberg P, Kohn W. Density functional theory (DFT)[J]. Phys. Rev, 1964, 136: B864.
154. Hadjisavvas N, Theophilou A. Rigorous formulation of the Kohn and Sham theory[J]. Physical Review A, 1984, 30(5): 2183.
155. Jackson K, Pederson M R. Accurate forces in a local-orbital approach to the local-density approximation[J]. Physical Review B, 1990, 42(6): 3276.

156. Perdew J P, Yue W. Accurate and simple density functional for the electronic exchange energy: Generalized gradient approximation[J]. Physical review B, 1986, 33(12): 8800.
157. Perdew J P, Burke K, Ernzerhof M. Perdew, burke, and ernzerhof reply[J]. Physical Review Letters, 1998, 80(4): 891.
158. Hammer B, Hansen L B, Nørskov J K. Improved adsorption energetics within density-functional theory using revised Perdew-Burke-Ernzerhof functionals[J]. Physical review B, 1999, 59(11): 7413.
159. Matveev A, Staufer M, Mayer M, et al. Density functional study of small molecules and transition-metal carbonyls using revised PBE functionals[J]. International journal of quantum chemistry, 1999, 75(4-5): 863-873.
160. Shepherd J J, Booth G, Grüneis A, et al. Full configuration interaction perspective on the homogeneous electron gas[J]. Physical Review B, 2012, 85(8): 081103.
161. Wang V, Xu N, Liu J C, et al. VASPKIT: a user-friendly interface facilitating high-throughput computing and analysis using VASP code[J]. Computer Physics Communications, 2021: 108033.
162. Troullier N, Martins J L. Efficient pseudopotentials for plane-wave calculations[J]. Physical review B, 1991, 43(3): 1993.
163. Clark S J, Segall M D, Pickard C J, et al. First principles methods using CASTEP[J]. Zeitschrift für Kristallographie-Crystalline Materials, 2005, 220(5-6): 567-570.
164. Kresse G, Furthmüller J. Efficiency of ab-initio total energy calculations for metals and semiconductors using a plane-wave basis set[J]. Computational materials science, 1996, 6(1): 15-50.
165. Sun G, Kürti J, Rajczy P, et al. Performance of the Vienna ab initio simulation package (VASP) in chemical applications[J]. Journal of Molecular Structure: THEOCHEM, 2003, 624(1-3): 37-45.
166. Colliot-Thélene J L, Hoobler R T, Kahn B. The Bloch-Ogus-Gabber theorem[J]. Algebraic K-Theory (Toronto, ON, 1996), 1997, 16: 31-94.
167. Morvan B, Hladky-Hennion A C, Leduc D, et al. Ultrasonic guided waves on a periodical grating: Coupled modes in the first Brillouin zone[J]. Journal of applied physics, 2007, 101(11): 114906.
168. Wang V, Liang Y Y, Kawazoe Y, et al. High-Throughput Computational Screening of Two-Dimensional Semiconductors[J]. arXiv preprint arXiv:1806.04285, 2018.
169. de Chialvo M R G, Chialvo A C. Hydrogen evolution reaction: analysis of the Volmer-Heyrovsky-Tafel mechanism with a generalized adsorption model[J]. Journal of Electroanalytical Chemistry, 1994, 372(1-2): 209-223.
170. Yang T, Patil R, McKone J R, et al. Revisiting Trends in the Exchange Current for Hydrogen Evolution[J]. Catalysis Science & Technology, 2021.
171. Kakaei K, Esrafili M D, Ehsani A. Alcohol oxidation and hydrogen evolution[M]//Interface Science and Technology. Elsevier, 2019, 27: 253-301.
172. Yang Y, Liu J, Liu F, et al. FeS_2-anchored transition metal single atoms for highly efficient overall water splitting: a DFT computational screening study[J]. Journal of Materials Chemistry A, 2021, 9(4): 2438-2447.
173. Nie X, Luo W, Janik M J, et al. Reaction mechanisms of CO_2 electrochemical reduction on Cu (1 1 1) determined with density functional theory[J]. Journal of catalysis, 2014, 312: 108-122.
174. Zhang G R, Straub S D, Shen L L, et al. Probing CO_2 reduction pathways for copper catalysis using an ionic liquid as a chemical trapping agent[J]. Angewandte Chemie International Edition, 2020, 59(41): 18095-18102.
175. Zhou Y, Yeo B S. Formation of C–C bonds during electrocatalytic CO_2 reduction on non-copper electrodes [J]. Journal of Materials Chemistry A, 2020, 8(44): 23162-23186.
176. Calvinho K U D, Laursen A B, Yap K M K, et al. Selective CO_2 reduction to C_3 and C_4 oxyhydrocarbons on nickel phosphides at overpotentials as low as 10 mV[J]. Energy & Environmental Science, 2018, 11(9): 2550-2559.
177. Kuhl G C, De Dea Lindner J. Biohydrogenation of linoleic acid by lactic acid bacteria for the production of functional cultured dairy products: A review[J]. Foods, 2016, 5(1): 13.
178. Guo X, Lin S, Gu J, et al. Establishing a Theoretical Landscape for Identifying Basal Plane Active 2D Metal Borides (MBenes) toward Nitrogen Electroreduction[J]. Advanced Functional Materials, 2021, 31(6): 2008056.
179. Sun J, Yang S, Liang Z, et al. Two-dimensional/one-dimensional molybdenum sulfide (MoS_2) nanoflake/graphitic carbon nitride (g-C_3N_4) hollow nanotube photocatalyst for enhanced photocatalytic hydrogen production activity[J]. Journal of colloid and interface science, 2020, 567: 300-307.
180. Bai Y, Mavrikakis M. Mechanistic study of nitric oxide reduction by hydrogen on Pt (100)(I): a DFT analysis of the reaction network[J]. The Journal of Physical Chemistry B, 2017, 122(2): 432-443.
181. Saeidi N, Esrafili M D, Sardroodi J J. NO electrochemical reduction over Si-N_4 embedded graphene: A DFT investigation[J]. Applied Surface Science, 2021, 544: 148869.
182. Weiss R L, Cerreto M C. The Marital Status Inventory: Development of a measure of dissolution potential[J]. American Journal of Family Therapy, 1980, 8(2): 80-85.
183. Ren Y, Yu C, Tan X, et al. Strategies to suppress hydrogen evolution for highly selective electrocatalytic nitrogen reduction: challenges and perspectives[J]. Energy & Environmental Science, 2021, 14(3): 1176-1193.
184. Rowlinson* J S. The Maxwell–Boltzmann distribution[J]. Molecular Physics, 2005, 103(21-23): 2821-2828.

Journal Publications (2018.10-present)

First Author

1. Xiao Y, Shen C, Xiong Z, et al. A Strategy to Address the Challenge of Electrochemical CO2 and N2 Coupling to Synthesis Urea on Two-Dimensional Metal Borides (MBenes) by Computational Screening[J]. Materials Today Physics, 2022: 100726.

2. Xiao Y, Shen C, Zhang W B. Screening and prediction of metal-doped α-borophene monolayer for nitric oxide elimination[J]. Materials Today Chemistry, 2022, 25: 100958.

3. **Xiao Y***, Shen C. Transition - Metal Borides (MBenes) as New High - Efficiency Catalysts for Nitric Oxide Electroreduction to Ammonia by a High-Throughput Approach[J]. ***Small*****,** 2021: 2100776.

4. **Xiao Y***, Shen C, Long T. Theoretical Establishment and Screening of an Efficient Catalyst for N_2 Electroreduction on Two-Dimensional Transition-Metal Borides (MBenes)[J]. ***Chemistry of Materials***, 2021 33 (11), 4023-4034.

5. **Yi Xiao***, Chen Shen, Niloofar Hadaeghi. Quantum Mechanical Screening of 2D MBenes for the Electroreduction of CO_2 to C1 Hydrocarbon Fuels. ***Journal of Physical Chemistry Letters***. 2021, 12, 6370−6382.

6. **Xiao Y***, Zhang W. High throughput screening of M_3C_2 MXenes for efficient CO_2 reduction conversion into hydrocarbon fuels[J]. ***Nanoscale***, 2020, 12(14): 7660-7673.

7. **Xiao Y***, Shen C, Chen R. Mechanistic Study of Efficient Producing CO_2 Electroreduction via 2D Metal Organic Frameworks $M_3(HITP)_2$ Surface[J]. ***Electrochimica Acta***, 2021: 138028.

8. **Xiao Y***, Wang J, Wang Y, et al. A new promising catalytic activity on blue phosphorene nitrogen-doped nanosheets for the ORR as cathode in nonaqueous Li–air batteries[J]. ***Applied Surface Science,*** 2019, 488: 620-628.

9. **Xiao Y***, et al. Adsorption mechanisms of Mo_2CrC_2 MXenes as potential anode materials for metal-ion batteries: A first-principles investigation[J]. ***Applied Surface Science***, 2020: 145883.

10. Xiao Y, Shen C. Predicted Electrocatalyst Properties on Metal Insulator $MoTe_2$ for Hydrogen Evolution Reaction and Oxygen Reduction Reaction Application in Fuel Cells[J]. ***Energy & Fuels***, 2021, 35(9): 8275-8285.

11. **Yi Xiao***, Li Tang, Weibin Zhang, Chen Shen. Theoretical Insighting for Efficient Energy Conversion with ORR and CO_2RR via CuAu Surface. ***Computational Materials Science*** 192 (2021) 110402.

12. **Xiao Y*,** Tang L. High-Throughput Approach Exploitation: Two-Dimensional Double-Metal Sulfide (M_2S_2) of Efficient Electrocatalysts for Oxygen Reduction Reaction in Fuel Cells[J]. ***Energy & Fuels***, 2020, 34(4): 5006-5015.

13. **Xiao Y***, Zhang W. DFT analysis elementary reaction steps of catalytic activity for ORR on metal-, nitrogen-co-doped graphite embedded structure[J]. ***SN Applied Sciences***, 2020, 2(2): 194.

14. **Xiao Y***, Zhang W. High-Throughput Calculation Investigations on the Electrocatalytic Activity of Co-doped Single Metal–Nitrogen Embedded in Graphene for ORR Mechanism[J]. ***Electrocatalysis***, 2020: 1-12.

15. **Xiao, Yi**, et al. "The potential application of 2D Ti_2CT_2 (T= C, O and S) monolayer MXenes as anodes for Na-ion batteries: A theoretical study." ***Computational Materials Science*** 163 (2019): 267-277.

Co-first Author

16. Xiong W, Zhang J, **Xiao Y,** et al. Oxygen-rich nanoflake-interlaced carbon microspheres for potassium-ion battery anodes [J]. ***Chemical Communications***, 2020, 56(23): 3433-3436.

Corresponding Author

17. Chen R, Chen D, **Xiao Y***. Theoretical Scanning of Bimetallic Alloy for Designing Efficient N_2 Electroreduction Catalyst[J]. ***Materials Today Energy***, 2021: 100684.

18. Liu L, **Xiao Y***. Theoretical exploration electrocatalytic active of spinel M_2CoO_4 (M= Co, Fe and Ni) as efficient catalyst for water splitting[J]. ***Computational Materials Science,*** 2021, 187: 110082.

19. Zhang, W., & **Xiao, Y***. Mechanism of electrocatalytically active precious metal (Ni, Pd, Pt, and Ru) complexes in the graphene basal plane for ORR applications in novel fuel cells. ***Energy & Fuels***, 34(2), (2020). 2425-2434.

Co-author

20. Mwankemwa N, Chen S, Gao S, **Xiao Y** et al. First-principles calculations to investigate the electronic and optical properties of $(MoS_2)_{4-n}/(MoSSe)_n$ lateral heterostructure[J]. ***Journal of Physics and Chemistry of Solids***, 2021: 110049.

21. Wang J, Zhang W, Wu Q, **Xiao Y** et al. The electronic and optical properties of Au decorated $(10\bar{1}4)$ dolomite surface: A first principles calculations[J]. ***Results in Physics***, 2021, 21: 103827.

22. Zhang X, Song Y, Zhang F, **Xiao Y,** et al. The electronic properties of hydrogenated Janus MoSSe monolayer: a first principles investigation[J]. ***Materials Research Express***, 2019, 6(10): 105055.

23. Wei Xiong, Xingyu Fenga, **Yi Xiao**, Tao Huanga, Xiaoyan Li, et al. Fluorine-free prepared two-dimensional molybdenum boride (MBene) as a promising anode for lithium-ion batteries with superior electrochemical performance [J]. ***Chemical Engineering Journal,*** https://doi.org/10.1016/j.cej.2022.137466.

Acknowledgment

First of all, I would like to express my sincere gratitude to my advisor, Prof. Hongbin Zhang, for his trust and the admission to join the TMM group. In my three years research period, he devoted many efforts in giving me suggestions in my Ph.D. study and related research, provided my great freedom in the research field and suggested me with new research directions. I have benefited and learned a lot from him, especially from his immense knowledge and strict logic. His guidance helped me in all the time of research and writing of this thesis. Besides my advisor, I would also like to thank Prof. Karsten Albe, who gave me many times kind and constructive discussions. His insightful knowledge regarding the course of computational materials science impressed me. My sincere thanks also go to Prof. Jan Philipp Hoffmann for his insightful comments and encouragement during the paper writing. I wish to acknowledge Prof. Vera Krewald for the careful reading and commenting on the paper we published as well as this dissertation. I would also thank Prof. Karsten Albe for the kind suggestions during the discussions and agreement to join the defence commission board. I am grateful to Prof. Ye Han, who guides me into the simulation field and held countless helpful discussions. Without him, I would not be in this field. I would like to thank Chen Shen, who gave me many supports with the software VASP and VASPKIT. I would also like to thank Dr. Qiang Gao, Dr. Xinru Li, Dr. Lei Xu, Teng Long, Fortunato Nuno, Hadaeghi Niloofar, and the other colleagues for their professional discussions and help from all the aspects. I appreciate Mrs Walker's help for the assistant in handling documentation whenever I had a Germany language problem. I would like to acknowledge the financial support from Chinese Scholarship Council (CSC) and the LOEWE project FLAME funded by the Ministry of Higher Education, Research, and the Arts (HMWK) of the Hessen state. I gratefully acknowledge computational time on the Lichtenberg High Performance Supercomputer. Financial support comes from the China Scholarship Council (CSC:201808440416) of China.

Finally, I would thank the support from my family, for their care and supports in my life. I wish to give my special thanks to my girlfriend Yizhi Xu, who accompanied me writing the dissertation all the time and gave me many supports and encouragement, being with her was the happiest time in my life.

Curriculum Vitae

Personal

Name: Yi Xiao
Place of Birth: Nanchong, Sichuan Province, China.
Date of Birth: 1986-07-29
Employment: Technische Universität Darmstadt (TU Darmstadt)
Position: Doctor (Department of Materials Science)
E-**mail:** yixiao@tmm.tu-darmstadt.de
Nationality: Chinese (Han).
Address: Department of Materials Science, Technische Universität Darmstadt, Alarich-Weiss-Str. 2, 64287 Darmstadt, Hessen, Germany.

Research Areas

Understanding of electrocatalytic processes which are occurring on the electrolyte-electrode interfaces is the key to predict and to ultimately design properties of materials in different length and time scales.

1. Doped carbon material as innovative support for electrocatalyst in fuel cell and batteries.

2. Catalytic properties of nanostructured electrodic materials.

3. Single-Atom Catalysts Embedded Design of Nonaqueous Metal–Air and Metal-Ion Batteries.

4. Theoretical Screening of Ammonia Synthesis Catalysts Based on Two-Dimensional Transition Metal Borides (MBenes) under Ambient Conditions.

5. Theoretical Scanning of Bimetallic Alloy for Designing Efficient N_2 Electroreduction Catalyst.

6. Mechanistic Study of Efficient Producing CO_2 Electroreduction via 2D Metal Organic Frameworks (MOFs).

7. Theoretical Establishing a new prototypes Catalysts for CO_2 Electroreduction on 2D MBenes.

8. Theoretical Insights into the Mechanism of Selective Nitrate-to-Ammonia Electroreduction on MBenes.

9. Transition-Metal Borides (MBenes) as a New high-efficiency Catalysts for Producing Nitric Oxide Electroreduction to Ammonia by High Throughput Approach.

Education

1. 2018-09-30 to 2022-08-01
Technische Universität Darmstadt: 64287, Darmstadt, Hessen, Germany.
Doctor (Department of Materials Science)
2. 2011-09-01 to 2014-07-01
Department of Chemistry and Chemical Engineering, Southwest University, 400715, Chongqing, China.
Master of Science.
3. 2007-09-01 to 2011-06-27
Faculty of Science, Agricultural University of Hebei, 071001, Baoding, China.
Bachelor of Science

Work Experience

1. 2017-07-01 to 2018-09-27
School of Materials Science and Engineering, Southern University of Science and Technology (SUSTech). China,
(Research Assistant).
2. 2017-01-01 to 2017-07-01
Department of Physics and Materials Science, City University of Hong Kong (CityU). Tat Chee Avenue Kowloon, 999077, Hong Kong, China,
(Research Assistant).
3. 2015-09-01 to 2016-11-30
Department of Chemical and Biochemical Engineering, Dongguk University-Seoul, 100715, South Korea.
(Doctor)
4. 2014-09-01 to 2015-09-01
Luxian No.1 High Middle School, Luzhou, 646100, Sichuan, China.
(Teacher)

Research interests

Theoretical Screening; Density Functional Theory; 2D Materials; Atomic-Scale Design of Catalysts for Electrochemical Synthesis Electrochemical (Such as **ORR/OER** in fuel cell; **CO_2 reduction**, **N_2 reduction** and **NO reduction**); High Activity and Selectivity Catalysts Designing; High-throughput Screening; Energy Storage and Conversion; Machine Learning.